

**OFFICE OF CIVILIAN RADIOACTIVE WASTE MANAGEMENT  
ANALYSIS/MODEL COVER SHEET**

1. QA: QA

Page: 1 of 457

**Complete Only Applicable Items**

<p><input type="checkbox"/> <b>Analysis</b>      Check all that apply</p> <table border="1" style="width:100%; border-collapse: collapse;"> <tr> <td style="width:20%;">Type of Analysis</td> <td> <input type="checkbox"/> Engineering  <input type="checkbox"/> Performance Assessment  <input type="checkbox"/> Scientific                 </td> </tr> <tr> <td>Intended Use of Analysis</td> <td> <input type="checkbox"/> Input to Calculation  <input type="checkbox"/> Input to another Analysis or Model  <input type="checkbox"/> Input to Technical Document  <input type="checkbox"/> Input to other Technical Products                 </td> </tr> <tr> <td colspan="2">Describe use:</td> </tr> </table>	Type of Analysis	<input type="checkbox"/> Engineering <input type="checkbox"/> Performance Assessment <input type="checkbox"/> Scientific	Intended Use of Analysis	<input type="checkbox"/> Input to Calculation <input type="checkbox"/> Input to another Analysis or Model <input type="checkbox"/> Input to Technical Document <input type="checkbox"/> Input to other Technical Products	Describe use:		<p>3. <input checked="" type="checkbox"/> <b>Model</b>      Check all that apply</p> <table border="1" style="width:100%; border-collapse: collapse;"> <tr> <td style="width:20%;">Type of Model</td> <td> <input checked="" type="checkbox"/> Conceptual Model      <input type="checkbox"/> Abstraction Model  <input checked="" type="checkbox"/> Mathematical Model      <input type="checkbox"/> System Model  <input checked="" type="checkbox"/> Process Model                 </td> </tr> <tr> <td>Intended Use of Model</td> <td> <input type="checkbox"/> Input to Calculation  <input checked="" type="checkbox"/> Input to another Model or Analysis  <input checked="" type="checkbox"/> Input to Technical Document  <input checked="" type="checkbox"/> Input to other Technical Products                 </td> </tr> <tr> <td colspan="2">Describe use: This model provides TH information and data for other reports</td> </tr> </table>	Type of Model	<input checked="" type="checkbox"/> Conceptual Model <input type="checkbox"/> Abstraction Model <input checked="" type="checkbox"/> Mathematical Model <input type="checkbox"/> System Model <input checked="" type="checkbox"/> Process Model	Intended Use of Model	<input type="checkbox"/> Input to Calculation <input checked="" type="checkbox"/> Input to another Model or Analysis <input checked="" type="checkbox"/> Input to Technical Document <input checked="" type="checkbox"/> Input to other Technical Products	Describe use: This model provides TH information and data for other reports	
Type of Analysis	<input type="checkbox"/> Engineering <input type="checkbox"/> Performance Assessment <input type="checkbox"/> Scientific												
Intended Use of Analysis	<input type="checkbox"/> Input to Calculation <input type="checkbox"/> Input to another Analysis or Model <input type="checkbox"/> Input to Technical Document <input type="checkbox"/> Input to other Technical Products												
Describe use:													
Type of Model	<input checked="" type="checkbox"/> Conceptual Model <input type="checkbox"/> Abstraction Model <input checked="" type="checkbox"/> Mathematical Model <input type="checkbox"/> System Model <input checked="" type="checkbox"/> Process Model												
Intended Use of Model	<input type="checkbox"/> Input to Calculation <input checked="" type="checkbox"/> Input to another Model or Analysis <input checked="" type="checkbox"/> Input to Technical Document <input checked="" type="checkbox"/> Input to other Technical Products												
Describe use: This model provides TH information and data for other reports													

4. Title:  
Multiscale Thermohydrologic Model

5. Document Identifier (including Rev. No. and Change No., if applicable):  
ANL-EBS-MD-000049 REV 00 ICN 02

6. Total Attachments:	7. Attachment Numbers - No. of Pages in Each: Attachment I - <sup>2 Rpt 1/14/02</sup> 7 pages      Attachment II - 13 pages
-----------------------	--

	Printed Name	Signature	Date
8. Originator	Thomas A. Buscheck	<i>Randolph L Schreier for</i>	12/21/01
9. Checker	Jim Kam/Ming Lin	<i>Norma Bigler for Jim Kam + Ming Lin</i>	12/21/01
10. Lead/Supervisor	James Blink	<i>Randolph L Schreier for</i>	12/21/01
11. Responsible Manager	Robert J. MacKinnon	<i>Randolph L Schreier for</i>	12/21/01

12. Remarks:

**OFFICE OF CIVILIAN RADIOACTIVE WASTE MANAGEMENT  
ANALYSIS/MODEL REVISION RECORD**

***Complete Only Applicable Items***

1. Page: 2 of 457

2. Analysis or Model Title:

Multiscale Thermohydrologic Model

3. Document Identifier (including Rev. No. and Change No., if applicable):

ANL-EBS-MD-000049 REV00 ICN 02

4. Revision/Change No.

5. Description of Revision/Change

00

Original issue. Supported TSPA-SR, Rev 00 for the Backfill Case. Used 1.54 kW/m line load.

00 ICN 01

This ICN was developed to include the No Backfill Case supporting TSPA-SR Rev 00 ICN 01. The DTN:SN9908T0872799.004 references were removed. The data and inputs were referenced to updated DTNs and references, or entered as assumptions. Revised invert thermal conductivity values and an adjusted heat load of 1.45 kW/m were used for the no-backfill case.

00 ICN 02

This ICN was developed to address the NRC KTI Agreement TEF 2.9 and show the influence of drift-scale fracture heterogeneity on TH behavior for the No Backfill Case. This was accomplished with the use of the 3-D heterogeneous Line-averaged-heat-source Drift-scale TH (LDTH) model, which was developed for this ICN, and which is completely described in Section 6.14. The 3-D heterogeneous LDTH model is based on the 2-D homogeneous LDTH model. The data and inputs were referenced to updated DTNs and references, or entered as assumptions. Section 7 has also been updated to include the conclusions developed from the 3-D heterogeneous LDTH model. A postprocessor, XLDTH, was developed and used to address the influence of drift-scale heterogeneity of fracture properties as described above. This postprocessor is qualified in accordance with the currently approved version of AP-SI.1Q, Software Management.

Deficiency Report LVMO-00-D-039, Inaccurate Documentation and Validation of Software Routines and/or Macros, identified software issues that are addressed in MOL.20010910.0181 (Schreiner, R.L. 2001; *Stand Alone DR-39 package for ANL-EBS-MD-000049, Rev. 00, ICN01, Multiscale Thermohydrologic Model*). Attachment I contains a cross-walk between attachments in the Stand Alone Package and the attachments formerly included in this AMR. The Stand Alone package provides additional software documentation, e.g., source code listings, validation text files, input/output files and other corrections for routines formerly documented in Attachments I through XVII and XIX through XX of ICN 01 of this AMR.

Attachment II in this ICN 02 lists files supporting each version of this document, including the file lists previously documented in Attachment XVIII of ICN 01. ICN 02 also addresses in Section 2 the issues and concerns identified in Deficiency Report BSC-01-D-100, pertaining to control of electronic information. ICN 02 also addresses NRC KTI agreements pertinent to this AMR, in Section 1.

The following sections have been affected by this ICN: Section 1, Section 2, Section 3, Section 4, Section 5, Section 6, Section 7, Section 8, Attachment I and Attachment II

## CONTENTS

	<b>Page</b>
1. PURPOSE .....	25
1.1 OBJECTIVES .....	25
1.2 WORK SCOPE .....	25
1.3 PRIMARY TASKS .....	29
1.4 RELATIONSHIP TO NUCLEAR REGULATORY COMMISSION KEY TECHNICAL ISSUES .....	29
2. QUALITY ASSURANCE .....	35
3. COMPUTER SOFTWARE AND MODEL USAGE .....	37
3.1 DESCRIPTION OF SOFTWARE .....	38
3.1.1 NUFT v3.0s .....	38
3.1.2 RADPRO v3.22 .....	38
3.1.3 XTOOL v10.1 .....	39
3.1.4 MSTHAC v6.2 .....	39
3.1.5 MSTHAC v6.3 .....	39
3.2 DESCRIPTION OF ROUTINES AND MACROS .....	40
3.2.1 MakeColumns v1.0 .....	40
3.2.2 Rme6 v1.1 .....	40
3.2.3 Define_EBS_fineGrid v1.3 .....	40
3.2.4 ReadsUnits v1.0 .....	40
3.2.5 AddLayers v1.0 .....	41
3.2.6 Heat_DDT v1.0 .....	41
3.2.7 Heat_SMT v1.0 .....	41
3.2.8 Cover v1.1 .....	41
3.2.9 ColumnInfiltration v1.1 .....	41
3.2.10 Chim_surf_TP v1.0 .....	41
3.2.11 Chim_wt_TP v1.0 .....	42
3.2.12 Xairtab v1.8 .....	42
3.2.13 Infiltrab v1.0 .....	42
3.2.14 Rock_sun v1.0 .....	42
3.2.15 SMT_surf_bc v1.1 .....	42
3.2.16 SMT_bot_bc v1.1 .....	43
3.2.17 Bound v1.0 .....	43
3.2.18 Addlay v1.0 .....	43
3.2.19 Assembly Scripts LDTH*corey, SDT-01*v1.0 .....	43
3.2.20 HeatgenAge v1.2 .....	43
3.2.21 SplitEXT v1.0 .....	44
3.2.22 YMESH v1.53 .....	44
3.2.23 CONVERTCOORDS v1.1 .....	44
3.2.24 XLDTH v1.0 .....	44
3.3 Data Flow .....	44

## CONTENTS (Continued)

	Page
4. INPUTS.....	81
4.1 DATA AND PARAMETERS.....	81
4.1.1 Geometric Description of the EBS and Material Properties .....	81
4.1.2 Drift Spacing .....	81
4.1.3 Waste Package Spacing.....	81
4.1.4 Drift Diameter .....	81
4.1.5 Properties of Air at Model Boundaries.....	81
4.1.6 Properties of EBS Materials.....	81
4.1.7 Hydrologic and Thermal Properties of Stratigraphic Units.....	82
4.1.8 Thermal Properties of Air Inside the Drifts.....	83
4.1.9 Thermal Properties of Stratigraphic Units for SMT Submodels.....	83
4.1.10 Effective Thermal Conductivity of Cavities Inside Drifts .....	83
4.1.11 Stratigraphy .....	87
4.1.12 Infiltration Flux .....	87
4.1.13 Heat-Generation Rate.....	87
4.1.14 Boundary Conditions.....	87
4.1.15 Enthalpy.....	88
4.2 CRITERIA.....	88
4.3 CODES AND STANDARDS .....	88
5. ASSUMPTIONS .....	90
5.1 Boundary Conditions.....	90
5.1.1 Areal Block Model.....	90
5.1.2 Gaussian Interpolation.....	90
5.1.3 Inverse Distance Interpolation.....	90
5.1.4 Relative Humidity at Ground Surface .....	91
5.1.5 LDTH Boundary Conditions .....	91
5.1.6 SMT, DDT, and SDT Boundary Conditions.....	91
5.2 MATERIAL PROPERTIES.....	91
5.2.1 Permeability of Drip Shield and Waste Package.....	91
5.2.2 Tortuosity of Backfill and Invert Materials.....	92
5.2.3 Satiated Saturation of Invert and Backfill Materials .....	92
5.2.4 Thermal Conductivity Used in Conduction-Only Submodels.....	92
5.2.5 Saturated-Zone Thermal Conductivity.....	92
5.2.6 Thermal Conductivity and Density for the Active Fracture Model.....	93
5.2.7 Thermal Properties of the Backfill and Invert for the Backfill Case.....	93
5.2.8 Thermal Conductivity, the Lower and Upper Invert Layer for the No- Backfill Case .....	94
5.3 HEAT GENERATION AND HEAT TRANSFER.....	95
5.3.1 Heat Generation.....	95
5.3.2 Constant Heat Flux.....	95
5.3.3 Effective Thermal Conductivity.....	95

## CONTENTS (Continued)

	Page
5.3.4	Random Fields for Stochastic Realizations..... 96
5.4	Geometric description of the ebs and material properties ..... 96
5.4.1	Repository Footprint..... 96
5.4.2	Waste Package Lengths and Sequencing ..... 97
5.4.3	Cross Section Geometry of the Backfilled Emplacement Drift ..... 97
5.4.3.1	Angle of Repose of Backfill ..... 97
5.4.3.2	Minimum Depth of Backfill Cover..... 97
5.4.3.3	Location of Backfill Peak ..... 97
5.4.3.4	Intersection Between Backfill and Drift Wall ..... 98
5.4.3.5	Drip Shield Radius..... 98
5.4.3.6	Location of Waste Package..... 98
5.4.3.7	Waste Package Diameter ..... 98
5.4.3.8	Gap Between Waste Package and Drip Shield ..... 99
5.4.3.9	Gap Between Waste Package and Invert ..... 99
5.4.3.10	Invert Height..... 99
5.4.3.11	Drip-Shield Height..... 99
6.	ANALYSIS/MODEL ..... 103
6.1	MSTHM CONCEPTUAL MODEL..... 104
6.2	SMT SUBMODELS ..... 105
6.2.1	SMT Repository Footprint ..... 105
6.2.2	SMT-Submodel Mesh ..... 106
6.2.3	SMT Submodel Boundary Conditions ..... 106
6.2.4	SMT Submodel Heat Generation Rates ..... 106
6.2.5	SMT Submodel Material Properties..... 106
6.2.6	Submodel Simulations ..... 107
6.3	LDTH SUBMODELS ..... 107
6.3.1	LDTH Submodel Locations ..... 108
6.3.1.1	Stratigraphic Columns ..... 108
6.3.1.2	Vertical Location of Repository Horizon ..... 108
6.3.2	LDTH Submodel Mesh ..... 108
6.3.2.1	Pre-closure LDTH Submodel Mesh ..... 108
6.3.2.2	Post-closure LDTH Submodel Mesh..... 113
6.3.3	LDTH Submodel Boundary Conditions..... 114
6.3.4	LDTH Submodel Heat Generation Rates ..... 114
6.3.5	LDTH Submodel Material Properties ..... 114
6.3.6	Infiltration Flux ..... 116
6.3.7	LDTH Submodel Simulations..... 116
6.4	SDT SUBMODELS ..... 116
6.4.1	SDT Submodel Locations ..... 117
6.4.2	SDT Submodel Mesh ..... 117
6.4.3	SDT Submodel Boundary Conditions..... 117

## CONTENTS (Continued)

	<b>Page</b>
6.4.4	SDT Submodel Heat Generation Rates ..... 118
6.4.5	SDT Submodel Material Properties ..... 118
6.4.6	SDT Submodel Simulations ..... 118
6.5	DDT SUBMODELS..... 118
6.5.1	DDT Submodel Location ..... 119
6.5.2	DDT Submodel Mesh..... 119
6.5.2.1	Pre-closure DDT Submodel..... 120
6.5.2.2	Pre-closure (Restart) DDT Submodel..... 120
6.5.2.3	Post-closure DDT Submodel ..... 120
6.5.3	DDT Submodel Boundary Conditions ..... 120
6.5.4	DDT Submodel Heat Generation Rates ..... 121
6.5.5	DDT Submodel Material Properties..... 121
6.5.6	DDT Submodel Simulations ..... 122
6.6	MSTHAC METHODOLOGY ..... 122
6.6.1	Accounting for the Influence of Drift Ventilation..... 122
6.6.2	Accounting for the Emplacement of the Drip Shield and Backfill ..... 123
6.6.3	Computing Drift-Wall Temperatures ..... 123
6.6.3.1	Computing Drift-Wall Temperatures for the Backfill Case ..... 124
6.6.3.2	Computing Drift-Wall Temperatures for the No-Backfill Case..... 125
6.6.4	Computing Host-Rock Temperatures..... 127
6.6.5	Computing Backfill, Drip-Shield, and Invert Temperatures ..... 127
6.6.6	Computing Waste Package Temperatures..... 127
6.6.7	Computing Drift-Wall Relative Humidity ..... 127
6.6.8	Computing Host-Rock Relative Humidity ..... 128
6.6.9	Computing Relative Humidity on the Drip Shield..... 128
6.6.10	Computing Relative Humidity in the Backfill ..... 128
6.6.11	Computing Relative Humidity in the Invert..... 129
6.6.12	Computing Waste-Package Relative Humidity..... 129
6.6.13	Computing Liquid-Phase Flux in the Host Rock ..... 130
6.6.14	Computing Liquid-Phase Flux on the Drip Shield..... 130
6.6.15	Computing Liquid-Phase Flux in the Backfill ..... 130
6.6.16	Computing Liquid-Phase Flux in the Invert..... 130
6.6.17	Computing Liquid Saturation at the Drift Wall ..... 131
6.6.18	Computing Liquid Saturation on the Drip Shield ..... 131
6.6.19	Computing Liquid Saturation in the Invert ..... 131
6.6.20	Computing Gas-Phase Air-Mass Fraction Adjacent to Drip Shield..... 131
6.6.21	Computing Gas-Phase Pressure Adjacent to Drip Shield ..... 131
6.6.22	Computing Gas-Phase Flux of Air ..... 132
6.6.23	Computing Gas-Phase Flux of Water Vapor..... 132
6.6.24	Computing Capillary Pressure on the Drip Shield ..... 132
6.6.25	Computing Capillary Pressure on the Drift Wall ..... 132

## CONTENTS (Continued)

	Page
6.6.26	Computing Capillary Pressure in the Invert ..... 133
6.6.27	Computing Evaporation Rate on the Drip Shield..... 133
6.6.28	Computing Evaporation Rate at the Top of the Backfill..... 133
6.6.29	Computing Evaporation Rate in the Invert..... 133
6.6.30	Binning TH Results..... 133
6.7	OVERVIEW OF DATA FLOW ..... 134
6.8	SUBMODEL PREPARATION ..... 134
6.8.1	Mesh Generation ..... 135
6.8.1.1	YMESH Input ..... 135
6.8.1.2	Drift-Scale-Submodel Meshes..... 136
6.8.1.3	Mountain-Scale Submodel Mesh..... 137
6.8.2	Material Properties ..... 137
6.8.3	Heat-Generation Rate ..... 138
6.8.4	Infiltration Flux ..... 138
6.8.5	Boundary Conditions..... 139
6.9	SUBMODEL EXECUTION ..... 139
6.9.1	LDTH Simulations ..... 140
6.9.2	SDT Simulations ..... 141
6.9.3	DDT Simulations ..... 141
6.9.4	SMT Simulations ..... 142
6.10	MSTHAC EXECUTION ..... 142
6.11	MSTHM RESULTS FOR THE BACKFILL CASE..... 143
6.11.1	Temperature Distributions..... 144
6.11.1.1	Temperature Distributions for Mean Infiltration Case ..... 144
6.11.1.2	Temperature Distributions for High Infiltration Case ..... 146
6.11.1.3	Temperature Distributions for Low Infiltration Case ..... 146
6.11.1.4	Temperature Analysis ..... 146
6.11.2	Relative Humidity Distributions ..... 148
6.11.2.1	Relative Humidity Distributions for Mean Infiltration Case ..... 148
6.11.2.2	Relative Humidity Distributions for High Infiltration Case ..... 148
6.11.2.3	Relative Humidity Distributions for Low Infiltration Case ..... 149
6.11.2.4	Relative Humidity Analysis..... 149
6.11.3	Gas-Phase Air-Mass Fraction Distributions..... 150
6.11.3.1	Gas-Phase Air-Mass Fraction Distributions for Mean Infiltration Case ..... 150
6.11.3.2	Gas-Phase Air-Mass Fraction Distributions for High Infiltration Case ..... 150
6.11.3.3	Gas-Phase Air-Mass Fraction Distributions for Low Infiltration Case ..... 151
6.11.3.4	Gas-Phase Air-Mass Fraction Analysis ..... 151
6.11.4	Liquid-Phase Flux Distributions ..... 151
6.11.4.1	Liquid-Phase Flux Distributions for Mean Infiltration Case ..... 151

## CONTENTS (Continued)

	Page
6.11.4.2	Liquid-Phase Flux Distributions for High Infiltration Case ..... 155
6.11.4.3	Liquid-Phase Flux Distributions for Low Infiltration Case..... 157
6.11.4.4	Liquid-Phase Flux Analysis..... 159
6.11.5	Evaporation Rate Distributions ..... 160
6.11.5.1	Evaporation Rate Distributions for Mean Infiltration Case..... 160
6.11.5.2	Evaporation Rate Distributions for High Infiltration Case..... 160
6.11.5.3	Evaporation Rate Distributions for Low Infiltration Case..... 161
6.11.5.4	Evaporation Rate Analysis..... 161
6.11.6	Influence of Variability of Heat Generation from Waste Packages ..... 162
6.11.6.1	Temperature and Relative Humidity on Different Waste- Package Types ..... 162
6.11.7	Influence of Overburden Thickness ..... 162
6.12	MSTHM RESULTS FOR THE NO-BACKFILL CASE..... 162
6.12.1	Temperature Distributions..... 164
6.12.2	Liquid-Phase Saturation and Relative Humidity Distributions..... 164
6.12.3	Evaporation Rate Distributions ..... 165
6.12.4	Capillary-Pressure Distributions ..... 165
6.12.5	Liquid-Phase Flux Distributions ..... 165
6.13	MODEL VALIDATION ..... 166
6.13.1	Comparison of NUFT TH Model against the Large Block Test ..... 167
6.13.2	Comparison of NUFT TH Model against the Drift Scale Test ..... 168
6.13.3	Comparison of MSTHM against an Alternative Conceptual Model..... 169
6.14	THREE-DIMENSIONAL HETEROGENEOUS LDTH MODEL ..... 171
6.14.1	Physics of Seepage into an Open Cavity..... 172
6.14.2	Random-Field Generation..... 173
6.14.3	Findings from Previous Seepage-Model Studies ..... 174
6.14.4	Description of 3-D Heterogeneous LDTH Model..... 174
6.14.5	3-D Heterogeneous LDTH-Model Results..... 177
6.14.5.1	Thermohydrologic Seepage Behavior for Realizations A-56 and A-34 ..... 183
6.14.5.2	Thermohydrologic Seepage Behavior for Realizations B-56 and B-34..... 184
6.14.5.3	Thermohydrologic Seepage Behavior for Realizations C-56 and C-34..... 185
6.14.5.4	Thermohydrologic Seepage Behavior for Realizations D-56 and D-34 ..... 185
6.14.5.5	Summary of the Results of the Three-Dimensional Heterogeneous LDTH Model ..... 185
7.	CONCLUSIONS..... 443
7.1	UNCERTAINTIES OF THE AMBIENT AND THERMALLY PERTURBED SYSTEM..... 448

## CONTENTS (Continued)

	<b>Page</b>
7.2 Drift-scale fracture heterogeneity .....	449
8. INPUTS AND REFERENCES .....	451
8.1 DOCUMENTS CITED .....	451
8.2 PROCEDURES CITED .....	455
8.3 SOURCE DATA .....	455
8.4 SOFTWARE SOURCES .....	456
8.5 OUTPUT DATA .....	457
9. ATTACHMENTS .....	457

## FIGURES

	Page
1-1. Schematic of conceptual models used by the MSTHM, including (a) SDT submodel, (b) LDTH submodel, (c) DDT submodel, and (d) SMT submodel .....	32
1-2. Overall data flow diagram for the MSTHM.....	33
1-3. Data flow diagram for the MSTHM that shows the relationship between the input data and submodels for the three infiltration flux scenarios addressed in Rev 00 .....	34
3-1. Legend for data flow diagrams.....	70
3-2. Generation of numerical meshes for all submodels .....	71
3-3. Preparation of heat generation curves for all submodels.....	72
3-4. Preparation of infiltration data for LDTH submodels .....	73
3-5. Preparation of boundary conditions for submodels.....	74
3-6. Creation of scripts to generate families of LDTH submodels .....	75
3-7. Material properties of the natural system .....	76
3-8. Material properties of the EBS.....	76
3-9. Execution of LDTH submodels.....	77
3-10. Execution of SDT submodels.....	78
3-11. Execution of DDT submodels .....	79
3-12. Execution of SMT submodels .....	80
4-1. Diagram showing drift spacing, WP lengths, and WP spacing. The names of the respective WPs (hlw 1, bwr 1, etc.) used in the DDT submodel (Section 6.5) are given above each WP. ....	89
5-1. Comparison of the actual repository footprint and the approximation of the repository footprint that is assumed in the MSTHM.....	100
5-2. The 31 drift-scale submodel locations used in the MSTHM .....	101
5-3. The cross-sectional geometry of the emplacement drift after backfill is emplaced .....	102
6-1a. Repository-scale numerical mesh of the repository area used in the MSTHM showing the 623 repository subdomains used in backfill case.....	187
6-1b. Repository-scale numerical mesh of the repository area used in the MSTHM showing the 610 repository subdomains used in no-backfill case .....	188
6-2a. Cross-sectional view of the numerical mesh used in the pre-closure LDTH submodels for the backfill case (REV 00), and no-backfill case (ICN 01). This is also the post-closure LDTH-submodel mesh for no-backfill case (ICN 01).....	189
6-2b. Cross-sectional view of numerical mesh used in the pre-closure and post-closure LDTH submodels for the ICN-02 no-backfill case .....	190
6-3. Cross-sectional view of the numerical mesh used in the post-closure LDTH submodels for the backfill case. The post-closure LDTH-submodel mesh for no-backfill case is shown in Figure 6-2. ....	191
6-4. Cross-sectional view of the numerical mesh used in the pre-closure DDT submodel for backfill and no-backfill cases.....	192
6-5. Cross-sectional view of the numerical mesh used in the pre-closure DDT submodel that is used to generate the restart file to start the post-closure DDT submodel for backfill case.....	193

## FIGURES (Continued)

	Page
6-6a. Cross-sectional view of the numerical mesh used in the post-closure DDT submodel for backfill case.....	194
6-6b. Cross-sectional view of the numerical mesh used in the post-closure DDT submodel for the no backfill case.....	195
6-7. Temperature on the surface of a 21-PWR WP for the mean infiltration-flux backfill case for the indicated times.....	196
6-8. Temperature on the crown of the drift (or upper drift wall) immediately above a 21-PWR WP for the mean infiltration-flux backfill case for the indicated times.....	202
6-9. Temperature on the lower drift wall immediately below a 21-PWR WP for the mean infiltration-flux backfill case for the indicated times.....	205
6-10. Temperature on the surface of a 21-PWR WP for the high infiltration-flux backfill case for the indicated times.....	208
6-11. Temperature on the surface of a 21-PWR WP for the low infiltration-flux backfill case for the indicated times.....	214
6-12. The complementary cumulative distribution function (CCDF) for the maximum lateral extent of the boiling point ( $T = 96^{\circ}\text{C}$ ) isotherm is plotted for the mean, high, and low infiltration-flux backfill cases.....	220
6-13. Temperature history on the surface of a 21-PWR WP for the mean infiltration-flux backfill case at (a) the geographical center of the repository and (b) a location 27.5 m from the eastern edge of the repository. Note that the Nevada State coordinates are given.....	221
6-14. Peak WP temperature for the low, mean, and high infiltration-flux backfill cases.....	222
6-15. Peak temperature on the lower drift wall (below the invert) for the low, mean, and high infiltration-flux backfill cases.....	223
6-16. Relative humidity on the surface of a 21-PWR WP for the mean infiltration-flux backfill case for the indicated times.....	224
6-17. Relative humidity on the surface of a 21-PWR WP for the high infiltration-flux backfill case for the indicated times.....	232
6-18. Relative humidity on the surface of a 21-PWR WP for the low infiltration-flux backfill case for the indicated times.....	240
6-19. (a) The complementary cumulative distribution function (CCDF) for the time required to attain a relative humidity RH of 85% is plotted for the mean, high, and low infiltration-flux backfill cases. CCDF of the WP temperature at which WPs reach an RH of 85% is plotted for the same cases.....	249
6-20. Relative humidity history on the surface of a 21-PWR WP for the mean infiltration-flux backfill case at (a) the geographical center of the repository and (b) a location 27.5 m from the eastern edge of the repository. Note that the Nevada State coordinates are given.....	250
6-21. Relative humidity history on the surface of a 21-PWR WP for the high infiltration-flux backfill case at (a) the geographical center of the repository and (b) a location 27.5 m from the eastern edge of the repository. Note that the Nevada State coordinates are given.....	251

## FIGURES (Continued)

	Page
6-22. Relative humidity history on the surface of a 21-PWR WP for the low infiltration-flux backfill case at (a) the geographical center of the repository and (b) a location 27.5 m from the eastern edge of the repository. Note that the Nevada State coordinates are given.....	252
6-23. Gas-phase air-mass fraction averaged over the perimeter of the drip shield at the location of a 21-PWR WP for the mean infiltration-flux backfill case for the indicated times.....	253
6-24. Gas-phase air-mass fraction averaged over the perimeter of the drip shield at the location of a 21-PWR WP for the high infiltration-flux backfill case for the indicated times.....	257
6-25. Gas-phase air-mass fraction averaged over the perimeter of the drip shield at the location of a 21-PWR WP for the low infiltration-flux backfill case for the indicated times.....	261
6-26. Liquid-phase flux 5 m above the crown of the drift for the mean infiltration-flux backfill case for the indicated times.....	265
6-27. Liquid-phase flux 0.2 m above the crown of the drift for the mean infiltration-flux backfill case for the indicated times.....	270
6-28. Liquid-phase flux averaged over the upper surface of the drip shield for the mean infiltration-flux backfill case for the indicated times.....	274
6-29. Liquid-phase flux adjacent to the lower side of the drip shield (i.e., adjacent to the base of the drip shield) for the mean infiltration-flux backfill case for the indicated times.....	278
6-30. Liquid-phase flux averaged over the invert for the mean infiltration-flux backfill case for the indicated times.....	281
6-31. Liquid-phase flux 5 m above the crown of the drift for the high infiltration-flux backfill case for the indicated times.....	285
6-32. Liquid-phase flux 0.2 m above the crown of the drift for the high infiltration-flux backfill case for the indicated times.....	290
6-33. Liquid-phase flux averaged over the upper surface of the drip shield for the high infiltration-flux backfill case for the indicated times.....	294
6-34. Liquid-phase flux backfill adjacent to the lower side of the drip shield (i.e., adjacent to the base of the drip shield) for the high infiltration-flux backfill case for the indicated times.....	298
6-35. Liquid-phase flux backfill averaged over the invert for the high infiltration-flux backfill case for the indicated times.....	301
6-36. Liquid-phase flux backfill 5 m above the crown of the drift for the low infiltration-flux backfill case for the indicated times.....	305
6-37. Liquid-phase flux backfill 0.2 m above the crown of the drift for the low infiltration-flux backfill case for the indicated times.....	312
6-38. Liquid-phase flux averaged over the upper surface of the drip shield for the low infiltration-flux backfill case for the indicated times.....	316

## FIGURES (Continued)

	Page
6-39. Liquid-phase flux adjacent to the lower side of the drip shield (i.e., adjacent to the base of the drip shield) for the low infiltration-flux backfill case for the indicated times.....	321
6-40. Liquid-phase flux averaged over the invert for the low infiltration-flux backfill case for the indicated times .....	325
6-41. Liquid-phase flux history at indicated drift-scale locations for the mean infiltration-flux case at (a) the geographical center of the repository and (b) a location 27.5 m from the eastern edge of the repository. Note that the Nevada State coordinates are given.....	329
6-42. Evaporation rate summed over the upper surface of the drip shield for the mean infiltration-flux backfill case for the indicated times .....	330
6-43. Evaporation rate summed over the upper surface of the drip shield for the high infiltration-flux backfill case for the indicated times .....	336
6-44. Evaporation rate summed over the upper surface of the drip shield for the low infiltration-flux backfill case for the indicated times .....	341
6-45. Evaporation rate summed over the upper surface of the drip shield for the mean infiltration-flux backfill case at (a) the geographical center of the repository and (b) a location 27.5 m from the eastern edge of the repository. Note that the Nevada State coordinates are given.....	346
6-46. Temperature and relative humidity on the WP surface for the mean infiltration-flux backfill case is plotted at the geographical center of the repository for the 4 different WP types and 8 different WP locations (along the drift) considered in the MSTHM (see Figure 4-1 for WP locations).....	347
6-47. The infiltration-flux distribution for the mean infiltration-flux case is plotted, including the present-day, monsoonal, and glacial climate periods.....	348
6-48. The infiltration-flux distribution for the high infiltration-flux case is plotted, including the present-day, monsoonal, and glacial climate periods.....	349
6-49. The infiltration-flux distribution for the low infiltration-flux case is plotted, including the present-day, monsoonal, and glacial climate periods.....	350
6-50. Perimeter-averaged temperature on the drift wall $T_{dw}$ and temperature on the WP $T_{wp}$ for a 21-PWR WP for the mean infiltration-flux no-backfill case for the indicated times.....	351
6-51. Temperature 5 m above the crown of the drift in the vicinity of a 21-PWR WP for the mean infiltration-flux no-backfill case for the indicated times.....	355
6-52. Temperature 7.39 m laterally away from the springline of the drift in the vicinity of a 21-PWR WP for the mean infiltration-flux no-backfill case for the indicated times. This location is almost exactly one-quarter of the distance in toward the midline of the pillar. This temperature is called $T_{pillar}$ .....	359
6-53. Temperature history at the indicated locations at (a) the geographical center of the repository and (b) a location 27.5 m from the eastern edge of the repository. The temperatures occur in the vicinity of a 21-PWR WP for the mean infiltration-flux no-backfill case for the indicated times.....	363

## FIGURES (Continued)

	Page
6-54. (a) The complementary cumulative distribution function (CCDF) for the peak temperature on waste packages and for the peak perimeter-averaged drift-wall temperature is plotted for the mean infiltration-flux no-backfill case. (b) The CCDF of the maximum lateral extent of the boiling point ( $T = 96^{\circ}\text{C}$ ) is plotted for the mean infiltration-flux case. ....	364
6-55. Liquid-phase saturation $S_{\text{liq}}$ averaged around the perimeter of the drift wall in the vicinity of a 21-PWR WP for the mean infiltration-flux no-backfill case for the indicated times. ....	365
6-56. Perimeter-averaged drift-wall relative humidity $RH_{\text{dw}}$ and relative humidity on the surface of the WP $RH_{\text{wp}}$ for a 21-PWR WP for the mean infiltration-flux no-backfill case for the indicated times. ....	371
6-57. Perimeter-averaged drift-wall liquid-phase saturation history and relative humidity history (a) at the geographical center of the repository and (b) a location 27.5 m from the eastern edge of the repository. These conditions occur in the vicinity of a 21-PWR WP for the mean infiltration-flux no-backfill case for the indicated times. ....	376
6-58. Evaporation rate $Q_{\text{evap}}$ in the host rock at the crown of the drift in the vicinity of a 21-PWR WP for the mean infiltration-flux no-backfill case for the indicated times. ....	377
6-59. Evaporation rate history in the host rock at the crown of the drift at the geographical center of the repository and a location 27.5 m from the eastern edge of the repository. These conditions occur in the vicinity of a 21-PWR WP for the mean infiltration-flux no-backfill case for the indicated times. Center of repository, Nevada State coordinates: Easting = 170535.03 m, Northing = 233640.08 m. Eastern edge of repository, Nevada State coordinates: Easting = 171195.16 m, Northing = 233605.06 m. ....	385
6-60. Capillary pressure in the fractures $P_{\text{cap,frac}}$ and in the matrix $P_{\text{cap,mat}}$ averaged around the perimeter of the drift wall in the vicinity of a 21-PWR WP for the mean infiltration-flux no-backfill case for the indicated times. ....	386
6-61. Capillary pressure history in (a) the fractures and in (b) the matrix averaged around the perimeter of the drift wall at the geographical center of the repository and a location 27.5 m from the eastern edge of the repository. These conditions occur in the vicinity of a 21-PWR WP for the mean infiltration-flux no-backfill case for the indicated times. ....	394
6-62. Liquid-phase flux 5 m and 3 m above the crown of the drift $q_{\text{liq},5\text{m}}$ and $q_{\text{liq},3\text{m}}$ in the vicinity of a 21-PWR WP for the mean infiltration-flux no-backfill case for the indicated times. ....	395
6-63. Liquid-phase flux at the upper drift wall $q_{\text{liq,dwTop}}$ in the vicinity of a 21-PWR WP for the mean infiltration-flux no-backfill case for the indicated times. ....	400
6-64. Liquid-phase flux history at the indicated locations above the drift at (a) the geographical center of the repository and (b) a location 27.5 m from the edge of	

## FIGURES (Continued)

	Page
the repository. These conditions occur in the vicinity of a 21-PWR WP for the mean infiltration-flux no-backfill case for the indicated times. ....	404
6-65. Comparison of the NUFT-simulated and measured temperatures along Borehole TT1 is given at six times from 30 to 400 days. The NUFT simulation used the drift-scale hydrologic property set that was used in the MSTHM calculations in this AMR. ....	405
6-66. Comparison of the NUFT-simulated and measured liquid-phase saturation along Borehole TN3 is given at three times from 100 to 500 days. The NUFT simulation used the drift-scale hydrologic property set that was used in the MSTHM calculations in this AMR. ....	406
6-67. Comparison of the NUFT-simulated and measured temperatures along Borehole ESF-HD-137 is given at 365 and 547 days. The NUFT simulation used the drift-scale hydrologic property set that was used in the MSTHM calculations in this AMR. ....	407
6-68. Comparison of predicted temperatures at (a) center of the repository (l4c3 location in Table 2-2 of Buscheck et al., 1998) and (b) 100 m from the edge of the repository (l4c1 location) for the 12/97 TSPA-VA base-case $I \times 1 \alpha_{f,mean}$ parameter set, where the symbol I stands for the nominal infiltration-flux $q_{inf}$ map (average $q_{inf} = 7.8$ mm/yr) for the present-day climate and the variable $\alpha_f$ is the van Genuchten “alpha” parameter for fractures. The MSTHM is used to predict drift-wall temperature adjacent to an “average” 21-PWR medium-heat CSNF WP. The east-west cross-sectional mountain-scale TH model is used to predict the drift temperature, which is averaged over the cross section of the drift, arising from a line-averaged heat-source representation of WP decay heat. ....	408
6-69. Contours of the log10 of the bulk permeability $k$ field are plotted for stochastic realization A-56. Contours are given (a, b, c, d, e) for vertical xz planes at five locations ( $j = 1, 2, 3, 4, 5$ ), located at axial distances of 0.5, 1.5, 2.5, 3.5, and 4.5 m, respectively. A contour plot is also given (f) for the vertical yz plane located along the central axis of the drift ( $i = 1$ ). ....	409
6-70. Contours of liquid-phase saturation $S_{liq}$ in the fractures (a, b, c) and in the matrix (d, e, f) at two vertical xz planes ( $j = 3, 5$ ) and one vertical yz plane ( $i = 2$ , which is 0.765 m from the centerline of the drift) plotted at 50 yr for stochastic realization A-56 and an AML of 56 MTU/acre. ....	410
6-71. Contours of temperature $T$ (a, b, c) and relative humidity $RH$ (d, e, f) at two vertical xz planes ( $j = 3, 5$ ) and one vertical yz plane ( $i = 2$ , which is 0.765 m from the centerline of the drift), plotted at 50 yr for stochastic realization A-56 and an AML of 56 MTU/acre. Note that the white area in panels d, e, and f correspond to the region where $RH$ is not predicted in the model. ....	411
6-72. Contours of liquid-phase saturation $S_{liq}$ in the fractures (a, b, c) and in the matrix (d, e, f) at two vertical xz planes ( $j = 3, 5$ ) and one vertical yz plane ( $i = 2$ , which is 0.765 m from the centerline of the drift), plotted at 60 yr for stochastic realization A-56 and an AML of 56 MTU/acre. ....	412

## FIGURES (Continued)

	Page
6-73. Contours of temperature $T$ (a, b, c) and relative humidity $RH$ (d, e, f) at two vertical $xz$ planes ( $j = 3, 5$ ) and one vertical $yz$ plane ( $i = 2$ , which is 0.765 m from the centerline of the drift) are plotted at 60 yr for stochastic realization A-56 and an AML of 56 MTU/acre. Note that the white area in panels d, e, and f correspond to the region where $RH$ is not predicted in the model .....	413
6-74. Contours of liquid-phase saturation $S_{liq}$ in the fractures (a, b, c) and in the matrix (d, e, f) at two vertical $xz$ planes ( $j = 3, 5$ ) and one vertical $yz$ plane ( $i = 2$ , which is 0.765 m from the centerline of the drift) are plotted at 1900 yr for stochastic realization A-56 and an AML of 56 MTU/acre.....	414
6-75. Contours of temperature $T$ (a, b, c) and relative humidity $RH$ (d, e, f) at two vertical $xz$ planes ( $j = 3, 5$ ) and one vertical $yz$ plane ( $i = 2$ , which is 0.765 m from the centerline of the drift), are plotted at 1900 yr for stochastic realization A-56 and an AML of 56 MTU/acre. Note that the white area in panels d, e, and f correspond to the region where $RH$ is not predicted in the model .....	415
6-76. Contours of liquid-phase flux $q_{iq}$ in the fractures and in the drift at (a, c) two vertical $xz$ planes ( $j = 2, 5$ ) and (b, d) two vertical $yz$ planes ( $i=1$ , which is at the centerline of the drift and $i = 2$ , which is 0.765m from the centerline of the drift) are plotted at 1900 yr for stochastic realization A-56 and an AML of 56 MTU/acre. The arrows show the direction of flow .....	416
6-77. Contours of liquid-phase saturation $S_{liq}$ in the fractures (a, b, c) and in the matrix (d, e, f) at two vertical $xz$ planes ( $j = 2, 5$ ) and one vertical $yz$ plane ( $i = 4$ , which is 1.4671 m from the centerline of the drift) are plotted at 50 yr for stochastic realization A-34 and an AML of 34 MTU/acre.....	417
6-78. Contours of temperature $T$ (a, b, c) and relative humidity $RH$ (d, e, f) at two vertical $xz$ planes ( $j = 2, 5$ ) and one vertical $yz$ plane ( $i = 4$ , which is 1.4671 m from the centerline of the drift) are plotted at 50 yr for stochastic realization A-34 and an AML of 34 MTU/acre. Note that the white area in panels d, e, and f correspond to the region where $RH$ is not predicted in the model .....	418
6-79. Contours of liquid-phase saturation $S_{liq}$ in the fractures (a, b, c) and in the matrix (d, e, f) at two vertical $xz$ planes ( $j = 2, 5$ ) and one vertical $yz$ plane ( $i = 4$ , which is 1.4671 m from the centerline of the drift) are plotted at 60 yr for stochastic realization A-34 and an AML of 34 MTU/acre.....	419
6-80. Contours of temperature $T$ (a, b, c) and relative humidity $RH$ (d, e, f) at two vertical $xz$ planes ( $j = 2, 5$ ) and one vertical $yz$ plane ( $i = 4$ , which is 1.4671 m from the centerline of the drift) are plotted at 60 yr for stochastic realization A-34 and an AML of 34 MTU/acre. Note that the white area in panels d, e, and f correspond to the region where $RH$ is not predicted in the model. ....	420
6-81. Contours of liquid-phase saturation $S_{liq}$ in the fractures (a, b, c) and in the matrix (d, e, f) at two vertical $xz$ planes ( $j = 2, 5$ ) and one vertical $yz$ plane ( $i = 4$ , which is 1.4671 m from the centerline of the drift) are plotted at 700 yr for stochastic realization A-34 and an AML of 34 MTU/acre.....	421

## FIGURES (Continued)

	Page
6-82. Contours of temperature $T$ (a, b, c) and relative humidity $RH$ (d, e, f) at two vertical $xz$ planes ( $j = 2, 5$ ) and one vertical $yz$ plane ( $i = 4$ , which is 1.4671 m from the centerline of the drift) are plotted at 700 yr for stochastic realization A-34 and an AML of 34 MTU/acre. Note that the white area in panels d, e, and f correspond to the region where $RH$ is not predicted in the model. ....	422
6-83. Temperature and relative-humidity histories are given at the drift wall and drip shield for stochastic realization A-56 and an AML of 56 MTU/acre. Temperature at the upper drift wall (a) is averaged from springline to springline. Relative humidity at the drift wall (b) is averaged over the entire perimeter of the drift. Drip-shield temperature (c) and relative humidity (d) are averaged over the entire drip shield. Histories are given at five axial locations ( $j = 1, 2, 3, 4$ , and 5) for the equivalent 2-D homogeneous LDTH model. ....	423
6-84. Temperature histories are given at the drift wall and drip shield for stochastic realization A-56 and an AML of 56 MTU/acre. Temperature at the upper drift wall (a) is averaged from springline to springline. Drip-shield temperature (b) is averaged over the entire drip shield. Histories are given at five axial locations ( $j = 1, 2, 3, 4$ , and 5) for the corresponding 2-D LDTH model with an homogeneous drift-scale bulk permeability distribution. This plot focuses on the end of the boiling period. ....	424
6-85. Evaporation-rate history is given at the drip shield for stochastic realization A-56 and an AML of 56 MTU/acre. Drip-shield evaporation rate is averaged over the entire drip shield. Histories are given at five axial locations ( $j = 1, 2, 3, 4$ , and 5) and for the corresponding 2-D LDTH model with an homogeneous drift-scale bulk permeability distribution. ....	425
6-86. Liquid-phase-flux histories are given at various locations in the host rock and in the drift for stochastic realization A-56 and an AML of 56 MTU/acre. Liquid-phase flux 5 m above the drift is averaged over the entire rock pillar from the drift centerline to the rock-pillar centerline. Liquid-phase flux 3 m above the drift is averaged over the lateral extent of the drift. Liquid-phase seepage flux at the upper drift wall is averaged from springline to springline. Liquid-phase seepage flux at the upper drip shield is averaged over the lateral extent of the drip shield. Histories are given at five axial locations ( $j = 1, 2, 3, 4$ , and 5), as well as for an average of the five axial locations. ....	426
6-87. The distribution of seepage locations is plotted at (a) 1100 yr, (b) 1900 yr, (c) 2200 yr, and (d) 1,000,000 yr for stochastic realization A-56 and an AML of 56 MTU/acre. The light stippled blocks correspond to the footprint of the drip shield. The dark blue blocks correspond to blocks that have a non-zero liquid-phase seepage flux at the upper drift wall. ....	427
6-88. Temperature and relative-humidity histories are given at the drift wall and drip shield for stochastic realization A-34 and an AML of 34 MTU/acre. Temperature at the upper drift wall (a) is averaged from springline to springline. Relative humidity at the drift wall (b) is averaged over the entire perimeter of the drift.	

## FIGURES (Continued)

	Page
Drip-shield temperature (c) and relative humidity (d) are averaged over the entire drip shield. Histories are given at five axial locations ( $j = 1, 2, 3, 4,$ and $5$ ) for the equivalent 2-D homogeneous LDTH model. ....	428
6-89. Liquid-phase-flux histories are given at various locations in the host rock and in the drift for stochastic realization A-34 and an AML of 34 MTU/acre. Liquid-phase flux 5 m above the drift is averaged over the entire rock pillar from the drift centerline to the rock-pillar centerline. Liquid-phase flux 3 m above the drift is averaged over the lateral extent of the drift. Liquid-phase seepage flux at the upper drift wall is averaged from springline to springline. Liquid-phase seepage flux at the upper drip shield is averaged over the lateral extent of the drip shield. Histories are given at five axial locations ( $j = 1, 2, 3, 4,$ and $5$ ), as well as for an average of the five axial locations. ....	429
6-90. Liquid-phase-seepage-flux history at the crown of the drift for (a) stochastic realization A-56 and an AML of 56 MTU/acre and for (b) stochastic realization A-34 and an AML of 34 MTU/acre. This seepage flux is averaged over the lateral extent of the drip shield. Histories are given at five axial locations ( $j = 1, 2, 3, 4,$ and $5$ ), as well as for an average of the five axial locations. ....	430
6-91. Temperature and relative-humidity histories are given at the drift wall and drip shield for stochastic realization B-56 and an AML of 56 MTU/acre. Temperature at the upper drift wall (a) is averaged from springline to springline. Relative humidity at the drift wall (b) is averaged over the entire perimeter of the drift. Drip-shield temperature (c) and relative humidity (d) are averaged over the entire drip shield. Histories are given at five axial locations ( $j = 1, 2, 3, 4,$ and $5$ ) for the equivalent 2-D homogeneous LDTH model. ....	431
6-92. Liquid-phase-flux histories are given at various locations in the host rock and in the drift for stochastic realization B-56 and an AML of 56 MTU/acre. Liquid-phase flux 5 m above the drift is averaged over the entire rock pillar from the drift centerline to the rock-pillar centerline. Liquid-phase flux 3 m above the drift is averaged over the lateral extent of the drift. Liquid-phase seepage flux at the upper drift wall is averaged from springline to springline. Liquid-phase seepage flux at the upper drip shield is averaged over the lateral extent of the drip shield. Histories are given at five axial locations ( $j = 1, 2, 3, 4,$ and $5$ ), as well as for an average of the five axial locations. ....	432
6-93. Temperature and relative-humidity histories are given at the drift wall and drip shield for stochastic realization B-34 and an AML of 34 MTU/acre. Temperature at the upper drift wall (a) is averaged from springline to springline. Relative humidity at the drift wall (b) is averaged over the entire perimeter of the drift. Drip-shield temperature (c) and relative humidity are (d) averaged over the entire drip shield. Histories are given at five axial locations ( $j = 1, 2, 3, 4,$ and $5$ ) for the equivalent 2-D homogeneous LDTH model. ....	433
6-94. Liquid-phase-flux histories are given at various locations in the host rock and in the drift for stochastic realization B-34 and an AML of 34 MTU/acre. Liquid-	

**FIGURES (Continued)**

**Page**

phase flux 5 m above the drift is averaged over the entire rock pillar from the drift centerline to the rock-pillar centerline. Liquid-phase flux 3 m above the drift is averaged over the lateral extent of the drift. Liquid-phase seepage flux at the upper drift wall is averaged from springline to springline. Liquid-phase seepage flux at the upper drip shield is averaged over the lateral extent of the drip shield. Histories are given at five axial locations ( $j = 1, 2, 3, 4,$  and  $5$ ), as well as for an average of the five axial locations. .... 434

6-95. Temperature and relative-humidity histories are given at the drift wall and drip shield for stochastic realization C-56 and an AML of 56 MTU/acre. Temperature at the upper drift wall (a) is averaged from springline to springline. Relative humidity at the drift wall (b) is averaged over the entire perimeter of the drift. Drip-shield temperature (c) and relative humidity (d) are averaged over the entire drip shield. Histories are given at five axial locations ( $j = 1, 2, 3, 4,$  and  $5$ ) for the equivalent 2-D homogeneous LDTH model. .... 435

6-96. Liquid-phase-flux histories are given at various locations in the host rock for stochastic realization C-56 and an AML of 56 MTU/acre. Liquid-phase flux 5 m above the drift is averaged over the entire rock pillar from the drift centerline to the rock-pillar centerline. Liquid-phase flux 3 m above the drift is averaged over the lateral extent of the drift. All liquid-phase fluxes at the drift wall and in the drift are zero for this case. Histories are given at five axial locations ( $j = 1, 2, 3, 4,$  and  $5$ ), as well as for an average of the five axial locations. Note that there is no seepage flux across the upper drift wall or onto the drip shield for this realization. .... 436

6-97. Temperature and relative-humidity histories are given at the drift wall and drip shield for stochastic realization C-34 and an AML of 34 MTU/acre. Temperature at the upper drift wall (a) is averaged from springline to springline. Relative humidity at the drift wall (b) is averaged over the entire perimeter of the drift. Drip-shield temperature (c) and relative humidity (d) are averaged over the entire drip shield. Histories are given at five axial locations ( $j = 1, 2, 3, 4,$  and  $5$ ) for the equivalent 2-D homogeneous LDTH model. .... 437

6-98. Liquid-phase-flux histories are given at various locations in the host rock for stochastic realization C-34 and an AML of 34 MTU/acre. Liquid-phase flux 5 m above the drift is averaged over the entire rock pillar from the drift centerline to the rock-pillar centerline. Liquid-phase flux 3 m above the drift is averaged over the lateral extent of the drift. All liquid-phase fluxes at the drift wall and in the drift are zero for this case. Histories are given at five axial locations ( $j = 1, 2, 3, 4,$  and  $5$ ), as well as for an average of the five axial locations. Note that there is no seepage flux across the upper drift wall or onto the drip shield for this realization. .... 438

6-99. Temperature and relative-humidity histories are given at the drift wall and drip shield for stochastic realization D-56 and an AML of 56 MTU/acre. Temperature at the upper drift wall (a) is averaged from springline to springline. Relative

## FIGURES (Continued)

Page

humidity at the drift wall (b) is averaged over the entire perimeter of the drift. Drip-shield temperature (c) and relative humidity (d) are averaged over the entire drip shield. Histories are given at five axial locations ( $j = 1, 2, 3, 4,$ and $5$ ) for the equivalent 2-D homogeneous LDTH model. ....	439
6-100. Liquid-phase-flux histories are given at various locations in the host rock and in the drift for stochastic realization D-56 and an AML of 56 MTU/acre. Liquid-phase flux 5 m above the drift is averaged over the entire rock pillar from the drift centerline to the rock-pillar centerline. Liquid-phase flux 3 m above the drift is averaged over the lateral extent of the drift. Liquid-phase seepage flux at the upper drift wall is averaged from springline to springline. Liquid-phase seepage flux at the upper drip shield is averaged over the lateral extent of the drip shield. Histories are given at five axial locations ( $j = 1, 2, 3, 4,$ and $5$ ), as well as for an average of the five axial locations. ....	440
6-101. Temperature and relative-humidity histories are given at the drift wall and drip shield for stochastic realization D-34 and an AML of 34 MTU/acre. Temperature at the upper drift wall (a) is averaged from springline to springline. Relative humidity at the drift wall (b) is averaged over the entire perimeter of the drift. Drip-shield temperature (c) and relative humidity (d) are averaged over the entire drip shield. Histories are given at five axial locations ( $j = 1, 2, 3, 4,$ and $5$ ) for the equivalent 2-D homogeneous LDTH model. ....	441
6-102. Liquid-phase-flux histories are given at various locations in the host rock and in the drift for stochastic realization D-34 and an AML of 34 MTU/acre. Liquid-phase flux 5 m above the drift is averaged over the entire rock pillar from the drift centerline to the rock-pillar centerline. Liquid-phase flux 3 m above the drift is averaged over the lateral extent of the drift. Liquid-phase seepage flux at the upper drift wall is averaged from springline to springline. Liquid-phase seepage flux at the upper drip shield is averaged over the lateral extent of the drip shield. Histories are given at five axial locations ( $j = 1, 2, 3, 4,$ and $5$ ), as well as for an average of the five axial locations. ....	442

## TABLES

	<b>Page</b>
1-1. List of NFE and EBS TH variables calculated with the MSTHM at each of the 623 repository subdomains for the backfill case .....	27
1-2. List of NFE and EBS TH variables calculated with the MSTHM at each of the 610 repository subdomains for the no-backfill case.....	28
1-3. List of TEF KTI Subissue Acceptance Criteria Related to this AMR (NRC 2000).....	30
1-4. List of NRC-DOE Technical Exchange (TE) Agreements Related to this AMR (Williams, D., 2001).....	31
3-1a. Software validation .....	37
3-1b. Software execution.....	38
3-2a. N-table for backfill case .....	46
3-2b. N-table for no-backfill case .....	47
3-3a. E-table for backfill case.....	48
3-3b. E-table for no-backfill case .....	49
3-4a. File groups for backfill case .....	50
3-4b. File groups for no-backfill case.....	52
3-5a. Software routine input and output files for backfill case .....	54
3-5b. Software routine input and output files for no-backfill case .....	58
3-6a. LDTH NUFT input and output files for backfill case .....	62
3-6b. LDTH NUFT input and output files for no-backfill case.....	63
3-7a. SDT NUFT input and output files for backfill case .....	64
3-7b. SDT NUFT input and output files for no-backfill case.....	65
3-8a. DDT NUFT input and output files for backfill case .....	66
3-8b. DDT NUFT input and output files for no-backfill case .....	67
3-9a. SMT NUFT input and output files for backfill case .....	68
3-9b. SMT NUFT input and output files for no-backfill case .....	69
4-1. Backfill and invert material properties for the backfill and no-backfill cases .....	82
4-2. Matrix properties of stratigraphic units .....	84
4-3. Fracture properties of stratigraphic units.....	85
4-4. Thermal properties of stratigraphic units .....	86
6-1. Stratigraphic columns used in the 31 drift-scale-submodel locations.....	109
6-2. Summary of the vertical location of the repository horizon at the 31 drift-scale-submodel locations.....	113
6-3. Boundary conditions used in the drift-scale submodels (LDTH, SDT, and DDT). Note that the gas-phase pressure and gas-phase air-mass fraction only apply to the LDTH submodels .....	115
6-4. List of plots of TH conditions for the backfill case.....	145
6-5. List of plots of TH conditions for the no-backfill case .....	163
6-6. RMSD and MD for temperature profile along TT1 using driftscale data set.....	168
6-7. Infiltration-flux values for the mean infiltration-flux case.....	175
6-8. List of statistical parameters used in the 3-D heterogeneous LDTH-model realizations .....	177

## TABLES (Continued)

	<b>Page</b>
6-9. List of plots of TH conditions calculated with the 3-D heterogeneous LDTH and 2-D homogeneous LDTH models .....	178
6-10. Summary of seepage conditions at 1,000,000 yr where seepage percentage is the fraction of the incident average percolation flux.....	180

## ACRONYMS

AFC	Active-Fracture Concept
AML	Areal Mass Loading
CCDF	Complementary Cumulative Distribution Function
CRWMS M&O	Civilian Radioactive Waste Management System Management and Operating Contractor
CSNF	Commercial Spent Nuclear Fuel
DDT	Discrete-heat-source, Drift-scale, Thermal-conduction Submodel
DHLW	Defense High-Level Waste
DKM	Dual-Permeability Method
DMTH	Discrete-heat-source, Mountain-scale, Thermohydrologic Submodel
DSNF	Defense Spent Nuclear Fuel
EBS	Engineered Barrier System
EDA	Enhanced Design Alternative
HLW	High-Level Waste
IRSR	Issue Resolution Status Report
KTI	Key Technical Issue
LADS	License Application Design Selection
LDTH	Line-averaged-heat-source, Drift-scale, Thermohydrologic Submodel
LMTH	Line-averaged-heat-source, Mountain-scale, Thermohydrologic Submodel
MSTHAC	Multiscale Abstraction Code
MSTHM	Multiscale Thermohydrologic Model
NF	Near Field
NFE	Near-Field Environment
NRC	Nuclear Regulatory Commission
NUFT	Nonisothermal Unsaturated-Saturated Flow and Transport
RH	Relative Humidity
SDT	Smeared-heat-source, Drift-scale, Thermal-conduction Submodel
SMT	Smeared-heat-source, Mountain-scale, Thermal-conduction Submodel
SR	Site Recommendation
SZ	Saturated Zone
TBV	To Be Verified
TEF	Thermal Effects on Flow
TH	Thermohydrologic
THC	Thermohydrologic-chemical

## ACRONYMS (Continued)

TSPA	Total System Performance Assessment
TSPA-SR	Total System Performance Assessment for Site Recommendation
TSPAI	Total System Performance Assessment Integration
UZ	Unsaturated Zone
WP	Waste Package

## 1. PURPOSE

The purpose of the Multiscale Thermohydrologic Model (MSTHM) is to describe the thermohydrologic evolution of the near-field environment (NFE) and engineered barrier system (EBS) throughout the potential high-level nuclear waste repository at Yucca Mountain for a particular engineering design (CRWMS M&O 2000c). The process-level model will provide thermohydrologic (TH) information and data (such as in-drift temperature, relative humidity, liquid saturation, etc. (see Table 1-1)) for use in other technical products. This data is provided throughout the entire repository area as a function of time.

The MSTHM (Figure 1-1) couples the Smearred-heat-source Drift-scale Thermal-conduction (SDT), Line-average-heat-source Drift-scale Thermohydrologic (LDTH), Discrete-heat-source Drift-scale Thermal-conduction (DDT), and Smearred-heat-source Mountain-scale Thermal-conduction (SMT) submodels such that the flow of water and water vapor through partially-saturated fractured rock is considered. The MSTHM accounts for 3-D drift-scale and mountain-scale heat flow, repository-scale variability of stratigraphy and infiltration flux, and waste package (WP)-to-WP variability in heat output from WPs. All submodels use the nonisothermal unsaturated-saturated flow and transport (NUFT) simulation code. The MSTHM is implemented in several data-processing steps (Figure 1-2 and Figure 1-3). The four major steps are (1) submodel input-file preparation, (2) execution of the four submodel families with the use of the NUFT code, (3) execution of the multiscale thermohydrologic abstraction code (MSTHAC), and (4) binning and post-processing (i.e., graphics preparation) of the output from MSTHAC. Section 6 describes the MSTHM in detail.

Rev 00 ICN 02 of this AMR has been developed as documented in the Technical Work Plan *Technical Work Plan for EBS Department Modeling FY01 Work Activities* (BSC 2001), which was prepared in accordance with AP-2.21Q, *Quality Determinations And Planning For Scientific, Engineering, And Regulatory Compliance Activities*.

This model is important because it is used in assessing post-closure performance.

### 1.1 OBJECTIVES

The objectives of this Analyses and Model Report (AMR) are to investigate near field (NF) and EBS thermohydrologic environments throughout the repository area at various evolution periods, and to provide TH data that may be used in other process model reports.

### 1.2 WORK SCOPE

The calculations described in this report do not include the coupling of geochemical or geomechanical processes to predicted TH behavior. Coupled geochemical processes are addressed in the *Drift-Scale Coupled Processes (Drift-Scale Test and THC Seepage) Models* AMR (CRWMS M&O 2001a). The calculations in this report are conducted using the MSTHM and will be based on the following information:

- a. Repository footprint for Enhanced Design Alternative (EDA) II will be modeled for a total of 70,000 MTU of waste, including 63,000 MTU of commercial spent nuclear

fuel (CSNF) and 7000 MTU of Defense high-level waste (DHLW). (Extended waste inventories may be addressed in subsequent revisions)

- b. The Total System Performance Assessment for Site Recommendation (TSPA-SR) base-case hydrologic properties set for the case of no perching, including three infiltration-flux scenarios: (1) low flux, (2) mean flux, and (3) high flux. Each infiltration-flux scenario has a time-varying infiltration flux that includes the influence of three climate states: (1) present-day, (2) monsoonal, and (3) glacial.
- c. Emplacement drifts are ventilated for the entire pre-closure period, which is assumed to be 50 years. (Extended ventilation periods will be addressed in subsequent revisions.)
- d. Emplacement drifts are backfilled at the end of the pre-closure period. Drip shields are emplaced at the same time as backfill.
- e. The distribution of hydrostratigraphic units used in the site-scale unsaturated zone (UZ) flow model (based on GFM version 3.1) will be used in the numerical grids that are built (using the YMESH numerical-mesh generator), for all of the submodels used in the MSTHM.
- f. The drift-scale models will use grid discretization that is comparable to or better than that used in the Multiscale NF/EBS TH Model calculations for Phase II of the License Application Design Selection (LADS).
- g. This AMR includes a no-backfill case, where the emplacement drifts will remain open after pre-closure and the drip shields have been installed. The no-backfill case is the Site-Recommendation (SR) current design basis (CRWMS M&O 1999f) and the reason for ICN 01 of this document; ICN 01 supports the TSPA-SR. The backfill case is being maintained in this document to also support the TSPA-SR.
- h. The 38 and 39 TH variables are identified in Table 1-1 and Table 1-2 for the backfill and no-backfill case respectively. The number of subdomains that delineates the area of repository heating for the backfill and no-backfill cases are slightly different, 623 subdomains for backfill versus 610 subdomains for no-backfill, due to small differences in the representation of the northwestern and southwestern repository boundaries. The total heat loading is the same between these two cases, which results in a slightly lower, negligible, difference in the areal heat loading for the backfill case.
- i. ICN 02 of this AMR was developed to address the NRC KTI agreement TEF 2.9 and show the influence of drift-scale fracture heterogeneity on TH behavior for the no-backfill case. This ICN also addresses the issues and concerns identified in deficiency report BSC-01-D-100, pertaining to control of electronic information.

Table 1-1. List of NFE and EBS TH variables calculated with the MSTHM at each of the 623 repository subdomains for the backfill case

TH Variable	Drift-Scale Location
Temperature	NFE host rock (5 m above crown of drift)
	NFE host rock (mid-pillar at repository horizon)
	Maximum lateral extent of boiling
	Upper drift wall (crown of the drift)
	Lower drift wall (below invert)
	Drift wall (perimeter average)
	Backfill (crown)
	Drip shield (perimeter average)
	Drip shield (upper surface)
	WP (surface average)
	Invert (average)
Relative humidity	Drift wall (perimeter average)
	Backfill (crown)
	Drip shield (perimeter average)
	Waste package
	Invert (average)
Liquid-phase saturation (matrix)	Drift wall (perimeter average)
	Drip shield (perimeter average)
	Invert (average)
Liquid-phase flux	NFE host rock (5 m above crown of drift)
	NFE host rock (3 m above crown of drift)
	NFE host rock (0.2 m above crown of drift)
	Drip shield (crown)
	Drip shield (upper surface average)
	Drip shield (lower side at the base)
	Invert (average)
Gas-phase air-mass fraction	Drip shield (perimeter average)
Gas-phase pressure	Drip shield (perimeter average)
Capillary pressure	Drip shield (perimeter average)
	Invert (average)
	Drift wall (crown, in matrix)
	Drift wall (crown, in fractures)
Gas-phase (water vapor) flux	Drift wall (perimeter average)
Gas-phase (air) flux	Drift wall (perimeter average)
Evaporation rate	Backfill (crown)
	Drip shield (crown)
	Drip shield (perimeter total)
	Invert (total)

Table 1-2. List of NFE and EBS TH variables calculated with the MSTHM at each of the 610 repository subdomains for the no-backfill case

TH Variable	Drift-Scale Location
Temperature	NFE host rock (5 m above crown of drift)
	NFE host rock (mid-pillar at repository horizon)
	Maximum lateral extent of boiling
	Drift wall (perimeter average)
	Drift (midway between drip-shield crown and drift crown)
	Drip shield (perimeter average)
	Drip shield (upper surface)
	WP (surface average)
	Invert (average)
	Relative humidity
Drift (midway between drip-shield crown and drift crown)	
Drip shield (perimeter average)	
Waste package	
Invert (average)	
Liquid-phase saturation (matrix)	Drift wall (perimeter average)
	Drip shield (perimeter average)
	Invert (average)
Liquid-phase flux	NFE host rock (5 m above crown of drift)
	NFE host rock (3 m above crown of drift)
	Drift wall (upper surface)
	Drift wall (lower surface below invert)
	Drip shield (crown)
	Drip shield (upper surface average)
	Drip shield (lower side at the base)
	Invert (average)
Gas-phase air-mass fraction	Drip shield (perimeter average)
Gas-phase pressure	Drip shield (perimeter average)
Capillary pressure	Drip shield (perimeter average)
	Invert (average)
	Drift wall (crown, in matrix)
	Drift wall (crown, in fractures)
Gas-phase (water vapor) flux	Drift wall (perimeter average)
Gas-phase (air) flux	Drift wall (perimeter average)
Evaporation rate	Drift (midway between drip-shield crown and drift crown)
	Drip shield (crown)
	Drip shield (perimeter total)
	Drift wall (upper surface)
	Drift wall (lower surface below invert)
	Invert (total)

Section 4.2 gives the specific criteria for the calculations conducted in this AMR.

### 1.3 PRIMARY TASKS

The primary tasks completed in the preparation of this document are to:

1. Calculate TH conditions (i.e., performance measures) in the NF host rock and in the EBS throughout the repository area, using the MSTHM. The TH performance measures include temperature, liquid-phase saturation, relative humidity, gas-phase air-mass fraction, evaporation rate, and liquid-phase flux. These performance measures will be given in histogram bins for each of the repository subregions. The distribution of these performance measures will also be described for the entire repository area, using complementary cumulative distribution functions.
2. Describe all submodels that are implemented in the MSTHM as well as the MSTHAC.

### 1.4 RELATIONSHIP TO NUCLEAR REGULATORY COMMISSION KEY TECHNICAL ISSUES

This AMR is closely related to the *Nuclear Regulatory Commission (NRC) Key Technical Issues (KTI) on the Thermal Effects on Flow (TEF)* (NRC 2000). The primary applicable subissue of the TEF KTI is Subissue 2, which asks the question “Is the Department of Energy thermohydrologic modeling approach sufficient to predict the nature and bounds of thermal effects on flow in the near field?” Table 1-3 lists the acceptance criteria for Subissue 2 and the sections of this AMR that address these criteria. Table 1-4 lists the NRC-DOE Technical Exchange (TE) agreements related to this AMR (Williams, D., 2001).

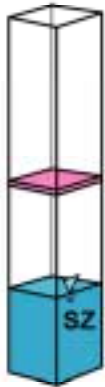
Table 1-3. List of TEF KTI Subissue Acceptance Criteria Related to this AMR (NRC 2000)

Subissue 2: Is the U.S. Department of Energy thermohydrologic modeling approach sufficient to predict the nature and bounds of thermal effects on flow in the near field?		
Acceptance Criterion	Description of Criterion	Relevant Sections of this AMR
Programmatic Acceptance Criterion 1	DOE's thermohydrologic modeling analyses were developed and documented under acceptable QA procedures.	Section 2
Technical Acceptance Criterion 1	<p>Sufficient data are available to adequately define relevant parameters, parameter values, and conceptual models. Specifically DOE should demonstrate that:</p> <ul style="list-style-type: none"> <li>• Uncertainties and variabilities in parameter values are accounted for using defensible methods. The technical bases for parameter ranges, probability distributions or bounding values used are provided. Parameter values (single values, ranges, probability distributions, or bounding values) are derived from site-specific data or an analysis is included to show the assumed parameter value lead to a conservative effect on performance.</li> <li>• Analyses are consistent with site characteristics in establishing initial conditions, boundary conditions, and computational domains for conceptual models evaluated.</li> </ul>	<p>Sections 4,6,7</p> <p>Sections 4,6</p>
Technical Acceptance Criterion 2	<p>Descriptions of process-level conceptual and mathematical models used in the analyses are reasonably complete. Further, DOE should demonstrate that:</p> <ul style="list-style-type: none"> <li>• Models are based on well-accepted principles of heat and mass transfer applicable to unsaturated geologic media.</li> <li>• Models include, at a minimum, the processes of evaporation and condensation and the effects of discrete geologic features.</li> <li>• Models include, at a minimum, an evaluation of important thermohydrological phenomena, such as: (i) multidrift dryout zone coalescence, (ii) lateral movement of condensate, (iii) cold-trap effects, and (v) condensate drainage through fractures.</li> <li>• Models include all significant repository design features.</li> <li>• Models are capable of accommodating variation in infiltration.</li> <li>• Conceptual model uncertainties have been defined and documented and effects on conclusions regarding performance assessed.</li> <li>• Mathematical models are consistent with conceptual models, bases on consideration of site characteristics.</li> <li>• Alternative models and modeling approaches, which are consistent with available data and current scientific understanding, have been investigated, limitations defined, and results appropriately considered.</li> <li>• Results from different mathematical models have been compared to judge robustness of results</li> </ul>	<p>In future Rev</p> <p>Section 6</p> <p>Section 6</p> <p>Sections 4,5,6</p> <p>Sections 4,6</p> <p>In Future Rev</p> <p>Section 6</p> <p>Section 6.14</p> <p>Section 6.14</p>

Table 1-4. List of NRC-DOE Technical Exchange (TE) Agreements Related to this AMR (Williams, D., 2001)

Agreement	Description of Agreement	Relevant Sections of this AMR
TEF 2.9	Provide the Multi-scale Thermohydrologic Model AMR, ICN 03. The DOE will provide the Multi-scale Thermohydrologic Model AMR (ANL-EBS-MD-000049), Rev 00, ICN 03 to the NRC. Note: This should have read ICN 02 instead of ICN 03	Section 6.14
TSPA 3.07	Provide technical basis for representation of or the neglect of dripping from rockbolts in the ECRB in performance assessment, including the impact on hydrology, chemistry, and other impacted models	Section 6
TSPA 3.09	Provide the documentation that presents the representation of uncertainty and variability in the near-field environment abstractions in the TSPA (ENG3.1.4)	Section 6.14
TSPA 3.11	DOE should account for appropriate integration between the 3-D UZ flow model, the MSTH model, and the drift seepage model. In particular, DOE should ensure that relevant spatial distributions are propagated appropriately between the UZ flow model, the thermohydrology model, and the seepage model (ENG3.1.6).	Sections 4,6
TSPA 3.27	Provide an overview of water flow rates used in the UZ model above and below the repository, in the MSTHM, in the seepage abstraction, and in the in-drift flow path models, to ensure appropriate integration between the various models (UZ2.TT.3).	Section 6

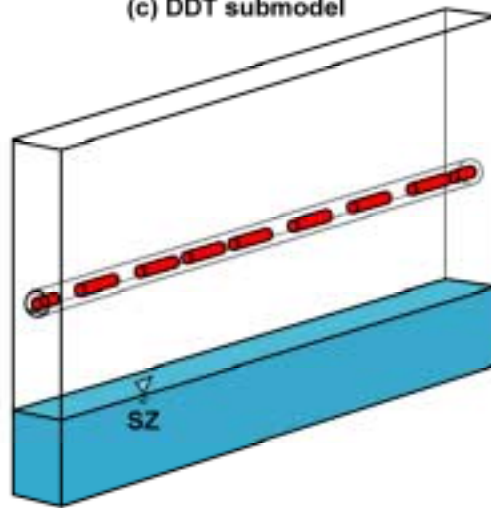
(a) SDT submodel



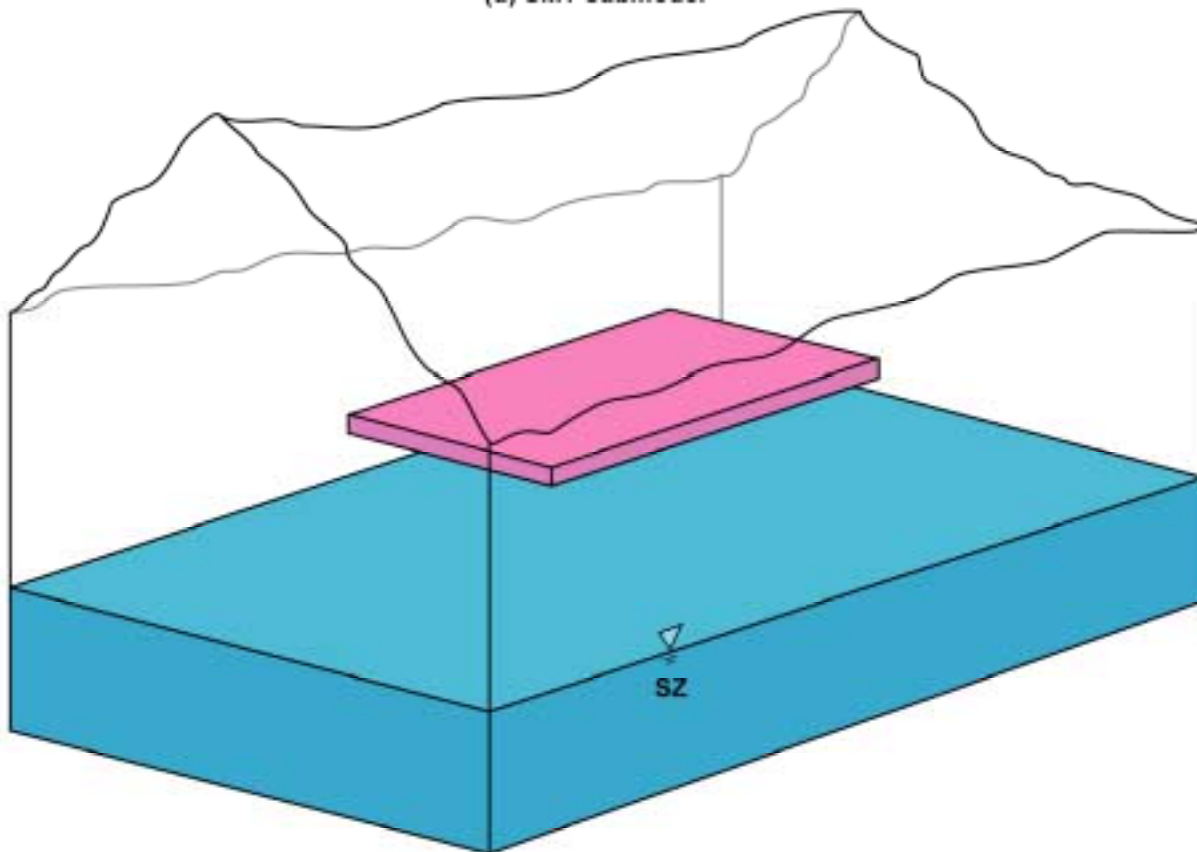
(b) LDTH submodel



(c) DDT submodel

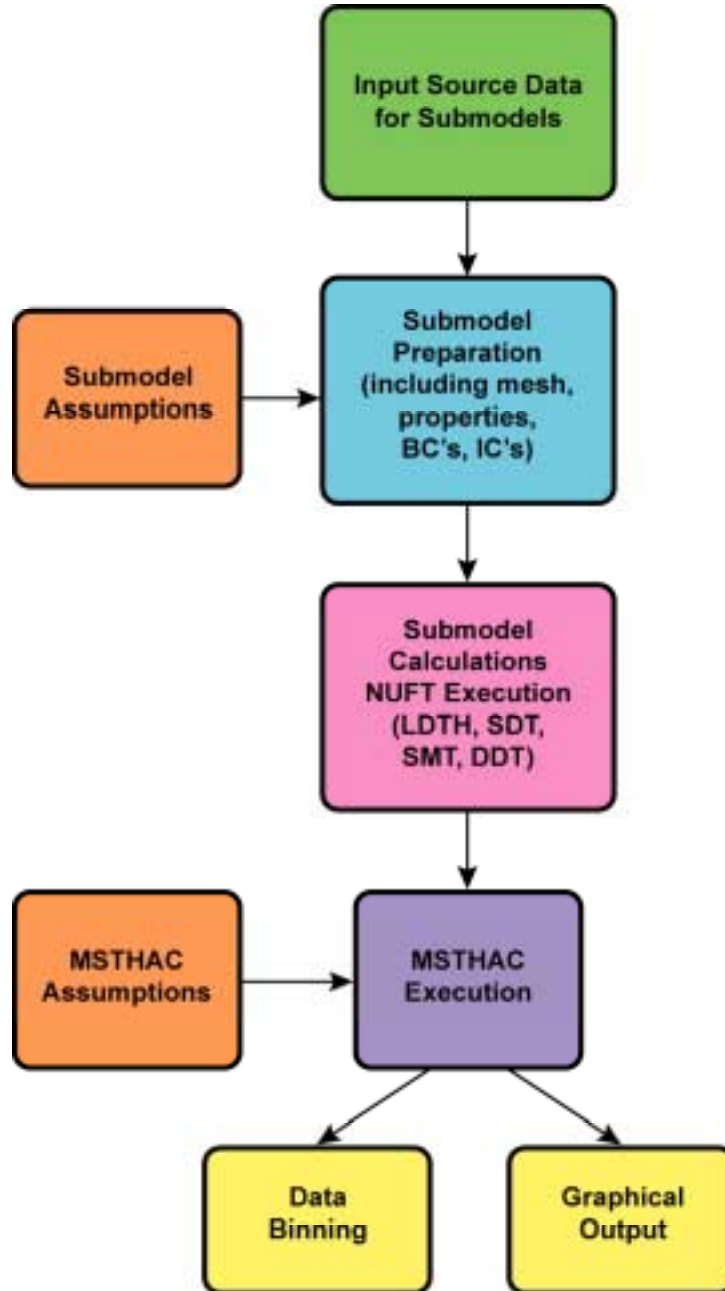


(d) SMT submodel



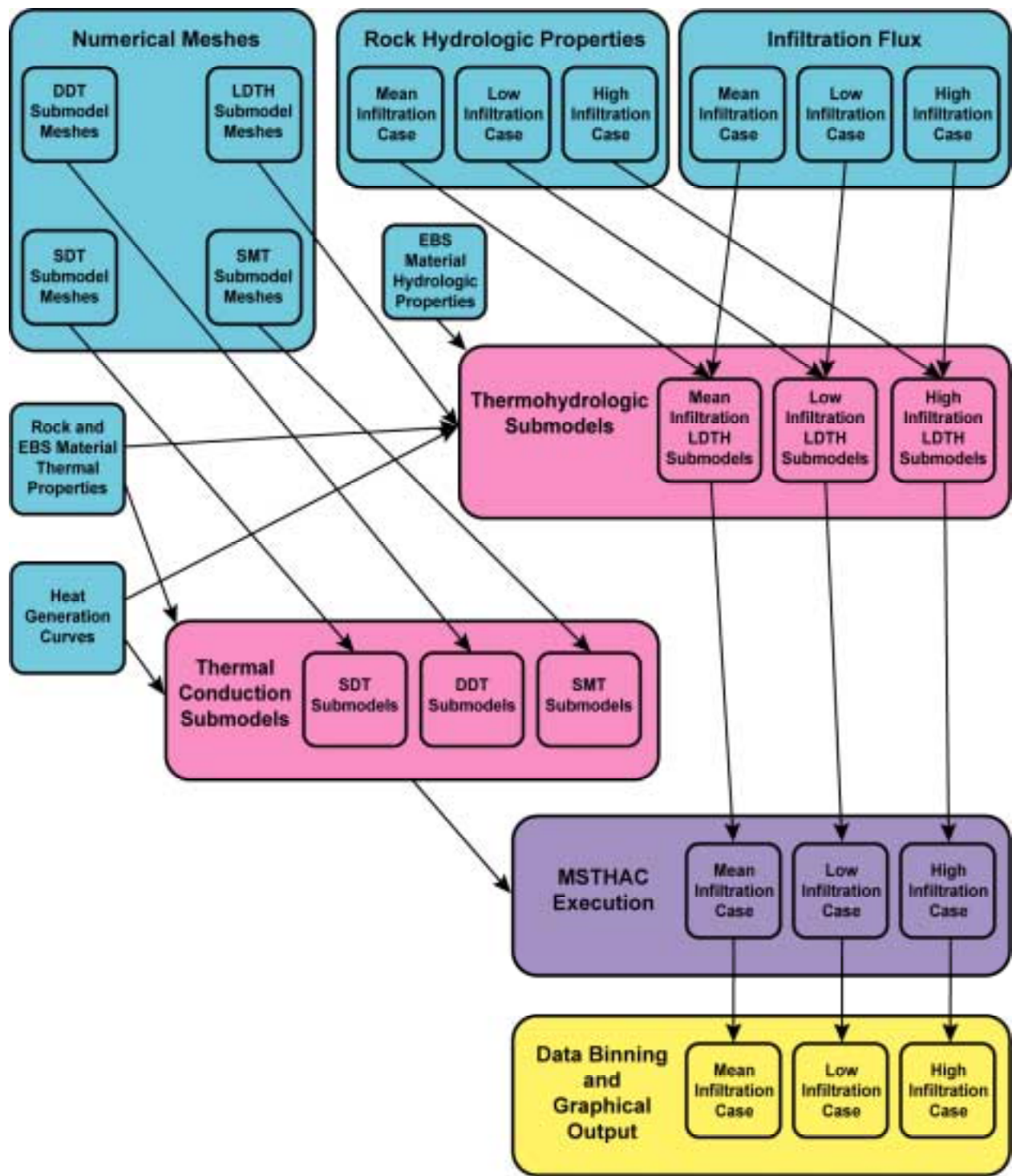
TB\_AMR\_fig1-1submod-schem

Figure 1-1. Schematic of conceptual models used by the MSTHM, including (a) SDT submodel, (b) LDTH submodel, (c) DDT submodel, and (d) SMT submodel



TB\_AMR\_fig1-2\_MSTHM\_flow

Figure 1-2. Overall data flow diagram for the MSTHM



TB\_AMR\_fig1-3\_MSTHM\_flow2

Figure 1-3. Data flow diagram for the MSTHM that shows the relationship between the input data and submodels for the three infiltration flux scenarios addressed in Rev 00

## 2. QUALITY ASSURANCE

The activity related to preparing Rev 0 ICN 01 of this document was evaluated (CRWMS M&O 1999b) in accordance with QAP-2-0, *Conduct of Activities*, and was determined to be subject to the requirements of the Quality Assurance Requirements and Description (DOE 2000). The QAP-2-3, Classification of Permanent Items, evaluation, Classification of the MGR Ex-Container System, (CRWMS M&O 1999c, p. 8) identified the ex-container system as QL-1, important to radiological safety. Water drainage is not specifically addressed in the Q-List (YMP 1998, p. II-9), but is a characteristic of the ex-container system. For this document, the classification of water drainage features are considered QL-1, important to radiological safety. The engineered barrier system is identified on the *Q-List* (YMP 1998, p. II-9) and is identified as QL-1, important to radiological safety; and QL-2, important to waste isolation.

Rev 0 and ICN 1 of this AMR were prepared in accordance with the development plan (CRWMS M&O 2000c), which was developed in accordance with the applicable versions of procedures listed in AP-2.13Q, *Technical Product Development Plan*, as documented in *Development Plan for Multiscale Thermohydrologic Model* (CRWMS M&O 2000c). ICN 2 of this AMR was initiated under the Technical Work Plan (CRWMS M&O 2000i) but was completed in accordance with the AP-2.21Q, *Quality Determinations and Planning for Scientific, Engineering, and Regulatory Compliance Activities*, as documented in *Technical Work Plan For EBS Department Modeling FY01 Work Activities* (BSC 2001) and is subject to quality assurance program controls. The applicability of the QA Program to ICN 02 of this AMR is documented in Addendum B of the technical work plan.

Qualified and accepted input data and references are identified in Section 8 of this AMR. AP-3.10Q, *Analyses and Models*, requires that output resulting from unqualified software be designated as unqualified to-be-verified (TBV) in accordance with AP-3.15Q, *Managing Technical Product Inputs*. Unqualified data used in this report have been tracked in accordance with AP-3.15Q, *Managing Technical Product Inputs*. Section 6.13 of this AMR discusses model validation. Software and routines used in this report are subject to AP-SI.1Q, *Software Management*, as discussed in Section 3 of this document.

Methods used to control electronic data as required by AP-SV.1Q, *Control of the Electronic Management of Information* were accomplished in accordance with the applicable controls specified in the *Technical Work Plan for EBS Department Modeling FY01 Work Activities*, (BSC 2001) and the *Electronic Management of Information Checklist For Management of Electronic Information Related to AMR ANL-EBS-MD-000049, Revision 00, ICN 2 and Calculation Report of TH Calculations Supporting SSPA* (LLNL 2001). Electronic media is stored, maintained, retrieved, modified, updated, and transmitted in a manner that ensures the quality of information used on the project. Data is stored on a password-protected computer hard drive stored away from heat sources, liquids, etc. Data on systems are backed up daily onto tapes and periodically transferred to CDs. Data transferred to computers outside the local computer network is accomplished using CDs, FTP, or email as appropriate in a manner that allows the user to verify the completeness and accuracy of the files sent. All data input entries pertaining to the natural systems, (i.e., host rock) are conducted through the use of qualified software routines. Entries are

periodically checked using independent hand calculations. Data input pertaining to EBS are done by hand and are checked against the source data for accuracy and completeness.

Per Section 5.9 of AP-3.10Q, *Analyses and Models*, if the data developed in this document are determined to be needed by organizations outside of the Engineered Barrier Systems Operations, the results of this model will be submitted to the Technical Data Management System in accordance with AP-SIII.3Q, *Submittal and Incorporation of Data to the Technical Data Management System*. For the backfill case, the resulting data tracking numbers (DTNs) are LL000113904242.089, LL000114004242.090, and LL000114104242.091. For the no-backfill case, the resulting DTNs are LL000509112312.003, LL000509012312.002, and LL000509212312.004. For the three-dimensional heterogeneous LDTH model (Section 6.14), the resulting DTN is LL010802723122.019.

### 3. COMPUTER SOFTWARE AND MODEL USAGE

Software and routines were used in the preparation of this AMR. Table 3-1a gives a complete list of software and routines used. Table 3-1b contains a list of the CPUs where these programs were executed. These programs were all executed at Lawrence Livermore National Laboratory. Software was obtained from Software Configuration Management, was appropriate for the application, and was used within the range of validation in accordance with AP-SI.1Q. Use of software has been documented in accordance with AP-SI.1Q. This documentation identifies the type of computer used.

Table 3-1a. Software validation

Code	Attachment where qualified (or STN)	Software Type
NUFT v3.0s	10088-3.0s-00	Software
RADPRO v3.22	10204-3.22-00	Software
XTOOL v10.1	10208-10.1-00	Software
MSTHAC v6.2 (for backfill case)	10290-6.2-00	Software
MSTHAC v6.3 (for no-backfill case)	10419-6.3-00	Software
CONVERTCOORDS v1.1	10209-1.1-00	Routine
YMESS v1.53	10172-1.53-00	Routine
makeColumns v1.0	Schreiner, 2001	Routine
define_EBS_fineGrid v1.3	Schreiner, 2001	Routine
readsUnits v1.0	Schreiner, 2001	Routine
addLayers v1.0 & addlay v1.0	Schreiner, 2001	Routine
heat_DDT v1.0 & heat_SMT v1.0	Schreiner, 2001	Routine
xairtab v1.8	Schreiner, 2001	Routine
infiltrab v1.0	Schreiner, 2001	Routine
rock_sun v1.0	Schreiner, 2001	Routine
SMT_surf_bc v1.1 & SMT_bot_bc v1.1	Schreiner, 2001	Routine
bound v1.0	Schreiner, 2001	Routine
assembly scripts LDTH*corey, SDT-01* v1.0	Schreiner, 2001	Routine
heatgenAge v1.0	Schreiner, 2001	Routine
chim_surf_TP v1.0 & chim_wt_TP v1.0	Schreiner, 2001	Routine
columnInfiltration v1.1	Schreiner, 2001	Routine
cover v1.1	Schreiner, 2001	Routine
rme6 v1.1	Schreiner, 2001	Routine
splitEXT v1.0	Schreiner, 2001	Routine
XLDTH v1.0	10581-1.0-00	Level 3

The use of any unqualified software that is to support Site Recommendation is controlled in accordance with AP-SI.1Q and is identified in the following descriptions.

The previous versions of this AMR contained the attachments that qualified the single use routines. For ICN 02 the attachments have been removed and reference is now made to the *Stand alone DR-39 Package for ANL-EBSI-MD-000049, Rev. 00, ICN 01, Multiscale Thermohydrologic Model* (Schreiner 2001). Attachment I now contains the index of those routines that were in the previous versions.

Table 3-1b. Software execution

Workstation Name	Physical Location
s139	T1487 Rm 150A
s89	T1487 Rm 150
s116	T1401 Rm 1119
s117	T1487 Rm 112
s187	T1487 Rm 153
s70	T1487 Rm 149
s11	T1487 Rm 146
s08	T1487 Rm 145
s28	T1487 Rm 154
s13	T1487 Rm 124
s188	T1487 Rm 138
s175	T1487 Rm 114

### 3.1 DESCRIPTION OF SOFTWARE

The names and software tracking numbers for the qualified codes used in this document are NUFT v3.0s (NUFT, STN: 10088-3.0s-00), RADPRO v3.22 (RADPRO, STN: 10204-3.22-00), XTOOL v10.1 (XTOOL, STN: 10208-10.1-00), MSTHAC v6.2 (MSTHAC, STN: 10290-6.2-00), MSTHAC v6.3 (MSTHAC, STN:10419-6.3-00) and XLDTH v1.0 (XLDTH, STN: 10581-1.0-00). MSTHAC v6.2 was used in Rev 0 0 of this AMR. MSTHAC v6.3 was used in ICN 01 of this AMR; neither of these versions are used in ICN 02 of this AMR; moreover, ICN 02 did not require the use of any version of MSTHAC. All other software/routines described in this AMR were qualified in the Stand Alone DR-39 Package (Schreiner 2001) and therefore do not require documentation changes per AP-SI.1Q. The software described in this section is used in the following data-flow diagrams (Figure 3-1 through Figure 3-12). A more detailed description of these diagrams is given in following sections of this AMR. The computer software used was run on computers located in Lawrence Livermore National Laboratory. Table 3-1b gives the specific office locations.

#### 3.1.1 NUFT v3.0s

NUFT v3.0s is classified as a qualified software program (per AP-SI.1Q, *Software Management*), and was obtained from configuration management. NUFT was run on a Sun Ultra 10 workstation with a SunOS 5.6 operating system. NUFT is used to predict the conditions in the EBS and natural barrier system. NUFT is appropriate for this task. (Nitao, 1998).

The stochastic near field properties generator (random field generator) option of NUFT Version 3.0s was not included in the qualification of the software. That option is being qualified in parallel with the development of Rev 00 ICN02 of this AMR. The qualification documentation is tracked as STN:10088-3.0s-01. That option is used in the analyses described in Section 6.14.

#### 3.1.2 RADPRO v3.22

RADPRO v3.22 is classified as a qualified software program (per AP-SI.1Q, *Software Management*), and was obtained from configuration management. RADPRO was run on a Sun

Ultra 10 workstation with a SunOS 5.6 operating system. RADPRO is used to predict the radiative heat transfer in the drift. RADPRO is appropriate software for this task.

### **3.1.3 XTOOL v10.1**

XTOOL v10.1 is classified as a qualified software program (per AP-SI.1Q, *Software Management*), and was obtained from configuration management. The output from XTOOL is graphical (no actual data is produced with XTOOL). XTOOL is tracked in accordance with AP-SI.1Q because it is not commercial software. XTOOL is used to develop graphical representations of the results in the NUFT output files (XVIII-files: \*.out). XTOOL is appropriate software for this task. Software programs used to produce figures that are not used for model validation are exempt from AP-SI.1Q requirements. XTOOL was run on a Sun Ultra 10 workstation with a SunOS 5.6 operating system.

### **3.1.4 MSTHAC v6.2**

MSTHAC v6.2 is classified as a qualified software program (per AP-SI.1Q, *Software Management*), and was obtained from configuration management. MSTHAC v6.2 was run on a Sun Ultra 10 workstation with a SunOS 5.6 operating system. MSTHAC v6.2 is used to predict the multiscale TH conditions for the backfill case (Rev 00) based on the various NUFT submodel runs. MSTHAC v6.2 is appropriate software for this task.

During checking of R00 ICN02 of this AMR, a defect was found in MSTHAC Version 6.2. This defect was documented on a Software Defect Notice ( SDN009020010730, Software Defect Notification). The results in this process level AMR are not affected by the defect. The defect was incorrect binning of results which are used in the MSTH Abstraction AMR (CRWMS M&O 2001c). The software was removed from the qualified software list as a result of the Defect Notice, pending impact evaluations.

### **3.1.5 MSTHAC v6.3**

MSTHAC v6.3 is classified as a qualified software program (per AP-SI.1Q, *Software Management*), and was obtained from configuration management. MSTHAC v6.3 was run on a Sun Ultra 10 workstation with a SunOS 5.6 operating system. MSTHAC v6.3 is used to predict the multiscale TH conditions for the no-backfill case (ICN 01) based on the various NUFT submodel runs. MSTHAC v6.3 is appropriate software for this task.

During checking of R00 ICN02 of this AMR, a defect was found in MSTHAC Version 6.3. This defect was documented on a Software Defect Notice (SDN009120010730, Software Defect Notification). The results in this process level AMR are not affected by the defect. The defect was incorrect binning of results, which are used in the MSTH Abstraction AMR (CRWMS M&O 2001c). The software was removed from the qualified software list as a result of the Defect Notice, pending impact evaluations.

## **3.2 DESCRIPTION OF ROUTINES AND MACROS**

All routines and macros used in the preparation of this document are qualified (see Table 3-1) or have associated software tracking numbers. The qualified routines used in this document are CONVERTCOORDS v1.1 (CONVERTCOORDS, STN: 10209-1.1-00), YMESH v1.53 (YMESH, STN: 10172-1.53-00) and XLDTH v1.0, (XLDTH, STN: 10581-1.0-00). All other software/routines described in this AMR were qualified in accordance with AP-SI-1Q, Rev 2 and therefore do not require documentation changes per AP-SI.1Q, Rev 3.

### **3.2.1 MakeColumns v1.0**

MakeColumns v1.0 is classified as a routine per AP-SI.1Q. It creates a family of YMESH input files to generate a family of chimney meshes at a set of specified locations. The input files to makeColumns are column\_template and column.data (CRWMS M&O 2000a). This routine is qualified in (Schreiner, 2001) and is appropriate for its purpose. MakeColumns was run on a Sun Ultra 2 workstation with a SunOS 5.5.1 operating system. MakeColumns was developed using a C++ compiler.

### **3.2.2 Rme6 v1.1**

Rme6 v1.1 is classified as a routine per AP-SI.1Q. It converts world view data files to a format readable by YMESH. The input files to rme6 are tspa99\_primary\_mesh and UZ99\_3.grd (CRWMS M&O 2000a). The output file is LBL99-YMESH (CRWMS M&O 2000a). Rme6 is qualified in (Schreiner, 2001) and is appropriate for its purpose. Rme6 was run on a Sun Ultra 2 workstation with a SunOS 5.5.1 operating system. Rme6 was developed using a C++ compiler.

### **3.2.3 Define\_EBS\_fineGrid v1.3**

Define\_EBS\_fineGrid v1.3 is classified as a routine per AP-SI.1Q. Its purpose is to convert NUFT genmsh files, created with YMESH, to separate sets of “matrix” and “fracture” mesh definition instructions, and to add a mapping of materials for the EBS to the mesh. Input files for the routine are \*.nft (CRWMS M&O 2000a). Output files are \*.nft.msh.dkm.m, \*.nft.msh.dkm.f, \*.nft.msh.dkm0, \*.nft.msh.dkm0.m, and \*.nft.msh.dkm0.f (CRWMS M&O 2000a). Define\_EBS\_fineGrid is qualified in (Schreiner, 2001), and is appropriate for its purpose. Define\_EBS\_fineGrid was run on a Sun Ultra 2 workstation with a SunOS 5.5.1 operating system. Define\_EBS\_fineGrid was developed using a C++ compiler.

### **3.2.4 ReadsUnits v1.0**

ReadsUnits v1.0 is classified as a routine per AP-SI.1Q. It converts YMESH column type output to NUFT comments indicating for each rock layer how thick the layer is for a given column. It adds together the widths of adjoining zones of the same material, if any. The input to readsUnits is a file “results” and the output is called “results.units” (CRWMS M&O 2000a). ReadsUnits is qualified in (Schreiner, 2001) and is appropriate for its purpose. ReadsUnits was run on a Sun Ultra 2 workstation with a SunOS 5.5.1 operating system. ReadsUnits was developed using a C++ compiler.

### **3.2.5 AddLayers v1.0**

AddLayers v1.0 is classified as a routine per AP-SI.1Q. AddLayers modifies NUFT mesh input data by adding an atmosphere or “atm” layer to the top and a water table or “wt” layer to the bottom of the zones for a chimney. The atm layer has depth zero, and the wt layer falls below the lowest rock layer. The routine is qualified in (Schreiner, 2001) and is appropriate for its purpose. AddLayers was run on a Sun Ultra 2 workstation with a SunOS 5.5.1 operating system. AddLayers was developed using a C++ compiler.

### **3.2.6 Heat\_DDT v1.0**

Heat\_DDT v1.0 is classified as a macro per AP-SI.1Q. It extracts heat generation data for chimneys from file DWperimeter (CRWMS M&O 2000a) and rewrites it in NUFT heat generation input data format. Heat\_DDT is qualified in (Schreiner, 2001) and is appropriate for its purpose. Heat\_DDT was run on a Sun Ultra 2 workstation with a SunOS 5.5.1 operating system. Heat\_DDT was developed using Matlab.

### **3.2.7 Heat\_SMT v1.0**

Heat\_SMT v1.0 is classified as a macro per AP-SI.1Q. It extracts heat generation data for the mountain scale model from file heatTSPA00.dat and rewrites it in NUFT heat generation input data format. Heat\_SMT is qualified in (Schreiner, 2001) and is appropriate for its purpose. Heat\_SMT was run on a Sun Ultra 2 workstation with a SunOS 5.5.1 operating system. Heat\_SMT was developed using Matlab.

### **3.2.8 Cover v1.1**

Cover v1.1 is classified as a macro per AP-SI.1Q. The purpose of cover.m v1.1 is to make a block model of the plan view of the repository that approximates the area and location of the emplacement. This macro is qualified in (Schreiner, 2001) and is appropriate for its purpose. Cover was run on a Sun Ultra 2 workstation with a SunOS 5.5.1 operating system. Cover was developed using Matlab.

### **3.2.9 ColumnInfiltration v1.1**

ColumnInfiltration v1.1 is classified as a routine per AP-SI.1Q. The purpose of this routine is to interpolate the infiltration at a given (x,y) location using a Gaussian weighting function (4.1.2).

This routine is qualified in (Schreiner, 2001) and is appropriate for its purpose. This routine was run on a Sun Ultra 2 workstation with a SunOS 5.5.1 operating system. ColumnInfiltration was developed using a C++ compiler.

### **3.2.10 Chim\_surf\_TP v1.0**

Chim\_surf\_TP v1.0 is classified as a routine per AP-SI.1Q. The purpose of chim\_surf\_TP is to interpolate the temperature and pressure at the ground surface for a given location using the inverse distance cubed method. This routine is qualified in (Schreiner, 2001) and is appropriate

for its purpose. Chim\_surf\_TP was run on a Sun Ultra 2 workstation with a SunOS 5.5.1 operating system. Chim\_surf\_TP was developed using a Fortran compiler.

### **3.2.11 Chim\_wt\_TP v1.0**

Chim\_wt\_TP v1.0 is classified as a routine per AP-SI.1Q. The purpose of chim\_wt\_TP is to interpolate the temperature and pressure at the water table for a given location using the inverse distance cubed method. This routine is qualified in (Schreiner, 2001) and is appropriate for its purpose. Chim\_wt\_TP was run on a Sun Ultra 2 workstation with a SunOS 5.5.1 operating system. Chim\_wt\_TP was developed using a Fortran compiler.

### **3.2.12 Xairtab v1.8**

Xairtab v1.8 is classified as a routine per AP-SI.1Q. Xairtab reads the boundary condition file chimney\_surface\_TP (CRWMS M&O 2000a) and computes air mass fraction and liquid enthalpy at the surface for each chimney. Xairtab is qualified in (Schreiner, 2001) and is appropriate for its purpose. Xairtab was run on a Sun Ultra 2 workstation with a SunOS 5.5.1 operating system. Xairtab was developed using a C++ compiler.

### **3.2.13 Infiltrab v1.0**

Infiltrab v1.0 is classified as a macro per AP-SI.1Q. It extracts infiltration flux data from the input file infiltration.tex (CRWMS M&O 2000a) and writes the following 9 output files (CRWMS M&O 2000a) in matrix format: Median\_g.dat, Median\_m.dat, Median\_p.dat, low\_g.dat, low\_m.dat, low\_p.dat, upper\_g.dat, upper\_m.dat, and upper\_p.dat. Infiltrab.m is qualified in (Schreiner, 2001) and is appropriate for its purpose. Infiltrab was run on a Sun Ultra 2 workstation with a SunOS 5.5.1 operating system. Infiltrab was developed using Matlab.

### **3.2.14 Rock\_sun v1.0**

Rock\_sun v1.0 is classified as a macro per AP-SI.1Q. Its purpose is to extract material property data from the 1d\_driftscale\*.prn files (CRWMS M&O 2000a) and rewrite it formatted as input for NUFT. Rock\_sun is qualified in (Schreiner, 2001) and is appropriate for its purpose. Rock\_sun was run on a Sun Ultra 2 workstation with a SunOS 5.5.1 operating system. Rock\_sun was developed using Matlab.

### **3.2.15 SMT\_surf\_bc v1.1**

SMT\_surf\_bc v1.1 is classified as a routine per AP-SI.1Q. The purpose of SMT\_surf\_bc is to interpolate the temperature at the ground surface for a given location using the inverse distance squared method. It was demonstrated to perform in the expected manner (Schreiner, 2001). SMT\_surf\_bc was run on a Sun Ultra 2 workstation with a SunOS 5.5.1 operating system. SMT\_surf\_bc was developed using a Fortran compiler.

### **3.2.16 SMT\_bot\_bc v1.1**

SMT\_bot\_bc v1.1 is classified as a routine per AP-SI.1Q. The purpose of SMT\_bot\_bc is to interpolate the temperature at the ground botace for a given (x,y) location using the inverse distance squared method. It was demonstrated to perform in the expected manner (see Schreiner, 2001). SMT\_bot\_bc was run on a Sun Ultra 2 workstation with a SunOS 5.5.1 operating system. SMT\_bot\_bc was developed using a Fortran compiler.

### **3.2.17 Bound v1.0**

Bound v1.0 is classified as a macro per AP-SI.1Q. Bound computes temperatures at 1000 m below the water table. Bound takes as input a thermal conductivity file, tcond\_wet.dat, the \*.units file generated by readsUnits from YMESH column output (containing material thicknesses), the temperature\_S surface temperature from LDTH boundary conditions, and the temperature\_W water table temperature also from LDTH boundary conditions. It writes the file T\_bottom.dat. Bound was demonstrated to behave according to expectations (see Schreiner, 2001). Bound was run on a Sun Ultra 2 workstation with a SunOS 5.5.1 operating system. Bound was developed using Matlab.

### **3.2.18 Addlay v1.0**

Addlay v1.0 is classified as a routine per AP-SI.1Q. Addlay v1.0, like addLayers, reads a NUFT genmsh file generated by YMESH and inserts an atmospheric and a water table layer at the top and bottom of the mesh. In addition, it removes the five lines of NUFT instructions preceding the vertical zone thickness definitions and the final closing parenthesis. Addlay demonstrated correct behavior relative to its objective (see Schreiner, 2001). Addlay was run on a Sun Ultra 2 workstation with SunOS 5.5.1 operating system. Addlay was developed using a C++ compiler.

### **3.2.19 Assembly Scripts LDTH\*corey, SDT-01\*v1.0**

The following twelve input assembly scripts, all v1.0, are classified as routines per AP-SI.1Q: LDTH-i-li-corey, LDTH-i-mi-corey, LDTH-i-ui-corey, LDTH-01-li-corey, LDTH-01-mi-corey, LDTH-01-ui-corey, LDTH-01v-li-corey, LDTH-01v-mi-corey, LDTH-01v-ui-corey, SDT-01i, SDT-01, SDT-01v. These scripts build NUFT input files from component subfiles of various types. The scripts were shown to perform in the expected manner (see Schreiner, 2001). The scripts were run on a Sun Ultra 2 workstation with a SunOS 5.5.1 operating system. Input assembly scripts were developed using the c-shell V5.1.1.

### **3.2.20 HeatgenAge v1.2**

HeatgenAge v1.2 is classified as a routine per AP-SI.1Q. HeatgenAge reads a heat generation file and performs two transformations on it: (1) aging the fuel by a number of years, skipping ahead a number of years in the data set and subtracting that number of years from the times of the remaining entries, and (2) ventilating the system for a number of years, removing a specified fraction of the heat during the aging period. HeatgenAge performed as expected (see Schreiner 2001). HeatgenAge was run on a Sun Ultra 2 workstation with a SunOS 5.5.1 operating system. HeatgenAge was developed using a C++ compiler.

### **3.2.21 SplitEXT v1.0**

SplitEXT v1.0 is classified as a routine per AP-SI.1Q. SplitEXT splits the .ext output file from MSTHAC into separate .ext files containing the output for each variable. If the input file is <name>.ext, then the output files will be <name>.<var>.ext for all variables. SplitEXT is qualified in (Schreiner, 2001). It was run on a Sun Ultra 2 workstation with a SunOS 5.5.1 operating system. SplitEXT was developed using a C++ compiler.

### **3.2.22 YMESH v1.53**

YMESH v1.53 is classified as a routine per AP-SI.1Q, has the following associated STN: 10172-1.53-00, and was obtained from configuration management. YMESH is used in this model to interpolate the thickness of the stratigraphic units at given locations. The input file for YMESH is LBL99-YMESH (CRWMS M&O 2000a). The output from this software is column.dat (CRWMS M&O 2000a). YMESH is appropriate software for this task. YMESH was run on a Sun Ultra 2 workstation with a SunOS 5.5.1 operating system.

### **3.2.23 CONVERTCOORDS v1.1**

CONVERTCOORDS v1.1 is classified as a routine per AP-SI.1Q, has the following associated STN: 10209-1.1-00, and was obtained from configuration management. CONVERTCOORDS is used to convert from Universal Transverse Mercator coordinates to Nevada State Plane coordinates, as well as to reformat the data (CRWMS M&O 2000a, files: \*.inf). The desired format is columns of data, with the input files in a matrix format. CONVERTCOORDS is appropriate software for this task. CONVERTCOORDS was run on a Sun Ultra 2 workstation with a SunOS 5.5.1 operating system.

### **3.2.24 XLDTH v1.0**

XLDTH v1.0, which is classified as a Level 3 Code per AP-SI.1Q, is a data-extraction routine that reads the .ext output file from 3-D LDTH models, described in Section 6.14. The output of XLDTH is .ptlsc files that can be read by XTOOL v10.1 (or any other version of XTOOL). XLDTH was run on a Sun Ultra 2 workstation with a SunOS 5.7 operating system. XLDTH v1.0 was developed using a C++ compiler.

## **3.3 DATA FLOW**

Tables 3-2 – 3-9 allow for more efficient use of Figures 3-1 – 3-12. There are three kinds of alpha-numeric codes used in the data flowchart figures.

1. Those starting with an N represent an operation explained in a footnote that results in the creation of one or more files. These operations have output files, but no input files. Table 3-2 explains the operations involved.

2. Alpha-numeric codes starting with an E represent editing type operations. These operations have input and output files. Table 3-3 explains the operations involved.
3. All other codes represent groups of files that flow from one page to the next. Table 3-4 lists these files as well as the figures of origin and destination.

Table 3-5 gives the name of the input and output file for software routines used in this document, as well as the figure(s) where the routine is used and the input source(s). Tables 3-6 – 3-9 give similar information for NUFT. Attachment I provides the names of the input and output files for RADPRO, XTOOL, MSTHAC, YMESH, and CONVERTCOORDS.

Table 3-2a. N-table for backfill case

α# *	Fig.	Output File Names	Notes
N:M1	3-2	SDT:\column_template	Mesh column_template for LDTH and SDT
N:M2	3-2	LDTH:\column_template	The grid files for the SMT model are specified by applying several criteria: <ul style="list-style-type: none"> <li>- The east boundary is to be parallel to the actual repository boundary.</li> <li>- The repository edge has a finer grid to allow the MSTHM algorithm to treat edge effects appropriately.</li> <li>- The grid blocks are each to correspond to an integral number of drifts in order to simplify the final parameter mapping.</li> </ul>
N:L1	3-9	run_control_param_LDTH-v00 run_control_param_LDTH-v01	Run control parameters provide setup of the numerical control of the simulation code itself to achieve reasonable efficiency in the computation
N:L2	3-9	<aml>infil <aml>pre-closure <aml>post-closure	LDTH Templates
N:L3	3-9	output.times-00v output.times-<aml>-00	Run control parameters provide setup of the numerical control of the simulation code itself to achieve reasonable efficiency in the computation
N:S1	3-10	SDT-00tplt	SDT Templates
N:S2	3-10	output.times-00v output.times-<aml>-00	The output times files contain the list of times for which parameter values are to be written to the output stream. The criterion for the choice of times is to achieve suitable time resolution, especially when the relative humidity in the drift is varying rapidly. An appropriate choice of times was discovered empirically
N:D1	3-11	run_control_param_DDT-v01 run_control_param_DDT-v02	Run control parameters provide setup of the numerical control of the simulation code itself to achieve reasonable efficiency in the computation
N:D2	3-11	output.times-DDT60-00	The output times files contain the list of times for which parameter values are to be written to the output stream. The criterion for the choice of times is to achieve suitable time resolution, especially when the relative humidity in the drift is varying rapidly. An appropriate choice of times was discovered empirically
N:D3	3-11	DDT60-03.radin DDT60-03v.radin DDT60-03pbf.radin	The radin files are used to specify which surfaces may be coupled via radiation, and to provide emissivity assignments to the surfaces.
N:T1	3-12	run_control_param_SMT-v01	Run control parameters provide setup of the numerical control of the simulation code itself to achieve reasonable efficiency in the computation.
N:T2	3-12	output.times-SMT60-00	The output times files contain the list of times for which parameter values are to be written to the output stream. The criterion for the choice of times is to achieve suitable time resolution, especially when the relative humidity in the drift is varying rapidly. An appropriate choice of times was discovered empirically
N:T3	3-12	SMT-1Dds-mi-sz	Set properties of natural system materials in the saturated zone. The material is assumed to be identical to that found at the bottom of the unsaturated zone.
<p>* This column gives the alpha numeric designator used in the figure referenced in the "Fig." column.                      N:xx allows a free-form textual note to be attached to a given operation. In this case, there is not typically an input file to the step, but the information is originated in some sort of analyst input from domain expertise, and is at this point encapsulated.                      The analyst input involved is briefly described in the table notes, and a larger explanation may be found in the text.</p>			

Table 3-2b. N-table for no-backfill case

$\alpha$ # *	Fig.	Output File Names	Notes
N:M1	3-2	SDT:\column_template	Mesh column_template for LDTH and SDT
N:M2	3-2	LDTH:\column_template	The grid files for the SMT model are specified by applying several criteria: - The east boundary is to be parallel to the actual repository boundary. - The repository edge has a finer grid to allow the MSTHM algorithm to treat edge effects appropriately. - The grid blocks are each to correspond to an integral number of drifts in order to simplify the final parameter mapping.
N:L1	3-9	run_control_param_LDTH-v00 run_control_param_LDTH-v01	Run control parameters provide setup of the numerical control of the simulation code itself to achieve reasonable efficiency in the computation
N:L2	3-9	<aml>infil <aml>pre-closure <aml>post-closure	LDTH Templates
N:L3	3-9	output.times-00v output.times-<aml>-00	Run control parameters provide setup of the numerical control of the simulation code itself to achieve reasonable efficiency in the computation
N:S1	3-10	SDT-00tplt	SDT Templates
N:S2	3-10	output.times-00v output.times-<aml>-20	The output times files contain the list of times for which parameter values are to be written to the output stream. The criterion for the choice of times is to achieve suitable time resolution, especially when the relative humidity in the drift is varying rapidly. An appropriate choice of times was discovered empirically
N:D1	3-11	run_control_param_DDT-v01 run_control_param_DDT-v02	Run control parameters provide setup of the numerical control of the simulation code itself to achieve reasonable efficiency in the computation
N:D2	3-11	output.times-DDT60-20	The output times files contain the list of times for which parameter values are to be written to the output stream. The criterion for the choice of times is to achieve suitable time resolution, especially when the relative humidity in the drift is varying rapidly. An appropriate choice of times was discovered empirically
N:D3	3-11	DDT60-03.radin DDT60-03v.radin DDT60-03pbf.radin	The radin files are used to specify which surfaces may be coupled via radiation, and to provide emissivity assignments to the surfaces.
N:T1	3-12	run_control_param_SMT-v01	Run control parameters provide setup of the numerical control of the simulation code itself to achieve reasonable efficiency in the computation.
N:T2	3-12	output.times-SMT56-20	The output times files contain the list of times for which parameter values are to be written to the output stream. The criterion for the choice of times is to achieve suitable time resolution, especially when the relative humidity in the drift is varying rapidly. An appropriate choice of times was discovered empirically
N:T3	3-12	SMT-1Dds-mi-sz	Set properties of natural system materials in the saturated zone. The material is assumed to be identical to that found at the bottom of the unsaturated zone.

\* This column gives the alpha numeric designator used in the figure referenced in the "Fig." column.

N:xx allows a free-form textual note to be attached to a given operation. In this case, there is not typically an input file to the step, but the information is originated in some sort of analyst input from domain expertise, and is at this point encapsulated.

The analyst input involved is briefly described in the table notes, and a larger explanation may be found in the text.

Table 3-3a. E-table for backfill case

$\alpha$ # *	Fig.	Input File Name(s)**	Output File Names**	Notes
E:M1	3-2	I4c3.dat	I4c3.03v.dat	Refine the input LDTH grid to sufficiently describe thermal radiation processes.
E:M2	3-2	DTN file, I4c3.03v.dat	I4c3.dat	Refine grid within drift to properly describe post-closure engineered system material distribution, especially drip shield emplacement.
E:M3	3-2	shape.dat	column.data	Chimney locations are chosen in a regular array parallel to the major axis (East side) of the MSTHM repository footprint.
E:M4	3-2	PALtem1Att10817	dft1.dat	Removed the column headers.
E:H1	3-3	heatTSPA-SR-99184.dat	heatTSPA00.dat	Removed the column headers and reorganized the parameter values into a matrix format for Matlab to read.
E:H2	3-3	2-DWperimeter.dat	Dwperimeter.txt	
E:H3	3-3	2-DWperimeter.dat	line-load-heat	Place the data columns of Time and Averaged Heat Transfer into NUET format (in a compflux block).
E:B1	3-5	chimney_surface_TP	temperature_s	The files chimney_wt_TP and chimney_surface_TP are transformed into temperature_W and temperature_S, respectively, by laying out the temperature data found in the source file into an array format of 7x5 rather than a list. All other (non-temperature) source data is discarded.
E:B1	3-5	chimney_wt_TP	temperature_w	
E:C1	3-6	B-1, B-2, I-L0	LDTH-i-li-corey	LDTH initial script
E:C1	3-6	B-1, B-2, I-M0	LDTH-i-mi-corey	
E:C1	3-6	B-1, B-2, I-U0	LDTH-i-ui-corey	
E:C2	3-6	B-1, B-2, I-L0, I-L1	LDTH-01v-li-corey	LDTH ventilation script
E:C2	3-6	B-1, B-2, I-M0, I-M1	LDTH-01v-mi-corey	
E:C2	3-6	B-1, B-2, I-U0, I-U1	LDTH-01v-ui-corey	
E:C3	3-6	B-1, B-2, I-L0, I-L1	LDTH-01-li-corey	LDTH main script
E:C3	3-6	B-1, B-2, I-M0, I-M1	LDTH-01-mi-corey	
E:C3	3-6	B-1, B-2, I-U0, I-U1	LDTH-01-ui-corey	
E:R1	3-7	dkm-afc-1Dds-mc-mi-00	SDT-1Dds-mi	Removed all hydrologic properties and set thermal properties to the appropriate wet material properties.
E:P1	3-8	DTN unknown file name	R-1,R-1v,R-2,R-3,R-D	Tabulated In-drift and Thermal Properties Used in Drift-scale Models for TSPA-SR (Rev 01) to create EBS material properties files.
E:S1	3-10	B-1	SDT-01i	SDT initial script
E:S2	3-10	B-1	SDT-01v	SDT ventilation script
E:S3	3-10	B-1	SDT-01	SDT main script
E:D1	3-11	M-D1	I4c3-DDT60-03v.in	DDT initial script
E:D2	3-11	M-D2	I4c3-DDT60-03pbf.in	DDT ventilation script
E:D3	3-11	M-D2	I4c3-DDT60-03bff.in	DDT main script
E:T1	3-12	thermal_UZ.xls	SMT-1Dds-mi-flt	Manually format rock property information for materials in fault areas into NUET input file format.

\* This column gives the alpha numeric designator used in the figure referenced in the "Fig." column.

\*\* File sets denoted with alpha numeric designators are listed in Table 3-4.

E:xx refers to an editing operation. This indicates that the transformation from input to output file incorporates some analyst input not previously encapsulated in the input file to the step, or that unnecessary information was removed.

The analyst input involved is briefly described in the table notes, and a larger explanation may be found in the text.

Table 3-3b. E-table for no-backfill case

α# *	Fig.	Input File Name(s)**	Output File Names**	Notes
E:M1	3-2	l4c3.dat	l4c3.03v.dat	Refine the input LDTH grid to sufficiently describe thermal radiation processes.
E:M2	3-2	DTN file, l4c3.03v.dat	l4c3.dat	Refine grid within drift to properly describe post-closure engineered system material distribution, especially drip shield emplacement.
E:M3	3-2	shape.dat	column.data	Chimney locations are chosen in a regular array parallel to the major axis (East side) of the MSTHM repository footprint.
E:M4	3-2	PAItem1Att10817	dft1.dat	Removed the column headers.
E:H1	3-3	heatTSPA-SR-99184.dat	heatTSPA00.dat	Removed the column headers and reorganized the parameter values into a matrix format for Matlab to read.
E:H2	3-3	2-DWperimeter.dat	Dwperimeter.txt	
E:H3	3-3	2-DWperimeter.dat	line-load-heat-1.45	Place the data columns of Time and Averaged Heat Transfer into NUFT format (in a complux block).
E:B1	3-5	chimney_surface_TP	temperature_s	The files chimney_wt_TP and chimney_surface_TP are transformed into temperature_W and temperature_S, respectively, by laying out the temperature data found in the source file into an array format of 7x5 rather than a list. All other (non-temperature) source data is discarded.
E:B1	3-5	chimney_wt_TP	temperature_w	
E:C1	3-6	B-1, B-2, I-L0	LDTH-i-li-corey	LDTH initial script
E:C1	3-6	B-1, B-2, I-M0	LDTH-i-mi-corey	
E:C1	3-6	B-1, B-2, I-U0	LDTH-i-ui-corey	
E:C2	3-6	B-1, B-2, I-L0, I-L1	LDTH-20v-li-corey	LDTH ventilation script
E:C2	3-6	B-1, B-2, I-M0, I-M1	LDTH-20v-mi-corey	
E:C2	3-6	B-1, B-2, I-U0, I-U1	LDTH-20v-ui-corey	
E:C3	3-6	B-1, B-2, I-L0, I-L1	LDTH-20-li-corey	LDTH main script
E:C3	3-6	B-1, B-2, I-M0, I-M1	LDTH-20-mi-corey	
E:C3	3-6	B-1, B-2, I-U0, I-U1	LDTH-20-ui-corey	
E:R1	3-7	dkm-afc-1Dds-mc-mi-00	SDT-1Dds-mi	Removed all hydrologic properties and set thermal properties to the appropriate wet material properties.
E:P1	3-8	DTN unknown file name	R-1,R-1v,R-2,R-3,R-D	Tabulated In-drift and Thermal Properties Used in Drift-scale Models for TSPA-SR (Rev 01) to create EBS material properties files
E:S1	3-10	B-1	SDT-01i	SDT initial script
E:S2	3-10	B-1	SDT-20v	SDT ventilation script
E:S3	3-10	B-1	SDT-20	SDT main script
E:D1	3-11	M-D1	l4c3-DDT60-20v.in	DDT initial script
E:D2	3-11	M-D2	l4c3-DDT60-20pbf.in	DDT ventilation script
E:D3	3-11	M-D2	l4c3-DDT60-20ss.in	DDT main script
E:T1	3-12	thermal_UZ.xls	SMT-1Dds-mi-flt	Manually format rock property information for materials in fault areas into NUFT input file format.

\* This column gives the alpha numeric designator used in the figure referenced in the "Fig." column.

\*\* File sets denoted with alpha numeric designators are listed in Table 3-4.

E:xx refers to an editing operation. This indicates that the transformation from input to output file incorporates some analyst input not previously encapsulated in the input file to the step, or that unnecessary information was removed.

The analyst input involved is briefly described in the table notes, and a larger explanation may be found in the text.

Table 3-4a. File groups for backfill case

$\alpha$ #*	Figure		File names
	Created in	Used in	
M-1	3-2	3-5	column.data
M-M0	3-2	3-5	tspa00-mesh00
M-M1	3-2	3-12	tspa00-mesh01
M-M2	3-2	3-12	tspa00-mesh02
M-D1	3-2	3-11	l4c3.03v.nft.msh.ddt
M-D2	3-2	3-11	l4c3.nft.msh.ddt
M-L0<column>	3-2	3-9	LDTH:\<column >.col.units <column >.nft.msh.dkm0.f <column >.nft.msh.dkm0.m
M-L1<column>	3-2	3-9	<column >.col.units <column >.nft.msh.dkm.f <column >.nft.msh.dkm.m
M-S<column >	3-2	3-5, 3-10	<column >.nft.msh.dkm0 SDT:\<column >.col.units
H-D0	3-3	3-11	SMT-0.3Qheat-1e6y_vent-00v
H-D1	3-3	3-11	SMT-0.3Qheat-50y_vent-00
H-L0	3-3	3-9, 3-10	LDTH-SDT-0.3Qheat-1e6y_vent-00v
H-L1	3-3	3-9, 3-10	LDTH-SDT-0.3Qheat-50y_vent-00
H-M0	3-3	3-12	SMT-0.3Qheat-1e6y_vent-02v
H-M1	3-3	3-12	SMT-0.3Qheat-50y_vent-02
I-L0	3-4	3-6	low_p.dat
I-L1	3-4	3-6	low_g.dat low_m.dat
I-M0	3-4	3-6	Median_p.dat
I-M1	3-4	3-6	Median_g.dat Median_m.dat
I-U0	3-4	3-6	upper_p.dat
I-U1	3-4	3-6	upper_g.dat upper_m.dat
B-1	3-5	3-6, 3-10	chimney_wt_TP chimney_surface_TP
B-2	3-5	3-6	Enthalpy.dat X.air
B-3	3-5	3-12	SMT_surfbc
B-4	3-5	3-12	SMT_bsmtbc
XL-0<infil>	3-6	3-9	LDTH-i-li-corey LDTH-i-mi-corey LDTH-i-ui-corey
XL-1<infil>	3-6	3-9	LDTH-01v-li-corey LDTH-01v-mi-corey LDTH-01v-ui-corey
XL-2<infil>	3-6	3-9	LDTH-01-li-corey LDTH-01-mi-corey LDTH-01-ui-corey

\* This column gives the alpha numeric designator used in the respective figure

Table 3-4a. File groups for backfill case (Continued)

$\alpha$ #	Figure		File names
	Origin	Dest.	
R-S	3-7	3-10, 3-11, 3-12	SDT-1Dds-mi
R-L<umn>	3-7	3-9	dkm-afc-1Dds-mc-li-00 dkm-afc-1Dds-mc-mi-00 dkm-afc-1Dds-mc-ui-00
R-1	3-8	3-9, 3-11	modprop_dr-up-00
R-1v	3-8	3-9, 3-11	modprop_dr-up-00v
R-2	3-8	3-9	dkm-afc-pbf-EBS_Rev10
R-3	3-8	3-9	dkm-afc-EBS_Rev10
R-D	3-8	3-9, 3-11	DDT-EBS_Rev00
LDTH-0<AIC>	3-9	LDTH out	<column>-LDTH<aml>-1Dds_mc-<infil>-01v.ext
LDTH-1<AIC>	3-9	LDTH out	<column>-LDTH<aml>-1Dds_mc-<infil>-01.ext
SDT-0<AC>	3-10	SDT out	<column>-SDT-<aml>-01v.ext
SDT-1<AC>	3-10	SDT out	<column>-SDT-<aml>-01.ext
S-Z	3-10	3-11	l4c3-SDT-01-i.ztab
DDT-0	3-11	DDT out	l4c3-DDT60-03v.EBS.ext
DDT-1	3-11	DDT out	l4c3-DDT60-03bff.EBS.ext
SMT-0	3-12	SMT out	SMT60-02v.rep.ext
SMT-1	3-12	SMT out	SMT60-02.rep.ext

\* This column gives the alpha numeric designator used in the respective figure.

Table 3-4b. File groups for no-backfill case

α#	Figure		File names
	Created in	Used in	
M-1	3-2	3-5	column.data
M-M0	3-2	3-5	tspa00-mesh00
M-M1	3-2	3-12	tspa00-mesh01
M-M2	3-2	3-12	tspa00-mesh02
M-D1	3-2	3-11	l4c3.03v.nft.msh.ddt
M-D2	3-2	3-11	l4c3.nft.msh.ddt
M-L0 <column>	3-2	3-9	LDTH:\< column >.col.units < column >.nft.msh.dkm0.f < column >.nft.msh.dkm0.m
M-L1 <column>	3-2	3-9	< column >.col.units < column >.nft.msh.dkm.f < column >.nft.msh.dkm.m
M-S <column >	3-2	3-5, 3-10	< column >.nft.msh.dkm0 SDT:\< column >.col.units
H-D0	3-3	3-11	SMT-0.3Qheat-1e6y_vent-20v
H-D1	3-3	3-11	SMT-0.3Qheat-50y_vent-20
H-L0	3-3	3-9, 3-10	LDTH-SDT-0.3Qheat-1e6y_vent-20v
H-L1	3-3	3-9, 3-10	LDTH-SDT-0.3Qheat-50y_vent-20
H-M0	3-3	3-12	SMT-0.3Qheat-1e6y_vent-20v
H-M1	3-3	3-12	SMT-0.3Qheat-50y_vent-20
I-L0	3-4	3-6	low_p.dat
I-L1	3-4	3-6	low_g.dat low_m.dat
I-M0	3-4	3-6	Median_p.dat
I-M1	3-4	3-6	Median_g.dat Median_m.dat
I-U0	3-4	3-6	upper_p.dat
I-U1	3-4	3-6	upper_g.dat upper_m.dat
B-1	3-5	3-6, 3-10	chimney_wt_TP chimney_surface_TP
B-2	3-5	3-6	Enthalpy.dat X.air
B-3	3-5	3-12	SMT_surfbc
B-4	3-5	3-12	SMT_bsmtbc
XL-0<infil>	3-6	3-9	LDTH-i-li-corey LDTH-i-mi-corey LDTH-i-ui-corey
XL-1<infil>	3-6	3-9	LDTH-20v-li-corey LDTH-20v-mi-corey LDTH-20v-ui-corey
XL-2<infil>	3-6	3-9	LDTH-20-li-corey LDTH-20-mi-corey LDTH-20-ui-corey

\* This column gives the alpha numeric designator used in the respective figure

Table 3-4b. File groups for no-backfill case (Continued)

$\alpha$ #	Figure		File names
	Origin	Dest.	
R-S	3-7	3-10, 3-11, 3-12	SDT-1Dds-mi
R-L<umn>	3-7	3-9	dkm-afc-1Dds-mc-li-00 dkm-afc-1Dds-mc-mi-00 dkm-afc-1Dds-mc-ui-00
R-1	3-8	3-9, 3-11	modprop_dr-up-00
R-1v	3-8	3-9, 3-11	modprop_dr-up-00v
R-2	3-8	3-9	dkm-afc-pbf-EBS_Rev10
R-3	3-8	3-9	dkm-afc-EBS_Rev10
R-D	3-8	3-9, 3-11	DDT-EBS_Rev00
LDTH-0<AIC>	3-9	LDTH out	<column>-LDTH<aml>-1Dds_mc-<infil>-01v.ext
LDTH-1<AIC>	3-9	LDTH out	<column>-LDTH<aml>-1Dds_mc-<infil>-01.ext
SDT-0<AC>	3-10	SDT out	<column>-SDT-<aml>-01v.ext
SDT-1<AC>	3-10	SDT out	<column>-SDT-<aml>-01.ext
S-Z	3-10	3-11	l4c3-SDT-01-i.ztab
DDT-0	3-11	DDT out	l4c3-DDT60-03v.EBS.ext
DDT-1	3-11	DDT out	l4c3-DDT60-03bff.EBS.ext
SMT-0	3-12	SMT out	SMT60-02v.rep.ext
SMT-1	3-12	SMT out	SMT60-02.rep.ext

\* This column gives the alpha numeric designator used in the respective figure.

Table 3-5a. Software routine input and output files for backfill case

Name/Number	Description	Number or location of validation	Data Flowchart Figure	Input source	Input File name	# of files	Output File Name	# of files
addLayers v1.0	Routine	Attach. I	3-2	YMESS output	l4c3.nft	1	l4c3.nft.msh.ddt	1
			3-2	YMESS output	l4c3.03v.nft	1	l4c3.03v.nft.msh.ddt	1
addlay v1.0	Routine	Attach. I	3-2	YMESS output	SDT:\<column>.nft	31	SDT:\<column>.nft.msh.dkm0	31
bound v1.0	Routine	Attach. I	3-5	E:B1 output	temperature_W	1	T_bottom.dat	1
				E:B1 output	temperature_S	1		
				addlay output	<column>.nft.msh.dkm0	31		
				readUnits output	SDT:\<column>.col.units	31		
LB990701233129.001	tcond_wet.dat	1						
Chim_Surf_TP v1.0	Routine	Attach. I	3-5	LB990701233129.001	tspa99_primary_mesh	1	outpt	1
				LB991201233129.001	bcs_99.dat	1	surf_TP.out	1
Chim_wt_TP v1.0	Routine	Attach. I	3-5	LB990701233129.001	tspa99_primary_mesh	1	oupt_wt	1
				LB991201233129.001	bcs_99.dat	1		
ColumnInfiltration v1.1	Routine	Attach. I	3-4	convertCoords output	*.NV	9	infiltration.tex	1
				E:M3	column.data	1		
Cover v1.1	Routine	Attach. I	3-2	MO9911MWDEBSWD .000	dft1.dat	1	shape1.dat figure1.dat	1
define_EBS_fine Grid v1.3	Routine	Attach. I	3-2	YMESS output	LDTH:\<column>.nft	31	<column>.nft.msh.dkm.f	31
							<column>.nft.msh.dkm.m	31
							<column>.nft.msh.dkm0.f	31
							<column>.nft.msh.dkm0.m	31

Table 3-5a. Software routine input and output files for backfill case (Continued)

Name/Number	Description	Number or location of validation	Data Flowchart Figure	Input source	Input File name	# of files	Output File Name	# of files
heat_DDT v1.0	Routine	Attach. I	3-3	E:H2	DWperimeter.txt	1	DDT-heat-01	1
heat_SMT v1.0	Routine	Attach. I	3-3	E:H1	heatTSPA00.dat	1	SMT-heat-00	1
heatgenAge v1.2	Routine	Attach. I	3-3	E:H3	DDT-heat-01	1	DDT-0.3Qheat-1e6y_vent-00v DDT-0.3Qheat-50y_vent-00	1 1
				heat_DDT ouput	line-load-heat	1	LDTH-SDT-0.3Qheat-1e6y_vent-00v LDTH-SDT-0.3Qheat-50y_vent-00	1 1
				heat_SMT output	SMT-heat-00	1	SMT-0.3Qheat-1e6y_vent-00v SMT-0.3Qheat-50y_vent-00	1 1
infiltab v1.0	Routine	Attach. I	3-4	columnInfiltration output	infiltration.tex	1	low_g.dat low_m.dat low_p.dat Median_g.dat Median_m.dat Median_p.dat upper_g.dat upper_m.dat upper_p.dat	1 1 1 1 1 1 1 1 1
LDTH assembly scripts: LDTH*corey v1.0	Routine	Attach. I	3-9	XL-0<infil> N:L2 XL-1<infil> N:L2 XL-2<infil> XL-2	LDTH-i-<infil>-corey <aml>infil LDTH-01v-<infil>-corey <aml>pre-closure LDTH-01-<infil>-corey <aml>post-closure	3 1 3 1 3 1	<aml><infil><column> <aml><infil><column> <aml><infil><column>	

Table 3-5a. Software routine input and output files for backfill case (Continued)

Name/Number	Description	Number or location of validation	Data Flowchart Figure	Input source	Input File name	# of files	Output File Name	# of files
makeColumns v1.0	Routine	Attach. I	3-2	N:M1	LDTH:\column_template	1	LDTH:\<column>.dat	31
				E:M3	column.data	1		
				N:M1	SDT:\column_template	1	SDT:\<column>.dat	31
				E:M3	column.data	1		
readsUnits v1.0	Routine	Attach. I	3-2	YMESH output	LDTH:\<column>.col	31	LDTH:\<column>.col.units	31
				YMESH output	SDT:\<column>.col	31	SDT:\<column>.col.units	31
rme6 v1.1	Routine	Attach. I	3-2	LB990701233129.001	tspa99_primary_mesh	1	LBL99-YMESH	1
				LB990701233129.001	UZ99_3.grd	1		
					<column>.dat	1		
rock_sun v1.0	Routine	Attach. I	3-7	LB990861233129.001	1d-driftscale_basecase2_flow.prn	1	dkm-afc-1Dds-mc-mi-00	1
				LB990861233129.001	1d-driftscale_basecase2_th.prn	1		
				LB990861233129.003	1d-driftscale_lowinf_flow.prn	1	dkm-afc-1Dds-mc-li-00	1
				LB990861233129.003	1d-driftscale_lowinf_th.prn	1		
				LB990861233129.002	1d-driftscale_upperinf_flow.prn	1	dkm-afc-1Dds-mc-ui-00	1
LB990861233129.002	1d-driftscale_upperinf_th.prn	1						
SDT assembly scripts: SDT-01* v1.0	Routine	Attach. I	3-10	E:S1	SDT-01i	1	SDT initial.<column><aml>	1
				N:S1	SDT-00-i-tplt	1		
				E:S2	SDT-01v	1	<column>-SDT<aml>-01.in	1
				N:S1	SDT-00-tplt	1		
				E:S3	SDT-01	1	<column>-SDT<aml>-01v.in	1
N:S1	SDT-00-tplt	1						
SMT_surf_bc v1.1	Routine	Attach. I	3-5	chim_surf_TP output	surf_TP.out	1	SMT_surf_bc.out	1
				YMESH output	tspa00-mesh00	1		

Table 3-5a. Software routine input and output files for backfill case (Continued)

Name/Number	Description	Number or location of validation	Data Flowchart Figure	Input source	Input File name	# of files	Output File Name	# of files
SMT_bot_bc v1.1	Routine	Attach. I	3-5	bound output	T_bottom.dat	1	SMT_bsmtbc.out	1
				YMESH output	tspa00-mesh00	1		
				E:M3	column.data	1		
splitEXT v1.0	Routine	Attach. I	NA	MSTHAC output	TSPA_SR_<infil>.ext	3	TSPA_SR_<infil>_ <variable>.ext	111
					TSPA_SR_<infil>_T_pillar_Xdist.ext	3		
xairtab v1.8	Routine	Attach. I	3-5	renamed from outpt	chimney_surface_TP	1	Enthalpy.dat X.air	1 1

Table 3-5b. Software routine input and output files for no-backfill case

Name/Number	Description	Number or location of validation	Data Flowchart Figure	Input source	Input File name	# of files	Output File Name	# of files
addLayers v1.0	Routine	Attach. I	3-2	YMESS output	l4c3.nft	1	l4c3.nft.msh.ddt	1
			3-2	YMESS output	l4c3.03v.nft	1	l4c3.03v.nft.msh.ddt	1
addlay v1.0	Routine	Attach. I	3-2	YMESS output	SDT:\<column>.nft	31	SDT:\<column>.nft.msh.dkm0	31
bound v1.0	Routine	Attach. I	3-5	E:B1 output E:B1 output addlay output readUnits output LB99EBS1233129.001	temperature_W temperature_S <column>.nft.msh.dkm0 SDT:\<column>.col.units tcond_wet.dat	1 1 31 31 1	T_bottom.dat	1
Chim_Surf_TP v1.0	Routine	Attach. I	3-5	LB99EBS1233129.001	tspa99_primary_mesh	1	outpt	1
				LB99EBS1233129.003	bcs_99.dat	1	surf_TP.out	1
Chim_wt_TP v1.0	Routine	Attach. I	3-5	LB99EBS1233129.001	tspa99_primary_mesh	1	oupt_wt	1
				LB99EBS1233129.003	bcs_99.dat	1		
ColumnInfiltration v1.1	Routine	Attach. I	3-4	convertCoords output	*.NV	9	infiltration.tex	1
				E:M3	column.data	1		
Cover v1.1	Routine	Attach. I	3-2	MO9911MWDEBSWD .000	dft1.dat	1	shape1.dat figure1.dat	1
define_EBS_fine Grid v1.3	Routine	Attach. I	3-2	YMESS output	LDTH:\<column>.nft	31	<column>.nft.msh.dkm.f <column>.nft.msh.dkm.m <column>.nft.msh.dkm0.f <column>.nft.msh.dkm0.m	31 31 31 31

Table 3-5b. Software routine input and output files for no-backfill case (Continued)

Name/Number	Description	Number or location of validation	Data Flowchart Figure	Input source	Input File name	# of files	Output File Name	# of files
heat_DDT v1.0	Routine	Attach. I	3-3	E:H2	DWperimeter.txt	1	DDT-heat-01	1
heat_SMT v1.0	Routine	Attach. I	3-3	E:H1	heatTSPA00.dat	1	SMT-heat-20	1
heatgenAge v1.2	Routine	Attach. I	3-3	E:H3	DDT-heat-01	1	DDT-0.3Qheat-1e6y_vent-20v DDT-0.3Qheat-50y_vent-20	1 1
				heat_DDT output	line-load-heat-1.45	1	LDTH-SDT-0.3Qheat-1e6y_vent-20v LDTH-SDT-0.3Qheat-50y_vent-20	1 1
				heat_SMT output	SMT-heat-20	1	SMT-0.3Qheat-1e6y_vent-20v SMT-0.3Qheat-50y_vent-20	1 1
infiltab v1.0	Routine	Attach. I	3-4	columnInfiltration output	infiltration.tex	1	low_g.dat low_m.dat low_p.dat Median_g.dat Median_m.dat Median_p.dat upper_g.dat upper_m.dat upper_p.dat	1 1 1 1 1 1 1 1 1
LDTH assembly scripts: LDTH*corey v1.0	Routine	Attach. I	3-9	XL-0<infil> N:L2 XL-1<infil> N:L2 XL-2<infil> XL-2	LDTH-i-<infil>-corey <aml>infil LDTH-20v-<infil>-corey <aml>pre-closure LDTH-20-<infil>-corey <aml>post-closure	3 1 3 1 3 1	<aml><infil><column> <aml><infil><column>	

Table 3-5b. Software routine input and output files for no-backfill case (Continued)

Name/Number	Description	Number or location of validation	Data Flowchart Figure	Input source	Input File name	# of files	Output File Name	# of files
makeColumns v1.0	Routine	Attach. I	3-2	N:M1 E:M3	LDTH:\column_template column.data	1 1	LDTH:\<column>.dat	31
				N:M1 E:M3	SDT:\column_template column.data	1 1	SDT:\<column>.dat	31
readsUnits v1.0	Routine	Attach. I	3-2	YMESS output	LDTH:\<column>.col	31	LDTH:\<column>.col.units	31
				YMESS output	SDT:\<column>.col	31	SDT:\<column>.col.units	31
rme6 v1.1	Routine	Attach. I	3-2	LB99EBS1233129.001 LB99EBS1233129.001 ? If so, from <column>.dat	tspa99_primary_mesh UZ99_3.grd l4c3.dat	1 1 1	LBL99-YMESS	1
rock_sun v1.0	Routine	Attach. I	3-7	LB990861233129.001	1d-driftscale_ basecase2_flow.prn	1	dkm-afc-1Dds-mc-mi-20	1
				LB990861233129.001	1d-driftscale_ basecase2_th.prn	1		
				LB990861233129.003 LB990861233129.003	1d-driftscale_lowinf_flow.prn 1d-driftscale_lowinf_th.prn	1 1	dkm-afc-1Dds-mc-li-20	1
				LB990861233129.002 LB990861233129.002	1d-driftscale_ upperinf_flow.prn 1d-driftscale_upperinf_th.prn	1 1	dkm-afc-1Dds-mc-ui-20	1
SDT assembly scripts: SDT-01* v1.0	Routine	Attach. I	3-10	E:S1 N:S1	SDT-01i SDT-00-i-tplt	1 1	SDT initial.<column><aml>	1
				E:S2 N:S1	SDT-20v SDT-00-tplt	1 1	<column>-SDT<aml>-20.in	1
				E:S3 N:S1	SDT-20 SDT-00-tplt	1 1	<column>-SDT<aml>-20v.in	1
SMT_surf_bc v1.1	Routine	Attach. I	3-5	chim_surf_TP output YMESS output	surf_TP.out tspa00-mesh00	1 1	SMT_surf_bc.out	1

Table 3-5b. Software routine input and output files for no-backfill case (Continued)

Name/Number	Description	Number or location of validation	Data Flowchart Figure	Input source	Input File name	# of files	Output File Name	# of files
SMT_bot_bc v1.1	Routine	Attach. I	3-5	bound output	T_bottom.dat	1	SMT_bsmtbc.out	1
				YMESS output	tspa00-mesh00	1		
				E:M3	column.data	1		
splitEXT v1.0	Routine	Attach. I	NA	MSTHAC output	TSPA_SR_<infil>.ext	3	TSPA_SR_<infil>_ <variable>.ext	111
					TSPA_SR_<infil>_T_pil	3		
					lar_Xdist.ext			
xairtab v1.8	Routine	Attach. I	3-5	renamed from outpt	chimney_surface_TP	1	Enthalpy.dat X.air	1 1

Table 3-6a. LDTH NUFT input and output files for backfill case

Description	Data Flowchart Figure	Input source	File α #	Input File name	# of files	Output File Name	# of files
LDTH Initialization	3-9a	define_EBS_fineGrid output	M-L0	<column>.nft.msh.dkm0.f	31	Include files	
		define_EBS_fineGrid output	<column>	<column>.nft.msh.dkm0.m	31		
		readUnits output		LDTH:\<column>.col.units	31		
		rock_sun output	R-L0	dkm-afc-1Dds-mc-mi-00	1		
		rock_sun output	<infil>	dkm-afc-1Dds-mc-li-00	1		
		rock_sun output		dkm-afc-1Dds-mc-ui-00	1		
		N:L1		run_control_param_LDTH-v00	1		
corey output		<column>-LDTH<aml>-1Dds_mc-<infil>-i.in	465	<column>-LDTH<aml>-1Dds_mc-<infil>-i.ext	465		
LDTH restart include files	3-9a	define_EBS_fineGrid output	M-L1	<column>.nft.msh.dkm.f	31	Include files	
		define_EBS_fineGrid output	<column>	<column>.nft.msh.dkm.m	31		
		readUnits output		LDTH:\<column>.col.units	31		
		rock_sun output		dkm-afc-1Dds-mc-mi-00	1		
		rock_sun output	R-L <infil>	dkm-afc-1Dds-mc-li-00	1		
		rock_sun output		dkm-afc-1Dds-mc-ui-00	1		
		E:P1	R-1v	modprop_dr-up-00v	1		
		E:P1	R-2	dkm-afc-pbf-EBS_Rev10	1		
		heatgenAge output	H-L0	LDTH-SDT-0.3Qheat-1e6y_vent-00v	1		
		NUFT output	Init.	LDTH:\<aml><infil><column>			
		N:L1		run_control_param_LDTH-v01	1		
N:L3		output.times-00v	1				
Pre-closure		corey output		<column>-LDTH<aml>-1Dds_mc-<infil>-01v.in	465	<column>-LDTH<aml>-1Dds_mc-<infil>-01v.ext	465
LDTH restart include files	3-9a	define_EBS_fineGrid output	M-L1	listed in LDTH restart above		Include files	
		readUnits & roack_sun output	R-L <infil>	listed in LDTH restart above			
		E:P1	R-1	modprop_dr-up-00	1		
		E:P1	R-3	dkm-afc-EBS_Rev10	1		
		heatgenAge output	H-L1	LDTH-SDT-0.3Qheat-50y_vent-00	1		
		NUFT output	pre-clos	LDTH:\<aml><infil><column>			
		N:L1		run_control_param_LDTH-v01	1		
N:L3		output.times-<aml>-00					
Post-closure		corey output		<column>-LDTH<aml>-1Dds_mc-<infil>-01.in	465	<column>-LDTH<aml>-1Dds_mc-<infil>-01.ext	465

Table 3-6b. LDTH NUFT input and output files for no-backfill case

Description	Data Flowchart Figure	Input source	File α#	Input File name	# of files	Output File Name	# of files
LDTH Initialization	3-9b	define_EBS_fineGrid output	M-L0	<column>.nft.msh.dkm0.f	31	Include files	
		define_EBS_fineGrid output	<column>	<column>.nft.msh.dkm0.m	31		
		readUnits output		LDTH:\<column>.col.units	31		
		rock_sun output	R-L0	dkm-afc-1Dds-mc-mi-00	1		
		rock_sun output	<infil>	dkm-afc-1Dds-mc-li-00	1		
		rock_sun output		dkm-afc-1Dds-mc-ui-00	1		
		N:L1		run_control_param_LDTH-v00	1		
corey output		<column>-LDTH<aml>-1Dds_mc-<infil>-i.in	465	<column>-LDTH<aml>-1Dds_mc-<infil>-i.ext	465		
LDTH restart include files	3-9b	define_EBS_fineGrid output	M-L1	<column>.nft.msh.dkm.f	31	Include files	
		define_EBS_fineGrid output	<column>	<column>.nft.msh.dkm.m	31		
		readUnits output		LDTH:\<column>.col.units	31		
		rock_sun output	R-L	dkm-afc-1Dds-mc-mi-00	1		
		rock_sun output	<infil>	dkm-afc-1Dds-mc-li-00	1		
		rock_sun output		dkm-afc-1Dds-mc-ui-00	1		
		E:P1	R-1v	modprop_dr-20v	1		
		E:P1	R-2	dkm-afc-pbf-EBS_Rev20	1		
		heatgenAge output	H-L0	LDTH-SDT-0.3Qheat-1e6y_vent-20v	1		
		NUFT output	Init.	LDTH:\<aml><infil><column>	1		
N:L1		run_control_param_LDTH-v01	1				
N:L3		output.times-00v	1				
Pre-closure		corey output		<column>-LDTH<aml>-1Dds_mc-<infil>-20v.in	465	<column>-LDTH<aml>-1Dds_mc-<infil>-20v.ext	465
LDTH restart include files	3-9b	define_EBS_fineGrid output	M-L1	listed in LDTH restart above		Include files	
		readUnits & roack_sun output	R-L	listed in LDTH restart above			
		E:P1	R-1	modprop_dr-20	1		
		E:P1	R-3	dkm-afc-EBS_Rev20	1		
		heatgenAge output	H-L1	LDTH-SDT-0.3Qheat-50y_vent-20	1		
		NUFT output	pre-clos	LDTH:\<aml><infil><column>	1		
		N:L1		run_control_param_LDTH-v01	1		
N:L3		output.times-<aml>-20	1				
Post-closure		corey output		<column>-LDTH<aml>-1Dds_mc-<infil>-20.in	465	<column>-LDTH<aml>-1Dds_mc-<infil>-20.ext	465

Table 3-7a. SDT NUFT input and output files for backfill case

Description	Data Flowchart Figure	Input source	File $\alpha$ #	Input File name	# of files	Output File Name	# of files
SDT Initialization	3-10a	define_EBS_fineGrid output	M-S	<column>.nft.msh.dkm0	31	Include files	31
		readUnits output	<column>	SDT:\<column>.col.units	31		
		rock_sun output	R-S	SDT-1Dds-mi	1		
		SDT-01i output		<column>-SDT-01-i.in	31		
SDT restart include files	3-10a	define_EBS_fineGrid output	M-S	<column>.nft.msh.dkm0	31	Include files	155
		readUnits output	<column>	SDT:\<column>.col.units	31		
		rock_sun output	R-S	SDT-1Dds-mi	1		
		heatgenAge output N:S2	H-L0	LDTH-SDT-0.3Qheat-1e6y_vent-00v output.times-00v	1		
		NUFT output	pre-clos	SDT:\<aml><column>. Ztab files	1		
Pre-closure		SDT-01v output		<column>-SDT<aml>-01v.in	155	<column>-SDT<aml>-01v.ext	155
SDT restart include files	3-10a	define_EBS_fineGrid output	M-S	<column>.nft.msh.dkm0	31	Include files	155
		readUnits output	<column>	SDT:\<column>.col.units	31		
		rock_sun output	R-S	SDT-1Dds-mi	1		
		heatgenAge output N:S2	H-L1	LDTH-SDT-0.3Qheat-50y_vent-00 output.times-<aml>-00	1		
		NUFT output	pre-clos	SDT:\<aml><column>. Ztab files	1		
Post-closure		SDT-01 output		<column>-SDT<aml>-01.in	155	<column>-SDT<aml>-01.ext	155

Table 3-7b. SDT NUFT input and output files for no-backfill case

Description	Data Flowchart Figure	Input source	File α#	Input File name	# of files	Output File Name	# of files
SDT Initialization	3-10b	define_EBS_fineGrid output	M-S	<column>.nft.msh.dkm0	31	Include files	
		readUnits output	<column>	SDT:\<column>.col.units	31		
		rock_sun output	R-S	SDT-1Dds-mi	1		
		SDT-01i output		<column>-SDT-01-i.in	31	<column>-SDT<aml>-i.ext	31
SDT restart include files	3-10b	define_EBS_fineGrid output	M-S	<column>.nft.msh.dkm0	31	Include files	
		readUnits output	<column>	SDT:\<column>.col.units	31		
		rock_sun output	R-S	SDT-1Dds-mi	1		
		heatgenAge output	H-L0	LDTH-SDT-0.3Qheat-1e6y_vent-20v	1		
		N:S2		output.times-00v	1		
		NUFT output	pre-clos	SDT:\<aml><column>. Ztab files			
Pre-closure		SDT-01v output		<column>-SDT<aml>-01v.in	155	<column>-SDT<aml>-20v.ext	155
SDT restart include files	3-10b	define_EBS_fineGrid output	M-S	<column>.nft.msh.dkm0	31	Include files	
		readUnits output	<column>	SDT:\<column>.col.units	31		
		rock_sun output	R-S	SDT-1Dds-mi	1		
		heatgenAge output	H-L1	LDTH-SDT-0.3Qheat-50y_vent-20	1		
		N:S2		output.times-<aml>-20	1		
		NUFT output	pre-clos	SDT:\<aml><column>. Ztab files			
Post-closure		SDT-01 output		<column>-SDT<aml>-20.in	155	<column>-SDT<aml>-20.ext	155

Table 3-8a. DDT NUFT input and output files for backfill case

Description	Data Flowchart Figure	Input source	File $\alpha$ #	Input File name	# of files	Output File Name	# of files
DDT Initialization	3-11a	define_EBS_fineGrid output	R-1	modprop_dr-up-00	1	Include files	
		readUnits output	R-S	SDT-1Dds-mi	1		
		E:P1	R-D	DDT-EBS_Rev00	1		
		NUFT output	S-Z	I4c3-SDT-01-I.ztab	1		
		heatgenAge output	H-D0	DDT-0.3Qheat-1e6y_vent-00v	1		
		N:D1		run_control_param_DDT-v01	1		
		N:D2		output.times-DDT60-00	1		
		Radpro output		DDT60-03v.radout	1		
		E:D1	M-D1	I4c3-DDT60-03v.in	1	I4c3-DDT60-03v.EBS.ext	1
DDT Preclosure	3-11a	E:P1	R-1v	modprop_dr-up-00v	1	Include files	
		readUnits output	R-S	SDT-1Dds-mi	1		
		E:P1	R-D	DDT-EBS_Rev00	1		
		NUFT output	S-Z	I4c3-SDT-01-I.ztab	1		
		heatgenAge output	H-D1	DDT-0.3Qheat-50y_vent-00	1		
		N:D1		run_control_param_DDT-v01	1		
		N:D2		output.times-DDT60-00	1		
		Radpro output		DDT60-03pbf.radout	1		
		E:D1	M-D1	I4c3-DDT60-03pbf.in	1	I4c3-DDT60-03pbf.res	1
DDT Postclosure	3-11a	define_EBS_fineGrid output	R-1	modprop_dr-up-00	1	Include files	
		readUnits output	R-S	SDT-1Dds-mi	1		
		E:P1	R-D	DDT-EBS_Rev00	1		
		NUFT output		I4c3-DDT60-03pbf.res	1		
		heatgenAge output	H-D1	DDT-0.3Qheat-50y_vent-00	1		
		N:D1		run_control_param_DDT-v02	1		
		N:D2		output.times-DDT60-00	1		
		Radpro output		DDT60-03pbf.radout	1		
		E:D1	M-D1	I4c3-DDT60-03bff.in	1	I4c3-DDT60-03bff.EBS.ext	1

Table 3-8b. DDT NUFT input and output files for no-backfill case

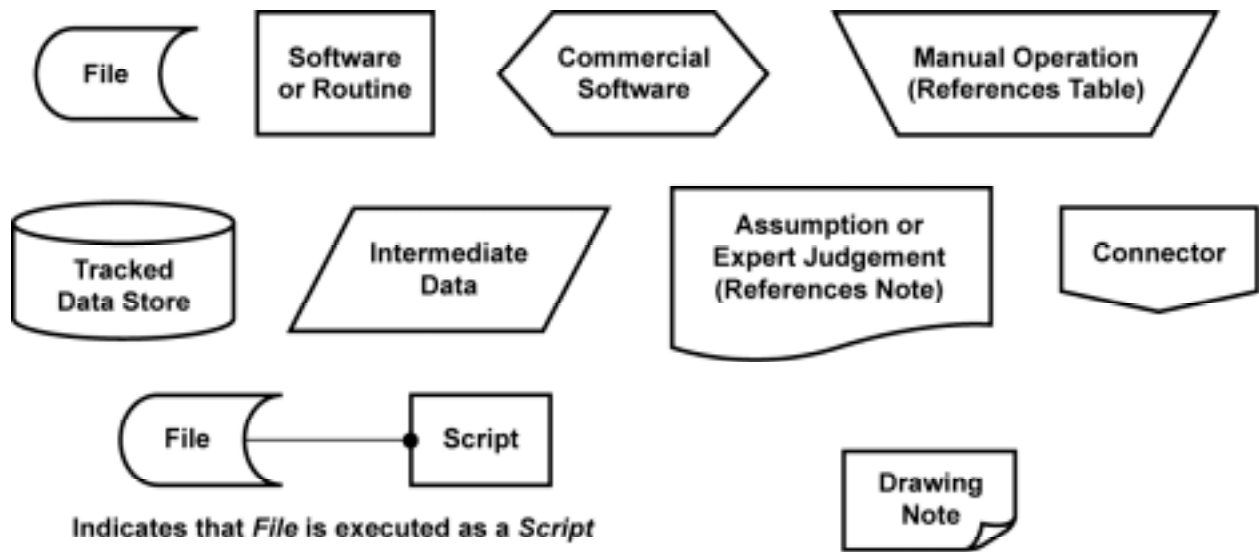
Description	Data Flowchart Figure	Input source	File $\alpha$ #	Input File name	# of files	Output File Name	# of files
DDT Initialization	3-11b	define_EBS_fineGrid output	R-1	modprop_dr-20	1	Include files	
		readUnits output	R-S	SDT-1Dds-mi	1		
		E:P1	R-D	DDT-EBS_Rev20	1		
		NUFT output	S-Z	I4c3-SDT-01-I.ztab	1		
		heatgenAge output	H-D0	DDT-0.3Qheat-1e6y_vent-00v	1		
		N:D1		run_control_param_DDT-v01	1		
		N:D2		output.times-DDT60-20	1		
		Radpro output		DDT60-03v.radout	1		
		E:D1	M-D1	I4c3-DDT60-20v.in	1	I4c3-DDT60-20v.EBS.ext	1
DDT Preclosure	3-11b	E:P1	R-1v	modprop_dr-20v	1	Include files	
		readUnits output	R-S	SDT-1Dds-mi	1		
		E:P1	R-D	DDT-EBS_Rev20	1		
		NUFT output	S-Z	I4c3-SDT-01-I.ztab	1		
		heatgenAge output	H-D1	DDT-0.3Qheat-50y_vent-00	1		
		N:D1		run_control_param_DDT-v01	1		
		N:D2		output.times-DDT60-20	1		
		Radpro output		DDT60-03pbf.radout	1		
		E:D1	M-D1	I4c3-DDT60-20pbf.in	1	I4c3-DDT60-20pbf.res	1
DDT Postclosure	3-11b	define_EBS_fineGrid output	R-1	modprop_dr-20	1	Include files	
		readUnits output	R-S	SDT-1Dds-mi	1		
		E:P1	R-D	DDT-EBS_Rev20	1		
		NUFT output		I4c3-DDT60-20pbf.res	1		
		heatgenAge output	H-D1	DDT-0.3Qheat-50y_vent-00	1		
		N:D1		run_control_param_DDT-v02	1		
		N:D2		output.times-DDT60-20	1		
		Radpro output		DDT60-03pbf.radout	1		
		E:D1	M-D1	I4c3-DDT60-20ss.in	1	I4c3-DDT60-20ss.EBS.ext	1

Table 3-9a. SMT NUFT input and output files for backfill case

Description	Data Flowchart Figure	Input source	File $\alpha$ #	Input File name	# of files	Output File Name	# of files
SMT Initialization	3-12	readUnits output	R-S	SDT-1Dds-mi	1	Include files	
		heatgenAge output	B-3	SMT_surfbc	1		
		YMESH output	M-M1	tspa00-mesh02	1		
		N:T1		run_control_param_SMT-v01	1		
			B-4	SMT_bsmtbc	1		
		N:T3		SMT-1Dds-mi-sz	1		
		E:T1		SMT-1Dds-mi-flt	1		
		user developed		SMT60-01-i-in	1	SMT60-01-i-rst	1
SMT Preclosure	3-12	readUnits output	R-S	SDT-1Dds-mi	1	Include files	
		heatgenAge output	H-M0	SMT-0.3Qheat-1e6y_vent-02v	1		
		YMESH output	M-M2	tspa00-mesh02	1		
		N:T1		run_control_param_SMT-v01	1		
		N:T2		output.times-SMT60-00	1		
		N:T3		SMT-1Dds-mi-sz	1		
		E:T1		SMT-1Dds-mi-flt	1		
		NUFT output		SMT60-01-i-rst	1		
		user developed		SMT60-02v.in	1	SMT60-02v.rep.ext	1
SMT Postclosure	3-12	readUnits output	R-S	SDT-1Dds-mi	1	Include files	
		heatgenAge output	H-M1	SMT-0.3Qheat-50y_vent-02v	1		
		YMESH output	M-M1	tspa00-mesh01	1		
		N:T1		run_control_param_SMT-v01	1		
		N:T2		output.times-SMT60-00	1		
		N:T3		SMT-1Dds-mi-sz	1		
		E:T1		SMT-1Dds-mi-flt	1		
		NUFT output		SMT60-01-i-rst	1		
		user developed		SMT60-02.in	1	SMT60-02.rep.ext	1

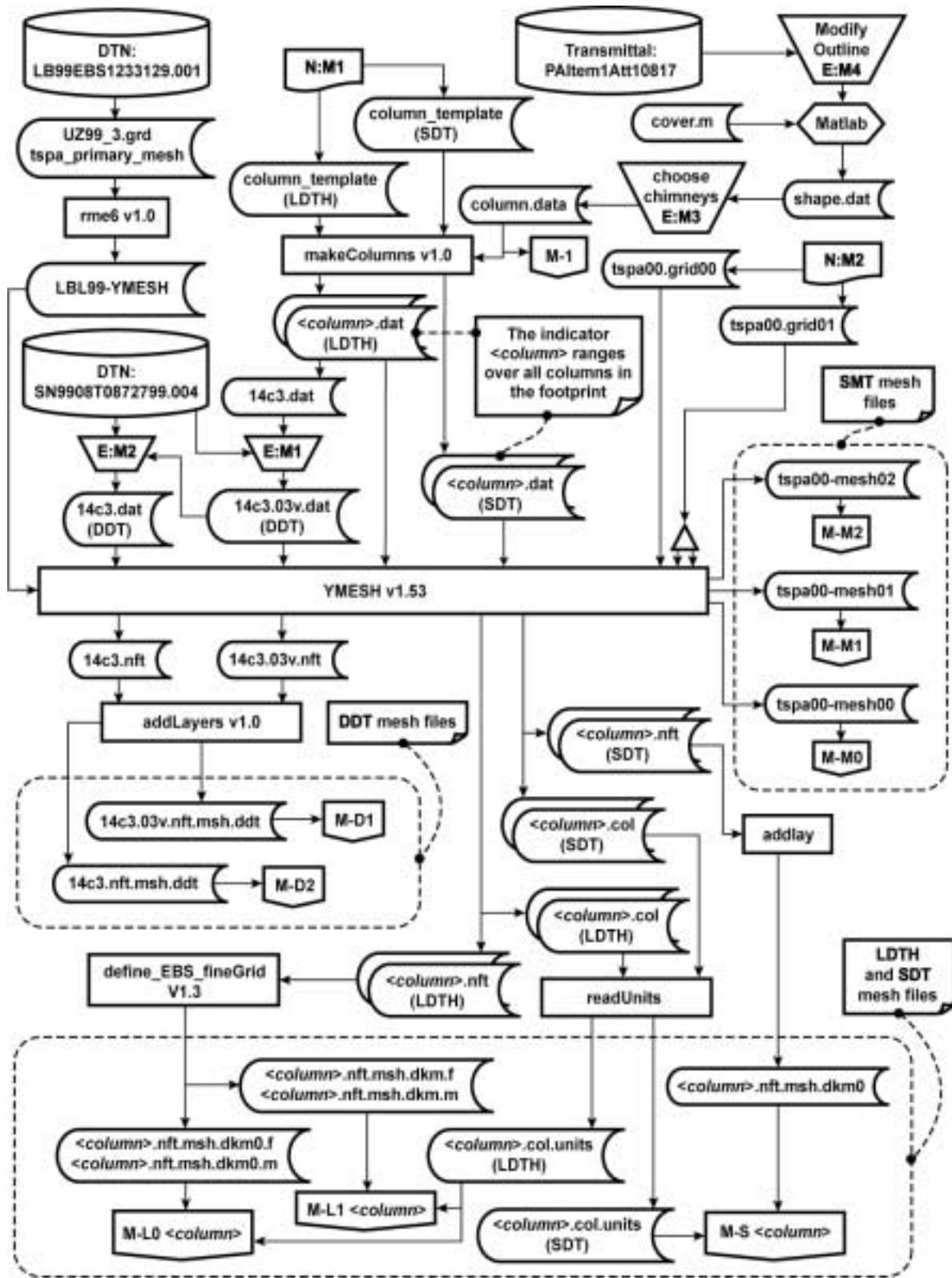
Table 3-9b. SMT NUFT input and output files for no-backfill case

Description	Data Flowchart Figure	Input source	File $\alpha$ #	Input File name	# of files	Output File Name	# of files
SMT Initialization	3-12	readUnits output	R-S	SDT-1Dds-mi	1	Include files	
		heatgenAge output	B-3	SMT_surfbc	1		
		YMESH output	M-M1	tspa00-mesh01	1		
		N:T1		run_control_param_SMT-v01	1		
			B-4	SMT_bsmtbc	1		
		N:T3		SMT-1Dds-mi-sz	1		
		E:T1		SMT-1Dds-mi-flt	1		
		user developed		SMT60-01-i-in	1	SMT60-01-i-rst	1
SMT Preclosure	3-12	readUnits output	R-S	SDT-1Dds-mi	1	Include files	
		heatgenAge output	H-M0	SMT-0.3Qheat-1e6y_vent-20v	1		
		YMESH output	M-M2	tspa00-mesh20	1		
		N:T1		run_control_param_SMT-v01	1		
		N:T2		output.times-SMT60-20	1		
		N:T3		SMT-1Dds-mi-sz	1		
		E:T1		SMT-1Dds-mi-flt	1		
		NUFT output		SMT60-01-i-rst	1		
		user developed		SMT60-20v.in	1	SMT60-20v.rep.ext	1
SMT Postclosure	3-12	readUnits output	R-S	SDT-1Dds-mi	1	Include files	
		heatgenAge output	H-M1	SMT-0.3Qheat-50y_vent-20v	1		
		YMESH output	M-M1	tspa00-mesh20	1		
		N:T1		run_control_param_SMT-v01	1		
		N:T2		output.times-SMT60-20	1		
		N:T3		SMT-1Dds-mi-sz	1		
		E:T1		SMT-1Dds-mi-flt	1		
		NUFT output		SMT60-01-i-rst	1		
		user developed		SMT60-20.in	1	SMT60-20.rep.ext	1



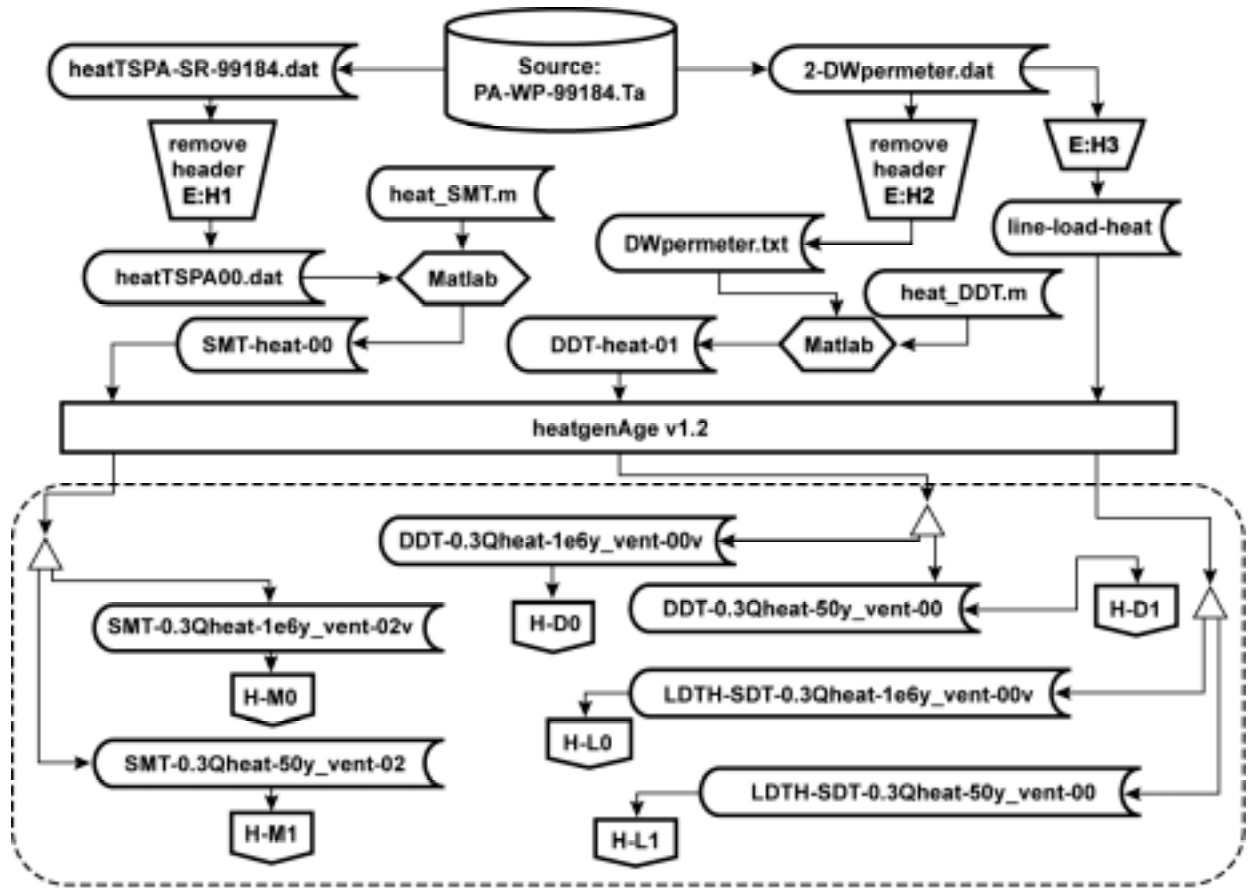
TB\_AMR\_fig3-1\_wr\_legend

Figure 3-1. Legend for data flow diagrams



TB\_AMR\_fig3-2\_wr\_mesh

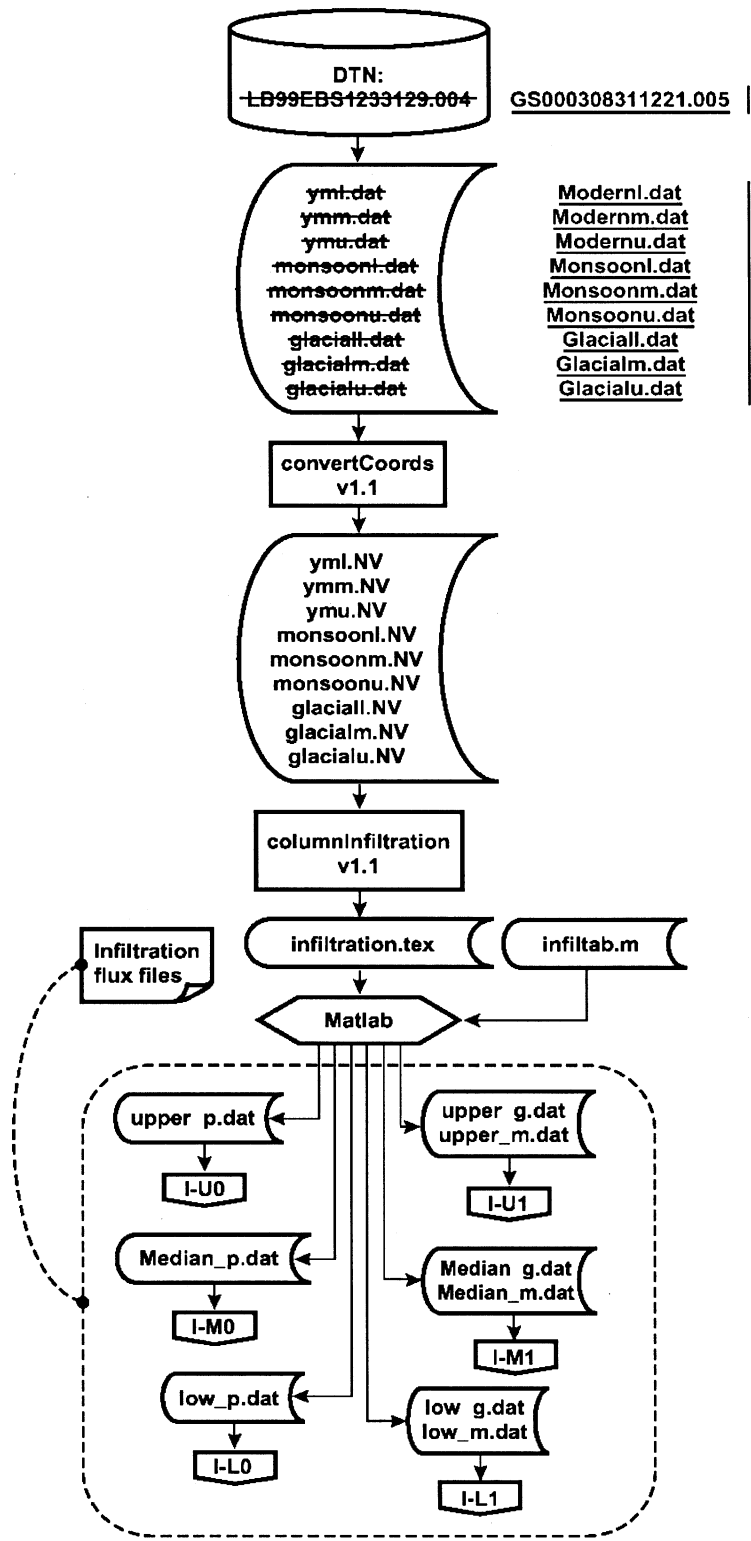
Figure 3-2. Generation of numerical meshes for all submodels



TB\_AMR\_fig3-3\_wr\_heat

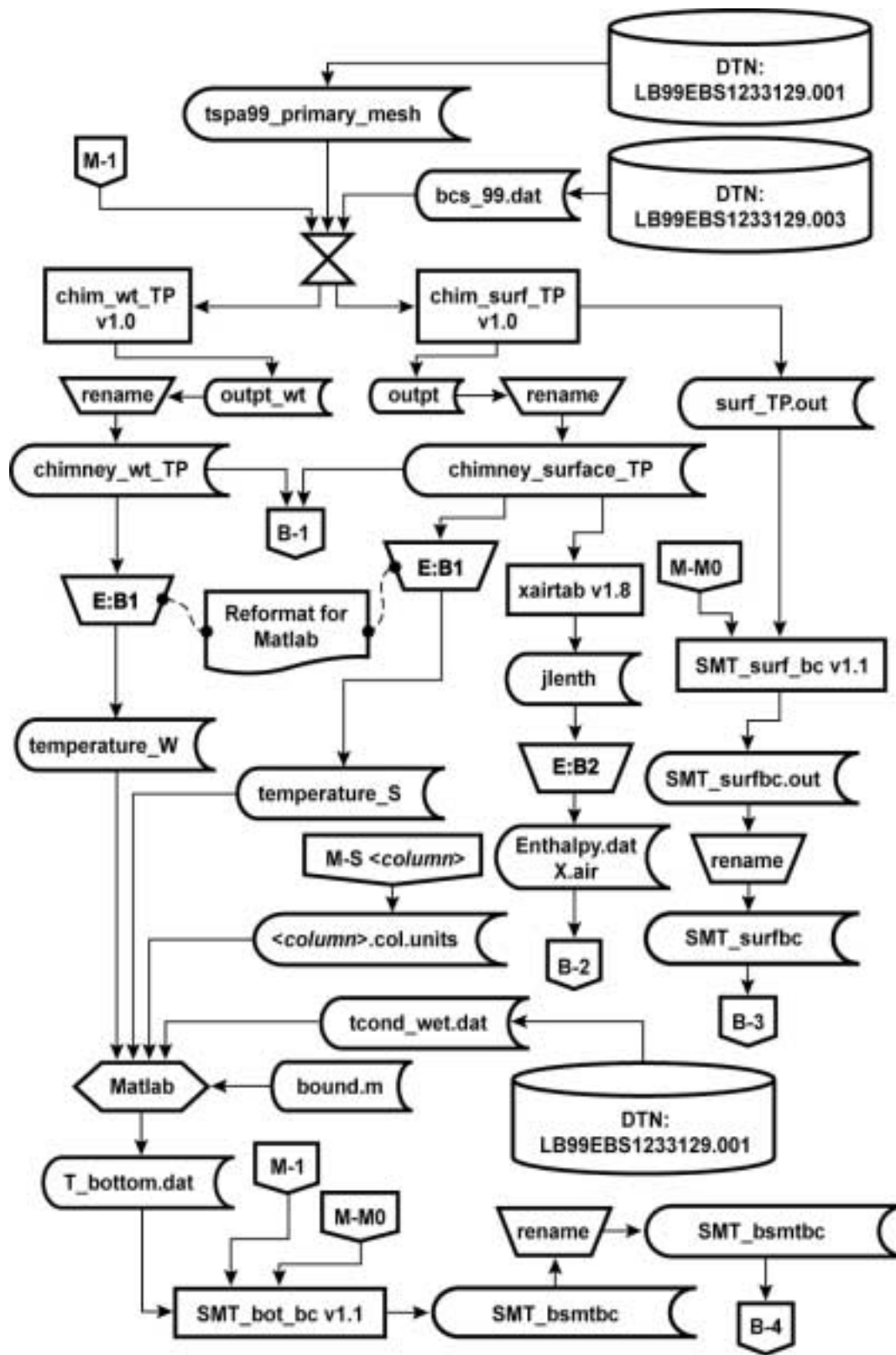
NOTE: This diagram shows the files for the backfill case, for the No-backfill case the file names SMT-0.3Qheat-1e6y\_vent-02v, SMT-0.3Qheat-50y\_vent-02, DDT-0.3heat-1e6y\_vent-00v, DDT-0.3Qheat-50y\_vent-00v, LDTH-SDT=0.3Qheat-1e6y\_vent-00v, and LDTH-SDT-0.3Qheat-50y\_vent-00 are changed to SMT-0.3Qheat-1e6y\_vent-20v, SMT-0.3Qheat-50y\_vent-20, DDT-0.3heat-1e6y\_vent-20v, DDT-0.3Qheat-50y\_vent-20v, LDTH-SDT=0.3Qheat-1e6y\_vent-20v, and LDTH-SDT-0.3Qheat-50y\_vent-20 respectively all else remains the same.

Figure 3-3. Preparation of heat generation curves for all submodels



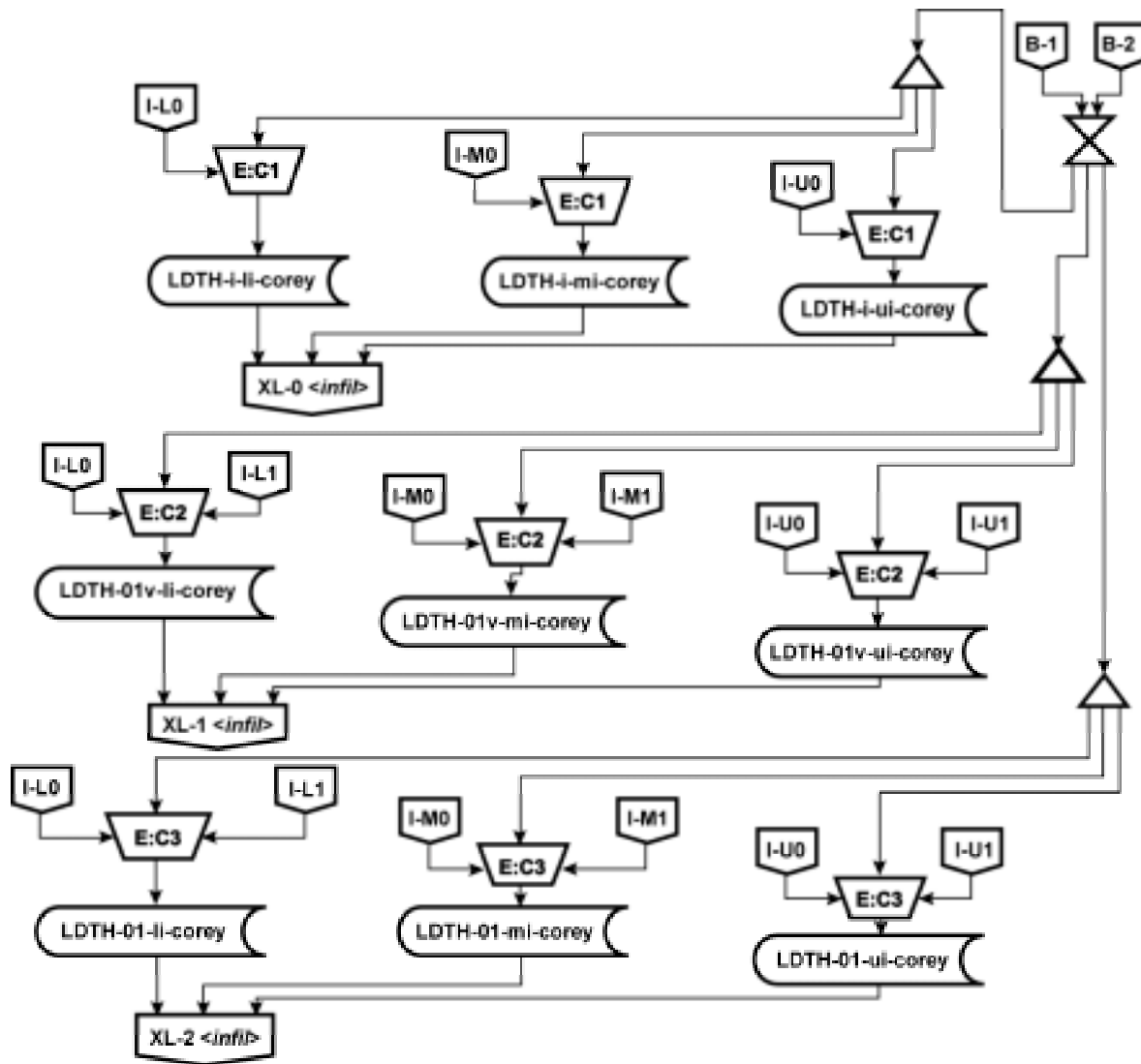
TB ICN fig3-4 wr infil

Figure 3-4. Preparation of infiltration data for LDTH submodels



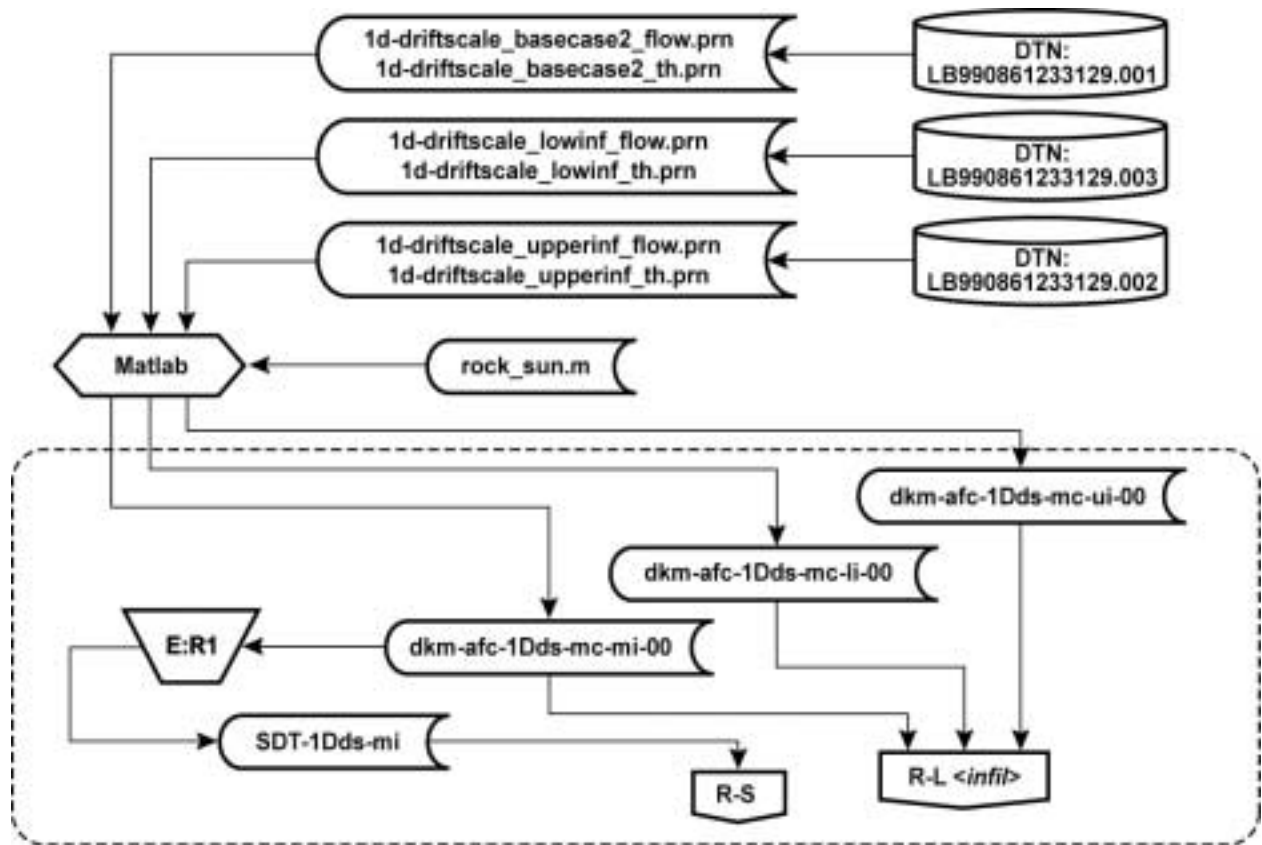
TB\_AMR\_fig3-5\_wr\_bc

Figure 3-5. Preparation of boundary conditions for submodels



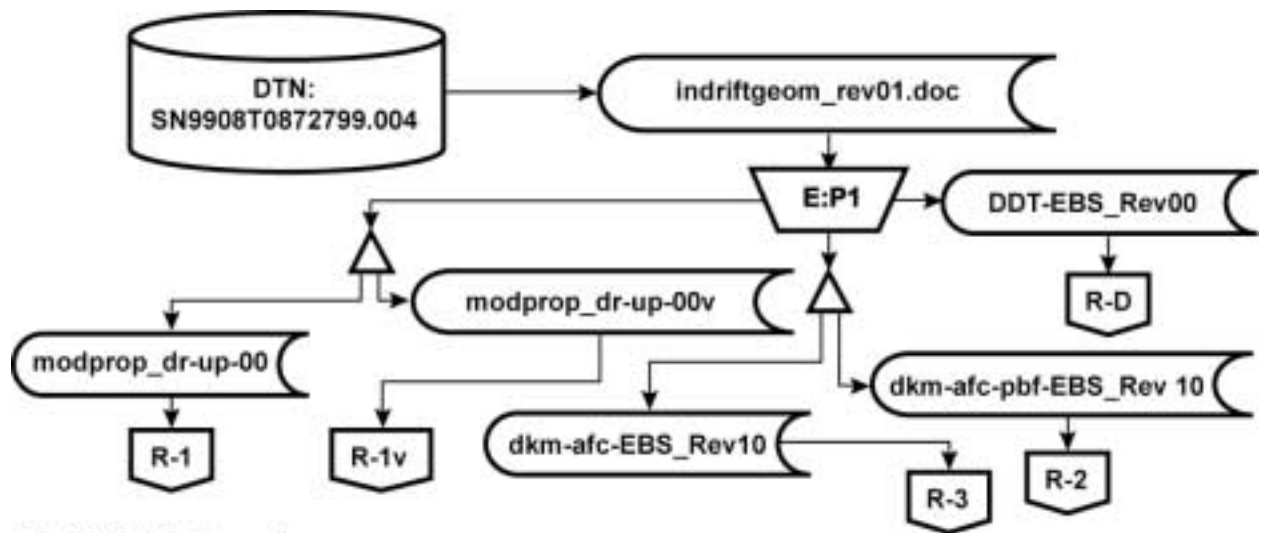
TB\_AMR\_fig3-6\_wr\_corey

Figure 3-6. Creation of scripts to generate families of LDTH submodels



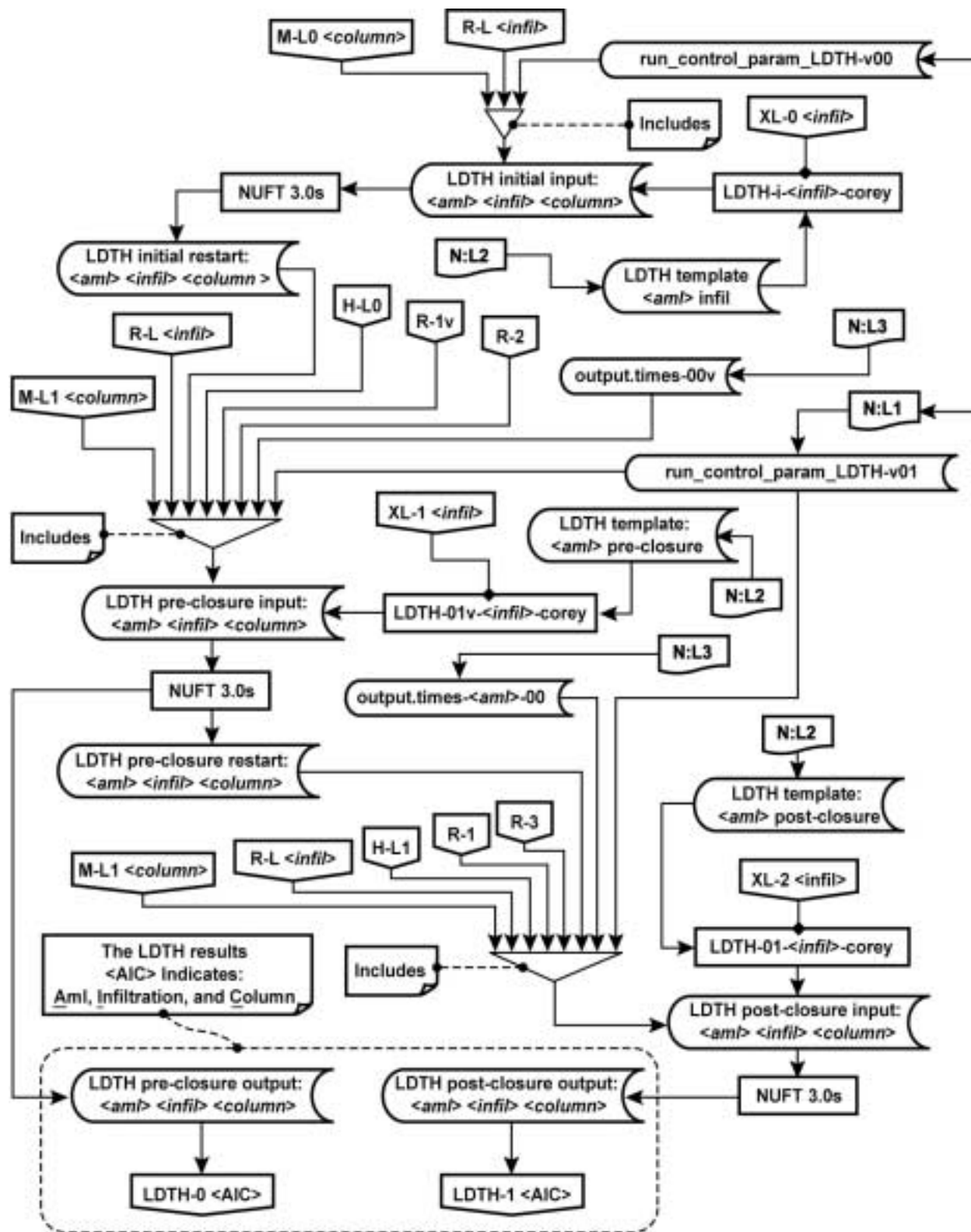
TB\_AMR\_fig3-7\_wr\_rock

Figure 3-7. Material properties of the natural system



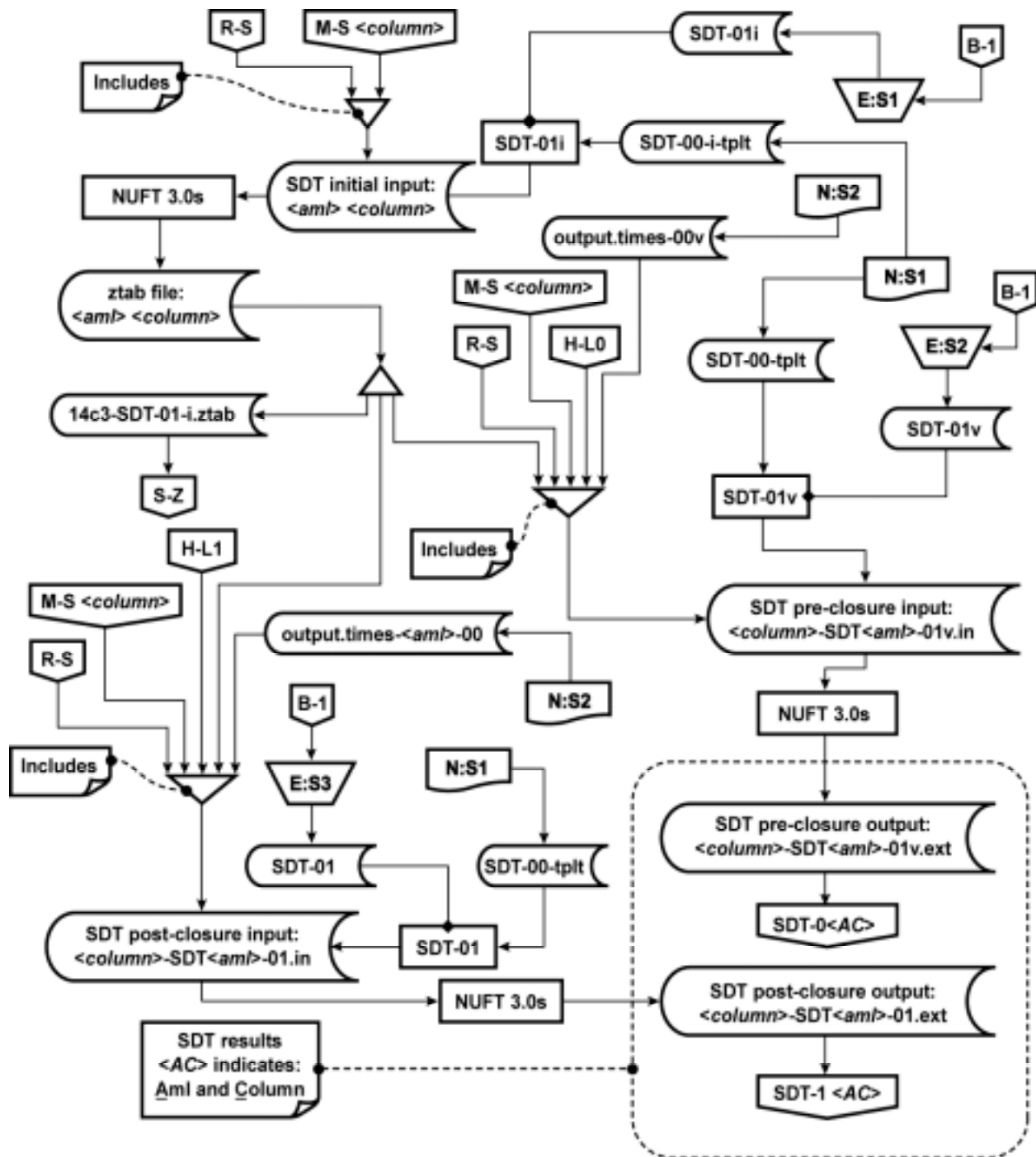
TB\_AMR\_fig3-8\_wr\_ebs

Figure 3-8. Material properties of the EBS



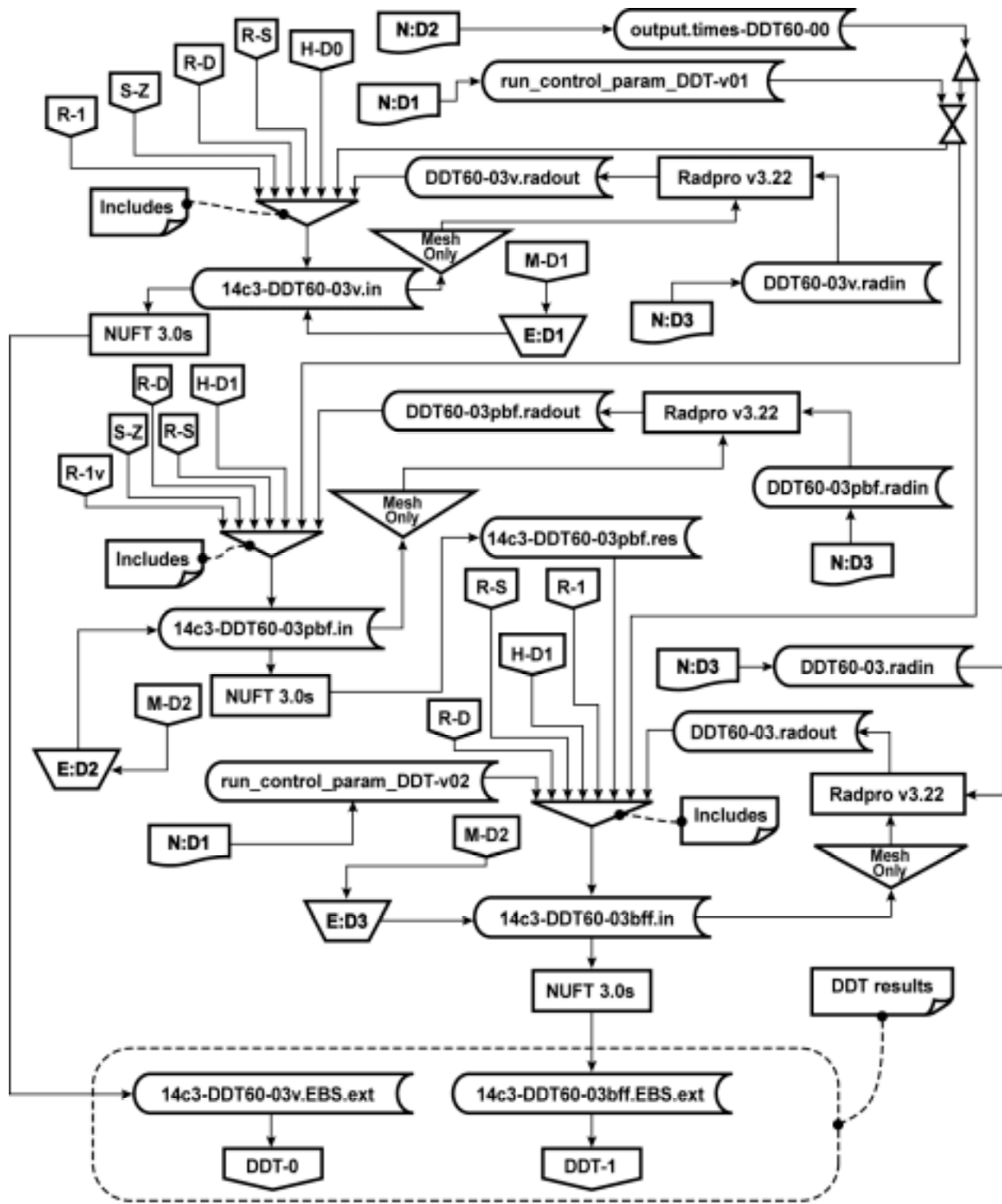
TB\_AMR\_fig3-9\_wr\_ldth

Figure 3-9. Execution of LDTH submodels



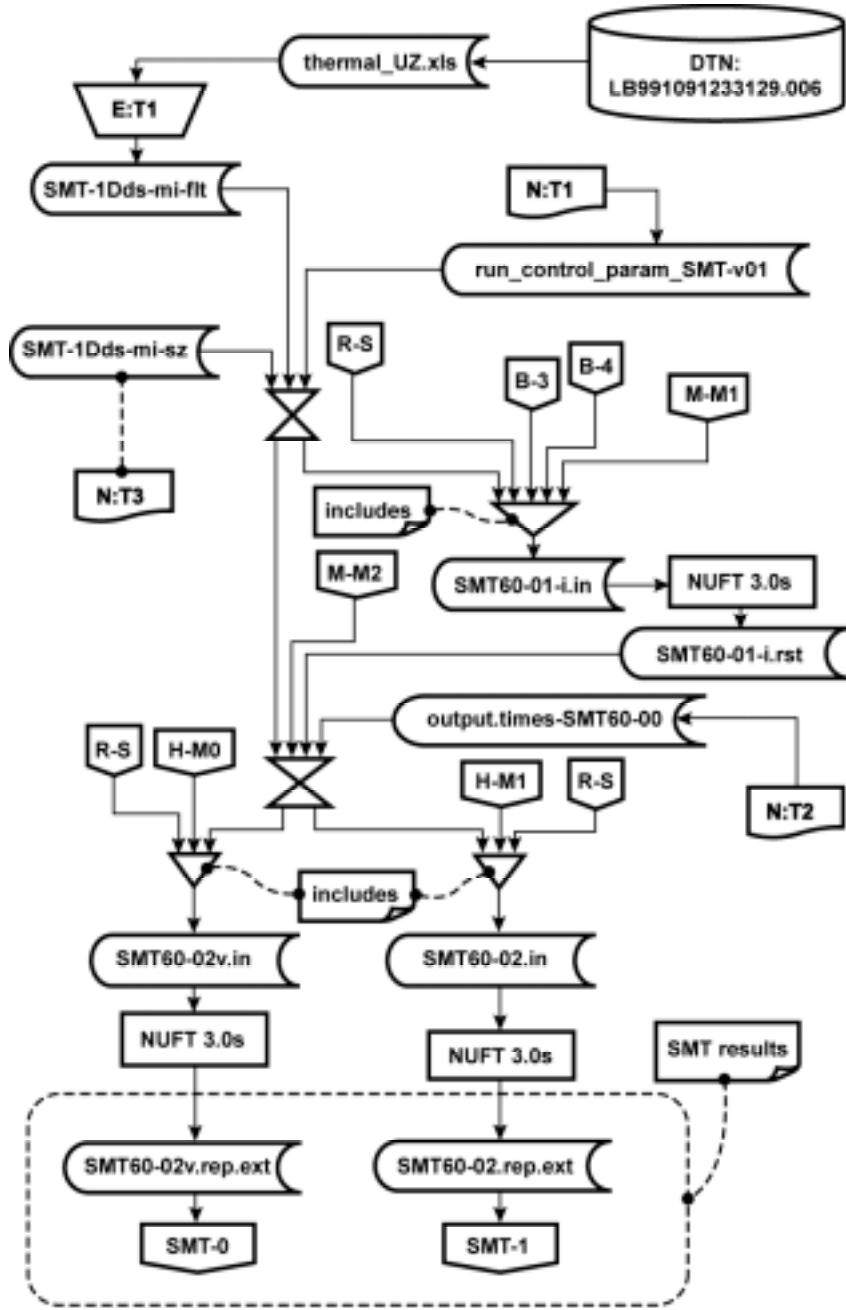
TB\_AMR\_fig3-10\_wr\_sdt

Figure 3-10. Execution of SDT submodels



TB\_AMR\_fig3-11\_wr\_ddt

Figure 3-11. Execution of DDT submodels



TB\_AMR\_fig3-12\_wr\_smt

Figure 3-12. Execution of SMT submodels

## 4. INPUTS

The inputs to the MSTHM are presented in the following sections: Section 4.1 Data and Parameters, Section 4.2 Criteria, and Section 4.3 Codes and Standards.

### 4.1 DATA AND PARAMETERS

Inputs are outlined in the following sections.

#### 4.1.1 Geometric Description of the EBS and Material Properties

The geometric description of the EBS consists of both longitudinal dimensions (along the longitudinal axis of the emplacement drifts) and the vertical and lateral dimensions in a vertical cross-sectional plane that is orthogonal to the longitudinal axis of the drifts.

#### 4.1.2 Drift Spacing

Emplacement drifts have an 81-m centerline to centerline spacing which is presented in the *Subsurface Facility System Description Document* (CRWMS M&O 2000d, Section 1.2.1.5). This information is used in the DDT submodels (Section 6.5).

#### 4.1.3 Waste Package Spacing

There is a 0.1-m gap between WPs shown in Figure 4-1 is taken from *Emplacement Drift System Description Document* (CRWMS M&O 2000e, Section 1.2.4.7). This information is used in the DDT submodels (Section 6.5). This input is appropriately used.

#### 4.1.4 Drift Diameter

The diameter of the emplacement drifts is 5.5m and is presented in the *Subsurface Facility System Description Document* (CRWMS M&O 2000d, Section 1.2.1.3).

#### 4.1.5 Properties of Air at Model Boundaries

The thermal conductivity of air at 16°C (ground surface) is 0.0254 W/m-K (Bolz and Tuve 1973, p. 11, interpolated). The solid density of air at 24.8°C (intake to emplacement drifts) is 1.185 kg/m<sup>3</sup> (Bolz and Tuve 1973, p. 11, interpolated). The specific heat of air at 25°C (intake to emplacement drifts) is 1006 joules/kg-k (Bolz and Tuve 1973, p. 11). This information is used in the SMT, DDT, and SDT models through incorporation in the file SDT-1Dds-mi. (Accepted data/established fact, handbook value.) This input is appropriately used.

#### 4.1.6 Properties of EBS Materials

Table 4.1 provides backfill and invert properties.

Backfill and crushed tuff invert hydrologic material properties for the EBS originate in source DTN:MO0009SEPTIHMP.000.

The emissivity of the waste package is 0.8 (Avallone, E.A. and Baumeister, T., III, ed. 1987, p. 4-68) and is established fact. The value for carbon steel is used as an approximation. This input is appropriately used.

The drip-shield properties comprised of titanium are discussed in *ANSYS Calculations in Support of Enhanced Design Alternatives* (CRWMS M&O 1999e, p. 21). The drip-shield thermal conductivity is 20.55 W/(m K) (ASME 1995, p. 611). The density is 4512 kg/m<sup>3</sup> (ASME 1995, p. 620). The drip-shield thermal diffusivity is 8.310 \* 10<sup>-6</sup> m<sup>2</sup>/sec (ASME 1995, p. 620). The specific heat capacity of the drip shield corresponding to these properties is 550 J/Kg-K.

Table 4-1. Backfill and invert material properties for the backfill and no-backfill cases

Property	Units	Overton Sand Backfill (backfill case)	Crushed Tuff Invert (backfill case)	Crushed Tuff Invert (no-backfill case)	Waste Package	Drip Shield
Permeability	m <sup>2</sup>	1.43 × 10 <sup>-11</sup>	6.15 × 10 <sup>-10</sup>	6.15 × 10 <sup>-10</sup>	NA	NA
Porosity	Fraction	0.41	0.545	0.545	NA	NA
Van Genuchten α	1/Pa	2.7523 × 10 <sup>-4</sup>	1.2232 × 10 <sup>-3</sup>	1.2232 × 10 <sup>-3</sup>	NA	NA
Van Genuchten β	Dimensionless	2	2.7	2.7	NA	NA
Residual Saturation	Fraction	0.024	0.092	0.092	NA	NA
Grain Density	Kg/m <sup>3</sup>	2700 <sup>3</sup>	2530 <sup>3</sup>	2530 <sup>3</sup>	8189.2	4501.72
Grain Specific Heat	J/Kg-K	795.492 <sup>3</sup>	948 <sup>3</sup>	948 <sup>3</sup>	488.86	551.32
Conductivity	W/m-K	0.33 <sup>3</sup>	0.66	1.52 (upper layer) <sup>2</sup> 0.15 (lower layer) <sup>2</sup>	14.42	20.55
Emissivity	Dimensionless	0.93	0.93	0.93	0.80 <sup>1</sup>	0.63

Sources:

<sup>1</sup> (Avallone, E.A. and Baumeister, T., III, ed. 1987, p. 4-68). The value from carbon steel is used as an approximation.

<sup>2</sup> See Section 5.2.8.

<sup>3</sup> See Section 5.2.7.

#### 4.1.7 Hydrologic and Thermal Properties of Stratigraphic Units

Each stratigraphic unit has two sets of properties, one for its matrix and the other for its fractures. The matrix properties are permeability, porosity, Van Genuchten α parameter, Van Genuchten β parameter, residual saturation, and saturated saturation. The fracture parameters include the six categories used for the matrix of the rock (although the values for the fractures are different) and three additional parameters: active fracture parameter, fracture frequency, and fracture to matrix area. The thermal properties include grain density, grain specific heat, wet thermal conductivity, dry thermal conductivity, and tortuosity. There are three infiltration cases (each corresponding to an expected climate) over which the repository is being modeled. There is a set of hydrologic properties for each of these infiltration cases.

The matrix properties, fracture properties, and thermal properties corresponding to the basecase infiltration flux are given in the file 1d-driftscale\_basecase.xls (LB990861233129.001). Properties corresponding to the upper infiltration flux are given in the file 1d-driftscale\_upperinf.xls (LB990861233129.002). Properties corresponding to the lower bound infiltration flux are given in the file 1d-driftscale\_lowinf.xls (LB990861233129.003).

The basecase matrix properties are reproduced in Table 4-2. The basecase fracture properties are reproduced in Table 4-3. Thermal properties are reproduced in Table 4-4. The tortuosity factor is 0.7.

The hydrologic property sets are used in Section 6.3.5. This input is appropriately used.

#### **4.1.8 Thermal Properties of Air Inside the Drifts**

The thermal conductivity of in-drift air in the DDT submodels is from *Fundamentals of heat and mass transfer* (Incropera and DeWitt 1996, pg. 839: lines 4-12 of the table). The input data is given as a function of temperature in Fahrenheit that is converted to Celsius and used in the file DDT-EBS-Rev00. This input is appropriately used.

#### **4.1.9 Thermal Properties of Stratigraphic Units for SMT Submodels**

The uncalibrated thermal properties of the stratigraphic units are given in Table 4-4. The source of this data is thermal\_UZ.xls (LB991091233129.006). This data is edited to create the file SMT-1Dds-mi-flt as described in the editing function E:T1 in Table 3-3 (also see Figure 3-12). This information is used in Section 6.5. This input is appropriately used.

#### **4.1.10 Effective Thermal Conductivity of Cavities Inside Drifts**

Thermal radiative heat transfer inside cavities within the emplacement drifts can be represented with the use of an effective thermal conductivity, which is given as a function of time. Effective thermal conductivity versus time relationships have been developed and are discussed in Assumption section 5.3.3. This input is appropriately used.

Table 4-2. Matrix properties of stratigraphic units

Unit	Permeability (m <sup>2</sup> )	Porosity (Fraction)	Van Genuchten $\alpha$ (Pa <sup>-1</sup> )	Van Genuchten $\beta$	Residual Saturation (Fraction)	Satiated Saturation (Fraction)
tcw11	3.86E-15	0.253	4.00E-05	0.47	0.07	1
tcw12	2.74E-19	0.082	1.81E-05	0.241	0.19	1
tcw13	9.23E-17	0.203	3.44E-06	0.398	0.31	1
ptn21	9.90E-13	0.387	1.01E-05	0.176	0.23	1
ptn22	2.65E-12	0.439	1.60E-04	0.326	0.16	1
ptn23	1.23E-13	0.254	5.58E-06	0.397	0.08	1
ptn24	7.86E-14	0.411	1.53E-04	0.225	0.14	1
ptn25	7.00E-14	0.499	5.27E-05	0.323	0.06	1
ptn26	2.21E-13	0.492	2.49E-04	0.285	0.05	1
tsw31	6.32E-17	0.053	3.61E-05	0.303	0.22	1
tsw32	5.83E-16	0.157	3.61E-05	0.333	0.07	1
tsw33	3.08E-17	0.154	2.13E-05	0.298	0.12	1
tsw34	4.07E-18	0.11	3.86E-06	0.291	0.19	1
tsw35	3.04E-17	0.131	6.44E-06	0.236	0.12	1
tsw36	5.71E-18	0.112	3.55E-06	0.38	0.18	1
tsw37	4.49E-18	0.094	5.33E-06	0.425	0.25	1
tsw38	4.53E-18	0.037	6.94E-06	0.324	0.44	1
tsw39	5.46E-17	0.173	2.29E-05	0.38	0.29	1
ch1z	1.96E-19	0.288	2.68E-07	0.316	0.33	1
ch1v	9.90E-13	0.273	1.43E-05	0.35	0.03	1
ch2v	9.27E-14	0.345	5.13E-05	0.299	0.07	1
ch3v	9.27E-14	0.345	5.13E-05	0.299	0.07	1
ch4v	9.27E-14	0.345	5.13E-05	0.299	0.07	1
ch5v	9.27E-14	0.345	5.13E-05	0.299	0.07	1
ch2z	6.07E-18	0.331	3.47E-06	0.244	0.28	1
ch3z	6.07E-18	0.331	3.47E-06	0.244	0.28	1
ch4z	6.07E-18	0.331	3.47E-06	0.244	0.28	1
ch5z	6.07E-18	0.331	3.47E-06	0.244	0.28	1
ch6	4.23E-19	0.266	3.38E-07	0.51	0.37	1
pp4	4.28E-18	0.325	1.51E-07	0.676	0.28	1
pp3	2.56E-14	0.303	2.60E-05	0.363	0.1	1
pp2	1.57E-16	0.263	2.67E-06	0.369	0.18	1
pp1	6.40E-17	0.28	1.14E-06	0.409	0.3	1
bf3	2.34E-14	0.115	4.48E-06	0.481	0.11	1
bf2	2.51E-17	0.259	1.54E-07	0.569	0.18	1

DTN: LB990861233129.001

Table 4-3. Fracture properties of stratigraphic units

Unit	Permeability (m <sup>2</sup> )	Porosity	Van Genuchten $\alpha$ (Pa <sup>-1</sup> )	Van Genuchten $\beta$	Residual Saturation (Fraction)	Saturated Saturation (Fraction)	Active Fracture Parameter	Frequency (1/m)	Fracture to matrix area (m <sup>2</sup> /m <sup>3</sup> )
tcw11	2.41E-12	0.028	3.15E-03	0.627	0.01	1	0.30	0.92	1.56
tcw12	1.00E-10	0.02	2.13E-03	0.613	0.01	1	0.30	1.91	13.39
tcw13	5.42E-12	0.015	1.26E-03	0.607	0.01	1	0.30	2.79	3.77
ptn21	1.86E-12	0.011	1.68E-03	0.58	0.01	1	0.09	0.67	1.00
ptn22	2.00E-11	0.012	7.68E-04	0.58	0.01	1	0.09	0.46	1.41
ptn23	2.60E-13	0.0025	9.23E-04	0.61	0.01	1	0.09	0.57	1.75
ptn24	4.67E-13	0.012	3.37E-03	0.623	0.01	1	0.09	0.46	0.34
ptn25	7.03E-13	0.0062	6.33E-04	0.644	0.01	1	0.09	0.52	1.09
ptn26	4.44E-13	0.0036	2.79E-04	0.552	0.01	1	0.09	0.97	3.56
tsw31	3.21E-11	0.0055	2.49E-04	0.566	0.01	1	0.06	2.17	3.86
tsw32	1.26E-12	0.0095	1.27E-03	0.608	0.01	1	0.41	1.12	3.21
tsw33	5.50E-13	0.0066	1.46E-03	0.608	0.01	1	0.41	0.81	4.44
tsw34	2.76E-13	0.01	5.16E-04	0.608	0.01	1	0.41	4.32	13.54
tsw35	1.29E-12	0.011	7.39E-04	0.611	0.01	1	0.41	3.16	9.68
tsw36	9.91E-13	0.015	7.84E-04	0.61	0.01	1	0.41	4.02	12.31
tsw37	9.91E-13	0.015	7.84E-04	0.61	0.01	1	0.41	4.02	12.31
tsw38	5.92E-13	0.012	4.87E-04	0.612	0.01	1	0.41	4.36	13.34
tsw39	4.57E-13	0.0046	9.63E-04	0.634	0.01	1	0.41	0.96	2.95
ch1z	3.40E-13	0.0002	1.43E-03	0.631	0.01	1	0.10	0.04	0.11
ch1v	1.84E-12	0.0007	1.09E-03	0.624	0.01	1	0.13	0.10	0.30
ch2v	2.89E-13	0.0009	5.18E-04	0.628	0.01	1	0.13	0.14	0.43
ch3v	2.89E-13	0.0009	5.18E-04	0.628	0.01	1	0.13	0.14	0.43
ch4v	2.89E-13	0.0009	5.18E-04	0.628	0.01	1	0.13	0.14	0.43
ch5v	2.89E-13	0.0009	5.18E-04	0.628	0.01	1	0.13	0.14	0.43
ch2z	3.12E-14	0.0004	4.88E-04	0.598	0.01	1	0.10	0.14	0.43
ch3z	3.12E-14	0.0004	4.88E-04	0.598	0.01	1	0.10	0.14	0.43
ch4z	3.12E-14	0.0004	4.88E-04	0.598	0.01	1	0.10	0.14	0.43
ch5z	3.12E-14	0.0004	4.88E-04	0.598	0.01	1	0.10	0.14	0.43
ch6	1.67E-14	0.0002	7.49E-04	0.604	0.01	1	0.10	0.04	0.11
pp4	3.84E-14	0.0004	5.72E-04	0.627	0.01	1	0.10	0.14	0.43
pp3	7.60E-12	0.0011	8.73E-04	0.655	0.01	1	0.46	0.20	0.61
pp2	1.38E-13	0.0011	1.21E-03	0.606	0.01	1	0.46	0.20	0.61
pp1	1.12E-13	0.0004	5.33E-04	0.622	0.01	1	0.10	0.14	0.43
bf3	4.08E-13	0.0011	9.95E-04	0.624	0.01	1	0.46	0.20	0.61
bf2	1.30E-14	0.0004	5.42E-04	0.608	0.01	1	0.10	0.14	0.43

DTN: LB990861233129.001

Table 4-4. Thermal properties of stratigraphic units

Model Layer	Rock Grain Density	Rock Grain Specific	Dry Conductivity	Wet Conductivity
	Kg/m <sup>3</sup>	Heat (J/Kg K)	W/m K	W/m K
tcw11	2550	823	1.6	2
tcw12	2510	851	1.24	1.81
tcw13	2470	857	0.54	0.98
ptn21	2380	1040	0.5	1.07
ptn22	2340	1080	0.35	0.5
ptn23	2400	849	0.44	0.97
ptn24	2370	1020	0.46	1.02
ptn25	2260	1330	0.35	0.82
ptn26	2370	1220	0.23	0.67
tsw31	2510	834	0.37	1
tsw32	2550	866	1.06	1.62
tsw33	2510	882	0.79	1.68
tsw34	2530	948	1.56	2.33
tsw35	2540	900	1.2	2.02
tsw36	2560	865	1.42	1.84
tsw37	2560	865	1.42	1.84
tsw38	2360	984	1.69	2.08
tsw39	2360	984	1.69	2.08
ch1z	2310	1060	0.7	1.31
ch1v	2310	1060	0.7	1.31
ch2v	2240	1200	0.58	1.17
ch3v	2240	1200	0.58	1.17
ch4v	2240	1200	0.58	1.17
ch5v	2240	1200	0.58	1.17
ch2z	2350	1150	0.61	1.2
ch3z	2350	1150	0.61	1.2
ch4z	2350	1150	0.61	1.2
ch5z	2350	1150	0.61	1.2
ch6	2440	1170	0.73	1.35
pp4	2410	577	0.62	1.21
pp3	2580	841	0.66	1.26
pp2	2580	841	0.66	1.26
pp1	2470	635	0.72	1.33
bf3	2570	763	1.41	1.83
bf2	2410	633	0.74	1.36

DTN: LB991091233129.006

#### 4.1.11 Stratigraphy

The primary input for stratigraphy to map rock materials onto the computational mesh is from two files. The first is `tspa99_primary_mesh` [renamed, original filename is `UZ99_3_3D.mesh` (LB990701233129.001)], which is the numerical mesh for the site-scale UZ flow model. The second is `UZ99_3.grd` (LB990701233129.001), which is the vertices file for that mesh. These two files, which define the numerical mesh for the 3-D site-scale UZ-flow model, are used to generate the numerical meshes for each submodel (Sections 6.2.2, 6.3.2, 6.4.2 and 6.5.2). This input is appropriately used.

#### 4.1.12 Infiltration Flux

Infiltration flux is given for three climate periods: [present climate ( $0 < t < 600$  yr), monsoonal climate ( $600 < t < 2000$  yr), and glacial climate ( $2000 < t < 1000000$  yr)] in the nine files `Monsoon*.dat`, `Glacial*.dat`, and `Modern*.dat` (\*represents l, m and u) (source of these nine files: GS000308311221.005). This information is used in Section 6.3.6. This input is appropriately used.

#### 4.1.13 Heat-Generation Rate

Heat-generation decay curves for each of the MSTHM submodel types are based on information in the files `2-Dwperimeter.xls` and `heatTSPA-SR-99184.txt`. The file `2-Dwperimeter.xls` contains:

- decay curves for CSNF (CRWMS M&O 1999d, Item 2: Table 2, pp 3-6),
- decay curves for DHLW (See Assumption 5.3.1),
- decay curves for DSNF (See Assumption 5.3.1), and
- a seven waste package model of the waste stream (CRWMS M&O 1999d, Item 2: Worksheet 2, p 16).

The CSNF decay curves in `2-Dwperimeter.xls` are duplicated in `heatTSPA-SR-99184.txt`.

This information is used by all submodels (Section 6.2, Section 6.3, Section 6.3, and Section 6.5) through inclusion in the above mentioned files. This input is appropriately used.

#### 4.1.14 Boundary Conditions

Temperature and pressure for the 3-D site-scale UZ-flow model are found in the file `bcs99.dat` (LB991201233129.001). This information is used to generate boundary conditions for all submodels (Section 6.2, Section 6.3, Section 6.3, and Section 6.5). This input is appropriately used.

#### **4.1.15 Enthalpy**

Liquid enthalpy at 16 and 17 degrees Celsius is 67.19 J/gram and 71.38 J/gram, respectively (Keenan et al. 1969, p. 2). Accepted Data (established fact, handbook value) used in (Schreiner 2001, Attachment VI). This input is appropriately used.

#### **4.2 CRITERIA**

Specific criteria for this AMR has not been developed at this time.

The calculations for this AMR are based on the following criteria:

1. Repository footprint for EDA II is modeled for a total of 70,000 MTU of waste, including 63,000 MTU of civilian spent nuclear fuel (CSNF) and 7000 MTU of defense high-level water (DHLW), which includes both high-level waste (HLW) WPs and defense spent nuclear fuel (DSNF) WPs.. Extended waste inventories may be addressed in subsequent revisions (Stroupe 2000, Attachment I, p.1).
2. Emplacement drifts are ventilated for the entire preclosure period. The preclosure period is assumed to be 50 yr and drift ventilation is assumed to remove 70% of the heat output from WPs throughout the repository area (Stroupe 2000, Attachment I, p.1).
3. Emplacement drifts are backfilled at the end of the preclosure period. Drip shields are emplaced at the same time as backfill (Stroupe 2000, Attachment I, p.1).
4. For the no-backfill case as identified in this AMR the emplacement drifts are to be left open with only the drip shield installed (CRWMS M&O 2000e).

#### **4.3 CODES AND STANDARDS**

No codes and standards were used in the preparation of this document.

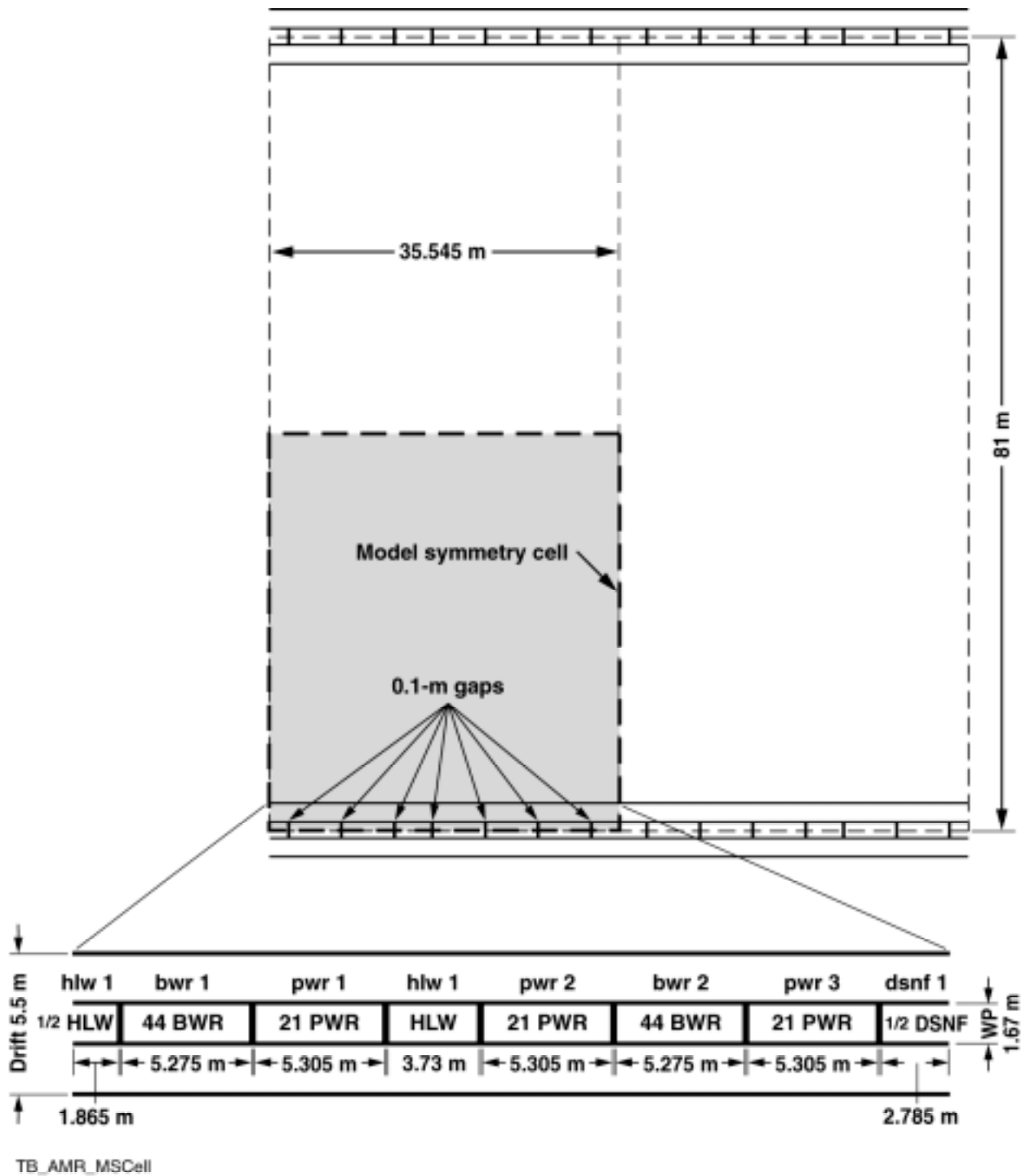


Figure 4-1. Diagram showing drift spacing, WP lengths, and WP spacing. The names of the respective WPs (hlw 1, bwr 1, etc.) used in the DDT submodel (Section 6.5) are given above each WP.

## 5. ASSUMPTIONS

### 5.1 BOUNDARY CONDITIONS

#### 5.1.1 Areal Block Model

The repository footprint is adequately represented with the repository model outline shown in Figure 5-1. The variability of stratigraphy, temperature, pressure, and infiltration across the top boundary of the repository is adequately represented by determining these values at the 31 locations in column.data (CRWMS M&O 2000a) and illustrated in Figure 5-2. This assumption is implicit in the file column.data (CRWMS M&O 2000a). Used in Sections 6.3.1 and 6.4.1.

Rationale: The actual repository footprint has an area of 4,310,041 m<sup>2</sup> (Schreiner 2001, Table XV-2) and the block model has a cross sectional area of 4,216,139 m<sup>2</sup> (Schreiner 2001, Table XV-1). This is a difference of less than three percent. As can be seen in Figure 5-1, the area enclosed by the actual and modeled repository is similar. The 31 locations are evenly spaced within the repository model. The MSTHM grid resolution is precise enough that the results would not be affected by increasing the grid resolution. This assumption does not require confirmation.

#### 5.1.2 Gaussian Interpolation

The normalized results from Gaussian interpolation [(Isaaks and Srivastava 1989, p. 208) and (Kitanidis 1997, p. 54); see Schreiner 2001, Eq. XIV-2] adequately represent infiltration rates.

This assumption is used in all LDTH submodels (Section 6.3) through incorporation in the NUFT input files (CRWMS M&O 2000a, files: \*.in). The interpolated data is in the files output from ColumnInfiltration (CRWMS M&O 2000a, 9 files: \*.out; see Figure 3-4). The normalization is done in (Schreiner 2001, Table XVII-1).

Rationale: The Gaussian method strongly weights the closest points. For a given point, the infiltration rates at relatively close points are the best indicators. It was authors choice to use this method for its application in this document. This assumption does not require confirmation.

#### 5.1.3 Inverse Distance Interpolation

The inverse distance equation (Isaaks and Srivastava 1989, p. 258. See Schreiner 2001, Table XIII-1 for this equation) is appropriate for interpolating temperature and pressures at model boundaries. Chim\_surf\_TP and chim\_wt\_TP (validated in Schreiner 2001) interpolate the temperature and pressure at the ground surface and water table using the inverse distance cubed equation. SMT\_surf\_TP and SMT\_bot\_TP use the inverse distance squared equation to interpolate temperatures at the boundaries of the SMT submodels (Section 6.2.3 and Schreiner 2001).

Rationale: The inverse distance method strongly weights the closest points. The actual power chosen is subjective and has a negligible effect on the numerical results. For a given point, the

temperature and pressure at relatively close points are the best indicators. It was authors choice to use this method for its application in this document. This assumption does not require confirmation.

#### **5.1.4 Relative Humidity at Ground Surface**

The relative humidity at the ground surface is assumed to be 100%. This assumption is used in Section 6.3.3, and impacts all LDTH submodel input files.

Rationale: This bounds humidity effects by minimizing evaporation. This assumption does not require confirmation.

#### **5.1.5 LDTH Boundary Conditions**

The density of the upper boundary is assumed to have a value of  $1 \times 10^8$  Kg/m<sup>3</sup>. The heat capacity of the upper boundary is assumed to have a value of  $1 \times 10^8$  J/Kg-K. The thermal conductivity of the upper boundary is assumed to have a value of 0.17 W/m-K.

Rationale: The values used for this boundary condition are required in the NUFT input files, but the specific values chosen have no numerical impact. The thickness of this boundary is  $1 \times 10^{-30}$ m and the conditions are held constant by NUFT. These values are used in 6.3.3 through incorporation in the files: dkm-afc-1Dds-mc-li-00, dkm-afc-1Dds-mc-mi-00, and dkm-afc-1Dds-mc-ui-00. This assumption does not require confirmation.

#### **5.1.6 SMT, DDT, and SDT Boundary Conditions**

The density of the upper boundary is assumed to have a value of 1.185 Kg/m<sup>3</sup>. The heat capacity of the upper boundary is assumed to have a value of  $1 \times 10^3$  J/Kg-K. The thermal conductivity of the upper boundary is assumed to have a value of 0.0254 W/m-K. These values are used in 6.2.3, 6.4.3, and 6.5.3 through incorporation in the file SDT-1Dds\_mi (CRWMS M&O 2000a).

Rationale: The values used for this boundary condition are required in the NUFT input files, but the specific values chosen have no numerical impact. The thickness of this boundary is  $1 \times 10^{-30}$ m and the conditions are held constant by NUFT. This assumption does not require confirmation.

### **5.2 MATERIAL PROPERTIES**

#### **5.2.1 Permeability of Drip Shield and Waste Package**

The drip shield and WP are assumed to be impermeable for the entire duration of the MSTHM simulation. This assumption is implicit by the absence of permeable or semi-permeable barriers in the EBS (used throughout).

Rationale: These EBS components will take a long time to fail, and it is beyond the scope of this document to model their failure. Even after these components have been perforated, the

capillarity of the overlying Overton sand backfill will prevent (or greatly limit) the flux of water that can enter the perforations. This assumption does not require confirmation.

### **5.2.2 Tortuosity of Backfill and Invert Materials**

The assumed value for tortuosity of the backfill and invert materials is 0.7. This assumption is used in all NUFT input files (used throughout).

Rationale: This value is consistent with the tortuosity values for the natural barrier system. This assumption does not require confirmation.

### **5.2.3 Satiated Saturation of Invert and Backfill Materials**

The assumed value for satiated saturation of the invert and backfill materials is 1.0. This assumption is used in all NUFT input files (used throughout).

Rationale: This is an upper bound for this parameter, and is therefore conservative. This assumption does not require confirmation.

### **5.2.4 Thermal Conductivity Used in Conduction-Only Submodels**

The thermal conductivity data is provided for both dry and wet conditions. The conduction-only submodels (SDT, DDT, and SMT submodels) cannot explicitly represent the influence of liquid saturation on thermal conductivity. Because the rock is predominately closer to being fully saturated (i.e., wet), it was decided to assume the wet value of thermal conductivity (See Table 4-4) for all of the conduction-only submodels. This assumption is used in Sections 6.2.5 and 6.4.5, and has no effect on the results of the MSTHM.

Rationale: This assumption has no effect on the MSTHM results because the influence of liquid saturation is explicitly represented by the LDTH submodels. The scanning curves that relate LDTH temperature to SDT temperature (see Section 6.6 for MSTHAC methodology) automatically correct for the influence of TH processes (including liquid saturation) on temperature. As long as the SDT and SMT submodels utilize consistent assumptions (and data) concerning the thermal conductivity of the stratigraphic units, then the influence of liquid saturation on temperature is rigorously accounted for. As for the validity of this assumption in the DDT submodel, it is important to note that the DDT submodel is only used for two purposes: (1) calculating the temperature difference between the WP and drip shield and (2) calculating the longitudinal temperature variations along the drift axis. Neither of these quantities are influenced by whether wet or dry thermal conductivity is applied in the host rock. This assumption does not require confirmation.

### **5.2.5 Saturated-Zone Thermal Conductivity**

The SMT submodel (Section 6.2) is the only submodel that explicitly represents the saturated zone (SZ). A description of the distribution of the stratigraphic units below the water table is not available; therefore, there was no available data source for determining the distribution of the stratigraphic units in the SZ portion of the SMT submodel. An assumption is made that the SZ is

comprised of the pp1 unit (Table 4-1) because it is the predominant stratigraphic unit at the water table for the 31 drift-scale-submodel locations. At 14 out of 31 drift-scale-submodel locations, the pp1 unit is at the water table. Used in Section 6.2.

Rationale: The pp1 unit is the predominant unit at the water table of the 31 drift-scale-submodel locations (with 14 out of 31 locations having the pp1 unit at the water table). Furthermore, for the 5 stratigraphic units (pp4, pp3, pp2, pp1, bf3, and bf2) that reside at the water table in the 31 drift-scale-submodel locations, the average wet thermal conductivity is 1.375 W/m-K [ $1.375 = (1.21 + 1.26 + 1.26 + 1.33 + 1.83 + 1.36)/6$ ], which is very close to the value of wet thermal conductivity in the pp1 unit (Table 4-4, 1.33 W/m-K). The output of this report is not sensitive to this assumption, and therefore this assumption does not need confirmation.

### 5.2.6 Thermal Conductivity and Density for the Active Fracture Model

The thermal conductivity and density values of the fracture and matrix are apportioned by the following

$$\begin{aligned} \text{fracture conductivity} &= \text{total conductivity} \times (\text{fracture porosity}) \\ \text{matrix conductivity} &= \text{total conductivity} \times (1 - \text{fracture porosity}) \\ \text{fracture density} &= \text{total density} \times (\text{fracture porosity}) \\ \text{matrix density} &= \text{total density} \times (1 - \text{fracture porosity}) \end{aligned}$$

Rationale: There is no commonly accepted approach to apportioning fracture and matrix conductivity and density. However, it is important to note that we conserve the total value of conductivity and the total value of density. Therefore, the total conductive heat flow is the same as a single continuum with the same total value of thermal conductivity. Similarly, during the transient (heatup) period, we honor the correct mass density of the rock mass. This assumption has no impact on this model. This method is used in all submodels (used throughout). This assumption does not require confirmation.

### 5.2.7 Thermal Properties of the Backfill and Invert for the Backfill Case

The thermal properties for the backfill and crushed tuff for the backfill case as reported in Table 4-1 were taken from *Repository Subsurface Design Information to Support TSPA-SR*. Input Transmittal PA-SSR-99218.Ta (CRWMS M&O 1999f, Item 2 pp. 3-4 and pp. 13-14). Used in sections 6.3.5 and 6.5.5.

It is assumed that these data from an unqualified source adequately describe the thermal properties of Overton sand and crushed tuff for the backfill case for the purposes of thermohydrological modeling. This assumption is justified because the data used are the best available data and were developed using sound engineering judgement. Any changes to these data during qualification are not expected to be of such magnitude to impact model results.

Rationale: This was the best available data at the time this AMR was produced. This assumption does not require confirmation since the current design basis does not include backfill.

### 5.2.8 Thermal Conductivity, the Lower and Upper Invert Layer for the No-Backfill Case

The thermal conductivity of the crushed tuff invert material were taken from the *Repository Subsurface Design Information to Support TSPA-SR*. Input Transmittal PA-SSR-99218.Tc (CRWMS M&O 2000g, p. 23). The specific heat capacity and density for the crushed tuff properties were taken from *Repository Subsurface Design Information to Support TSPA-SR*. Input Transmittal PA-SSR-99218.Ta (CRWMS M&O 1999f, Item 2 pp. 13-14). Used in section 6.3.5 and 6.5.5.

These data from unqualified sources are assumed to adequately describe the thermal conductivity, specific heat capacity and density of the crushed tuff invert material for the no-backfill case in the thermohydrologic model. This assumption is justified because the data are the best available and were developed by applying sound engineering judgement. Any variations in the data that may occur as the qualification process is advanced are not expected to be substantial enough to impact model conclusions.

In addition, the invert of the no-backfill case consists of two layers with respect to thermal conductivity  $K_{th}$ . The lower half of the invert (called the lower invert layer) has a  $K_{th}$  value for pure crushed tuff (Section 4.1.6). The document *Invert Effective Thermal Conductivity Calculation* (CRWMS M&O 2000i, pp. 15-24) presents a calculation of thermal conductivity for a composite upper invert comprised of steel beams and crushed tuff of various thicknesses. Because of the orientation of the steel beams, there is directional anisotropy for the effective  $K_{th}$  of the upper invert layer. Because NUFT does not handle directional anisotropy in  $K_{th}$ , it was judged that a lateral value of  $K_{th}$  (1.520 W/m-K) is the most appropriate single value of  $K_{th}$  for the upper invert layer in the no-backfill calculations in the DDT and LDTH submodels.

Rationale: The value of  $K_{th}$  in the upper invert layer is applied to the DDT submodels as well as to the LDTH submodels. An important function of the DDT submodels is to predict the WP-to-WP variability of temperature conditions along the emplacement drifts. It is important not to overpredict axial attenuation of WP-to-WP temperature variability of (by virtue of the choice of  $K_{th}$  in the upper invert layer in the DDT submodels). Note that in general the vertical  $K_{th}$  is much larger than the axial value of  $K_{th}$ , which is much closer to the lateral value of  $K_{th}$ . Had the vertical  $K_{th}$  value been chosen for the upper invert layer, this would have artificially added to the attenuation of WP-to-WP temperature variability in the DDT submodels, which would be nonconservative with respect to WP-to-WP temperature variability. It was judged that preserving the WP-to-WP variability of temperature conditions (by virtue of not using the large vertical  $K_{th}$  value) is a reasonably conservative choice. Because the axial value of  $K_{th}$  does not affect heat flow in the LDTH submodels, it was judged that it was best to choose the lateral value of  $K_{th}$ , which does influence heat flow in the LDTH submodels. Moreover, the lateral  $K_{th}$  value lies between the axial and vertical  $K_{th}$  values, and is therefore is closer to being an "average"  $K_{th}$  value for the upper invert layer; an average  $K_{th}$  value is preferred when only a single value of  $K_{th}$  can be used.

## 5.3 HEAT GENERATION AND HEAT TRANSFER

### 5.3.1 Heat Generation

(1) Heat-generation decay curves for the SMT, SDT, and LDTH submodels in the no-backfill case are slightly modified from those used in the backfill case (Section 4.1.13). The heat-generation decay curves for the DDT submodels are the same for the no-backfill and backfill cases. This assumption is used in Section 6.5.4.

(2) It is assumed that the decay curves for DHLW and DSNF calculated for the TSPA-VA describe the likely behavior of those waste forms in the repository. The decay curves are contained in DTN:SNT0571897001.004 (DHLW decay curves in file avgdhlw.tst and DSNF decay curves in file nrctor4pck.txt).

Rationale: (1) For the backfill case, the initial lineal power density is 1.5404 kW/m averaged over all of the emplacement drifts in the repository. For the no-backfill case, the initial lineal power density is specified to be 1.45 kW/m (Stroupe 2000, Attachment I p. 1). The heat-generation decay curves for the SMT, SDT, and LDTH submodels used in the backfill cases are multiplied by a factor of 1.45/1.5404 (= 0.94131) to obtain the revised curves for the no-backfill case. Because the heat-generation decay curves for individual WPs did not change (between the backfill and no-backfill cases), it was not necessary to modify the decay curves for the DDT submodels used in the no-backfill case. Moreover, the primary purpose of the DDT submodels is to determine the deviations of local temperatures at various WP locations from the line-averaged temperature conditions along the emplacement drifts. The DDT submodels are not used to determine absolute temperatures along emplacement drifts; therefore, the lineal power density in the DDT submodels does not have to be exactly equal to the repository-wide average. This assumption is used in all submodels.

(2) The justification for this assumption is that the calculations performed for the TSPA-VA are the best available information on thermal decay of these waste forms. The calculations are heat generation calculations similar to those used to produce the decay curves of CSNF, documented in CRWMS M&O 1999d, Item 2: Table 2, pp 3-6, and are based on the best available data for DHLW and DSNF. This assumption is used in Section 4.1.13.

### 5.3.2 Constant Heat Flux

The present day heat flux from the ground surface to the water table is constant. This assumption allows a simplification in the heat transfer equations used in Attachment I.

Rationale: This assumption has no impact on this model, and does not require confirmation. Used in Attachment I and Section 6.2.3.

### 5.3.3 Effective Thermal Conductivity

It is assumed that the data contained in the unqualified DTN SN9907T0872799.002 adequately describe the time-dependent thermal effective conductivity  $K_{\text{eff}}$  of the air in the emplacement

drift. The data contained in that DTN were developed from unqualified sources that do not meet current data quality requirements. This assumption used throughout the submodels.

For Rev 00, ICN 01, and ICN 02, there is an underlying assumption that the time-dependent effective thermal conductivity  $K_{\text{eff}}$  of air is not dependent on AML. It is also assumed that the time-dependent  $K_{\text{eff}}$  from DTN SN9907T0872799.002 is applicable to both 2-D and 3-D models.

Rationale: The primary justification for these assumptions is that these data are the only available source for these parameters and were developed using technically sound measurement and analytical methods. Because the 3-D LDTH model calculations performed for ICN 02 have negligible temperature variation along the third (axial) dimension, the assumption that  $K_{\text{eff}}$  applies to both the 2-D and 3-D models is justified for ICN 02. These assumptions do not require confirmation.

#### **5.3.4 Random Fields for Stochastic Realizations**

It is assumed that the results of the NUFT stochastic near field properties generator (random field generator) are consistent with the input parameters used as inputs to NUFT. This feature of NUFT is being qualified in parallel with development of this document. This assumption is only used in Section 6.14.

Rationale: Visual inspection of the results did not reveal any non-random structure.

### **5.4 GEOMETRIC DESCRIPTION OF THE EBS AND MATERIAL PROPERTIES**

Repository layout parameters, which include the footprint, waste package dimensions and drift geometry outlined in Sections 5.4.1 through 5.4.3.10 below are from CRWMS M&O 2000d, 1999f. The assumed parameters represent the repository design in effect at the time this document was developed and are the best available information for the purpose of thermohydrologic modeling. As the design of the repository is advanced, parameter changes will be evaluated for their affect upon the thermohydrologic model during future revisions.

#### **5.4.1 Repository Footprint**

The coordinates of the drift endpoints are given in the file dft1.dat and are based upon the EDA II Layout as presented in *Request for Repository Subsurface Design Information to Support TSPA-SR* (CRWMS M&O 1999f, Item 1). These coordinates were used to develop the repository footprint representation used in the SMT submodel (Section 6.2.1), and to generate the 31 LDTH submodel locations in Section 6.3.1. Figure 5-1 illustrates the actual and modeled repository footprint.

Rationale: This is a representative layout of the repository, the actual footprint may vary within the confines of this overall layout. This assumption does not require confirmation.

## **5.4.2 Waste Package Lengths and Sequencing**

The waste package (WP) lengths and WP sequencing (Figure 4-1) is taken from the *Enhanced Design Alternative (EDA) II Repository Estimated Waste Package Types and Quantities*. (CRWMS M&O 1999d Item 1 pp. 25-26). Figure 4-1 shows the WP lengths, and WP sequencing (including WP-to-WP spacing) that is used in this AMR.

Rationale: This is a representative layout of the waste package lengths and spacing, the final may vary from what is presented. This assumption does not require confirmation.

## **5.4.3 Cross Section Geometry of the Backfilled Emplacement Drift**

Figure 5-3 shows all of the details of the cross-sectional geometry of the emplacement drift after the drip shield and backfill are emplaced as presented in CRWMS M&O 1999f. Figure 5-3 applies to the backfill case; it also applies to the no-backfill case, except that the area shown as backfill is replaced with an open cavity. These geometric details are used in this AMR. This information is used in the LDTH submodels (Section 6.3) and in the DDT submodels (Section 6.5). This assumption does not require confirmation.

Rationale: This is a representative layout of the repository, the actual footprint may vary within the confines of this overall layout.

### **5.4.3.1 Angle of Repose of Backfill**

The angle of repose of the backfill is  $26^\circ$  as presented in CRWMS M&O 1999f. This information is used in the LDTH submodels.

Rationale: This assumption is only applicable to the backfill case and is a nominal construction value. This assumption is not required by the no-backfill case. This assumption does not require confirmation.

### **5.4.3.2 Minimum Depth of Backfill Cover**

The minimum depth of the backfill cover (occurs at an angle equivalent to the angle of repose measured off the vertical drawn from the WP centerline) is 1.495 m as presented in CRWMS M&O 1999f. This information is used in the LDTH submodels (Section 6.3).

Rationale: This assumption is only applicable to the backfill case and is not required by the no-backfill case. This assumption does not require confirmation.

### **5.4.3.3 Location of Backfill Peak**

The backfill peak crosses the drift centerline 2.25 m above the drift springline as presented in CRWMS M&O 1999f. This information is used in the LDTH submodels (Section 6.3).

Rationale: This assumption is only applicable to the backfill case and is not required by the no-backfill case. This assumption does not require confirmation.

#### **5.4.3.4 Intersection Between Backfill and Drift Wall**

The backfill profile intersects the drift wall 1.0 m above the drift springline as presented in CRWMS M&O 1999f. This information is used in the LDTH submodels (Section 6.3).

Rationale: This assumption is only applicable to the backfill case and is not required by the no-backfill case. This assumption does not require confirmation.

#### **5.4.3.5 Drip Shield Radius**

The portion of the drip shield above the centerline of the WP has an inside radius of 1.231 m as presented in CRWMS M&O 1999f. This information is used in the LDTH submodels (Section 6.3) and in the DDT submodels (Section 6.5). For ICN 2 of this AMR, the drip-shield radius is 1.256 m (See Section 6.14.4).

Rationale: This assumption is a representation of the drip shield, the final version may vary within the confines of these general parameters. This assumption does not require confirmation.

#### **5.4.3.6 Location of Waste Package**

The WP centerline is 1.945 m above the bottom of the drift and 0.805 m below the springline as presented in CRWMS M&O 1999f. This information is used in the LDTH (Section 6.3) and DDT submodels (Section 6.5).

Rationale: This assumption depicts the general location of the waste package within the confines of the emplacement drift and may vary in the final configuration. This assumption does not require confirmation.

#### **5.4.3.7 Waste Package Diameter**

The WP outer diameter is 1.67 m and is taken as the average diameter for the inventory from the *Enhanced Design Alternative (EDA) II Repository Estimated Waste Package Types and Quantities*. (CRWMS M&O 1999d Item 1 pp. 25-26). This information is used in the DDT submodels (Section 6.5).

Rationale: This assumption only influences two aspects of the MSTHM: (1) the temperature difference between the waste package and drip shield and (2) the waste-package-to-waste-package variation of this temperature difference. Note that this temperature difference also depends on the waste-package heat output. The 21-PWR and 44-BWR CSNF waste packages, comprising nearly all waste packages with an appreciable heat output (CRWMS M&O 1999d Worksheet 3 p.18), have diameters of 1.564 m and 1.594 m, respectively (CRWMS M&O 1999d Table 8 p. 25), which are very close to the value of 1.67 m in the DDT submodels; these waste packages also comprise a large portion (71.3 percent) of the overall waste-package inventory (CRWMS M&O 1999d Worksheet 3 p. 18). Waste packages that deviate more from this average diameter, such as the 24-BWR 1.238-m-diameter CSNF waste packages and the 5-DHLW/DOE 2.03-m-diameter co-disposal waste packages, generate much less heat and also comprise a relatively small portion of the overall waste-package inventory. Therefore, the assumed diameter

of 1.67 m is very close to the actual diameter for the majority of waste packages in the overall inventory and is also very close to the diameter of the waste packages generating an appreciable temperature difference between the waste package and drip shield. This assumption does not require confirmation.

#### **5.4.3.8 Gap Between Waste Package and Drip Shield**

The gap between the top half of the WP and the drip shield is 0.396 m as presented in CRWMS M&O 1999f. This information is used in the DDT submodels (Section 6.5).

Rationale: This assumption is consistent with the waste-package-diameter assumption (Section 5.4.3.7). Because thermal radiation is the dominant mode of heat transfer between the waste package and the drip shield, the gap between the waste package and drip shield has little influence on predicted behavior in the MSTHM. This assumption does not require confirmation.

#### **5.4.3.9 Gap Between Waste Package and Invert**

The gap between the bottom of the WP and the invert is 0.504 m as presented in CRWMS M&O 1999f. This information is used in the DDT submodels (Section 6.5).

Rationale: This is an overall representation of this dimension. This assumption does not require confirmation.

#### **5.4.3.10 Invert Height**

The top of the invert is 0.606 m above the bottom of the drift as presented in CRWMS M&O 1999f. This information is used in the LDTH (Section 6.3) and DDT submodels (Section 6.5). For ICN 2 of this AMR, the invert height is 0.806 m (See Section 6.14.4).

Rationale: This is an overall representation of the invert, actual conditions may vary within the overall confines of this assumption. This assumption does not require confirmation.

#### **5.4.3.11 Drip-Shield Height**

For Rev 00 and ICN 1 of this AMR, the top of the drip shield is 2.566 m above the top of the invert. For ICN 2 of this AMR, the top of the drip shield is 2.521 m above the top of the invert (See Section 6.14.4).

Rationale: This assumption is a representation of the drip shield, the final version may vary within the confines of these general parameters. This assumption does not require confirmation.

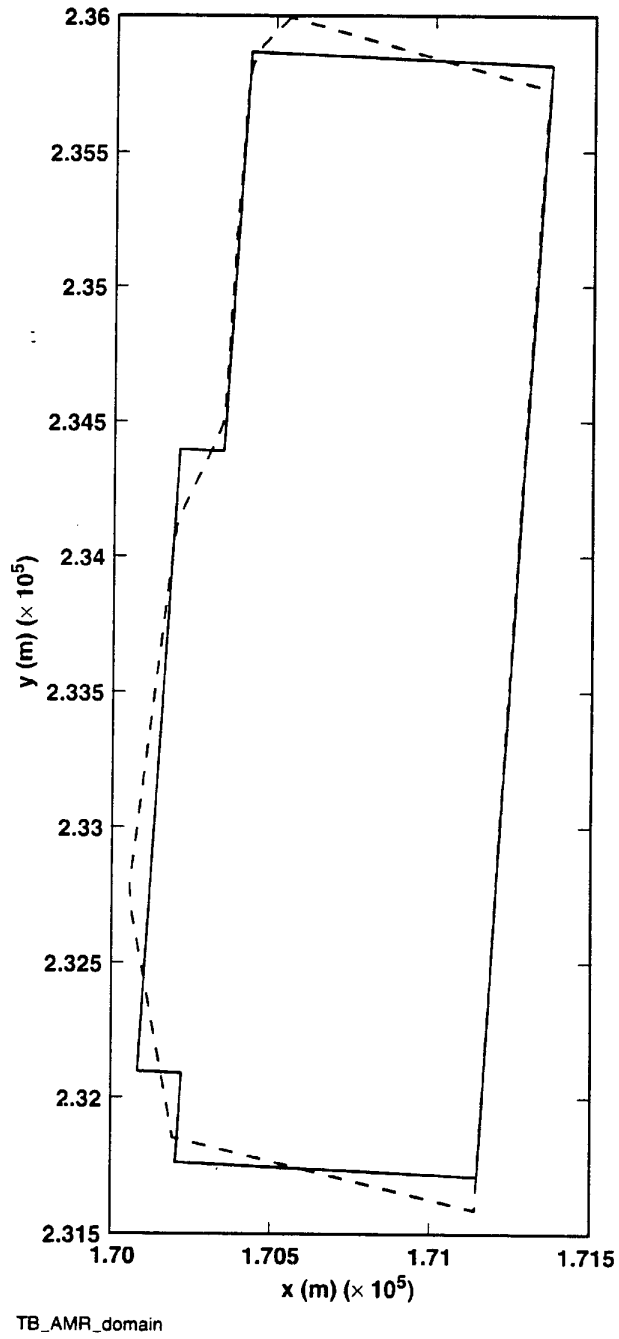


Figure 5-1. Comparison of the actual repository footprint and the approximation of the repository footprint that is assumed in the MSTHM

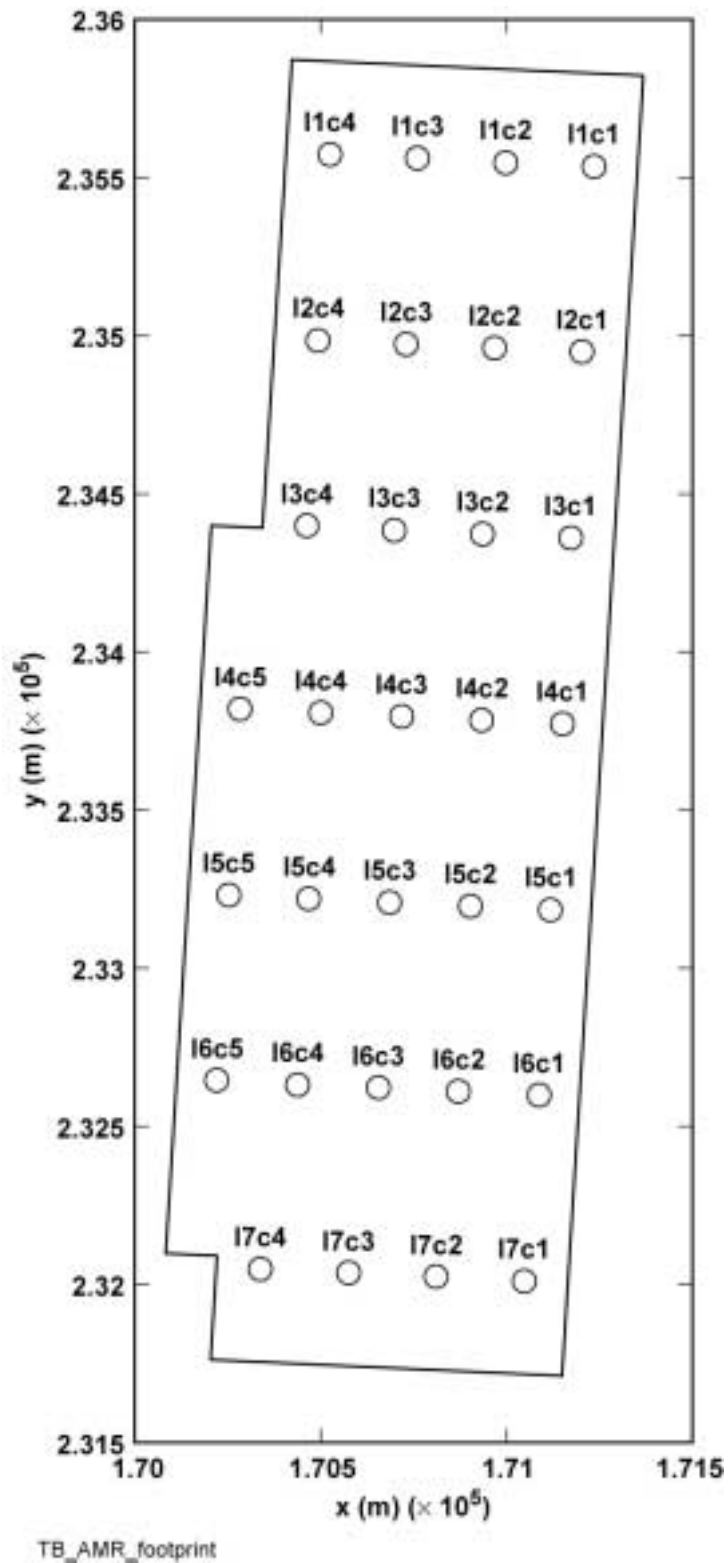
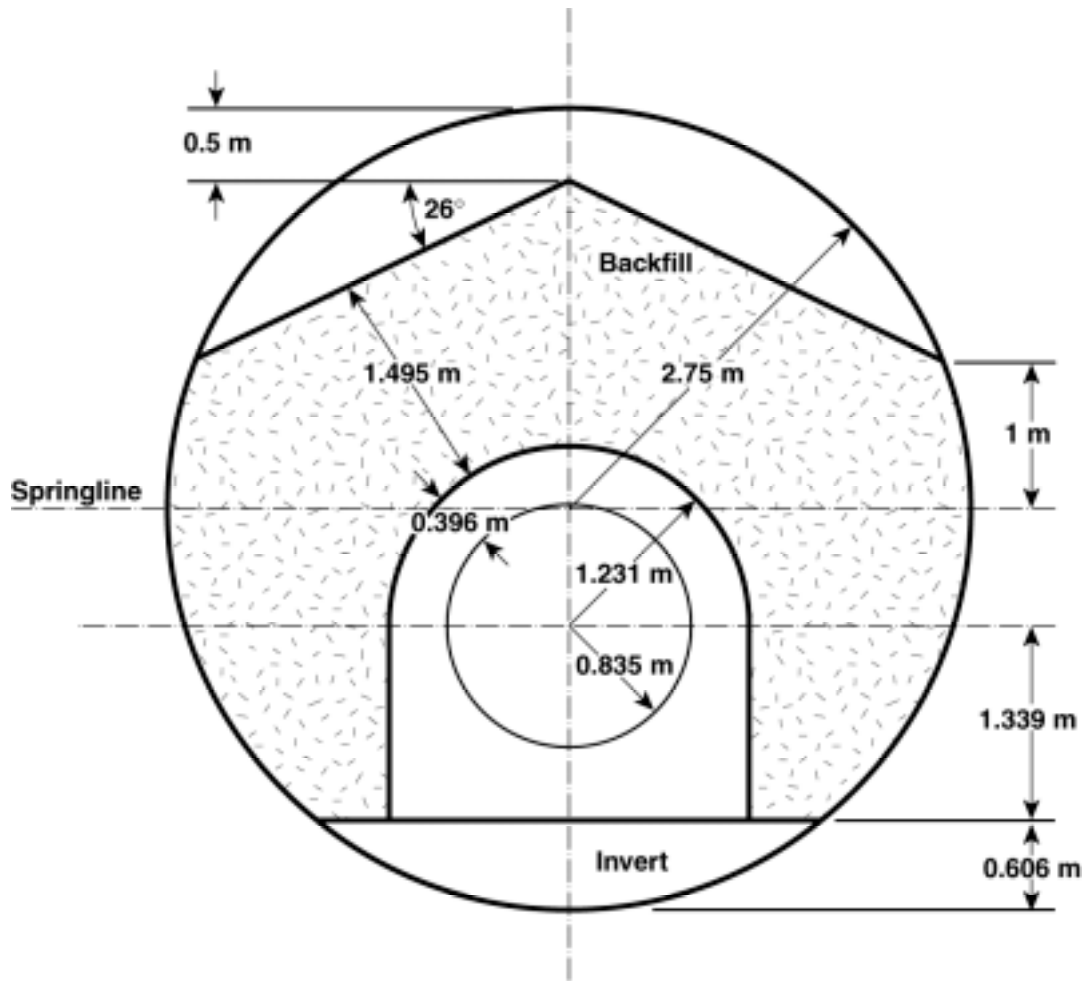


Figure 5-2. The 31 drift-scale submodel locations used in the MSTHM



TB\_AMR\_In-drift\_data

Figure 5-3. The cross-sectional geometry of the emplacement drift after backfill is emplaced

## 6. ANALYSIS/MODEL

The MSTHM is a computationally efficient means of determining TH conditions in the NFE and EBS as a function of location in the repository and WP type; such determination would otherwise require millions of grid blocks if a brute-force monolithic numerical model were used. The MSTHM captures the key factors affecting NFE and EBS TH conditions:

- Repository-scale variability of percolation flux.
- Temporal variability of percolation flux (as influenced by climate change).
- Uncertainty in percolation flux (as addressed by the mean, high, and low flux scenarios).
- Repository-scale variability in hydrologic properties (e.g., those governing matrix imbibition diffusivity and capillary wicking in fractures).
- Edge-cooling effect (which increases with proximity to the edge of the repository).
- Dimensions and properties of the EBS components, such as the drip shield, engineered backfill (if present) and the invert.
- WP-to-WP variability in heat-generation rate.
- Repository-scale variability in overburden thickness.
- Repository-scale variability in thermal conductivity (with an emphasis on the host-rock units).

The influence of these factors on NFE and EBS TH conditions is analyzed in Sections 6.11 and 6.12.

The MSTHM calculates 38 NFE and EBS TH variables (Table 1-1). These TH variables are calculated for 623 repository subdomains distributed throughout the repository area for the backfill case (Figure 6-1a); for the no-backfill case these TH variables are calculated for 610 repository subdomains (Figure 6-1b). Four different WP types (in the specific sequence shown Figure 4-1) are modeled. Because there are 8 different WP locations, this results in 8 different WPs that are considered at each of the 623 repository subdomains. Thus, at each of the 623 repository subdomains, 38 TH variables are calculated for 8 different WPs, resulting in  $623 \times 38 \times 8 = 189,392$  TH variables at each calculational timestep. Because there are 352 timesteps, this results in  $189,392 \times 353 = 66,855,376$  TH data points per infiltration-flux case. Because there are three infiltration-flux cases (mean, high, and low flux) considered in this AMR, there are a total of  $66,855,376 \times 3 = 200,566,128$  TH data points calculated by the MSTHM in this AMR for the backfill case.

For the no-backfill case there are 610 repository subdomains, 38 TH variables (Table 1-2), and 8 different WPs, resulting in  $610 \times 38 \times 8 = 185,440$  TH variables at each timestep. Because there are 99 timesteps, this results in  $185,440 \times 99 = 18,358,560$  TH data points per infiltration-flux case. Because there are three infiltration-flux cases, there are a total of  $18,358,560 \times 3 = 55,075,680$  TH data points calculated by the MSTHM for the no-backfill case.

The number of subdomains that delineates the area of repository heating for the backfill and no-backfill cases are slightly different, 623 subdomains for backfill and 610 subdomains for

No-backfill, due to small differences in the representation of the northwestern and southwestern repository boundaries. The total heat loading is the same between these two cases which results in a slightly lower, negligible, difference in the areal heat loading for the backfill case.

## 6.1 MSTHM CONCEPTUAL MODEL

The need for a multiscale modeling approach stems from the fact that the performance measures depend on TH behavior within a few meters of the emplacement drifts and also on thermal and TH behavior on a repository (or mountain) scale. A single numerical model (e.g., embedding a 3-D drift-scale model with a relatively fine mesh into a 3-D mountain-scale model with a coarse mesh) would require an unfeasible number (millions) of grid blocks. The MSTHM has been developed for estimating the results that would be obtained if such a single model were possible. In addition to coupling the drift scale and mountain scale, the MSTHM also allows for consideration of the effect of different waste packages types (e.g., different CSNF waste packages, co-disposal of defense HLW on the various performance measures.

The MSTHM consists of 4 major submodels (Figure 1-1) and includes multiple scales (mountain and drift), multiple dimensions (1-D, 2-D and 3-D) and varying assumptions regarding the coupling of heat transfer to fluid flow (conduction-only and fully coupled thermohydrologic). These 4 submodels are as follows:

- LDTH (Line-averaged-heat-source, Drift-scale, Thermohydrologic) Submodel
- SMT (Smearred-heat-source, Mountain-scale, Thermal-conduction) Submodel
- SDT (Smearred-heat-source, Drift-scale Thermal-conduction) Submodel
- DDT (Discrete-heat-source, Drift-scale Thermal-conduction) Submodel

It is useful to think of the LDTH submodel as the “core” submodel. These 2-D drift-scale TH submodels are run for 31 locations (Figure 5-2) spaced evenly throughout the repository area for several Areal Mass Loading (AML) values (nominal value and lower) to represent the influence of edge-cooling effects. The LDTH submodel includes the hydrologic processes and parameters (e.g., surface infiltration rates, hydrologic properties) used to describe a location, given specific coordinates within the repository.

The remaining three submodels, which are conduction only, are required to account for the influence of 3-D mountain-scale heat flow and 3-D drift-scale heat flow on drift-scale TH behavior. The coupling of 3-D mountain-scale heat flow to 2-D drift-scale TH behavior is accomplished with the SMT and the SDT submodels. The SMT is 3-D and includes the influence of thermal-property variation in the mountain, lateral heat loss at the repository edges, and overburden-thickness variation with location, assuming a uniform, planar (i.e., smearred) heat source throughout the repository area. The SDT submodel is a 1-D (vertical) submodel, run at the same 31 locations and for the same AMLs as the LDTH submodels. To obtain the “line-averaged” drift-wall temperature (which is roughly equivalent to an average WP location), the relationship between the drift-wall temperature in the LDTH submodel and the “smearred” repository-plane temperature in the SDT submodel is used to modify the temperatures in the SMT submodel, thereby resulting in an MSTHM drift-wall temperature that approximates the effects of the most important TH processes at the drift-scale and the geometry effects of the

mountain scale. At this stage of the MSTHM abstraction methodology, the influence of 3-D drift-scale heat flow has not yet been added.

Because the SMT and SDT submodels both share the same smeared-heat-source approximation and thermal-conduction representation of heat flow, the relationship between the SDT submodel temperature and the LDTH submodel drift-wall temperature allows for the SMT submodel temperature to be “corrected” for both the influence of TH processes on temperature and for the influence of 2-D drift-scale dimensionality (orthogonal to the axis of the drift). The SMT, SDT, and LDTH submodels all share a blended heat-generation history, which blends the heat-generation histories of the entire WP repository; hence, the heat-generation history is effectively that of an “average” WP. The DDT submodel is a 3-D drift-scale submodel which includes individual WPs (with distinctive heat-generation histories) and accounts for thermal radiation in addition to thermal conduction between the WPs and drift surfaces. The drift-wall temperatures for an average WP, calculated with the combined use of the LDTH, SMT and SDT submodels, are then further modified to account for waste-package-specific deviations using the DDT submodel. This is accomplished by relationships between local temperatures at various “point” locations along the drift (such as on the drift wall, drip-shield surface, and WP surface) and the corresponding “line-averaged” temperature in the DDT submodel.

The results of the MSTHM submodels are integrated with the use of the MSTHAC. Details of MSTHAC and the 4 submodels (LDTH, SMT, SDT and DDT) are discussed in Section 6.11.

## **6.2 SMT SUBMODELS**

The 3-D SMT submodel is used to determine the repository-scale variations in host-rock temperature  $T$  resulting from the heat output from the entire inventory of 70,000 MTU of waste, including 63,000 MTU of civilian spent nuclear fuel (CSNF) and 7000 MTU of DHLW, which includes both HLW WPs and DSNF WPs (Section 4.1.13). The SMT submodel includes the influence of mountain-scale thermal-property distribution, the edge-cooling effect, which results from lateral heat loss at the repository edges, and the overburden-thickness distribution. (Overburden thickness is defined to be the depth of the repository horizon below the ground surface.) The SMT submodel domain extends from the ground surface to 1000 m below the present-day water table and the lateral (adiabatic) boundaries are far enough away from the repository so that they do not affect repository temperatures. The temperature 1000m below the water table is found by extrapolation using the routine bound. The extrapolation equation used is developed in Attachment I, and the use of results from bound requires assumptions.

### **6.2.1 SMT Repository Footprint**

The actual and modeled repository footprint (Figure 5-1) both cover similar areas of approximately 4 km<sup>2</sup> (Schreiner 2001, XV-2). The repository footprint corresponds to the area that is heated by the smeared-heat-source representation of heat generation from WPs. The areal distribution of gridblocks in the repository area of the SMT submodel is the same as that shown in Figure 6-1, except that the northernmost and southernmost rows of repository subdomains are further subdivided in the SMT submodel to better represent the influence of edge cooling along

the northern and southern edges of the repository. (MO9911MWDEBSWD; infiltration rates file: dft1.dat and drift end points file: dft1dat).

### **6.2.2 SMT-Submodel Mesh**

The SMT-submodel mesh is constructed so that boundary effects have a negligible effect on the predicted temperatures near the repository. This is accomplished by extending the lateral boundaries beyond the repository edges and extending the lower boundary 1000m below the water table.

The SMT mesh files are output from YMESH (CRWMS M&O 2000a; tspa00-mesh00, tspa00-mesh01, and tspa00-mesh02) and tspa00-mesh20 for the no-backfill case. The process of generating the numerical mesh for the SMT submodel is illustrated in Figure 3-2.

### **6.2.3 SMT Submodel Boundary Conditions**

The SMT submodel domain extends from the ground surface to 1000 m below the present-day water table. The lateral boundaries, which are adiabatic boundaries, are situated far enough away from the repository so that they do not affect thermal behavior in the repository. The temperature at the lower boundary of the model domain is extrapolated vertically from the temperature gradient at the water table, based on the calculated temperature field from the UZ Site-Scale Model (Section 4.1.3) and the equation developed in Attachment I based on Assumptions 5.3.1, 5.3.2 and Equation 5. Thermal conditions at the water table vary with location, so the extrapolated temperature varies on the model boundary. The temperature at the ground surface are calculated from the UZ Site-Scale Model, using an inverse distance cubed method discussed in Section 5.1.3. The data-flow chart for the preparation of boundary conditions is given in Figure 3-5; this process is described in Section 6.8.5.

The density of the upper boundary is  $1.185 \text{ kg/m}^3$  (5.1.6). The heat capacity of the upper boundary is  $1 \times 10^3 \text{ J/Kg-K}$  (5.1.6). The thermal conductivity of the upper boundary is  $0.0254 \text{ W/m-K}$  (5.1.6). This data is incorporated into the SMT submodel through inclusion in the file: SDT-Dds\_mi (CRWMS M&O 2000a).

### **6.2.4 SMT Submodel Heat Generation Rates**

The heat generation rate for the SMT submodel is in the form of a heat versus time table located in NUFT include files. During preclosure the file used is output from heatgenAge (CRWMS M&O 2000a, SMT-0.3Qheat-50y\_vent-02) and SMT-0.3Qheat-50y\_vent-20 for no-backfill. The heat output represented in this file accounts for removal of 70% of the total heat due to ventilation. The postclosure heat generation table is also output from heatgenAge (CRWMS M&O 2000a, SMT-0.3Qheat-1e6y\_vent-02v) and SMT-0.3Qheat-1e6y\_vent-20v for no-backfill.

### **6.2.5 SMT Submodel Material Properties**

The SMT submodel uses thermal-conduction properties (for the stratigraphic units) consistent with the SDT submodel (Section 6.4.5). These properties are based on Sections 4.1.1.20 and Section 5.2.4 through incorporation in the include file SDT-1Dds-mi (CRWMS M&O 2000a) as

illustrated in Figures 3-7 and 3-12. This file incorporates assumption 5.2.4 by using the wet thermal conductivity. Where SZ thermal properties are required the wet thermal conductivity of pp1 are used (Section 5.2.5).

### **6.2.6 Submodel Simulations**

Two SMT-submodel simulations were conducted for this AMR. The first, which is required to calculate pre-closure TH conditions in the MSTHM, was run with the heat-generation rate reduced by 70%. However, only the first 50 years of this simulation is used as the ventilation period ends at that point (Section 4.2). The second, which is required to calculate post-closure TH conditions in the MSTHM, was run for a simulation period of 1,000,000 yr using a step-function heat-generation rate, with the rate reduced by 70% for the first 50 yr and the full nominal rate from 50 yr to 1,000,000 yr. The two SMT simulations are used in all three infiltration-flux (mean, high, and low flux) cases.

## **6.3 LDTH SUBMODELS**

The 2-D LDTH submodels use the dual-permeability method (DKM), modified with the active-fracture concept (AFC), to represent two-phase heat and fluid flow in the fractured porous rock. The LDTH submodels are run at the 31 drift-scale-submodel locations (Figure 5-2) and for 5 different values of Areal Mass Loading (AML = 15, 25, 36, 50, and 60 MTU/acre). Representing the influence of edge-cooling effects requires that most of the LDTH submodel runs use an AML that is less than the nominal value.

These submodels are required to obtain functional relationships (also called “scanning curves”) between “line-averaged” temperatures predicted by the LDTH submodel and the “smeared” host-rock temperatures predicted by the SDT submodel.

The USNT module of NUFT, is used to model flow through a fractured porous media in the LDTH submodels. The key NUFT options used for LDTH simulations include the DKM and the AFC. These modeling methods are NUFT options selected in the NUFT input files.

The DKM conceptualizes the fractured rock as having two interacting materials, one representing the matrix and one representing the fractures. The interaction between the fractures and the matrix is explicitly calculated from the local temperature and pressure differences, thus allowing transient behavior to be predicted. The DKM underestimates the fracture-matrix interaction for steep temperature and pressure gradients (Hardin 1998, p. 2). Simulations in this model are at isothermal, so there are no steep temperature or pressure gradients. Therefore, the DKM is appropriate for the model developed in this document.

The active fracture concept accounts for the contact area between the fracture and the matrix (Table 4-3), as well as the frequency of fractures (Table 4-3). The AFC is that fracture flow only occurs through some of the fractures. This is more conservative than assuming the influx flows evenly through all fractures. The flux through a fracture is greater when it has higher saturation and, therefore, focusing flow through a portion of the fractures (i.e., to active fractures) maximizes flux and results in fast pathways for flux through the mountain.

The rock properties in Section 4.1.7 were calibrated using an inverse modeling technique that assumes the properties will only be used in DKM employing AFC. Therefore, the DKM and AFC are appropriate NUFT options.

### **6.3.1 LDTH Submodel Locations**

The LDTH submodel locations are in the file `column.data`. The repository footprint is output from Cover in the file `shape.dat` (CRWMS M&O 2000a). The manual operation E:M3 in Figure 3-2 is used to grid the repository into 31 representative locations, which are located in the file `column.data`.

The LDTH submodel locations are shown in Figure 5-2, and represent repository-scale variability of thermal properties, hydrologic properties, infiltration flux, and overburden thickness.

#### **6.3.1.1 Stratigraphic Columns**

The stratigraphic columns corresponding to the LDTH submodel locations are output from YMESH in the file `<column>.nft` (CRWMS M&O 2000a). The software used in manipulating the source data into a YMESH input file (excluding the location file, `column.data`) are `rme6` and `makeColumns`. The thickness of the stratigraphic units at each location is output from `readUnits` (CRWMS M&O 2000a, 31 files: `<column.col.units>`), and is tabulated in Table 6-1.

#### **6.3.1.2 Vertical Location of Repository Horizon**

The EBS is added to the stratigraphic columns (CRWMS M&O 2000a, `<column>.nft`) by the routine `define_EBS_fineGrid`. This routine changes the grid blocks at the location of the EBS to the appropriate material. The routine also changes the size of the mesh near the EBS.

The vertical location of the repository horizon at the LDTH submodel locations `column.data`, in the stratigraphic columns `<column>.nft`, are tabulated by `readUnits` (CRWMS M&O 2000a, `<column>.col.units`) and shown in Table 6-2.

### **6.3.2 LDTH Submodel Mesh**

The cross-sectional dimensions of the drift for the post-closure period is shown in Figure 4-2; these dimensions were used to build the numerical meshes of the LDTH submodels.

#### **6.3.2.1 Pre-closure LDTH Submodel Mesh**

The numerical mesh for the pre-closure LDTH submodel (Figure 6-2a) assumes the same representation for the WP and drip shield as is used in the numerical mesh for the post-closure LDTH submodel (Figure 6-3). This lumped approximation of the drip shield and WP is corrected by the manner in which the pre-closure DDT submodel (Figure 6-4), which rigorously accounts for the actual dimensions of the WP (without the presence of the drip shield), is applied in the MSTHAC methodology (Section 6.6).

Table 6-1. Stratigraphic columns used in the 31 drift-scale-submodel locations

Stratigraphic unit	Drift-scale submodel location								
	I1c1	I1c2	I1c3	I1c4	I2c1	I2c2	I2c3	I2c4	I3c1
tcw11	0.000	1.904	34.922	0.000	0.000	0.000	0.000	0.000	15.908
tcw12	36.856	0.000	36.504	0.000	33.692	0.000	0.000	48.955	90.996
tcw13	7.910	7.617	6.885	3.838	3.867	0.000	1.816	4.746	4.805
ptn21	6.855	7.354	8.115	8.701	6.797	7.500	7.764	8.496	5.918
ptn22	8.760	8.496	8.555	9.111	6.445	5.654	5.156	5.420	6.211
ptn23	6.621	6.387	6.387	6.885	5.010	4.307	3.779	4.043	5.068
ptn24	24.844	22.910	20.449	19.336	15.762	14.707	12.305	10.986	10.254
ptn25	48.164	48.955	50.479	50.947	31.728	33.252	38.408	39.756	22.939
ptn26	11.309	11.514	12.100	12.393	10.137	10.430	11.309	12.773	12.041
tsw31	1.992	1.992	1.992	2.021	1.992	1.992	1.992	1.992	1.992
tsw32	47.139	45.176	41.132	37.442	49.570	48.633	45.732	41.836	52.354
tsw33	76.465	79.160	81.211	81.064	84.160	83.780	85.478	86.982	85.616
tsw34	35.820	36.552	37.051	36.826	32.270	31.352	33.320	34.092	35.700
tsw35	107.316	103.389	98.263	97.218	116.003	113.171	101.807	98.603	115.600
tsw36	7.422	10.625	12.432	11.500	16.406	18.750	28.271	22.422	31.729
tsw37	3.691	5.273	6.240	8.852	8.203	9.375	14.121	11.172	15.850
tsw38	16.348	16.729	16.914	17.559	17.168	16.875	17.461	18.867	18.281
tsw39	6.680	7.207	7.344	7.471	5.713	6.006	6.973	6.943	3.281
ch1v	0.000	0.000	0.000	0.000	0.000	0.000	0.000	0.000	0.000
ch2v	0.000	0.000	0.000	0.000	0.000	0.000	0.000	0.000	0.000
ch3v	0.000	0.000	0.000	0.000	0.000	0.000	0.000	0.000	0.000
ch4v	0.000	0.000	0.000	0.000	0.000	0.000	0.000	0.000	0.000
ch5v	0.000	0.000	0.000	0.000	0.000	0.000	0.000	0.000	0.000
ch1z	13.623	13.594	11.162	8.828	18.721	19.365	14.648	9.785	15.527
ch2z	33.105	28.682	28.330	26.387	24.082	23.818	21.592	19.219	21.299
ch3z	33.135	28.682	28.330	26.367	24.082	23.789	21.562	19.248	21.328
ch4z	33.105	28.652	28.330	26.367	24.082	23.818	21.592	19.248	21.328
ch5z	33.105	28.682	28.301	26.367	24.082	23.818	21.562	19.219	21.299
ch6	20.596	19.248	19.219	18.779	18.896	18.867	17.783	16.963	17.666

Table 6-1. Stratigraphic columns used in the 31 drift-scale-submodel locations

Stratigraphic unit	Drift-scale submodel location								
	I3c2	I3c3	I3c4	I4c1	I4c2	I4c3	I4c4	I4c5	I5c1
pp4	14.766	16.875	16.758	16.816	18.369	19.365	19.863	19.541	13.652
pp3	7.617	7.676	6.064	6.211	16.084	15.762	13.066	13.359	0.000
Pp2	27.041	30.850	35.977	37.178	6.738	16.729	15.293	15.557	0.000
Pp1	0.000	22.881	48.955	76.465	0.000	0.000	25.869	73.330	0.000
Bf3	0.000	0.000	0.000	0.000	0.000	0.000	0.000	0.000	0.000
Bf2	0.000	0.000	0.000	0.000	0.000	0.000	0.000	0.000	0.000
tcw11	0.000	0.000	30.762	0.000	9.199	0.000	32.900	0	0.000
tcw12	38.702	77.930	79.307	73.652	81.416	83.086	89.004	20.801	41.426
tcw13	5.010	4.629	4.541	5.537	5.625	5.391	4.951	4.717	4.717
ptn21	6.152	7.207	8.232	3.838	4.014	4.893	5.947	6.768	2.842
ptn22	5.303	4.600	4.512	3.809	3.750	3.193	2.490	2.812	1.641
ptn23	4.365	3.838	3.838	2.578	2.812	2.754	2.373	2.49	0.000
ptn24	9.727	9.316	8.379	7.236	7.324	7.061	6.533	6.475	6.738
ptn25	22.412	24.785	25.723	16.611	16.025	15.410	14.443	14.561	7.939
ptn26	11.953	11.777	13.096	13.096	13.682	14.619	15.498	15.41	12.393
tsw31	1.992	2.021	1.992	1.992	1.992	2.021	1.992	2.021	2.021
tsw32	49.951	46.260	41.250	50.918	49.482	46.318	42.070	38.466	42.626
tsw33	87.178	88.438	90.176	86.664	84.258	87.412	88.711	89.062	82.676
tsw34	33.750	31.524	31.836	29.700	34.200	31.586	30.254	31.084	32.824
tsw35	117.687	118.965	113.262	105.082	104.424	108.981	111.895	112.638	101.912
tsw36	28.857	24.756	22.725	37.295	35.625	31.348	27.119	23.184	39.375
tsw37	14.414	12.393	11.367	18.633	17.812	15.674	13.594	12.305	19.688
tsw38	19.922	20.654	22.412	15.850	17.842	21.035	23.408	24.688	11.104
tsw39	3.369	4.219	4.717	1.875	2.051	2.871	3.779	4.16	3.545
ch1v	0.000	0.000	8.145	0.000	0.000	0.000	10.166	8.027	20.596
ch2v	0.000	0.000	0.000	0.000	0.000	0.000	0.000	0	16.758
ch3v	0.000	0.000	0.000	0.000	0.000	0.000	0.000	0	16.729
ch4v	0.000	0.000	0.000	0.000	0.000	0.000	0.000	0	0.000
ch5v	0.000	0.000	0.000	0.000	0.000	0.000	0.000	0	0.000
ch1z	15.234	12.451	0.000	17.109	17.080	14.004	0.000	0	0.000
ch2z	19.688	18.281	15.938	20.537	18.926	16.523	14.414	13.096	0.000
ch3z	19.688	18.281	15.908	20.537	18.896	16.523	14.414	13.066	0.000
ch4z	19.688	18.252	15.938	20.566	18.926	16.523	14.414	13.096	16.758
ch5z	19.688	18.281	15.938	20.537	18.926	16.523	14.414	13.096	16.758
ch6	18.135	18.252	17.900	17.666	17.988	18.896	19.629	19.277	16.670
pp4	15.938	16.553	15.498	11.865	11.338	9.932	8.086	8.027	9.258
pp3	22.939	23.115	24.170	17.168	27.246	30.732	33.691	33.34	31.582
pp2	5.273	16.582	16.025	0.000	9.961	16.846	14.707	14.561	18.105
pp1	0.000	25.488	78.457	0.000	0.000	29.619	61.055	55.752	7.295
bf3	0.000	0.000	0.000	0.000	0.000	0.000	17.402	51.533	0.000
bf2	0.000	0.000	0.000	0.000	0.000	0.000	0.000	14.766	0.000

Table 6-1. Stratigraphic columns used in the 31 drift-scale-submodel locations (Continued)

Stratigraphic unit	Drift-scale submodel location								
	I5c2	I5c3	I5c4	I5c5	I6c1	I6c2	I6c3	I6c4	I6c5
tcw11	0.000	0.000	17.080	0.000	0.000	0.000	0.000	28.418	25.723
tcw12	47.607	76.465	92.724	79.805	82.910	63.721	82.324	96.006	97.266
tcw13	5.039	5.068	6.445	6.709	4.834	4.980	4.863	4.658	4.482
ptn21	2.900	2.607	2.314	2.783	2.285	2.461	2.725	2.461	3.164
ptn22	1.992	1.875	2.197	2.637	0.000	0.000	1.904	2.930	3.076
ptn23	0.000	0.000	1.523	1.699	0.000	1.699	0.000	1.963	2.109
ptn24	7.412	7.178	6.240	6.562	4.863	4.482	6.885	7.061	7.002
ptn25	9.023	7.793	7.412	8.145	4.922	4.834	4.189	4.043	3.398
ptn26	13.477	13.242	13.916	14.912	10.400	10.957	11.455	12.451	11.953
tsw31	2.021	1.992	2.021	1.992	1.992	1.992	1.992	1.992	1.992
tsw32	42.568	40.694	38.614	36.446	35.450	34.952	33.632	32.900	31.612
tsw33	83.926	82.520	81.826	82.998	74.297	75.225	73.184	72.480	69.814
tsw34	32.656	31.406	33.555	33.486	36.200	37.422	38.632	39.288	41.338
tsw35	103.194	104.054	103.331	108.507	90.354	92.149	94.933	95.812	97.737
tsw36	36.211	36.211	32.920	25.625	43.740	40.693	35.908	33.740	29.706
tsw37	18.105	18.105	16.436	14.141	21.885	20.361	17.959	16.054	15.664
tsw38	14.912	14.385	16.992	21.055	7.852	9.785	12.305	14.805	14.648
tsw39	3.281	3.691	3.984	4.102	7.090	5.947	5.332	4.805	4.883
ch1v	18.105	18.164	15.264	11.221	23.613	22.354	18.398	14.092	13.184
ch2v	15.264	14.209	12.480	11.279	15.000	13.008	10.576	9.258	8.496
ch3v	15.234	14.209	12.451	0.000	15.000	13.037	10.576	0.000	0.000
ch4v	0.000	0.000	0.000	0.000	15.000	0.000	0.000	0.000	0.000
ch5v	0.000	14.209	0.000	0.000	15.029	13.008	10.576	0.000	0.000
ch1z	0.000	0.000	0.000	0.000	0.000	0.000	0.000	0.000	0.000
ch2z	0.000	0.000	0.000	0.000	0.000	0.000	0.000	0.000	0.000
ch3z	0.000	0.000	0.000	11.309	0.000	0.000	0.000	9.258	8.496
ch4z	15.264	14.209	12.451	11.279	0.000	13.037	10.576	9.229	8.496
ch5z	15.264	0.000	12.480	11.309	0.000	0.000	0.000	9.258	8.496
ch6	17.549	17.168	17.578	18.252	14.092	14.561	15.264	15.938	15.732
pp4	8.350	8.057	7.207	6.826	10.430	8.613	7.324	7.383	7.500
pp3	33.838	34.980	36.943	36.797	32.666	35.215	38.115	39.053	39.668
pp2	15.820	14.883	12.773	12.217	20.977	17.227	13.154	10.840	10.635
pp1	38.760	53.438	63.545	55.137	17.314	58.066	70.312	64.365	64.629
bf3	0.000	0.000	28.389	79.336	0.000	0.000	39.580	88.916	107.051
bf2	0.000	0.000	0.000	0.000	0.000	0.000	0.000	0.000	0.000

Table 6-1. Stratigraphic columns used in the 31 drift-scale-submodel locations (Continued)

Stratigraphic unit	Drift-scale submodel location			
	I7c1	I7c2	I7c3	I7c4
tcw11	0.000	0.000	0.000	5.391
tcw12	68.730	91.142	104.122	105.908
tcw13	6.035	6.006	5.186	6.240
ptn21	3.018	3.164	3.633	3.545
ptn22	0.000	0.000	1.641	1.611
ptn23	0.000	0.000	0.000	0.000
ptn24	5.068	5.244	5.508	5.127
ptn25	0.000	2.139	2.432	2.256
ptn26	11.602	9.990	10.107	10.020
tsw31	2.021	1.992	1.992	1.992
tsw32	27.188	27.129	28.477	27.393
tsw33	67.168	66.826	66.416	65.391
tsw34	39.492	40.772	41.914	41.894
tsw35	87.227	85.997	87.028	90.234
tsw36	36.855	35.146	35.297	29.738
tsw37	18.428	17.578	16.641	16.094
tsw38	12.334	13.184	12.656	13.164
tsw39	10.049	9.229	7.939	8.906
ch1v	23.906	23.906	18.809	18.047
ch2v	12.861	10.723	0.000	0.000
ch3v	12.861	10.723	0.000	0.000
ch4v	12.861	10.723	0.000	0.000
ch5v	12.861	10.723	0.000	0.000
ch1z	0.000	0.000	0.000	0.000
ch2z	0.000	0.000	8.965	8.525
ch3z	0.000	0.000	8.965	8.555
ch4z	0.000	0.000	8.965	8.525
ch5z	0.000	0.000	8.965	8.525
ch6	16.963	15.264	14.678	14.531
pp4	3.516	4.834	6.328	6.270
pp3	35.654	37.441	39.229	39.756
pp2	23.555	21.211	16.934	18.604
pp1	64.277	77.490	70.312	69.668
bf3	0.000	27.158	75.586	89.238
bf2	0.000	0.000	0.000	0.000

Table 6-2. Summary of the vertical location of the repository horizon at the 31 drift-scale-submodel locations

Submodel location	Host-rock unit	Repository elevation (m)	Overburden thickness (m)	Repository height above water table (m)
I1c1	tsw35	1047.788	352.483	317.799
I1c2	tsw35	1048.672	328.371	318.688
I1c3	tsw35	1049.553	418.821	319.576
I1c4	tsw35	1050.438	360.480	320.446
I2c1	tsw35	1055.706	294.329	325.729
I2c2	tsw35	1056.589	264.504	326.608
I2c3	tsw35	1057.473	281.038	327.486
I2c4	tsw35	1058.356	355.187	328.366
I3c1	tsw34	1063.624	333.000	333.639
I3c2	tsw35	1064.506	282.492	334.518
I3c3	tsw35	1065.390	343.449	335.396
I3c4	tsw35	1066.274	405.744	336.295
I4c1	tsw34	1071.505	278.830	341.520
I4c2	tsw34	1072.314	308.479	342.340
I4c3	tsw35	1073.124	326.642	343.131
I4c4	tsw35	1073.934	395.403	343.951
I4c5	tsw35	1074.744	324.505	344.772
L5c1	tsw34	1079.423	234.543	349.429
L5c2	tsw35	1080.232	267.521	350.250
L5c3	tsw35	1081.042	299.739	351.070
L5c4	tsw35	1081.851	359.211	351.881
L5c5	tsw35	1082.662	363.880	352.682
L6c1	tsw34	1087.340	250.852	357.340
L6c2	tsw35	1088.149	261.623	358.160
L6c3	tsw35	1088.960	313.693	358.980
L6c4	tsw35	1089.770	389.661	359.790
L6c5	tsw35	1090.580	397.366	360.582
L7c1	tsw35	1095.294	249.221	365.308
L7c2	tsw35	1096.178	299.543	366.188
L7c3	tsw35	1097.062	341.653	367.067
L7c4	tsw35	1097.944	357.200	367.944

### 6.3.2.2 Post-closure LDTH Submodel Mesh

The numerical mesh for the post-closure submodel (Figure 6-3) assumes that the drip shield and WP are lumped. This lumped approximation of the drip shield and WP allows for the representation of thermohydrologic behavior down to the surface of the drip shield. The post-closure DDT submodel (Figure 6-5), which rigorously accounts for the actual WP and drip-shield dimensions (including the correct dimensions of the gap between the WP and drip shield), is applied in the MSTHAC methodology (Section 6.6) to represent thermohydrologic behavior between the drip shield and waste package.

### 6.3.3 LDTH Submodel Boundary Conditions

Because the LDTH submodels are for a symmetry cell between the vertical plane down the center of the drift and the vertical midplane between drifts, the lateral boundaries are adiabatic and no-mass-flow boundaries. The LDTH submodels require temperature, pressure, and gas-phase air-mass fraction at the upper boundary, which represents the ground surface and the lower boundary, which represents the water table (Table 6.3). Both boundaries have constant conditions with time. The density of the upper boundary is  $1 \times 10^8 \text{ Kg/m}^3$  (5.1.5). The heat capacity of the upper boundary is  $1 \times 10^8 \text{ Kg/m}^3$  (5.1.5). The thermal conductivity of the upper boundary is 0.17 (5.1.5). These values are incorporated in the files dkm-afc-1Dds-mc-li-00, dkm-afc-1Dds-mc-mi-00, and dkm-afc-1Dds-mc-ui-00 (CRWMS M&O 2000a).

The temperature and pressure are based on the grid in Section 4.1.11, the temperatures and pressures in Section 4.1.14, and the locations in column.data (CRWMS M&O 2000a). An interpolation routine is used to relate the temperatures and pressures at various points to the LDTH submodel locations. The routines used for this interpolation are chim\_surf\_TP and chim\_wt\_TP. The air mass fraction and liquid enthalpy is found given the resulting temperature and pressure, along with a bounding assumption of 100% humidity (Section 5.1.4). The routine used for this calculation is X.air.

### 6.3.4 LDTH Submodel Heat Generation Rates

The heat generation rates for the LDTH submodels are in the form of heat versus time tables located in NUFT include files. During preclosure the file used is output from heatgenAge (CRWMS M&O 2000a, LDTH-SDT-0.3Qheat-50y\_vent-00) and LDTH-SDT-0.3Qheat-50y\_vent-20 for no-backfill. The heat output represented in this file accounts for removal of 70% of the total heat due to ventilation. The postclosure heat generation table is also output from heatgenAge (CRWMS M&O 2000a, LDTH-SDT-0.3Qheat-1e6y\_vent-00v) and LDTH-SDT-0.3Qheat-1e6y\_vent-20v for the no-backfill case.

Because any given LDTH submodel cover the same model domain (including the same area in plan view) as the corresponding SDT submodel, the LDTH and corresponding SDT submodel use the same heat-generation rate versus time tables (files).

### 6.3.5 LDTH Submodel Material Properties

Material properties are output from rock\_sun into three files (CRWMS M&O 2000a, dkm-afc-1Dds-mc-mi-00, dkm-afc-1Dds-mc-li-00, dkm-afc-1Dds-mc-ui-00), each one corresponding to an infiltration rate.

1d-driftscale\_basecase.xls (LB990861233129.001). Properties corresponding to the upper infiltration flux are given in the file 1d-driftscale\_upperinf.xls (LB990861233129.002). Properties corresponding to the lower bound infiltration flux are given in the file 1d-driftscale\_lowinf.xls (LB990861233129.003).

Table 6-3. Boundary conditions used in the drift-scale submodels (LDTH, SDT, and DDT). Note that the gas-phase pressure and gas-phase air-mass fraction only apply to the LDTH submodels

Submodel location	Ground-surface			Water Table
	Temperature (°C)	Gas-phase pressure (Pa <sup>-1</sup> )	Gas-phase air-mass fraction	Temperature (°C)
l1c1	16.779	8.5320688e+04	0.9860	28.658
l1c2	16.633	8.5178711e+04	0.9861	28.651
l1c3	15.903	8.4462820e+04	0.9866	28.765
l1c4	16.436	8.4987852e+04	0.9862	28.871
l2c1	17.032	8.5583062e+04	0.9858	29.083
l2c2	17.175	8.5722703e+04	0.9857	29.049
l2c3	16.944	8.5497703e+04	0.9859	29.203
l2c4	16.355	8.4923633e+04	0.9863	29.508
l3c1	16.654	8.5236117e+04	0.9861	30.719
l3c2	16.817	8.5393297e+04	0.9860	30.683
l3c3	16.415	8.4996156e+04	0.9862	30.781
l3c4	16.036	8.4626445e+04	0.9865	30.895
l4c1	16.994	8.5587211e+04	0.9858	32.356
l4c2	16.826	8.5418938e+04	0.9860	32.350
l4c3	16.544	8.5134164e+04	0.9862	32.390
l4c4	15.910	8.4510758e+04	0.9866	32.544
l4c5	16.193	8.4794422e+04	0.9864	32.460
l5c1	17.390	8.5986297e+04	0.9855	32.505
l5c2	16.915	8.5510719e+04	0.9859	32.517
l5c3	16.522	8.5125812e+04	0.9862	32.472
l5c4	16.186	8.4795891e+04	0.9864	32.549
l5c5	16.119	8.4729391e+04	0.9865	32.596
l6c1	17.085	8.5700695e+04	0.9858	31.199
l6c2	16.941	8.5551477e+04	0.9859	31.455
l6c3	16.519	8.5129719e+04	0.9862	31.815
l6c4	15.949	8.4569531e+04	0.9866	31.915
l6c5	16.295	8.4910359e+04	0.9863	31.920
l7c1	17.063	8.5692555e+04	0.9858	30.259
l7c2	16.734	8.5359688e+04	0.9860	30.682
l7c3	16.422	8.5048141e+04	0.9862	31.007
l7c4	16.139	8.4765539e+04	0.9864	31.258

The fracture and matrix properties are in the files 1d-driftscale\_basecase.xls, 1d-driftscale\_upperinf.xls, 1d-driftscale\_lowerinf.xls (4.1.7). These files are renamed and read into the routine rock\_sun. ). These files are renamed and read into the routine rock\_sun (see Figure 3-8). There are three sets of matrix and fracture properties that correspond to the three infiltration cases.

The LDTH EBS properties are based on inputs in Sections 4.1.2-4.1.5 and assumptions in Sections 5.2.7 and 5.2.8.

### 6.3.6 Infiltration Flux

Infiltration data is in the nine files from Section 4.1.12, representing three cases (low, mean, and upper, each having three climates (present day, monsoon, and glacial). Infiltration rates at each submodel location in column.data (CRWMS M&O 2000a) are found using a routine that interpolates, and then normalizing the results from the 31 locations.

ConvertCoords prepares the input data for the interpolation routine, columnInfiltration (see Figure 3-4). The output from columnInfiltration is one large file (CRWMS M&O 2000a, infiltration.tex). This file is split into the nine constituent infiltration rates with the routine infiltrab. The average of the 31 infiltration rates was found to differ from the average of all the infiltration rates in the source data that were within the repository footprint. To account for this the infiltration rates are normalized with respect to the average of the source data over the repository footprint. The normalization is completed in Attachment I.

### 6.3.7 LDTH Submodel Simulations

Because of the manner in which the MSTHM temperatures are abstracted, it is necessary to account for drift ventilation scenarios by conducting two complete (parallel) MSTHM abstractions (with one that pertains to the pre-closure period and one that pertains to the post-closure period) and then splicing the results of these two MSTHM abstractions at the end of the pre-closure period (i.e., when ventilation ceases). Therefore, it is necessary to run two complete sets of MSTHM submodels to account for ventilation for a given infiltration-flux case.

The LDTH submodel is the only submodel type that has to be run for each of the three infiltration-flux cases (mean, high, and low flux). The simulations for the other three submodel types are applied to all three flux cases.

For a given infiltration-flux case, two sets of LDTH-submodel simulations are required. The first set, which is required to calculate pre-closure TH conditions in the MSTHM, was run with the heat-generation rate reduced by 70%. The second set, which is required to calculate post-closure TH conditions in the MSTHM, was run for a simulation period of 1,000,000 yr using a step-function heat-generation rate, with the rate reduced by 70% for the first 50 yr, and with the full nominal rate applied from 50 yr to 1,000,000 yr.

Each LDTH-submodel set consists of 155 simulations, which comes from 31 drift-scale-submodel locations (Section 6.3.1) and 5 AML values run at each location ( $31 \times 5 = 155$ ). Thus, because there are two sets, a total of 310 LDTH simulations are conducted for a given infiltration-flux case. Because there are three infiltration-flux cases, there are a total of 930 LDTH simulations conducted for this AMR.

## 6.4 SDT SUBMODELS

The 1-D smeared-heat-source drift-scale thermal-conduction (SDT) submodels are run in parallel with the LDTH submodels at the same 31 locations and for the same AMLs (15, 25, 36, 50, and 60 MTU/acre). These submodels are required to obtain functional relationships (also called

“scanning curves”) between “line-averaged” temperatures predicted by the LDTH submodel and the “smeared” host-rock temperatures predicted by the SDT submodel.

#### **6.4.1 SDT Submodel Locations**

The SDT submodels are run at the same 31 drift-scale-submodel locations as the LDTH submodel (Section 6.3.1).

#### **6.4.2 SDT Submodel Mesh**

The SDT submodels use the same vertical discretization of grid blocks as is used in the SMT submodels (Section 6.2.2). The manner in which the LDTH-SDT temperature scanning curves are developed and used to modify SMT-predicted host-rock temperatures (Section 6.6.3) demands consistency between how heat flow is modeled in the respective SDT and SMT submodels, including consistency in the vertical grid-block discretization in the respective submodels.

#### **6.4.3 SDT Submodel Boundary Conditions**

The SDT boundary temperature conditions are the same as the corresponding LDTH submodel (Section 6.3.3). Consistent upper and lower boundary temperatures assures self-consistency with respect to how the LDTH and SDT submodels are used to generate LDTH-temperature versus SDT-temperature scanning curves and how these scanning curves are used in the MSTHAC methodology to correct SMT-predicted temperatures to LMTH conditions (Section 6.3.3). The data-flow chart for the preparation of boundary conditions is given in Figure 3-5; this process is described in Section 6.8.5.

Because the SDT submodels are for a symmetry cell between the vertical plane down the center of the drift and the vertical midplane between drifts, the lateral boundaries are adiabatic and no-mass-flow boundaries. The SDT submodels require temperature at the upper boundary, which represents the ground surface and the lower boundary, which represents the water table (Table 6.3). Both boundaries have constant temperature conditions with time.

The density of the upper boundary is  $1 \times 10^8 \text{ Kg/m}^3$  (5.1.6). The heat capacity of the upper boundary is  $1 \times 10^8 \text{ J/Kg-K}$  (5.1.6). The thermal conductivity of the upper boundary is 0.17 (5.1.6). This data is incorporated into the SDT submodel through inclusion in the file: SDT-Dds\_mi (CRWMS M&O 2000a).

The temperature and pressure are based on the grid in Section 4.1.11, the temperatures and pressures in Section 4.1.14, and the locations in column.data (CRWMS M&O 2000a). An interpolation routine is used to relate the temperatures and pressures at various points to the SDT submodel locations. The routines used for this interpolation are chim\_surf\_TP and chim\_wt\_TP. The air mass fraction and liquid enthalpy is found given the resulting temperature and pressure, along with a bounding assumption of 100% humidity (Section 5.1.4). The routine used for this calculation is X.air.

#### **6.4.4 SDT Submodel Heat Generation Rates**

Because any given SDT submodel covers the same model domain (including the same area in plan view) as the corresponding LDTH submodel, the SDT and corresponding LDTH submodel use the same heat-generation rate versus time tables. These are nuft include files output from heatgenAge (CRWMS M&O 2000a, LDTH-SDT-0.3Qheat-50y\_vent-00 and LDTH-SDT-0.3Qheat-1e6y\_vent-00v) and LDTH-SDT-0.3Qheat-50y\_vent-20 and LDTH-SDT-0.3Qheat-1e6y\_vent-20v for the no-backfill case, as discussed in Section 6.3.4.

#### **6.4.5 SDT Submodel Material Properties**

The SDT submodel uses the same thermal-conduction properties (for the stratigraphic units) that are used in the SMT submodel (Section 6.2.5). These properties are based on Sections 4.1.9 and Section 5.2.4 through incorporation in the include file SDT-1Dds-mi (CRWMS M&O 2000a) as illustrated in Figures 3-7 and 3-10.

#### **6.4.6 SDT Submodel Simulations**

Two sets of SDT-submodel simulations were conducted for this AMR. The first set, which is required to calculate pre-closure TH conditions in the MSTHM, was run with the heat-generation rate reduced by 70%. The second set, which is required to calculate post-closure TH conditions in the MSTHM, was run for a simulation period of 1,000,000 yr using a step-function heat-generation rate, with the rate reduced by 70% for the first 50 yr, and with the full nominal rate applied from 50 yr to 1,000,000 yr.

Each SDT-submodel set consists of 155 simulations, which comes from 31 drift-scale-submodel locations (Figure 5-2) and 5 AML values run at each location ( $31 \times 5 = 155$ ). Thus, a total of 310 SDT simulations are conducted for this AMR. These two sets of SDT simulations are used in all three infiltration-flux (mean, high, and low flux) cases.

### **6.5 DDT SUBMODELS**

The 3-D DDT submodel is used to account for WP-specific heat output and for thermal radiation between all WP and drift surfaces to determine WP-specific deviations (relative to line-averaged-heat-source conditions) in temperatures in the NFE and EBS (e.g., drift wall, drip shield, and WP). For the pre-closure period (prior to the emplacement of the drip shield and backfill) and for the post-closure period of the no-backfill case, thermal radiation between the WP and drift surfaces controls the longitudinal temperature deviations along the drift. For the post-closure period of the backfill case, heat conduction in the backfill controls temperature deviations along the drift. In either case, the values of thermal conductivity in the host rock play a minor role on the magnitude of longitudinal temperature deviations along the drift (Hardin 1998, Section 3.7.5.4).

The DDT submodel is only run at one drift-scale-submodel location (14c3 in Figure 5-2). The DDT submodel is only used for two purposes: (1) calculating the temperature difference between the WP and drip shield and (2) calculating the longitudinal temperature variations along the drift axis. Neither of these quantities are significantly influenced by the thermal conductivity

in the host rock (or in any of the other stratigraphic units). Therefore, it is not necessary to run the DDT submodels at multiple locations because the only potential benefit of running at multiple locations would be to capture the influence of the local thermal conductivity values, which is relatively unimportant with regards to the two quantities that the DDT submodel is required to predict. Advective heat transfer driven by TH behavior in the host rock has little effect on axial temperature variation in the drift. In other words, TH processes in the host rock do not contribute significantly to equalization of axial temperature variations in the drift. Therefore, the conduction-only DDT model adequately represents longitudinal deviations in NFE and EBS temperatures (relative to line-average-heat-source conditions) along the drift.

### **6.5.1 DDT Submodel Location**

The 14c3 drift-scale-submodel location (CRWMS M&O 2000a, column.data) is used for all DDT submodels.

### **6.5.2 DDT Submodel Mesh**

The cross-sectional dimensions of the drift for the post-closure period is shown in Figure 5-3; these dimensions were used to build the numerical meshes of the DDT submodels. For the pre-closure period, the backfill and drip shield in Figure 5-3 are not present; otherwise all other dimensions are the same as in the post-closure case. For the no-backfill case, the backfill in Figure 5-3 is not present. All of the DDT-submodel meshes assume a square cross section for the WP, drift wall, and drip shield (were it is present). As was demonstrated previously (Wilder 1996, Table 1.10.4.1), a circular WP in a circular drift can be accurately represented by a square WP in a square drift, provided that the respective circular and square cross-sectional areas are equal.

The longitudinal dimensions of the drift are shown in Figure 4-1. The DDT submodel utilizes symmetry in all four directions: (1) about the vertical midplane down the center of the drift, (2) the vertical midplane down the center of the rock pillar between drifts, (3) the vertical plane that is orthogonal to and intersects the “hlw1” WP, and (4) the vertical plane that is orthogonal to and intersects the “dsnf1” WP (Figure 4-1).

Two DDT-submodel meshes are used; both meshes share the same grid-block spacing in the longitudinal direction. Two of the DDT submodels share the same mesh (Section 6.5.2.2 and Section 6.5.2.3), which uses fine grid-block spacing in the lateral and vertical direction in the drift to account for the drip-shield cross section, the gap between the WP and drip shield, and (3) thermal conduction in the backfill (for the backfill case) and invert. The only difference between these two submodels (Section 6.5.2.2 and Section 6.5.2.3) is the material distributions inside the drift. The other mesh, which is used in the pre-closure DDT submodel, is able to utilize coarser grid-block spacing without diminishing its ability to accurately account for thermal radiation within the drift.

### **6.5.2.1 Pre-closure DDT Submodel**

The pre-closure DDT-submodel mesh (Figure 6-4) is designed to address thermal radiation inside the emplacement; therefore, it does not require to have as fine gridding inside the drift as is required by the post-closure DDT submodel. The grid-block spacing used in this submodel is fine enough to accurately represent thermal radiation inside the drift.

### **6.5.2.2 Pre-closure (Restart) DDT Submodel**

Because the pre-closure DDT submodel and the post-closure DDT submodel have different grid-block spacing inside the drift, it is necessary to have a second pre-closure DDT submodel to produce the restart file required by the post-closure DDT submodel at 50 yr (when the post-closure submodel is started). The “restart” DDT submodel (Figure 6-5) is the same as the post-closure DDT submodel except that all of the gridblocks between the WP and drift wall have air as the specified material; the air in this submodel uses the effective thermal conductivity versus time relationship that was developed to represent thermal radiation inside the drift (Section 4.1.2.6).

### **6.5.2.3 Post-closure DDT Submodel**

The post-closure DDT-submodel mesh for the backfill case (Figure 6-6a) is designed to address the details of (1) thermal radiation between the WP and drip shield, (2) thermal conduction in the relatively thin drip shield, and (3) thermal conduction in the backfill and invert. The grid-block spacing used in this submodel (Figure 6-6a) is fine enough to accurately model these processes. For the post-closure DDT submodel for the no-backfill case (Figure 6-6b), the area designated as backfill in Figure 6-6a is replaced with air, with an effective thermal conductivity representing thermal radiation.

## **6.5.3 DDT Submodel Boundary Conditions**

The boundary conditions for the DDT submodels are the same as those for the SDT submodel (Figure 6-4) at the l4c3 drift-scale-submodel location (Figure 5-2).

The DDT boundary conditions are the same as the corresponding LDTH submodel (Section 6.3.3).

Because the DDT submodels are for a symmetry cell between the vertical plane down the center of the drift and the vertical midplane between drifts, the lateral boundaries are adiabatic and no-mass-flow boundaries. The DDT submodels require temperature at the upper boundary, which represents the ground surface and the lower boundary, which represents the water table (Table 6.3). Both boundaries have constant temperature conditions with time.

The density of the upper boundary is  $1 \times 10^8$  Kg/m<sup>3</sup> (5.1.6). The heat capacity of the upper boundary is  $1 \times 10^8$  J/Kg-K (5.1.6). The thermal conductivity of the upper boundary is 0.17 (5.1.6). This data is incorporated into the DDT submodel through inclusion in the file: SDT-Dds\_mi (CRWMS M&O 2000a).

The temperature and pressure are based on the grid in Section 4.1.11, the temperatures and pressures in Section 4.1.14, and the locations in column.data (CRWMS M&O 2000a). An interpolation routine is used to relate the temperatures and pressures at various points to the DDT submodel locations. The routines used for this interpolation are chim\_surf\_TP and chim\_wt\_TP.

#### **6.5.4 DDT Submodel Heat Generation Rates**

Heat-generation-rate versus time tables, taken from the source data described in Section 4.1.13, are required for the 8 different WPs represented in the DDT submodels (Figure 4-1). The heat generation rate for the DDT submodel is in the form of a heat versus time table located in NUFT include files. During preclosure the file used is output from heatgenAge (CRWMS M&O 2000a, DDT-0.3Qheat-50y\_vent-00). The heat output represented in this file accounts for removal of 70% of the total heat due to ventilation. The postclosure heat generation table is also output from heatgenAge (CRWMS M&O 2000a, SMT-0.3Qheat-1e6y\_vent-00v). The heat-generation decay curves for this submodel are the same for the no-backfill and backfill cases (Assumption 5.3.1).

#### **6.5.5 DDT Submodel Material Properties**

The DDT submodel uses the same thermal-conduction properties (for the stratigraphic units) that are used in the SMT and SDT submodels (Section 6.2.5 and Section 6.4.5). These properties are based on Sections 4.1.9 and Section 5.2.4 through incorporation in the include file SDT-1Dds-mi (CRWMS M&O 2000a) as illustrated in Figures 3-7 and 3-12. This file incorporates assumption 5.2.4 by using the wet thermal conductivity. In addition to the properties for the stratigraphic units, the DDT submodels require the thermal-conduction properties for the EBS materials (Table 4-1). For the Overton-sand backfill, drip shield, and crushed-tuff invert, the DDT submodels use the same thermal-property values as those used in the LDTH submodels.

For the pre-closure DDT submodel (Figure 6-4), the thermal properties of the gap between the WP and drip shield are those of air (Section 4.1.8).

For the pre-closure DDT submodel (Figure 6-5), which is used to start the post-closure DDT submodel (Figure 6-6), the same effective thermal conductivity versus time table (Section 4.1.8) is used for the air gap between the WP and drift wall as is used in the pre-closure LDTH submodels (Figure 6-2a). For the post-closure DDT submodel (Figure 6-6a) for the backfill case, the same effective thermal conductivity versus time table (Section 4.1.8) is used for the air gap between the upper backfill surface and the crown of the drift as is used in the post-closure LDTH submodels (Figure 6-3). The solid density and specific heat of the air gap in the drift are standard handbook values (Section 4.1.8). For the post-closure DDT submodel (Figure 6-6b) for the no-backfill case, the same effective thermal conductivity versus time table (Section 4.1.8) is used for the air gap between the drip shield and drift wall. Assumption 5.2.7 is used for thermal properties of the backfill and invert for the backfill case. Assumption 5.2.8 is used for thermal conductivity for the invert for the no-backfill case.

### **6.5.6 DDT Submodel Simulations**

Three DDT-submodel simulations were conducted for this AMR. The three DDT simulations are used in all three infiltration-flux (mean, high, and low flux) cases.

The first, which is required to calculate pre-closure TH conditions in the MSTHM, was run with the heat-generation rate reduced by 70%. The first DDT submodel has no backfill or drip shield in the drift (Figure 6-4).

The second DDT submodel has the same heat-generation rate used in the first DDT submodel and uses the same grid spacing used in the third DDT submodel; however, it has no backfill or drip shield in the drift (Figure 6-5). The second submodel is run for a simulation time of 50 yr to generate the restart file (i.e., initial conditions) for the third DDT submodel.

The third DDT submodel, which is required to calculate post-closure TH conditions in the MSTHM, was run for a simulation period of 50 to 1,000,000 yr using the full nominal heat-generation rate. The third submodel has backfill in the drift (Figure 6-6a) for the backfill case. The third submodel for the no-backfill case (Figure 6-6b) does not have backfill in the drift.

## **6.6 MSTHAC METHODOLOGY**

The conceptual model for the MSTHAC is discussed in Section 6.1. The MSTHAC methodology involves a sequence of calculational steps that is described in the following sections.

### **6.6.1 Accounting for the Influence of Drift Ventilation**

For an MSTHM scenario that does not involve drift ventilation, the calculation sequence described in the following sections is executed once. For an MSTHM scenario that involves drift ventilation during the pre-closure period (which is the case for this AMR), the following MSTHM calculational sequence is executed twice.

As discussed in Section 6.2, Section 6.3, Section 6.4 and Section 6.5, the influence of drift ventilation is approximated by reducing the heat-generation rate during the ventilation period. Then, as ventilation ceases, the heat-generation rate abruptly jumps from its reduced value up to its nominal value. For this AMR, the heat-generation rate is reduced by 70% during the ventilation period. Because of the manner in which the MSTHM temperatures are abstracted it is necessary to account for drift ventilation scenarios by conducting two complete (parallel) MSTHM abstractions. One abstraction pertains to the pre-closure period and one pertains to the post-closure period). The results of these two MSTHM abstractions are then spliced at the end of the pre-closure period (i.e., when ventilation ceases). Therefore, it is necessary to run two complete sets of MSTHM submodels to account for ventilation for a given MSTHM scenario (e.g., for a particular infiltration-flux scenario).

For the MSTHM abstraction that pertains to the ventilated pre-closure period, the submodels are run with a reduced heat-generation rate for the entire simulation period. For this AMR, the pre-closure submodels were run for 600 yr with the heat-generation rate reduced in all submodels by 70%, which assures that the scanning curves adequately incorporated the influence of the

initial portion of the cool-down period. For the MSTHM abstraction for the post-closure period, all submodels are run with a step-function heat-generation-rate history that is reduced by 70% during the pre-closure period and then followed by an abrupt increase to the nominal heat-generation rate at the time of closure (which occurs at 50 yr for this AMR). The second set of submodels calculations are run for 1,000,000 yr.

### **6.6.2 Accounting for the Emplacement of the Drip Shield and Backfill**

If an MSTHM abstraction involves the emplacement of either a drip shield or a drip shield overlain by backfill at the time of closure (as is the case in this AMR), it is necessary to break up the LDTH and DDT submodel calculations into two parts. For the pre-closure period, the LDTH and DDT submodels are conducted with a drift without the drip shield and backfill. A restart file is generated for each of the pre-closure submodel runs to start the corresponding post-closure submodel run that includes either a drip shield or a drip shield overlain by backfill in the drift; the post-closure submodel is started at the time of closure (50 yr).

### **6.6.3 Computing Drift-Wall Temperatures**

To obtain the MSTHM drift-wall temperature for an average WP location at each of the 623 repository subdomains (see Figure 6-1a) for the backfill case and for each of the MSTHM timesteps, the relationship between the "line-averaged" drift-wall temperature in the LDTH submodel and the "smeared" temperature in the repository plane of the SDT submodel is used to modify the "smeared" temperatures calculated with the SMT submodel. For the no-backfill case the MSTHM drift-wall temperature for an average WP location is obtained at each of the 610 repository subdomains (Figure 6-1b) just as is done for the backfill case. The result of this stage of the abstraction are the "line-averaged" drift-wall temperatures at each of the 623 repository subdomains for the backfill case (610 repository subdomains for the no-backfill case) and each of the MSTHM timesteps.

The "model" that results from this intermediate step in the MSTHAC calculational sequence could be called the LMTH model, which stands for line-averaged-heat-source mountain-scale thermohydrologic model. The LMTH drift-wall temperatures are further modified to account for waste-package-specific deviations using the DDT submodel. After the DDT submodel has been used to modify the drift-wall temperatures, the result are drift-wall temperatures calculated by a discrete-heat-source mountain-scale TH model (or DMTH model). Thus, the MSTHM is a DMTH model. Details of this procedure are described below.

An overview of the calculational sequence for determining drift-wall temperatures in the MSTHM is as follows:

- SMT-submodel-predicted host-rock temperatures, which is a "smeared" representation of host-rock temperatures in the plane of the repository.
- LMTH-abstracted-model-predicted drift-wall temperatures, which is a "line-averaged" representation of drift-wall temperatures along each emplacement drift in the repository.

- DMTH-abstracted-model-predicted drift-wall temperatures, which is a “discrete” representation of drift-wall temperatures at various points (i.e., specific WP locations with specific heat-generation-rate histories) along each emplacement drift in the repository.

The calculational sequence for determining drift-wall temperatures can be broken down into six steps.

### 6.6.3.1 Computing Drift-Wall Temperatures for the Backfill Case

**Step 1: Conduct the appropriate submodel simulations.** For the case of a pre-closure MSTHM abstraction, this consists of 155 LDTH submodels, 155 SDT submodels, one SMT submodel and one DDT submodel. The number 155 comes from submodel simulations being conducted at 31 drift-scale-submodel locations (Figure 5-2) and for five AML values ( $31 \times 5 = 155$ ). In this case, the nominal repository AML is 60 MTU/acre so the five AML values chosen are: 60 MTU/acre, 50 MTU/acre, 36 MTU/acre, 25 MTU/acre and 15 MTU/acre. The SMT and DDT submodels are both run with an AML of 60 MTU/acre. Because the MSTHM requires pre-closure and post-closure submodels, the number of submodels is doubled; thus, there are 310 LDTH submodels, 310 SDT submodels, 2 SMT submodels and 2 DDT submodels.

**Step 2: Tabulate the SMT-submodel-predicted host-rock temperature histories.** For the backfill case this step is conducted at each of the 623 repository subdomains (Figure 6-1a) and for each of the 352 MSTHM timesteps. The result of this step is the SMT-submodel-predicted host-rock temperature, which is the average (thermal-conduction) host-rock temperature at each of the 623 repository subdomains.

**Step 3: Build 155 scanning curves at the 31 drift-scale-submodel locations.** These curves are plots of the “line-averaged” temperature at the drift wall in the LDTH submodels versus the “smeared” host-rock temperature in the SDT submodels; five curves (for five AMLs) are constructed at each of the 31 locations.

**Step 4: Build 3115 scanning curves at the 623 repository subdomains.** This step is the construction of five scanning curves (for five AMLs) at each of the 623 repository subdomains (Figure 6-1a), which results in 3115 scanning curves ( $623 \times 5 = 3115$ ). This step involves an interpolation process that utilizes the scanning curves at all of the 31 drift-scale-submodel locations. For a given repository-subdomain location and a given AML scanning curve (e.g., the curve for 60 MTU/acre), a new scanning curve is developed, based on an exponentially weighted average of the scanning curves at the 31 drift-scale-submodel locations. Because the influence of any drift-scale-submodel location drops off exponentially with distance, the scanning curve at a repository location is most heavily influenced by its closest (three or four) drift-scale-submodel neighbors. The result of this step is equivalent to having had run 3115 LDTH submodels and 3115 SDT submodels and developing the scanning curve from each LDTH-SDT-submodel pair.

**Step 5: Calculate LMTH drift-wall temperature at the 623 repository subdomains.** This step determines a line-averaged drift-wall temperature at each of the 623 repository subdomains. This is done by interpolating a new scanning curve on the basis of the five AML scanning curves (at a given repository subdomain) and the peak SMT-submodel temperature in that subdomain.

The peak SMT-submodel temperature is compared to the peak SDT-submodel temperatures in each of the five scanning curves. The new scanning curve lies between the scanning curves that have peak SDT-submodel temperatures that bracket the peak SMT-submodel temperature. The relative distance between the new scanning curve and the two bracketing scanning curves is proportional to the relative distance between the peak SMT-submodel temperature and the two peak SDT-submodel temperatures that bracket it. The relationship between the SDT-submodel temperature and the LDTH-submodel temperature in this scanning curve is then used to adjust the SMT-submodel temperature time-history plot from step #2. This step provides 623 values of drift-wall temperature for line-averaged-heat-source conditions.

**Step 6: Calculate 4984 DMTH drift-wall temperatures at the 623 repository subdomains.**

This step adjusts the 623 line-averaged drift-wall temperatures from step #5 to provide WP-specific point values. The DDT submodel is used to calculate local temperature “deviations” along the drift. A local temperature deviation is the difference between the local temperature at a “point” on the drift wall and the line-averaged drift-wall temperature along the entire drift in the DDT submodel (Figure 4-1). The temperature histories from step #5 are adjusted for each of the WP locations represented in the DDT submodel (see Figure 4-1). Because there are eight different WPs treated in the DDT submodel, this results in 4984 values ( $623 \times 8 = 4984$ ) of drift-wall temperature.

This procedure is repeated at different locations along the drift wall, including the upper drift wall (i.e., crown of the drift), the lower drift wall (below the invert), and perimeter-averaged temperature on the drift wall.

### **6.6.3.2 Computing Drift-Wall Temperatures for the No-Backfill Case**

**Step 1: Conduct the appropriate submodel simulations.** For the case of a pre-closure MSTHM abstraction, this consists of 93 LDTH submodels, 93 SDT submodels, one SMT submodel and one DDT submodel. The number 93 comes from submodel simulations being conducted at 31 drift-scale-submodel locations (Figure 5-2) and for three AML values ( $31 \times 3 = 93$ ). For this case, it was decided to conduct one set of submodels at a slightly higher than nominal repository AML (60 MTU/acre) and two sets of submodels at lower than nominal AMLs. The three AML values chosen are: 66 MTU/acre, 56 MTU/acre, and 14 MTU/acre. The SMT and DDT submodels are both run with an AML of 60 MTU/acre. Because the MSTHM requires pre-closure and post-closure submodels, the number of submodels is doubled; thus, there are 186 LDTH submodels, 186 SDT submodels, 2 SMT submodels and 2 DDT submodels.

**Step 2: Tabulate the SMT-submodel-predicted host-rock temperature histories.** For the no-backfill case this step is conducted at each of the 610 repository subdomains (Figure 6-1b) and for each of the 99 MSTHM timesteps. The result of this step is the SMT-submodel-predicted host-rock temperature, which is the average (thermal-conduction) host-rock temperature at each of the 610 repository subdomains.

**Step 3: Build 93 scanning curves at the 31 drift-scale-submodel locations.** These curves are plots of the “line-averaged” temperature at the drift wall in the LDTH submodels versus the

“smeared” host-rock temperature in the SDT submodels; five curves (for five AMLs) are constructed at each of the 31 locations.

**Step 4: Build 1830 scanning curves at the 610 repository subdomains.** This step is the construction of three scanning curves (for three AMLs) at each of the 610 repository subdomains (Figure 6-1b), which results in 1830 scanning curves ( $610 \times 3 = 1830$ ). This step involves an interpolation process that utilizes the scanning curves at all of the 31 drift-scale-submodel locations. For a given repository-subdomain location and a given AML scanning curve (e.g., the curve for 56 MTU/acre), a new scanning curve is developed, based on an exponentially weighted average of the scanning curves at the 31 drift-scale-submodel locations. Because the influence of any drift-scale-submodel location drops off exponentially with distance, the scanning curve at a repository location is most heavily influenced by its closest (three or four) drift-scale-submodel neighbors. The result of this step is equivalent to having had run 1830 LDTH submodels and 1830 SDT submodels and developing the scanning curve from each LDTH-SDT-submodel pair.

**Step 5: Calculate LMTH drift-wall temperature at the 610 repository subdomains.** This step determines a line-averaged drift-wall temperature at each of the 610 repository subdomains. This is done by interpolating a new scanning curve on the basis of the three AML scanning curves (at a given repository subdomain) and the peak SMT-submodel temperature in that subdomain. The peak SMT-submodel temperature is compared to the peak SDT-submodel temperatures in each of the three scanning curves. The new scanning curve lies between the scanning curves that have peak SDT-submodel temperatures that bracket the peak SMT-submodel temperature. The relative distance between the new scanning curve and the two bracketing scanning curves is proportional to the relative distance between the peak SMT-submodel temperature and the two peak SDT-submodel temperatures that bracket it. The relationship between the SDT-submodel temperature and the LDTH-submodel temperature in this scanning curve is then used to adjust the SMT-submodel temperature time-history plot from step #2. This step provides 610 values of drift-wall temperature for line-averaged-heat-source conditions.

**Step 6: Calculate 4880 DMTH drift-wall temperatures at the 610 repository subdomains.** This step adjusts the 610 line-averaged drift-wall temperatures from step #5 to provide WP-specific point values. The DDT submodel is used to calculate local temperature “deviations” along the drift. A local temperature deviation is the difference between the local temperature at a “point” on the drift wall and the line-averaged drift-wall temperature along the entire drift in the DDT submodel (Figure 4-1). The temperature histories from step #5 are adjusted for each of the WP locations represented in the DDT submodel (see Figure 4-1). Because there are eight different WPs treated in the DDT submodel, this results in 4880 values ( $610 \times 8 = 4880$ ) of drift-wall temperature.

This procedure is repeated at different locations along the drift wall, including the upper drift wall (i.e., crown of the drift), the lower drift wall (below the invert), and perimeter-averaged temperature on the drift wall.

#### **6.6.4 Computing Host-Rock Temperatures**

The calculational procedure in 6.6.3 is repeated for other locations, including those in the near-field host rock, producing WP-specific host-rock temperatures.

#### **6.6.5 Computing Backfill, Drip-Shield, and Invert Temperatures**

The calculational procedure in 6.6.3 is repeated for other locations, including those in the backfill, on the drip shield, and in the invert, producing WP-specific (backfill, drip-shield, or invert) temperatures. For the no-backfill case, temperature is provided in the drift (midway between the crown of the drift and the crown of the drip shield), which is at the same location within the drift as where the backfill temperature is provided for the backfill case.

#### **6.6.6 Computing Waste Package Temperatures**

For the pre-closure period, the procedure for calculating WP temperatures is analogous to the procedure described in section 6.6.4 for drift-wall temperatures, with the following minor distinction. The LDTH-SDT scanning curves are constructed with the average of temperatures in the grid blocks that form the outer perimeter of the modeled WP (Figure 6-2a) rather than the host-rock grid blocks on the perimeter of the drift wall.

For the post-closure period, which is the time after ventilation has ceased and backfill and the drip shield have been emplaced, an additional calculational step is added to account for the fact that the WP and drip shield are modeled as one lumped material in the LDTH submodel. To do this, the DDT submodel is used to compute the difference between the WP temperature and the perimeter-averaged drip-shield temperature. This temperature difference is added to the WP temperature (which is the temperature of the lumped drip shield and WP) computed by the LDTH submodel. The result of this step are WP-specific WP temperatures. Because there are 8 different WPs treated in the DDT submodel (Figure 4-1) and 623 repository subdomains (Figure 6-1a), this results in 4984 values ( $623 \times 8 = 4984$ ) of WP temperature for the backfill case. Because there are 610 repository subdomains in the no-backfill case (Figure 6-1b), this results in 4880 values ( $610 \times 8 = 4880$ ) of WP temperature.

This procedure applies to both the backfill and no-backfill cases.

#### **6.6.7 Computing Drift-Wall Relative Humidity**

The procedure for calculating *RH* on the drift wall is similar to the procedure for calculating drift-wall temperature, described in Section 6.6.3. The primary distinction is that scanning curves are completely derived from the LDTH submodels (rather than from LDTH-SDT pairs) and that the scanning curves relate the drift-wall *RH* to the drift-wall temperature. After drift-wall temperature has been calculated for the 623 repository subdomains (Figure 6-1a) and eight different WP locations (Figure 4-1) from Step 6 in Section 6.6.3, *RH* is determined from the drift-wall *RH* versus drift-wall *T* scanning curve. Note that the no-backfill case involves 610 repository subdomains (Figure 6-1b).

This procedure applies to both the backfill and no-backfill cases.

### 6.6.8 Computing Host-Rock Relative Humidity

The procedure for calculating  $RH$  at various locations in the host rock is analogous to that used to calculate drift-wall  $RH$ . After local host-rock temperatures (e.g., five m above the crown of the drift) have been calculated for the 623 repository subdomains (Figure 6-1a) and eight WP locations (Figure 4-1) from Section 6.6.4,  $RH$  is determined from the host-rock  $RH$  versus host-rock  $T$  scanning curve. Note that the no-backfill case involves 610 repository subdomains (Figure 6-1b).

This procedure applies to both the backfill and no-backfill cases.

### 6.6.9 Computing Relative Humidity on the Drip Shield

The procedure for calculating drip-shield relative humidity  $RH_{ds}$  is different from that used to calculate relative humidity on the drift-wall  $RH_{dw}$ , in that time is explicitly incorporated into the interpolation process. The necessity of explicitly including time in the calculation of  $RH$  in the drift arises from the following:

1.  $RH$  in the drift is very dependent on the magnitude of seepage flux into the drift.
2. The magnitude of seepage flux into the drift is very dependent on the magnitude of percolation flux in the host rock.
3. The magnitude of percolation flux in the host-rock is very dependent on the magnitude of infiltration flux at the ground surface.
4. Infiltration flux at the ground surface is a function of time (with three distinctive values pertaining to each of the three climate periods).

This procedure requires that  $RH_{dw}$  (Section 6.6.7) and the drip-shield temperature  $T_{ds}$  (Section 6.6.5) have already been determined. Instead of using temperature as the independent variable, two value versus time curves are plotted for the five AMLs:  $RH_{ds}/RH_{dw}$  versus time and  $T_{ds}$  versus time. For each timestep, the local value of  $T_{ds}$ , (Section 6.6.5) is compared against the five values of  $T_{ds}$  in the five  $T_{ds}$  history curves. The relative position of the local  $T_{ds}$  among the five  $T_{ds}$  history curves determines the relative position of the interpolated  $RH_{ds}/RH_{dw}$  among the five  $RH_{ds}/RH_{dw}$  history curves. For example, if the local  $T_{ds}$  is halfway between the values of  $T_{ds}$  in the 50 and 60 MTU/acre  $T_{ds}$  history curves, then the value of  $RH_{ds}/RH_{dw}$  will be halfway between the values of  $RH_{ds}/RH_{dw}$  in the 50 and 60 MTU/acre  $RH_{ds}/RH_{dw}$  history curves. Finally, for each timestep, the local value of  $RH_{ds}$  is determined by multiplying  $RH_{dw}$  (Section 6.6.7) by  $RH_{ds}/RH_{dw}$ .

This procedure applies to both the backfill and no-backfill cases.

### 6.6.10 Computing Relative Humidity in the Backfill

The procedure for calculating  $RH$  at various locations in the backfill is analogous to that used to calculate  $RH$  on the drip shield. This step requires that the local relative humidity at the drift wall

(Section 6.6.7) and the local temperature in the backfill (Section 6.6.5) have already been determined.

This procedure only applies to the backfill case.

### 6.6.11 Computing Relative Humidity in the Invert

The procedure for calculating  $RH$  in the invert is analogous to that used to calculate  $RH$  on the drip shield. This step requires that the local relative humidity at the drift wall (Section 6.6.7) and the local temperature in the invert (Section 6.6.5) have already been determined.

This procedure applies to both the backfill and no-backfill cases.

### 6.6.12 Computing Waste-Package Relative Humidity

For the pre-closure period, the procedure for calculating relative humidity on the WP  $RH_{wp}$  requires that the following have already been determined:  $RH_{dw}$  (Section 6.6.7),  $T_{dw}$  (Section 6.6.3), and WP temperature  $T_{wp}$  (Section 6.6.6);  $RH_{wp}$  is given by

$$RH_{wp} = RH_{dw} \frac{P_{sat}(T_{dw})}{P_{sat}(T_{wp})}, \quad (7)$$

where  $P_{sat}$  is the saturated vapor pressure. Summarizing,  $RH$  on the WP is determined by  $RH$  on the drift wall and the temperature difference between the drift wall and WP. This equation is arrived at by realizing that the vapor density is constant. This precludes a gradient of absolute humidity across an open space. Relative humidity is the ratio of actual vapor pressure to saturated vapor pressure. Therefore, the product of relative humidity and saturated vapor pressure is absolute humidity. Rearranging these terms yields equation 7.

For the post-closure, which is the time after ventilation has ceased and backfill and the drip shield have been emplaced, the procedure for calculating  $RH$  on the WP requires that the following have already been determined: drip-shield relative humidity  $RH_{ds}$  (Section 6.6.7), drift-wall temperature  $T_{ds}$  (Section 6.6.3), and WP temperature  $T_{wp}$  (Section 6.6.6). Relative humidity on the WP ( $RH_{wp}$ ) is given by

$$RH_{wp} = RH_{ds} \frac{P_{sat}(T_{ds})}{P_{sat}(T_{wp})}, \quad (8)$$

Summarizing,  $RH$  on the WP is primarily dependent on  $RH$  on the drip shield and the temperature difference between the drip shield and WP. Therefore, the temperature difference between the WP and drip shield plays a role in reducing  $RH$  on the WP.

This procedure applies to both the backfill and no-backfill cases.

### 6.6.13 Computing Liquid-Phase Flux in the Host Rock

Just as with  $RH$  in the emplacement drifts, the liquid-phase flux has a time dependence. This dependence is associated with the change of infiltration rate reflecting a change in climate. The process of calculating liquid-phase flux in the host rock  $q_{liq,hr}$  is similar to that for calculating  $RH$  in the drift (Section 6.6.9, Section 6.6.10, and Section 6.6.11).

This procedure requires that the local host-rock temperature  $T_{hr}$  has already been determined (Section 6.6.4). Two value versus time curves are plotted for the five AMLs:  $q_{liq,hr}$  versus time and  $T_{hr}$  versus time. For each timestep, the local value of  $T_{hr}$ , (Section 6.6.4) is compared against the five values of  $T_{hr}$  in the five  $T_{hr}$  history curves. The relative position of the local  $T_{hr}$  among the five  $T_{hr}$  history curves determines the relative position of the interpolated  $q_{liq,hr}$  among the five  $q_{liq,hr}$  history curves. For example, if the local  $T_{hr}$  is halfway between the values of  $T_{hr}$  in the 50 and 60 MTU/acre  $T_{hr}$  history curves, then the local value of  $q_{liq,hr}$  will be halfway between the values of  $q_{liq,hr}$  in the 50 and 60 MTU/acre  $q_{liq,hr}$  history curves.

This procedure is repeated for different locations in the host rock. This procedure applies to both the backfill and no-backfill cases.

### 6.6.14 Computing Liquid-Phase Flux on the Drip Shield

The procedure for calculating liquid-phase flux  $q_{liq,ds}$  on the drip shield is analogous to that used to calculate liquid-phase flux  $q_{liq,hr}$  in the host rock (Section 6.6.13). This step requires that the local temperature on the drip shield  $T_{ds}$  (Section 6.6.5) has already been determined.

This procedure is repeated for different locations on the drip shield. This procedure applies to both the backfill and no-backfill cases.

### 6.6.15 Computing Liquid-Phase Flux in the Backfill

The procedure for calculating liquid-phase flux  $q_{liq,bf}$  at various locations in the backfill is analogous to that used to calculate liquid-phase flux  $q_{liq,hr}$  in the host rock (Section 6.6.13). This step requires that the local temperature in the backfill  $T_{bf}$  (Section 6.6.5) has already been determined.

This procedure is repeated for different locations in the backfill. This procedure only applies to the backfill case.

### 6.6.16 Computing Liquid-Phase Flux in the Invert

The procedure for calculating liquid-phase flux  $q_{liq,inv}$  in the invert is analogous to that used to calculate liquid-phase flux  $q_{liq,hr}$  in the host rock (Section 6.6.13). This step requires that the local temperature on the drip shield  $T_{inv}$  (Section 6.6.5) has already been determined.

This procedure is repeated for different locations in the invert. This procedure applies to both the backfill and no-backfill cases.

### 6.6.17 Computing Liquid Saturation at the Drift Wall

The procedure for calculating liquid saturation  $S_{\text{liq,dw}}$  at the drift wall is analogous to that used to calculate drift-wall  $RH$ . After local drift-wall temperatures (Step 6 in Section 6.6.3) have been calculated for the 623 repository subdomains (Figure 6-1a) and eight WP locations (Figure 4-1),  $S_{\text{liq,dw}}$  is determined from the drift-wall  $S_{\text{liq,dw}}$  versus drift-wall  $T$  scanning curve. Note that the no-backfill case involves 610 repository subdomains (Figure 6-1b).

This procedure applies to both the backfill and no-backfill cases.

### 6.6.18 Computing Liquid Saturation on the Drip Shield

The procedure for calculating liquid saturation  $S_{\text{liq,ds}}$  on the drip shield is analogous to that used to calculate drift-wall  $RH$ . After local drip-shield temperatures (Section 6.6.5) have been calculated for the 623 repository subdomains (Figure 6-1a) and eight WP locations (Figure 4-1),  $S_{\text{liq,ds}}$  is determined from the drift-wall  $S_{\text{liq,ds}}$  versus drip-shield  $T$  scanning curve. Note that the no-backfill case involves 610 repository subdomains (Figure 6-1b).

This procedure applies to both the backfill and no-backfill cases.

### 6.6.19 Computing Liquid Saturation in the Invert

The procedure for calculating liquid saturation  $S_{\text{liq,inv}}$  at the drift wall is analogous to that used to calculate drift-wall  $RH$ . After local invert temperatures (Section 6.6.5) have been calculated for the 623 repository subdomains (Figure 6-1a) and eight WP locations (Figure 4-1),  $S_{\text{liq,inv}}$  is determined from the drift-wall  $S_{\text{liq,inv}}$  versus invert  $T$  scanning curve. Note that the no-backfill case involves 610 repository subdomains (Figure 6-1b).

This procedure applies to both the backfill and no-backfill cases.

### 6.6.20 Computing Gas-Phase Air-Mass Fraction Adjacent to Drip Shield

The procedure for calculating gas-phase air-mass fraction  $X_{\text{air,gas,ds}}$  adjacent to the drip shield is analogous to that used to calculate drift-wall  $RH$ . After local drip-shield temperatures (Section 6.6.5) have been calculated for the 623 repository subdomains (Figure 6-1a) and eight WP locations (Figure 4-1),  $X_{\text{air,gas,ds}}$  is determined from the  $X_{\text{air,gas,ds}}$  versus drip-shield  $T$  scanning curve. Note that the no-backfill case involves 610 repository subdomains (Figure 6-1b).

This procedure applies to both the backfill and no-backfill cases.

### 6.6.21 Computing Gas-Phase Pressure Adjacent to Drip Shield

The procedure for calculating gas-phase pressure  $P_{\text{gas,ds}}$  adjacent to the drip shield is analogous to that used to calculate drift-wall  $RH$ . After local drip-shield temperatures (Section 6.6.5) have been calculated for the 623 repository subdomains (Figure 6-1a) and eight WP locations (Figure 4-1),  $P_{\text{gas,ds}}$  is determined from the  $P_{\text{gas,ds}}$  versus drip-shield  $T$  scanning curve. Note that the no-backfill case involves 610 repository subdomains (Figure 6-1b).

This procedure applies to both the backfill and no-backfill cases.

### **6.6.22 Computing Gas-Phase Flux of Air**

The procedure for calculating gas-phase (air) flux  $Q_{\text{gas,air,dr}}$  around the perimeter of the drift is analogous to that used to calculate drift-wall  $RH$ . After local drift-wall temperatures (Step 6 in Section 6.6.3) have been calculated for the 623 repository subdomains (Figure 6-1a) and eight WP locations (Figure 4-1),  $Q_{\text{gas,air,dr}}$  is determined from the  $Q_{\text{gas,air,dr}}$  versus drift-wall  $T$  scanning curve. Note that the no-backfill case involves 610 repository subdomains (Figure 6-1b).

This procedure applies to both the backfill and no-backfill cases.

### **6.6.23 Computing Gas-Phase Flux of Water Vapor**

The procedure for calculating gas-phase (water vapor) flux  $Q_{\text{gas,wat,dr}}$  around the perimeter of the drift is analogous to that used to calculate drift-wall  $RH$ . After local drift-wall temperatures (Step 6 in Section 6.6.3) have been calculated for the 623 repository subdomains (Figure 6-1a) and eight WP locations (Figure 4-1),  $Q_{\text{gas,wat,dr}}$  is determined from the  $Q_{\text{gas,wat,dr}}$  versus drift-wall  $T$  scanning curve. Note that the no-backfill case involves 610 repository subdomains (Figure 6-1b).

This procedure applies to both the backfill and no-backfill cases.

### **6.6.24 Computing Capillary Pressure on the Drip Shield**

The procedure for calculating capillary pressure  $P_{\text{c,ds}}$  on the drip shield is analogous to that used to calculate drift-wall  $RH$ . After local drip-shield temperatures (Section 6.6.5) have been calculated for the 623 repository subdomains (Figure 6-1a) and eight WP locations (Figure 4-1),  $P_{\text{c,ds}}$  is determined from the  $P_{\text{c,ds}}$  versus drip-shield  $T$  scanning curve. Note that the no-backfill case involves 610 repository subdomains (Figure 6-1b).

This procedure applies to both the backfill and no-backfill cases.

### **6.6.25 Computing Capillary Pressure on the Drift Wall**

The procedure for calculating capillary pressure  $P_{\text{c,dw}}$  on the drift wall is analogous to that used to calculate drift-wall  $RH$ . After local drift-wall temperatures (Step 6 in Section 6.6.3) have been calculated for the 623 repository subdomains (Figure 6-1a) and eight WP locations (Figure 4-1),  $P_{\text{c,dw}}$  is determined from the  $P_{\text{c,dw}}$  versus drift-wall  $T$  scanning curve. Note that the no-backfill case involves 610 repository subdomains (Figure 6-1b).

This procedure is repeated for both the fracture and matrix continuum. This procedure applies to both the backfill and no-backfill cases.

### 6.6.26 Computing Capillary Pressure in the Invert

The procedure for calculating capillary pressure  $P_{c,inv}$  in the invert is analogous to that used to calculate drift-wall  $RH$ . After local invert temperatures (Section 6.6.5) have been calculated for the 623 repository subdomains (Figure 6-1a) and eight WP locations (Figure 4-1),  $P_{c,inv}$  is determined from the  $P_{c,inv}$  versus invert  $T$  scanning curve. Note that the no-backfill case involves 610 repository subdomains (Figure 6-1b).

This procedure applies to both the backfill and no-backfill cases.

### 6.6.27 Computing Evaporation Rate on the Drip Shield

The procedure for calculating evaporation rate  $E_{ds}$  on the drip shield is analogous to that used to calculate drift-wall  $RH$ . After local drip-shield temperatures (Section 6.6.5) have been calculated for the 623 repository subdomains (Figure 6-1a) and eight WP locations (Figure 4-1),  $E_{ds}$  is determined from the  $E_{ds}$  versus drip-shield  $T$  scanning curve. Note that the no-backfill case involves 610 repository subdomains (Figure 6-1b).

This procedure is conducted for top of the drip shield and for a sum over the entire perimeter of the drip shield. This procedure applies to both the backfill and no-backfill cases.

### 6.6.28 Computing Evaporation Rate at the Top of the Backfill

The procedure for calculating evaporation rate  $E_{tbf}$  at the top of the backfill is analogous to that used to calculate drift-wall  $RH$ . After local backfill temperatures (Section 6.6.5) have been calculated for the 623 repository subdomains (Figure 6-1a) and eight WP locations (Figure 4-1),  $E_{tbf}$  is determined from the  $E_{tbf}$  versus backfill  $T$  scanning curve. Note that the no-backfill case involves 610 repository subdomains (Figure 6-1b).

This procedure applies to both the backfill and no-backfill cases.

### 6.6.29 Computing Evaporation Rate in the Invert

The procedure for calculating evaporation rate  $E_{inv}$  in the invert is analogous to that used to calculate drift-wall  $RH$ . After local invert temperatures (Section 6.6.5) have been calculated for the 623 repository subdomains (Figure 6-1a) and eight WP locations (Figure 4-1),  $E_{inv}$  is determined from the  $E_{inv}$  versus invert  $T$  scanning curve. Note that the no-backfill case involves 610 repository subdomains (Figure 6-1b).

This procedure applies to both the backfill and no-backfill cases.

### 6.6.30 Binning TH Results

For each of the repository subdomains, a typical WP is selected for each of the two major WP groups: CSNF and HLW. The CSNF group includes bwr1, bwr2, pwr1, pwr2, and pwr3 WPs (Figure 4-1). The HLW group includes only hlw1 and hlw2. The DSNF WPs are excluded from

the binning process because they constitute such a small fraction of the inventory in the repository.

For a given repository subdomain and WP group, an average WP temperature history and an average WP relative humidity history are calculated on the basis of a simple average. For each WP in the group, the sum of the normalized differences is summed over time as follows:

$$\sum_{t=0}^{t=1,000,000} \frac{(T_{WP} - T_{WP,avg})}{(T_{WP,avg})^2} + \frac{(RH_{WP} - RH_{WP,avg})}{(T_{WP,avg})^2} \quad (8)$$

where  $T_{WP}$  is the WP temperature,  $RH_{WP}$  is the WP relative humidity,  $T_{WP,avg}$  is the average WP temperature (based on a simple average) and  $RH_{WP,avg}$  is the average WP relative humidity (based on a simple average) in that repository subdomain and WP group. The WP with the minimum sum is selected as being represented of that repository subdomain and WP group (Figure 6-1a).

This procedure applies to both the backfill and no-backfill cases.

## 6.7 OVERVIEW OF DATA FLOW

The overall data flow in the MSTHM is shown in Figure 1-2. A more detailed description is shown in Figure 1-3. The first components (shown in blue) involve submodel preparation, which are covered in Section 0. The next set of components (shown in violet) involve submodel execution, which are covered in Section 0. The next component (shown in purple) is the execution of MSTHAC, which is covered in Section 0. The last component (shown in yellow) is data binning and graphical-output preparation.

## 6.8 SUBMODEL PREPARATION

Generation of the full MSTHM abstraction is dependent upon the four major submodel types (LDTH, SDT, DDT, and SMT) as described in Sections 0 through Section 6.5. The quality of the final output is dependent on both the quality of the input data and the self-consistency of the multitude of NUFT simulation runs needed for a single MSTHM abstraction. These demands are met through the combination of automated tools for generating NUFT input files, along with a modular input file format making extensive use of the include function of NUFT.

The map of input data described in the previous section through the various stages of model generation is shown in the Data Flow Diagrams depicted in Figure 3-1 through Figure 3-12. The data manipulation required to prepare the raw input data (Section 4) for use by the NUFT-based submodels includes reformatting, change of units, averaging, and interpolation (various schemes). These operations are applied to the data in a well-defined sequence of steps to assure data consistency between all simulation runs.

Figure 3-1 provides the symbol legend applicable to all the diagrams in the following subsections. These Data Flow Diagrams comprehensively describe the processing steps applied in the modeling tasks.

## 6.8.1 Mesh Generation

There are two major categories of numerical meshes, corresponding to the mountain- and drift-scale submodels. For the mountain-scale (SMT) submodels, the numerical mesh is generated entirely by YMESH, prior to NUFT run time; using YMESH, the user builds the mountain-scale mesh such that the approximated shape of the heated repository footprint can be accurately represented, with sufficiently fine grid-block definition close to the edges of the repository. For the drift-scale (SDT, LDTH, and DDT) submodels, YMESH is used to generate the information that assigns the vertical distribution of the stratigraphic units as well as the grid-block resolution in the vertical direction. A combination of software scripts and hand editing is required to generate the grid-block spacing and material-type specification for the grid blocks (e.g., Figure 6-3) that represents the geometry of the EBS inside the emplacement drifts (Figure 5-3). For the drift-scale submodels, the genmsh feature of NUFT is utilized, whereby the numerical mesh is built at run time.

Mesh generation covers two main categories: the creation of a numerical grid for the computational algorithm, and the assignment of the proper material type, from natural stratigraphy or engineering design, to each grid block. The majority of the actual mapping operations are performed by YMESH, but additional steps are necessary both prior and subsequent to the use of YMESH. For all practical purposes, these pre- and post-fix operations serve as interface modules to the data pipeline.

The processing steps for generating all the numerical meshes required for the MSTHM are depicted in Figure 3-2 and described in the following sections.

### 6.8.1.1 YMESH Input

YMESH can be executed either in a 3-D sense or in a 1-D sense. For the mountain-scale (SMT) submodel, YMESH produces the 3-D numerical mesh file that is utilized directly by NUFT. For the 1-D and 2-D drift-scale submodels, YMESH produces information describing the 1-D vertical distribution of the grid blocks and material types of each of those grid-block layers; this information is placed in the genmsh block of the NUFT input file. For the 2-D and 3-D drift-scale submodels, the grid-block definition in the second and third dimension is assigned by scripts that the modeler develops the template for.

YMESH requires two inputs in order to generate a NUFT-compatible mesh:

- **User input.** This file includes specification of (1) the model domain (i.e., model boundaries), (2) the orientation and depth of the repository horizon, (3) the vertical dimensions (and/or the maximum allowable vertical dimensions) of the grid blocks as a function of distance from the repository horizon. For generating an SMT submodel, the areal location of the repository footprint (Figure 5-1) is accomplished by specifying a prefix to the name of the grid blocks in the repository footprint; different prefixes can be used to specify subareas of the repository.
- **World grid.** This is the stratigraphy primary input for YMESH to map rock materials onto the computational mesh (called the “user’s mesh”). The world grid is a combination of items

tspa99\_primary\_mesh, which is the numerical mesh for the site-scale UZ flow model, and UZ99\_3.grd, which is the vertices file for that mesh (4.1.11). The files UZ99\_3.grd and tspa99\_primary\_mesh are processed by rme6 (Attachment I) to create the file LBL99-YMESH, which is subsequently used in all YMESH operations for both the mountain- and drift-scale submodels.

The file PAItem1Att10817 (CRWMS M&O 2000a) is used to guide the modeler in approximating the repository footprint (Figure 5-1) for use in the mountain-scale (SMT) submodel (tspa00.grid00 and tspa00.grid01). Having chosen a reasonable representation of the repository footprint, the next step is choosing the 31 locations for use in the drift scale submodels (column.data). In this model-building process, the modeler's judgment in producing the input files to YMESH is as important as the quality of the input data in its affect on the quality of the final model result.

Several different output types are available from YMESH. For the purposes of the work at hand, the main YMESH output type is NUFT input, and the secondary output type is rock column description, which is placed into NUFT input files as comment lines. This secondary output is also used in generating Table 6.1.

#### 6.8.1.2 Drift-Scale-Submodel Meshes

The generation of the drift-scale meshes begins with the creation of the *column\_template* files along with the *column.data* file (Figure 3-2). The *column.data* information records the locations of the individual 31 locations for the LDTH and SDT submodels, and is represented graphically in Figure 5-2. There are two *column\_template* files, one for LDTH submodels, and one for SDT submodels. In each of these cases they serve the same purpose—to describe the vertical mesh resolution for the submodel type.

The routine *makeColumns* (Attachment I) reads in the *column.data* file along with a *column\_template* file to produce one individual YMESH input files for each of the 31 drift-scale submodel locations (<column>.dat). Each of these files is run through YMESH to generate a NUFT genmsh file (<column>.nft) and a rock column file (<column>.col) for its respective submodel type and location. These drift scale mesh files then contain information of both mesh geometry, as well as one-dimensional mapping of the materials in the natural system. (The approach of mapping material in one single dimension for the drift scale model is deemed appropriate due to the comparatively small horizontal extent of these submodels.)

In both SDT and LDTH models, the rock column files are used for informational purposes. The information is extracted by *readUnits* (Attachment I) and output as NUFT comment lines (<column>.col.units). These files will be included in the same NUFT input files which contain the contents of the corresponding <column>.nft information. As a final step in the production of SDT meshes, the routine *addlay* (Attachment I) is run on each of the <column>.nft files to add atmosphere and water table material layers at the top and bottom of the mesh, respectively.

The LDTH <column>.nft files require a more complex set of modifications, because of two additional requirements on these submodels—that they include both the engineered system and

hydrologic behavior. The hydrologic modeling of the LDTH submodels utilizes the implicit dual-permeability (implicit DKM) capability of NUFT. The implicit DKM requires mapping of materials for both fracture and matrix continua. To include the engineered system, some of the material mappings of the natural system stratigraphy must be overwritten with mapping to the engineered system materials. Both these tasks are achieved with *define\_EBS\_fineGrid* (Attachment I). The files *<column>.nft.msh.dkm0.f* and *<column>.nft.msh.dkm0.m* contain implicit-DKM format, but no engineered system, and are for use in the initialization runs of the LDTH submodel. The files *<column>.nft.msh.dkm0.f* and *<column>.nft.msh.dkm0.m* are for use in the remaining LDTH modeling stages.

The mesh for the DDT submodel is derived from an early stage in the development of the LDTH meshes. The YMESH input file at a single submodel location (14c3) is the starting point for development of the DDT meshes. To develop the pre-closure period file 14c3.03v.dat for the DDT model, the grid divisions in the z dimension are redefined to accommodate the eventual addition of radiation connections. For the post-closure DDT file (14c3.dat) the mesh is further refined in order to describe the drip shield and backfill. The resulting NUFT input files are then run through *addLayers* (Attachment I), which, similar to *addlay*, adds atmosphere and water table material layers.

### 6.8.1.3 Mountain-Scale Submodel Mesh

The mountain-scale mesh is the entire set of mesh information delivered, with the extrapolation of edges constrained to the needs of the abstraction modeling technique. The various modifications of the *tspa00-meshNN* files were for the purpose of marking regions of interest in grid block names. These tags had no impact on the data values transferred to the next stage in the pipeline.

The mountain-scale numerical mesh is based on the file *tspa00.grid01*, which derives itself from the motivating concerns outlined in Sections 6.2.1 and 6.2.2 (The mesh processing steps for the SMT mesh are shown in Figure 3-2.). This file is processed by YMESH to create both *tspa00-mesh01* and *tspa00-mesh02*. The differences in these two outputs are only in the names given to some of the grid blocks. In the latter file, the blocks at the repository horizon were given special names to aid in the later steps of the abstraction algorithm.

The YMESH input file *tspa00.grid00* differs from *tspa00.grid01* in that it contains a much finer mesh in the vertical direction. The file generated from this one (*tspa00-mesh00*) is only used in generation of boundary conditions (Figure 3-5), and in that role, only the horizontal dimensions of the mesh information are used, incomplete agreement with the other SMT mesh files.

## 6.8.2 Material Properties

The primary function of the processing performed on the material property data inputs is to reformat them in a form compatible for NUFT (see Figure 3-7 and Figure 3-8). This task involved both modifying the syntax and format of the file, and providing proper units, as well as proper assignments within the separate matrix and fracture continua simulated by NUFT in

implicit DKM simulations (using the LDTH submodels). The material properties of the stratigraphic units and those of the EBS are kept in separate input files to maintain modularity.

The input files for the material properties of the stratigraphic units were processed by the routine *rock\_sun.m* (Attachment I), to prepare them for the LDTH submodels. Each set of rock properties (from LB990861233129.001, LB990861233129.002, and LB990861233129.003), corresponding to three infiltration-flux cases (mean, high, and low flux) is processed in this manner. The rock property set used in the thermal conduction submodels is constructed from the mean infiltration file produced for the LDTH submodels by keeping only the wet thermal conduction data (Section 5.2.4).

The materials incorporated in the EBS are required only in the LDTH and DDT models. The files *dkm-afc-pbf-EBS\_Rev10* and *dkm-afc-EBS\_Rev10* contain the EBS material properties for the pre-closure and post-closure LDTH submodels, respectively. The EBS material properties in the DDT submodels are found in the file *DDT-EBS\_Rev00*. The effective thermal conductivity of air, which is used to represent thermal radiation (Section 4.1.8), is found in the files *modprop\_dr-up-00* and *modprop\_dr-up-00v*.

### 6.8.3 Heat-Generation Rate

Heat-generation-rate versus time information was extracted into individual heat-generation files in NUFT syntax, as shown in Figure 3-3. For the SMT submodel, the Matlab script *heat\_SMT.m* (Attachment I) extracts the data from the appropriate data source files. For the DDT submodel, the Matlab script *heat\_DDT.m* (Attachment I) extracts the data from the appropriate data source files. In both of these cases, the header lines are removed in order to simplify the script code, then the script is executed to produce the intermediate file. In the case of SDT and LDTH models, the file *line-load-heat* contains the heat-generation data, which was manually transcribed into the file. Incorporating the effects of ventilation and aging of WPs into the heat-generation-rate versus time tables is accomplished via the routine *heatgenAge* (Attachment I).

### 6.8.4 Infiltration Flux

To prepare the infiltration flux source data for use in the NUFT input file requires several steps. First, the routine *convertCoords* is executed on all source data to transform the coordinate representations from UTM NAD 27 coordinates to Nevada State Plane coordinates. Next, the local infiltration flux is interpolated at each of the drift-scale-submodel locations using a Gaussian weighting function implemented in the routine *columnInfiltration* (Attachment I). This interpolation is done for each of the three climate states (present-day, monsoonal, and glacial), and for each of the three infiltration-flux cases (mean, high, and low); for each drift-scale submodel location (Figure 5-2), this results in nine values of infiltration flux. The resulting file, *infiltration.tex*, then contains each of the nine infiltration-flux values for each of the drift-scale submodel locations. These values are then extracted from this file by the routine *infiltrab.m* (Attachment I) and written into individual files. The contents of these files are included in the LDTH input file creation scripts (Attachment I). These steps are depicted in Figure 3-4 and Figure 3-6.

At the time of LDTH input file creation (*i.e.* execution of the LDTH input file creation scripts), the three different tables of infiltration flux are used to create a time dependent infiltration flux definition. This results in an infiltration flux versus time table with a constant present-day-flux value from 0 to 600 yr, an abrupt transition at 600 yr to a constant monsoonal-flux value that lasts from 600 to 2000 yr, and an abrupt transition at 2000 yr to a constant glacial-flux value that lasts from 2000 to 1,000,000 yr.

### 6.8.5 Boundary Conditions

With respect to the process of building boundary conditions, the four submodel types share certain aspects, as well as having certain distinctions (Figure 3-5). All submodels have lateral boundaries that are no-heat-flow (or adiabatic) boundaries; the thermohydrologic (LDTH) submodel also has no-mass-flow lateral boundaries. Thus, the only boundary conditions that are specified in the four submodel types are at the upper and lower boundaries.

The conduction-only submodels, which include the SMT submodel (Section 6.2), SDT submodel (Section 6.4), and the DDT submodel (Section 6.5), only require that temperatures be specified at the boundaries. The thermohydrologic (LDTH) submodel (Section 6.3) requires temperature, pressure, and gas-phase air-mass fraction be specified at the boundaries. All four submodel types have the ground surface as the upper boundary; thus, at a given coordinate location, all four submodels share the same upper-boundary temperature. The three drift-scale submodels (SDT, LDTH, and DDT) have the water table as the lower boundary; thus the three drift-scale submodels share the same lower-boundary temperature. The SMT submodel has a lower boundary that is 1000 m below the water table.

The drift-scale submodels boundary conditions for temperature and pressure are interpolated using inverse distance cubed weighting (Section 4.1.5), implemented in the routines *chim\_surf\_TP* and *chim\_wt\_TP*. The input files are *tspa99\_primary\_mesh* and *bcs\_99.dat*, and the output files are *outpt* and *outpt\_wt* (CRWMS M&O 2000a). The additional parameters needed for the LDTH model (air-mass fraction and liquid enthalpy) are computed with *xairtab* (Attachment I).

For the mountain-scale submodel, the routine *bound* (Attachment I) computes the expected temperatures at 1000 m below the water table. This procedure is based upon assuring the same heat flux (driven by the geothermal gradient) above and below the water table. The vertical temperature profiles for ambient conditions, as predicted by the SDT submodels at each of the 31 drift-scale model locations, are used to extrapolate the temperature to a depth of 1000 m below the water table. These calculated temperatures are interpolated on the mountain-scale grid using inverse distance squared weighting implemented in routines *SMT\_surf\_bc* and *SMT\_bot\_bc* (Attachment I) resulting in the lower boundary conditions for the SMT submodel.

## 6.9 SUBMODEL EXECUTION

Several types of NUFT simulation runs are required to produce a single abstracted output dataset. The NUFT submodel-execution procedure is depicted in Figure 3-9 through Figure 3-12. Each submodel type fills a particular set of requirements, as described in Sections 6.1 through 6.5. These varying needs determine the volume of NUFT models to be run for each type of

simulation. The most demanding submodels in terms of number of simulation runs required are the LDTH and SDT submodels. For this reason, these two submodel types have received the greatest attention in automation tools. In general, these submodel types are first created at a single drift-scale-submodel location (Figure 5-2), the submodel is run and refined until the analyst has deemed it ready for production, then the automation components are refined as necessary and the submodel set is generated.

### 6.9.1 LDTH Simulations

The LDTH submodels are run at each of the 31 drift-scale-submodel locations for five AMLs (Section 6.3). In order to be assured of consistency between the data used in these simulations, a set of scripts were developed to generate the required NUFT input files (Attachment I). When one of these scripts is run, it generates a family of 155 NUFT input files, one for each of the five AMLs at each one of 31 locations. A total of nine such scripts were necessary for the LDTH submodels—each of the three infiltration-flux cases requires one script for each of the three stages of LDTH submodel execution: (1) initialization run (to obtain initial ambient conditions), (2) the pre-closure simulation, and (3) the post-closure simulation.

The data developed for boundary conditions and infiltration are embedded directly in the generating scripts as parameter arrays. These arrays contain one value for each drift-scale submodel location, which are transcribed into these scripts from their respective source files (Figure 3-6). The concept of operation of these scripts is that for each output file (*i.e.* generated NUFT input file), various placeholders in a template file (Figure 3-9) are replaced with data relevant to the given scenario. A single value from the data arrays described above, along with filenames containing the other important parameters for the submodel, constitute the information provided to the template by the script.

The LDTH-submodel template files serve the purpose of providing a skeleton NUFT input file for each of the three stages (initialization, pre- and post-closure) of LDTH submodel execution and for each of the five AMLs, resulting in a total of 15 LDTH template files. These files contain the description of the components of the numerical mesh in the x and y dimensions. Since the LDTH model is 2-D, the y-dimensions is only a single layer. On the other hand, the x-dimension is the item in the submodel that determines the drift spacing and thereby determines the effective AML being represented in the submodel.

The NUFT input files generated in this procedure reference mesh files (Section 6.8.1), heat generation files (Section 6.8.3), material property files (Section 6.8.2), run control parameter files, and output time files via the NUFT *include* directive. The run control parameters are chosen to meet efficiency needs in the execution of the NUFT simulations, and the output times are chosen to give the required temporal resolution.

Execution of a single LDTH submodel takes place in three stages, each of them feeding into the next one. These stages are initialization, pre-closure, and post-closure. The initialization stage is a numerical simulation of the unperturbed natural system, which is run out until the numerical simulation of the natural system achieves equilibrium. This provides the starting point for the pre-closure simulation, which simulates a ventilated system. This stage outputs a NUFT restart

file at 50 years (for starting the post-closure simulation), as well as providing data output for MSTHAC (Section 6.6). The post-closure simulation, which starts with the conditions at 50 yr from the pre-closure simulation, is conducted from 50 to 1,000,000 yr.

The NUFT output data files from the pre- and post-closure LDTH simulations are later used as input to MSTHAC (Section 6.6).

### 6.9.2 SDT Simulations

The MSTHAC methodology (Section 6.1 and Section 6.6) requires that the SDT-submodel simulations are conducted at all locations and AMLs as the LDTH submodels. The production of the NUFT input files for the SDT submodels is automated in a similar method as for the LDTH submodels (Section 6.9.1), but the task is simpler, largely due to the lack of hydrologic data in the SDT models. Three SDT generating scripts are required, one for each stage (initialization, pre-closure, and post-closure) of the submodel execution; and only two template files are required, one for the initialization runs, and one covering both the pre- and post-closure simulations. The script files contain the data concerning boundary conditions, as well as the mesh data for the x dimension (which determines the AML).

The initialization run is used to provide the starting vertical temperature profile, not only for the pre-closure and post-closure simulation periods in the SDT submodel, but also for the DDT submodels (Section 6.9.3). The pre- and post-closure simulations are almost identical, except that the heat-generation curves for the pre-closure period is reduced by 70% to simulate ventilation (Figure 3-10).

### 6.9.3 DDT Simulations

The DDT submodel need only be run at a single drift-scale submodel location, as discussed in Section 6.5. The 14c3 location (Figure 5-2) was chosen because it is at the geographic center of the repository area and because the host-rock unit at this location is the tsw35, which is the predominant host-rock unit in the repository; 25 of the 31 drift-scale-submodel locations have tsw35 as the host-rock unit (Table 5-2). As discussed in Section 6.5, it would have been acceptable to have chosen any of the other 31 drift-scale-submodel locations. The MSTHM methodology also only requires DDT-submodel results for a single (*i.e.* the nominal) AML of the repository. To meet the needs for DDT-submodel results, only two sets of NUFT outputs are necessary: one for the pre-closure period, and one for the post-closure period. This greatly simplifies the task of preparing the input files, so that it is feasible to create them without automation tools (Figure 3-11).

The DDT submodel represents a much greater level of detail within the drift than the other submodels. This is the only component of the MSTHM strategy that simulates heat transfer by thermal radiation explicitly. The thermal radiative components are prepared for NUFT with the use of RADPRO, which requires both a numerical mesh and a some additional setup information (provided in the files *DDT60-03v.radin*, *DDT60-03pbf.radin*, and *DDT60-03.radin*). The mesh is read directly from the respective NUFT input file. The additional file contains information of

which combination of surfaces may radiate (to each other), and the emissivity values of the respective surfaces.

The pre-closure DDT submodel (*l4c3-DDT60-03v.in*) has a coarser mesh than that for post-closure DDT submodel (*l4c3-DDT60-03bff.in*). The post-closure DDT submodel (Figure 6-6) is more refined than the pre-closure DDT submodel (Figure 6-4) inside the drift to represent the details of the in-drift geometry of drip-shield and backfill (Figure 5-3). This difference in mesh makes the pre-closure submodel incompatible for producing a restart file for the post-closure DDT submodel, as had been done in the LDTH submodel. Instead, an additional pre-closure submodel (for the purpose of producing a restart file for the post-closure DDT submodel) is required; it is built from the post-closure mesh, but with in-drift materials and heat-generation curves appropriate to the pre-closure period.

#### 6.9.4 SMT Simulations

The overall mountain scale effects of heat flow are simulated with the SMT submodel. This submodel is prepared without the assistance of automation tools, since only two simulations are required (one pre- and one post-closure simulation), which in turn requires only three NUFT input files: initialization, pre-closure, and post-closure (Figure 3-12). The initialization file is used for the generation of initial conditions for use in each of the other simulations, and the pre- and post-closure simulations are run independently of each other, with the only difference being the heat-generation curves, as in the case of the SDT submodels.

The SMT submodel uses the same material properties as the other thermal conduction submodels, except that some additional materials appear in this submodel (in files *SMT-IDds-mi-flt* and *SMT-IDds-mi-sz*), which are not required for the SDT or DDT submodels. The file *SMT-IDds-mi-flt* contains the thermal properties for the fault zones. The fault-zone materials are additional material type appearing in the site-scale UZ flow model mesh (Section 4.1.3), with property assignments derived from Section 4.1.1.20. None of the drift-scale-submodel locations intersected any of the fault zone; therefore the thermal properties for the fault zones were not required in the SDT and DDT submodels. The file *SMT-IDds-mi-sz* contains the thermal properties for the saturated zone (SZ). Because the SDT and DDT submodels have a lower boundary at the water table, they do not include the SZ in their respective model domains; therefore, these submodels do not require the SZ thermal properties. The thermal properties of the pp1 unit (Table 4-4) are assumed for the entire SZ in the SMT (Section 5.2.5).

#### 6.10 MSTHAC EXECUTION

For each of the three infiltration-flux cases (mean, high, and low flux), MSTHAC is executed in a series of steps.

**Step 1: Extract TH data from the all pre-closure submodels.** On the basis of the requested TH data (Table 1-1) and the MSTHAC methodology (Section 6.9), specific variables are extracted from specific locations in each of the pre-closure submodels.

**Step 2: Abstract TH data from the all pre-closure submodels.** Using the TH data that was extracted from the pre-closure submodels (step 1), the MSTHAC methodology (Section 6.9) is applied to abstract the requested TH data (Table 1-1) for the pre-closure period. This results in 600 yr of MSTHM results that corresponds to a scenario with 600 yr of drift ventilation, where the nominal heat-generation rate is reduced by 70%.

**Step 3: Extract TH data from the all post-closure submodels.** On the basis of the requested TH data (Table 1-1) and the MSTHAC methodology (Section 6.9), specific variables are extracted from specific locations in each of the post-closure submodels.

**Step 4: Abstract TH data from the all post-closure submodels.** Using the TH data that was extracted from the post-closure submodels (step 3), the MSTHAC methodology (Section 6.9) is applied to abstract the requested TH data (Table 1-1) for the post-closure period. This results in MSTHM results from 50 to 1,000,000 yr that corresponds to a scenario with 50 yr of drift ventilation, where the nominal heat-generation rate is reduced by 70%, followed by a 50 to 1,000,000 yr period where the full nominal heat-generation rate is used.

**Step 5: Combine the pre-closure and post-closure abstracted TH data.** The abstracted TH results for the pre-closure period (step 3) and the post-closure period (step 4) are spliced together, resulting in the 38 TH variables (Table 1-1) at each of the 623 repository subdomains (Figure 6-1a) for each of the 8 WP locations (Figure 4-1) for 352 timesteps, resulting in 66,665,984 data points for a given infiltration-flux backfill case. For the no-backfill case, the splicing applies to the 38 TH variables at each of the 610 repository subdomains (Figure 6-1b) for each of the 8 WP locations for 99 timesteps, resulting in 18,358,560 data points for a given infiltration-flux case.

**Step 6: Bin the abstracted TH data.** At each of the 623 repository subdomains, a binning procedure is used (Section 6.6.30) to obtain the average CSNF WP and the average HLW WP. This step results in the 38 TH variables (Table 1-1) at each of the 623 repository subdomains (Figure 6-1a) for 2 WP groups (CSNF and HLW) for 352 timesteps, resulting in 16,666,496 data points for a given infiltration-flux backfill case. For the no-backfill case, this step results in 38 TH variables at each of the 610 repository subdomains (Figure 6-1b) for 2 WP groups for 99 timesteps, resulting in 4,589,640 data points for a given infiltration-flux case.

## 6.11 MSTHM RESULTS FOR THE BACKFILL CASE

The MSTHM calculates 38 TH variables for 623 repository subdomains (Figure 6-1a) and eight different WP locations (Figure 4-1) as a function of time for more than 352 calculational timesteps. For each timestep there are  $38 \times 623 \times 8$  different data values, resulting in 189,392 data values. Multiplying by 352 calculational timesteps results in 66 million TH data values for a complete time evolution of a given infiltration flux case. The following subsections provide a comprehensive description of the variables that are of key interest to the evolution of the TH environment in the NF and EBS. This description is provided for the three infiltration-flux cases that were modeled in this AMR: mean, high, and low infiltration flux.

Contour plots are provided on a sufficiently frequent time basis to capture the major trends, as well as the peaks and major transitions, of the spatial and temporal distributions of the major TH variables. This information is provided for a 21-PWR WP (which is the fifth WP from the left in Figure 4-1). This WP location resulted in the highest temperatures with respect to WP-to-WP variability. It should be noted that the repository design analyzed in this report employs several design measures (such as fuel blending and line-load WP spacing) that minimize WP-to-WP variability in temperature. Therefore, the following results should be considered to be fairly typical of temperature distributions in the repository. Section 6.11.6 addresses the influence of WP-to-WP variability that arises from differences in heat-generation rate among WPs. Table 6-4 lists all of the plots of TH conditions that are given in Section 6.11.

In addition to the contour plots of TH conditions, history plots of TH conditions are also provided for several repository locations, including a location at the geographical center of the repository and a location that is relatively close to the eastern edge of the repository.

### **6.11.1 Temperature Distributions**

Contour plots of temperature are provided for (1) the WP surface, (2) the upper drift wall (or crown of the drift), and (3) the lower drift wall (below the bottom of the invert). Contour plots of peak WP temperature and peak temperature of the lower drift wall are also provided.

#### **6.11.1.1 Temperature Distributions for Mean Infiltration Case**

The temperature evolution on WPs and on the upper and lower drift wall is summarized for the entire 1,000,000-yr simulation period in Figure 6-7, Figure 6-8, and Figure 6-9 for the mean infiltration-flux case. For the pre-closure period, peak temperatures on WPs occur around 15 yr (Figure 6-7b). For the post-closure period, peak WP temperatures occur around 60 yr, with nearly half of the 21-PWR WPs exceeding 300°C. Edge-cooling effects have a minor affect on temperatures during the pre-closure; therefore, the temperature distribution is fairly uniform throughout the repository. During the post-closure period, edge-cooling effects are seen to significantly affect the repository-scale temperature distribution. For example, at 100 yr there is a 120°C difference in WP temperature between the center and edge of the repository (Figure 6-7e).

There is a large temperature difference between the upper and lower drift wall, particularly at early time (compare Figure 6-8d with Figure 6-9d). Boiling persists considerably longer on the lower drift wall than on the upper drift wall (compare Figure 6-8h and Figure 6-8i with Figure 6-9h and Figure 6-9i).

Table 6-4. List of plots of TH conditions for the backfill case

Figure Number	TH Variable	Source DTN	Source File Name
Figure 6-7	WP temperature	LL000114004242.090	TSPA_SR_mean.ext
Figure 6-8	Upper drift-wall temperature	LL000114004242.090	TSPA_SR_mean.ext
Figure 6-9	Lower drift-wall temperature	LL000114004242.090	TSPA_SR_mean.ext
Figure 6-10	WP temperature	LL000114104242.091	TSPA_SR_upper.ext
Figure 6-11	WP temperature	LL000113904242.089	TSPA_SR_lower.ext
Figure 6-12	Maximum lateral extent of boiling isotherm	LL000114004242.090 LL000114104242.091 LL000113904242.089	TSPA_SR_mean.ext TSPA_SR_upper.ext TSPA_SR_lower.ext
Figure 6-13	Temperatures in EBS	LL000114004242.090	TSPA_SR_mean.ext
Figure 6-14	Peak WP temperature	LL000114004242.090 LL000114104242.091 LL000113904242.089	TSPA_SR_mean.ext TSPA_SR_upper.ext TSPA_SR_lower.ext
Figure 6-15	Peak lower drift-wall temperature	LL000114004242.090 LL000114104242.091 LL000113904242.089	TSPA_SR_mean.ext TSPA_SR_upper.ext TSPA_SR_lower.ext
Figure 6-16	WP relative humidity	LL000114004242.090	TSPA_SR_mean.ext
Figure 6-17	WP relative humidity	LL000114104242.091	TSPA_SR_upper.ext
Figure 6-18	WP relative humidity	LL000113904242.089	TSPA_SR_lower.ext
Figure 6-19	WP relative humidity and temperature	LL000114004242.090 LL000114104242.091 LL000113904242.089	TSPA_SR_mean.ext TSPA_SR_upper.ext TSPA_SR_lower.ext
Figure 6-20	Relative humidity in EBS	LL000114004242.090	TSPA_SR_mean.ext
Figure 6-21	Relative humidity in EBS	LL000114104242.091	TSPA_SR_upper.ext
Figure 6-22	Relative humidity in EBS	LL000113904242.089	TSPA_SR_lower.ext
Figure 6-23	Gas-phase air-mass on drip shield	LL000114004242.090	TSPA_SR_mean.ext
Figure 6-24	Gas-phase air-mass on drip shield	LL000114104242.091	TSPA_SR_upper.ext
Figure 6-25	Gas-phase air-mass on drip shield	LL000113904242.089	TSPA_SR_lower.ext
Figure 6-26	Liquid-phase flux 5 m above drift	LL000114004242.090	TSPA_SR_mean.ext
Figure 6-27	Liquid-phase flux 0.2 m above drift	LL000114004242.090	TSPA_SR_mean.ext
Figure 6-28	Liquid-phase flux above drip shield	LL000114004242.090	TSPA_SR_mean.ext
Figure 6-29	Liquid-phase flux next to lower drip shield	LL000114004242.090	TSPA_SR_mean.ext
Figure 6-30	Liquid-phase flux in invert	LL000114004242.090	TSPA_SR_mean.ext
Figure 6-31	Liquid-phase flux 5 m above drift	LL000114104242.091	TSPA_SR_upper.ext
Figure 6-32	Liquid-phase flux 0.2 m above drift	LL000114104242.091	TSPA_SR_upper.ext
Figure 6-33	Liquid-phase flux above drip shield	LL000114104242.091	TSPA_SR_upper.ext
Figure 6-34	Liquid-phase flux next to lower drip shield	LL000114104242.091	TSPA_SR_upper.ext
Figure 6-35	Liquid-phase flux in invert	LL000114104242.091	TSPA_SR_upper.ext
Figure 6-36	Liquid-phase flux 5 m above drift	LL000113904242.089	TSPA_SR_lower.ext
Figure 6-37	Liquid-phase flux 0.2 m above drift	LL000113904242.089	TSPA_SR_lower.ext
Figure 6-38	Liquid-phase flux above drip shield	LL000113904242.089	TSPA_SR_lower.ext
Figure 6-39	Liquid-phase flux next to lower drip shield	LL000113904242.089	TSPA_SR_lower.ext
Figure 6-40	Liquid-phase flux in invert	LL000113904242.089	TSPA_SR_lower.ext
Figure 6-41	Liquid-phase flux in NFE& EBS	LL000114004242.090	TSPA_SR_mean.ext
Figure 6-42	Evaporation rate on upper drip shield	LL000114004242.090	TSPA_SR_mean.ext
Figure 6-43	Evaporation rate on upper drip shield	LL000114104242.091	TSPA_SR_upper.ext
Figure 6-44	Evaporation rate on upper drip shield	LL000113904242.089	TSPA_SR_lower.ext

Figure Number	TH Variable	Source DTN	Source File Name
Figure 6-45	Evaporation rate & gas-phase air-mass fraction on drip shield	LL000114004242.090	TSPA_SR_mean.ext
Figure 6-46	WP temperature and relative humidity	LL000114004242.090	TSPA_SR_mean.ext

### 6.11.1.2 Temperature Distributions for High Infiltration Case

The temperature evolution on WPs is summarized for the entire 1,000,000-yr simulation period in Figure 6-10 for the high infiltration-flux case. The magnitude of infiltration flux has a small effect on WP temperatures during the pre-closure period (compare Figure 6-10a, Figure 6-10b, and Figure 6-10c with Figure 6-7a, Figure 6-7b, and Figure 6-7c). During the early post-closure period, the enhanced cooling effect of the higher infiltration flux is small (compare Figure 6-10d with Figure 6-7d). At the end of the boiling period, the enhanced cooling effect of the higher infiltration flux is also small (compare Figure 6-10k with Figure 6-7k).

### 6.11.1.3 Temperature Distributions for Low Infiltration Case

The temperature evolution on WPs is summarized for the entire 1,000,000 yr simulation period in Figure 6-11 for the low infiltration-flux case. During the pre-closure period, the low infiltration-flux case is noticeably hotter than the mean infiltration-flux case (compare Figure 6-11 with Figure 6-7b). During the early post-closure period, the low infiltration-flux case is slightly hotter (with the region of hotter WPs also being more extensive) than in the mean-flux case (compare Figure 6-11d and Figure 6-11e with Figure 6-7e and Figure 6-7f). The duration of boiling for the low infiltration-flux case is longer than for the mean-flux case (compare Figure 6-11i with 6-7l).

### 6.11.1.4 Temperature Analysis

The maximum lateral extent of boiling (away from the drift wall) is a good indication of spatial extent of rock dryout around the emplacement drifts. The spatial extent of dryout decreases with increasing infiltration (or percolation) flux. The lateral extent of boiling is considerably greater for the low infiltration-flux case than for the mean or high infiltration-flux cases (Figure 6-12). For the median WP location, the maximum lateral extent of boiling is 8.4 m, 9.1 m, and 10.5 m for the high, mean, and low infiltration-flux cases, respectively. For the 90th percentile WP location, the maximum lateral extent of boiling is 9.1 m, 9.6 m, and 14.6 m for the high, mean, and low infiltration-flux cases, respectively. The hottest (and driest) WP location in the low infiltration-flux case has a maximum lateral extent of boiling of 18 m; therefore, because the drifts are 81 m apart (Figure 4-1), a maximum of 44.4% of the repository horizon is driven to the boiling point. The hottest (and driest) WP location in the mean infiltration-flux case has a maximum lateral extent of boiling of 9.7 m; therefore, a maximum of 24% of the repository horizon is driven to the boiling point. The hottest (and driest) WP location in the high infiltration-flux case has a maximum lateral extent of boiling of 9.7 m (which is the same as that for the mean-flux case). For the range of infiltration flux considered in this AMR, the maximum percentage of the repository horizon that can be driven to the boiling point lies between 24% and 44.4%.

Summarizing, there is much less difference in lateral boiling extent between the mean and high infiltration-flux cases than between the mean and low-flux cases; this observation is particularly true for the hottest (and driest) WP location. Therefore, if one considers defining a percolation-flux threshold wherein rock dryout becomes significantly limited by percolation, then this percolation-flux threshold would appear to be close to that arising from the mean infiltration-flux case. Increasing percolation fluxes above those of the mean infiltration-flux case has a diminishing effect on decreasing the extent of boiling (and rock dryout).

The time-varying influence of edge cooling is illustrated by Figure 6-13, which gives the temperature history at various locations in the EBS at the center and edge of the repository. The edge-cooling effect has a small influence on peak temperatures. However, by 100 yr, the influence of edge cooling is considerable. The large differences in WP temperature at 100 yr, with temperatures decreasing strongly with proximity to the edge (Figure 6-7d, Figure 6-10e, and Figure 6-11e), indicates a promising heat-management option for a repository with an extended ventilation period (e.g., 100 yr). Because the influence of edge-cooling has penetrated significantly (100 to 200 m) in from the edge by 100 yr, it would be possible to emplace the hottest WPs in this edge region without incurring very high peak temperatures. The cooler WPs would be emplaced in the central repository region that does not experience edge-cooling effects.

The large temperature difference between the upper and lower drift wall is very apparent in Figure 6-13. This large temperature difference arises from the drip-shield and backfill configuration in the emplacement drift (Figure 6-13). Because Overton sand backfill (Table 4-1) has a very low thermal conductivity (0.33 W/m-K), it is a very effective thermal insulator. Because much more of this insulation lies above the WP than below the WP, this focuses much of the decay heat generation from the WPs into the floor of the drift. To reduce the large difference between the upper and lower drift-wall temperatures, it would be necessary to balance the insulation above and below the WP. This balancing requires reducing the amount of backfill above the WP and increasing the thickness of the invert below the WP. Placing insulation between the WP and invert would serve to further balance the distribution of insulation in the drift.

The influence of the low thermal conductivity (0.33 W/m-K) of the Overton sand backfill (Table 4-1) is seen as a persistent temperature difference between the drip shield and drift wall (Figure 6-13). This temperature difference is independent of proximity to the edge of the repository. The temperature difference between the drip shield and WP is small because it is governed by thermal radiation, which is a very efficient means of heat transfer.

The influence of infiltration (or percolation) flux on peak WP and drift-wall temperatures is shown in Figure 6-14 and Figure 6-15, respectively. There is a relatively small difference (about 5°C) in peak WP between the mean and high infiltration-flux cases. There is a similar small difference in peak drift-wall temperature between these two cases. There is a slightly larger difference (of about 10°C) in peak WP temperature between the mean and low infiltration-flux cases. There is a similar difference in peak drift-wall temperature between these two cases.

The sensitivity of the WP and drift-wall temperatures on the thermal conductivity of the host rock is readily apparent in Figure 6-14 and Figure 6-15. The wet and dry thermal conductivity  $K_{th}$

values (Table 4-4) of the tsw34 unit (2.33 and 1.56 W/m-K, respectively) are considerably greater than in the tsw35 unit (2.02 and 1.2 W/m-K, respectively). With the exception of the central-eastern portion of the repository, the repository host rock is comprised of the tsw35 unit. The central-eastern portion is comprised of the tsw34 unit (Figure 5-2; Table 5-2). Using the 31 drift-scale-submodel locations (Figure 5-2; Table 5-2) as an indicator of the local host-rock unit, 26 of these locations have tsw35 as the host-rock unit and 5 of these locations have tsw34 as the host-rock unit: 11c3, 11c4, 11c5, 11c6, and 12c4. The five drift-scale-submodel locations wherein tsw34 is the host-rock unit correspond to the region of the repository with the lowest peak WP temperatures (Figure 6-15) and the lower peak drift-wall temperatures (Figure 6-15). This trend is the same for all three infiltration-flux cases. Thus, WP and drift-wall temperatures decrease with increasing  $K_{th}$  of the local host-rock unit.

### 6.11.2 Relative Humidity Distributions

Contour plots of relative humidity on the WP surface,  $RH_{wp}$ , are given for the mean, high, and low infiltration-flux cases. For the mean and high infiltration-flux cases it is only necessary to show the contour plots for the first 10,000 yr to show the complete evolution of  $RH_{wp}$ , while for the low infiltration-flux case it is necessary to show 100,000 yr. The difference in time required for the low infiltration-flux case to attain humid ambient conditions arises from the delayed onset of seepage into the drifts (relative to the mean and high-flux cases). The onset of seepage into the drifts (discussed in Section 6.11.4) is a critically important process governing how long it takes the backfill to attain humid ambient conditions.

#### 6.11.2.1 Relative Humidity Distributions for Mean Infiltration Case

The evolution of relative humidity on WPs,  $RH_{wp}$ , is summarized for 10,000 yr in Figure 6-16 for the mean infiltration-flux case. Within 10,000 yr,  $RH_{wp}$  has attained ambient humid conditions for the mean infiltration-flux case. At the end of the pre-closure period  $RH_{wp}$  has climbed up to 70 to 80% (Figure 6-16a). Immediately after backfill is emplaced the WP temperature abruptly climbs, which drastically reduces  $RH_{wp}$ . This effect occurs uniformly throughout the repository area (Figure 6-16b). The influence of edge-cooling on reducing rock dryout and  $RH$  reduction starts to become noticeable after 100 yr (Figure 6-16d, Figure 6-16e, and Figure 6-16f). The influence of the monsoonal climate and regions of higher infiltration flux (Figure 6-47) is seen after 600 yr, as the higher percolation flux begins to seep into the drift, causing more humid conditions (Figure 6-16h) inside the drifts. Regions of lower infiltration flux are seen as regions where  $RH_{wp}$  reduction is more persistent (Figure 6-16m through Figure 6-16x).

#### 6.11.2.2 Relative Humidity Distributions for High Infiltration Case

The evolution of relative humidity on WPs,  $RH_{wp}$ , is summarized for 10,000 yr in Figure 6-17 for the mean infiltration-flux case. During the pre-closure period, the difference between the high and the mean infiltration-flux case on  $RH_{wp}$  is small (compare Figure 6-17a with Figure 6-16a). During the early post-closure period  $RH_{wp}$  for the high infiltration-flux case is similar to that of the mean-flux case (compare Figure 6-17c and Figure 6-17d with Figure 6-16c and Figure 6-16d). At later time periods (particularly after 600 yr when the monsoonal climate begins),  $RH_{wp}$  in the high infiltration-flux case is slightly more humid than in the mean-flux case

(compare Figure 6-17h with Figure 6-16h). The more humid conditions arise due to the greater seepage flux into the drift for the high infiltration-flux case.

### 6.11.2.3 Relative Humidity Distributions for Low Infiltration Case

The evolution of relative humidity on WPs,  $RH_{wp}$ , is summarized for 100,000 yr in Figure 6-18 for the low infiltration-flux case. With a lower infiltration flux, rock dryout is more persistent and the onset of seepage into the drifts is delayed (relative to the higher flux cases), which delays rewetting the backfill to humid ambient conditions. For the preclosure period,  $RH_{wp}$  for the low infiltration-flux case is considerably drier than for the mean and high-flux cases (compare Figure 6-18a with Figure 6-16a and Figure 6-17a). For the postclosure period,  $RH_{wp}$  for the low infiltration flux is considerably drier (particularly after 600 yr when the monsoonal climate begins) than for the mean and high-flux cases (compare Figure 6-18i with Figure 6-16i and Figure 6-17i). After the glacial climate begins (at 2000 yr),  $RH_{wp}$  for the low infiltration-flux case continues to be considerably drier than it is for the mean and high-flux cases (compare Figure 6-18o with Figure 6-16o and Figure 6-17o).

### 6.11.2.4 Relative Humidity Analysis

Two important performance measures for the EBS are summarized in Figure 6-19. The first important performance measure is how long it takes WP to attain humid conditions. The distribution  $RH$ -reduction performance on WPs throughout the repository area is succinctly described with the complementary cumulative distribution function (CCDF) of the time required for WPs to attain an  $RH$  of 85% (Figure 6-19a). The second important performance measure is how hot the WP is once humid conditions are attained. Figure 6-19b is the CCDF of the WP temperature at which  $RH_{wp} = 85\%$  is attained. The CCDF curves in Figure 6-19a show that the mean and high infiltration-flux cases result in similar  $RH$ -reduction performance on WPs. This similarity is also indicated by the comparison of the  $RH_{wp}$  contours, which was discussed in Section 6.11.2.2. The CCDF curves in Figure 6-19a also clearly show that the low infiltration-flux case results in a much more persistent reduction in  $RH$  on WPs than the mean and high-flux cases. The mean and high infiltration-flux cases also result in similar WP temperatures once an  $RH$  of 85% is attained on the WPs (Figure 6-19b), whereas the low-flux case results in much lower WP temperatures at the time at which  $RH_{wp} = 85\%$  is attained.

Relative humidity histories on the drift wall, drip shield, and WP are given for locations at the center and edge of the repository for the mean, high, and low infiltration-flux cases in Figure 6-20, Figure 6-21, and Figure 6-22, respectively. Several important observations can be made, including:

**$RH$  reduction at the drift wall** (and in the host rock) decreases strongly with proximity to the edge of the repository. Significant reduction in  $RH_{dw}$  persists for about 100 to 1000 yr (depending on proximity to the repository edge) for the mean and high infiltration-flux cases and for about 200 to 2000 yr for the low infiltration-flux case.

**$RH$  reduction on the drip shield** is relatively insensitive to proximity to the edge of the repository. Eventually,  $RH$  on the drip shield becomes nearly 100%. For the mean and high

infiltration-flux cases this takes about 1000 to 2000 yr and for the low infiltration-flux case about 3000 to 6000 yr to occur. The end of the period of *RH* reduction on the drip shield corresponds to the time that the seepage into the backfill has reached a steady-state condition, essentially reaching a terminal state with respect to moisture content in the backfill.

***RH* reduction on the WP** persists long after *RH* reduction on the drip shield has ceased. The persistence of *RH* reduction between the drip shield and WP arises because of the temperature difference between the WP and drip shield. Because the interval between the WP and drip shield is an open cavity, thermal radiation controls this temperature difference. The use of an insulator (such as granular backfill) in the gap between the WP and drip shield would result in a much larger temperature difference, which would result in a much larger reduction in *RH* between the drip shield and WP.

### 6.11.3 Gas-Phase Air-Mass Fraction Distributions

Contour plots of gas-phase air-mass fraction on the drip-shield surface,  $X_{\text{air,gas,ds}}$ , are given for the mean, high, and low infiltration-flux cases for 20,000 yr; contours are given for this duration because it takes about 20,000 yr for  $X_{\text{air,gas,ds}}$  to return to ambient values.

#### 6.11.3.1 Gas-Phase Air-Mass Fraction Distributions for Mean Infiltration Case

The evolution of gas-phase air-mass fraction on the drip-shield surface,  $X_{\text{air,gas,ds}}$ , is summarized for 20,000 yr in Figure 6-23 for the mean infiltration-flux case. The value of  $X_{\text{air,gas,ds}}$  declines during the period of temperature increase as water vapor displaces air from the drifts and the rock adjacent to the drifts. Boiling conditions are required to drive a significant reduction in  $X_{\text{air,gas,ds}}$ . During the pre-closure period, the drift wall stays below the boiling point. As a consequence,  $X_{\text{air,gas,ds}}$  is not significantly reduced. During the post-closure period, after ventilation has ceased and the backfill emplaced, temperatures in the drift abruptly rise to well above the boiling point, thereby driving air away from the drifts. Consequently, during the early post-closure period, values of  $X_{\text{air,gas,ds}}$  become very small (Figure 6-23a). As water vapor displaces air from the drifts (by advection), binary diffusion of air and water vapor causes air to return to the drifts. The value of  $X_{\text{air,gas,ds}}$  reaches its minimum value about the same time that the peak WP and drip-shield temperatures are attained. As the drip-shield temperature then declines, the value of  $X_{\text{air,gas,ds}}$  gradually increases. Because temperatures decline more quickly at the edge of the repository (as a result of the edge-cooling effect),  $X_{\text{air,gas,ds}}$  increases more quickly at the repository edge (Figure 6-23b and Figure 6-23c) and the rate of increase of  $X_{\text{air,gas,ds}}$  increases with proximity to the edge of the repository. In general, the shape of the  $X$  contours are similar to the contours of WP temperature (for example, compare Figure 6-23g with Figure 6-7j).

#### 6.11.3.2 Gas-Phase Air-Mass Fraction Distributions for High Infiltration Case

The evolution of gas-phase air-mass fraction on the drip-shield surface,  $X_{\text{air,gas,ds}}$ , is summarized for 20,000 yr in Figure 6-24 for the high infiltration-flux case. Spatial and temporal evolution of  $X_{\text{air,gas,ds}}$  for the high and mean infiltration-flux cases are similar; however, the lower temperatures in the high infiltration-flux case result in slightly higher values of  $X_{\text{air,gas,ds}}$  than in the mean-flux case (for example, compare Figure 6-24f with Figure 6-23f).

### 6.11.3.3 Gas-Phase Air-Mass Fraction Distributions for Low Infiltration Case

The evolution of gas-phase air-mass fraction on the drip-shield surface  $X_{\text{air,gas,ds}}$  is summarized for 20,000 yr in Figure 6-25 for the low infiltration-flux case. The overall spatial and temporal evolution of  $X_{\text{air,gas,ds}}$  for the low infiltration-flux case is similar to that of the mean and high-flux case; however, values of  $X_{\text{air,gas,ds}}$  for the low infiltration-flux case are not as low as in the mean and high-flux cases (for example, compare Figure 6-25d with Figure 6-23d and Figure 6-24d). A secondary factor influencing  $X_{\text{air,gas,ds}}$  is the local percolation flux with  $X_{\text{air,gas,ds}}$  increasing slightly with decreasing percolation flux. Areas of lower percolation flux have less water returning to the boiling front; consequently the rate of water vapor generation in the immediate vicinity of the drifts is less than it is in areas where the local percolation flux is higher. In the mean and high infiltration-flux cases, the large return flux of water back to the boiling front causes the refluxing zone to remain closer to the drifts than in the low-flux case, which results in a larger vapor generation flux (close to the drifts) to drive air away from the drifts.

As the end of the boiling period is approached, the distribution of  $X_{\text{air,gas,ds}}$  for the low, mean, and high infiltration-flux cases become very similar (compare Figure 6-25g, Figure 6-23g, and Figure 6-24g). After boiling has ceased,  $X_{\text{air,gas,ds}}$  for the low infiltration-case is less than in the mean or high-flux cases (for example, compare Figure 6-25i with Figure 6-23i and Figure 6-24i).

### 6.11.3.4 Gas-Phase Air-Mass Fraction Analysis

The analysis of the factors affecting gas-phase air-mass fraction are discussed in Sections 6.11.3.1 through 6.11.3.3

## 6.11.4 Liquid-Phase Flux Distributions

The spatial and temporal evolution of liquid-phase flux in the NFE and EBS is strongly affected by decay heat from WPs. To illustrate this influence, liquid-phase flux contours are provided for five locations in the NFE and EBS: (1) 5 m above the crown of the drift, (2) 0.2 m above the crown of the drift, (3) in the sand backfill, averaged along the top of the drip shield, (4) in the sand backfill, adjacent to the lower side of the drip shield, and (5) in the crushed-tuff invert, averaged over the invert. In the host rock, this liquid-phase flux pertains to flux in the fractures; flux in the matrix (which is smaller) is not included. In the sand backfill and crushed-tuff invert, the liquid-phase flux in the following plots pertains to the total flux.

### 6.11.4.1 Liquid-Phase Flux Distributions for Mean Infiltration Case

The evolution of liquid-phase flux (in fractures) 5 m above the crown of the drift,  $q_{\text{liq},5\text{m}}$ , is summarized in Figure 6-26 for the mean infiltration-flux case. During the pre-closure period, because the host rock remains below the boiling point,  $q_{\text{liq},5\text{m}}$  is largely unaffected by decay heat. A comparison of Figure 6-26a and Figure 6-47a (which is the mean infiltration-flux contour map for present-day-climate conditions) shows the similarity between  $q_{\text{liq},5\text{m}}$  and the ambient infiltration flux.; note that the differences between these two plots arise from Figure 6-47 pertaining to the total (fracture + matrix) flux, while Figure 6-26 pertains only to flux in the fractures. Five years into the post-closure period (Figure 6-26b) decay heat has already noticeably

increased  $q_{\text{liq},5\text{m}}$ . The increase in  $q_{\text{liq},5\text{m}}$  arises from heat-driven condensate flow; which occurs in the refluxing zone (also called the heat-pipe zone), just beyond where dryout is occurring. Thirty years into the post-closure period (Figure 6-26d) the heart of the heat-pipe zone has reached at least 5 m above the drift. At earlier times (Figure 6-26b and Figure 6-26c), the heart of the heat-pipe zone is less than 5 m above the drift. At later times (Figure 6-26e and Figure 6-26f),  $q_{\text{liq},5\text{m}}$  is decreasing because it is proportional to the heat flux (from WPs), which is decaying with time. The decrease in  $q_{\text{liq},5\text{m}}$  continues through the present-day-climate period (which lasts 600 yr). At 500 yr,  $q_{\text{liq},5\text{m}}$  is comparable to the infiltration flux (compare Figure 6-26i to Figure 6-47a). Therefore, by 500 yr the influence of decay heat on  $q_{\text{liq},5\text{m}}$  has become small.

After the start of the monsoonal climate period  $q_{\text{liq},5\text{m}}$  increases to where it is comparable to the monsoonal-climate infiltration flux (compare Figure 6-26j with Figure 6-47b). Thus, the transition to steady-state percolation-flux conditions, controlled by the monsoonal-climate infiltration flux, occurs relatively quickly (compare Figure 6-26j, Figure 6-26k, and Figure 6-26l). Similarly, the transition to steady-state percolation-flux conditions, controlled by the glacial-climate infiltration flux, also progresses relatively quickly (compare Figure 6-26l, Figure 6-26m, Figure 6-26n, and Figure 6-26o).

The evolution of liquid-phase flux (in fractures) 0.2 m above the crown of the drift,  $q_{\text{liq},\text{cr}}$  (where “cr” stands for crown), is summarized in Figure 6-27 for the mean infiltration-flux case. During the pre-closure period when the host rock remains below the boiling point  $q_{\text{liq},\text{cr}}$  is largely unaffected by decay heat. After ventilation ceases, temperatures in the host rock abruptly rise above the boiling point, generating a heat-pipe zone immediately above the drift, which is manifested by very high values of  $q_{\text{liq},\text{cr}}$  (Figure 6-27a and Figure 6-27b). Five years into the post-closure period (Figure 6-27d) the heart of the heat-pipe zone no longer resides 0.2 m above the crown. Rather, it has moved at least 5 m above the drift (as indicated in Figure 6-26b). For most of the repository area, the value of  $q_{\text{liq},\text{cr}}$  is zero for the period from 55 to 200 yr. The exception being areas where the local ambient percolation flux is high enough to overwhelm the local heat flux from WPs (Figure 6-27e and Figure 6-27f). As the end of the present-day-climate period is approached, about half of the repository area has a nonzero value of  $q_{\text{liq},\text{cr}}$  (Figure 6-27g).

After the start of the monsoonal climate period,  $q_{\text{liq},\text{cr}}$  increases to where it is comparable to the monsoonal-climate infiltration flux (compare Figure 6-27h with Figure 6-47b). Thus, the transition to steady-state monsoonal-climate percolation-flux conditions (i.e., controlled by the monsoonal-climate infiltration flux) occurs relatively quickly (compare Figure 6-27h and Figure 6-27i). Similarly, the transition to steady-state glacial-climate percolation-flux conditions (i.e., controlled by the glacial-climate infiltration flux) also progresses quickly (compare Figure 6-27i, Figure 6-27j, Figure 6-27k, and Figure 6-27l).

The evolution of liquid-phase flux averaged over the upper surface of the drip shield,  $q_{\text{liq},\text{uds}}$ , (“uds” stands for upper drip shield), is summarized in Figure 6-28 for the mean infiltration-flux case. During the first 150 yr of the post-closure period,  $q_{\text{liq},\text{uds}}$  is zero everywhere in the repository. At 215 yr (Figure 6-28a) the first nonzero occurrence of  $q_{\text{liq},\text{uds}}$  is seen in a region of high ambient infiltration (and percolation) flux. The region of nonzero  $q_{\text{liq},\text{uds}}$  spreads (Figure 6-28b through Figure 6-28g), starting in the regions of highest infiltration flux, until it occupies all but the regions of low infiltration flux.

During the early part of the pre-closure period the backfill is dry. As the temperature at the drift wall declines below the boiling point, water is able to wick (by capillary flow) from the fractures into the Overton sand backfill. This wicking is facilitated by the van Genuchten  $\alpha$  value for Overton sand (Table 4-1:  $\alpha = 2.75 \times 10^{-4} \text{ Pa}^{-1}$ ) being smaller than that of the fractures in the host-rock units (Table 4-3: tsw34:  $\alpha = 5.16 \times 10^{-4} \text{ Pa}^{-1}$ ; tsw35:  $\alpha = 7.39 \times 10^{-4} \text{ Pa}^{-1}$ ; tsw36 and tsw37:  $\alpha = 7.84 \times 10^{-4} \text{ Pa}^{-1}$ ). Had a coarser, well-sorted sand been used as backfill, with a value of  $\alpha$  larger than that of the fractures in the host-rock units, then this wicking would not have taken place. The wicking flux that enters the drift is actually greater than the percolation flux in the overlying host rock because capillary suction (driven by the high capillarity of the Overton sand) augments the influence of gravity-driven fracture flow; this augmented flow “captures” flow in fractures that would have otherwise drained around the drift. Wicking into the drift occurs at the point that backfill contacts the drift wall, which occurs 1 m above the springline (Figure 4-2) down to the interface with the invert.

The magnitude of  $q_{\text{liq,uds}}$  is much larger than the ambient percolation flux because it arises from heat-driven condensate flow in the heat-pipe zone in the backfill above the drip shield. Just as the magnitude of liquid-phase flux in the heat-pipe zone in the host-rock above the drift can greatly exceed the background percolation flux, the magnitude of liquid-phase flux in the heat-pipe zone in the backfill can greatly exceed the seepage flux entering the drift. The large temperature gradient in the backfill facilitates a large vapor flux away from the drip shield, while the high capillarity of the Overton sand facilitates a large liquid-phase flux of water returning to the drip shield; when these gas-phase liquid-phase fluxes are equal, a heat pipe is established. As discussed in Section 6.11.5, this capillary-driven heat-pipe system in the Overton-sand backfill results in a very large evaporative flux on the surface of the drip shield.

Because it arises largely from heat-driven condensate flow, the value of  $q_{\text{liq,uds}}$  declines along with the decaying heat-generation rate from WPs. Thus, the value of  $q_{\text{liq,uds}}$  declines by more than a factor of two during the 1500-to-3000 yr time interval (Figure 6-28i and Figure 6-28j). This decrease occurred in spite of the fact that the transition from the monsoonal to glacial climate occurred over this time interval. Had the value of  $q_{\text{liq,uds}}$  been controlled by percolation flux, rather than by heat-pipe conditions, then the value of  $q_{\text{liq,uds}}$  should have increased significantly (rather than have decreased) during the 1500-to-3000 yr time interval. By 10,000 yr the value of  $q_{\text{liq,uds}}$  is much smaller than the background percolation flux (compare Figure 6-28k with Figure 6-26n and Figure 6-27k). As discussed below, the value of  $q_{\text{liq,uds}}$  is also much smaller than the liquid-phase flux at other locations in the drift. At 1,000,000 yr, the contrast between the value of  $q_{\text{liq,uds}}$  and liquid-phase flux at other locations in the host rock and drift is even greater (compare Figure 6-28l with Figure 6-26o and Figure 6-27l).

The evolution of liquid-phase flux adjacent to the lower side of the drip shield,  $q_{\text{liq,lds}}$  (“lds” stands for lower drip shield), is summarized in Figure 6-29 for the mean infiltration-flux case. During the first 425 yr of the post-closure period,  $q_{\text{liq,lds}}$  is zero everywhere in the repository. At 500 yr (Figure 6-29a) the first nonzero occurrence of  $q_{\text{liq,lds}}$  is seen in a region of high ambient infiltration (and percolation) flux. The region of nonzero  $q_{\text{liq,lds}}$  spreads (Figure 6-29b through Figure 6-29i), starting in the regions of highest infiltration flux, until it occupies all but the regions of low infiltration flux. The transition to a steady-state monsoonal-climate seepage-flux

condition occurs relatively quickly (compare Figure 6-29c and Figure 6-29d). The transition to a steady-state glacial-climate seepage-flux condition also occurs relatively quickly (compare Figure 6-29f through Figure 6-29i). Whereas the liquid-phase flux above the drip shield  $q_{\text{liq,uds}}$  declines to a very small value, the liquid-phase flux adjacent to the lower side of the drip shield  $q_{\text{liq,lds}}$  remains large.

The contour plot of  $q_{\text{liq,lds}}$  during the monsoonal climate (Figure 6-29f) is qualitatively the same as that of the monsoonal-climate infiltration flux (Figure 6-47b), with differences arising from how the geometry of the EBS results in flow focussing in the drift. The contour plot of  $q_{\text{liq,lds}}$  during the glacial climate (Figure 6-29h and Figure 6-29i) is also qualitatively similar to that of the glacial-climate infiltration flux (Figure 6-47c) and the contour map of  $q_{\text{liq,5m}}$  (Figure 6-26n and Figure 6-26o). However, the values of  $q_{\text{liq,lds}}$  are about four to five times larger than  $q_{\text{liq,5m}}$  in the host rock. Figure 4-2 and Figure 6-3 illustrate that the width of the backfill adjacent to the lower side of the drip shield becomes very narrow just above the interface with the invert. In the LDTH submodel, the backfill adjacent to the lower side of the drip shield is only 0.6907 m wide (Figure 6-3). If all of the water trying to shed around the drift were wicked into the drift, then this capillary-driven seepage flux into the drift would be contributed by the percolation flux in a region that is at least 2.75 m wide (which corresponds to the half-width of the drift). Because the value of the van Genuchten  $\alpha$  in the Overton sand backfill is smaller than in the fractures of the host rock, water draining down the side of the drip shield does not want to leave the backfill and enter the fractures in the host rock. Instead, all the water drains into the invert. If all of the percolation flux over a 2.75 m wide zone were focussed into the 0.6907 m wide zone next to the drip shield, this would result in a “focussing” factor of four, which is comparable to the ratio (of four to five) which is observed between  $q_{\text{liq,lds}}$  and  $q_{\text{liq,5m}}$  in the host rock. As observed earlier, because capillary suction augments gravity drainage into the drift, the source of seepage into the drift is actually contributed by percolation flux occurring over a region that is somewhat wider than 2.75 m.

The evolution of liquid-phase flux averaged across the invert,  $q_{\text{liq,inv}}$ , (“inv” stands for invert), is summarized in Figure 6-30 for the mean infiltration-flux case. During the first 200 yr of the post-closure period,  $q_{\text{liq,inv}}$  is zero everywhere in the repository. At 254 yr (Figure 6-30a) the first nonzero occurrence of  $q_{\text{liq,lds}}$  is seen in a region of high ambient infiltration (and percolation) flux. Initially, the values of  $q_{\text{liq,inv}}$  are negative, indicating that water is being wicked (by capillarity) vertically upward from below the drift. The region of nonzero  $q_{\text{liq,inv}}$  spreads (Figure 6-30b through Figure 6-30l), starting in the regions of highest infiltration (and percolation) flux, until it occupies all but the regions of low infiltration (and percolation) flux. As nonzero values of liquid-phase flux at the lower side of the drip shield  $q_{\text{liq,lds}}$  begin to occur, which causes water to drain from the Overton sand backfill into the invert, the direction of flow in the invert is forced to reverse, so that it is now flowing vertically downward, driven by gravity rather than by capillarity (Figure 6-30d through Figure 6-30f).

During the present-day and monsoonal climates, regions of negative  $q_{\text{liq,inv}}$  persist (Figure 6-30a through Figure 6-30f). Shortly after the glacial climate begins, all regions of negative  $q_{\text{liq,inv}}$  are eliminated and a steady-state drainage-flux condition is eventually established in the invert (Figure 6-30f through Figure 6-30l). Qualitatively, the contour plot of  $q_{\text{liq,inv}}$  (Figure 6-30h through Figure 6-30l) is similar to that of the glacial-climate infiltration flux (Figure 6-47c).

Because the area over which drainage occurs out the bottom of the invert is smaller than the overall footprint of the drift, a focussing effect occurs whereby the liquid-phase flux in the invert is larger than the percolation flux in the host rock.

#### 6.11.4.2 Liquid-Phase Flux Distributions for High Infiltration Case

The evolution of liquid-phase flux (in fractures) 5 m above the crown of the drift,  $q_{\text{liq},5\text{m}}$ , is summarized in Figure 6-31 for the high infiltration-flux case. The observations made for the mean infiltration-flux case generally apply to the high-flux case. During the pre-closure period, decay heat has almost no effect on liquid-phase flux in either the host rock or in the drift. During the early portion of the post-closure period, decay-heat-enhanced liquid-phase fluxes are seen above the drift (Figure 6-31c). However, because the higher infiltration (and percolation) flux slows down the upward advance of the boiling and dryout fronts above the drift (relative to the mean-flux case), it takes longer for the peak values of  $q_{\text{liq},5\text{m}}$  to occur (compare Figure 6-31e with Figure 6-31d with Figure 6-26d); accordingly, the upward advance of the heat-pipe zone is also slower for the high infiltration-flux case than in the mean-flux case. During the present-day climate, the contribution of heat on  $q_{\text{liq},5\text{m}}$  declines until  $q_{\text{liq},5\text{m}}$  approaches a steady-state condition, controlled by the present-day climate infiltration flux (compare Figure 6-31h and Figure 6-31i with Figure 6-48a). After the monsoonal climate begins,  $q_{\text{liq},5\text{m}}$  attains a steady-state condition controlled by the monsoonal-climate infiltration flux (compare Figure 6-31j and Figure 6-31k with Figure 6-48b). After the glacial climate begins,  $q_{\text{liq},5\text{m}}$  attains a steady-state condition controlled by the glacial-climate infiltration flux (compare Figure 6-31m, Figure 6-31n, and Figure 6-31o with Figure 6-48c).

The evolution of liquid-phase flux (in fractures) 0.2 m above the crown of the drift,  $q_{\text{liq},\text{cr}}$  (“cr” stands for crown), is summarized in Figure 6-32 for the high infiltration-flux case. The observations made for the mean infiltration-flux case also apply to the high-flux case. During the pre-closure period when the host rock remains below the boiling point,  $q_{\text{liq},\text{cr}}$  is largely unaffected by decay heat. During the early portion of the post-closure period, decay-heat-enhanced liquid-phase fluxes are seen above the drift (Figure 6-32a and Figure 6-32b). However, because the high percolation flux suppresses the advance of the dryout front above the drift (relative to the mean-flux case), dryout never completely obliterates the presence of the heat-pipe zone 5 m above the drift (Figure 6-32d). Relatively soon after the monsoonal climate begins,  $q_{\text{liq},\text{cr}}$  attains a steady-state condition controlled by the monsoonal-climate infiltration flux (compare Figure 6-32h and Figure 6-32i with Figure 6-48b). Similarly, relatively soon after the glacial climate begins,  $q_{\text{liq},\text{cr}}$  attains a steady-state condition controlled by the glacial-climate infiltration flux (compare Figure 6-32j, Figure 6-32k, and Figure 6-32l with Figure 6-48c).

The evolution of liquid-phase flux averaged over the upper surface of the drip shield,  $q_{\text{liq},\text{uds}}$  (“uds” stands for upper drip shield), is summarized in Figure 6-33 for the high infiltration-flux case. During the first 100 yr of the post-closure period,  $q_{\text{liq},\text{uds}}$  is zero everywhere in the repository area. At 162 yr (Figure 6-33a) the first nonzero occurrence of  $q_{\text{liq},\text{uds}}$  is seen in a region of high ambient infiltration (and percolation) flux. The region of nonzero  $q_{\text{liq},\text{uds}}$  spreads ( Figure 6-33b through Figure 6-33g), starting in the regions of highest infiltration (and percolation) flux, until it occupies nearly the entire repository area. The influence of the heat-pipe effect is apparent as the value of  $q_{\text{liq},\text{uds}}$  declines along with the decaying heat-generation-rate of WPs (compare

Figure 6-33g, Figure 6-33h, and Figure 6-33i). Unlike the mean infiltration-flux case, after the glacial climate begins, there is a small increase in  $q_{\text{liq,uds}}$ ; however, the magnitude of  $q_{\text{liq,uds}}$  is still much smaller than the magnitude of liquid-phase flux elsewhere in the drift or in the host rock (compare Figure 6-33j with Figure 6-34g and Figure 6-31m).

The evolution of liquid-phase flux adjacent to the lower side of the drip shield,  $q_{\text{liq,lds}}$  (“lds” stands for lower drip shield), is summarized in Figure 6-34 for the high infiltration-flux case. During the first 130 yr of the post-closure period,  $q_{\text{liq,lds}}$  is zero everywhere in the repository. At 184 yr (Figure 6-34a) the first nonzero occurrence of  $q_{\text{liq,lds}}$  is seen in a region of high ambient infiltration (and percolation) flux. The region of nonzero  $q_{\text{liq,lds}}$  spreads (Figure 6-34b through Figure 6-34i), starting in the regions of highest infiltration flux, until it occupies most of the repository area. The transition to a steady-state monsoonal-climate seepage-flux condition occurs relatively quickly (compare Figure 6-34d and Figure 6-34e). The transition to a steady-state glacial-climate seepage-flux condition also occurs relatively quickly (compare Figure 6-34e and Figure 6-34f).

The contour plot of  $q_{\text{liq,lds}}$  during the monsoonal climate (Figure 6-34d and Figure 6-34e) is qualitatively the same as that of the monsoonal-climate infiltration flux (Figure 6-48b), with differences arising from how the geometry of the EBS results in flow focussing in the drift. The contour plot of  $q_{\text{liq,lds}}$  during the glacial climate (Figure 6-34f through Figure 6-34i) is also qualitatively similar to that of the glacial-climate infiltration flux (Figure 6-48c) and is also qualitatively similar to the contour map of  $q_{\text{liq,5m}}$  (Figure 6-31m through Figure 6-31o); however, the values of  $q_{\text{liq,lds}}$  are about four times larger than  $q_{\text{liq,5m}}$  in the host rock. This factor of four corresponds to the ratio of the half-drift width divided by the width of the thickness of the backfill adjacent to the lower side of the drip shield (Figure 6-3). If all of the percolation flux over a 2.75 m wide zone were focussed into the 0.6907 m wide zone next to the drip shield, this would result in a “focussing” factor of four, which is comparable to the ratio (of four) which is observed between  $q_{\text{liq,lds}}$  and  $q_{\text{liq,5m}}$  in the host rock.

The evolution of liquid-phase flux averaged across the invert,  $q_{\text{liq,inv}}$  (“inv” stands for invert), is summarized in Figure 6-35 for the high infiltration-flux case. During the first 150 yr of the post-closure period,  $q_{\text{liq,inv}}$  is zero everywhere in the repository. At 200 yr (Figure 6-35a) the first nonzero occurrence of  $q_{\text{liq,lds}}$  is seen in a region of high ambient infiltration (and percolation) flux. Initially, the values of  $q_{\text{liq,inv}}$  are negative, indicating that water is being wicked (by capillarity) vertically upward from below the drift. The region of nonzero  $q_{\text{liq,inv}}$  spreads (Figure 6-35b through Figure 6-35f), starting in the regions of highest infiltration (and percolation) flux, until it occupies all but the regions of low infiltration (and percolation) flux. As nonzero values of liquid-phase flux at the lower side of the drip shield  $q_{\text{liq,lds}}$  begin to occur, which causes water to drain from the Overton sand backfill into the invert, the direction of flow in the invert is forced to reverse, so that it is now flowing vertically downward, driven by gravity rather than by capillarity (Figure 6-35d through Figure 6-35f).

During the present-day and monsoonal climates, regions of negative  $q_{\text{liq,inv}}$  persist (Figure 6-35a through Figure 6-35f). Shortly after the glacial climate begins, most of the regions of negative  $q_{\text{liq,inv}}$  are eliminated and a steady-state drainage-flux condition is eventually established in the invert (Figure 6-35g through Figure 6-35i). Qualitatively, the contour plot of  $q_{\text{liq,inv}}$  (Figure 6-35h

through Figure 6-35l) is similar to the that of the glacial-climate infiltration flux (Figure 6-48c). Because the area over which drainage occurs out the bottom of the invert is smaller than the overall footprint of the drift, a focussing effect occurs, whereby the liquid-phase flux in the invert is larger than the percolation flux in the host rock.

#### 6.11.4.3 Liquid-Phase Flux Distributions for Low Infiltration Case

The evolution of liquid-phase flux (in fractures) 5 m above the crown of the drift,  $q_{\text{liq},5\text{m}}$ , is summarized in Figure 6-36 for the low infiltration-flux case. Because of the low percolation flux in the host rock, boiling conditions occurred at the drift wall during the pre-closure period (Figure 6-13). Because the drift-wall attained a temperature of 100°C, boiling conditions occurred a short distance out into the host rock during the pre-closure period. However, the upper vertical extent of the heat-pipe zone has not reached 5 m above the drift at the end of the pre-closure period (compare Figure 6-36a with Figure 6-49a). Within 10 yr after the start of the post-closure period, decay-heat-enhanced values of  $q_{\text{liq},5\text{m}}$  are evident (compare Figure 6-36b through Figure 6-36d). The peak of  $q_{\text{liq},5\text{m}}$  occurs earlier in the low infiltration-flux case than in the mean and high-flux cases (compare Figure 6-36f with Figure 6-26d and Figure 6-31e). The earlier peak occurs in the low infiltration-flux case because rock dryout advances far enough vertically upward (above the drift) to displace the heat-pipe zone more than 5 m above the drift.

After the monsoonal climate begins,  $q_{\text{liq},5\text{m}}$  gradually transitions to a steady-state condition, controlled by the monsoonal-climate infiltration flux (compare Figure 6-36p, Figure 6-36q, Figure 6-36r, and Figure 6-49b). After the glacial climate begins,  $q_{\text{liq},5\text{m}}$  gradually transitions to a steady-state condition, controlled by the glacial-climate infiltration flux (compare Figure 6-36s, Figure 6-36t, Figure 6-36u, and Figure 6-49c).

The evolution of liquid-phase flux (in fractures) 0.2 m above the crown of the drift,  $q_{\text{liq},\text{cr}}$  (“cr” stands for crown), is summarized in Figure 6-37 for the low infiltration-flux case. During the early post-closure period, heat-enhanced values of  $q_{\text{liq},\text{cr}}$  are less in the low infiltration-flux case than in the mean-flux case (compare Figure 6-37a with Figure 6-27a). The values of  $q_{\text{liq},\text{cr}}$  are lower for the low-flux case (than for the mean-flux case) because the lower percolation flux allows for a more rapid advance of the dryout front above the drift, which more quickly obliterates heat-pipe conditions 0.2 m above the drift. Liquid flux  $q_{\text{liq},\text{cr}}$  is zero throughout the repository area for the low infiltration-flux case during the 55 to 198 yr time interval, and for the mean-flux case  $q_{\text{liq},\text{cr}}$  is zero for the 60 to 135 yr time interval (Figure 6-37d and Figure 6-27e). This illustrates that the lower infiltration case becomes dry earlier and stays dry longer than for higher infiltration fluxes.

After the monsoonal climate begins,  $q_{\text{liq},5\text{m}}$  gradually transitions to a steady-state condition, controlled by the monsoonal-climate infiltration flux (compare Figure 6-37e through Figure 6-37h, and Figure 6-49b). After the glacial climate begins,  $q_{\text{liq},5\text{m}}$  gradually transitions to a steady-state condition, controlled by the glacial-climate infiltration flux (compare Figure 6-37h through Figure 6-37l and Figure 6-49c).

The evolution of liquid-phase flux averaged over the upper surface of the drip shield,  $q_{\text{liq},\text{uds}}$ , (“uds” stands for upper drip shield), is summarized in Figure 6-38 for the low infiltration-flux

case. During the first 260 yr of the post-closure period,  $q_{\text{liq,uds}}$  is zero everywhere in the repository area. At 320 yr (Figure 6-38a) the first nonzero occurrence of  $q_{\text{liq,uds}}$  is seen in a region of relatively high ambient infiltration (and percolation) flux. The region of nonzero  $q_{\text{liq,uds}}$  spreads (Figure 6-33b through Figure 6-33d) in the regions of highest infiltration (and percolation) flux. The majority of the repository area continues to have a zero value of  $q_{\text{liq,uds}}$  throughout the present-day-climate period (Figure 6-38d). The influence of the heat-pipe effect is apparent as the nonzero values of  $q_{\text{liq,uds}}$  are much greater than the ambient infiltration (and percolation) flux (compare Figure 6-38a with Figure 6-49a).

During the monsoonal-climate period, the region of nonzero  $q_{\text{liq,uds}}$  spreads, starting in the regions of highest infiltration flux, and progressing into the regions of lower flux (Figure 6-38e through Figure 6-38h). The influence of the heat-pipe effect is apparent as the nonzero values of  $q_{\text{liq,uds}}$  are much greater than the ambient infiltration (and percolation) flux (compare Figure 6-38h with Figure 6-49b and Figure 6-36r). The influence of the heat-pipe effect is also exhibited by the decline in  $q_{\text{liq,uds}}$ , which corresponds to the decay in heat-generation rate from WPs (Figure 6-38h through Figure 6-38l). The value of  $q_{\text{liq,uds}}$  becomes much less than the infiltration and percolation flux (compare Figure 6-38l with Figure 6-49c and Figure 6-36u).

The evolution of liquid-phase flux adjacent to the lower side of the drip shield,  $q_{\text{liq,lds}}$  (“lds” stands for lower drip shield), is summarized in Figure 6-39 for the low infiltration-flux case. During the first 365 yr of the post-closure period,  $q_{\text{liq,lds}}$  is zero everywhere in the repository. At 420 yr (Figure 6-39a) the first nonzero occurrence of  $q_{\text{liq,lds}}$  is seen in a region of high ambient infiltration (and percolation) flux. The region of nonzero  $q_{\text{liq,lds}}$  spreads (Figure 6-39b through Figure 6-39c), starting in the regions of relative high infiltration (and percolation) flux; about half of the repository area continues to have a zero value of  $q_{\text{liq,lds}}$  throughout the present-day-climate period (Figure 6-39d). During the present-day-climate period, most of the nonzero values of  $q_{\text{liq,lds}}$  are negative, indicating that  $q_{\text{liq,lds}}$  is vertically upward, resulting from capillary-driven wicking up through the invert and into the backfill. During the present-day-climate and monsoonal-climate periods, a steady-state condition is never established in the backfill; thus decay heat continues to dominate liquid-phase flux conditions.

During the glacial-climate period,  $q_{\text{liq,lds}}$  eventually develops a steady-state condition that is controlled by the glacial-climate infiltration (and percolation) flux (compare Figure 6-39h through Figure 6-39l with Figure 6-49c and Figure 6-37l). The contour plot of  $q_{\text{liq,lds}}$  during the glacial climate (Figure 6-39j through Figure 6-39l) becomes qualitatively similar to that of the glacial-climate infiltration flux (Figure 6-49c) and is also qualitatively similar to the contour map of  $q_{\text{liq,5m}}$  (Figure 6-36s through Figure 6-36u); however, the values of  $q_{\text{liq,lds}}$  are about 4 times larger than  $q_{\text{liq,5m}}$  in the host rock. This factor of 4 corresponds to the ratio of the half-drift width divided by the width of the thickness of the backfill adjacent to the lower side of the drip shield (Figure 6-3). If all of the percolation flux over a 2.75 m wide zone were focussed into the 0.6907 m wide zone next to the drip shield, this would result in a “focussing” factor of four, which is comparable to the ratio (of four) which is observed between  $q_{\text{liq,lds}}$  and  $q_{\text{liq,5m}}$  in the host rock.

The evolution of liquid-phase flux averaged across the invert (called  $q_{\text{liq,inv}}$ , where “inv” stands for invert) is summarized in Figure 6-40 for the low infiltration-flux case. During the first 345 yr

of the post-closure period,  $q_{\text{liq,inv}}$  is zero everywhere in the repository. At 400 yr (Figure 6-40a) the first nonzero occurrence of  $q_{\text{liq,inv}}$  is seen in a region of high ambient infiltration (and percolation) flux. During the present-day-climate and monsoonal-climate periods, the values of  $q_{\text{liq,inv}}$  are negative, indicating that water is being wicked (by capillarity) vertically upward from below the drift. The region of nonzero  $q_{\text{liq,inv}}$  spreads (Figure 6-40b through Figure 6-40f), from the regions of highest infiltration (and percolation) flux. Most of the repository area continues to have a zero value of  $q_{\text{liq,inv}}$  throughout the present-day-climate period (Figure 6-40a and Figure 6-40b). During the monsoonal-climate period, the region of nonzero  $q_{\text{liq,inv}}$  spreads throughout most of the repository area (Figure 6-40c through Figure 6-40f).

During the glacial-climate period, a gradual transition occurs from nonzero values of  $q_{\text{liq,inv}}$  being primarily negative to all nonzero values of  $q_{\text{liq,inv}}$  being positive (Figure 6-40f through Figure 6-40l). This slow transition indicates the influence of decay heat from WPs on  $q_{\text{liq,inv}}$  persisting for nearly 50,000 yr for the low-infiltration flux case. The slow transition results because decay heat delays the onset of significant seepage into the Overton sand backfill. Eventually, seepage into the drift overwhelms the influence of decay heat and the resulting drainage of water into the invert dominates the direction of liquid-phase flow in the invert. When gravity flow finally dominates liquid flow in the drift (including the invert), the distribution of  $q_{\text{liq,inv}}$  (Figure 6-40l) becomes qualitatively similar to the distribution of  $q_{\text{liq,5m}}$  (Figure 6-36u) and that glacial-climate infiltration flux (Figure 6-49c).

#### 6.11.4.4 Liquid-Phase Flux Analysis

Most of the liquid-phase flux analysis is addressed in the previous three subsections (Section 6.11.4.1, Section 6.11.4.2, and Section 6.11.4.3). Not presented in the previous three subsections is a history plot of liquid-phase flux. Figure 6-41 plots the liquid phase flux at the five drift-scale locations in the NFE and EBS: (1) 5 m above the crown of the drift, (2) 0.2 m above the crown of the drift, (3) in the sand backfill, averaged along the top of the drip shield, (4) in the sand backfill, adjacent to the lower side of the drip shield, and (5) in the crushed-tuff invert, averaged over the invert. This information is given at two repository-scale locations, including the geographic center of the repository and a location 27.5 m from the eastern edge, which is approximately midway between the northern and southern boundaries of the repository.

Many of the observations made in the previous three subsections are illustrated in Figure 6-41. The early spike in the liquid-phase flux 0.2 m above the crown of the drift is seen just after 50 yr, while 5 m above the drift the heat-enhanced increase in liquid-phase flux occurs slightly later. At the edge of the repository, the heat-enhanced increase in liquid-phase flux 5 m above the drift is much less pronounced because edge-cooling prevents the neighboring drifts from reinforcing the temperature buildup enough to cause significant thermal effects on flow 5 m above the drift. At both the center and edge locations, the effect of the three climate states on liquid-phase flux above the drift is clearly evident. However, climate change has no effect on the liquid-phase flux above the drip shield. The dependence on liquid-phase flux above the drip shield on heat-generation rate is exhibited by an abrupt rise in flux at 50 yr, followed by a gradual decline to a value that is much less than the liquid-phase flux in the host rock.

Adjacent to the lower side of the drip shield and within the invert, the initial nonzero values of liquid-phase flux are negative, indicating that flow is being wicked from below the drift. Eventually, the direction of flow at these two directions is reversed and the liquid-phase flux at these locations in the drift is equal to a multiple of the percolation flux in the host rock. The factor by which the flux in the drift is greater than that in the host rock is attributed to how the EBS geometry causes flow focussing past the lower drip shield and into the invert.

### 6.11.5 Evaporation Rate Distributions

Evaporation can occur at a given location in the drift once the liquid-phase flux at that location is nonzero. Evaporation rate is considered to be an important performance measure because it is an indication of the rate at which mineral precipitates are being left behind. Negative values of evaporation rate indicate areas where condensation is occurring; in such regions, mineral dissolution may be occurring. A particularly important location within the EBS with respect to the effects of evaporation and condensation is the surface of the drip shield. The following three subsections provide the complete evolution of the total evaporation rate (summed over the outer perimeter of the drip shield) during the 1,000,000 yr simulation period. The reported values of evaporation rate (in kg/yr/m) pertain to the entire outer (perimeter) surface of a 1 m long interval of the drip shield (along the longitudinal axis of the drift). In the model, the evaporation (and condensation) actually occurs in the backfill gridblocks that are immediately adjacent to the drip shield. Note that the drip shield is emplaced after the pre-closure period (50 yr); therefore, the following results begin at 50 yr.

#### 6.11.5.1 Evaporation Rate Distributions for Mean Infiltration Case

The evolution of evaporation rate per unit length summed over the entire outer (perimeter) surface of the drip shield,  $Q_{\text{evap,ds}}$  (“ds” stands for drip shield), for the mean infiltration-flux case is summarized in Figure 6-42. The evaporation rate is given per unit length of drip shield (along the longitudinal axis of the drift). During the first 20 yr of the post-closure period, all values of  $Q_{\text{evap,ds}}$  are zero throughout the repository area. At 80 yr, the first nonzero values of  $Q_{\text{evap,ds}}$  are seen at the very outer edge of the repository (Figure 6-42a). The region of nonzero  $Q_{\text{evap,ds}}$  grows from the outer repository edges in towards the center of the repository (Figure 6-42a through Figure 6-42d). Within 1500 yr, the region of nonzero  $Q_{\text{evap,ds}}$  has reached most of the central region of the repository (Figure 6-42e), however, in regions of the lowest infiltration (and percolation) flux,  $Q_{\text{evap,ds}}$  is still zero at 1500 yr. Eventually, water has seeped into nearly every drift location, and nonzero  $Q_{\text{evap,ds}}$  prevails over most of the entire repository area (Figure 6-42g). Because  $Q_{\text{evap,ds}}$  decays along with heat-generation rate, the magnitude of  $Q_{\text{evap,ds}}$  declines with time (Figure 6-42e through Figure 6-42r). Even at 1,000,000 yr, there are nonzero values of  $Q_{\text{evap,ds}}$  throughout the repository area (Figure 6-42r).

#### 6.11.5.2 Evaporation Rate Distributions for High Infiltration Case

The evolution of evaporation rate per unit length summed over the entire outer (perimeter) surface of the drip shield,  $Q_{\text{evap,ds}}$  (“ds” stands for drip shield), for the high infiltration-flux case is summarized in Figure 6-43. The evaporation rate is given per unit length of drip shield (along the longitudinal axis of the drift). The evolution of  $Q_{\text{evap,ds}}$  for the high infiltration-flux case is

similar to that of the mean-flux case. During the first 40 yr of the post-closure period, all values of  $Q_{\text{evap,ds}}$  are zero throughout the repository area. At 100 yr, the first nonzero values of  $Q_{\text{evap,ds}}$  are seen at the very outer edge of the repository (Figure 6-43a). The region of nonzero  $Q_{\text{evap,ds}}$  grows from the outer repository edges in towards the center of the repository (Figure 6-43a through Figure 6-43c). Within 1000 yr, the region of nonzero  $Q_{\text{evap,ds}}$  has reached most of the central region of the repository (Figure 6-43d), however, in regions of the lowest infiltration (and percolation) flux,  $Q_{\text{evap,ds}}$  is still zero at 1000 yr. Eventually, water has seeped into nearly every drift location, and nonzero  $Q_{\text{evap,ds}}$  prevails over most of the entire repository area (Figure 6-43e). Because  $Q_{\text{evap,ds}}$  decays along with heat-generation rate, the magnitude of  $Q_{\text{evap,ds}}$  declines with time (Figure 6-43d through Figure 6-43o). Even at 1,000,000 yr, there are nonzero values of  $Q_{\text{evap,ds}}$  throughout the repository area (Figure 6-43o).

### 6.11.5.3 Evaporation Rate Distributions for Low Infiltration Case

The evolution of evaporation rate per unit length summed over the entire outer (perimeter) surface of the drip shield,  $Q_{\text{evap,ds}}$  (“ds” stands for drip shield), for the low infiltration-flux case is summarized in Figure 6-44. The evaporation rate is given per unit length of drip shield (along the longitudinal axis of the drift). The evolution of  $Q_{\text{evap,ds}}$  for the low infiltration-flux case is similar to that of the mean-flux case; however, the lower percolation flux results in the delayed onset of seepage into drifts, the onset of nonzero values of  $Q_{\text{evap,ds}}$  is delayed. During the first 60 yr of the post-closure period, all values of  $Q_{\text{evap,ds}}$  are zero throughout the repository area. At 120 yr, the first nonzero values of  $Q_{\text{evap,ds}}$  are seen at the very outer edge of the repository (Figure 6-43a). The region of nonzero  $Q_{\text{evap,ds}}$  grows from the outer repository edges in towards the center of the repository (Figure 6-44a through Figure 6-44d). Within 3000 yr, the region of nonzero  $Q_{\text{evap,ds}}$  has reached more than half of the repository area (Figure 6-44); however, in regions of the lowest infiltration (and percolation) flux,  $Q_{\text{evap,ds}}$  is still zero at 3000 yr. Eventually, water has seeped into most of the drift locations, and nonzero  $Q_{\text{evap,ds}}$  prevails over much of the entire repository area (Figure 6-44g). Because  $Q_{\text{evap,ds}}$  decays along with heat-generation rate, the magnitude of  $Q_{\text{evap,ds}}$  declines with time (Figure 6-44e through Figure 6-44o). Even at 1,000,000 yr, there are nonzero values of  $Q_{\text{evap,ds}}$  throughout the repository area (Figure 6-44o).

### 6.11.5.4 Evaporation Rate Analysis

Most of the analysis of evaporation rate is addressed in the previous three subsections (Section 6.11.5.1, Section 6.11.5.2, and Section 6.11.5.3). Not given in the previous three subsections is a history plot of evaporation rate. Figure 6-45a gives the evaporation rate on drip shields  $Q_{\text{evap,ds}}$  (summed over the outer perimeter on a unit length of drip shield). This information is given at two repository-scale locations, including the geographic center of the repository and a location 27.5 m from the eastern edge, which is approximately midway between the northern and southern boundaries of the repository. Figure 6-45b gives the gas-phase air-mass fraction in the drift, which is covered in Section 6.11.3.

Nonzero values of  $Q_{\text{evap,ds}}$  occur for about 950 yr at the geographic center of the repository and for about 80 yr at a location 27.5 m from the edge of the repository (Figure 6-45a). The magnitude of the peak value of  $Q_{\text{evap,ds}}$  is about the same for these two locations: (1) 615 kg/yr/m at the geographic center of the repository and (2) 510 kg/yr/m at the repository edge location.

The decline in  $Q_{\text{evap,ds}}$  is slower at the edge than at the geographic center of the repository. Eventually (after 30,000 yr), the magnitude of  $Q_{\text{evap,ds}}$  is nearly the same at these locations.

### 6.11.6 Influence of Variability of Heat Generation from Waste Packages

All of the results presented in Sections 6.11.1 through 6.11.5 are for the hottest WP location, which corresponds to the second 21-PWR WP shown in Figure 4-1. In this section, the sensitivity of WP temperature and WP relative humidity to the variability of WP heat-generation rate is examined for the mean infiltration-flux case.

#### 6.11.6.1 Temperature and Relative Humidity on Different Waste-Package Types

Temperature and relative humidity on the WP surface for the mean infiltration-flux case is plotted (Figure 6-46) at the geographical center of the repository for the 4 different WP types and 8 different WP locations (along the drift) considered in the MSTHM; the 4 WP types and 8 WP locations are shown in Figure 4-1. The WP temperature  $T_{\text{wp}}$  histories for these 8 WPs is relatively similar (Figure 6-46a). The difference in peak  $T_{\text{wp}}$  between the hottest and coldest WP is 42°C (Figure 6-46a). Note that the hottest WP is the 21-PWR WP that was considered throughout the rest of Section 6.11 and the coldest WP is a DSNF WP (see Figure 4-1). The duration of the boiling period (defined to be the period during which  $T_{\text{wp}} > 96^\circ\text{C}$ ) is 1540 yr and 1230 yr for the hottest and coldest WP, respectively. Therefore, the range in temperature for the different WP types (and locations) considered in this AMR is relatively small. The range in WP relative humidity  $RH_{\text{wp}}$  histories for the same group of WPs is also relatively small (Figure 6-46b). The minimum  $RH_{\text{wp}}$  is 1.7% for the hottest WP and is 3.9% for the coldest WP. The range in the time required for the WPs to attain  $RH_{\text{wp}} = 85\%$  varies from 1170 yr to 1460 yr.

### 6.11.7 Influence of Overburden Thickness

Overburden thickness (which is equal to the depth of the repository below the ground surface) affects temperatures in the repository because it determines the thickness of the (rock) insulation lying between the repository and the ground surface. Because the ground surface is a constant-temperature boundary, acts like a heat sink. The influence of overburden thickness is negligible during the first 300 to 500 yr (Hardin 1998, Section 3.7.7.1). This influence is also relatively unimportant close to the repository edges and are increasingly important toward the center of the repository (Hardin 1998, Section 3.7.7.1). The greatest long-term temperature rise occurs where the overburden thickness is greatest in the central region of the repository (Hardin 1998, Section 3.7.7.1).

Because the largest values of overburden thickness occur close to the center of the repository, it is difficult to discern the influence of the edge-cooling effect from the influence of overburden thickness (Figure 6-7h through Figure 6-7m); both influences cause higher long-term temperatures at the center and lower long-term temperatures at the edges of the repository.

## 6.12 MSTHM RESULTS FOR THE NO-BACKFILL CASE

The MSTHM calculates 38 TH variables for 610 repository subdomains (Figure 6-1b) and eight different WP locations (Figure 4-1) as a function of time for 99 calculational timesteps. For each

timestep there are  $38 \times 610 \times 8$  different data values, resulting in 185,440 data values. Multiplying by 99 calculational timesteps results in more than 18 million TH data values for a complete time evolution of a given infiltration-flux case. For the three infiltration-flux cases (mean, high, and low infiltration flux) there are a total of more than 55 million TH data points. The following subsections provide a comprehensive description of the variables that are of key interest to the evolution of the TH environment in the NF and EBS. This description focuses on the mean infiltration-flux case.

Contour plots are provided on a sufficiently frequent time basis to capture the major trends, as well as the peaks and major transitions, of the spatial and temporal distributions of the major TH variables. This information is provided for a 21-PWR WP (which is the fifth WP from the left in Figure 4-1). This WP location resulted in the highest temperatures with respect to WP-to-WP variability. It should be noted that the repository design analyzed in this report employs several design measures (such as fuel blending and line-load WP spacing) that minimize WP-to-WP variability in temperature. Therefore, the following results should be considered to be fairly typical of temperature distributions in the repository. Section 6.11.6 addresses the influence of WP-to-WP variability that arises from differences in heat-generation rate among WPs for the backfill case. Table 6-5 lists all of the plots of TH conditions that are given in Section 6.12.

Table 6-5. List of plots of TH conditions for the no-backfill case

Figure Number	TH Variable	Source DTN	Source File Name
Figure 6-50	Drift-wall & WP temperature	LL000509112312.003	TSPA_SR00nbf_mean_Infiltration.ext
Figure 6-51	Temperature 5 m above crown of drift	LL000509112312.003	TSPA_SR00nbf_mean_Infiltration.ext
Figure 6-52	Temperature 7.39 m laterally away from springline	LL000509112312.003	TSPA_SR00nbf_mean_Infiltration.ext
Figure 6-53	Temperature history at different EBS and NFE locations at center and eastern edge of repository	LL000509112312.003	TSPA_SR00nbf_mean_Infiltration.ext
Figure 6-54a	CCDF of the peak WP temperature	LL000509112312.003	TSPA_SR00nbf_mean_Infiltration.ext
Figure 6-54b	CCDF of the maximum lateral extent of boiling	LL000509112312.003	TSPA_SR00nbf_mean_Infiltration.ext
Figure 6-55	Drift-wall liquid-phase saturation	LL000509112312.003	TSPA_SR00nbf_mean_Infiltration.ext
Figure 6-56	Drift-wall relative humidity	LL000509112312.003	TSPA_SR00nbf_mean_Infiltration.ext
Figure 6-57	Drift-wall liquid saturation and relative humidity history at center and eastern edge of repository	LL000509112312.003	TSPA_SR00nbf_mean_Infiltration.ext
Figure 6-58	Evaporation-rate at the crown of the drift	LL000509112312.003	TSPA_SR00nbf_mean_Infiltration.ext
Figure 6-59	Evaporation-rate history at the crown of the drift at center and eastern edge of repository	LL000509112312.003	TSPA_SR00nbf_mean_Infiltration.ext
Figure 6-60	Drift-wall capillary pressure in fractures and matrix	LL000509112312.003	TSPA_SR00nbf_mean_Infiltration.ext
Figure 6-61	Capillary-pressure history in the fractures and matrix at center and eastern edge of repository	LL000509112312.003	TSPA_SR00nbf_mean_Infiltration.ext
Figure 6-62	Liquid-phase flux 5 m and 3 m above the crown of the drift	LL000509112312.003	TSPA_SR00nbf_mean_Infiltration.ext
Figure 6-63	Liquid-phase flux at the upper drift wall	LL000509112312.003	TSPA_SR00nbf_mean_Infiltration.ext

Figure 6-64	Liquid-phase-flux history at the upper drift wall at center and eastern edge of repository	LL000509112312.003	TSPA_SR00nbf_mean_Infiltration.ext
-------------	--	--------------------	------------------------------------

### 6.12.1 Temperature Distributions

Figure 6-50 shows the spatial distributions of perimeter-averaged drift-wall temperature, as well as the temperature on the WP. Preclosure drift-wall temperatures stay below the boiling point, while the WP temperature climbs above the boiling point as it peaks around 15 yr. Shortly after ventilation ceases, peak drift-wall and WP temperatures occur (Figures 6-50g and 6-50j). Peak drift-wall temperatures are generally less than 150°C. The edge-cooling effect is very evident thereafter, as temperatures around the repository edges are considerably less than at the repository center. Boiling at the drift wall ceases around 1000 yr (Figure 6-50n), while boiling on WPs ceases around 1400 yr.

Figure 6-51 shows the spatial distributions of temperature in the host rock 5 m above the crown of the drift. This location barely reaches the boiling point at about 100 yr (Figure 6-51e) and remains above the boiling point for less than 300 yr (Figure 6-51g).

Figure 6-52 shows the spatial distribution of temperature 7.39 m laterally away from the springline of the drift. Note that this location in the pillar is almost exactly one-quarter of the distance in toward the midline of the pillar. This location in the pillar never quite reaches the boiling point, indicating that at least 75% of the repository horizon remains below the boiling point. This condition virtually assures that condensate and percolation flux can readily shed between emplacement drifts.

Figure 6-53 shows the temperature history at various locations in the NFE host-rock, as well as on the WP, for the geographical center of the repository and a location 27.5 m from the eastern edge of the repository. The duration of boiling is considerably less at the edge than it is at the center of the repository. The duration of boiling at the drift wall is less than 1000 yr at the center of the repository and about 100 yr at the edge of the repository. The temperature history 5 m above the crown of the drift is similar to that 7.39 m laterally away from the springline of the drift.

Figure 6-54 shows the complementary cumulative distribution function (CCDF) for the peak temperature on WPs and on the drift wall, as well as showing the CCDF of the maximum lateral extent of the boiling point isotherm. The coolest WP location has a peak drift-wall temperature of about 115°C, while the hottest WP location has a peak of about 147°C. For the coolest WP location, the maximum lateral extent of boiling is about 6.5 m, while for the hottest WP location, the maximum lateral extent of boiling is about 8.9 m. Therefore, between 78 to 84% of the repository horizon remains below the boiling point, which will virtually assure that condensate and percolation flux can readily shed between emplacement drifts.

### 6.12.2 Liquid-Phase Saturation and Relative Humidity Distributions

Figure 6-55 shows the spatial distributions of liquid-phase saturation in the host-rock at the drift wall. Figure 6-56 shows the spatial distributions of relative humidity in the host-rock at the drift

wall and on the WP. Figure 6-57 shows the perimeter-averaged drift-wall liquid-phase saturation history and relative humidity history at the center and edge of the repository. Minimum liquid-phase saturations are about 0.2 at the repository center and slightly greater than 0.2 at the repository edge. Minimum values of drift-wall relative humidity are about 25% at the repository center and about 40% at the repository edge. The differences between the center and edge locations result from the edge-cooling effect. Significant reduction in drift-wall liquid-phase saturation (relative to ambient conditions) persist for up to about 2000 yr. Significant reduction in drift-wall *RH* (relative to humid ambient conditions) persist for up to about 2000 yr.

### **6.12.3 Evaporation Rate Distributions**

Figure 6-58 shows the spatial distribution of evaporation rate in the host rock at the crown of the drift. Figure 6-59 shows the evaporation-rate history at the crown of the drift for the repository center and edge. Immediately after ventilation ceases there is a sharp spike in evaporation rate as boiling commences in the host-rock around the drift wall. After this spike, the evaporation rate is close to zero at the repository center; a secondary sharp spike in evaporation rate occurs at the end of the boiling period (about 1000 yr in Figure 6-59). This spike results from the boiling front collapsing back into the emplacement drift. At the repository edge, there is a minimal period of zero values of evaporation rate because the boiling front never progresses very far away from the drift wall. Some time after the end of the boiling period the evaporation rate declines to relatively small values.

### **6.12.4 Capillary-Pressure Distributions**

Figure 6-60 shows the spatial distributions of capillary pressure in the fractures and in the matrix. Figure 6-61 shows the capillary-pressure histories in the fractures and in the matrix at the repository center and edge. Under ambient conditions, capillary pressure in the fractures is an order of magnitude less than that in the matrix (Figures 6-60a and 6-60d). During the preclosure period, changes in capillary pressure are small, primarily arising as a result of the temperature dependence of the surface tension of water. Shortly after ventilation ceases and boiling and dryout occur in the host rock around the drifts, the magnitude of capillary pressure in the matrix rises abruptly, attaining values about 3 to 4 orders of magnitude larger than ambient values. As the rock rewets to ambient liquid-phase saturation conditions, the capillary pressure declines to ambient values.

### **6.12.5 Liquid-Phase Flux Distributions**

Figure 6-62 shows the spatial distribution of liquid-phase flux 5 m and 3 m above the crown of the drift. Figure 6-63 shows the spatial distribution of liquid-phase flux at the drift wall. Figure 6-64 gives the liquid-phase-flux history at 5 m and 3 m above the crown of the drift, as well as at the drift wall for a repository center and edge location. The increase in liquid-phase flux (above ambient values) is called thermally-enhanced percolation.

At the repository center, the location 3 m above the crown of the drift experiences a very abrupt spike in liquid-phase flux just after ventilation ceases and boiling commences in the host rock around the drift. This primary spike is followed by a period of zero flux, which is then followed

by a secondary spike (much smaller than the primary spike) that occurs shortly after boiling ceases. At the repository center, the location 5 m above the drift experiences a less abrupt spike in liquid-phase flux. Liquid-phase flux remains above ambient values until the end of the present-day climate (at 600 yr); thereafter, the influence of thermally-enhanced percolation is swamped by the increased ambient percolation flux that results from the monsoonal and glacial climates.

At the repository edge, the duration of thermally-enhanced percolation flux (3 m and 5 m above the drift) is less than at the center of the repository. Percolation flux 3 m and 5 m above the drift returns to ambient values before the end of the present-day climate.

### 6.13 MODEL VALIDATION

The MSTHM is performed using industry standard finite-difference method that includes mass balance and energy balance. The results from finite-difference codes are only as good as the inputs. All inputs into this model are TBV, and therefore the results are TBV. The model validation includes various validation techniques described below:

- **Comparison of NUFT TH model results against the Large Block Test.** The Thermal Tests Thermal-Hydrological Analysis/Model Report (CRWMS M&O 2000b, Section 6.2.4.) documents the comparison of NUFT TH model calculations against measurements made in the Large Block Test. An agreement within about 10% would validate this model. A brief summary of this comparison is given in Section 6.13.1 of this report.
- **Comparison of NUFT TH model results against the Drift Scale Test.** The Thermal Tests Thermal-Hydrological Analysis/Model Report (CRWMS M&O 2000b, Section 6.2.3) documents the comparison of NUFT TH model calculations against measurements made in the Drift Scale Test. An agreement within about 10% would validate this model. A brief summary of this comparison is given in Section 6.13.2 of this AMR.
- **Comparison of MSTHM results against alternative numerical models.** Milestone Report SP4CK5M4 (Buscheck et al. 1998) documents a comparison between the results of the MSTHM against a 3-D east-west cross-sectional mountain-scale TH model developed at Lawrence Berkeley National Laboratory (Haukwa et al. 1998). An agreement within about 10% would validate this model. A brief summary of this comparison is given in Section 6.13.3 of this AMR.
- **Inspection of model inputs and outputs.** A detailed and comprehensive analysis was conducted (Section 6.11) that carefully compared the relationship between the model inputs and the model outputs. This comparison involved more than 150 pages of contour plots and time history plots of a wide range of input and output variables. This comparison uncovered no unexpected or difficult to explain model results; the relationships between the model outputs and the model inputs (for the range of inputs considered in this AMR) are consistent with the physical processes that are accounted for in the MSTHM.

- **Validation of software routines and macros.** The submodel input files were largely built using software routines and macros; very little hand editing was used in building the input files. Each one of these routines and macros are validated (Attachment I). By minimizing hand editing, the potential for human error is greatly reduced. Because the input files are built with validated software, this assures the accuracy with which the source-input data is faithfully represented in the submodels.
- **Inspection of model input files.** A detailed visual inspection of the submodel input files was conducted to verify that the submodels faithfully represented the intended conceptual model and accurately included all source-input data. Visual inspection was conducted for all templates (used in macros and scripts) and for the very few submodels that employed any hand editing in the building of the input files (e.g., the DDT submodel, described in Section 6.5). For the input files that are generated automatically (without hand editing), this inspection process is greatly facilitated by the validation of software routines and macros used to build these file (described in the preceding bullet).

On the basis of this multi-stage model validation effort, it is determined that the MSTHM is valid for its intended use.

#### 6.13.1 Comparison of NUFT TH Model against the Large Block Test

The NUFT model used to model the Large Block Test is described in the Thermal Tests Thermal-Hydrological Analysis/Model Report (CRWMS M&O 2000b, Section 5.4). Figure 6-65 shows the simulated versus measured temperature profile along Borehole TT1 at six times from 30 to 400 days. The DTN for all field temperatures is LL970803004244.036. The NUFT TH model of the Large Block Test, which used the same hydrologic property set as used in this AMR, shows some over-prediction of temperature at earlier times, but the difference between simulated and measured temperatures decreases at later times. At 300 and 400 days (25 days after power shutdown), the agreement is excellent.

Two statistical measures of goodness-of-fit, the root mean squared difference (RMSD) and mean difference (MD) between measured and simulated temperatures along Borehole TT1, were computed at various times from 30 days to 500 days. The results are tabulated in Table 6.6. As shown in the temperature profiles, the RMSD plot indicates a good fit between simulated and field temperatures. The match is good at 30 days, worsens at 100 days, and then consistently improves thereafter. The MD is always positive, which indicates that the NUFT TH model, in general, slightly overpredicts the temperatures. Again, the accuracy of the prediction consistently increases with time after 30 days, reducing to a mean error of less than 1°C at 500 days, 125 days into the cool-down phase.

Table 6-6. RMSD and MD for temperature profile along TT1 using driftscale data set

Time (days)	RMSD (°C)	MD (°C)
30	7.25	6.90
100	14.05	10.55
200	10.56	4.34
300	9.16	1.53
400	5.82	3.53
500	0.63	0.08

Figure 6-66 shows the simulated and measured liquid-phase saturation profile along TN3, which is a vertical borehole used for neutron probe measurements of water content. NUFT model results are compared to liquid-phase saturations measured by neutron probe (DTN LL971204304244.047, LL980919304244.075). The field measurement times, 103, 361, and 501 days are compared at model times of 100, 365, and 500 days. The small differences between model and field times should have a negligible effect on the comparisons since saturation changes develop relatively slowly. The simulated dryout zone develops more slowly than the measured dryout zone. The difference between the simulated and measure dryout zones decreases with increasing time. At 365 and 500 days, the comparison between the simulated and measured dryout zones is excellent.

The good agreement between the NUFT simulation and the measurements made in the LBT indicate that the NUFT LDTH submodels, together with the use of the drift-scale hydrologic property set, are validated for their intended use.

### 6.13.2 Comparison of NUFT TH Model against the Drift Scale Test

The NUFT model used to model the Drift Scale Test (DST) is described in the Thermal Tests Thermal-Hydrological Analysis/Model Report (CRWMS M&O 2000b, Section 5.1 and Section 5.3.2). Figure 6-67 compares the NUFT-simulated and measured temperatures along Borehole ESF-HD-137 at 365 and 547 days. The agreement between NUFT and the measured temperatures is good, with NUFT slightly overpredicting temperatures in the superheated zone and slightly underpredicting temperatures in the sub-boiling zone.

The RMSD, MD, and normalized averaged mean difference (NAMD) between simulated and measured temperatures were selected to serve as measures of the goodness-of-fit of the simulated values to the measured values. In general, the comparison between the simulated and measured temperatures is poor for all sensors very close to the heated drift at all times less than 100 days. This poor comparison results from the NUFT model of the DST representing the heated drift as an equivalent square rather than as the cylindrical cross section. On the other hand the LDTH submodels accurately represent the cylindrical cross-sectional geometry emplacement drift. It is judged that had the NUFT DST model accurately accounted for the cylindrical cross-sectional geometry of the heated drift, the agreement close to the heated drift would have been much better for all times and that the overall agreement between simulated and measured temperatures would have also been better.

At times in excess of 1 yr, the agreement between simulated and measured temperatures improves. The regions for which there is good agreement between simulated and measured temperatures fall into two categories: (1) the sub-boiling zone and (2) the boiling and above-boiling zone along the heated drift.

The good agreement in the sub-boiling zone indicates that heat flow there is dominated by conduction and that the assumed value of wet thermal conductivity is reasonable. Because of the relatively high liquid-phase saturation in the sub-boiling zone, the wet value of thermal conductivity applies. Because the bulk permeability  $k_b$  of the DST area is much less than the threshold  $k_b$  value at which buoyant gas-phase convection begins to significantly influence heat flow (Buscheck and Nitao, 1994), heat flow in the sub-boiling region is dominated by heat conduction.

The good agreement between the simulated and measured temperatures in the region close to the heated drift indicates the following three points. First, the representation of thermal radiation inside the heated drift is adequately represented in the NUFT DST model. Secondly, heat flow in the boiling and above-boiling zones is dominated by conduction. Thirdly, the value of dry thermal conductivity used in the NUFT DST model is reasonable.

The good agreement between the NUFT simulation and the measurements made in the DST indicate that the NUFT LDTH submodels, together with the use of the drift-scale hydrologic property set, are validated for their intended use. The good agreement also indicates that the DDT submodel (which represents how thermal radiation affects 3-D heat flow in the EBS and near field) is validated for its intended use.

### **6.13.3 Comparison of MSTHM against an Alternative Conceptual Model**

Figure 6-68 compares the drift-wall temperature predicted by the MSTHM (Buscheck et al. 1998) with those predicted by an east-west cross-sectional mountain-scale TH model (Haukwa et al. 1998). Because the east-west TH model does not predict in-drift TH conditions and because relative humidity  $RH$  and liquid-phase saturation was not provided from that model, the comparison is restricted to predictions of drift-wall temperatures by the respective modeling approaches.

Before discussing the differences in the temperatures predicted by the two approaches (Figure 6-68) it is important to discuss the differences in the models. The temperature predicted by the MSTHM is the perimeter-averaged drift-wall temperature adjacent to an “average” 21-PWR medium-heat CSNF WP. MSTHM discretely represents the decay-heat source from individual WPs—thus, some of the drift-wall locations are hotter than that shown in Figure 6-68, while some are considerably cooler. The drift-wall grid blocks over which the temperature is averaged extend 0.5 m into the host rock surrounding the drift. The temperature prediction in the east-west cross-sectional mountain-scale TH model is for a grid block that occupies the entire cross section of the drift—thus, it is a lumped representation of the drift temperature. Moreover, because the east-west cross-sectional mountain-scale model uses a line-averaged heat source, it axially smears out the differences between hot-WP locations and cold-WP locations along the drift.

Another difference between the modeling approaches concerns the mountains-scale dimensionality. The MSTHM represents 3-D mountain-scale heat flow for entire extent of the heated repository footprint, while the east-west cross-sectional mountain-scale TH model has a reflected boundary at the east-west midpoint of the repository. Thus, the east-west model assumes that the overburden thickness of the entire repository area can be approximated with the overburden thickness between the western repository boundary and the midpoint of the repository. Because the eastern half of the repository has much less overburden thickness than the western half, this east-west symmetry approximation effectively overrepresents the effective overburden thickness for the eastern half of the repository. The cross-sectional geometry of the east-west mountain-scale model implicitly assumes that mountain-scale heat loss in the north-south dimension is negligible, which is a reasonable assumption given the large north-south dimension of the repository.

Another difference between the two modeling approaches concerns the areal power density APD assumed in the models. The initial APD in the MSTHM is 92.3 kW/acre, while it is 99.4 kW/acre in the east-west cross-sectional mountain-sale model. Thus, the east-west model has a 7.7% larger APD than does the MSTHM.

At the center of the repository (the 14c3 location in Table 2-2 of Buscheck et al. 1998) the respective modeling approaches predict almost an identical duration of boiling (Figure 6-68a). At the edge repository location, which is 100 m from the western edge of the repository in the MSTHM (the 14c1 location in Table 2-2), the east-west cross-sectional mountain-scale model predicts a longer duration of boiling than does the MSTHM (Fig. 6-68b). One reason for this difference is that the east-west model representation of the heated repository footprint extends slightly further to the west than it does in the MSTHM.

During the post-boiling period, the temperatures predicted by the respective modeling approaches are in good agreement. During the early-time heat-up period, the coarse (lateral and axial) grid-block spacing in the east-west cross-sectional mountain-scale model does not capture the rapid drift-wall temperature rise that the more finely gridded MSTHM predicts. Because of the coarse lateral grid-block spacing in the east-west model, it smears out the lateral temperature gradient between the drift and the mid-pillar location—thus, it tends to overpredict the temperature at the mid-pillar location and thereby prevent condensate from shedding between drifts. The fine lateral grid-block spacing in the MSTHM captures the influence that the lateral temperature gradient has on allowing condensate to shed between drifts. The tendency for the east-west cross-sectional mountain-scale model to underrepresent condensate shedding results in a more substantial condensate buildup above the repository horizon. Also, the line-averaged heat-source approximation smears out differences in temperature between otherwise hot- and cold-WP locations and thereby preventing condensate from breaking through cold-WP locations along the drift. Altogether, the underprediction of condensate shedding between drifts and condensate breakthrough at cold-WP locations causes the east-west cross-sectional mountain-scale model to build up more condensate above the repository horizon that leads to unstable heat-pipe behavior. This unstable behavior is exhibited by the rapid decline from superheated conditions to heat-pipe conditions (Figure 6-68a) and the rapid rise once again to superheated conditions at about 400 yr. Notice that during the second superheated period predicted by the east-west model, the temperature climbs to be almost exactly that predicted by the MSTHM.

Given the differences between the MSTHM and the east-west cross-sectional mountain-scale model, the agreement between the two models is quite good. On the basis of this comparison, it is determined that the MSTHM is validated for its intended use.

#### **6.14 THREE-DIMENSIONAL HETEROGENEOUS LDTH MODEL**

Because it is computationally much more viable than three-dimensional TH models, the two-dimensional line-averaged-heat-source, drift-scale thermohydrologic (LDTH) model has been an important tool in investigating and analyzing thermohydrologic behavior at the drift scale. For example, LDTH models have been used to investigate coupled thermohydrologic-geochemical behavior in the *Drift-Scale Coupled Processes (Drift-Scale Test and THC Seepage) Models AMR REV01* (CRWMS M&O, 2001a, Section 6.) as well as in the *Water Distribution and Removal AMR REV01* (CRWMS M&O, 2001d). The LDTH model is also the “core” submodel used in the MSTHM methodology. Because the MSTHM incorporates LDTH submodels at 31 locations in the repository, it captures the influence of repository-scale variability of hydrologic properties and conditions, such as infiltration flux. However, as currently incorporated in the MSTHM, the 2-D LDTH submodels do not account for the influence of drift-scale heterogeneity, most notably, the influence of drift-scale heterogeneity of fracture properties, including permeability, porosity, and the capillary properties (the most important being the van Genuchten “alpha” parameter).

Over nearly the entire range of infiltration-flux conditions considered in the MSTHM calculations for the no-backfill case (see Section 6.12), seepage into the drift is not predicted to occur. Nonzero drift-seepage fluxes are only predicted to occur in regions of the repository having the highest infiltration (and percolation) flux for the “upper” infiltration-flux case. Two important reasons for the very low occurrence of predicted drift seepage is the fact that the 1-D drift-scale basecase hydrologic property set (Section 4.1.7) used throughout this AMR has fracture properties that are isotropic and homogeneous within any given hydrostratigraphic unit. Thus, the LDTH submodels incorporate a uniform (and isotropic) fracture continuum within any given hydrostratigraphic unit (particularly the host-rock units).. These conditions, together with the use of a 2-D LDTH submodel, reduces the tendency for the occurrence of drift seepage to be predicted (Tsang et al. 1997).

The purpose of this section (6.14) is to present results of a 3-D heterogeneous LDTH model that represents drift-scale heterogeneity of fracture properties in the host rock. This is the first major step in incorporating the influence of drift-scale heterogeneity in the MSTHM. To facilitate the ability of observing the influence of seepage on TH conditions in the drift, some of the stochastic realizations of heterogeneous fracture properties were deliberately chosen to assure that seepage would occur under the ambient present-day climate infiltration-flux conditions, as well as under the monsoonal- and glacial-climate conditions. This should not be interpreted as being an indication of whether such heterogeneous conditions are realistic. Rather, they should be regarded as extreme examples of fracture heterogeneity that were selected to be more heterogeneous than indicated by field measurements (CRWMS M&O, 2000j) and thereby substantially challenge the hypothesis that boiling conditions at the drift wall are capable of thwarting seepage. Therefore, a primary objective of this section (6.14) is determining whether fracture heterogeneity can result in liquid-phase flow penetrating through the boiling zone and/or a reduction in the duration of boiling. Another key objective is determining which TH variables

are caused (by drift-scale fracture heterogeneity) to deviate most significantly from the values predicted by the MSTHM (see Section 6.12). In this section a sensitivity analysis is also conducted to observe the importance of correlating capillary fracture properties with the fracture permeability  $k$  and to observe the influence of correlation lengths and standard deviation of fracture permeability.

Most of the heterogeneous cases selected for analysis in Section 6.14 lie outside of the range of expected heterogeneous characteristics based on field measurements (CRWMS M&O, 2000j). Consequently, the results reported in Section 6.14 are not expected to be comparable with seepage calculations that directly utilize those field measurements to characterize heterogeneity.

### **6.14.1 Physics of Seepage into an Open Cavity**

Flow in an unsaturated porous medium is governed by three forces: viscous, gravitational, and matric (capillary + osmotic). As long as the total head in fracture or matrix pore water is maintained to be less than total head in the drift, by virtue of matric forces, seepage cannot flow into the drift. Matric forces are caused by the sum of capillary pressure and surface forces at or near the pore walls. At high liquid-phase saturation, or for large pore sizes, such as in fractures, gravitational forces predominate. If flow is sufficiently high, a combination of gravitational and viscous forces will eventually overcome matric forces, and seepage into the drift can occur. In particular, as water flows around a drift, it has to travel a longer distance than does water following the flow lines farther away from the drift. From Darcy's law, the total head must therefore be higher in the vicinity of the crown of the drift than it is down the flanks of the upper drift wall (or at the sides of the drift). Because water is essentially incompressible, liquid flow diverted around a drift opening must flow faster than where there is no opening. The increased flux down the flanks of the upper drift wall (above the springline) also contributes to increased total head. If the magnitude of capillary pressure is reduced sufficiently (by virtue of the liquid-phase saturation increase) such that the gradient of total head allows downward flow above the opening, then seepage can enter the opening.

Natural heterogeneity in the hydrologic properties in the host rock (notably those of the fractures) can increase the likelihood for seepage through a variety of mechanisms. Low-permeability areas can obstruct flow and divert flow paths so they are longer, thus increasing the pressure above drift openings. Along preferential flow pathways, stream lines are concentrated, thus producing higher saturation than in the surrounding area. Because of spatial variability in hydrologic properties, there also may be localized regions with very low air-entry pressure (i.e., areas in which the fractures drain more readily). In some cases, heterogeneities may actually reduce the likelihood of seepage by diverting flow away from drift openings. However, reduction of seepage in certain areas of the repository may increase the likelihood of seepage in other locations.

The addition of boiling conditions introduces another mechanism that can attenuate potential seepage into the drift. However, boiling conditions in a highly heterogeneous fracture network can generate local liquid-phase fluxes that are much greater than would occur under ambient conditions. The key question is whether the focusing of ambient percolation and condensate flux can result in a local liquid-phase flux that overwhelms the local heat flux (and corresponding local evaporation rate). A modeling study by Pruess (1997) demonstrated that penetration of a

liquid front into the boiling zone is considerably greater for a heterogeneous case than it is for an equivalent homogeneous case. Capturing such behavior with a numerical model requires the use of very fine grid-block resolution. Pruess (1997) used grid blocks that were 0.2 m × 0.2 m in his modeling study.

Another key mechanism affecting the likelihood of seepage is nonequilibrium fracture-matrix flow. The dual-permeability model (DKM) conceptualizes fractured rock as having two interacting continua, one representing the matrix and the other representing the fracture network. Fluxes of mass and heat between the fracture network and the matrix at each point in the model domain, are calculated from the local temperature and pressure differences. These differences can be nonzero; thus, nonequilibrium conditions can exist at that point. This feature of the DKM allows for more realistic treatment of transient behavior when conditions such as saturation and temperature are changing with time.

The active-fracture concept (AFC) is a scheme for dynamic modification of the contact area between the fracture network and the matrix (Liu et al. 1998). The underlying concept is that fracture flow occurs through some, but not all, of the fractures at a given location and time. This tends to produce stronger nonequilibrium response than does assuming that flux is uniformly distributed through all fractures. Flow through a fracture is greater when it has higher saturation, and focusing of flux through a limited population of active fractures tends to maximize the saturation, thereby enhancing fast pathways for flux through the mountain.

Finally, thermal radiation in the drift cavity is an additional key mechanism that will influence whether seepage at the drift wall is capable of dripping onto the drip shield. Thermal-radiative heat flux is driven by the difference of the fourth power of temperature ( $T^4$ ). Thus very small deviations in temperature can result in a much greater delivery of heat flow to slightly cooler regions than would occur in a purely conductive heat flow system. As an incipient seep begins to form at the crown of the drift, the local temperature at this seep will be lower than the surrounding drift-wall surfaces. Thermal-radiative heat flow will be preferentially delivered to this incipient seep, increasing the local evaporation rate significantly above that which would be associated with a purely conductive heat-flow system.

### 6.14.2 Random-Field Generation

A random field is a set of random variables defined over either a continuous or a discrete portion of space (see Vanmarcke 1983, Chapter 1). The random variables are usually statistically correlated, with the degree of correlation depending on location and on the direction and separation distance between points. For the seepage calculations described in this section, the random field was generated by the Fourier spectral method in three dimensions (Nitao 1997); the random fields were for the key fracture properties: permeability, porosity, and the van Genuchten “alpha” parameter.

The value of the constant of proportionality used in the Fourier method is irrelevant because the resulting random field minus the mean is normalized by its standard deviation and then multiplied by the desired standard deviation. The random field algorithm is fully integrated into the NUFT code (Nitao 1993, 1998). The problem domain can be divided into subdomains, each

with its own random field structure. Any of the hydrologic parameters can be a function of as many as three independent random fields per subdomain. The random-field generator works seamlessly with the dual permeability capability in NUFT to generate matrix and fracture properties that can be statistically independent or dependent.

### **6.14.3 Findings from Previous Seepage-Model Studies**

Principal features that distinguish seepage models from other drift-scale hydrologic models is the fineness of the model grid and the incorporation of heterogeneous fracture properties. Studies of isothermal seepage (Tsang et al. 1997) and nonisothermal seepage (Nitao 1997; Hardin et al. 1998, Section 3.6) have resulted in the following major findings:

- Average seepage rate increases with introduction of heterogeneous fracture properties.
- The threshold percolation flux (wherein the onset seepage can occur) is reduced with the introduction of heterogeneous fracture properties.
- Average seepage rate increases when episodic infiltration is imposed on a DKM model.
- Seepage decreases for 3-D models when compared with corresponding 2-D models.
- In the absence of drift ventilation, water may be present in the drift immediately after emplacement as a result of condensation in the drift.

### **6.14.4 Description of 3-D Heterogeneous LDTH Model**

The 3-D heterogeneous LDTH models used in this section are all based on the 2-D LDTH submodel at the 14c3 location (see Section 6.3), which is close to the geographic center of the repository and which is used in the MSTHM no-backfill calculations (Section 6.12). The mean infiltration-flux case is modeled. As shown in Table 6-7, the 14c3 location has infiltration fluxes that are higher than the repository averages for the present-day, monsoonal, and glacial climates. The host-rock unit at this location is the tsw35 model unit (Ttptll unit), which is the predominant host-rock unit in the repository. For ICN2 of this AMR the assumed dimensions in the drift (Figure 6-2b) are nearly the same as in previous calculations in this AMR (Figure 6-2a), with the following minor exceptions:

- Invert height is 0.806 m (instead of 0.606 m) (Section 5.4.3.10).
- Drip-shield height is 2.521 m (instead of 2.566 m) (Section 5.4.3.11).
- Drip-shield radius is 1.256 m (instead of 1.251 m) (Section 5.4.3.5).
- These minor differences in the in-drift geometry resulted from minor revisions to the EBS design (CRWMS M&O, 2000e).

Table 6-7. Infiltration-flux values for the mean infiltration-flux case

	Present-day (mm/yr)	Monsoonal (mm/yr)	Glacial (mm/yr)
<b>14c3 location</b>	10.14	24.09	38.66
<b>Repository average</b>	5.98	16.07	24.86

In the vertical xz cross-sectional plane, the 2-D and 3-D LDTH models are nearly identical. The lateral gridding in the 2-D and 3-D LDTH models used in Section 6.14 is slightly more refined outside of the drift than was used in the LDTH submodels used in the MSTHM calculations described in Sections 6.11 and 6.12. This increased refinement was used to assure that drift-scale heterogeneity would be represented with adequate resolution in the immediate vicinity of the drift. Notice that the grid refinement in the LDTH model is greatest for the upper half of the drift above the springline (Figure 6.2) to assure adequate representation of flow diversion around the drift and seepage into the drift. In the vertical xz cross-sectional plane, the grid-block dimensions at the drift wall above the springline vary from a maximum of 0.58 m (wide)  $\times$  0.2 m (high) to a minimum of 0.2996 m  $\times$  0.2 m.

The 3-D LDTH model has an axial dimension of 5 m (approximately the length of one waste package). The grid-block spacing in the axial direction is 1.0 m. For the 56-MTU/acre cases, the 3-D LDTH models have a total of 6800 grid blocks (17 blocks laterally  $\times$  5 blocks axially  $\times$  80 blocks vertically). For the 34-MTU/acre cases, the 3-D LDTH models have a total of 7200 grid blocks (18 blocks  $\times$  5 blocks  $\times$  80 blocks). Because these models incorporate the DKM approximation (which doubles the number of grid blocks), the effective total number of grid blocks are 13,600 and 14,400 for the 56- and 34-MTU/acre models, respectively.

The influence of thermal radiation and natural convection on heat transfer in the drift is represented with the use of an effective thermal conductivity  $K_{\text{eff}}$  for the air in the drift (CRWMS M&O 2001b, Attachment I). The file modprop-dr-20 works in conjunction with the file dkm-afc-EBS\_Rev20a, which contains the hydrologic and thermal properties of the components in the EBS. The thermal conductivity for the air found in the file dkm-afc-EBS\_Rev20a is multiplied by the factor in the file modprop-dr-20, which is a function of time, yielding the effective thermal conductivity  $K_{\text{eff}}$  of the air in the cavity in the drift as a function of time. The value of  $K_{\text{eff}}$  in the drift declines as a function of time for two reasons. First, the effectiveness of thermal radiation, which is the primary mode of heat transfer in the drift, declines with temperature, which in turn declines with time. Second, the influence of natural convection declines with the temperature gradient between the drip shield and the drift wall. Because this gradient declines with time, the effectiveness of natural convection declines with time. It was determined in CRWMS M&O (2001b, Attachment I) that  $K_{\text{eff}}$  reaches its peak at 65 yr (when  $K_{\text{eff}} = 14.407 \text{ W/m}^{\circ}\text{C}$ ). Note that this is approximately when peak temperatures occur in the drift. At 1,000,000 yr, the value of  $K_{\text{eff}}$  has declined to 4.39  $\text{W/m}^{\circ}\text{C}$ .

As discussed in Section 5.3.3,  $K_{\text{eff}}$  is not dependent on AML. Therefore, the values of  $K_{\text{eff}}$  listed above for when peak temperature occurs ( $K_{\text{eff}} = 14.407 \text{ W/m}^{\circ}\text{C}$ ) and for 1,000,000 yr ( $K = 4.39 \text{ W/m}^{\circ}\text{C}$ ) pertain to both the 56- and 34-MTU/acre models, both of which are models that pertain to the no-backfill case. As discussed in Section 5.3.3, because the heterogeneous 3-D LDTH

model calculations have negligible temperature variation in the third (axial) direction (e.g., see Figure 6-83), the time-dependent  $K_{\text{eff}}$  are equally applicable to the 3-D LDTH and 2-D LDTH models.

The 3-D LDTH model treats the upper 39.7 m of the host-rock unit (Tptpl) as having heterogeneous fracture properties, including 17.4 m above the drift and 16.8 m below the drift, as well as the entire lateral extent of that region (i.e., to the mid-pillar location separating drifts). Eight stochastic realizations were modeled (Table 6-8). Four of the realizations were for an AML of 56 MTU/acre, which is representative of heating conditions at the center of the repository. Four of the realizations were for an AML of 34 MTU/acre, which is representative of heating conditions close to the repository edge.

In the heterogeneous fracture field, fracture permeability in any given gridblock is isotropic (just as it is in the hydrostratigraphic units that have homogeneous fracture permeability). All stochastic realizations use a log-normal distribution with values of  $\log_{10}$  standard deviation and correlation lengths in the principal directions listed in Table 6-8. Stochastic realizations A-56, A-34, B-56, and B-34 have a  $\log_{10}$  standard deviation of 0.652, which is closer to the value of 0.72 determined from air-permeability data performed at Niche 3650 (CRWMS M&O, 2000j, Table 5, p. 43). However, these realizations also have a larger correlation length in the vertical direction than in the horizontal directions, to increase the vertical focusing of flow and thereby increase the likelihood of seepage into the drift. Figure 6-69 shows the fracture-permeability field for stochastic realization A-56. The larger correlation length in the vertical direction results in a predominant vertical orientation to the heterogeneities. This vertical biasing of correlation length is qualitatively different from the gas-permeability measurements made in Niche 3650 (CRWMS M&O, 2000j, Figure 17, p. 49) that indicated no biasing in correlation length.

Capillary pressure and relative permeability are described by van Genuchten's function (Luckner et al. 1989, pp. 2191-2192), with the capillary-strength parameter  $1/\alpha$  correlated to the heterogeneous fracture permeability field according to Leverett's scaling rule (Leverett 1941, p. 159). Six of the stochastic realizations incorporate this correlation between capillary-strength and fracture permeability, while two of the cases (B-56 and B-34) incorporate a constant value of capillary strength throughout the domain with fracture heterogeneity (just as is done in the hydrostratigraphic units with homogeneous fracture permeability). All eight realizations have a fracture porosity  $\sigma$  that is correlated to the heterogeneous fracture permeability field according to the cubic law (Bear 1972, p. 164).

Because they utilized the same random-field-generation "seed" value, the fracture-permeability  $k$  fields of cases A-56 and B-56 are identical (Figure 6-69), just as are the  $k$  fields of cases A-34 and B-34. Comparisons between these two pairs of cases allows for observations about the significance of spatial heterogeneity of capillary strength in the fractures. Note that the fracture heterogeneity of cases A-56 and A-34 are similar, but not identical. Even though random-field generator started with the same seed value, the fact that the 34-MTU/acre case has a larger distance between drifts (and therefore generated random values over a spatially larger domain than the 56-MTU/acre case), it resulted in a different realization. Had we confined the lateral extent of the spatial domain of the random field to be a fixed distance from the drift centerline (e.g., 30 m) for both A-34 and A-56 cases, it would have resulted in identical stochastic

realizations for these respective cases. In future calculations we will take the approach of having a fixed lateral extent to the random-field domain so that the random fields for a suite of 3-D LDTH models (for example, with AMLs of 14, 34, 56, and 66 MTU/acre) will be identical for a given seed. As discussed in Section 6.6, it is necessary to have such a suite of models to generate scanning curves.

Table 6-8. List of statistical parameters used in the 3-D heterogeneous LDTH-model realizations

Stochastic Realization	Standard Deviation of $k$ ( $\log_{10}$ )	Correlation Length (m)			van Genuchten alpha value correlated to $k$
		lateral (x)	axial (y)	vertical (z)	
A-56	0.652	0.5	0.5	4.0	yes
A-34	0.652	0.5	0.5	4.0	yes
B-56	0.652	0.5	0.5	4.0	no
B-34	0.652	0.5	0.5	4.0	no
C-56	0.435	1.0	1.0	1.0	yes
C-34	0.435	1.0	1.0	1.0	yes
D-56	1.0	1.0	1.0	2.0	yes
D-34	1.0	1.0	1.0	2.0	yes

Stochastic realizations C-56 and C-34 have a value of  $\log_{10}$  standard deviation (0.435) in  $k$ , that is smaller than the value (0.72) determined from the gas-permeability measurements made in Niche 3650 (CRWMS M&O, 2000j, Table 5, p. 43). These realizations have no vertical biasing to the shape of heterogeneities, which is qualitatively consistent with the gas-permeability measurements made in Niche 3650 (CRWMS M&O, 2000j, Figure 17, p. 49). Because of the smaller standard deviations and lack of anisotropy, these realizations are less heterogeneous examples of fracture-permeability distributions than the other six realizations. Stochastic realizations D-56 and D-34 have a larger  $\log_{10}$  standard deviation (1.0) in fracture permeability  $k$  than the other cases. These realizations also have a smaller contrast in correlation lengths in the principal directions than do these A and B realizations. This vertical biasing of correlation length is qualitatively different from the gas-permeability measurements made in Niche 3650 (CRWMS M&O, 2000j, Figure 17, p. 49) that indicated no biasing in correlation length.

#### 6.14.5 3-D Heterogeneous LDTH-Model Results

The purpose of Section 6.14 is to investigate the influence of heterogeneous fracture properties on the potential for seepage during the boiling and post-boiling periods. A primary objective of this section is determining whether fracture heterogeneity can result in liquid-phase flow penetrating through the boiling zone and/or a reduction in the duration of boiling. Another objective is determining which TH variables are caused (by drift-scale fracture heterogeneity) to deviate most significantly from the values predicted by the MSTHM. Table 6-9 lists all of the plots of TH conditions that are discussed in Section 6.14. Table 6-10 summarizes the seepage conditions in the drift at 1,000,000 yr.

Table 6-9. List of plots of TH conditions calculated with the 3-D heterogeneous LDTH and 2-D homogeneous LDTH models

Figure No.	TH Variable	Source DTN	Source File Name
Figure 6-69	Contours of the bulk permeability field for stochastic realization A-56	LL010802723122.019	I4c3-LDTH56-1Dds_mc-mi-40-02.f.EBS.ext
Figure 6-70	Liquid-phase saturation in fractures and matrix for stochastic realization A-56 at 50 yr	LL010802723122.019	I4c3-LDTH56-1Dds_mc-mi-40-02.m.EBS.ext I4c3-LDTH56-1Dds_mc-mi-40-02.f.EBS.ext
Figure 6-71	Temperature and relative humidity for stochastic realization A-56 at 50 yr	LL010802723122.019	I4c3-LDTH56-1Dds_mc-mi-40-02.m.EBS.ext
Figure 6-72	Liquid-phase saturation in fractures and matrix for stochastic realization A-56 at 60 yr	LL010802723122.019	I4c3-LDTH56-1Dds_mc-mi-40-02.m.EBS.ext I4c3-LDTH56-1Dds_mc-mi-40-02.f.EBS.ext
Figure 6-73	Temperature and relative humidity for stochastic realization A-56 at 60 yr	LL010802723122.019	I4c3-LDTH56-1Dds_mc-mi-40-02.m.EBS.ext
Figure 6-74	Liquid-phase saturation in fractures and matrix for stochastic realization A-56 at 1900 yr	LL010802723122.019	I4c3-LDTH56-1Dds_mc-mi-40-02.m.EBS.ext I4c3-LDTH56-1Dds_mc-mi-40-02.f.EBS.ext
Figure 6-75	Temperature and relative humidity for stochastic realization A-56 at 1900 yr	LL010802723122.019	I4c3-LDTH56-1Dds_mc-mi-40-02.m.EBS.ext
Figure 6-76	Liquid-phase flux for stochastic realization A-56 at 1900 yr	LL010802723122.019	I4c3-LDTH56-1Dds_mc-mi-40-02.f.EBS.ext
Figure 6-77	Liquid-phase saturation in fractures and matrix for stochastic realization A-34 at 50 yr	LL010802723122.019	I4c3-LDTH34-1Dds_mc-mi-40-02.m.EBS.ext I4c3-LDTH34-1Dds_mc-mi-40-02.f.EBS.ext
Figure 6-78	Temperature and relative humidity for stochastic realization A-34 at 50 yr	LL010802723122.019	I4c3-LDTH34-1Dds_mc-mi-40-02.m.EBS.ext
Figure 6-79	Liquid-phase saturation in fractures and matrix for stochastic realization A-34 at 60 yr	LL010802723122.019	I4c3-LDTH34-1Dds_mc-mi-40-02.m.EBS.ext I4c3-LDTH34-1Dds_mc-mi-40-02.f.EBS.ext
Figure 6-80	Temperature and relative humidity for stochastic realization A-34 at 60 yr	LL010802723122.019	I4c3-LDTH34-1Dds_mc-mi-40-02.m.EBS.ext

Table 6-9. List of plots of TH conditions calculated with the 3-D heterogeneous LDTH and 2-D homogeneous LDTH models (Continued)

Figure No.	TH Variable	Source DTN	Source File Name
Figure 6-81	Liquid-phase saturation in fractures and matrix for stochastic realization A-34 at 700 yr	LL010802723122.019	I4c3-LDTH34-1Dds_mc-mi-40-02.m.EBS.ext I4c3-LDTH34-1Dds_mc-mi-40-02.f.EBS.ext
Figure 6-82	Temperature and relative humidity for stochastic realization A-34 at 700 yr	LL010802723122.019	I4c3-LDTH34-1Dds_mc-mi-40-02.m.EBS.ext
Figure 6-83	Temperature and relative humidity for stochastic realization A-56 and for 2-D homogeneous LDTH model	LL010802723122.019	I4c3-LDTH56-1Dds_mc-mi-40-02.f.EBS.ext I4c3-LDTH56-1Dds_mc-mi-40.f.EBS.ext
Figure 6-84	Temperature for stochastic realization A-56 and for 2-D homogeneous LDTH model	LL010802723122.019	I4c3-LDTH56-1Dds_mc-mi-40-02.f.EBS.ext I4c3-LDTH56-1Dds_mc-mi-40.f.EBS.ext
Figure 6-85	Evaporation rate for stochastic realization A-56 and for 2-D homogeneous LDTH model	LL010802723122.019	I4c3-LDTH56-1Dds_mc-mi-40-02.f.EBS.ext I4c3-LDTH56-1Dds_mc-mi-40.f.EBS.ext
Figure 6-86	Liquid-phase flux for stochastic realization A-56	LL010802723122.019	I4c3-LDTH56-1Dds_mc-mi-40-02.f.EBS.ext
Figure 6-87	Seepage pattern on crown of drift	LL010802723122.019	I4c3-LDTH56-1Dds_mc-mi-40-02.f.EBS.ext
Figure 6-88	Temperature and relative humidity for stochastic realization A-34 and for 2-D homogeneous LDTH model	LL010802723122.019	I4c3-LDTH34-1Dds_mc-mi-40-02.f.EBS.ext I4c3-LDTH34-1Dds_mc-mi-40.f.EBS.ext
Figure 6-89	Liquid-phase flux for stochastic realization A-34	LL010802723122.019	I4c3-LDTH34-1Dds_mc-mi-40-02.f.EBS.ext
Figure 6-90	Liquid-phase flux for stochastic realizations A-56 and A-34	LL010802723122.019	I4c3-LDTH56-1Dds_mc-mi-40-02.f.EBS.ext I4c3-LDTH34-1Dds_mc-mi-40-02.f.EBS.ext
Figure 6-91	Temperature and relative humidity for stochastic realization B-56 and for 2-D homogeneous LDTH model	LL010802723122.019	I4c3-LDTH56-1Dds_mc-mi-40-12.f.EBS.ext I4c3-LDTH56-1Dds_mc-mi-40.f.EBS.ext
Figure 6-92	Liquid-phase flux for stochastic realization B-56	LL010802723122.019	I4c3-LDTH56-1Dds_mc-mi-40-12.f.EBS.ext
Figure 6-93	Temperature and relative humidity for stochastic realization B-34 and for 2-D homogeneous LDTH model	LL010802723122.019	I4c3-LDTH34-1Dds_mc-mi-40-12.f.EBS.ext I4c3-LDTH34-1Dds_mc-mi-40.f.EBS.ext
Figure 6-94	Liquid-phase flux for stochastic realization B-34	LL010802723122.019	I4c3-LDTH34-1Dds_mc-mi-40-12.f.EBS.ext
Figure 6-95	Temperature and relative humidity for stochastic realization C-56 and for 2-D homogeneous LDTH model	LL010802723122.019	I4c3-LDTH56-1Dds_mc-mi-40-20.f.EBS.ext I4c3-LDTH56-1Dds_mc-mi-40.f.EBS.ext
Figure 6-96	Liquid-phase flux for stochastic realization C-56	LL010802723122.019	I4c3-LDTH56-1Dds_mc-mi-40-20.f.EBS.ext

Table 6-9. List of plots of TH conditions calculated with the 3-D heterogeneous LDTH and 2-D homogeneous LDTH models (Continued)

Figure No.	TH Variable	Source DTN	Source File Name
Figure 6-97	Temperature and relative humidity for stochastic realization C-34 and for 2-D homogeneous LDTH model	LL010802723122.019	I4c3-LDTH34-1Dds_mc-mi-40-20.f.EBS.ext I4c3-LDTH34-1Dds_mc-mi-40.f.EBS.ext
Figure 6-98	Liquid-phase flux for stochastic realization C-34	LL010802723122.019	I4c3-LDTH34-1Dds_mc-mi-40-20.f.EBS.ext
Figure 6-99	Temperature and relative humidity for stochastic realization D-56 and for 2-D homogeneous LDTH model	LL010802723122.019	I4c3-LDTH56-1Dds_mc-mi-40-01.f.EBS.ext I4c3-LDTH56-1Dds_mc-mi-40.f.EBS.ext
Figure 6-100	Liquid-phase flux for stochastic realization D-56	LL010802723122.019	I4c3-LDTH56-1Dds_mc-mi-40-01.f.EBS.ext
Figure 6-101	Temperature and relative humidity for stochastic realization D-34 and for 2-D homogeneous LDTH model	LL010802723122.019	I4c3-LDTH34-1Dds_mc-mi-40-01.f.EBS.ext I4c3-LDTH34-1Dds_mc-mi-40.f.EBS.ext
Figure 6-102	Liquid-phase flux for stochastic realization D-34	LL010802723122.019	I4c3-LDTH34-1Dds_mc-mi-40-01.f.EBS.ext

Table 6-10. Summary of seepage conditions at 1,000,000 yr where seepage percentage is the fraction of the incident average percolation flux

Stochastic Realization	Seepage Percentage Entering Drift (%)	Seepage Percentage Contacting Drip Shield (%)
A-56	37.5	30.4
A-34	54.8	13.6
B-56	27.9	0.1
B-34	21.3	4.4
C-56	0.0	0.0
C-34	0.0	0.0
D-56	42.9	11.0
D-34	85.5	26.4

Before discussing the various stochastic realizations in detail (shown in Figures 6-69 through 6-82), some general observations can be made, particularly from the history plots (Figures 6-83 through 6-86 and Figures 6-87 through 6-102) and from Table 6-10. Note that in the following discussion, the term “*RH* reduction” refers to the reduction of *RH* relative to ambient conditions, which are close to 100 percent. A primary outcome of temperature gradients in the drift is to cause a reduction in *RH* in the drift, relative to (humid) ambient conditions. General observations about the influence of heterogeneity on seepage and on thermohydrologic conditions in the drifts are as follows:

- The likelihood and magnitude of seepage increase with the  $\log_{10}$  of the standard deviation of the fracture permeability. (Compare Figures 6-96 and 6-100; also compare Figures 6-98 and 6-102).

- The likelihood and magnitude of seepage increase with the ratio of vertical to horizontal correlation length. (Compare Figures 6-86 and 6-100; also compare Figures 6-89 with 6-102).
- Correlating the capillary-strength parameter  $1/\alpha$  of the fractures with the fracture permeability according to Leverett's scaling rule resulted in a greater seepage magnitude than cases for which  $1/\alpha$  was constant. (Compare Figures 6-86 with 6-92; also compare Figures 6-89 with 6-94).
- The duration of boiling is never reduced as a result of fracture heterogeneity (for example, see Figures 6-83a, 6-83c, and 6-84). In fact, the duration of boiling is slightly greater for the heterogeneous cases than for the homogeneous cases. The greater duration of boiling for the heterogeneous cases results from the influence of buoyant gas-phase convection being reduced by the heterogeneous fracture-permeability distribution, with the low- $k$  features obstructing buoyant gas-phase convection. Thus, buoyant gas-phase convection plays a less significant role in the rate of cool down in the drift for the heterogeneous cases than for a corresponding homogeneous case.
- Temperatures at the drift wall or on the drip shield are insensitive to heterogeneity during both the boiling and post-boiling periods, with the exception that there is a slight increase in the duration of the boiling period for the heterogeneous cases. (See Figures 6-83, 6-88, 6-91, 6-93, 6-95, 6-97, 6-99, 6-101).
- Relative humidity in the drift is unaffected by fracture heterogeneity during the boiling period (See Figures 6-83, 6-88, 6-91, 6-93, 6-95, 6-97, 6-99, 6-101).
- Relative humidity reduction in the drift is diminished (as compared to that predicted by the 2-D homogeneous LDTH model) during the post-boiling period only for cases where seepage contacts the drip shield (for example, see Figures 6-83d and 6-88d). The diminishment of  $RH$  reduction is indicated by the fact that the drip-shield  $RH$  histories for the five axial locations ( $j = 1-5$ ) in the 3-D heterogeneous LDTH model deviate (by becoming more humid) from the  $RH$  history predicted by the 2-D homogeneous LDTH model (which has no seepage). For cases that have no seepage contacting the drip shield (Figures 6-95d and 6-97d)  $RH$  reduction is not diminished at all. The absence of the diminishment of  $RH$  reduction is indicated by the fact that the drip-shield  $RH$  histories for all five axial locations ( $j = 1-5$ ) in the 3-D heterogeneous LDTH model are identical to that predicted by the 2-D homogeneous LDTH model. Note that the magnitude of the differences in  $RH$  reduction between the cases with seepage and those without seepage is relatively small (generally less than 1 percent). These small differences in  $RH$  reduction should have a negligible effect on in-drift behavior.
- In the *Water Distribution and Removal Model* AMR (for example, see Figure 6-37 of CRWMS M&O 2001d)  $RH$  reduction was found to be increasingly diminished during the post-boiling period with increasing seepage flux onto the drip shield. All of the stochastic realizations with seepage contacting the drip shield (A-56, A-34, B-56, B-34, D-56, and D-34) resulted in large enough seepage fluxes wherein the distinctions in the diminishment of  $RH$  reduction among these cases is extremely small and therefore difficult to see when comparing the respective drip-shield  $RH$  histories during the post-boiling period (Figures 6-

83d, 6-88d, 6-91d, 6-93d, 6-99d, and 6-101d). In general, the differences in *RH* reduction are less than 1 percent among these cases, which is comparable to the differences observed in the *Water Distribution and Removal Model* AMR (CRWMS M&O 2001d). These small differences in *RH* reduction should have a negligible effect on in-drift behavior.

- For the cases with no seepage contacting the drip shield (Figure 6-95 and 6-97), the *T* and *RH* histories at the drift wall and drip shield for all five axial locations ( $j = 1-5$ ) in the 3-D heterogeneous LDTH model are virtually identical to that predicted by the 2-D homogeneous LDTH model, which is the core *TH* model used in the MSTHM. Therefore, a heterogeneous fracture permeability distribution in the host rock does not cause the *T* and *RH* distribution along the drift to deviate from that predicted by a homogeneous 2-D LDTH model. This means that the MSTHM adequately represents *T* and *RH* on the drip shield for situations with heterogeneous fracture permeability in the host rock as long as seepage onto the drip shield does not occur.
- For the cases with seepage contacting the drip shield (Figures 6-83, 6-88, 6-91, 6-93, 6-99 and 6-101), the drift-wall *T* and *RH* histories for all five axial locations ( $j = 1-5$ ) in the 3-D heterogeneous LDTH model are identical to that predicted by the 2-D homogeneous LDTH model, which is the core *TH* model used in the MSTHM. Therefore, a heterogeneous fracture permeability distribution in the host rock does not cause the *T* and *RH* distribution along the drift wall to deviate from that predicted by a homogeneous 2-D LDTH model. This means that the MSTHM adequately represents *T* and *RH* on the drift wall for situations with heterogeneous fracture permeability in the host rock even if seepage contacts the drip shield.

These observations clearly indicate that the thermohydrologic conditions calculated by the MSTHM for the no-backfill case (Section 6.12) would not be changed during the boiling period by virtue of adding the influence of drift-scale heterogeneity of fracture properties. These observations also indicate that temperatures calculated by the MSTHM for the no-backfill case would not be significantly changed during either the boiling or post-boiling period by virtue of adding the influence of fracture heterogeneity.

Note that the differences in seepage percentage (Table 6-10) between cases A-56 and A-34, or between B-56 and B-34, or between D-56 and D-34, are not related to the different AMLs for these respective pairs of cases. For each of these respective pairs of cases, the fracture heterogeneity is similar, but not identical. Even though random-field generator started with the same set of statistical parameters and the same seed value, the fact that the 34-MTU/acre case has a larger distance between drifts (and therefore generated random values over a spatially larger domain than the 56-MTU/acre case), it resulted in a different realization than the 56-MTU/acre case. The most significant difference between the 56-MTU/acre cases and the 34-MTU/acre cases is the duration of boiling and the onset of potential seepage into the drift. The seepage percentages listed in Table 6-10 pertain to the post-boiling period when the only potential AML-dependent factor is the temperature of the near-field host rock. The only way the sub-boiling temperature differences between a 56-MTU/acre case and a corresponding 34-MTU/acre could possibly influence seepage is with respect to the temperature-dependent properties of water. For the temperature differences between any given pair of cases (e.g., compare Figure 6-83a with Figure 6-88a) such differences in property values for water are much too small

to be the cause of the differences in seepage percentage shown in Table 6-10 between the pairs of cases.

The primary thermohydrologic quantities predicted by the MSTHM for the no-backfill case that would be affected by the inclusion of drift-scale heterogeneity are as follows:

- Relative humidity  $RH$  on the drip shield would be increased during the post-boiling period only for cases where seepage contacted the drip shield. Because  $RH$  during the post-boiling period is already relatively high for the post-boiling period of the no-backfill case, the magnitude of the increase of  $RH$  would be relatively small. The probability of occurrence of increased  $RH$  on the drip shield would also be small.
- Evaporation rate on the drip shield would be increased during the post-boiling only for cases where seepage contacted the drip shield. The magnitude of this increase in evaporation rate increases with the magnitude of seepage onto the drip shield and decreases with time (as the heat output from waste packages decreases).

#### 6.14.5.1 Thermohydrologic Seepage Behavior for Realizations A-56 and A-34

Figure 6-70 shows the distributions of liquid-phase saturation  $S_{liq}$  in the fractures and matrix for stochastic realization A-56 at 50 yr, which is the end of the pre-closure ventilation period. Figure 6-71 shows the corresponding distributions of temperature  $T$  and relative humidity  $RH$ . Note that the potential drying effects of drift ventilation are not represented in this calculation. Had a low- $RH$  boundary condition been imposed in the drift, this would have resulted in drier conditions in the drift and in the host rock. Notice that  $S_{liq}$  in the fractures show a very similar structure as the fracture permeability distribution (compare Figure 6-70a with Figure 6-69c and compare Figure 6-70b with Figure 6-69e). Figure 6-72 shows the  $S_{liq}$  distributions and Figure 6-73 shows the corresponding distributions of  $T$  and  $RH$  at 60 yr, which is about the time when drift-wall and waste-package temperatures reach their peak values. Whereas  $S_{liq}$  in the matrix,  $T$ , and  $RH$  have relatively smooth distributions,  $S_{liq}$  in the fractures is very heterogeneous outside of the boiling zone.

Boiling conditions at the drift wall persist for about 1050 yr for stochastic realization A-56 (Figures 6-83a and 6-84a). Seepage at the crown of the drift commences at 1100 yr, which is shortly after the end of the boiling period (Figure 6-86c). However, evaporation at the crown of the drift prevents this seepage from contacting the drip shield until 1900 yr (Figure 6-86d). Figure 6-74 shows the  $S_{liq}$  distributions and Figure 6-75 shows the corresponding distributions of  $T$  and  $RH$  at 1900 yr, which is time that seepage first contacts the drip shield. Figure 6-76 shows the liquid-phase flux  $q_{liq}$  distribution at the same time. This first occurrence of water contacting the drip shield is seen in distribution of  $S_{liq}$  (Figure 6-74b) as well as in the distribution of  $q_{liq}$  (Figure 6-76c). The point at which the seep contacts the drip shield is also seen as a local depression in the  $T$  contours (Figure 6-75b). The wicking of water into the invert is also evident as  $q_{liq}$  vectors pointing upward (Figure 6-76).

Figure 6-87 shows the pattern of seepage along the crown of the drift for stochastic realization A-56. At 1100 yr, incipient seepage occurs for 16.4% of the vertical projection of the upper drift

wall (Figure 6-87a). At 1900 yr, seepage occurs for 31.0% of the vertical projection of the upper drift wall (Figure 6-87b). Notice that most of this seepage occurs close to the crown of the drift. The influence of the glacial climate (which begins at 2000 yr) is evident at 2200 yr (Figure 6-87c), as the seepage area climbs to 50.5%, which is close to the maximum steady-state value of 57.8% (Figure 6-87d).

Figure 6-77 shows the distributions of  $S_{liq}$  in the fractures and matrix for stochastic realization A-34 at 50 yr, which is the end of the pre-closure ventilation period. Figure 6-78 shows the corresponding distributions of temperature  $T$  and relative humidity  $RH$ . These conditions are very similar to case A-56 at 50 yr (Figures 6-70 and 6-71), with one minor exception. In case A-34 there is evidence of a seep (Figures 6-77c and 6-78f). However, had the drying effect of ventilation been represented in this model it is unlikely that this seep could occur. Figure 6-79 shows the  $S_{liq}$  distributions and Figure 6-80 shows the corresponding distributions of  $T$  and  $RH$  at 60 yr, which are similar to the distributions predicted for case A-56 at 60 yr (Figures 6-72 and 6-73). Notice that the  $RH$  reduction in the drift is slightly less for case A-34 (Figures 6-80d, 6-80e, and 6-80f) than for case A-56 (Figure 6-73d, 6-73e, and 6-73f).

Boiling conditions persist at the drift wall for about 210 yr for stochastic realization A-34 (Figure 6-88a). Seepage at the crown of the drift commences at 280 yr (Figure 6-89c). However, evaporation at the crown of the drift prevents this seepage from immediately contacting the drip shield. Seepage contacts the drip shield at 700 yr, as is evidenced in Figure 6-81, which shows the  $S_{liq}$  distributions, and Figure 6-82, which shows the corresponding distributions of  $T$  and  $RH$  at 700 yr. The depression in the  $RH$  contours corresponds to the point where seepage is evaporating on the drip shield (Figure 6-82f). The waste-package heat generation rate is sufficient to evaporate 100% of this seepage flux on the drip shield until 1600 yr (Figure 6-89d). An important attribute of the line-load design is that the local heat-generation rate (expressed in kW/m of drift) is large enough to evaporate seepage entering the drift long after boiling conditions at the drift wall have ceased.

A comparison of Figures 6-86d and 6-89d would seem to imply that seepage flux onto the drip shield increases with AML. This difference actually occurred because stochastic realizations A-56 and A-34 involve two different random fields of fracture permeability (generated from the same statistical parameters). The permeability field in case A-56 results in a much heavier concentration of the drift seepage flux occurring close to the crown than in the A-34 case (compare Figures 6-90a and 6-90b). This heavy concentration of flux close to the crown in case A-56 is also evident in Figure 6-87.

#### **6.14.5.2 Thermohydrologic Seepage Behavior for Realizations B-56 and B-34**

Stochastic realization B-56 has the same fracture permeability distribution as case A-56. However, in case B-56 the capillary-strength parameter  $1/\alpha$  is not correlated with fracture permeability. Case B-56 results in much less seepage entering the drift and contacting the drip shield than case A-56 (Table 6-10; also compare 6-92 with 6-86). Because of the very small seepage flux reaching the drip shield,  $RH$  reduction on the drip shield is not greatly diminished by seepage (Figure 6-91d).

Stochastic realization B-34 has the same fracture permeability distribution as case A-34. However,  $1/\alpha$  is not correlated with fracture permeability for case B-34. Case B-34 results in much less seepage entering the drift and contacting the drip shield than case A-34 (Table 6-10; also compare 6-94 with 6-89). Because of the small seepage flux reaching the drip shield, *RH* reduction on the drip shield is not greatly diminished by seepage (Figure 6-93d).

#### **6.14.5.3 Thermohydrologic Seepage Behavior for Realizations C-56 and C-34**

Stochastic realizations C-56 and C-34 have a smaller  $\log_{10}$  standard deviation of fracture permeability than the other six cases (Table 6-8). Cases C-56 and C-34 also do not have any vertical biasing of correlation length, as in the other six cases. For cases C-56 and C-34 no seepage ever enters the drift or reaches the drip shield. Consequently, the *RH* histories for these two cases are identical to the corresponding *RH* histories predicted by the corresponding 2-D homogeneous LDTH models (Figures 6-95b, 6-95d, 6-97b, and 6-95d).

#### **6.14.5.4 Thermohydrologic Seepage Behavior for Realizations D-56 and D-34**

Stochastic realizations D-56 and D-34 have a larger  $\log_{10}$  standard deviation in fracture permeability  $k$  than cases A-56, A-34, B-56, and B-34, while having a smaller contrast in correlation lengths in the principal directions. Cases D-56 and D-34 resulted in approximately the same magnitude of seepage as cases A-56 and A-34 (Table 6-10; also compare Figures 6-100 and 6-102 with Figures 6-86 and 6-89). However, case D-56 resulted in a much greater delay (5000 yr) in the onset of seepage contacting the drip shield than in case A-56 (1900 yr).

#### **6.14.5.5 Summary of the Results of the Three-Dimensional Heterogeneous LDTH Model**

The primary purpose of the 3-D heterogeneous LDTH model was twofold: (1) test the hypothesis that boiling conditions at the drift wall are capable of thwarting seepage, even for highly heterogeneous fracture-permeability distributions and (2) determine how the incorporation of drift-scale fracture heterogeneity in the host rock would change (if at all) the MSTHM predictions of TH conditions in the host rock and in the drifts.

The results from Section 6.14 support the finding that boiling conditions at the drift wall will thwart any tendency for seepage into the drift, even for cases in which the fracture-permeability distribution is much more heterogeneous than indicated by field measurements (CRWMS M&O, 2000j). The results from Section 6.14 also support the finding that drift-scale fracture-permeability heterogeneity in the host rock has a negligible influence on temperatures at the drift wall and in the emplacement drift and also has a negligible influence on relative humidity at the drift wall; therefore, the MSTHM predictions of these variables are applicable even for cases in which fracture permeability in the host rock is highly heterogeneous. The results from Section 6.14 also support the finding that drift-scale fracture-permeability heterogeneity in the host rock has a negligible influence on relative humidity in the drift except locally where seepage contacts the drip shield.

Because the primary purpose of the results of Section 6.14 is to validate key assumptions in the MSTHM, on in-drift TH conditions it is not necessary to characterize the results of Section 6.14

as being either realistic, somewhat conservative, or conservative. Rather the results from Section 6.14 support the finding that the results from Sections 6.11 and 6.12 of this AMR are realistic with respect to the influence of drift-scale fracture heterogeneity in the host rock.

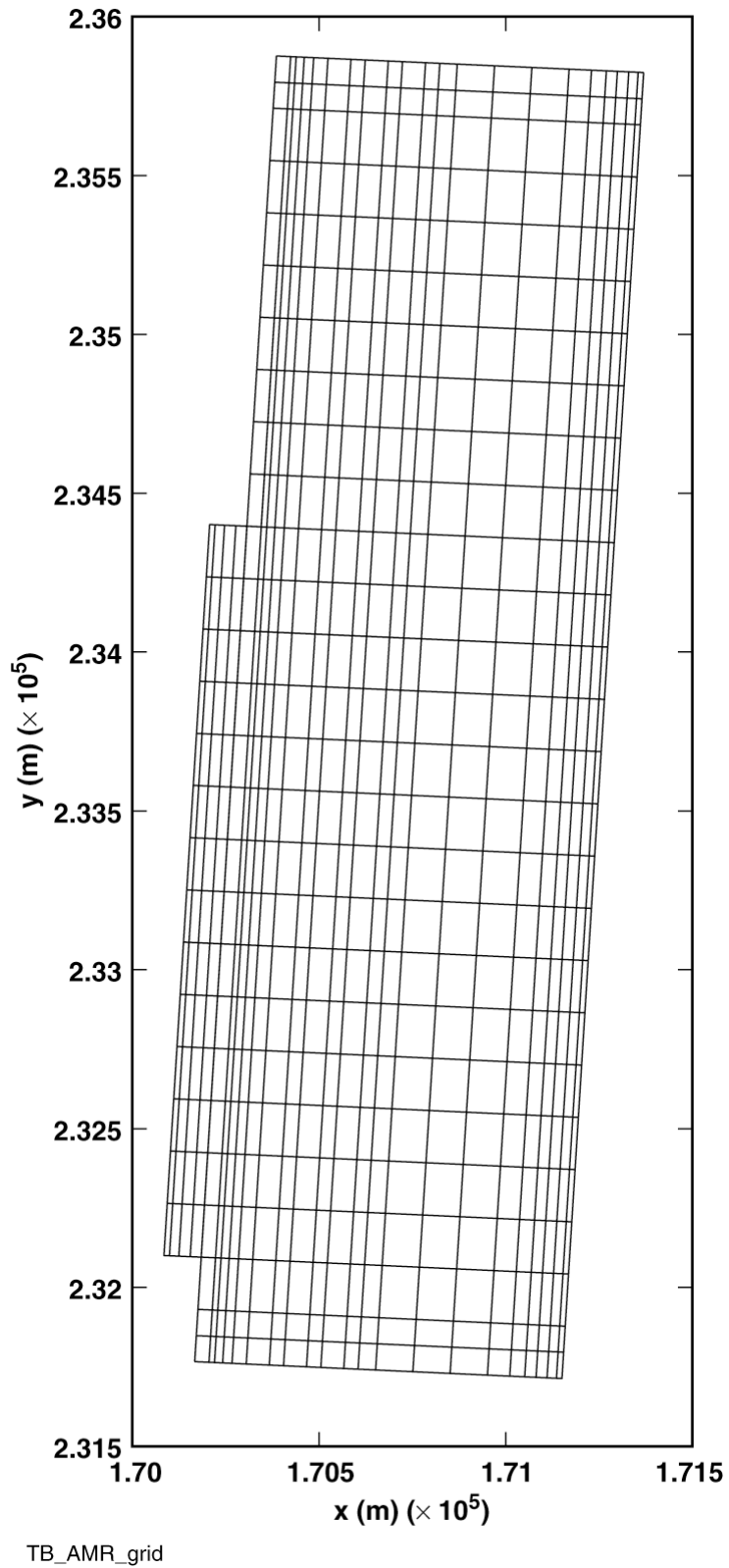
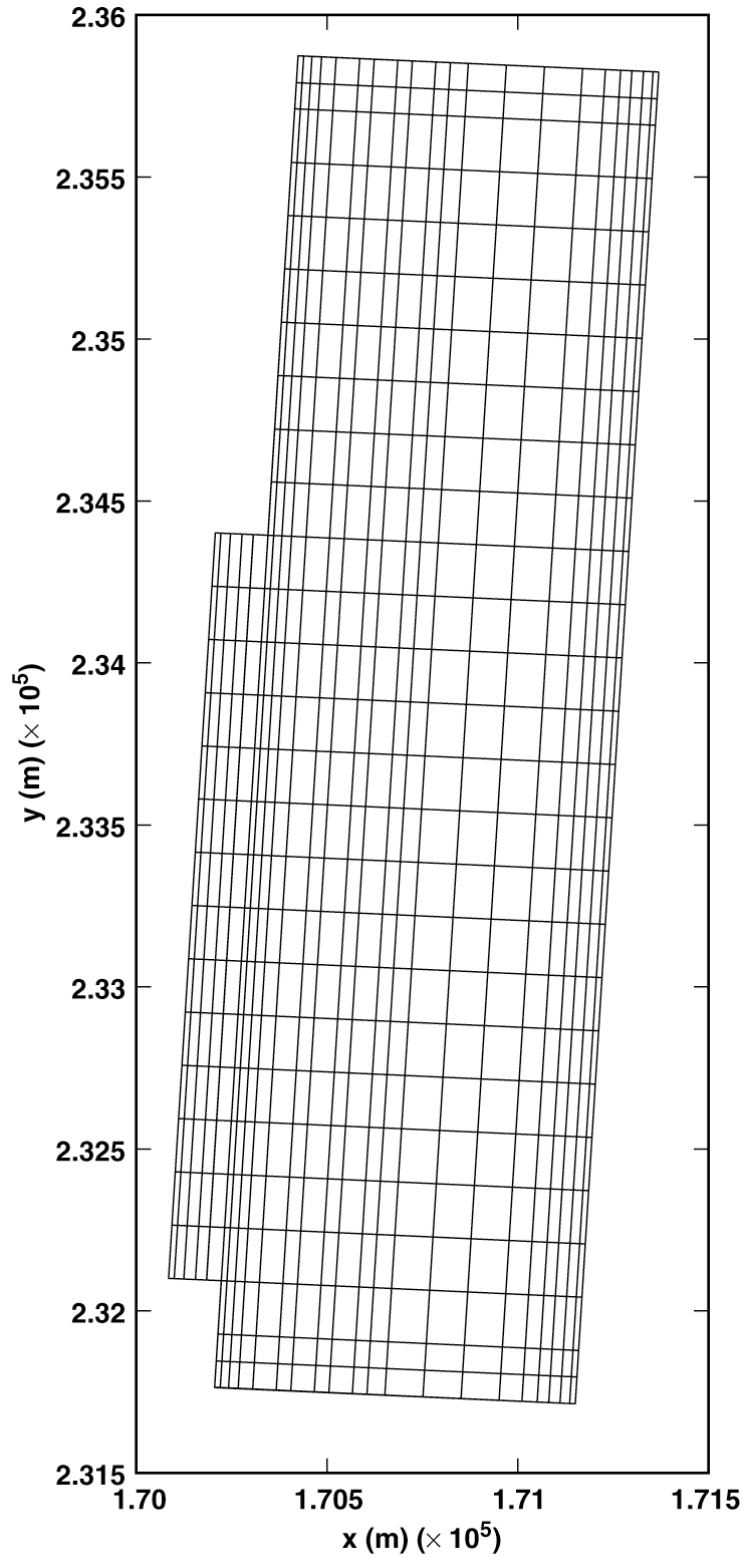


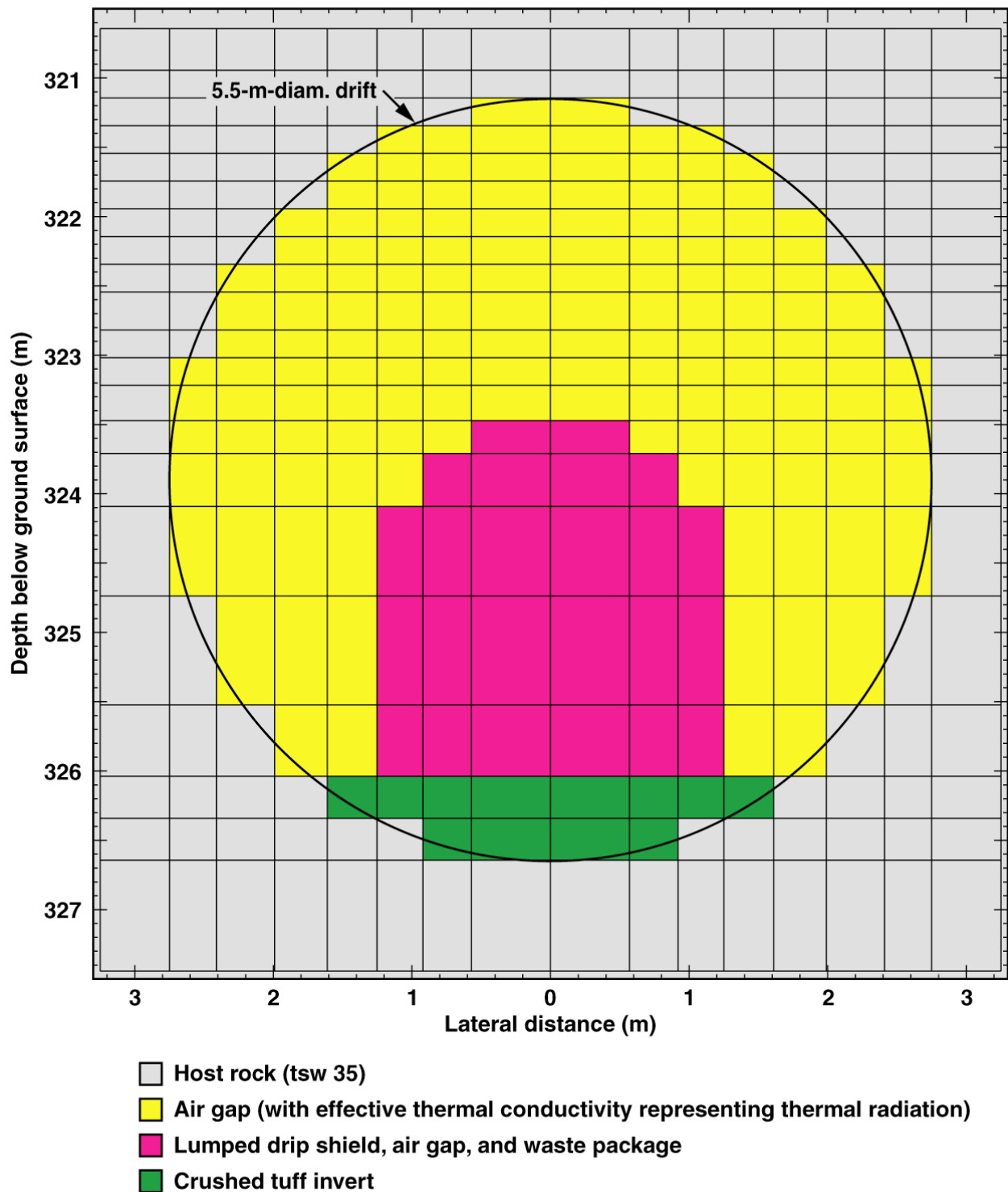
Figure 6-1a. Repository-scale numerical mesh of the repository area used in the MSTHM showing the 623 repository subdomains used in backfill case



TB\_AMR\_grid

Figure 6-1b. Repository-scale numerical mesh of the repository area used in the MSTHM showing the 610 repository subdomains used in no-backfill case

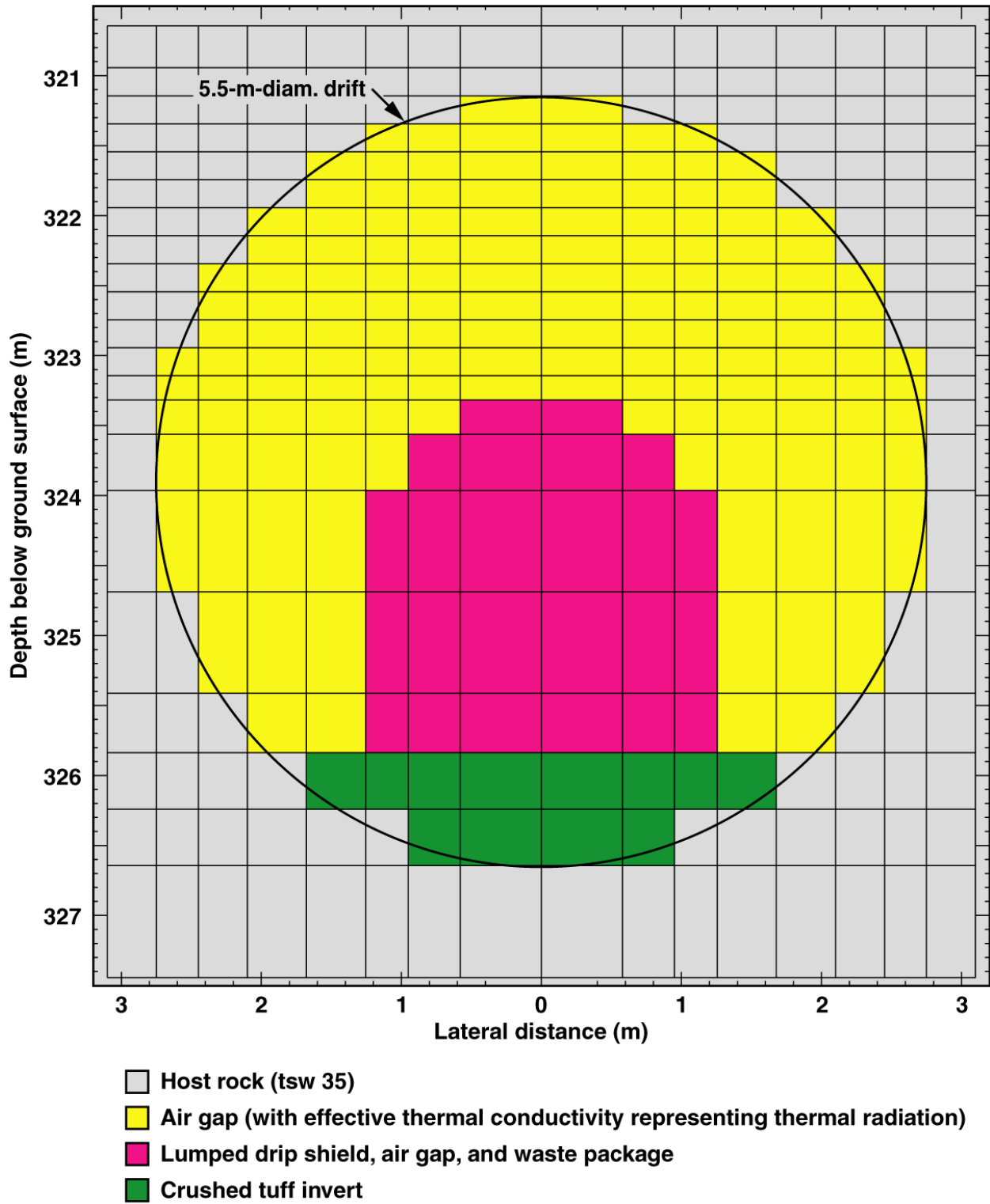
Pre-closure LDTH submodel



TB-LDTH-I4c3-pbf-grid

Figure 6-2a. Cross-sectional view of the numerical mesh used in the pre-closure LDTH submodels for the backfill case (REV 00), and no-backfill case (ICN 01). This is also the post-closure LDTH-submodel mesh for no-backfill case (ICN 01).

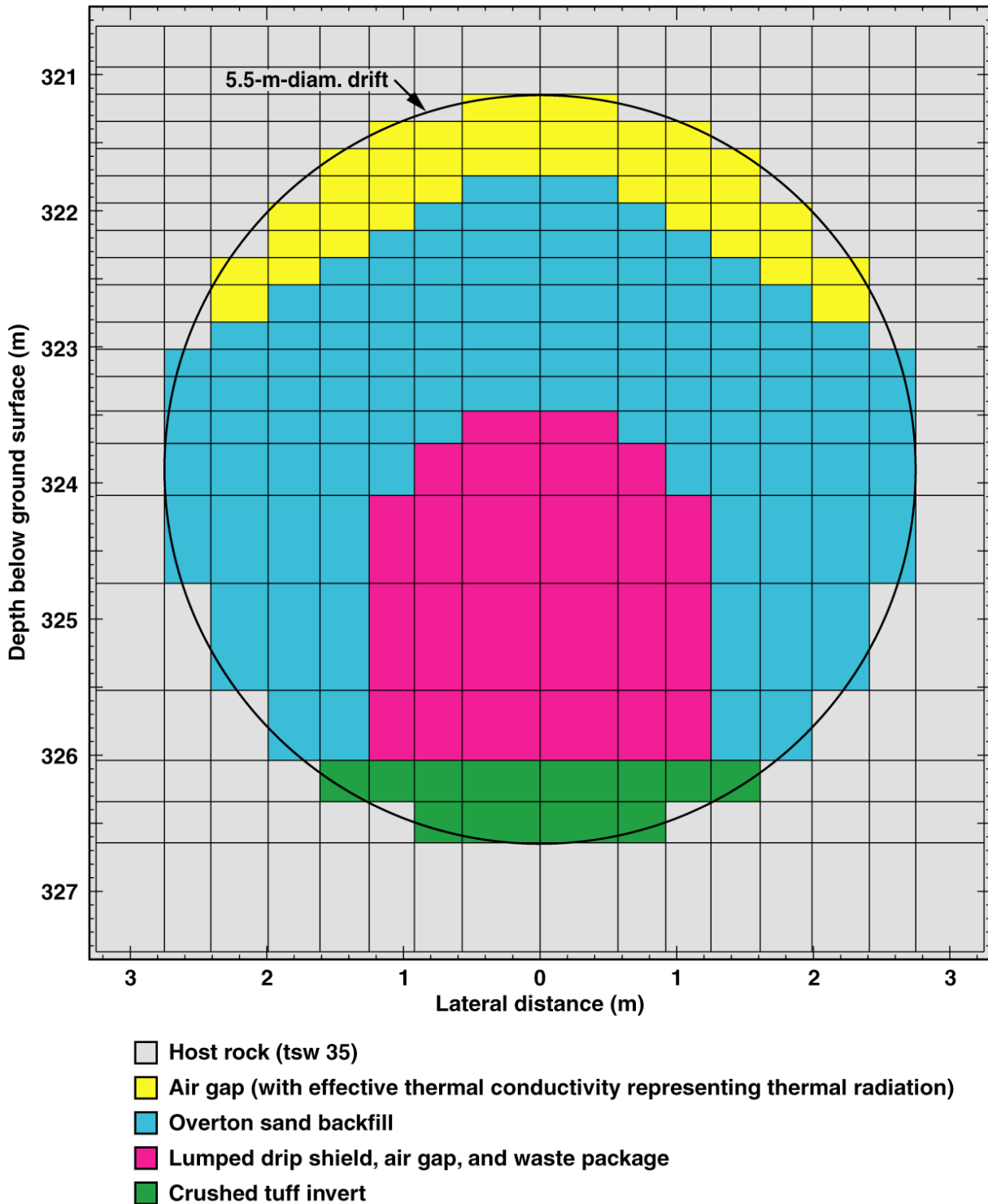
### Pre- and post-closure LDTH submodel



I4c3-LDTH-grid  
Figure 6-2b.

Cross-sectional view of numerical mesh used in the pre-closure and post-closure LDTH submodels for the ICN-02 no-backfill case

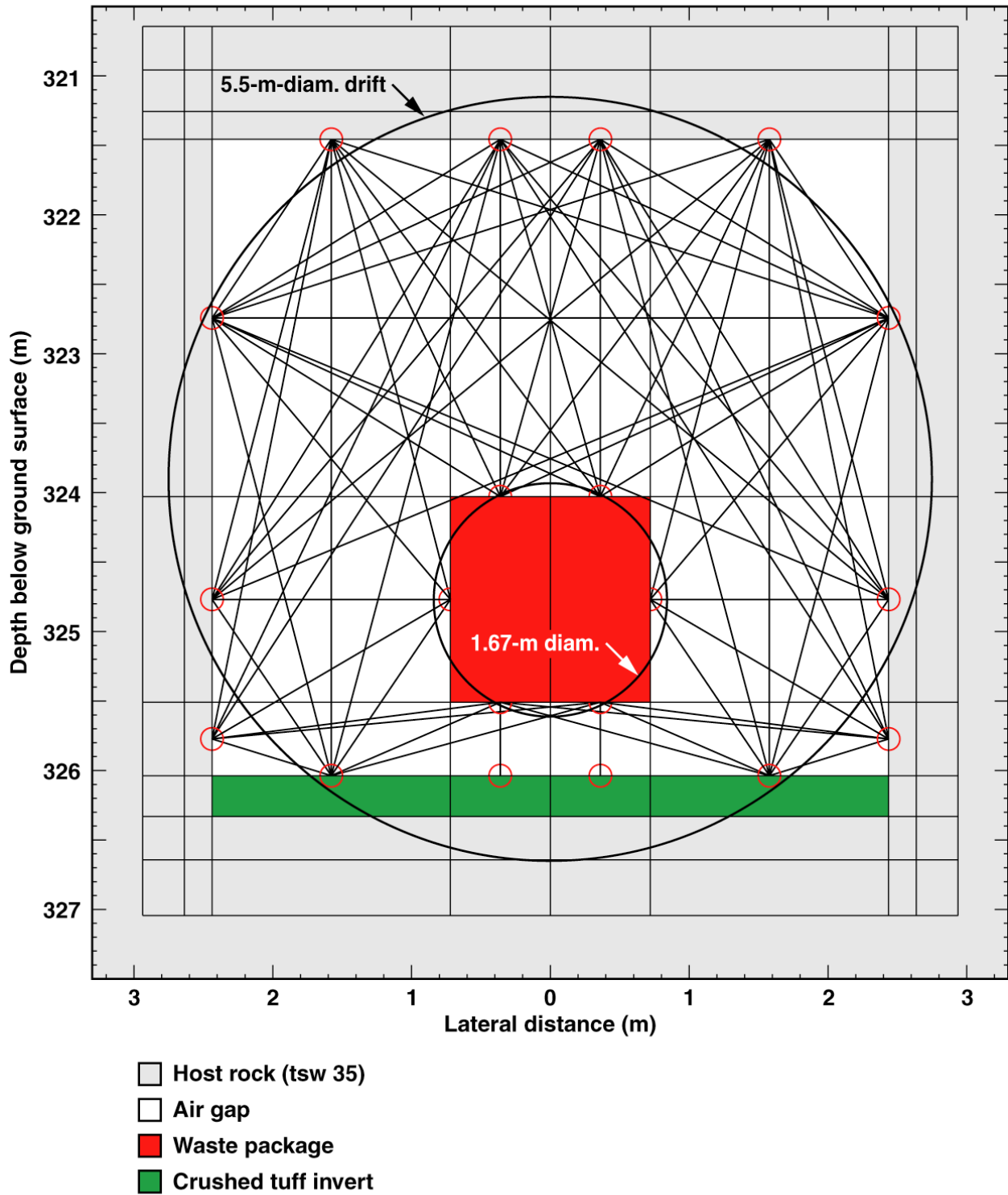
### Post-closure LDTH submodel



TB-LDTH-I4c3-bf-grid

Figure 6-3. Cross-sectional view of the numerical mesh used in the post-closure LDTH submodels for the backfill case. The post-closure LDTH-submodel mesh for no-backfill case is shown in Figure 6-2.

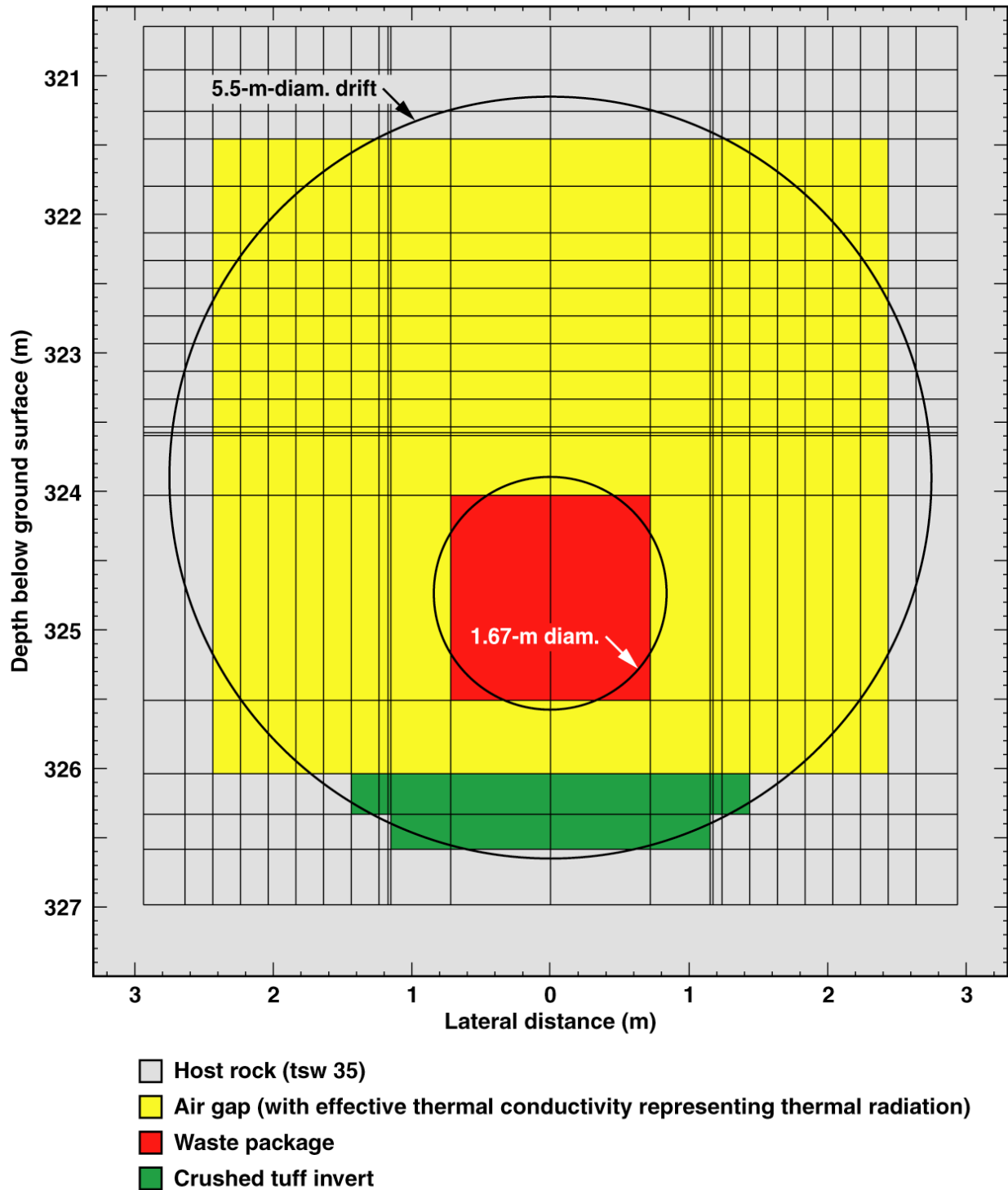
### Pre-closure DDT submodel



TB-DDT-I4c3-vent-grid

Figure 6-4. Cross-sectional view of the numerical mesh used in the pre-closure DDT submodel for backfill and no-backfill cases

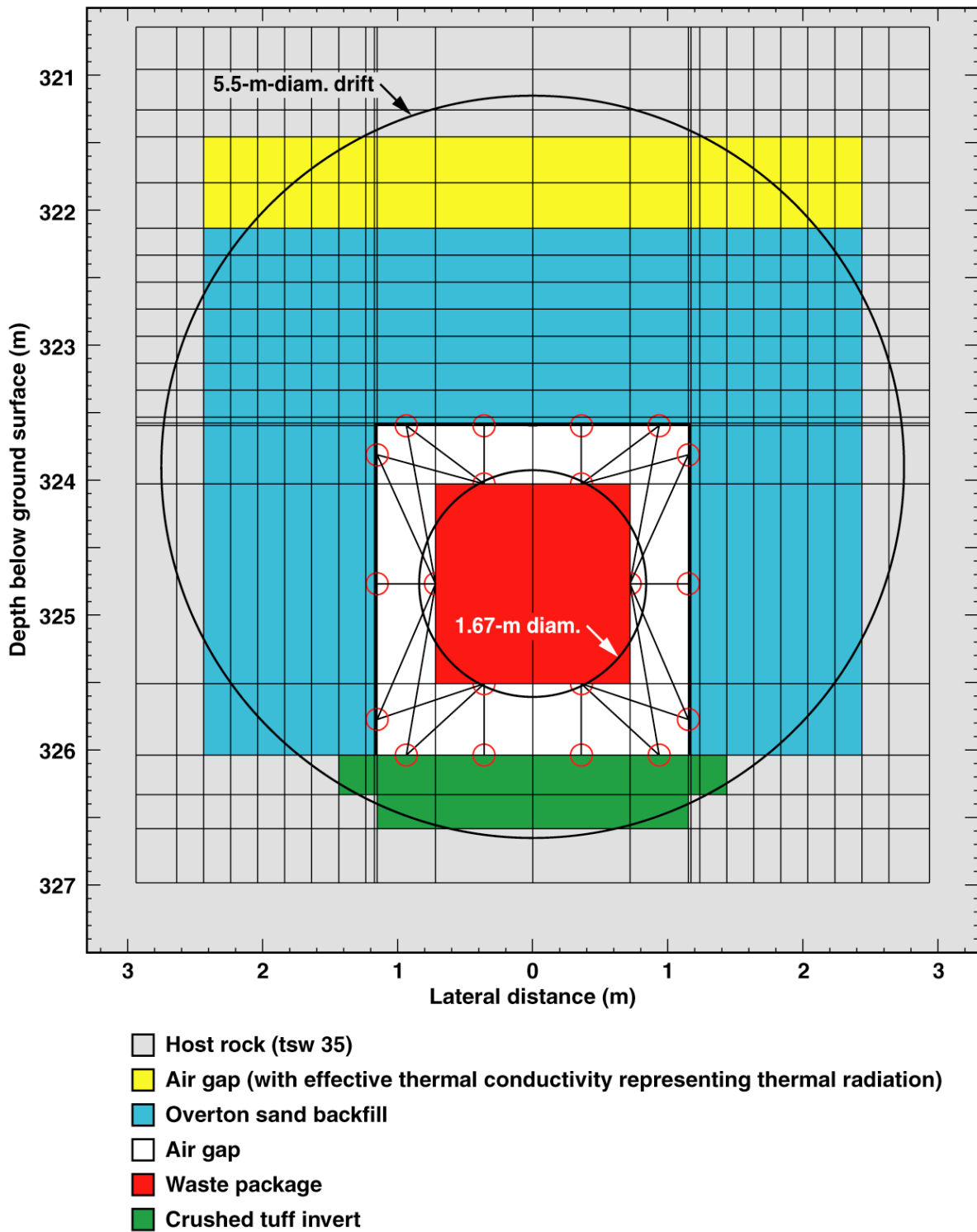
**Pre-closure DDT submodel  
(for restarting postclosure DDT submodel)**



TB-LDTH/DDT-I4c3-pbf-grid

Figure 6-5. Cross-sectional view of the numerical mesh used in the pre-closure DDT submodel that is used to generate the restart file to start the post-closure DDT submodel for backfill case

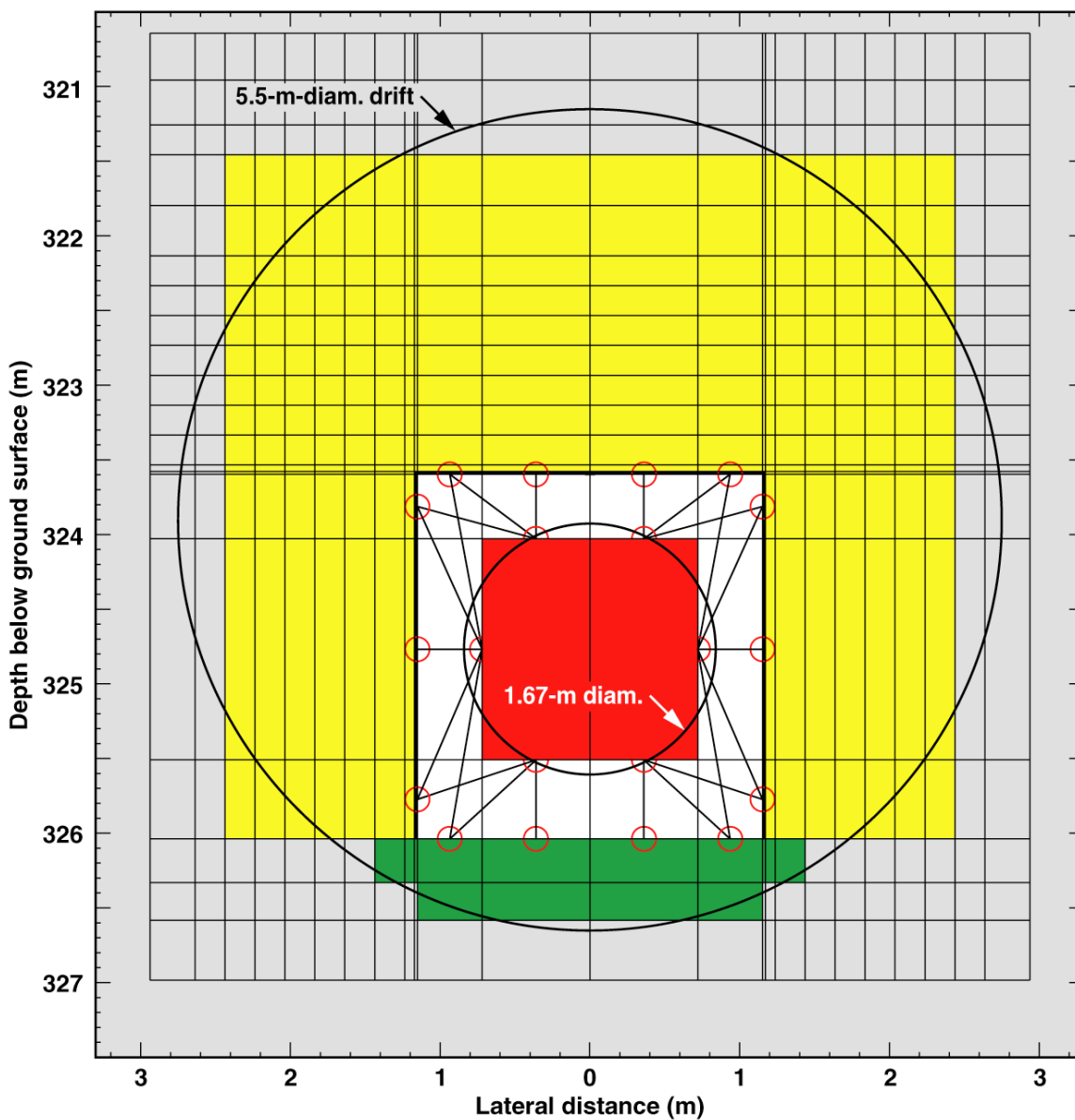
### Post-closure DDT submodel



TB-DDT-l4c3-bf-grid

Figure 6-6a. Cross-sectional view of the numerical mesh used in the post-closure DDT submodel for backfill case

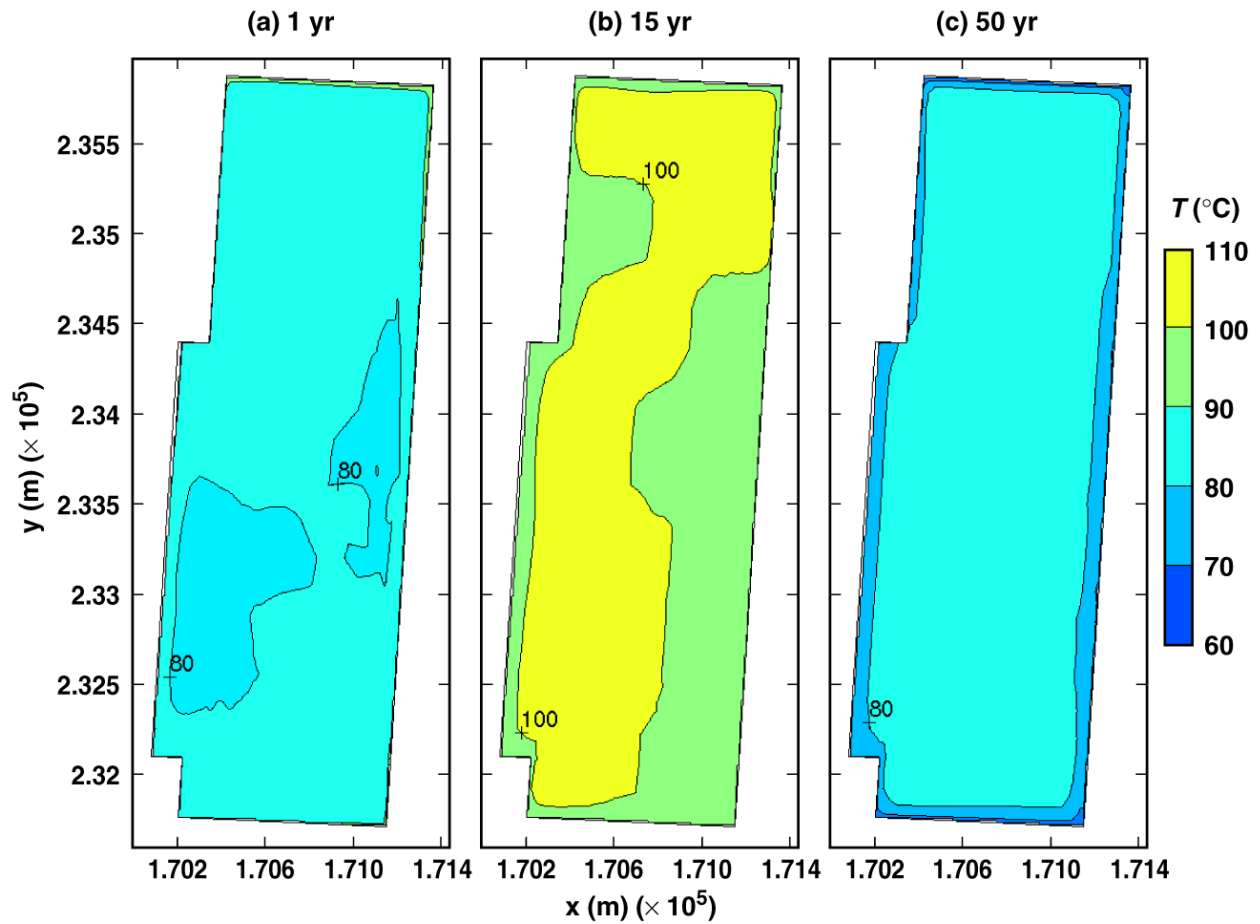
Post-closure DDT submodel



- Host rock (tsw 35)
- Air gap (with effective thermal conductivity representing thermal radiation)
- Overton sand backfill
- Air gap
- Waste package
- Crushed tuff invert

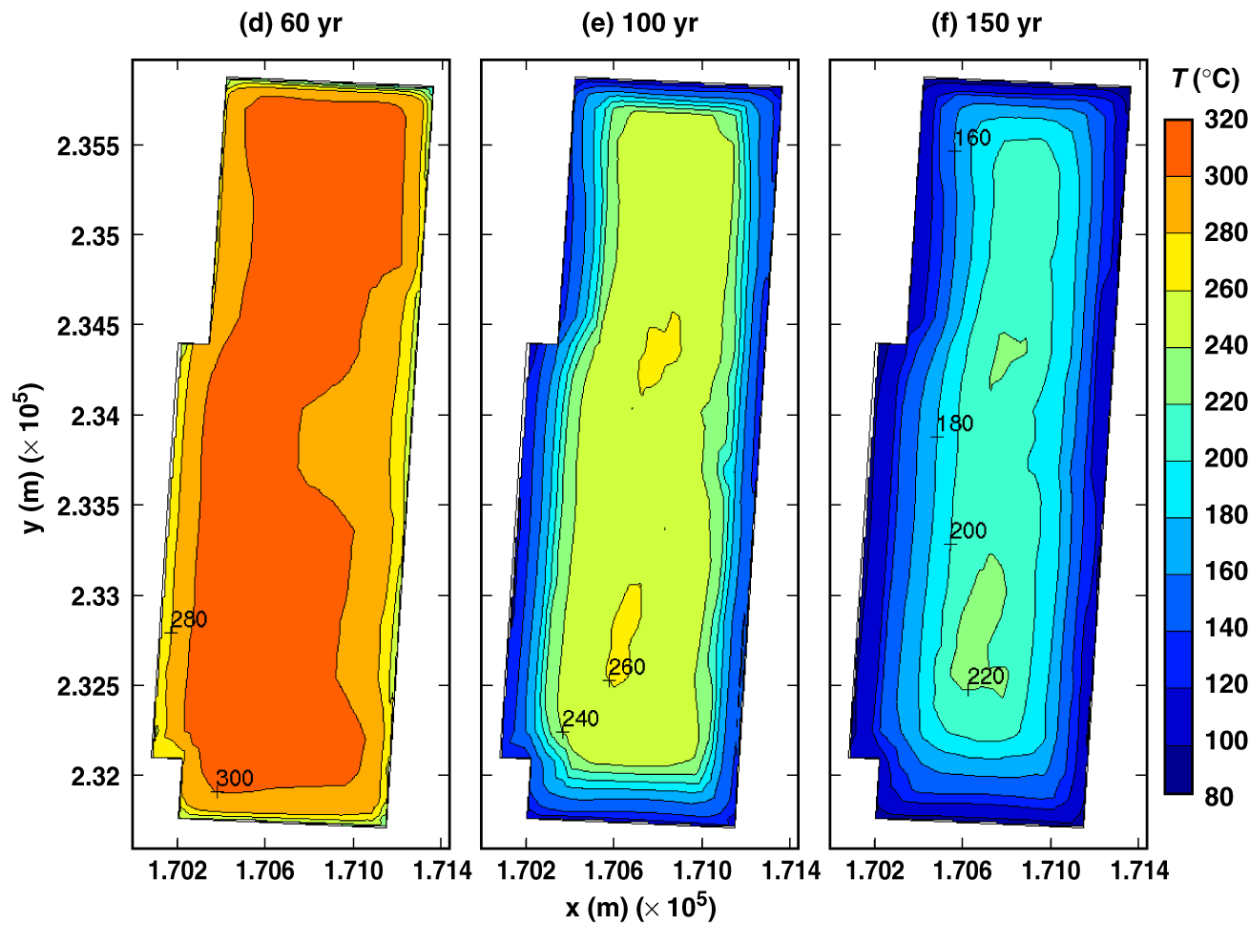
TB-DDT-l4c3-bf-grid

Figure 6-6b. Cross-sectional view of the numerical mesh used in the post-closure DDT submodel for the no backfill case



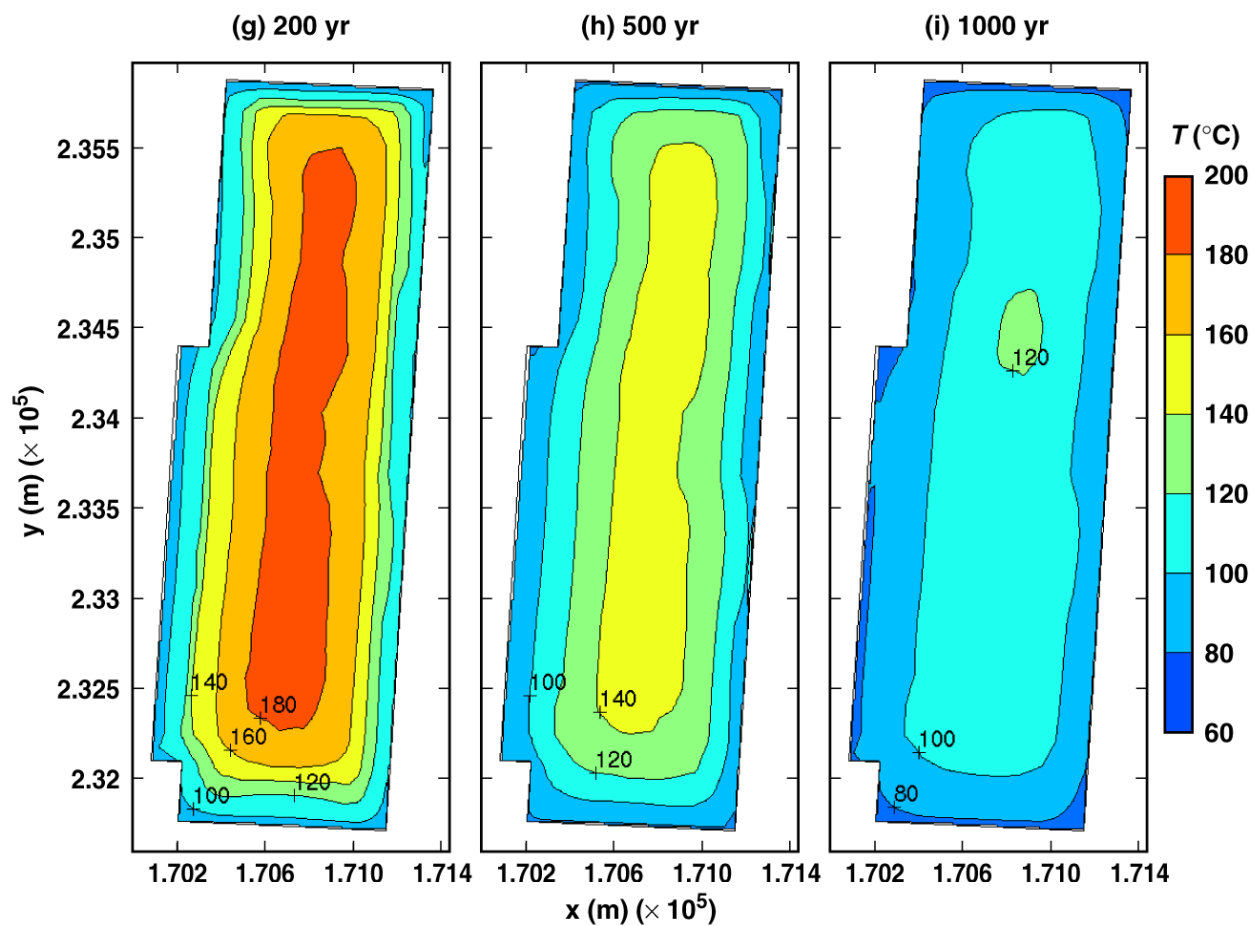
TB\_AMR\_mean\_T\_wp\_pwr2\_2-11

Figure 6-7. Temperature on the surface of a 21-PWR WP for the mean infiltration-flux backfill case for the indicated times



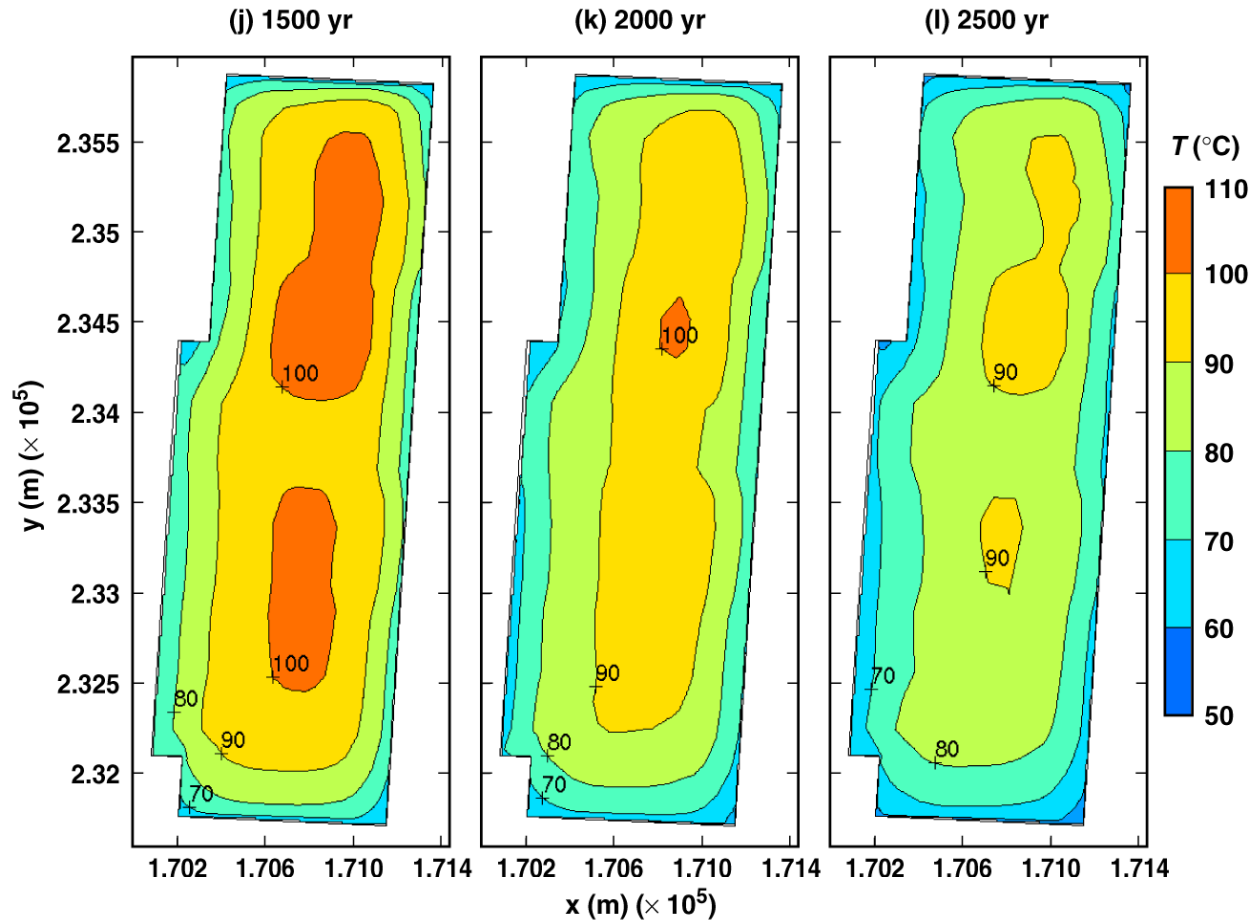
TB\_AMR\_mean\_T\_wp\_pwr2\_17-26

Figure 6-7. Temperature on the surface of a 21-PWR WP for the mean infiltration-flux backfill case for the indicated times (Continued)



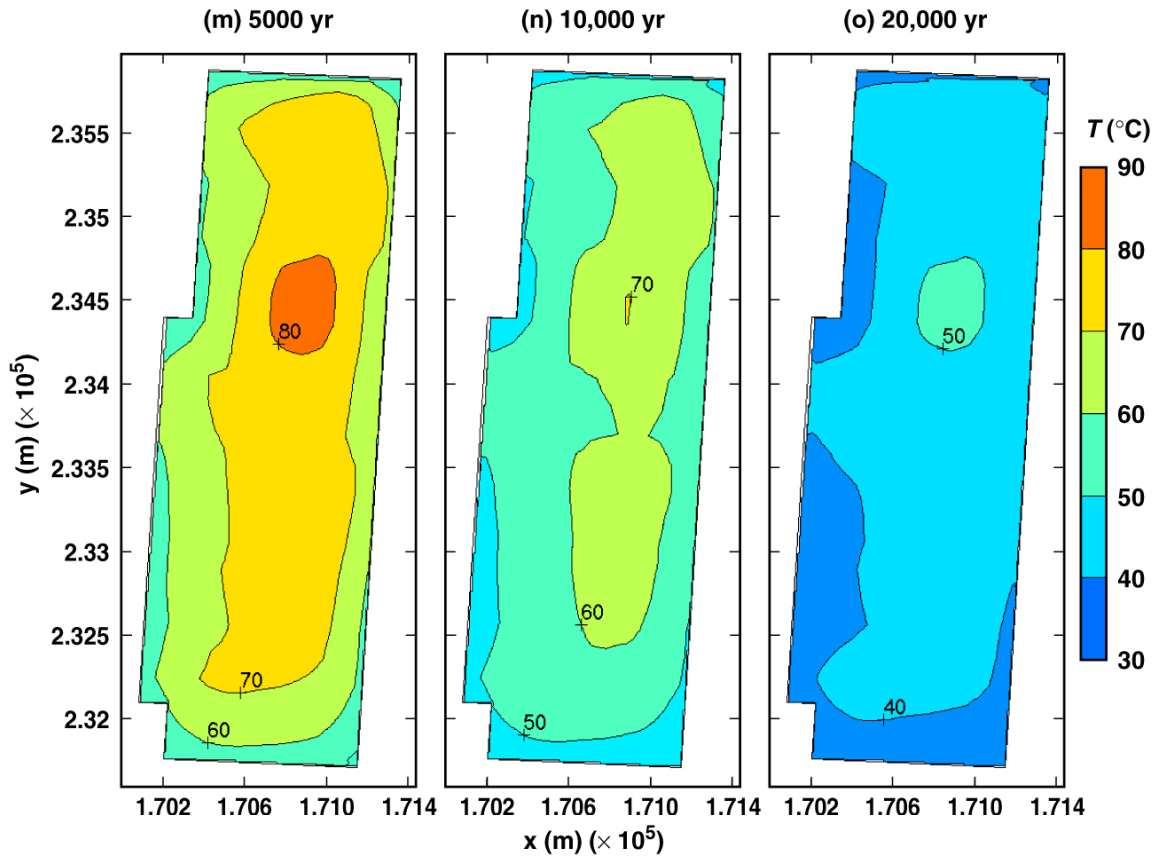
TB\_AMR\_mean\_T\_wp\_pwr2\_31-174

Figure 6-7. Temperature on the surface of a 21-PWR WP for the mean infiltration-flux backfill case for the indicated times (Continued)



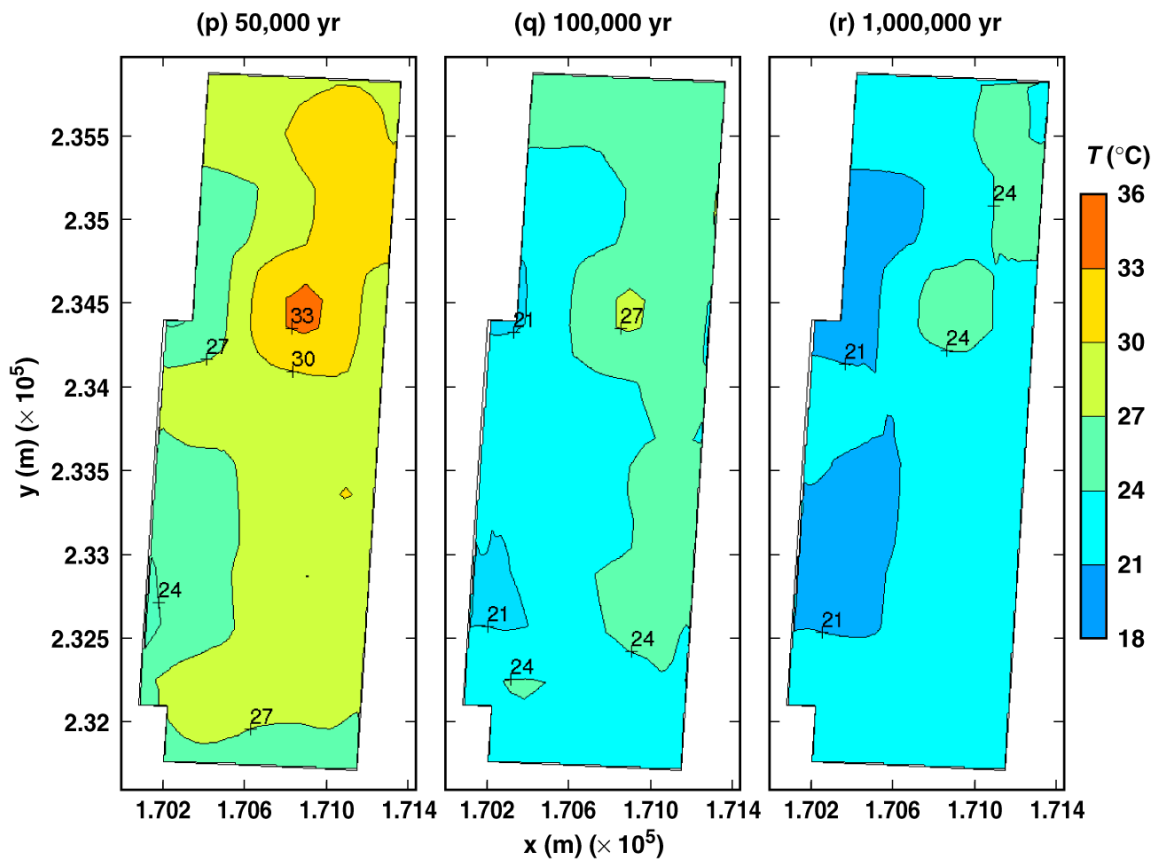
TB\_AMR\_mean\_T\_wp\_pwr2\_225-273

Figure 6-7. Temperature on the surface of a 21-PWR WP for the mean infiltration-flux backfill case for the indicated times (Continued)



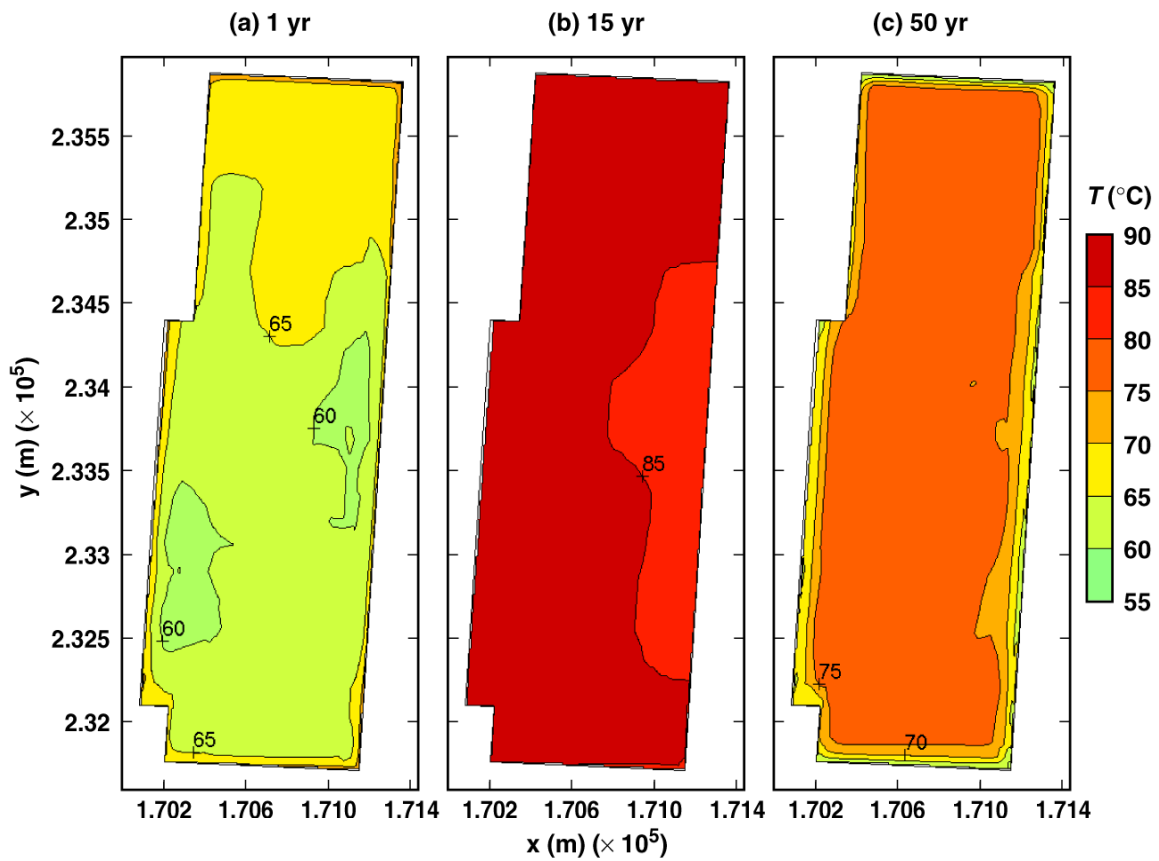
TB\_AMR\_mean\_T\_wp\_pwr2\_307-330

Figure 6-7. Temperature on the surface of a 21-PWR WP for the mean infiltration-flux backfill case for the indicated times (Continued)



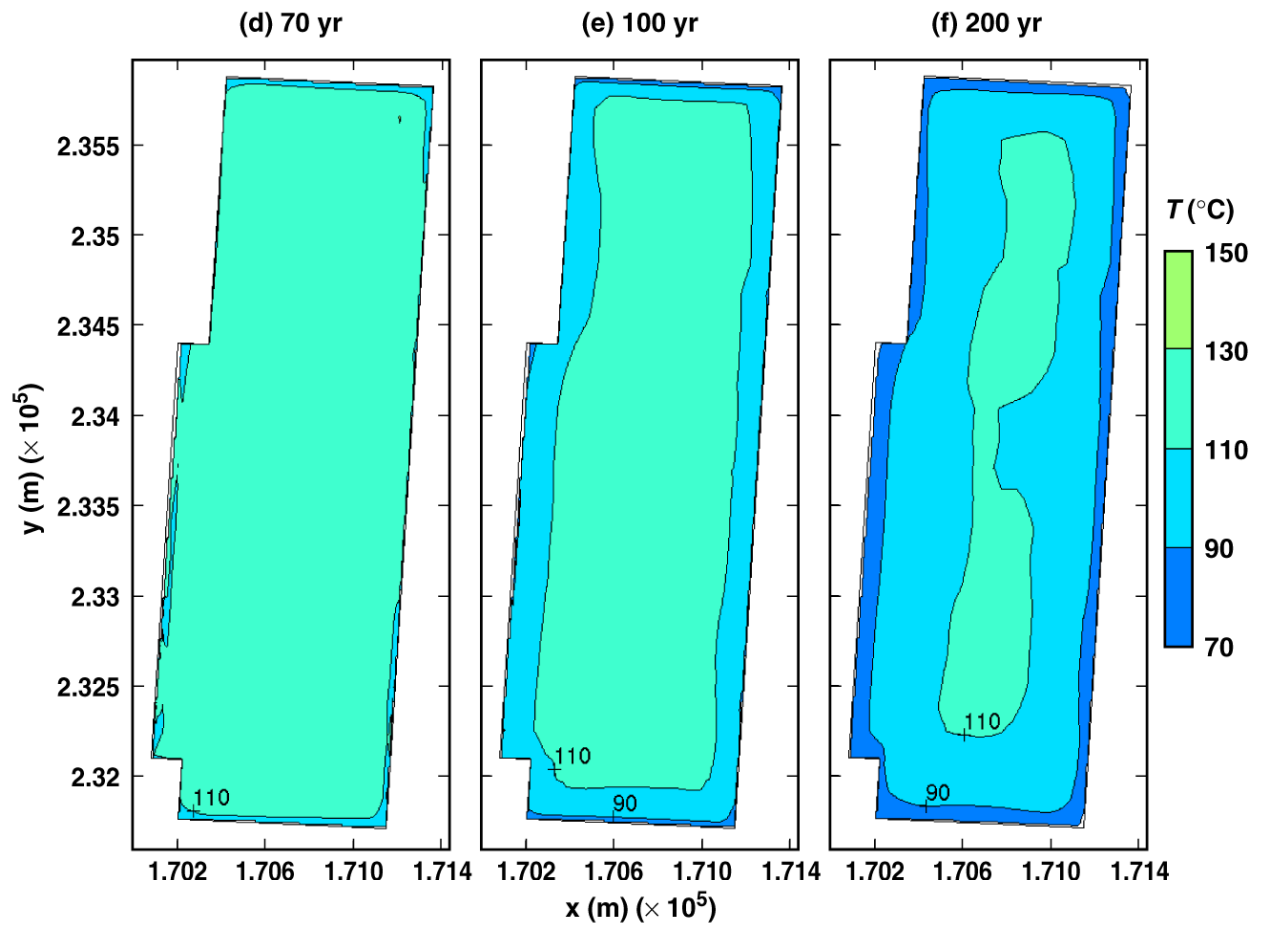
TB\_AMR\_mean\_T\_wp\_pwr2\_341-352

Figure 6-7. Temperature on the surface of a 21-PWR WP for the mean infiltration-flux backfill case for the indicated times (Continued)



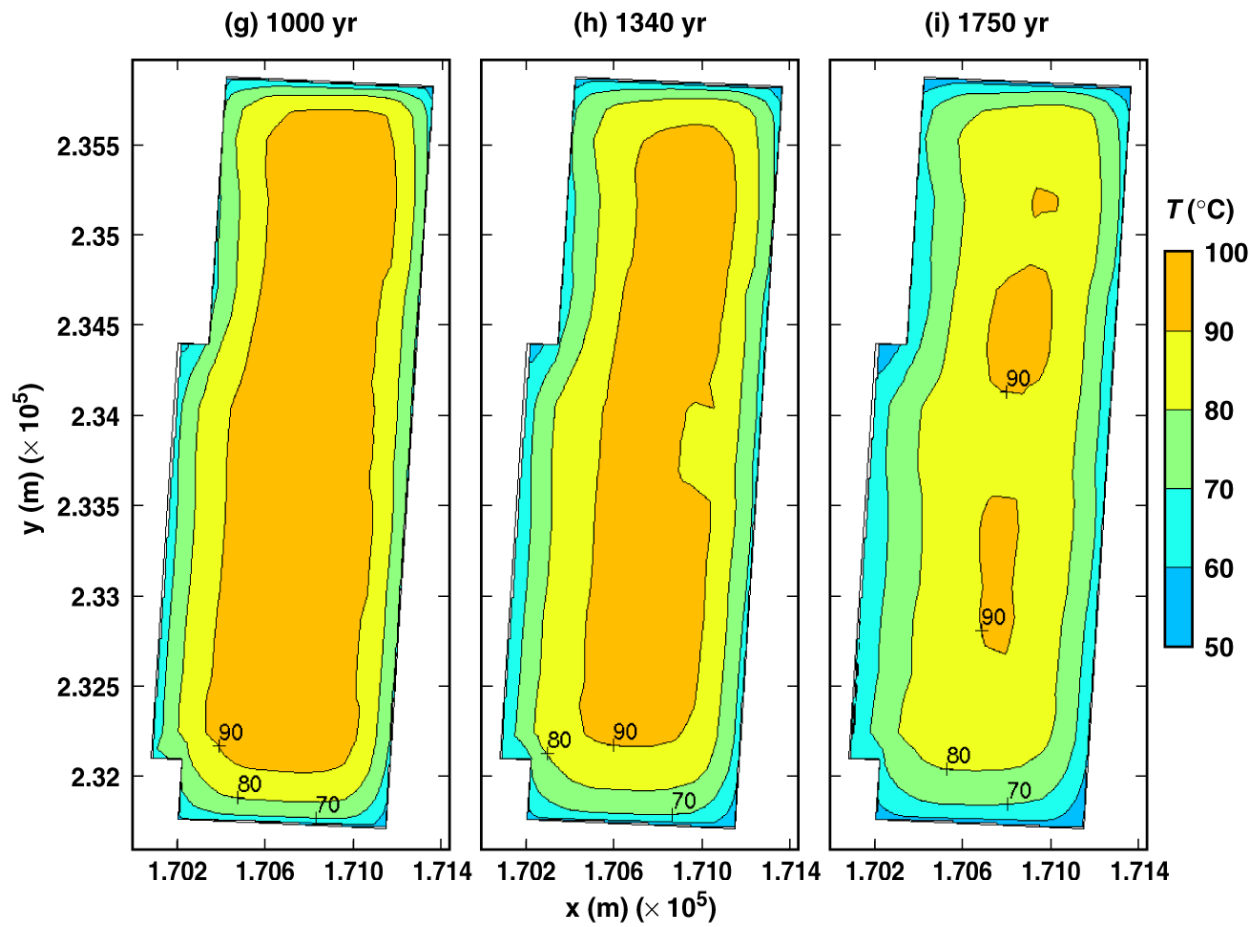
TB\_AMR\_mean\_T\_dw\_upper\_pwr2\_2-11

Figure 6-8. Temperature on the crown of the drift (or upper drift wall) immediately above a 21-PWR WP for the mean infiltration-flux backfill case for the indicated times



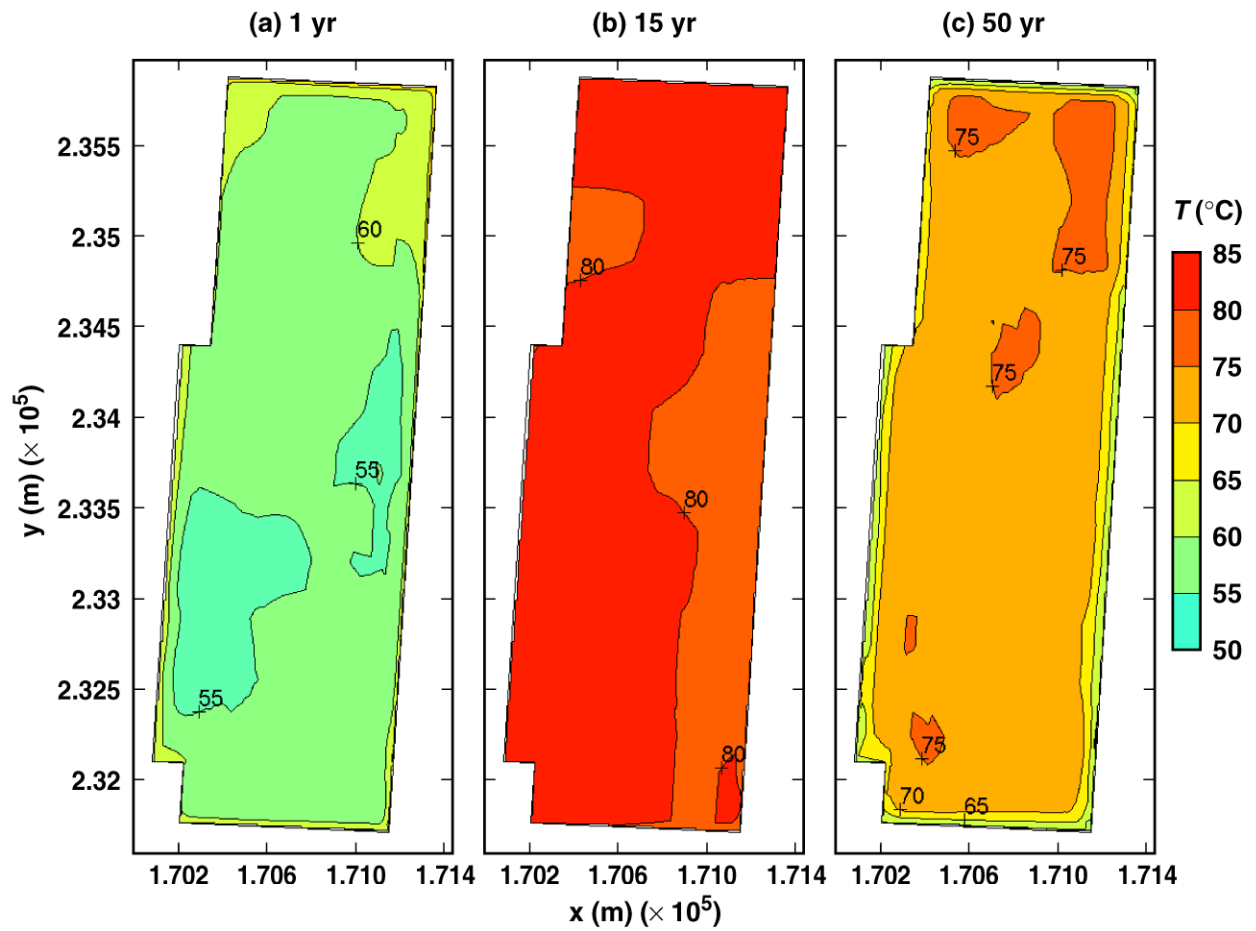
TB\_AMR\_mean\_T\_dw\_upper\_pwr2\_19-31

Figure 6-8. Temperature on the crown of the drift (or upper drift wall) immediately above a 21-PWR WP for the mean infiltration-flux backfill case for the indicated times (Continued)



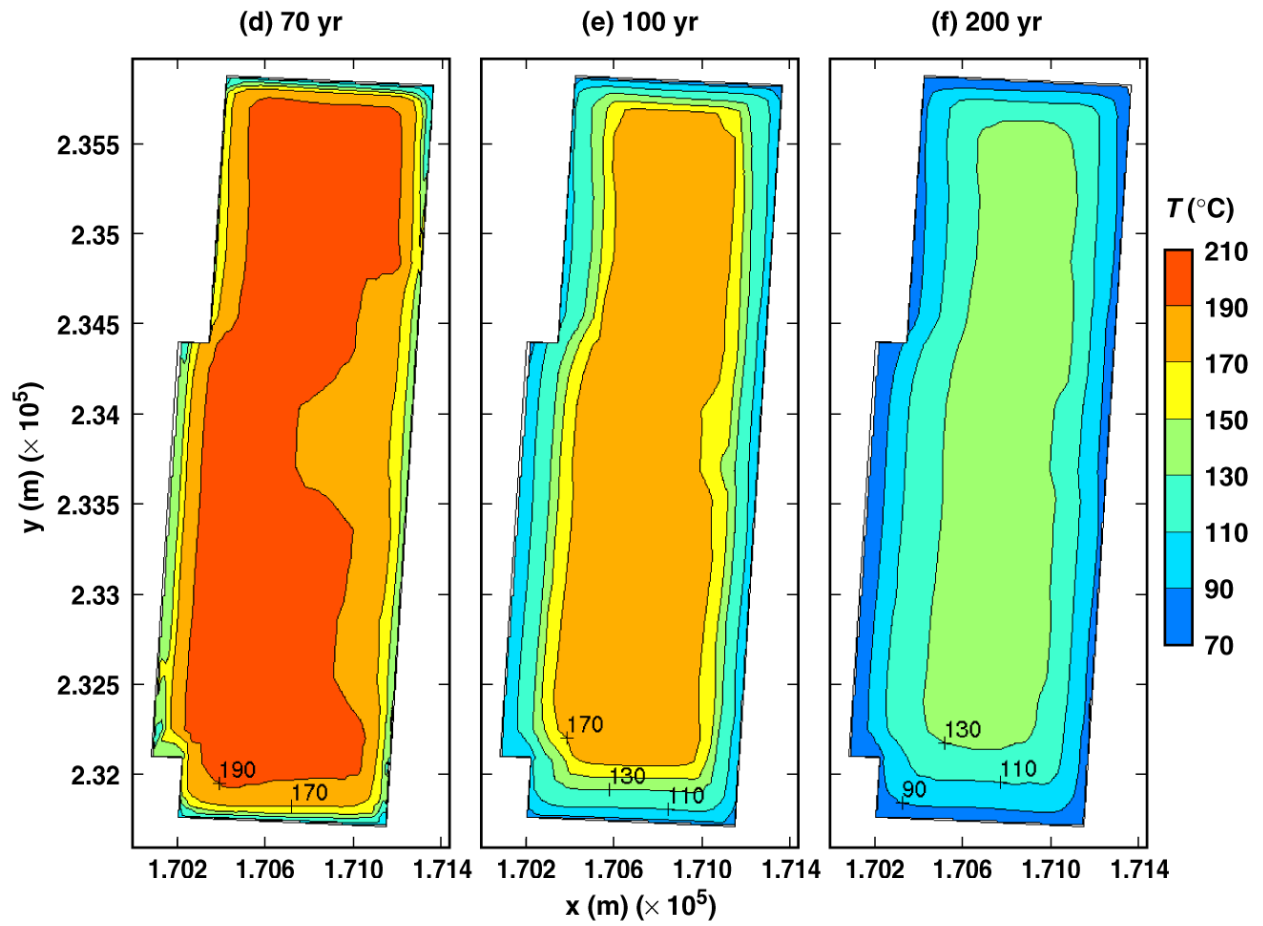
TB\_AMR\_mean\_T\_dw\_upper\_pwr2\_174-240

Figure 6-8. Temperature on the crown of the drift (or upper drift wall) immediately above a 21-PWR WP for the mean infiltration-flux backfill case for the indicated times (Continued)



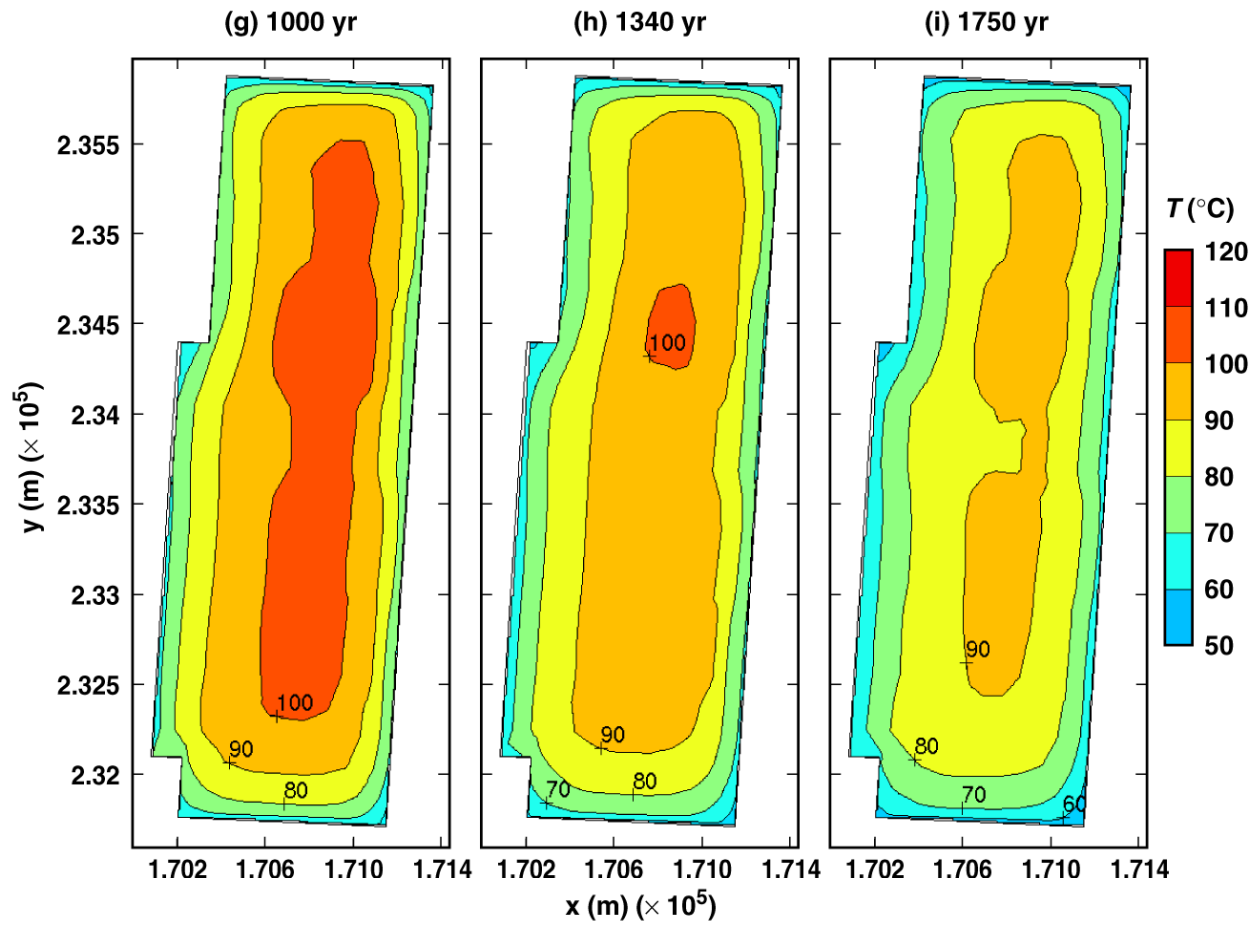
TB\_AMR\_mean\_T\_dw\_lower\_pwr2\_2-11

Figure 6-9. Temperature on the lower drift wall immediately below a 21-PWR WP for the mean infiltration-flux backfill case for the indicated times



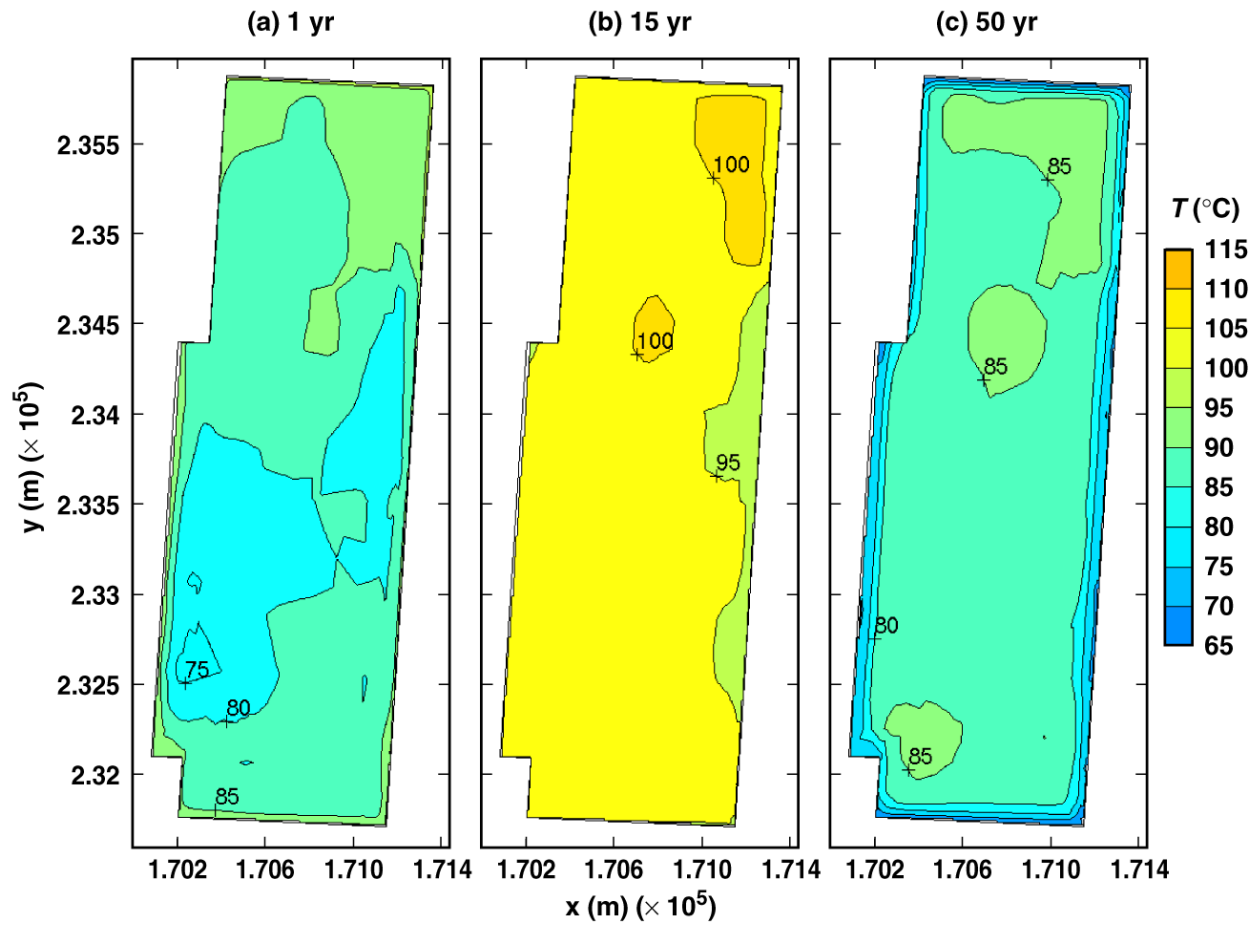
TB\_AMR\_mean\_T\_dw\_lower\_pwr2\_19-31

Figure 6-9. Temperature on the lower drift wall immediately below a 21-PWR WP for the mean infiltration-flux backfill case for the indicated times (Continued)



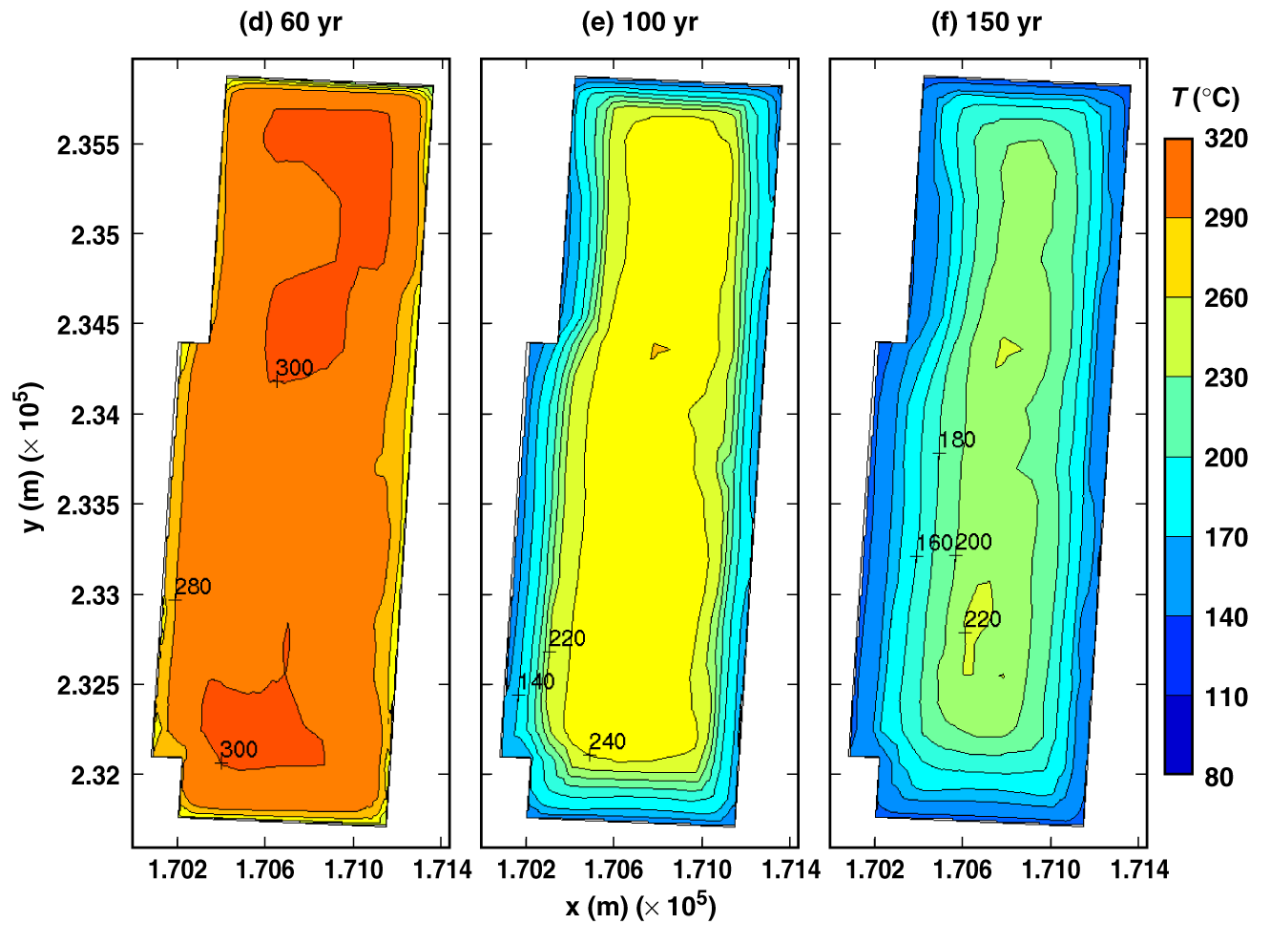
TB\_AMR\_mean\_T\_dw\_lower\_pwr2\_174-240

Figure 6-9. Temperature on the lower drift wall immediately below a 21-PWR WP for the mean infiltration-flux backfill case for the indicated times (Continued)



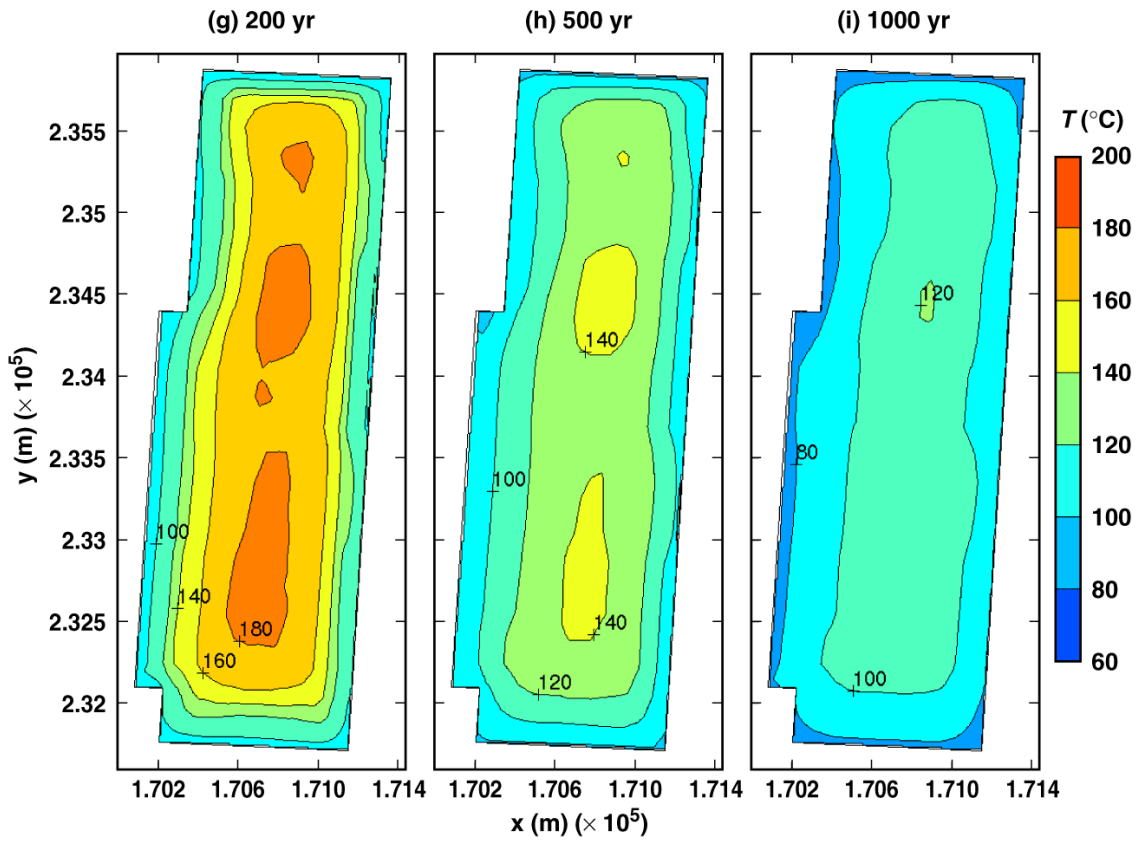
TB\_AMR\_upper\_T\_wp\_pwr2\_2-11

Figure 6-10. Temperature on the surface of a 21-PWR WP for the high infiltration-flux backfill case for the indicated times



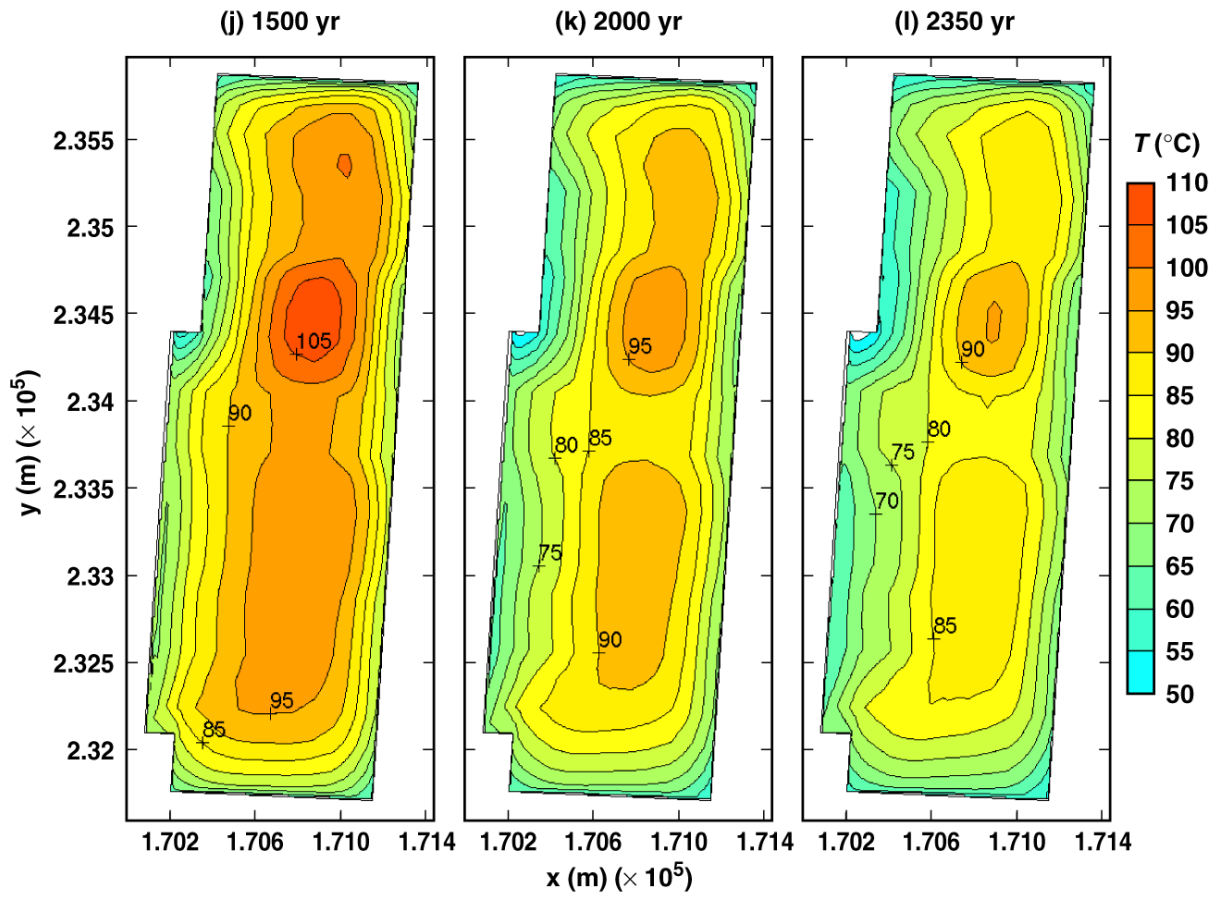
TB\_AMR\_upper\_T\_wp\_pwr2\_17-22

Figure 6-10. Temperature on the surface of a 21-PWR WP for the high infiltration-flux backfill case for the indicated times (Continued)

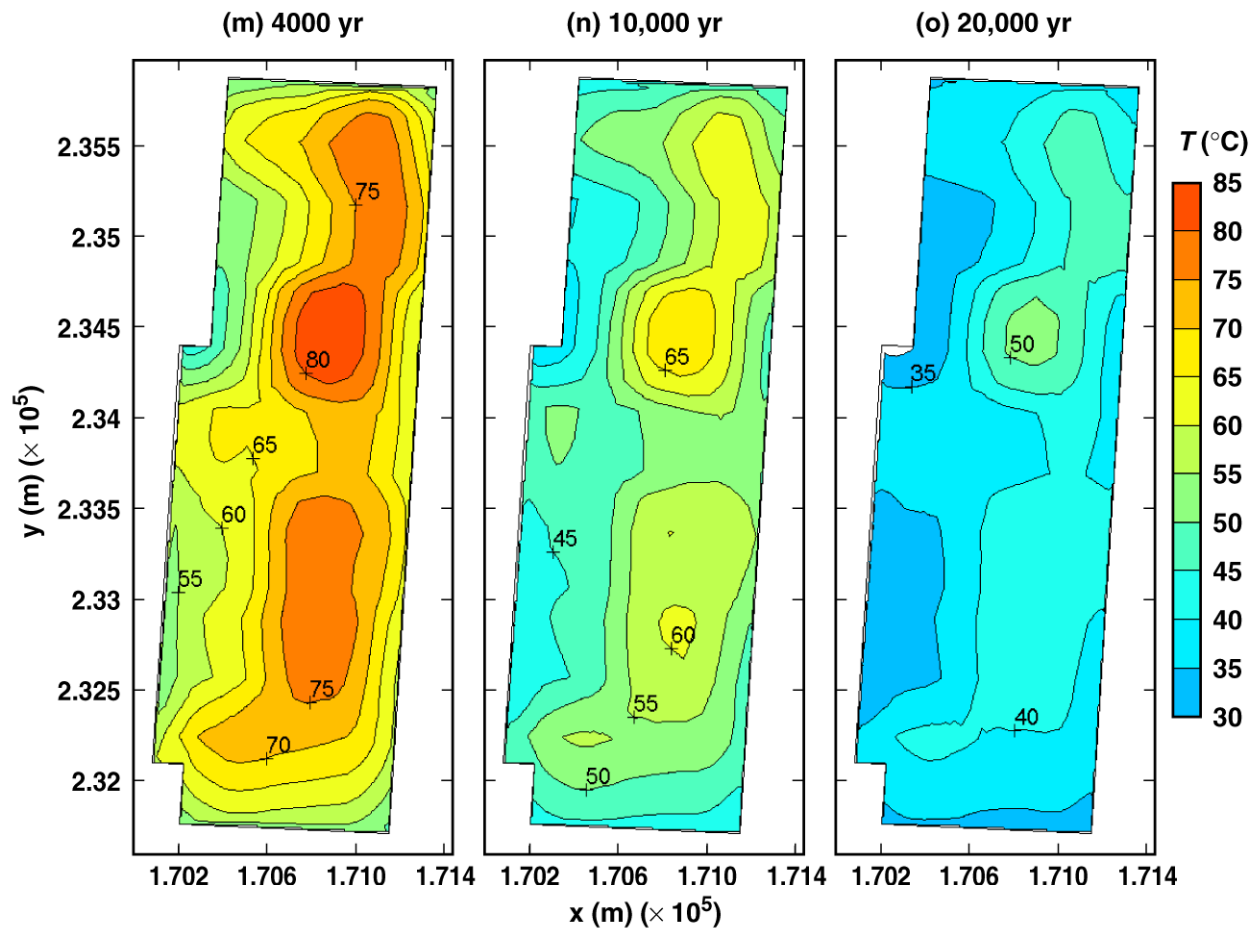


TB\_AMR\_upper\_T\_wp\_pwr2\_56-269

Figure 6-10. Temperature on the surface of a 21-PWR WP for the high infiltration-flux backfill case for the indicated times (Continued)

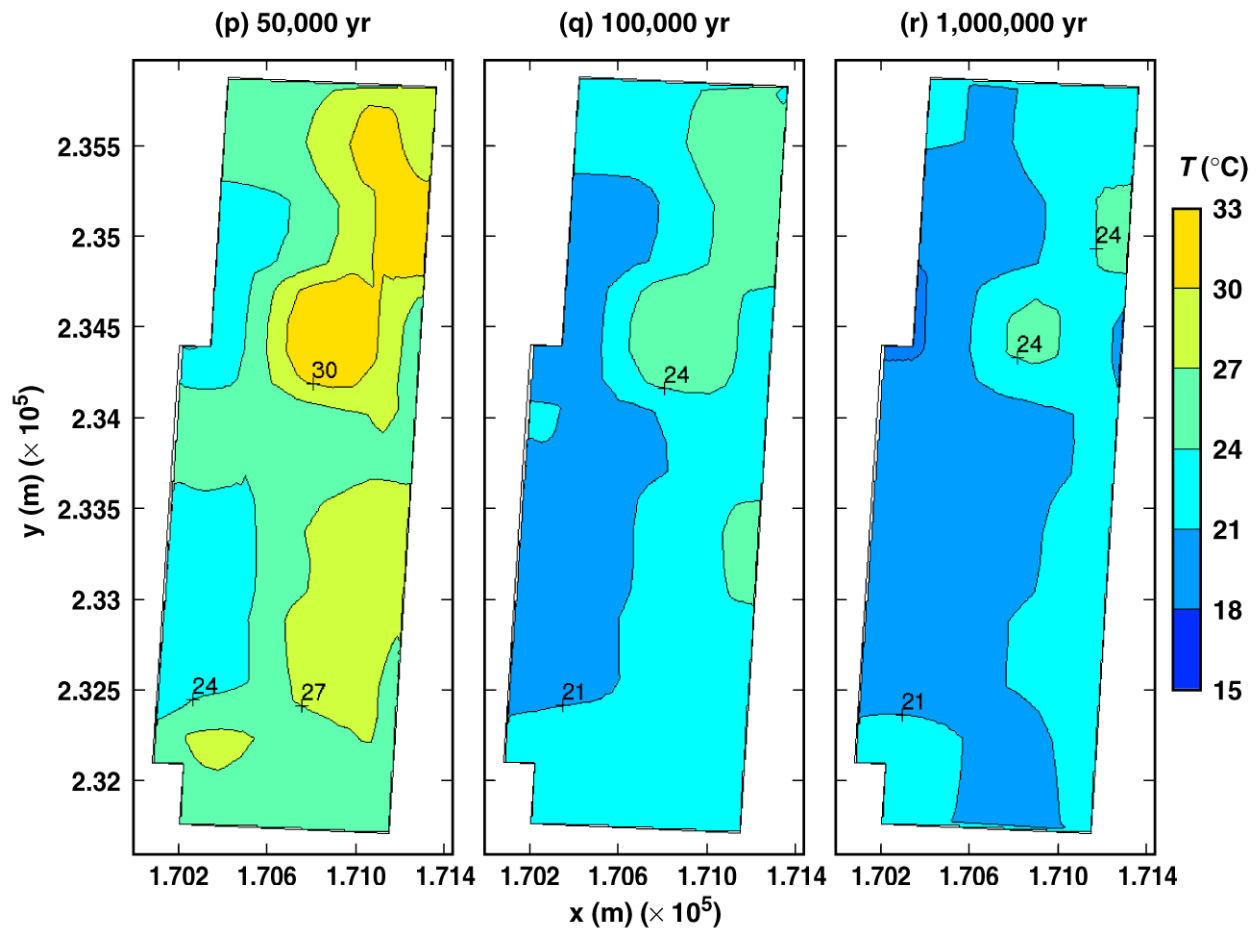


TB\_AMR\_upper\_T\_wp\_pwr2\_319-376  
 Figure 6-10. Temperature on the surface of a 21-PWR WP for the high infiltration-flux backfill case for the indicated times (Continued)



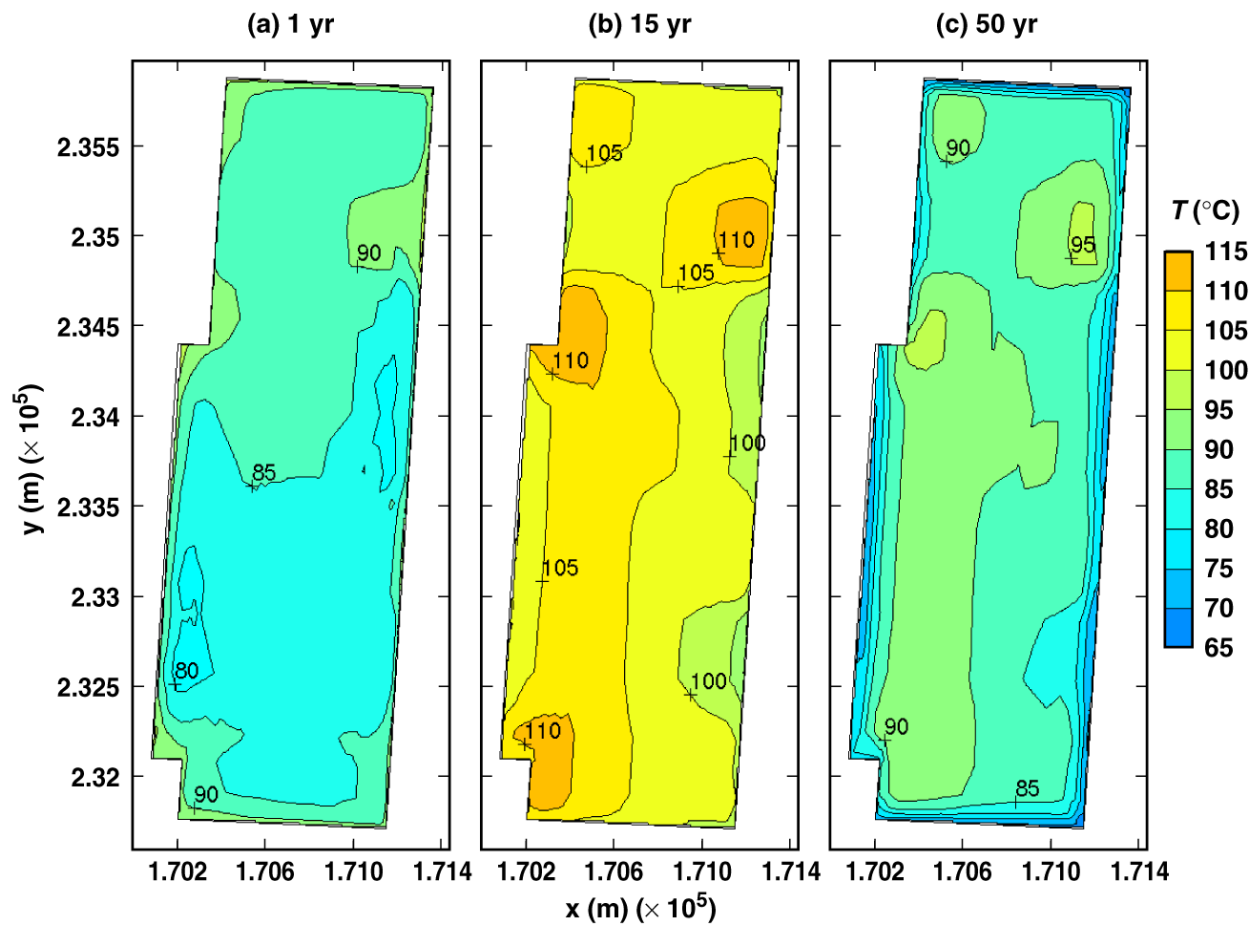
TB\_AMR\_upper\_T\_wp\_pwr2\_403-434

Figure 6-10. Temperature on the surface of a 21-PWR WP for the high infiltration-flux backfill case for the indicated times (Continued)



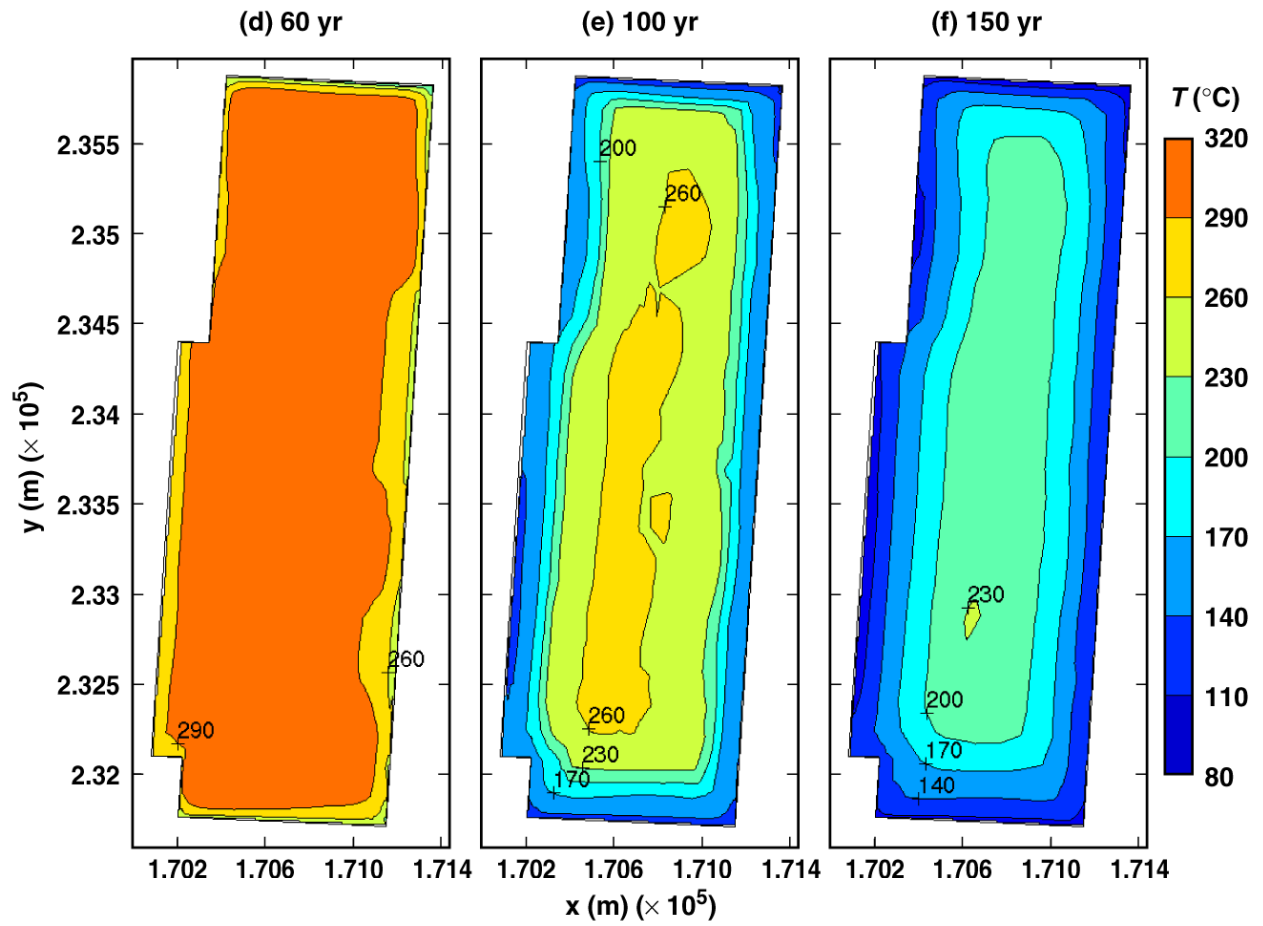
TB\_AMR\_upper\_T\_wp\_pwr2\_446-457

Figure 6-10. Temperature on the surface of a 21-PWR WP for the high infiltration-flux backfill case for the indicated times (Continued)



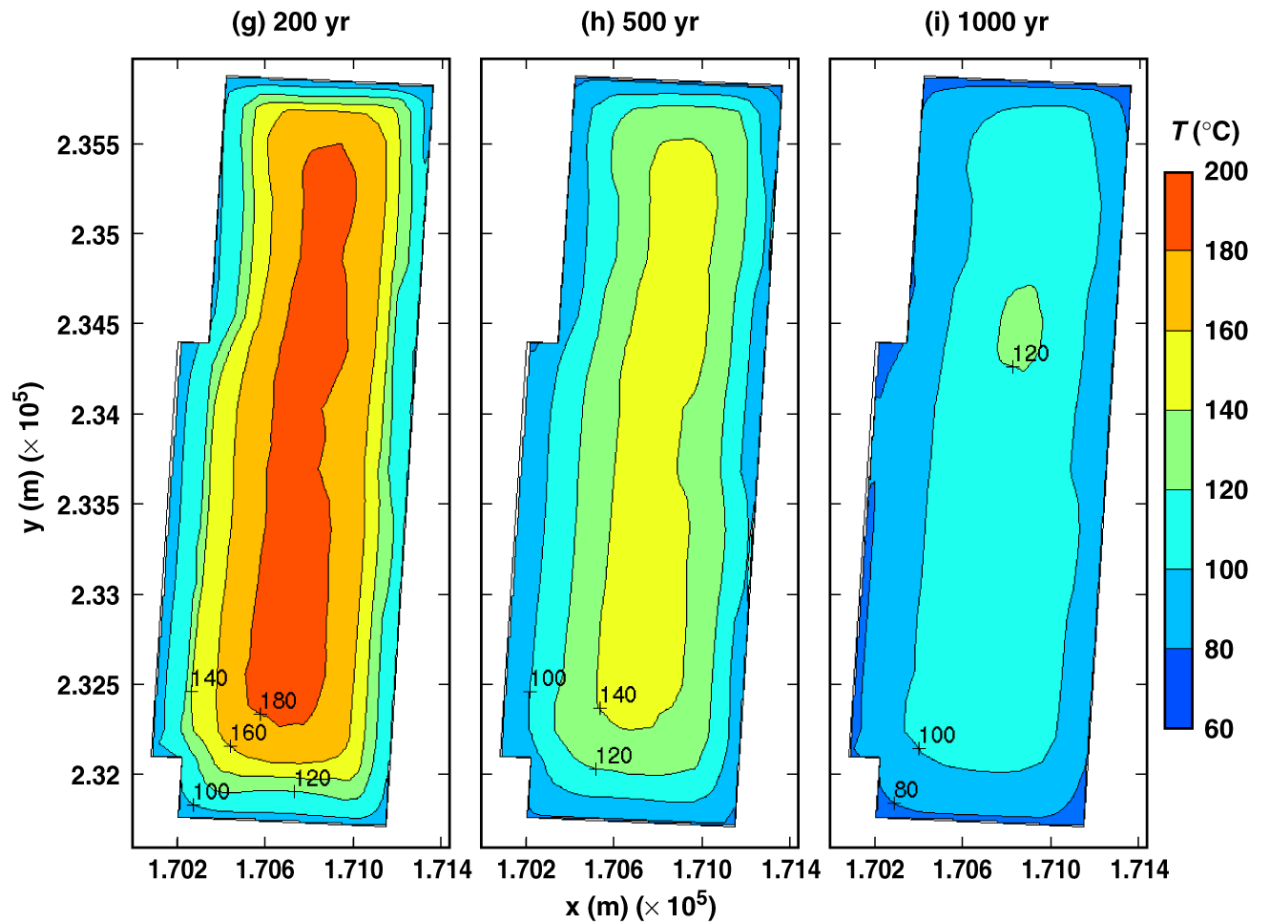
TB\_AMR\_lower\_T\_wp\_pwr2\_2-11

Figure 6-11. Temperature on the surface of a 21-PWR WP for the low infiltration-flux backfill case for the indicated times



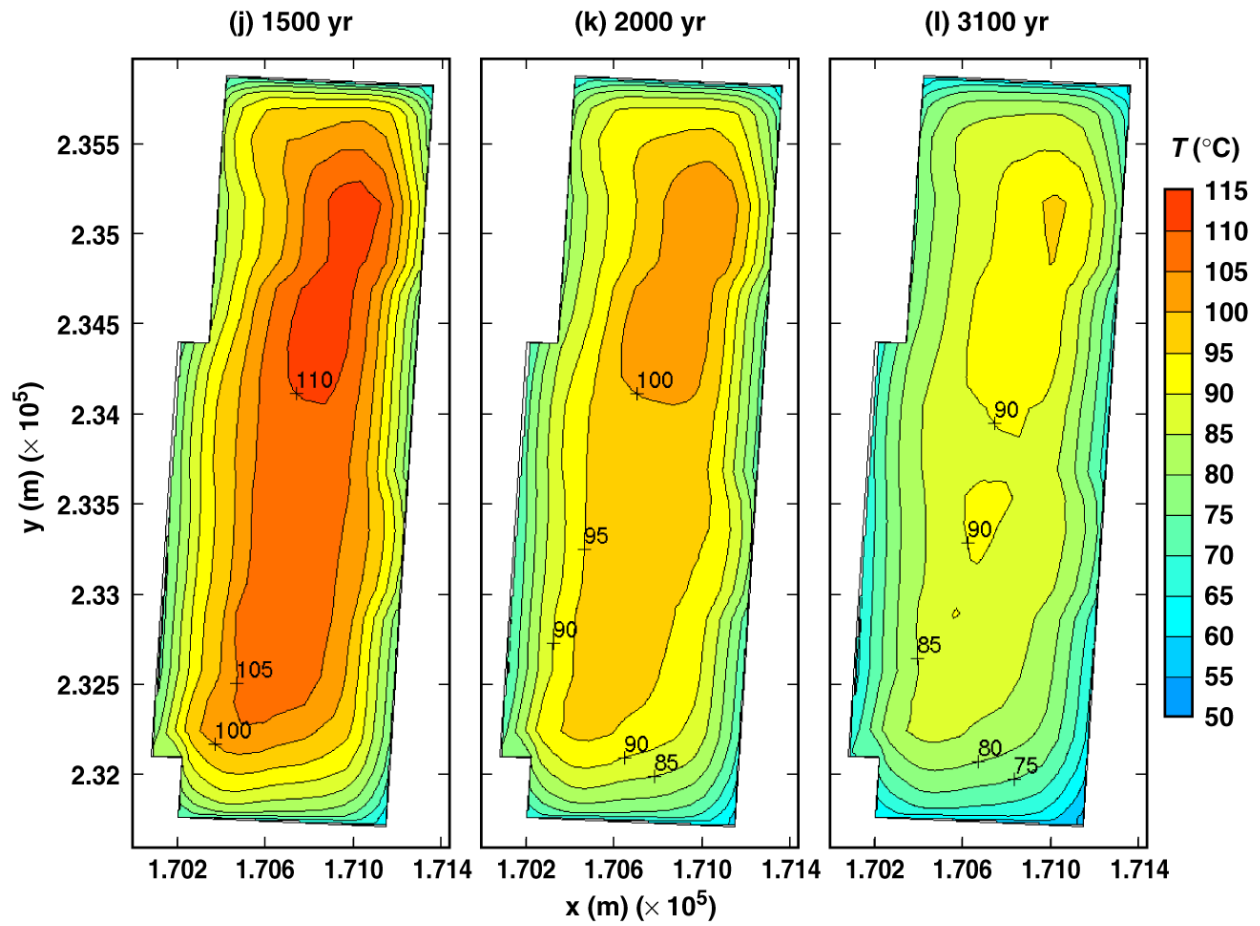
TB\_AMR\_lower\_T\_wp\_pwr2\_17-25

Figure 6-11. Temperature on the surface of a 21-PWR WP for the low infiltration-flux backfill case for the indicated times (Continued)



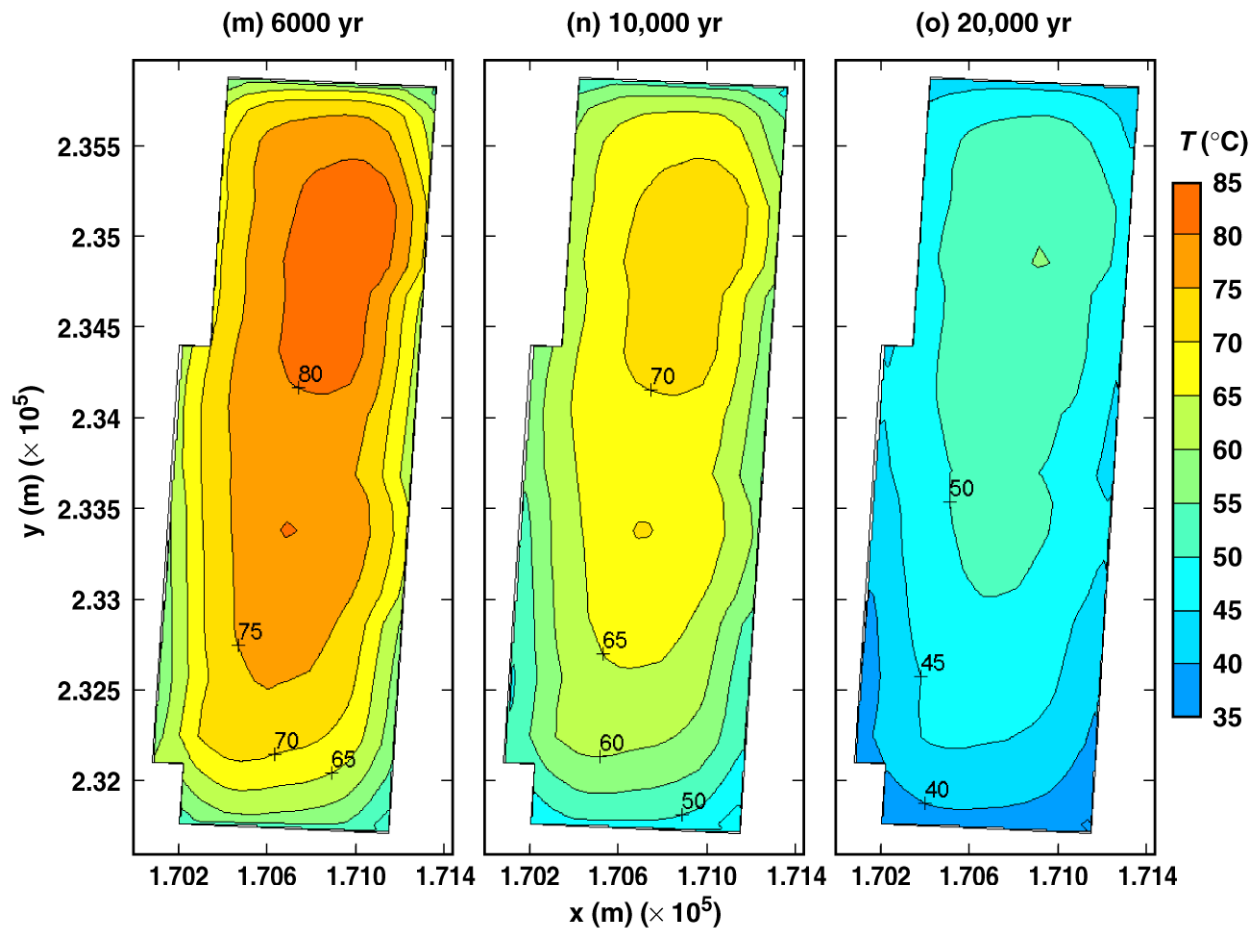
TB\_AMR\_lower\_T\_wp\_pwr2\_28-219

Figure 6-11. Temperature on the surface of a 21-PWR WP for the low infiltration-flux backfill case for the indicated times (Continued)



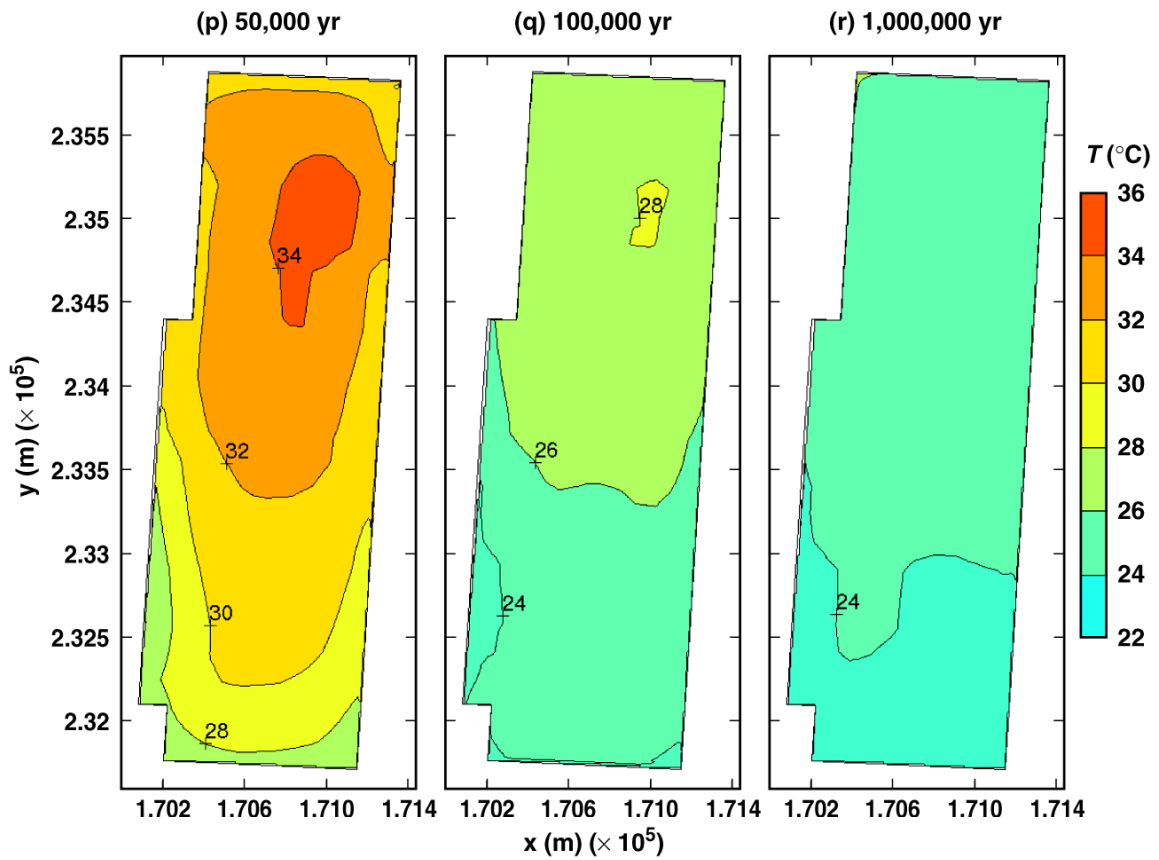
TB\_AMR\_lower\_T\_wp\_pwr2\_276-357

Figure 6-11. Temperature on the surface of a 21-PWR WP for the low infiltration-flux backfill case for the indicated times (Continued)



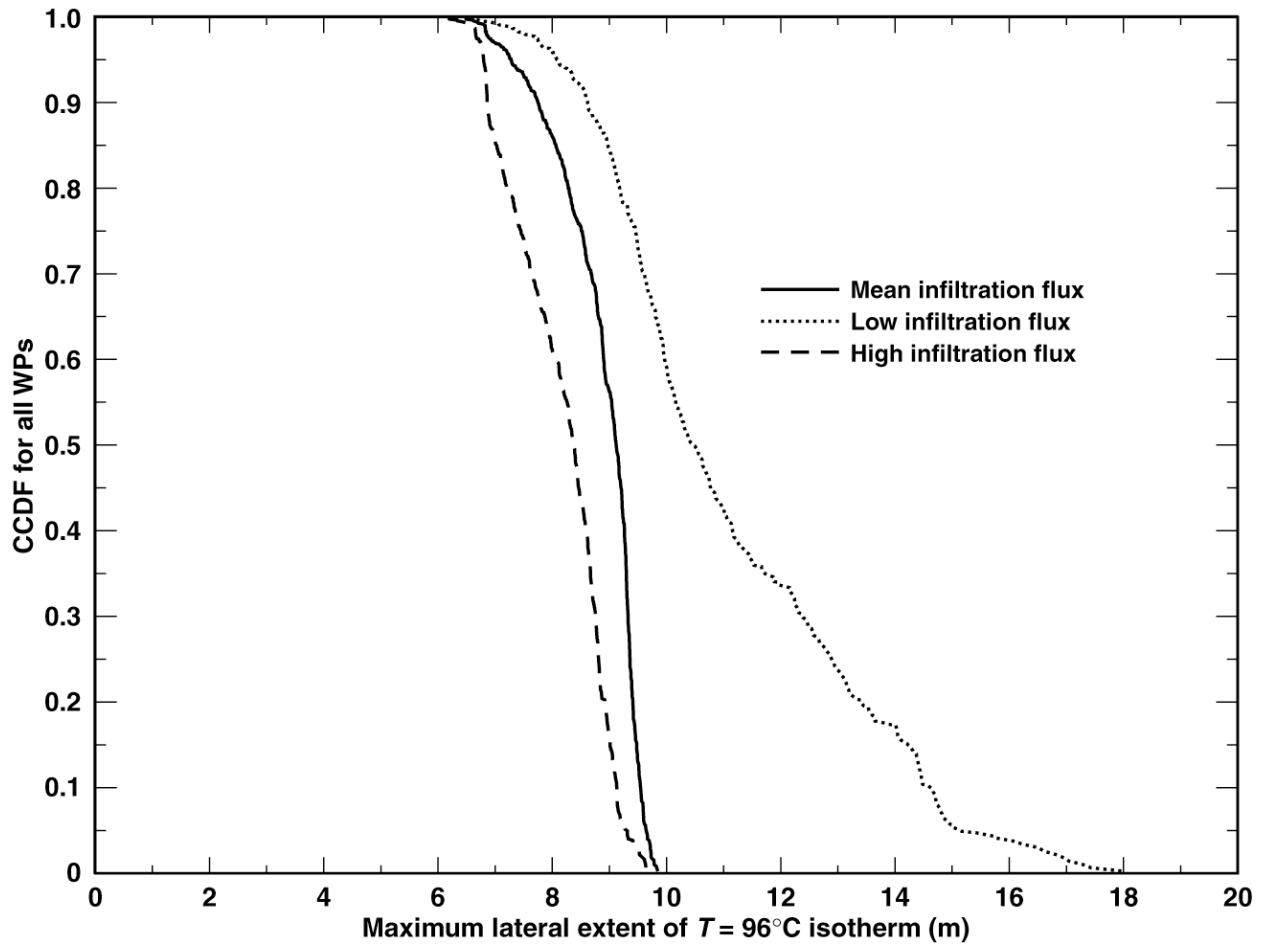
TB\_AMR\_lower\_T\_wp\_pwr2\_394-411

Figure 6-11. Temperature on the surface of a 21-PWR WP for the low infiltration-flux backfill case for the indicated times (Continued)



TB\_AMR\_lower\_T\_wp\_pwr2\_427-442

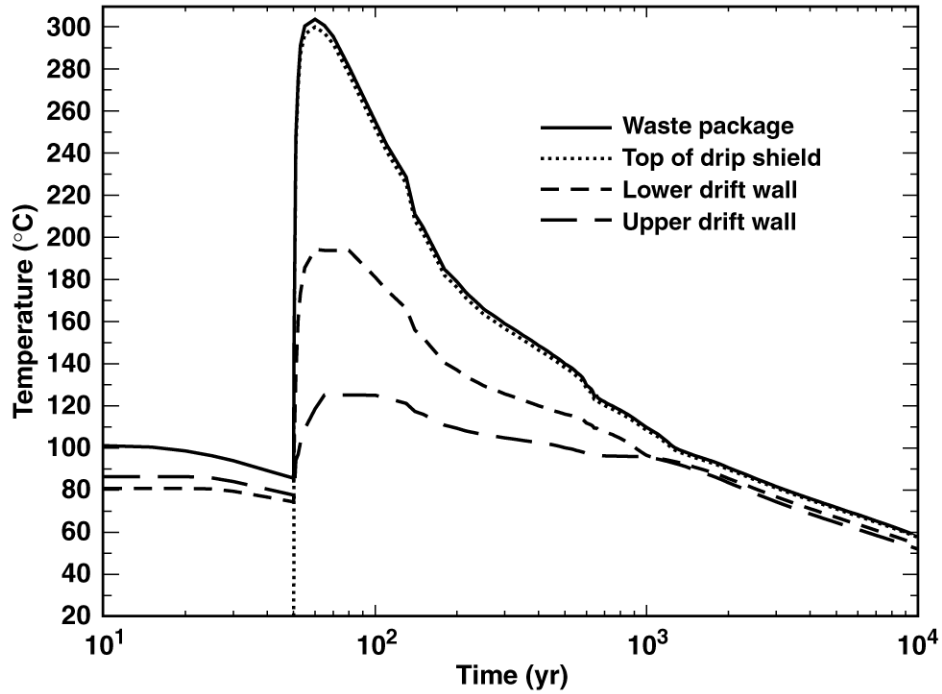
Figure 6-11. Temperature on the surface of a 21-PWR WP for the low infiltration-flux backfill case for the indicated times (Continued)



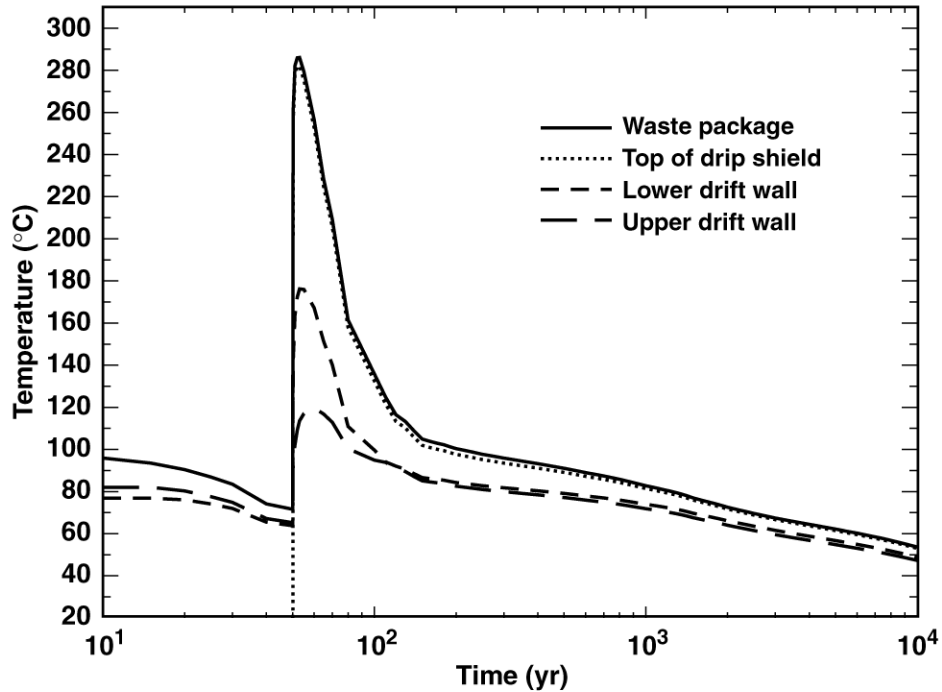
TB\_AMR\_CCDF\_xT=96C\_mlu

Figure 6-12. The complementary cumulative distribution function (CCDF) for the maximum lateral extent of the boiling point ( $T = 96^{\circ}\text{C}$ ) isotherm is plotted for the mean, high, and low infiltration-flux backfill cases

(a) Center of Repository  
 Nevada State Coordinates: Easting = 170535.03 m, Northing = 233640.08 m

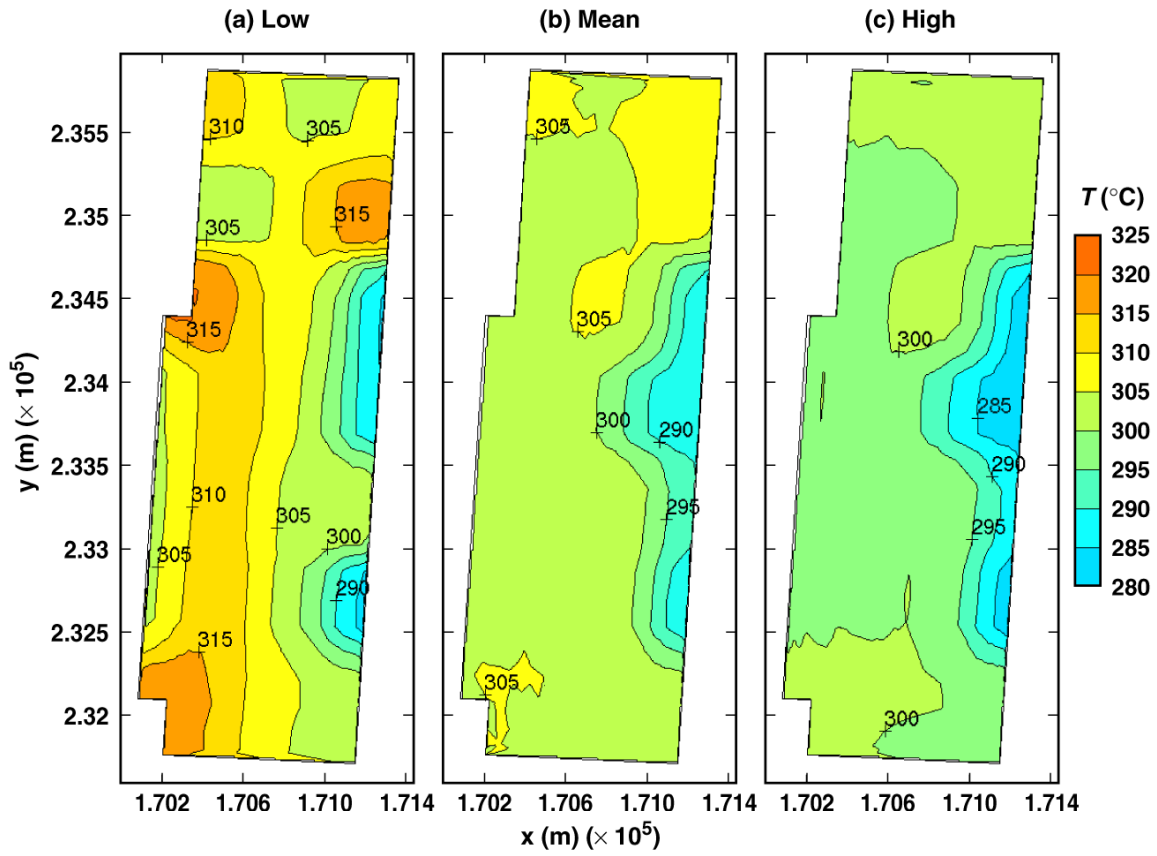


(b) Eastern Edge of Repository  
 Nevada State Coordinates: Easting = 171195.16 m, Northing = 233605.06 m



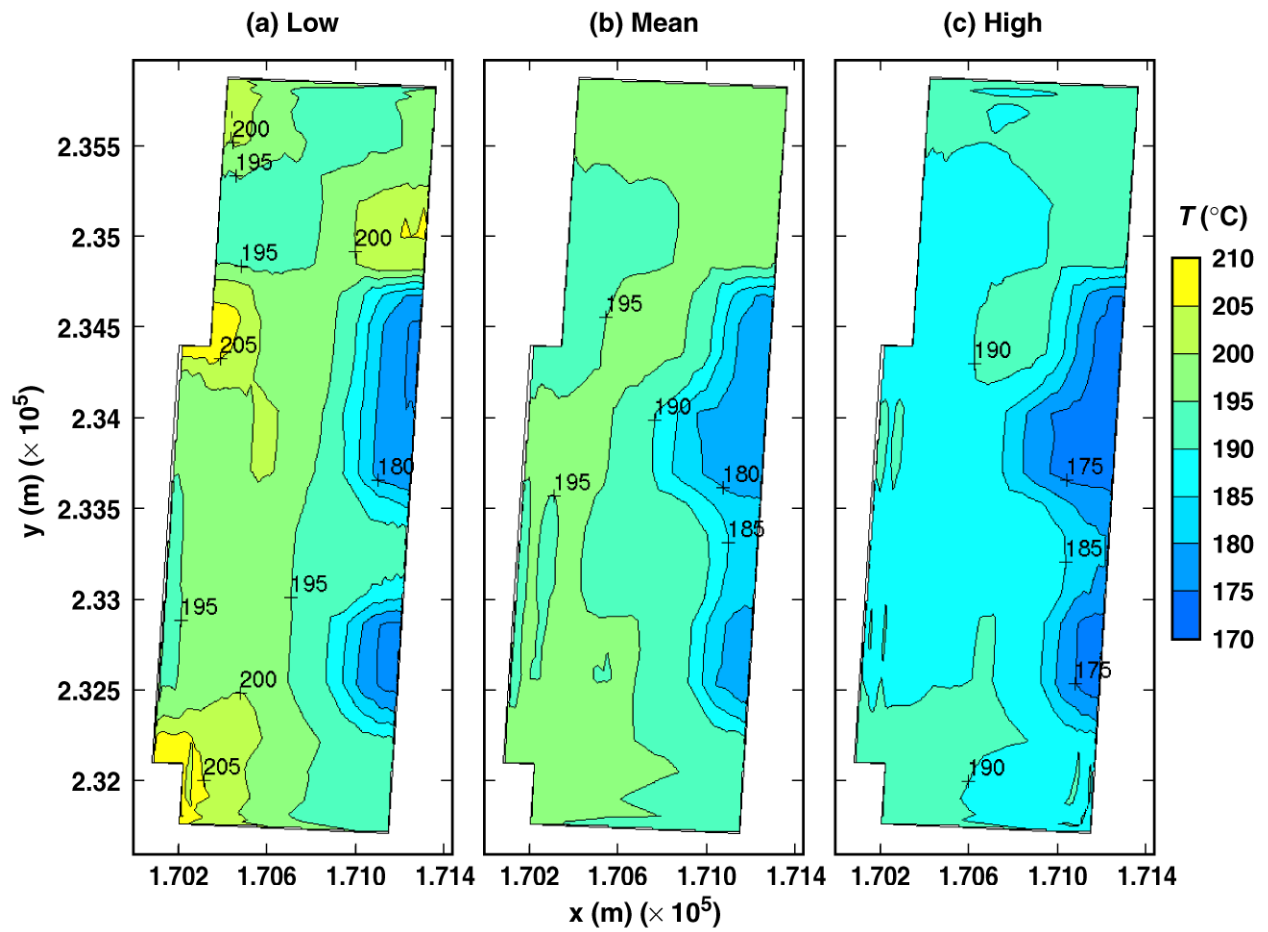
TB\_AMR\_T\_hist\_pwr2\_13&24\_17\_mean

Figure 6-13. Temperature history on the surface of a 21-PWR WP for the mean infiltration-flux backfill case at (a) the geographical center of the repository and (b) a location 27.5 m from the eastern edge of the repository. Note that the Nevada State coordinates are given.



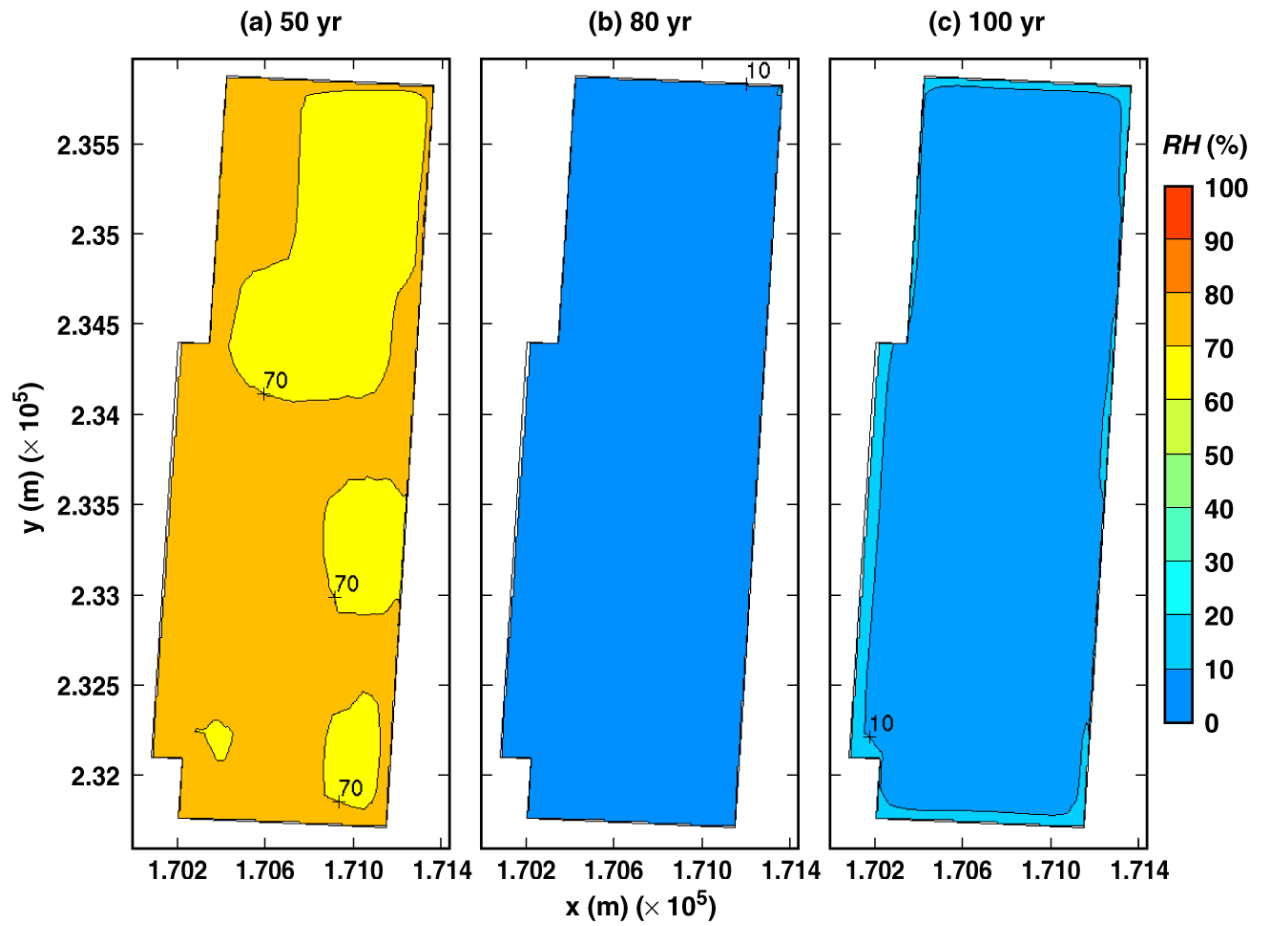
TB\_AMR\_lmu\_T\_wp\_max\_pwr2

Figure 6-14. Peak WP temperature for the low, mean, and high infiltration-flux backfill cases



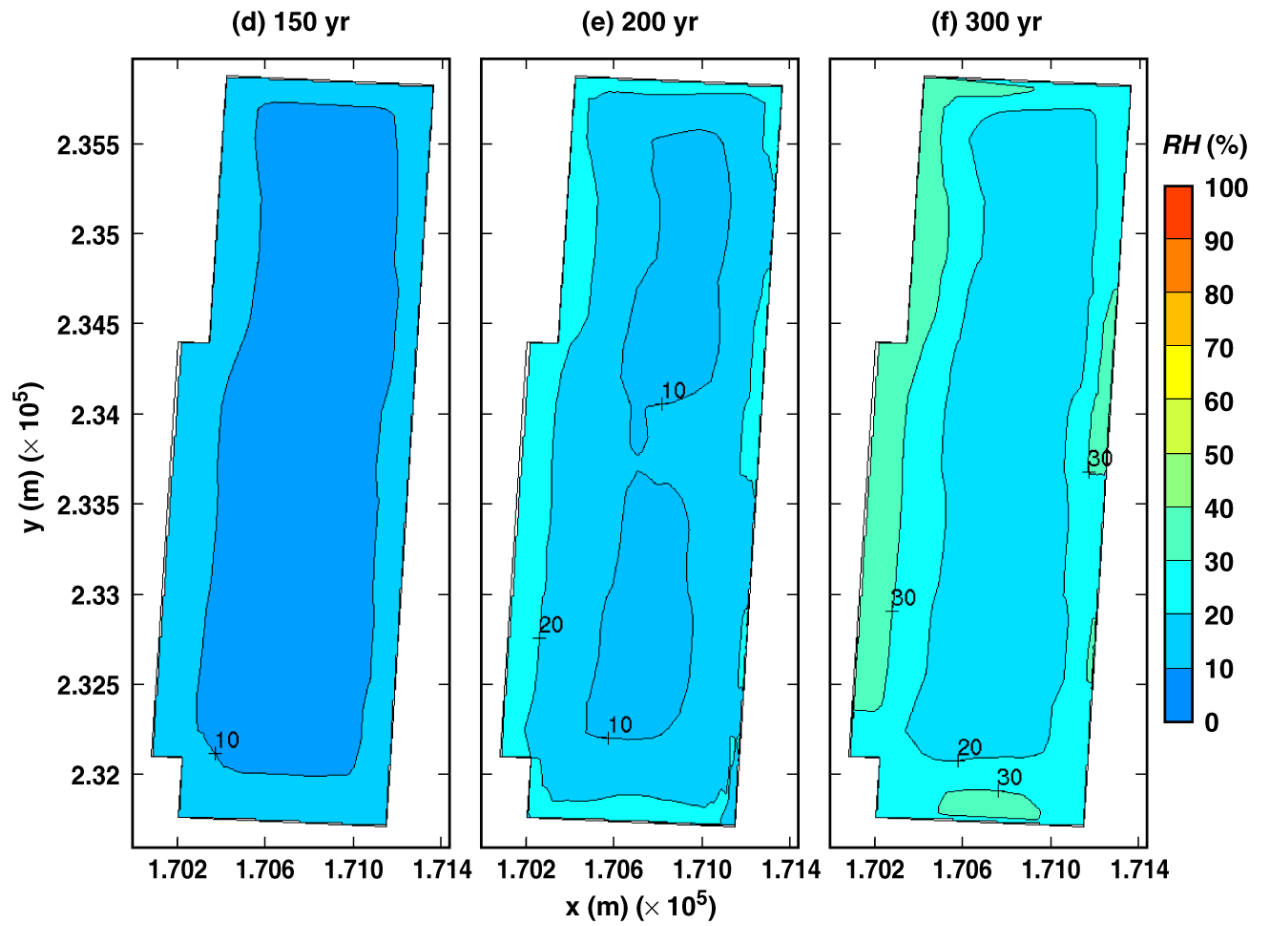
TB\_AMR\_lmu\_T\_dw\_lower\_max

Figure 6-15. Peak temperature on the lower drift wall (below the invert) for the low, mean, and high infiltration-flux backfill cases



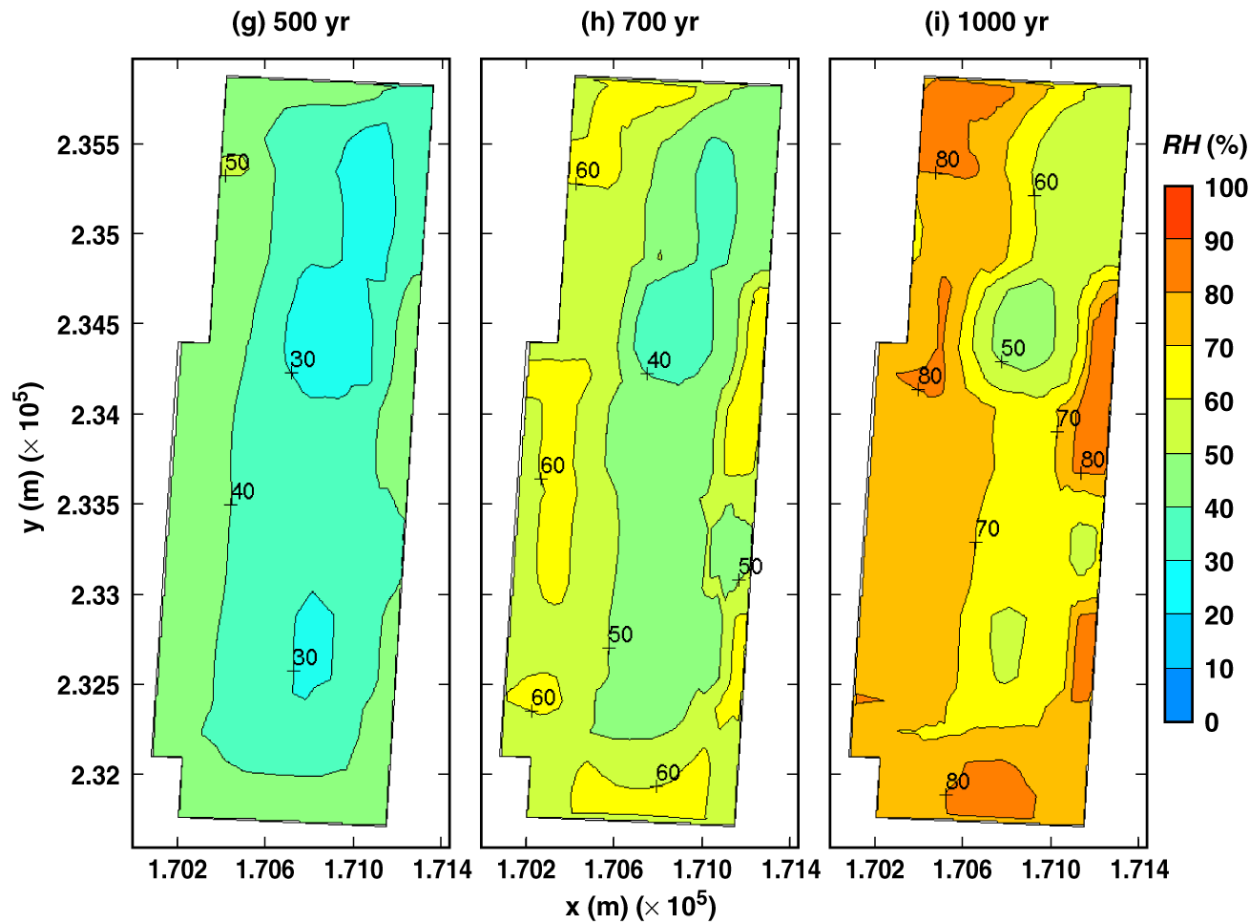
TB\_AMR\_mean\_RH\_wp\_pwr2\_11-21

Figure 6-16. Relative humidity on the surface of a 21-PWR WP for the mean infiltration-flux backfill case for the indicated times



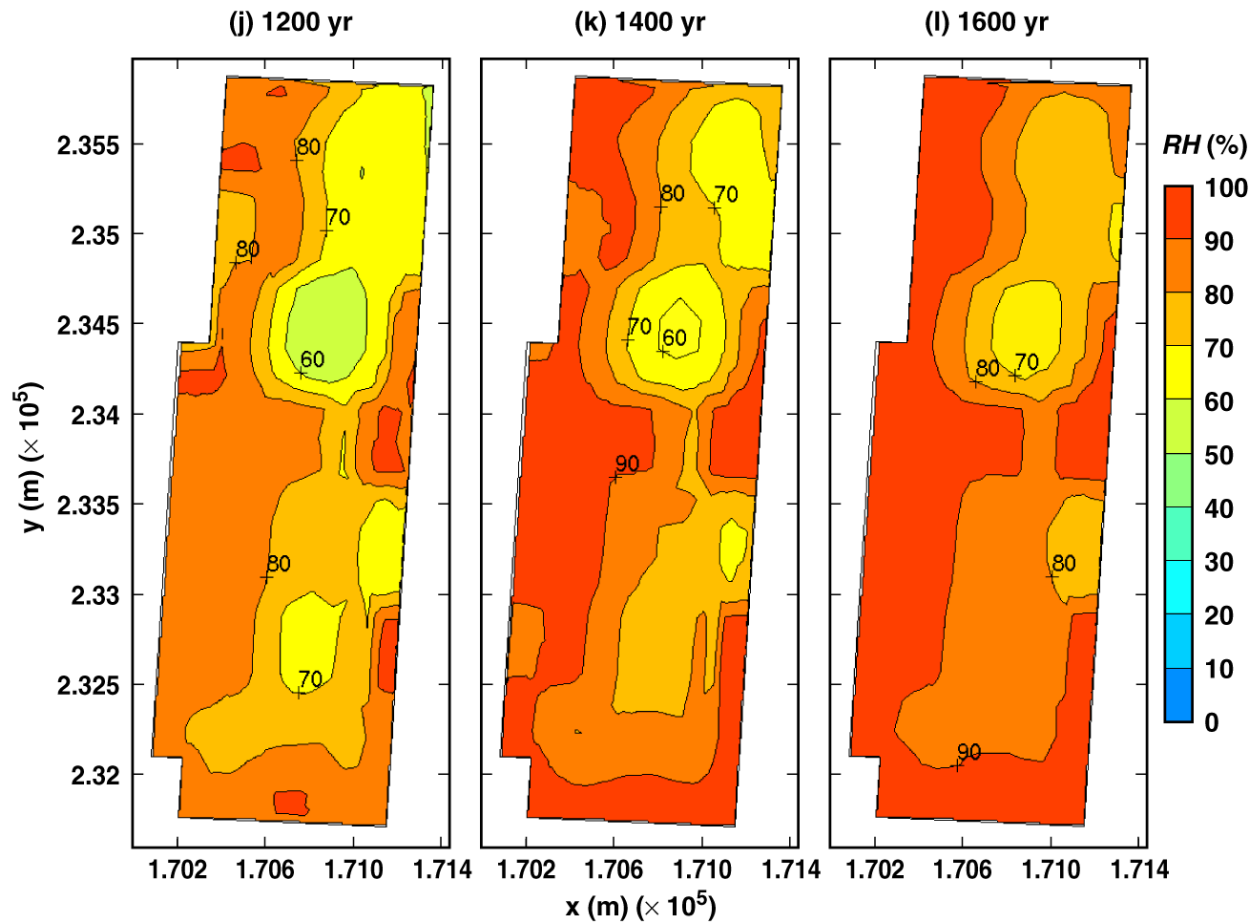
TB\_AMR\_mean\_RH\_wp\_pwr2\_26-64

Figure 6-16. Relative humidity on the surface of a 21-PWR WP for the mean infiltration-flux backfill case for the indicated times (Continued)



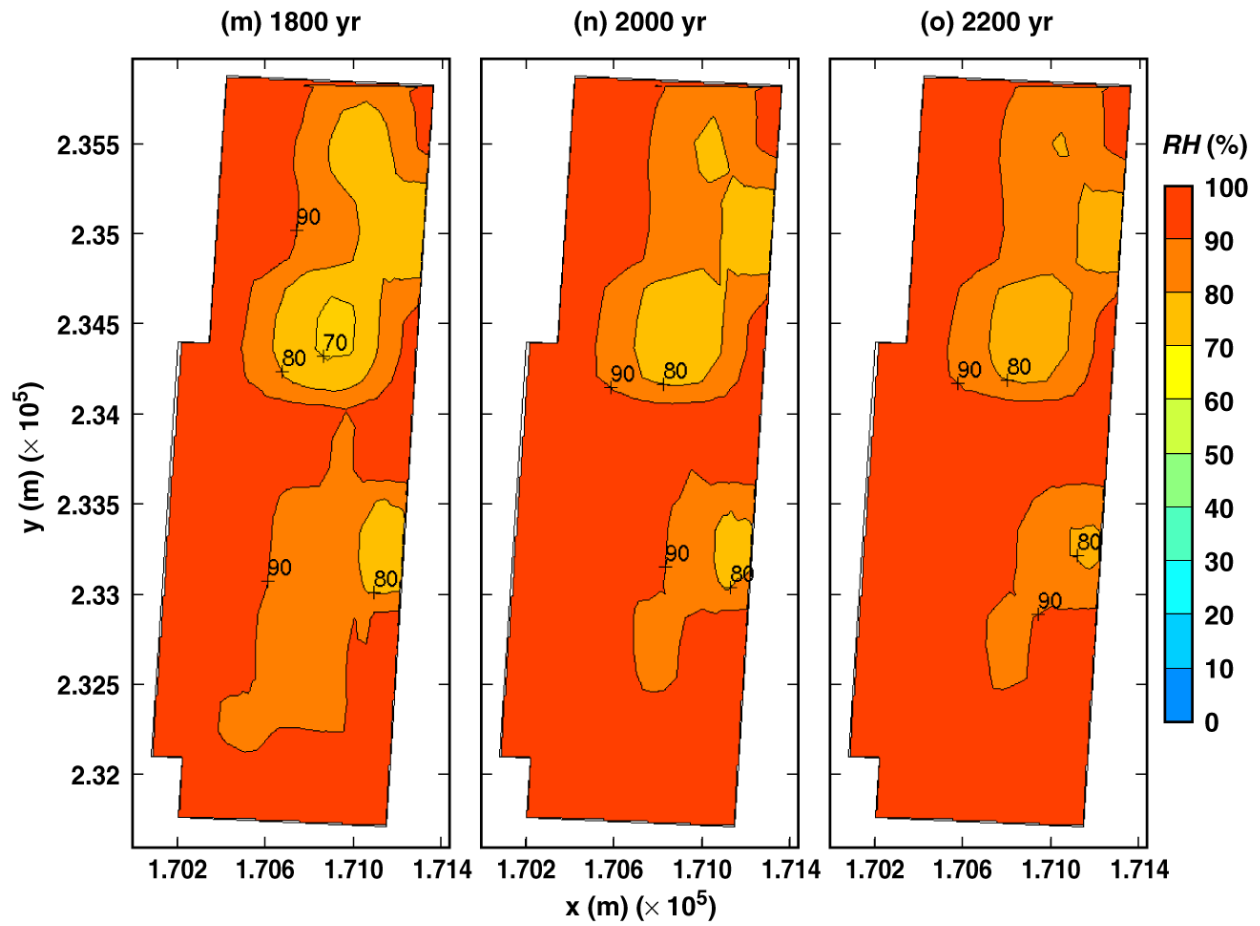
TB\_AMR\_mean\_RH\_wp\_pwr2\_104-174

Figure 6-16. Relative humidity on the surface of a 21-PWR WP for the mean infiltration-flux backfill case for the indicated times (Continued)



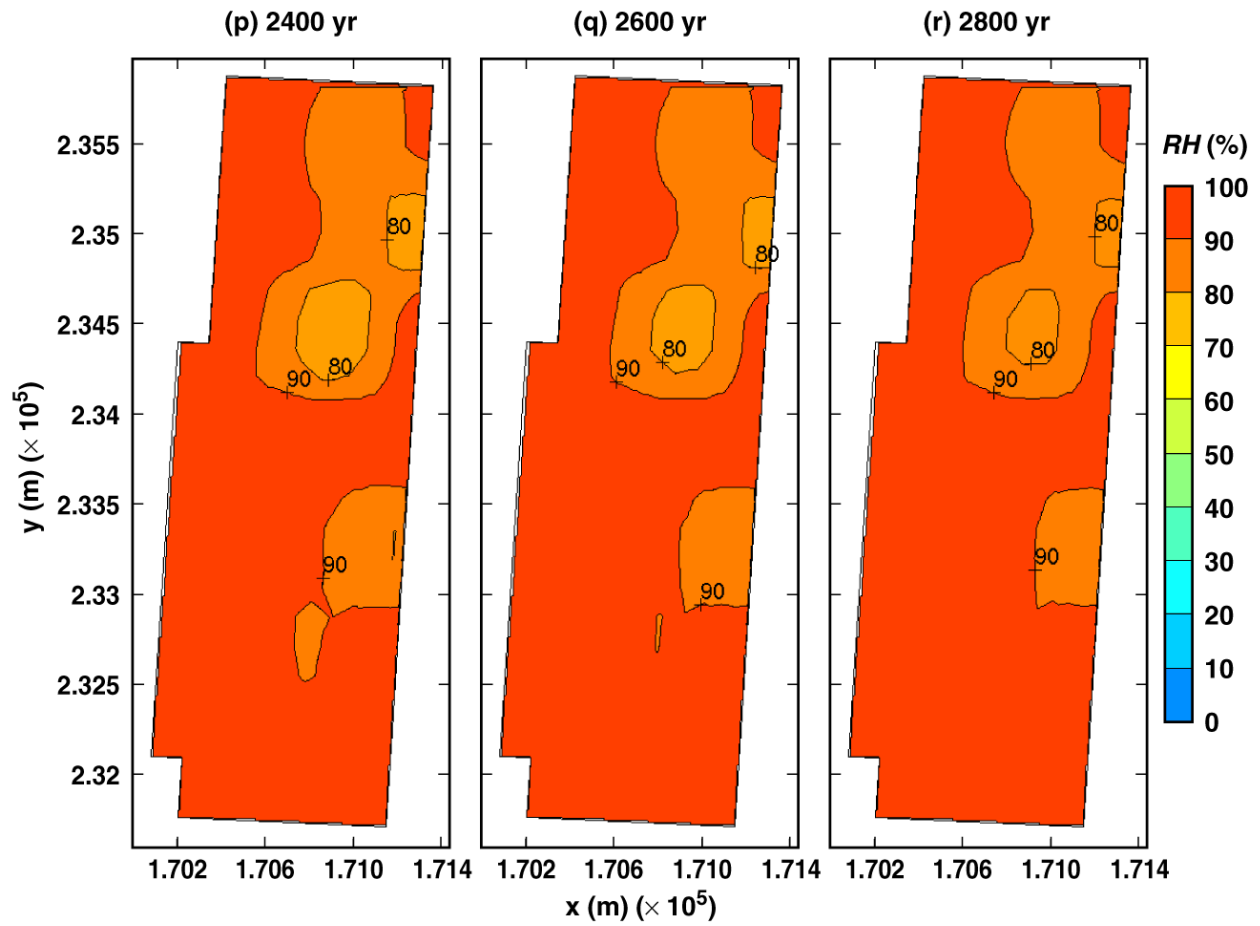
TB\_AMR\_mean\_RH\_wp\_pwr2\_204-231

Figure 6-16. Relative humidity on the surface of a 21-PWR WP for the mean infiltration-flux backfill case for the indicated times (Continued)



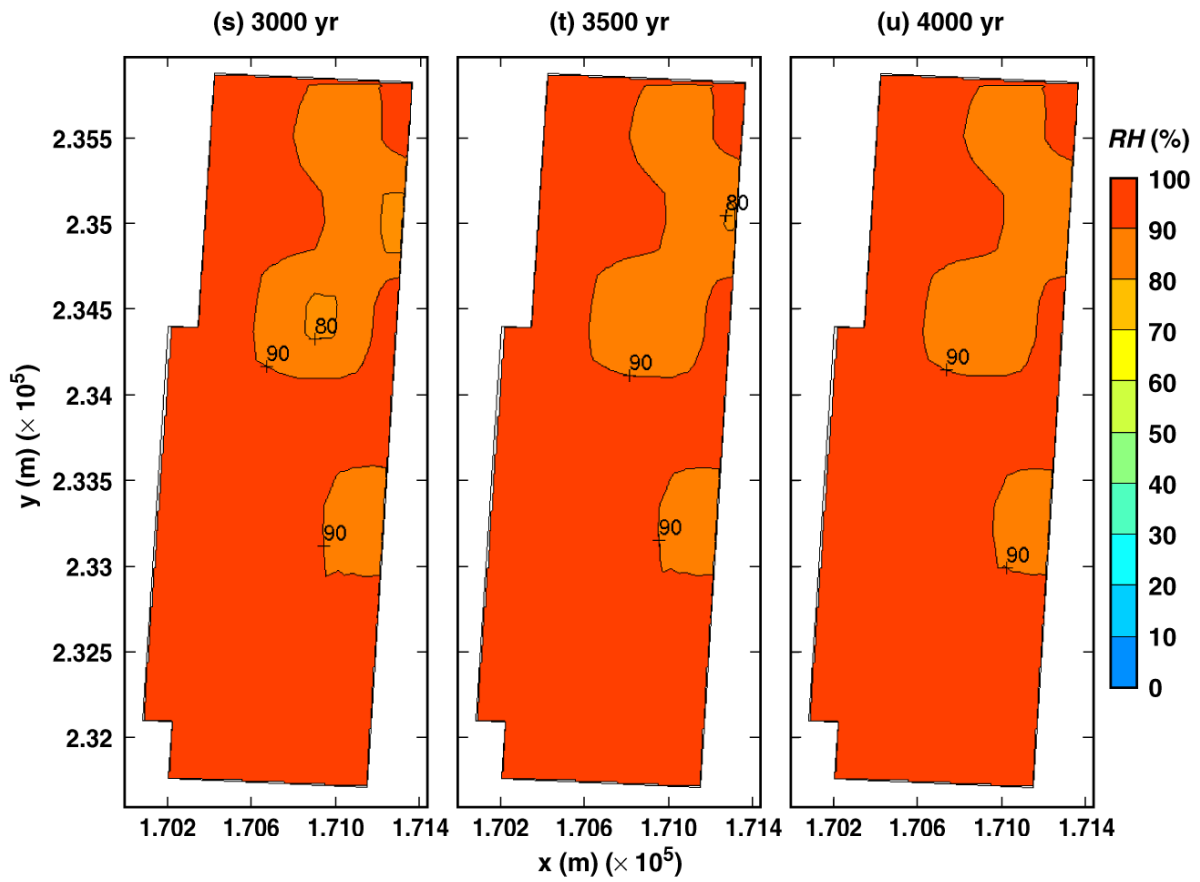
TB\_AMR\_mean\_RH\_wp\_pwr2\_243-266

Figure 6-16. Relative humidity on the surface of a 21-PWR WP for the mean infiltration-flux backfill case for the indicated times (Continued)



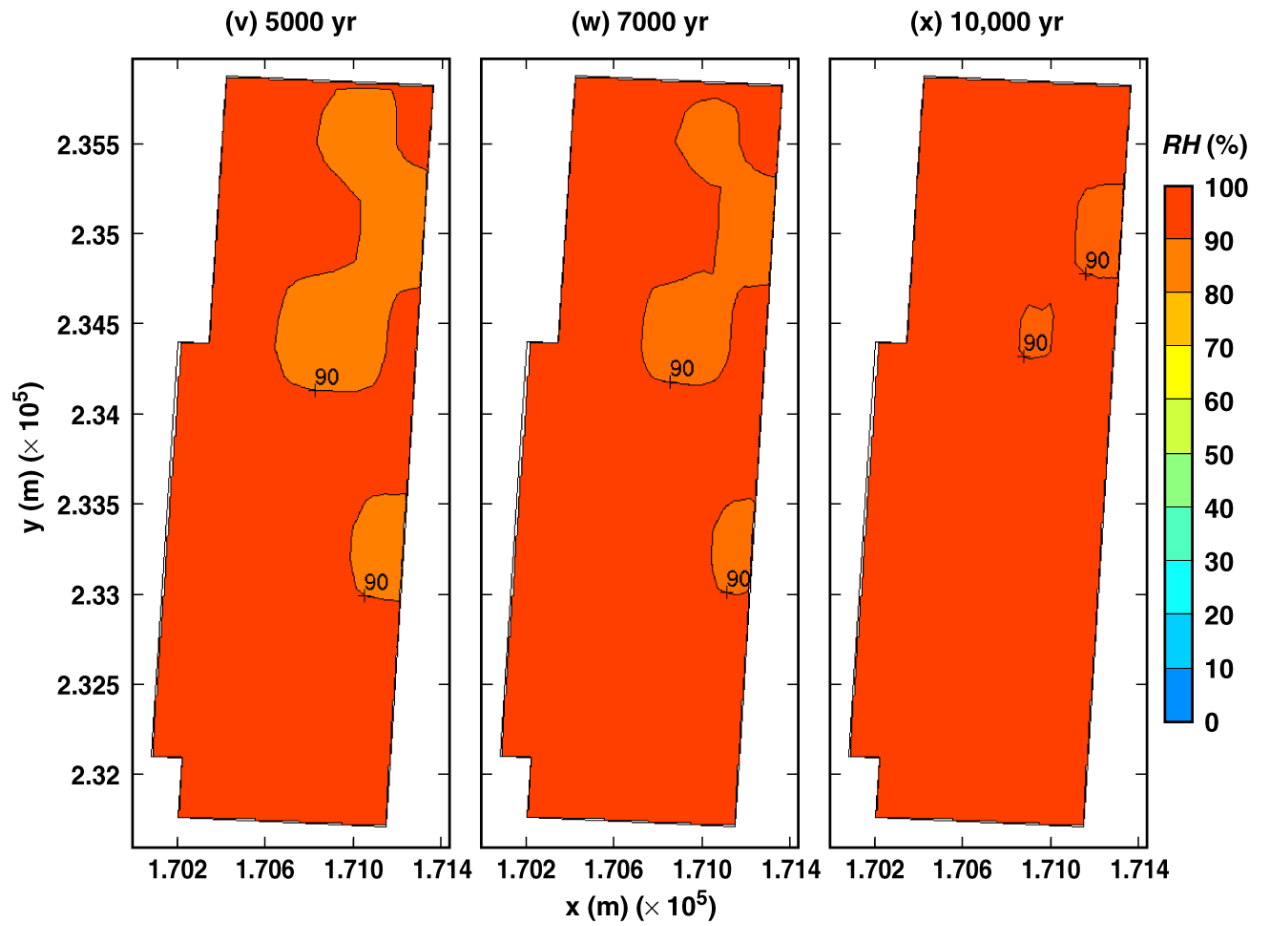
TB\_AMR\_mean\_RH\_wp\_pwr2\_271-279

Figure 6-16. Relative humidity on the surface of a 21-PWR WP for the mean infiltration-flux backfill case for the indicated times (Continued)



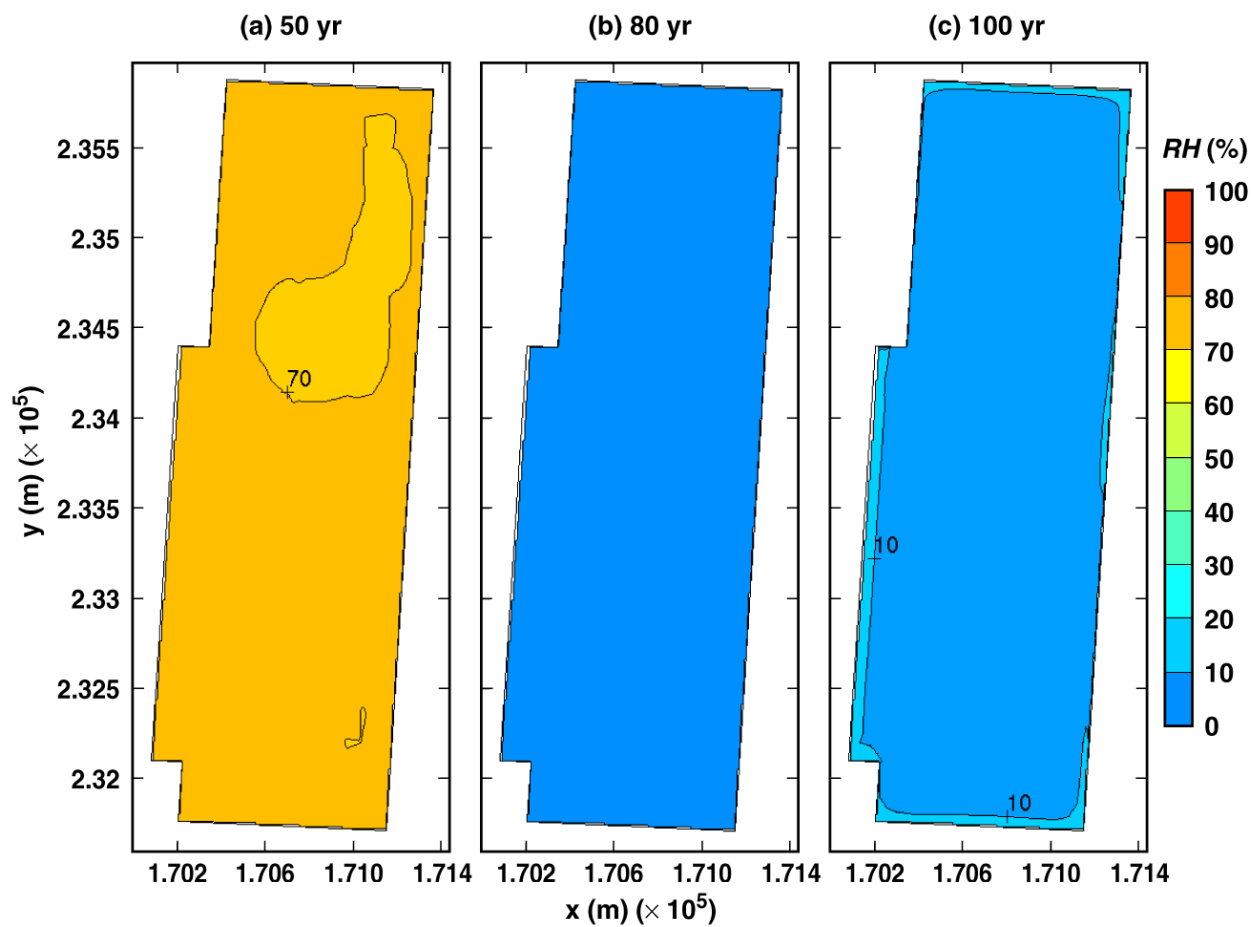
TB\_AMR\_mean\_RH\_wp\_pwr2\_283-297

Figure 6-16. Relative humidity on the surface of a 21-PWR WP for the mean infiltration-flux backfill case for the indicated times (Continued)



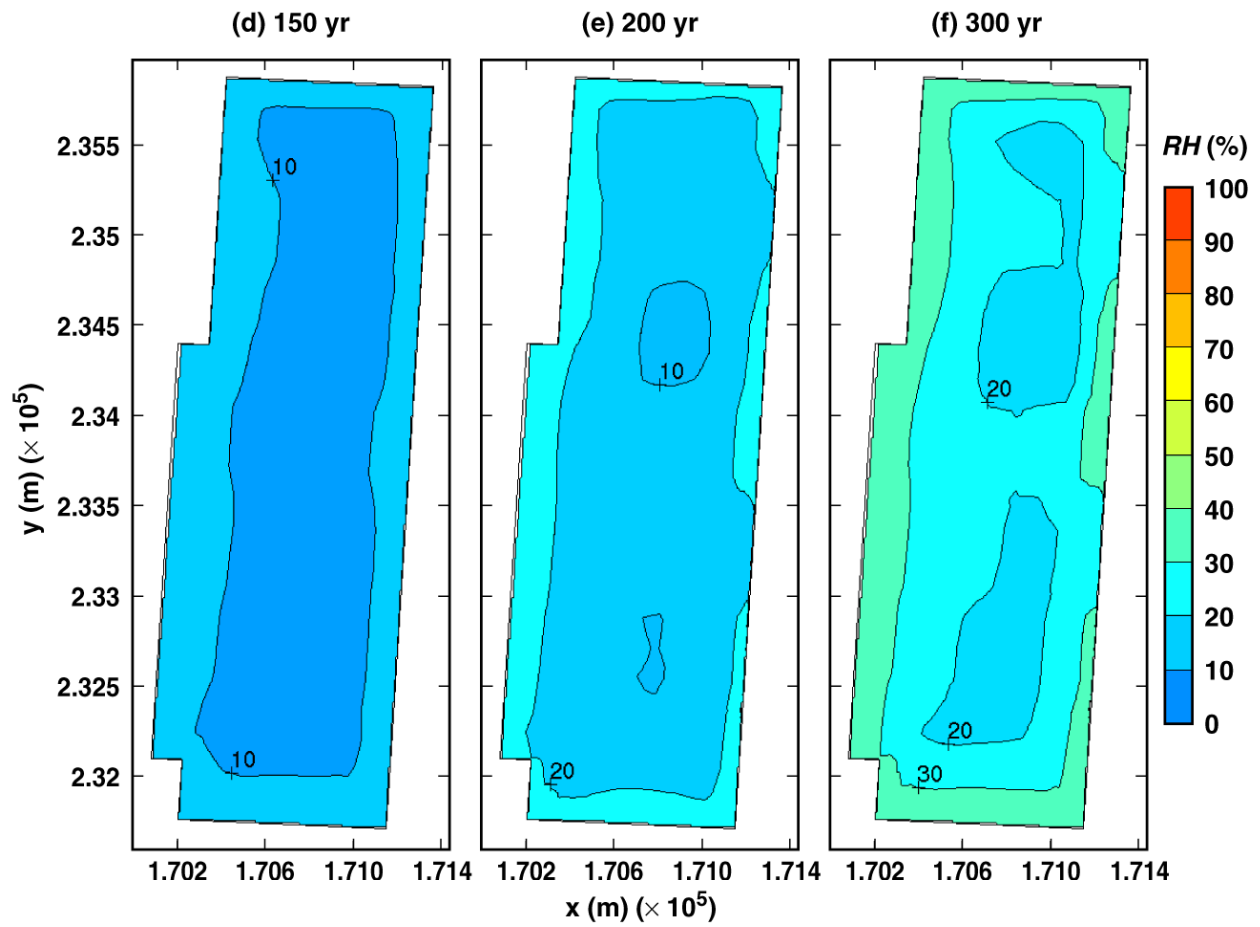
TB\_AMR\_mean\_RH\_wp\_pwr2\_307-319

Figure 6-16. Relative humidity on the surface of a 21-PWR WP for the mean infiltration-flux backfill case for the indicated times (Continued)



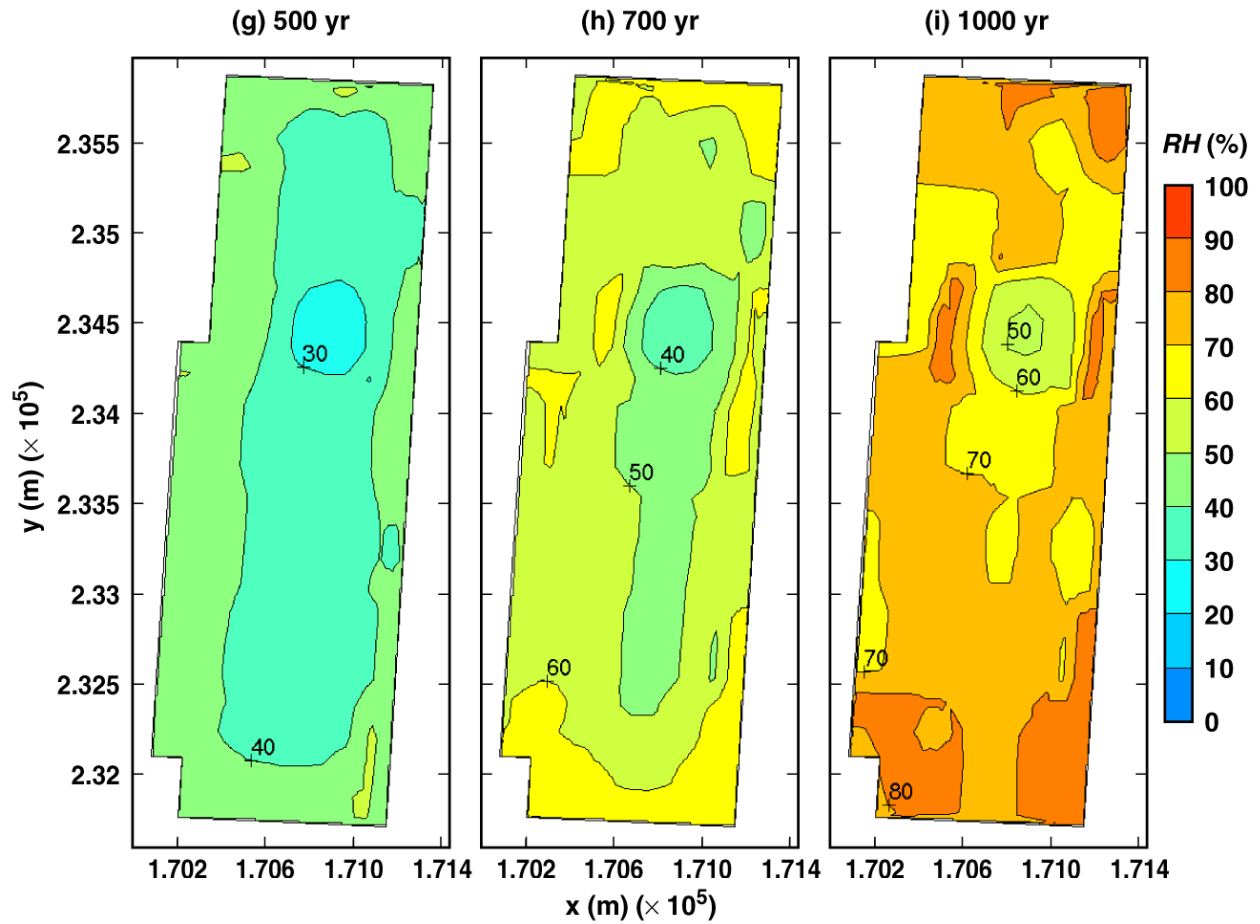
TB\_AMR\_upper\_RH\_wp\_pwr2\_11-22

Figure 6-17. Relative humidity on the surface of a 21-PWR WP for the high infiltration-flux backfill case for the indicated times



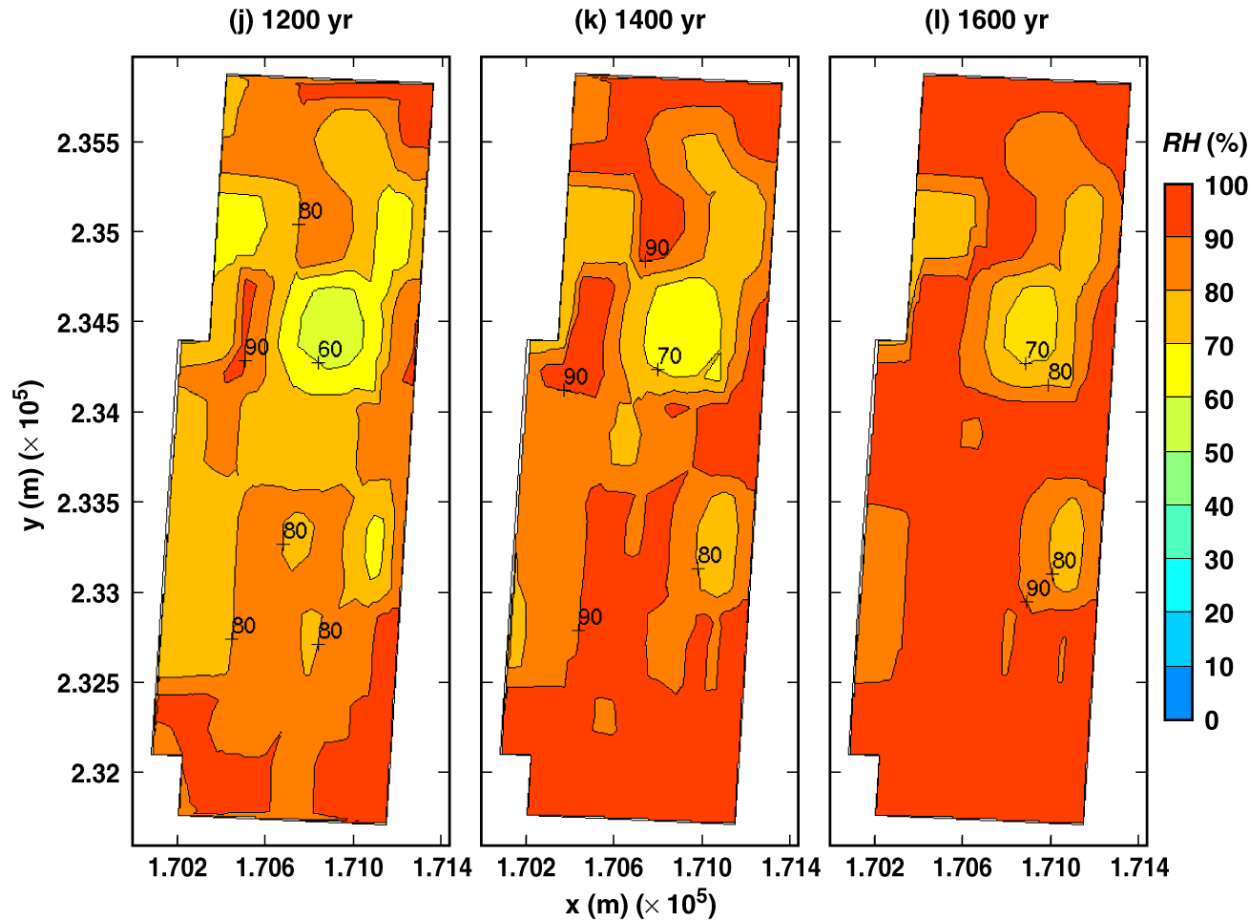
TB\_AMR\_upper\_RH\_wp\_pwr2\_31-107

Figure 6-17. Relative humidity on the surface of a 21-PWR WP for the high infiltration-flux backfill case for the indicated times (Continued)



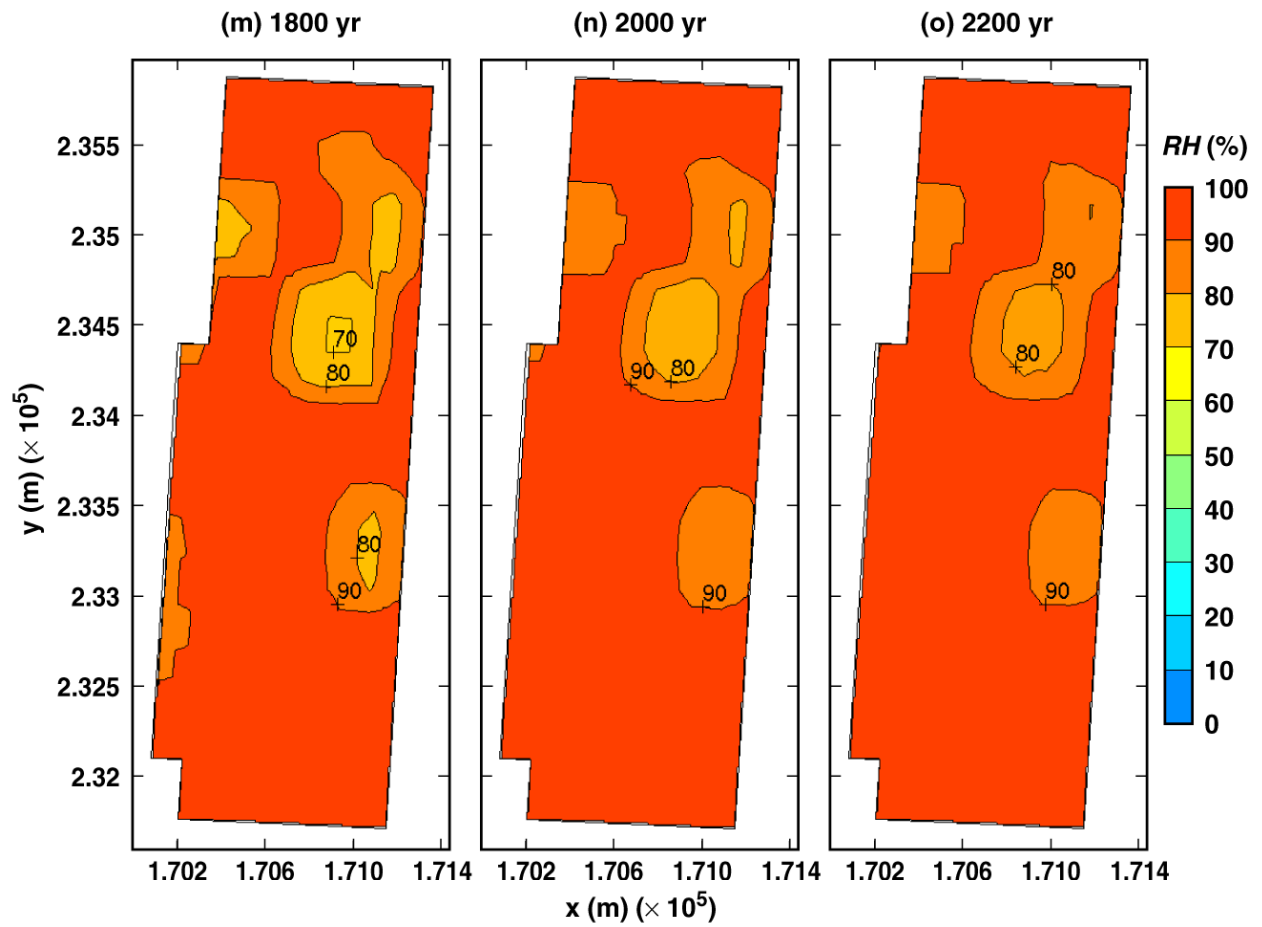
TB\_AMR\_upper\_RH\_wp\_pwr2\_177-269

Figure 6-17. Relative humidity on the surface of a 21-PWR WP for the high infiltration-flux backfill case for the indicated times (Continued)



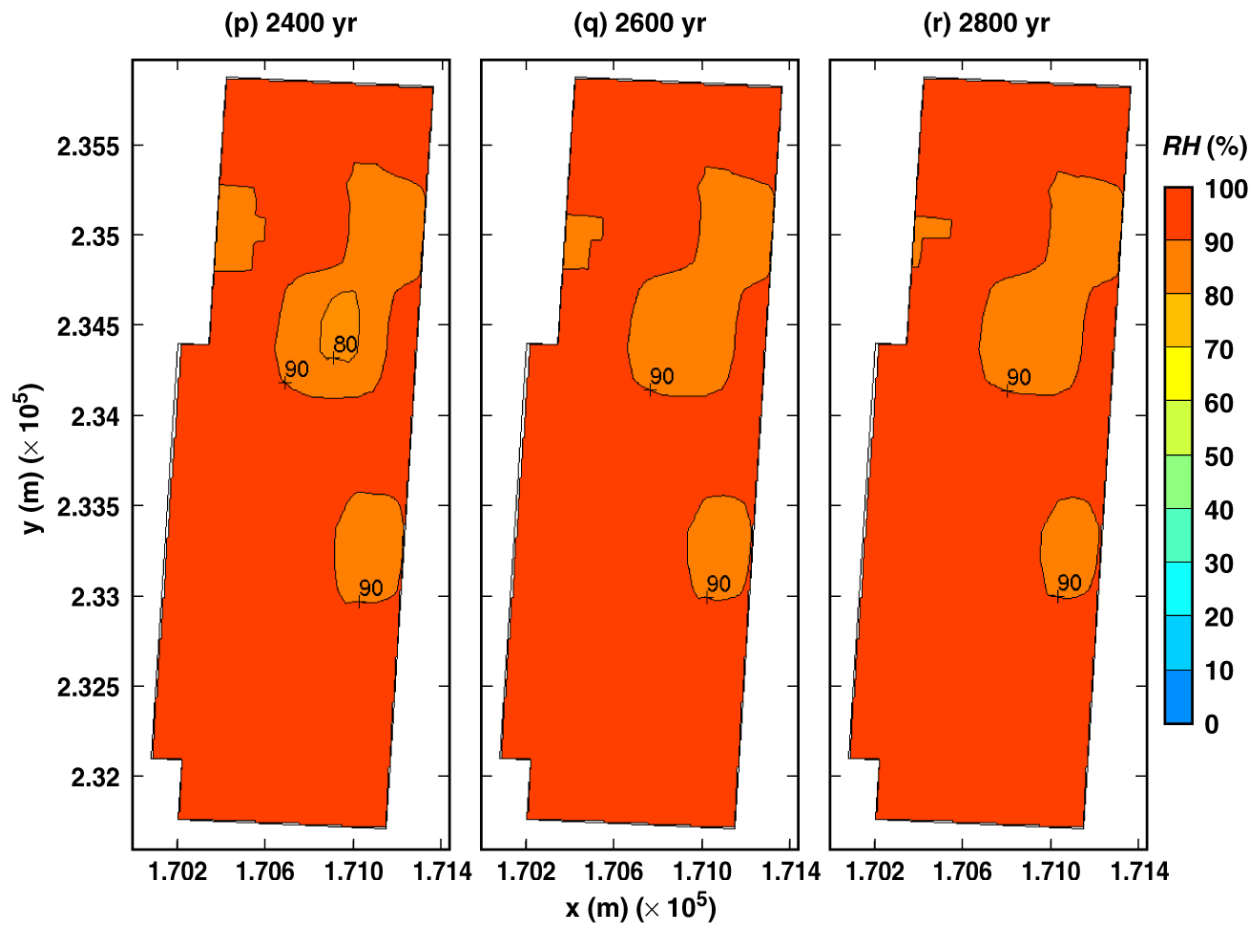
TB\_AMR\_upper\_RH\_wp\_pwr2\_289-329

Figure 6-17. Relative humidity on the surface of a 21-PWR WP for the high infiltration-flux backfill case for the indicated times (Continued)



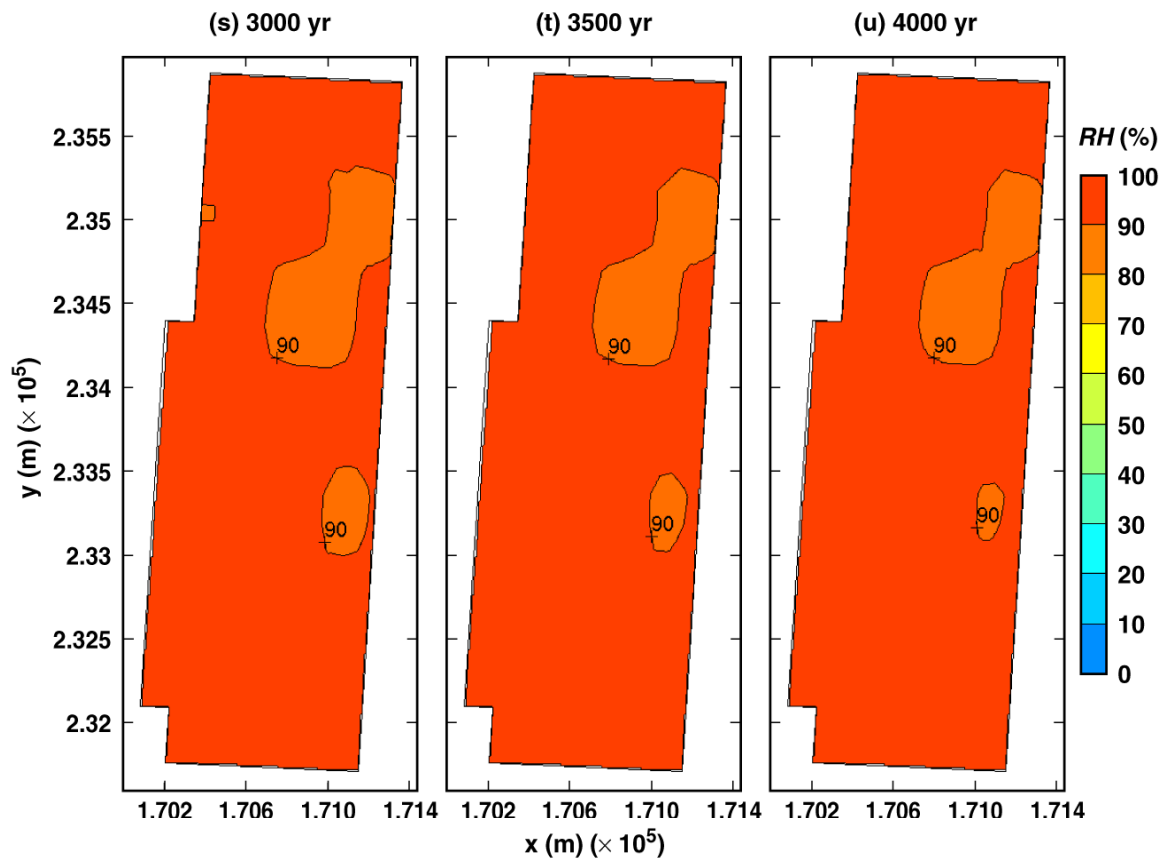
TB\_AMR\_upper\_RH\_wp\_pwr2\_347-372

Figure 6-17. Relative humidity on the surface of a 21-PWR WP for the high infiltration-flux backfill case for the indicated times (Continued)



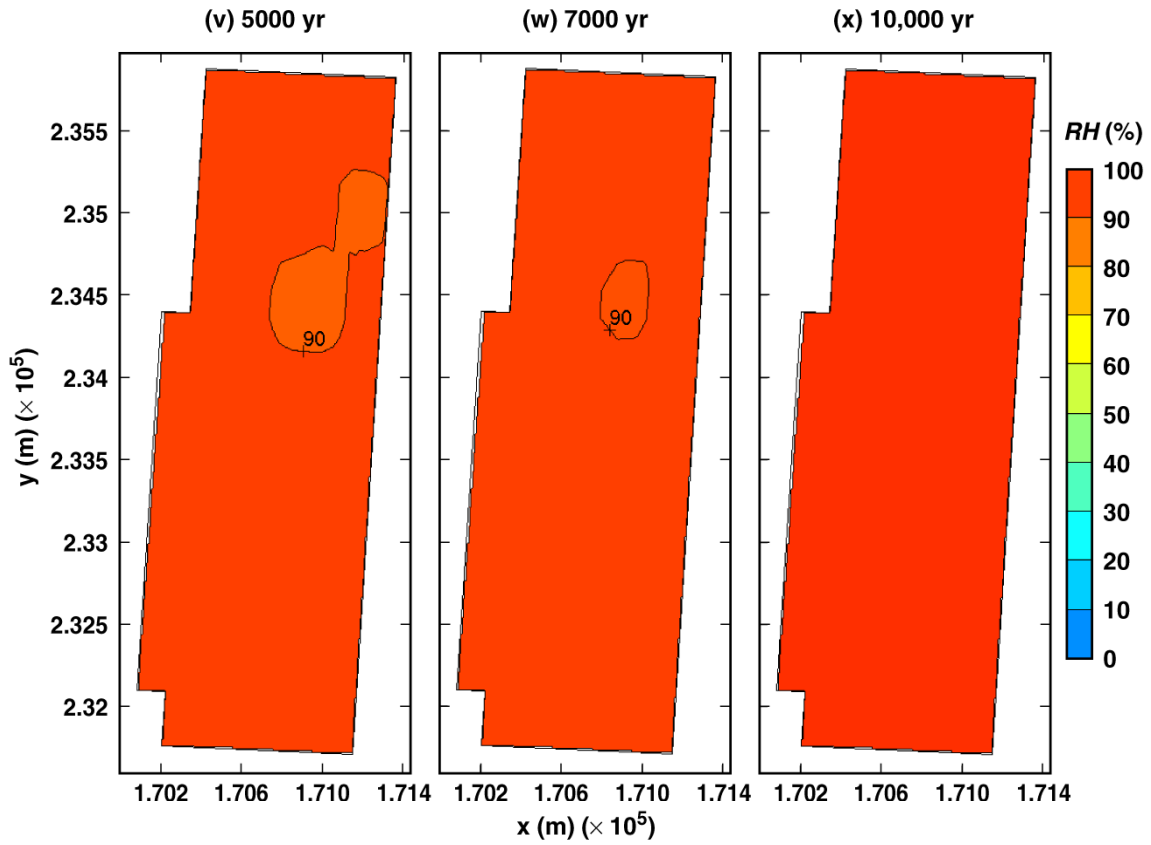
TB\_AMR\_upper\_RH\_wp\_pwr2\_377-385

Figure 6-17. Relative humidity on the surface of a 21-PWR WP for the high infiltration-flux backfill case for the indicated times (Continued)



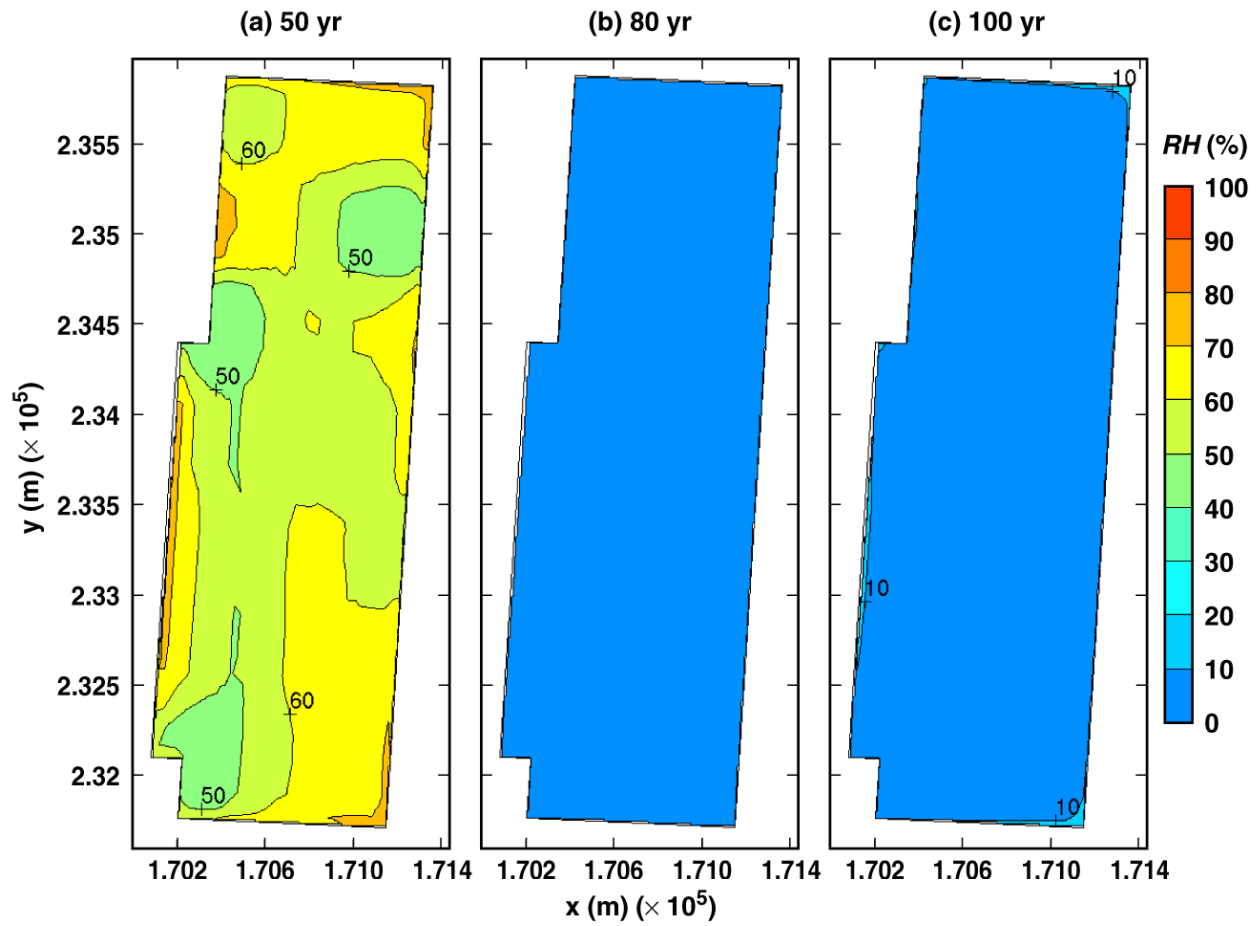
TB\_AMR\_upper\_RH\_wp\_pwr2\_389-403

Figure 6-17. Relative humidity on the surface of a 21-PWR WP for the high infiltration-flux backfill case for the indicated times (Continued)



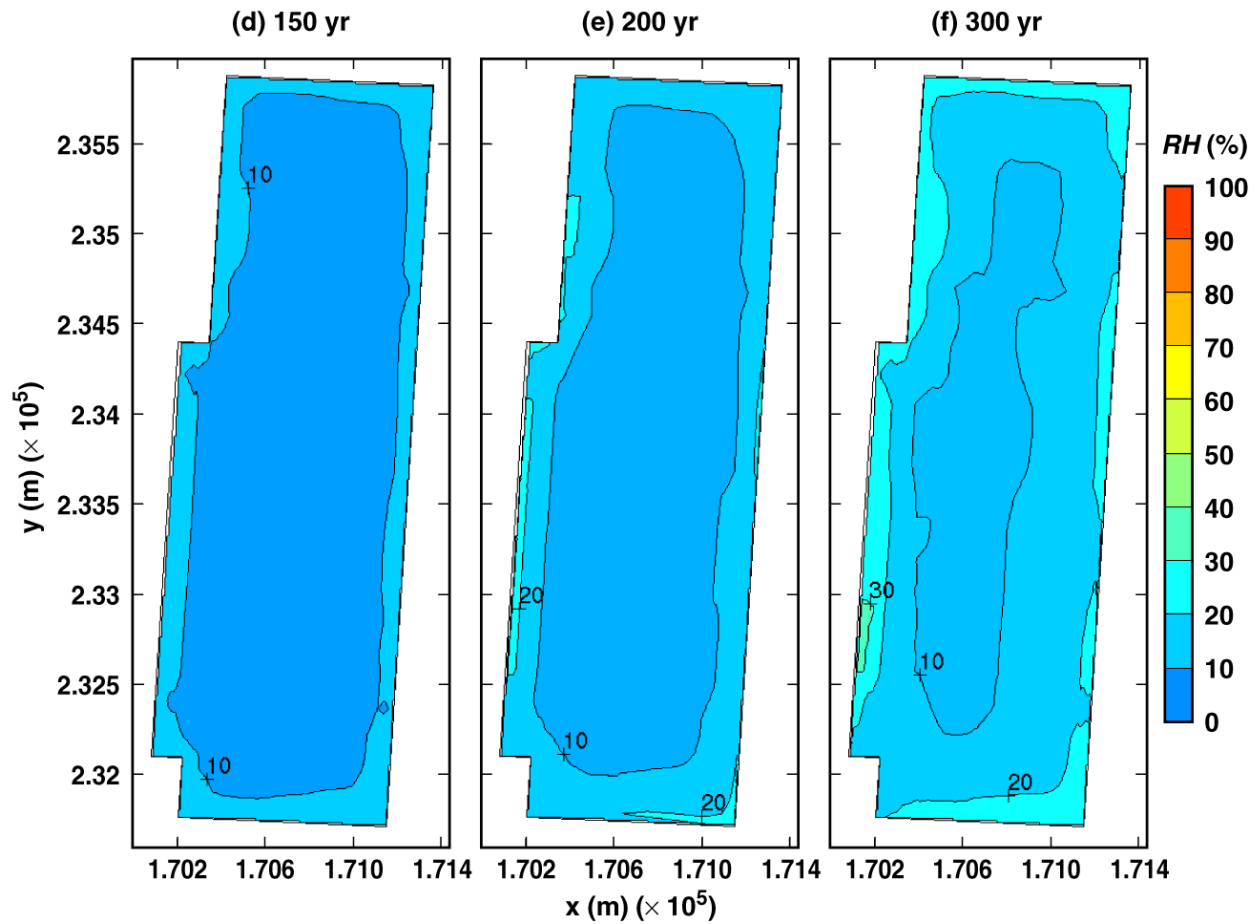
TB\_AMR\_upper\_RH\_wp\_pwr2\_413-425

Figure 6-17. Relative humidity on the surface of a 21-PWR WP for the high infiltration-flux backfill case for the indicated times (Continued)



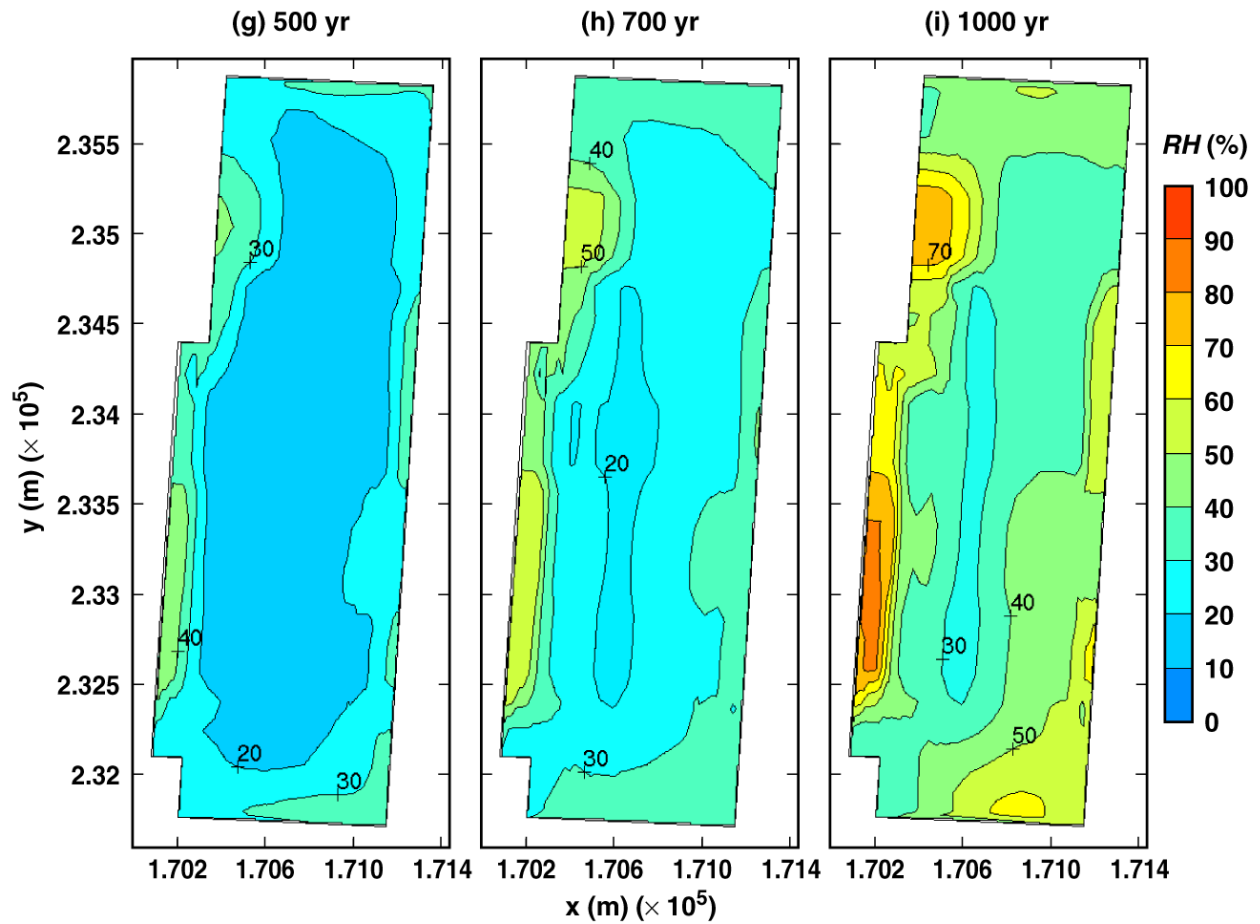
TB\_AMR\_lower\_RH\_wp\_pwr2\_11-22

Figure 6-18. Relative humidity on the surface of a 21-PWR WP for the low infiltration-flux backfill case for the indicated times



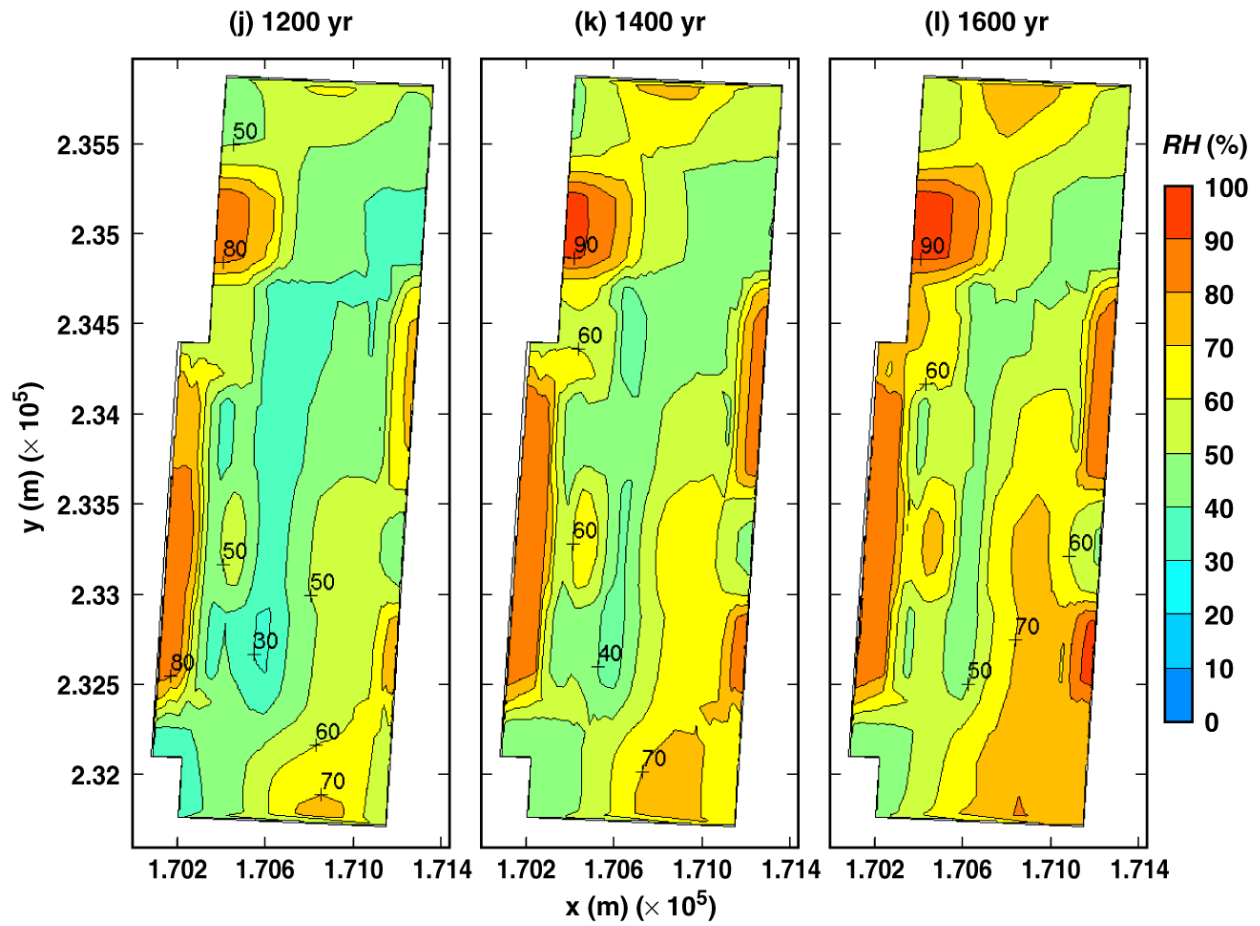
TB\_AMR\_lower\_RH\_wp\_pwr2\_25-36

Figure 6-18. Relative humidity on the surface of a 21-PWR WP for the low infiltration-flux backfill case for the indicated times (Continued)



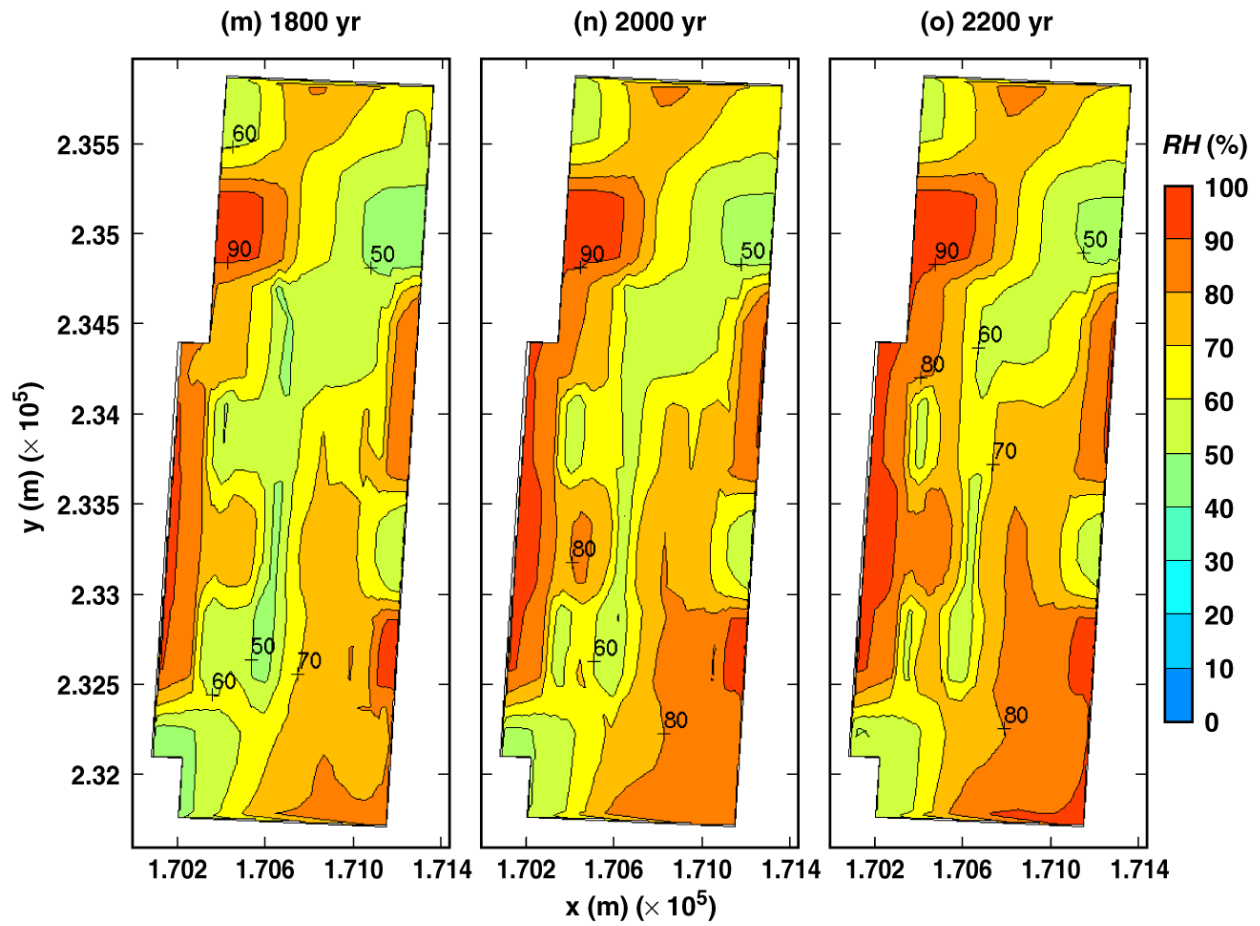
TB\_AMR\_lower\_RH\_wp\_pwr2\_77-219

Figure 6-18. Relative humidity on the surface of a 21-PWR WP for the low infiltration-flux backfill case for the indicated times (Continued)



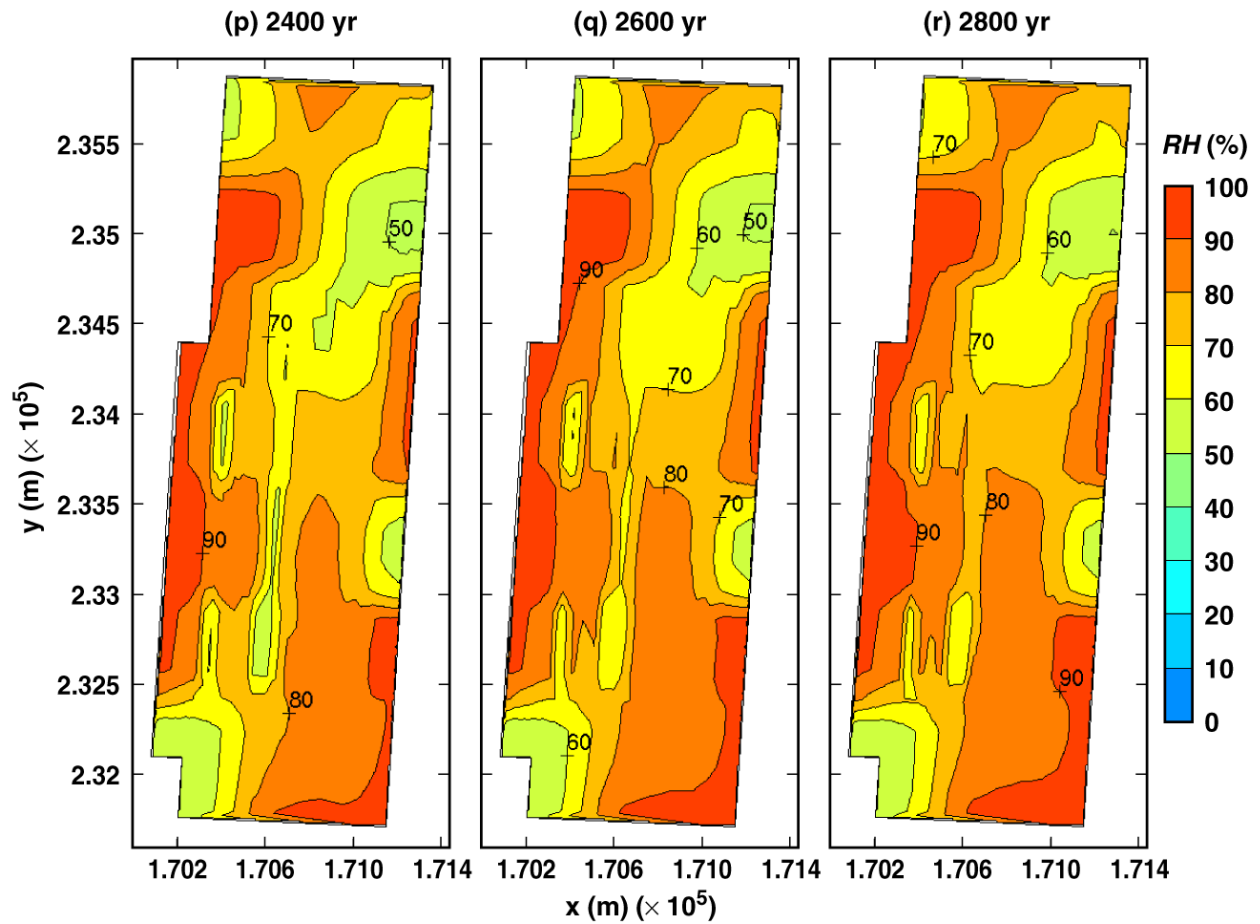
TB\_AMR\_lower\_RH\_wp\_pwr2\_246-286

Figure 6-18. Relative humidity on the surface of a 21-PWR WP for the low infiltration-flux backfill case for the indicated times (Continued)



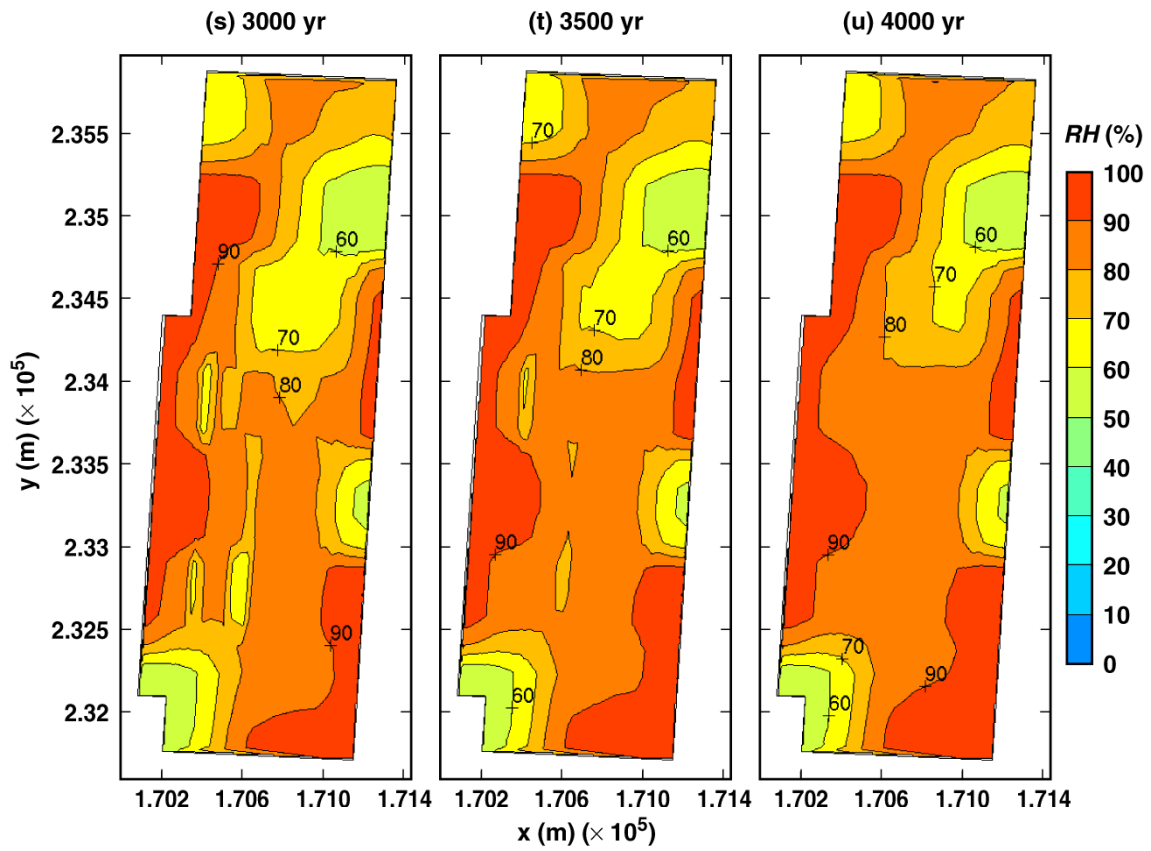
TB\_AMR\_lower\_RH\_wp\_pwr2\_305-335

Figure 6-18. Relative humidity on the surface of a 21-PWR WP for the low infiltration-flux backfill case for the indicated times (Continued)



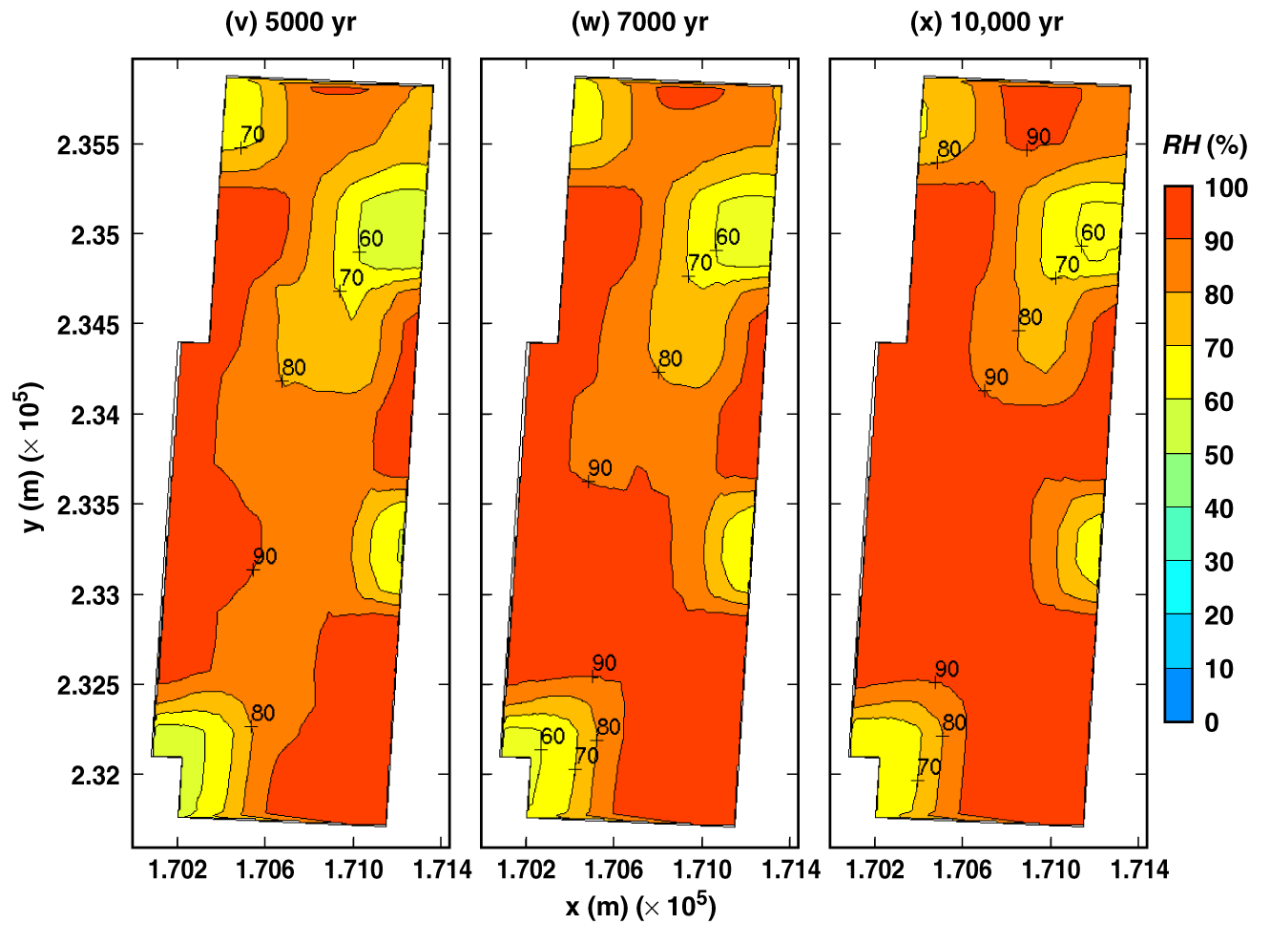
TB\_AMR\_lower\_RH\_wp\_pwr2\_343-351

Figure 6-18. Relative humidity on the surface of a 21-PWR WP for the low infiltration-flux backfill case for the indicated times (Continued)



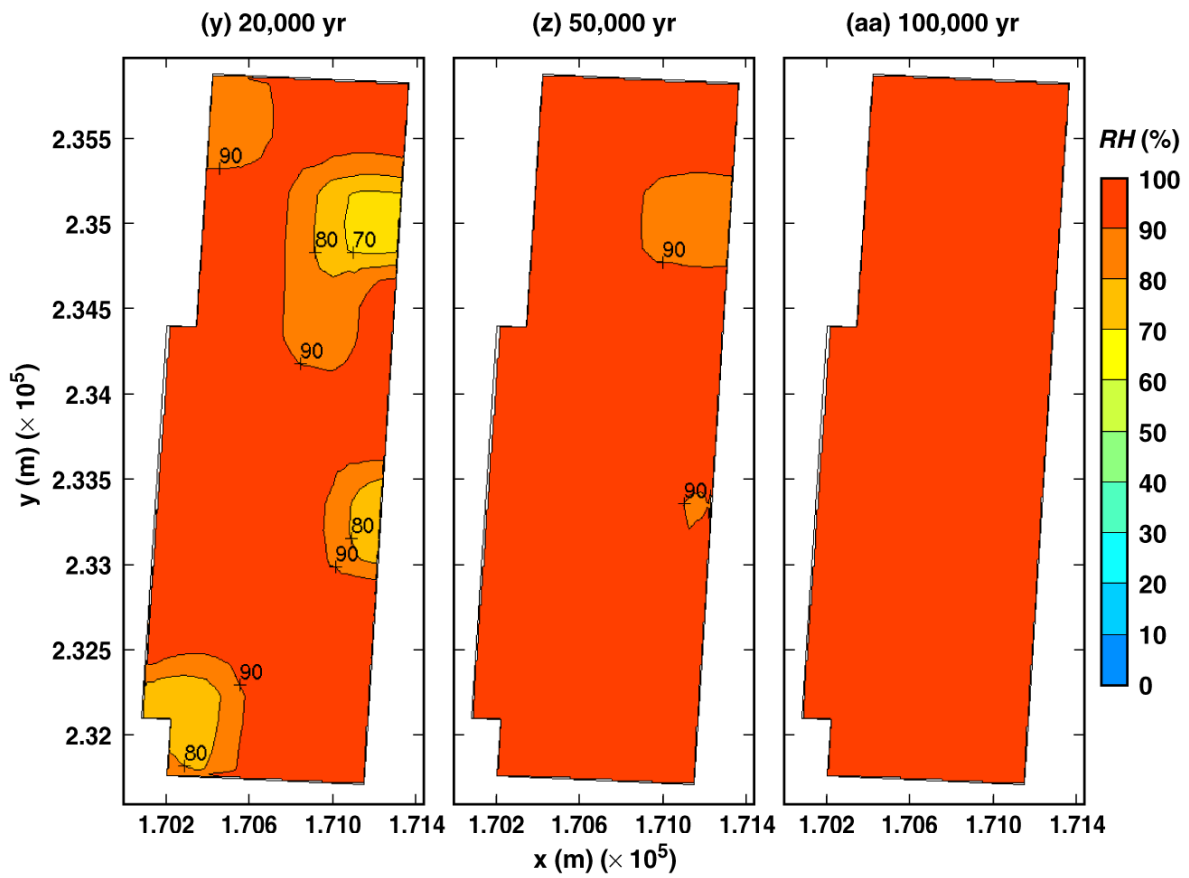
TB\_AMR\_lower\_RH\_wp\_pwr2\_355-372

Figure 6-18. Relative humidity on the surface of a 21-PWR WP for the low infiltration-flux backfill case for the indicated times (Continued)



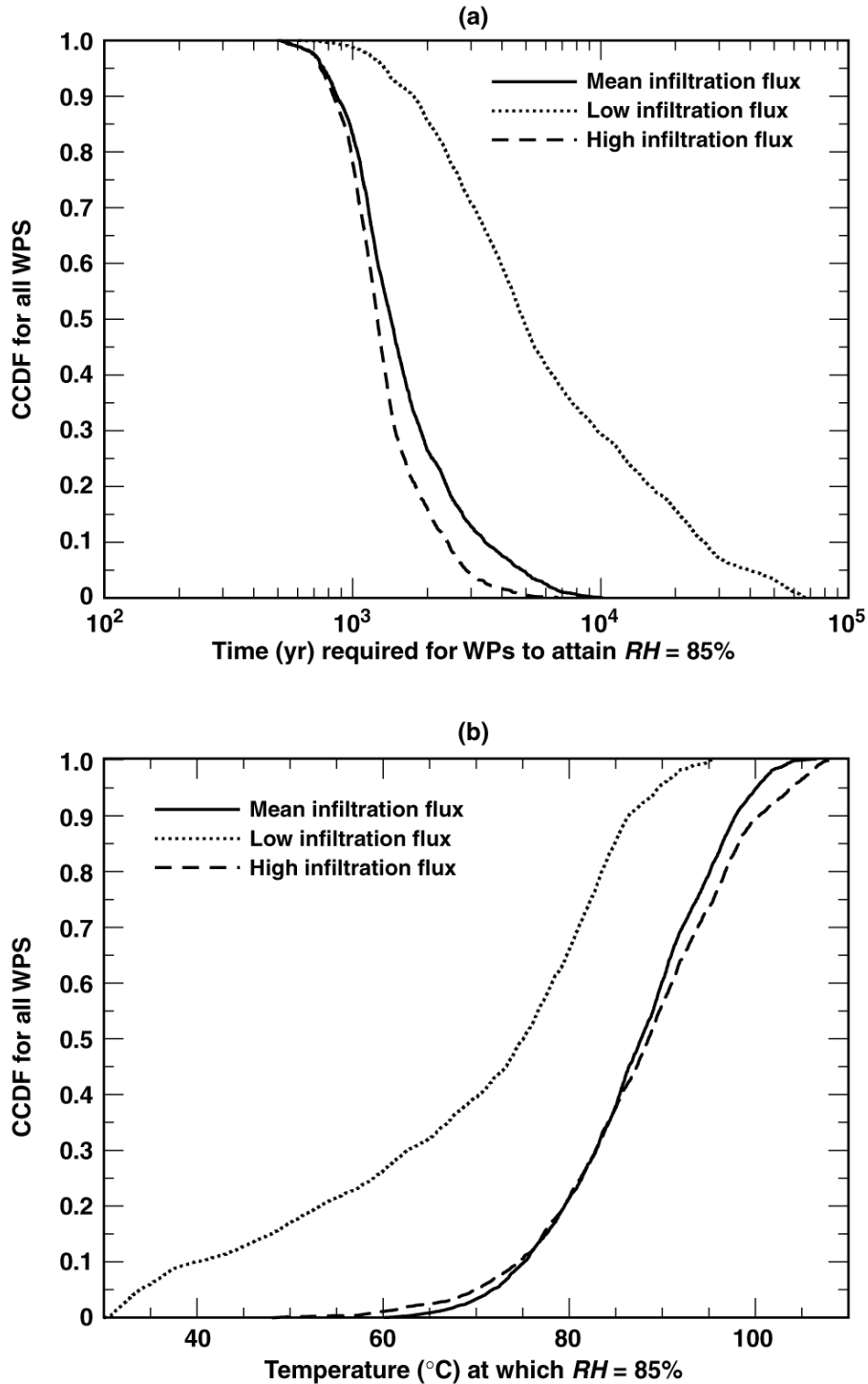
TB\_AMR\_lower\_RH\_wp\_pwr2\_390-402

Figure 6-18. Relative humidity on the surface of a 21-PWR WP for the low infiltration-flux backfill case for the indicated times (Continued)



TB\_AMR\_lower\_RH\_wp\_pwr2\_411-434

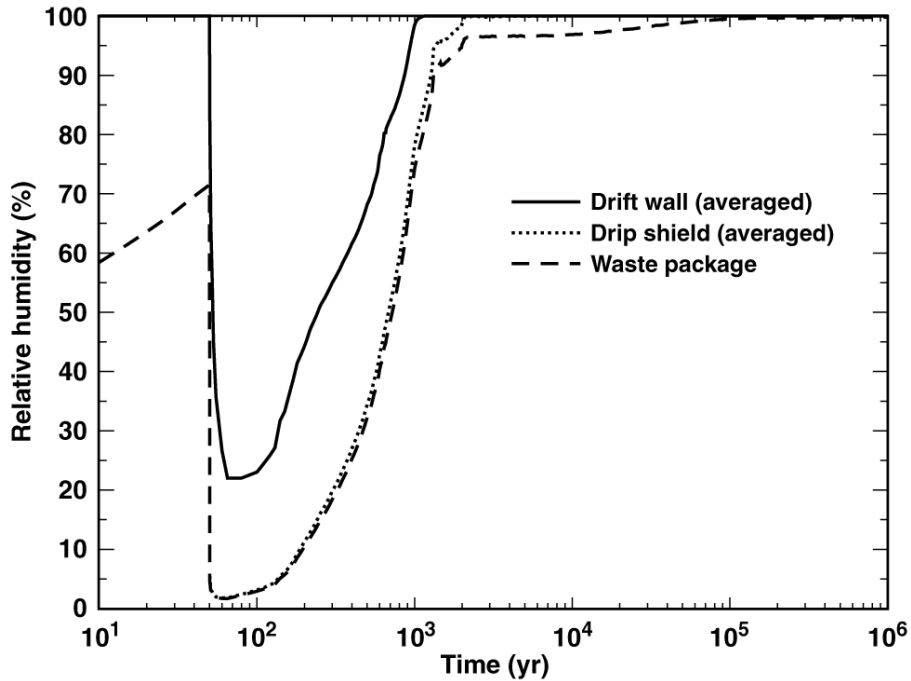
Figure 6-18. Relative humidity on the surface of a 21-PWR WP for the low infiltration-flux backfill case for the indicated times (Continued)



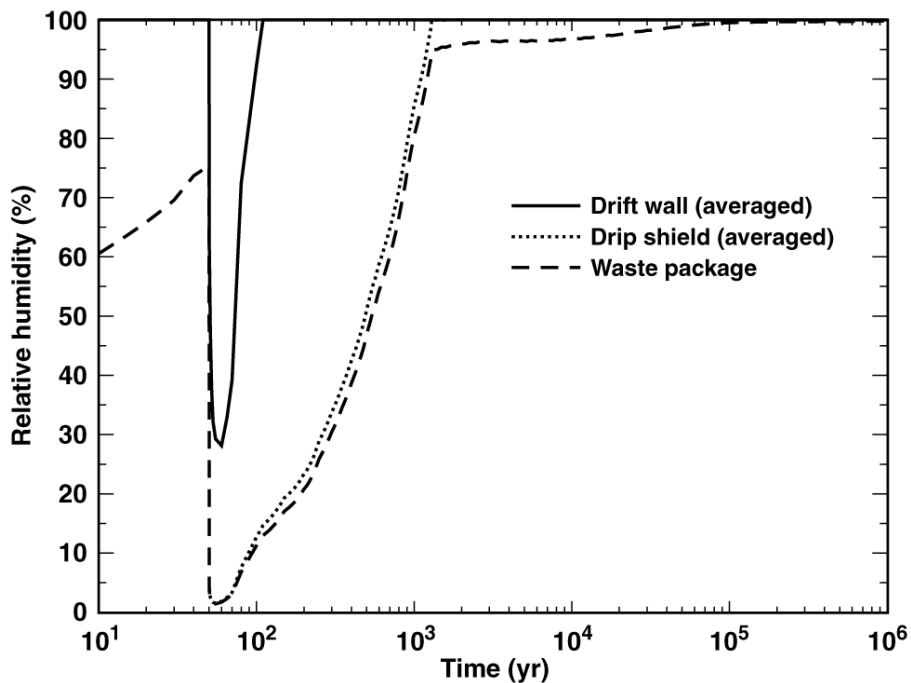
TB\_AMR\_CCDF\_RH85\_mlu

Figure 6-19. (a) The complementary cumulative distribution function (CCDF) for the time required to attain a relative humidity  $RH$  of 85% is plotted for the mean, high, and low infiltration-flux backfill cases. CCDF of the WP temperature at which WPs reach an  $RH$  of 85% is plotted for the same cases.

(a) Center of Repository  
 Nevada State Coordinates: Easting = 170535.03 m, Northing = 233640.08 m



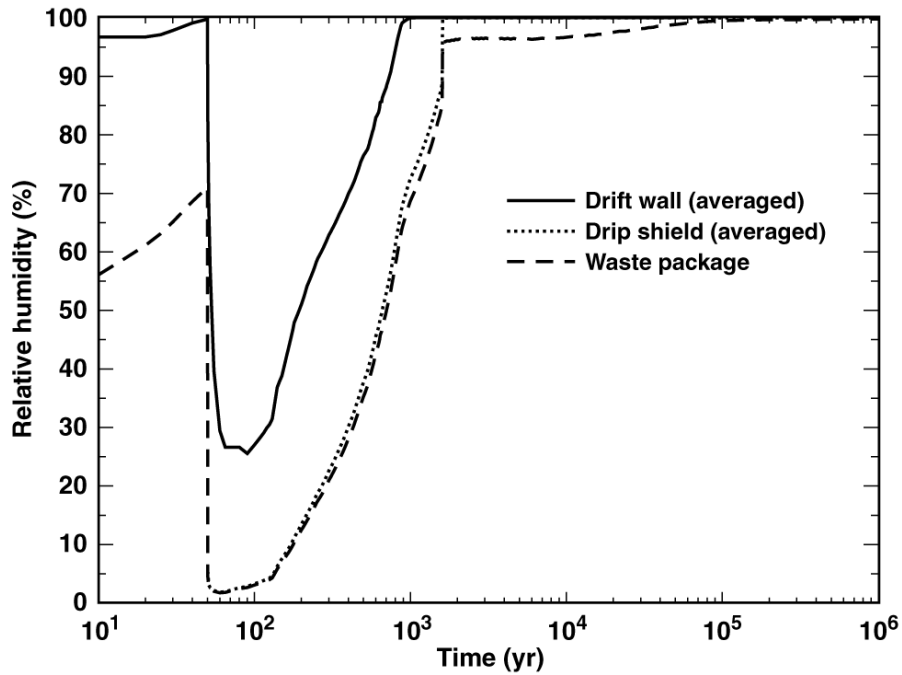
(b) Eastern Edge of Repository  
 Nevada State Coordinates: Easting = 171195.16 m, Northing = 233605.06 m



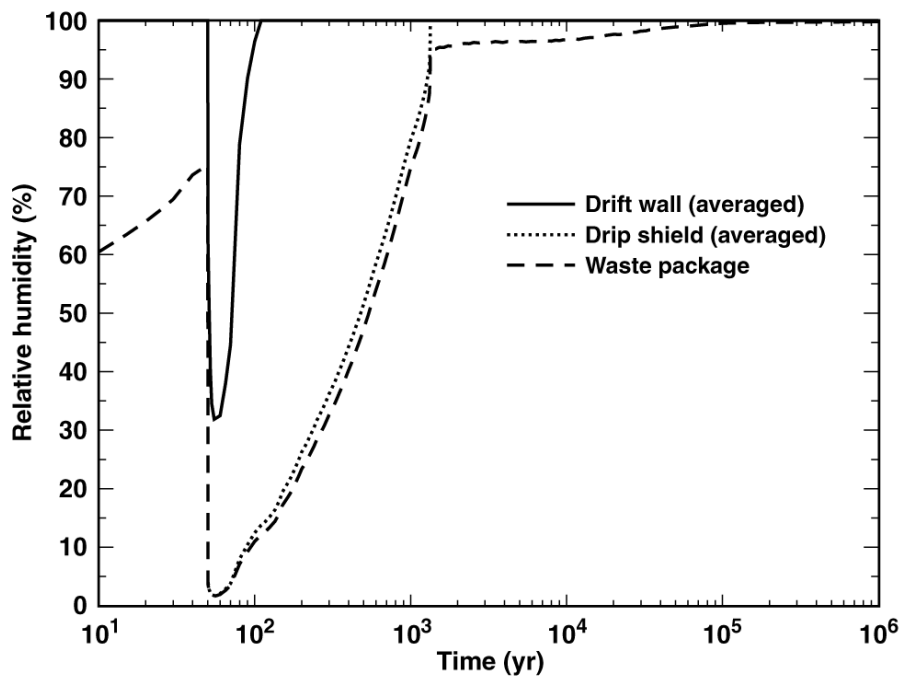
TB\_AMR\_RH\_pwr2\_13&24\_mean

Figure 6-20. Relative humidity history on the surface of a 21-PWR WP for the mean infiltration-flux backfill case at (a) the geographical center of the repository and (b) a location 27.5 m from the eastern edge of the repository. Note that the Nevada State coordinates are given.

(a) Center of Repository  
 Nevada State Coordinates: Easting = 170535.03 m, Northing = 233640.08 m



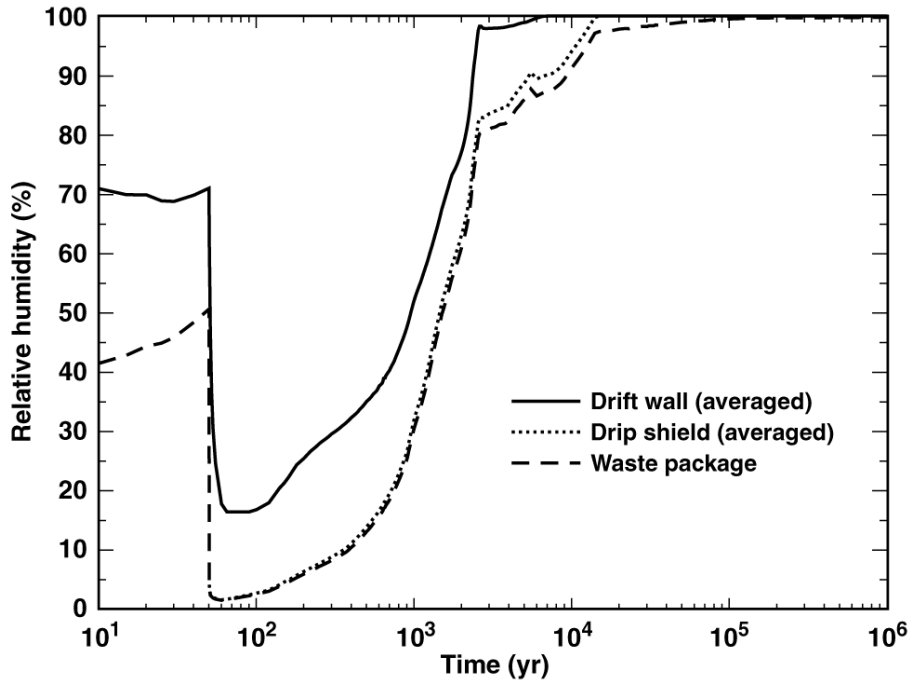
(b) Eastern Edge of Repository  
 Nevada State Coordinates: Easting = 171195.16 m, Northing = 233605.06 m



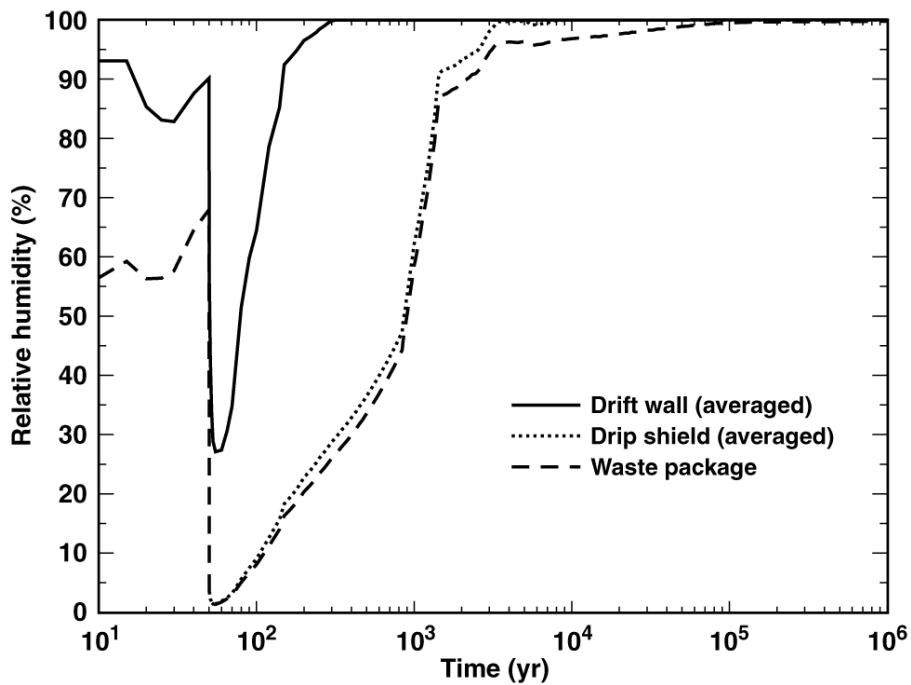
TB\_AMR\_RH\_pwr2\_13&24\_17\_upper

Figure 6-21. Relative humidity history on the surface of a 21-PWR WP for the high infiltration-flux backfill case at (a) the geographical center of the repository and (b) a location 27.5 m from the eastern edge of the repository. Note that the Nevada State coordinates are given.

(a) Center of Repository  
 Nevada State Coordinates: Easting = 170535.03 m, Northing = 233640.08 m

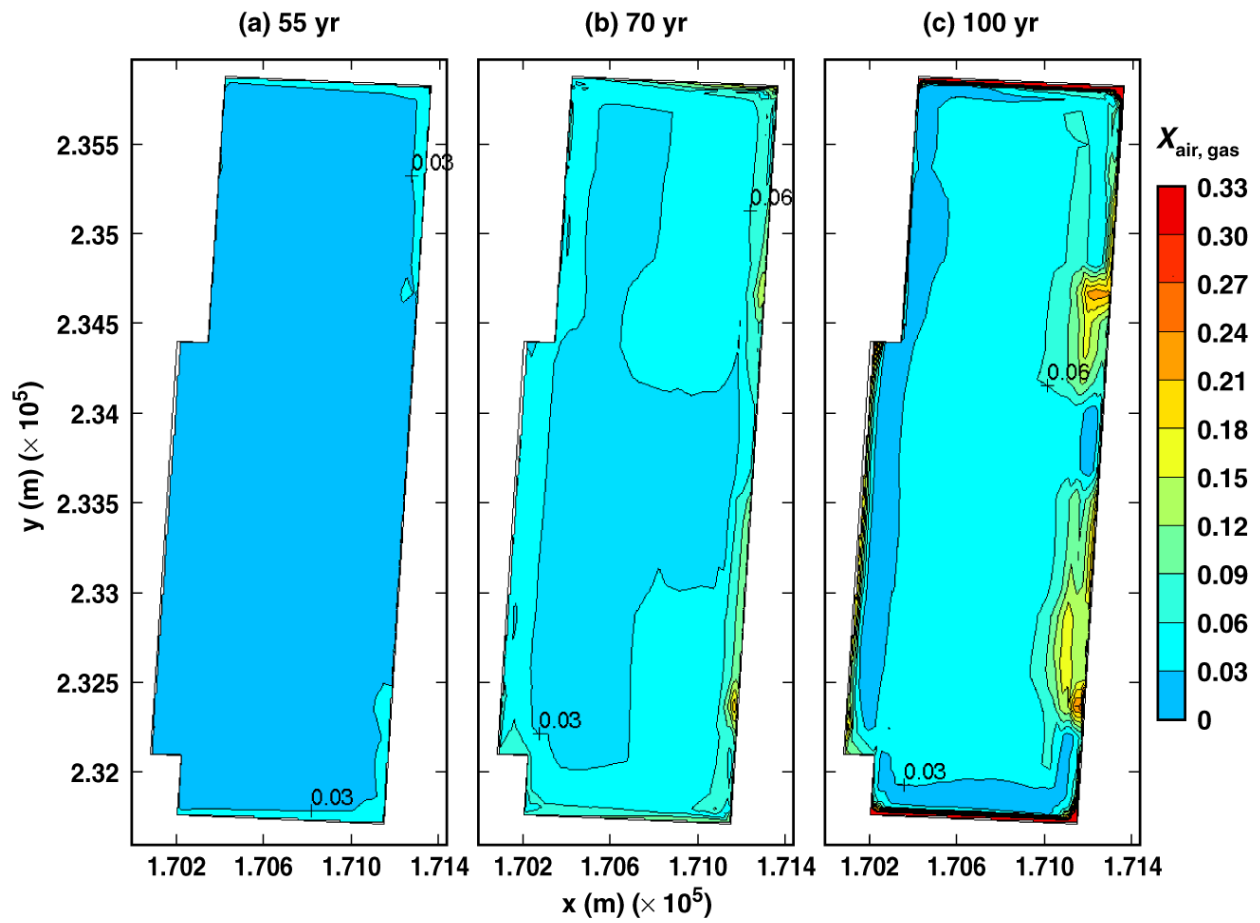


(b) Eastern Edge of Repository  
 Nevada State Coordinates: Easting = 171195.16 m, Northing = 233605.06 m



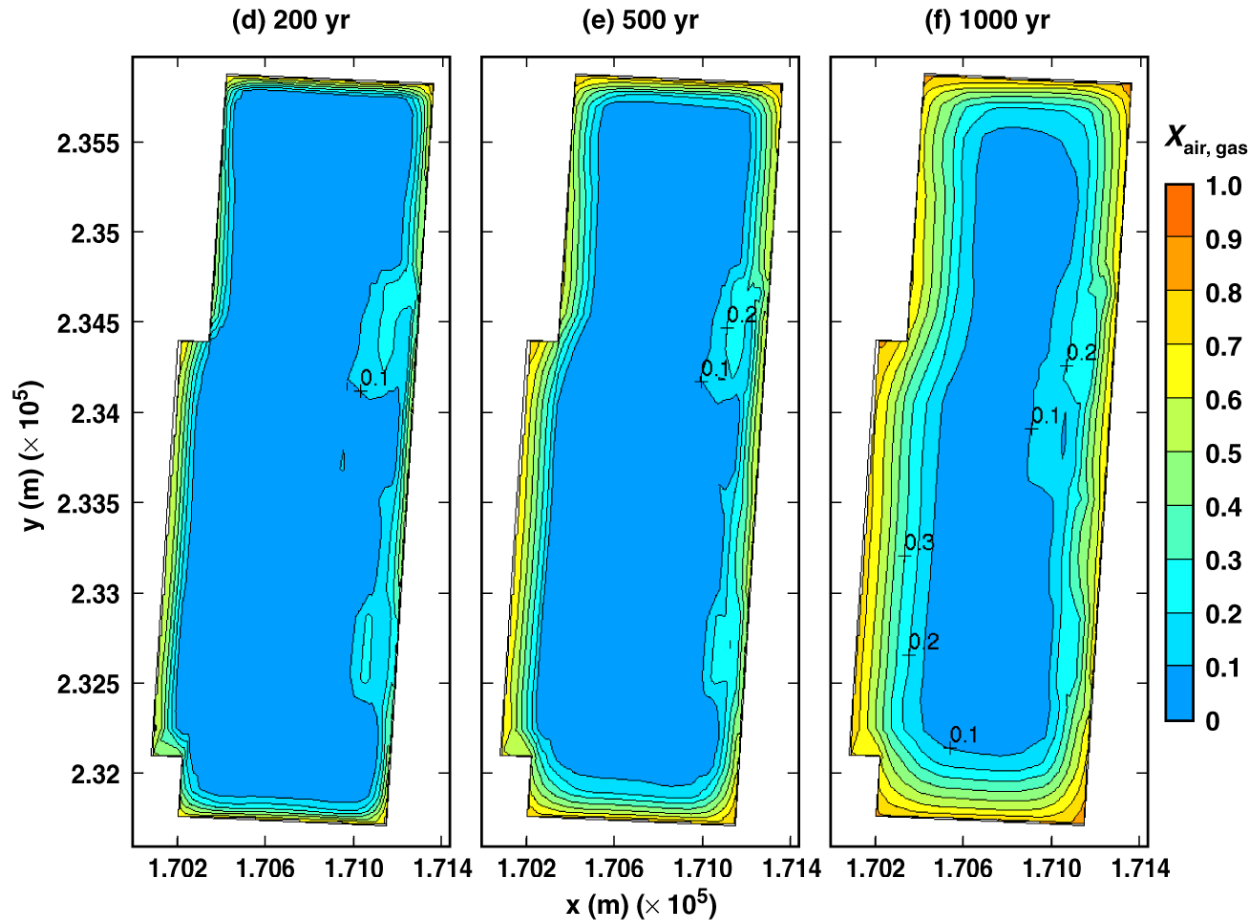
TB\_AMR\_RH\_pwr2\_13&24\_17\_lower

Figure 6-22. Relative humidity history on the surface of a 21-PWR WP for the low infiltration-flux backfill case at (a) the geographical center of the repository and (b) a location 27.5 m from the eastern edge of the repository. Note that the Nevada State coordinates are given.



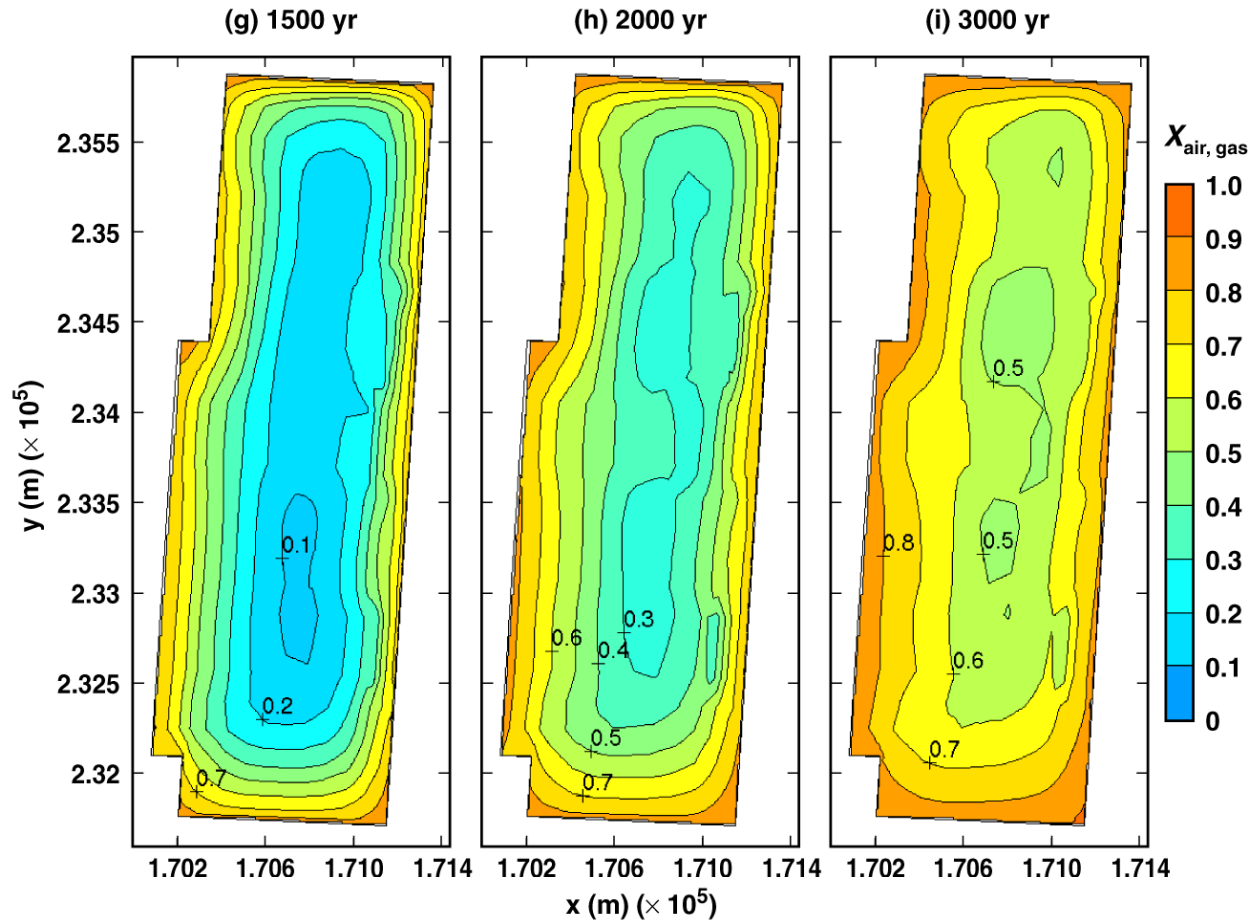
TB\_AMR\_mean\_Xair\_ds\_pwr2\_16-21

Figure 6-23. Gas-phase air-mass fraction averaged over the perimeter of the drip shield at the location of a 21-PWR WP for the mean infiltration-flux backfill case for the indicated times



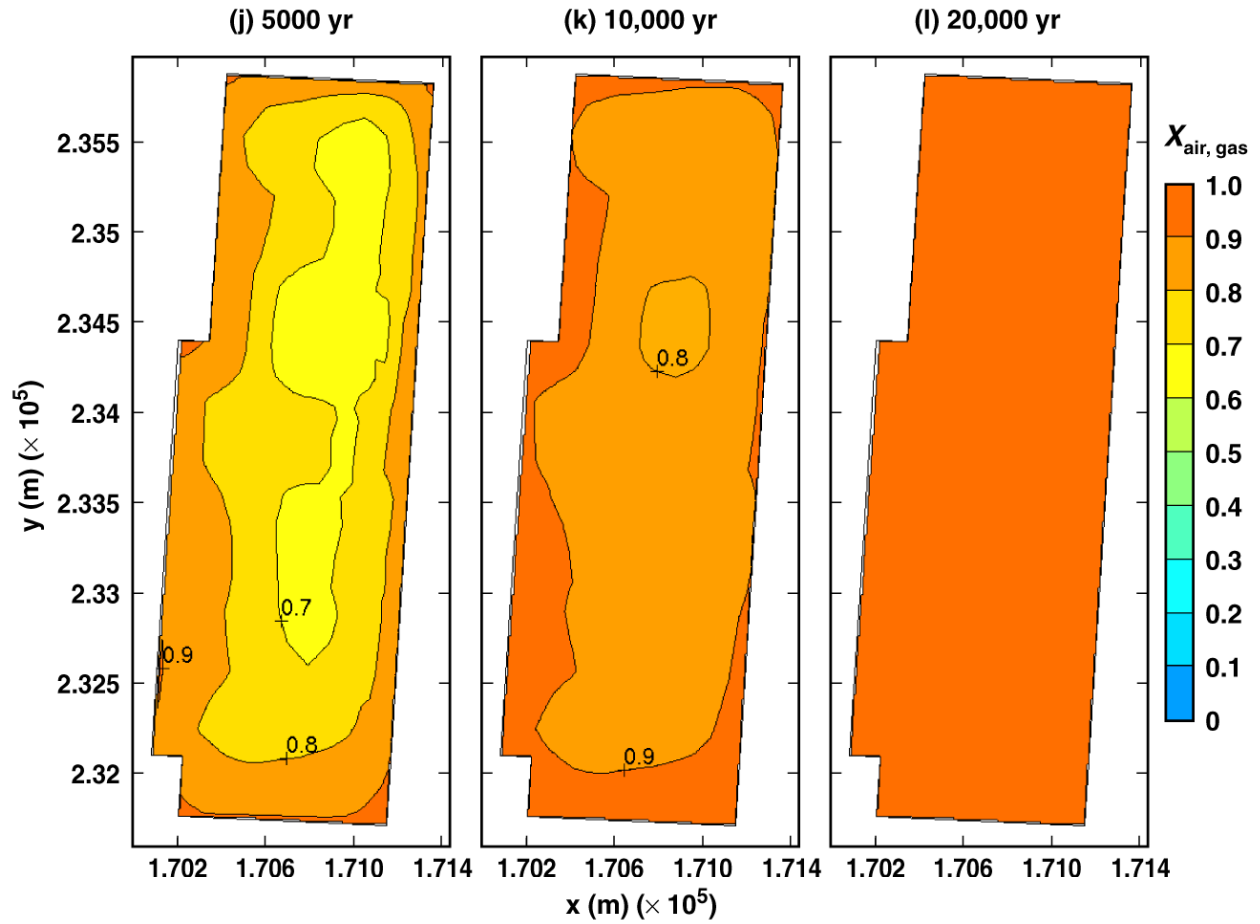
TB\_AMR\_mean\_Xair\_ds\_pwr2\_31-174

Figure 6-23. Gas-phase air-mass fraction averaged over the perimeter of the drip shield at the location of a 21-PWR WP for the mean infiltration-flux backfill case for the indicated times (Continued)



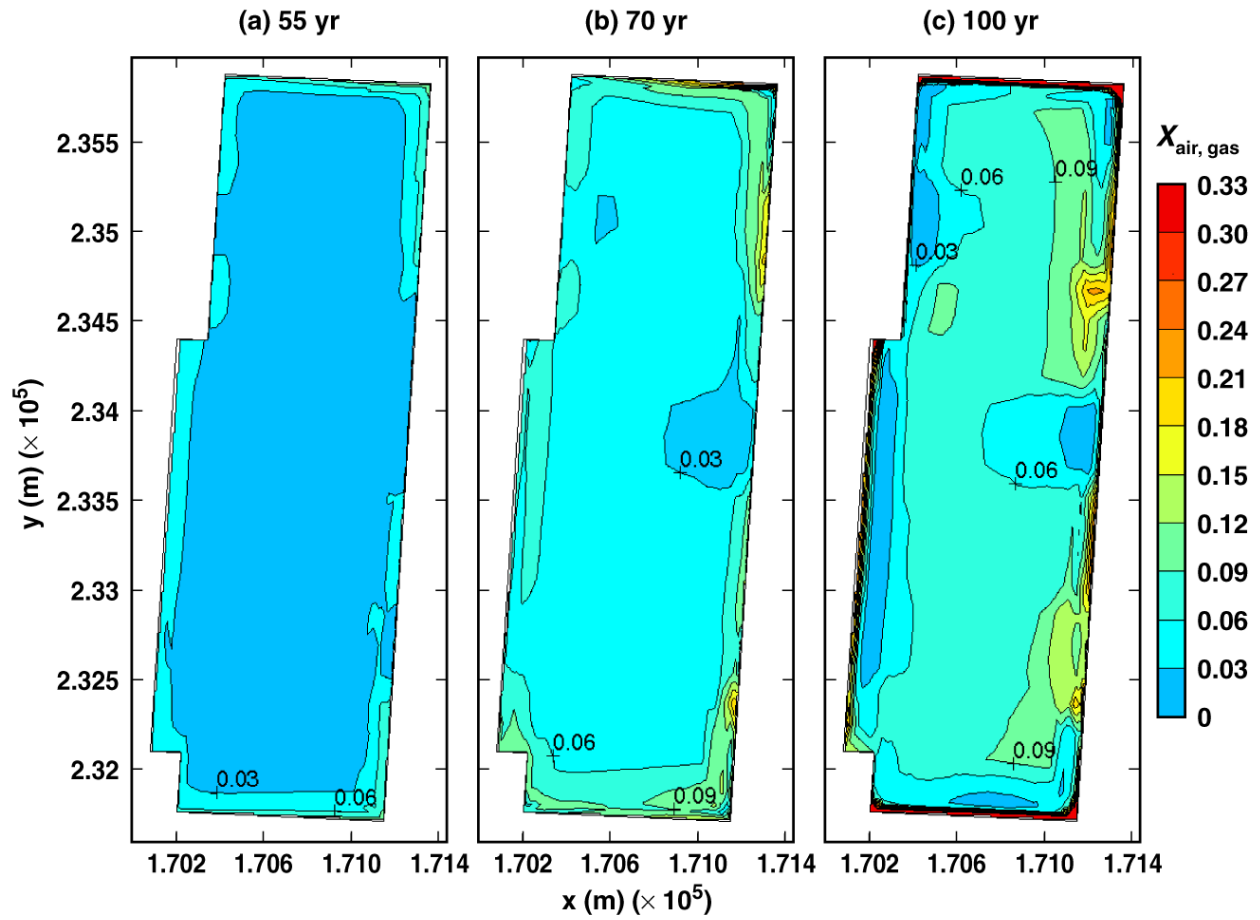
TB\_AMR\_mean\_Xair\_ds\_pwr2\_225-283

Figure 6-23. Gas-phase air-mass fraction averaged over the perimeter of the drip shield at the location of a 21-PWR WP for the mean infiltration-flux backfill case for the indicated times (Continued)



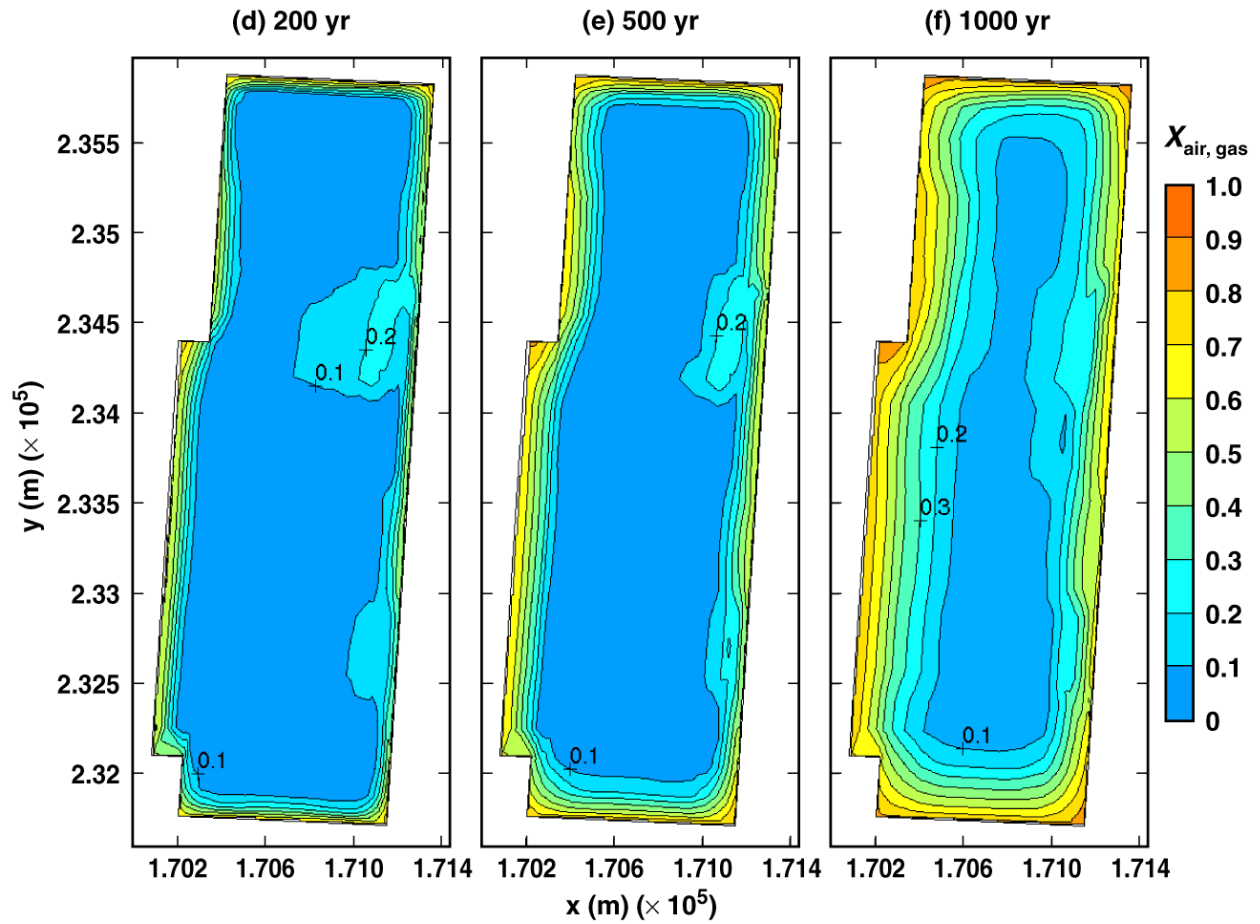
TB\_AMR\_mean\_Xair\_ds\_pwr2\_307-330

Figure 6-23. Gas-phase air-mass fraction averaged over the perimeter of the drip shield at the location of a 21-PWR WP for the mean infiltration-flux backfill case for the indicated times (Continued)



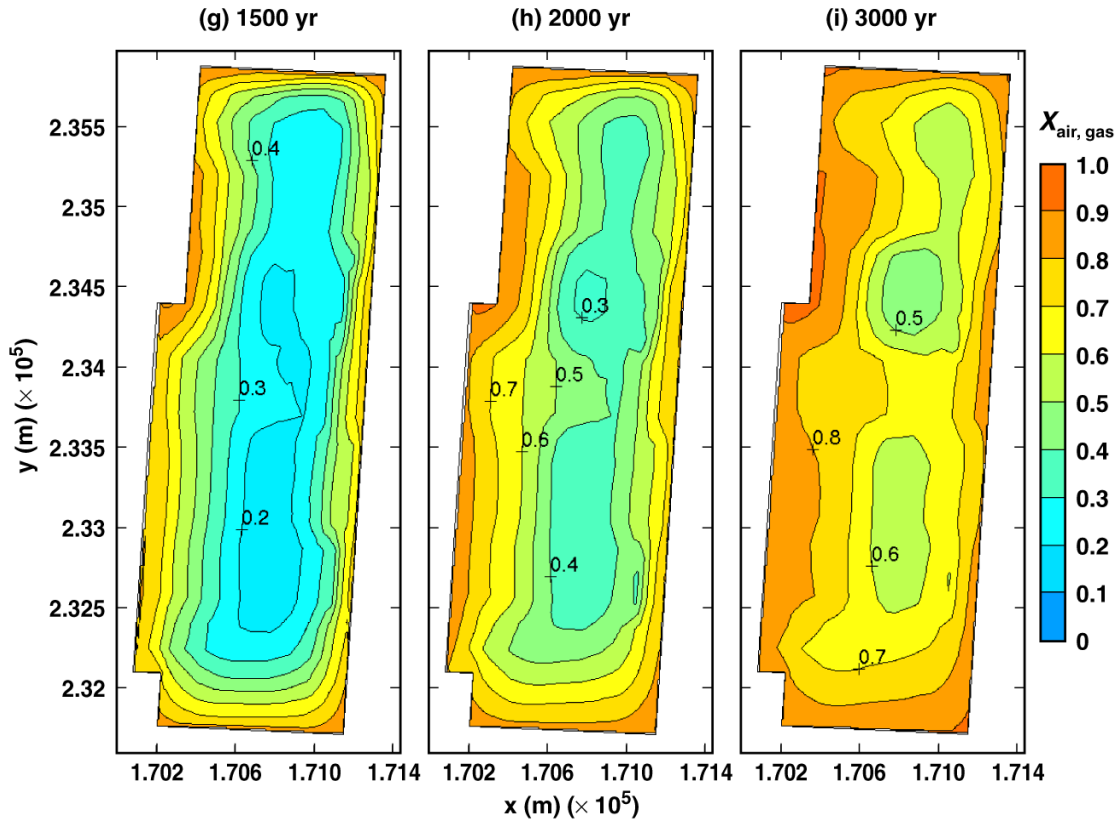
TB\_AMR\_upper\_Xair\_ds\_pwr2\_16-22

Figure 6-24. Gas-phase air-mass fraction averaged over the perimeter of the drip shield at the location of a 21-PWR WP for the high infiltration-flux backfill case for the indicated times



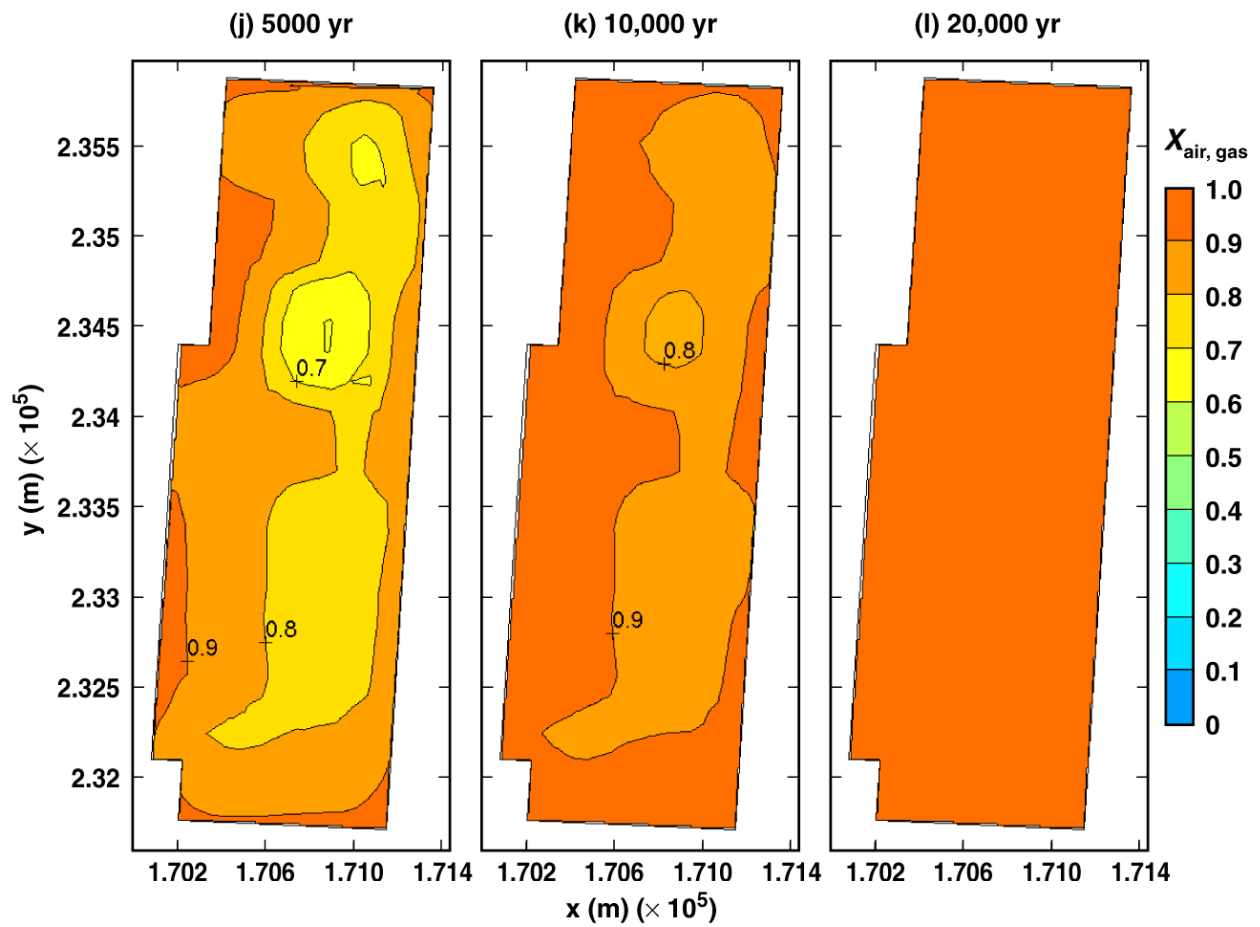
TB\_AMR\_upper\_Xair\_ds\_pwr2\_56-269

Figure 6-24. Gas-phase air-mass fraction averaged over the perimeter of the drip shield at the location of a 21-PWR WP for the high infiltration-flux backfill case for the indicated times (Continued)



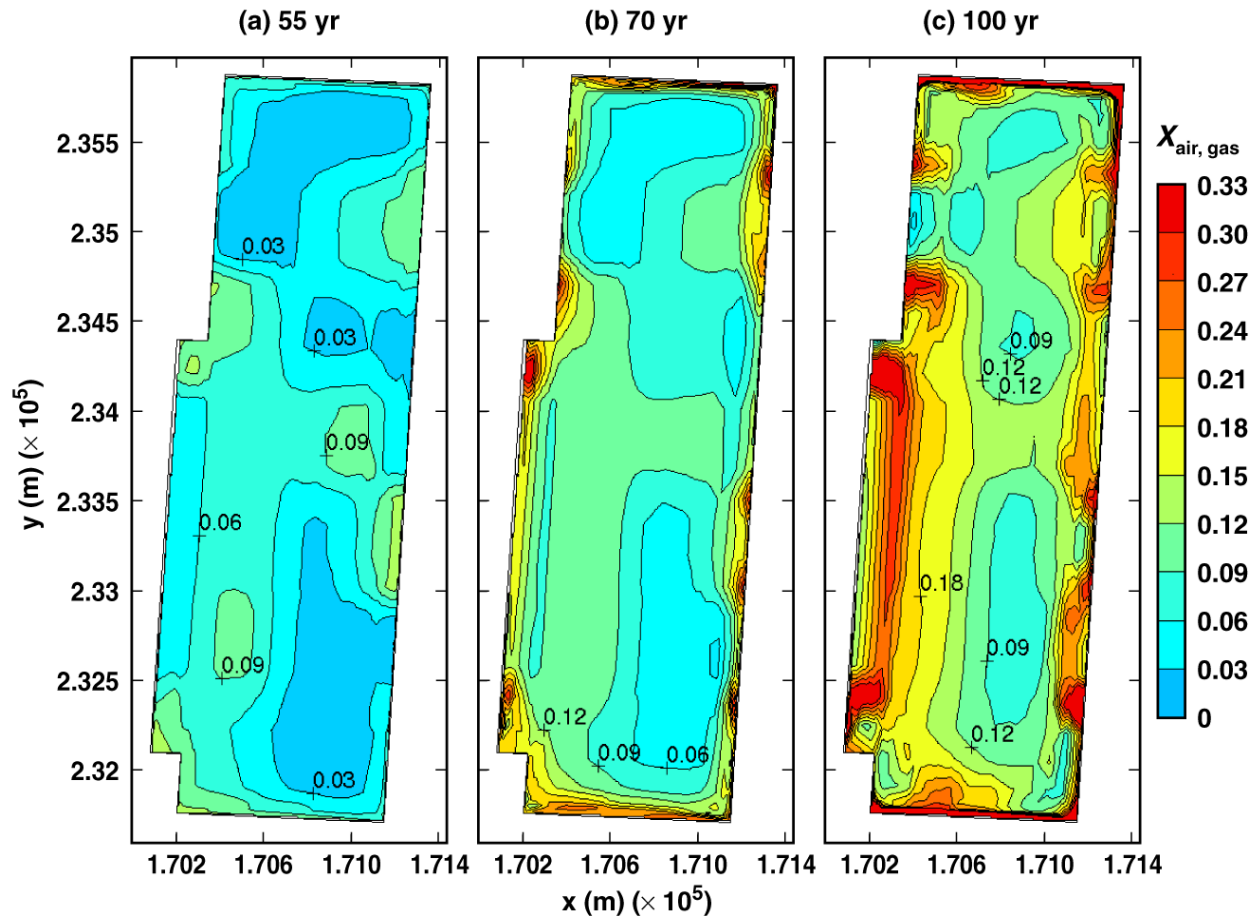
TB\_AMR\_upper\_Xair\_ds\_pwr2\_319-389

Figure 6-24. Gas-phase air-mass fraction averaged over the perimeter of the drip shield at the location of a 21-PWR WP for the high infiltration-flux backfill case for the indicated times (Continued)



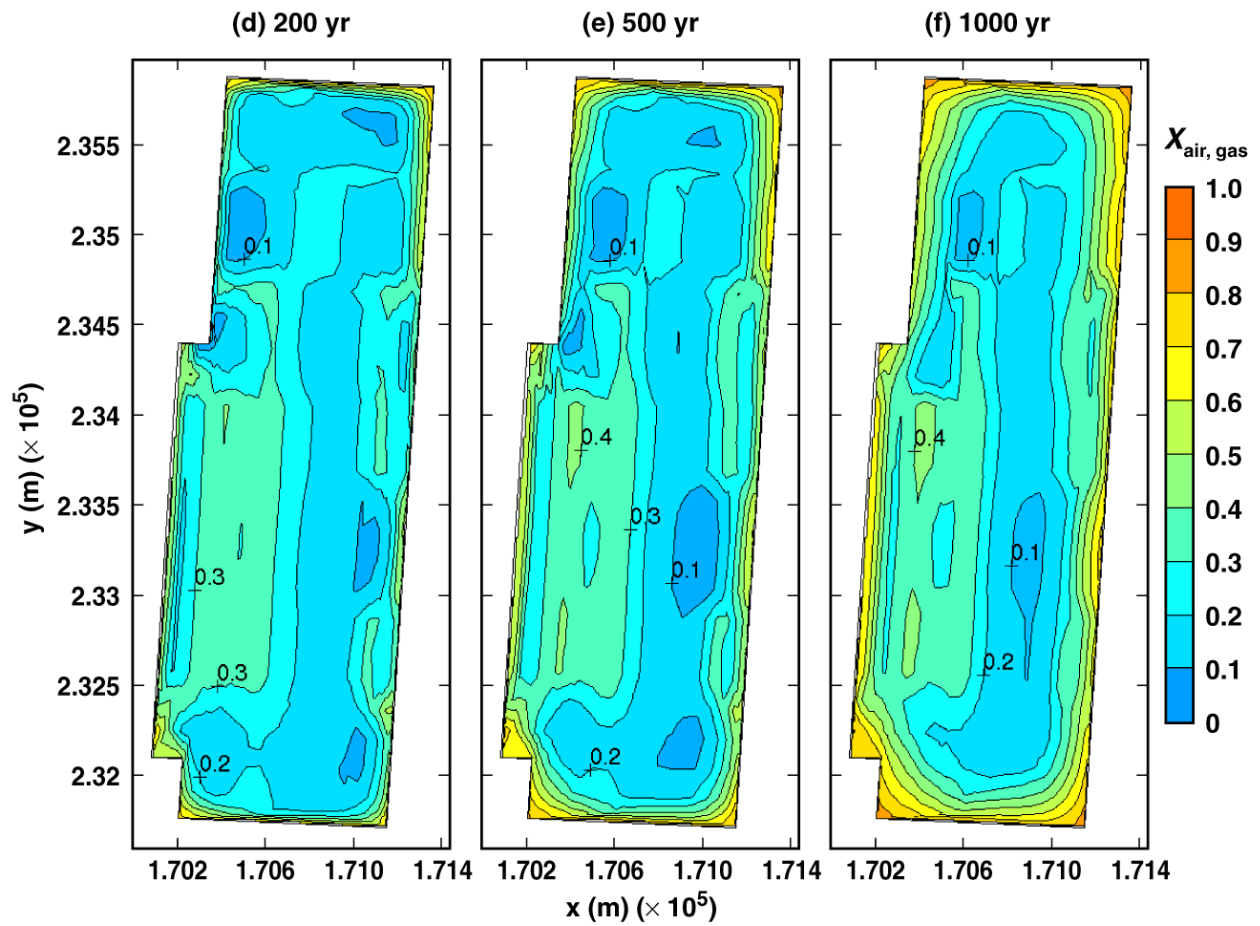
TB\_AMR\_upper\_Xair\_ds\_pwr2\_413-434

Figure 6-24. Gas-phase air-mass fraction averaged over the perimeter of the drip shield at the location of a 21-PWR WP for the high infiltration-flux backfill case for the indicated times (Continued)



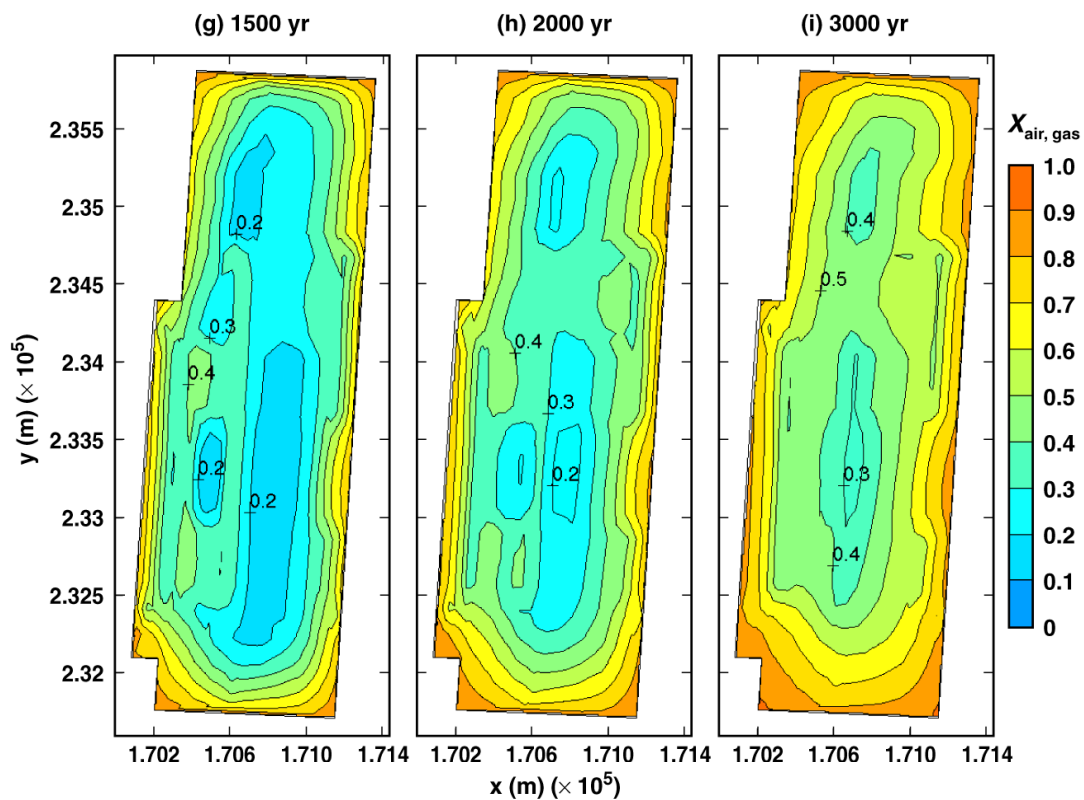
TB\_AMR\_lower\_Xair\_ds\_pwr2\_16-22

Figure 6-25. Gas-phase air-mass fraction averaged over the perimeter of the drip shield at the location of a 21-PWR WP for the low infiltration-flux backfill case for the indicated times



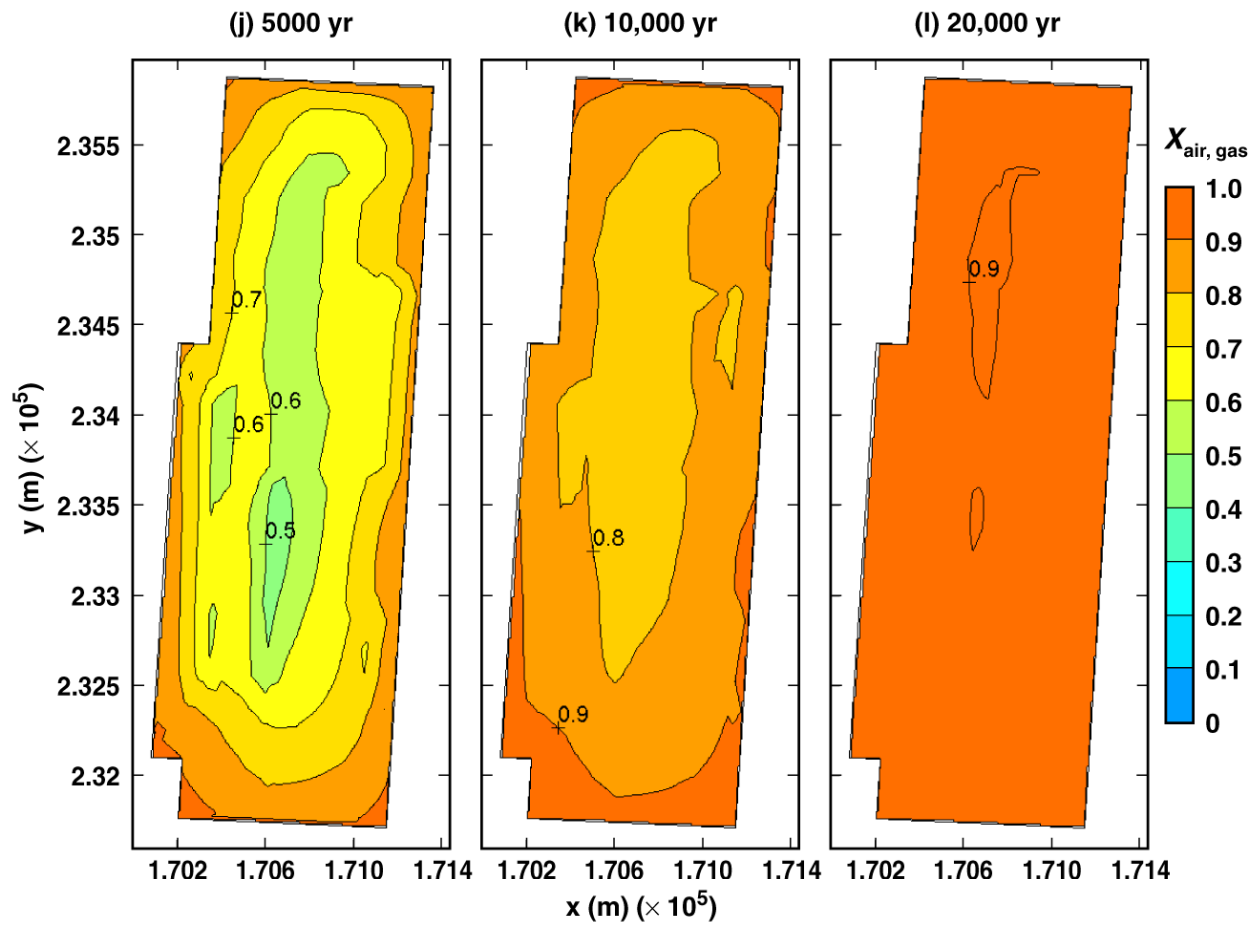
TB\_AMR\_lower\_Xair\_ds\_pwr2\_28-219

Figure 6-25. Gas-phase air-mass fraction averaged over the perimeter of the drip shield at the location of a 21-PWR WP for the low infiltration-flux backfill case for the indicated times (Continued)



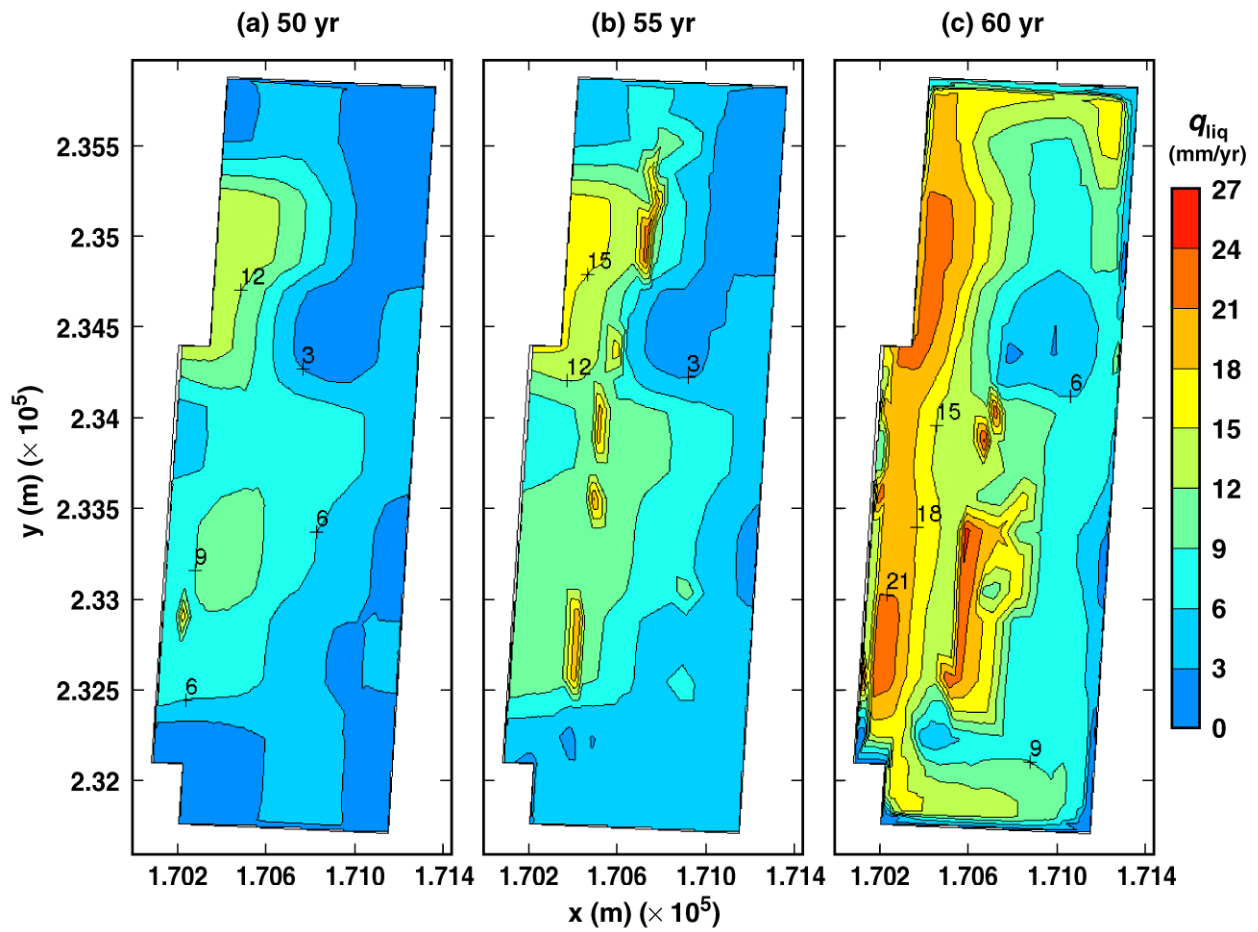
TB\_AMR\_lower\_Xair\_ds\_pwr2\_276-355

Figure 6-25. Gas-phase air-mass fraction averaged over the perimeter of the drip shield at the location of a 21-PWR WP for the low infiltration-flux backfill case for the indicated times (Continued)



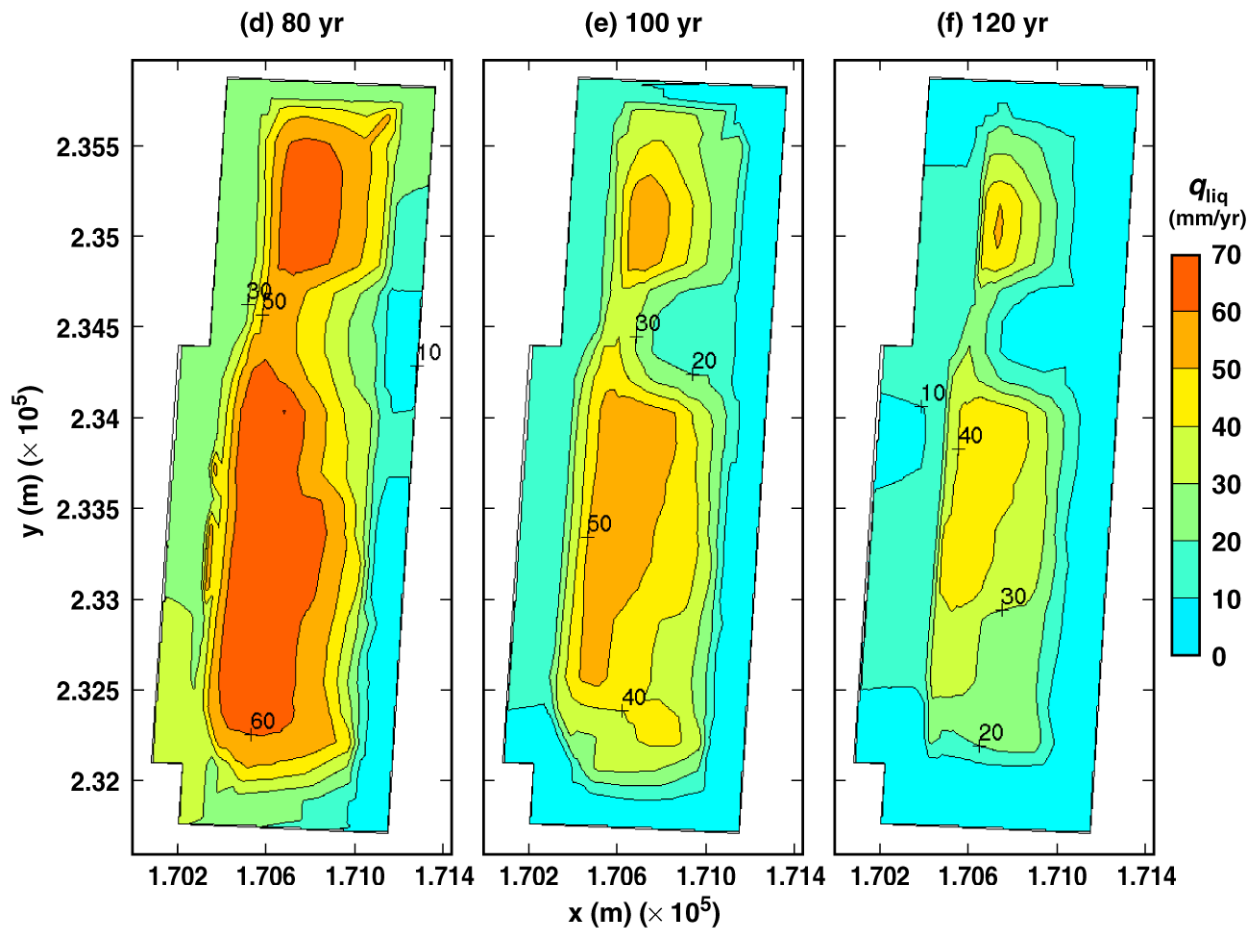
TB\_AMR\_lower\_Xair\_ds\_pwr2\_390-402

Figure 6-25. Gas-phase air-mass fraction averaged over the perimeter of the drip shield at the location of a 21-PWR WP for the low infiltration-flux backfill case for the indicated times (Continued)



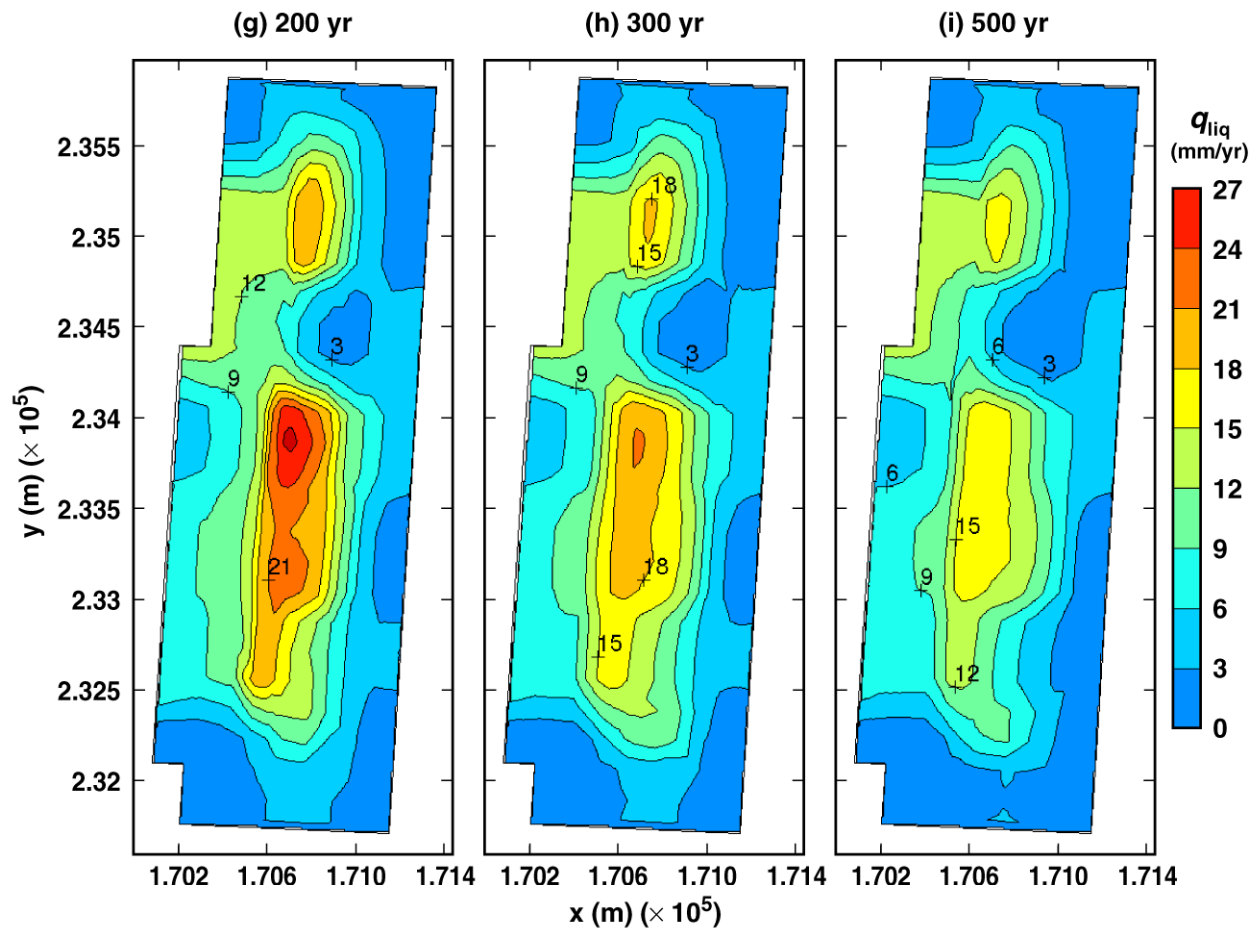
TB\_AMR\_mean\_qliq\_5m\_pwr2\_11-17

Figure 6-26. Liquid-phase flux 5 m above the crown of the drift for the mean infiltration-flux backfill case for the indicated times



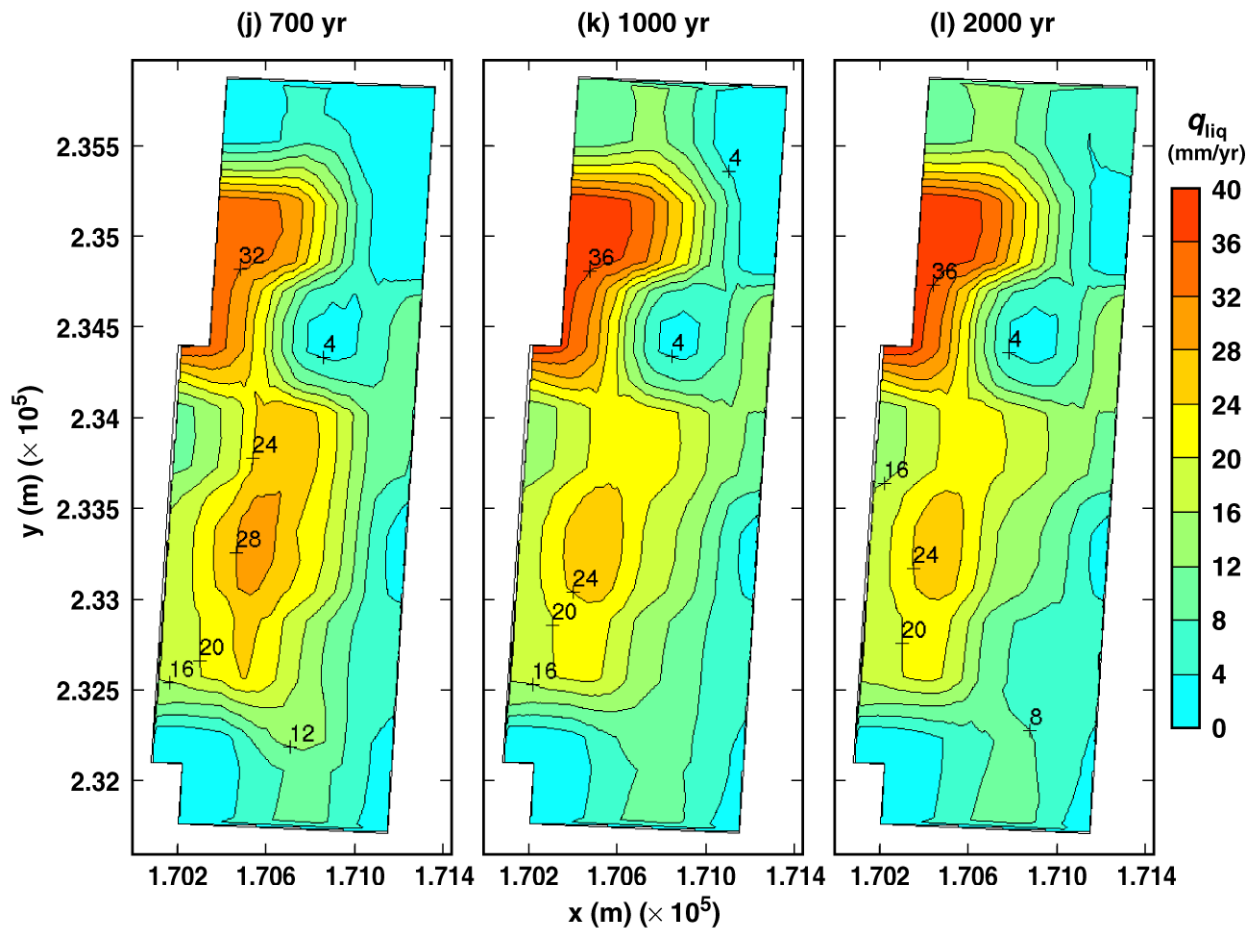
TB\_AMR\_mean\_qliq\_5m\_pwr2\_20-23

Figure 6-26. Liquid-phase flux 5 m above the crown of the drift for the mean infiltration-flux backfill case for the indicated times (Continued)



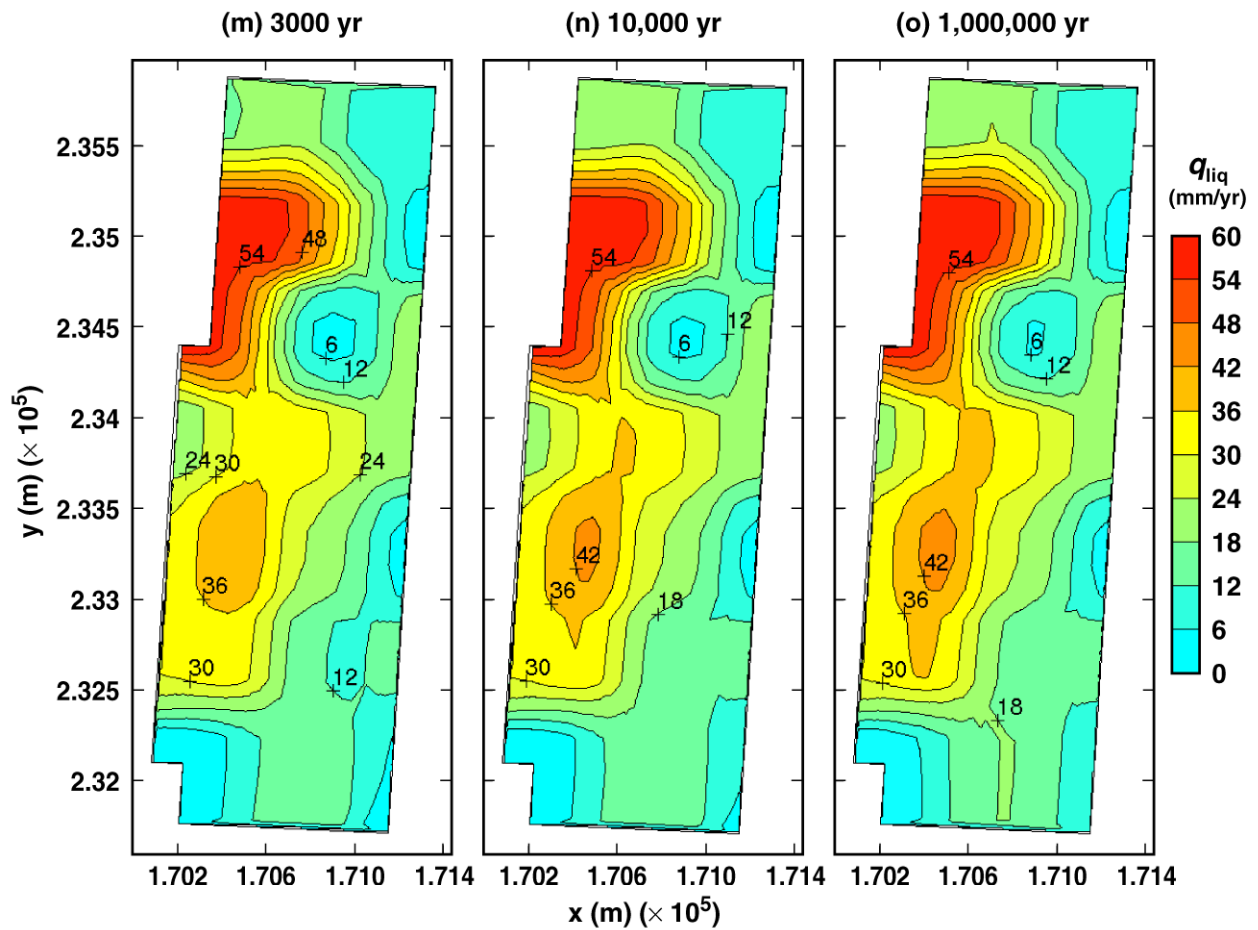
TB\_AMR\_mean\_qliq\_5m\_pwr2\_31-104

Figure 6-26. Liquid-phase flux 5 m above the crown of the drift for the mean infiltration-flux backfill case for the indicated times (Continued)



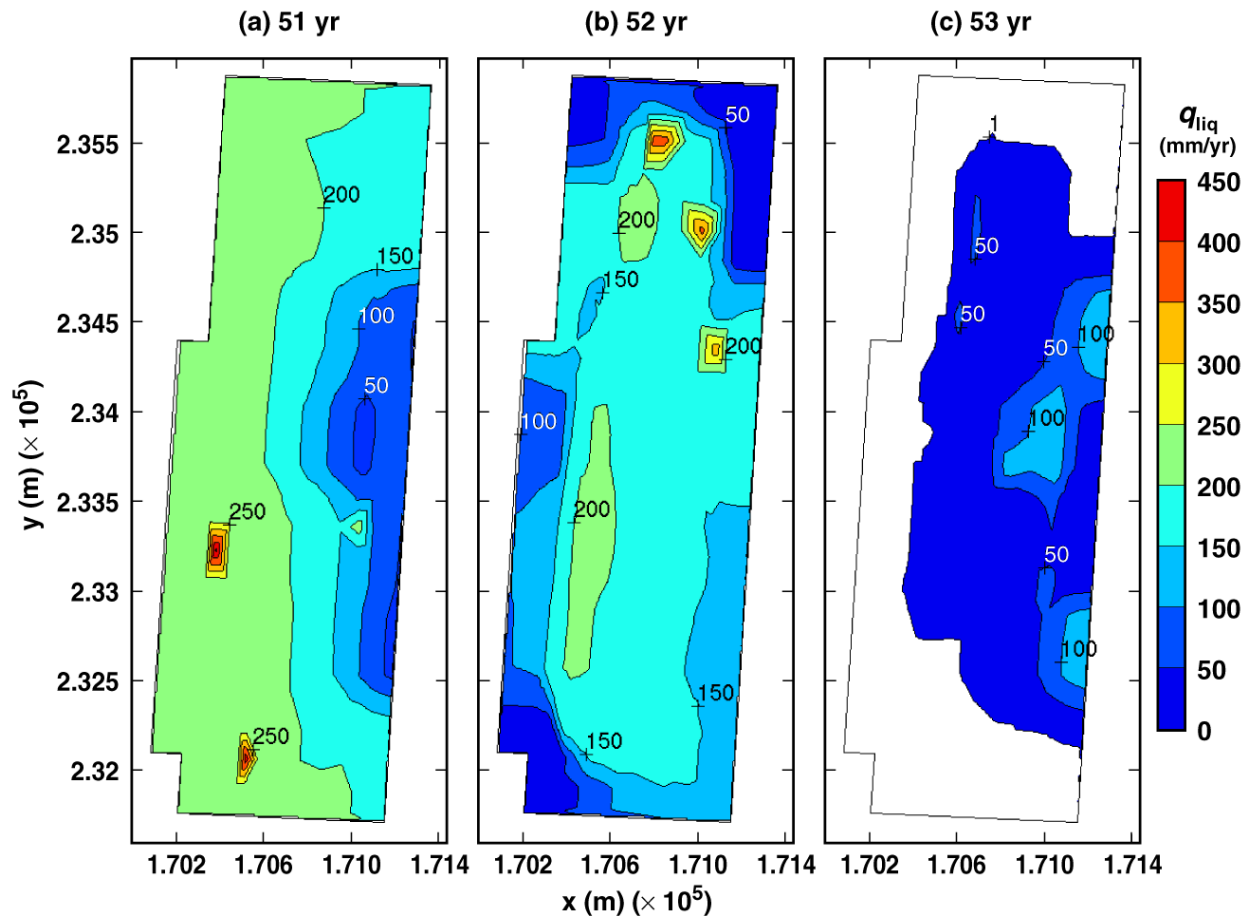
TB\_AMR\_mean\_qliq\_5m\_pwr2\_144-254

Figure 6-26. Liquid-phase flux 5 m above the crown of the drift for the mean infiltration-flux backfill case for the indicated times (Continued)



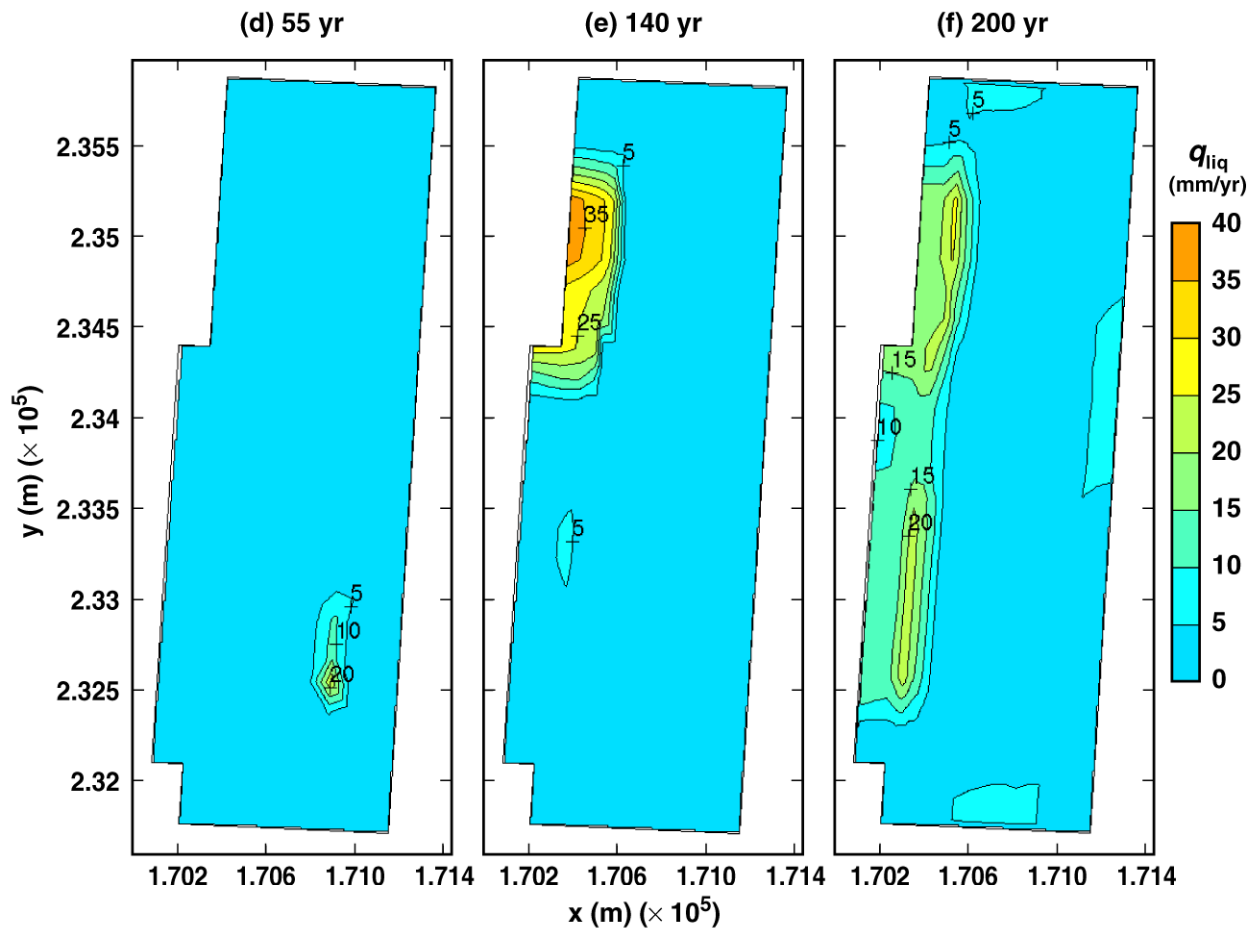
TB\_AMR\_mean\_qliq\_5m\_pwr2\_283-352

Figure 6-26. Liquid-phase flux 5 m above the crown of the drift for the mean infiltration-flux backfill case for the indicated times (Continued)



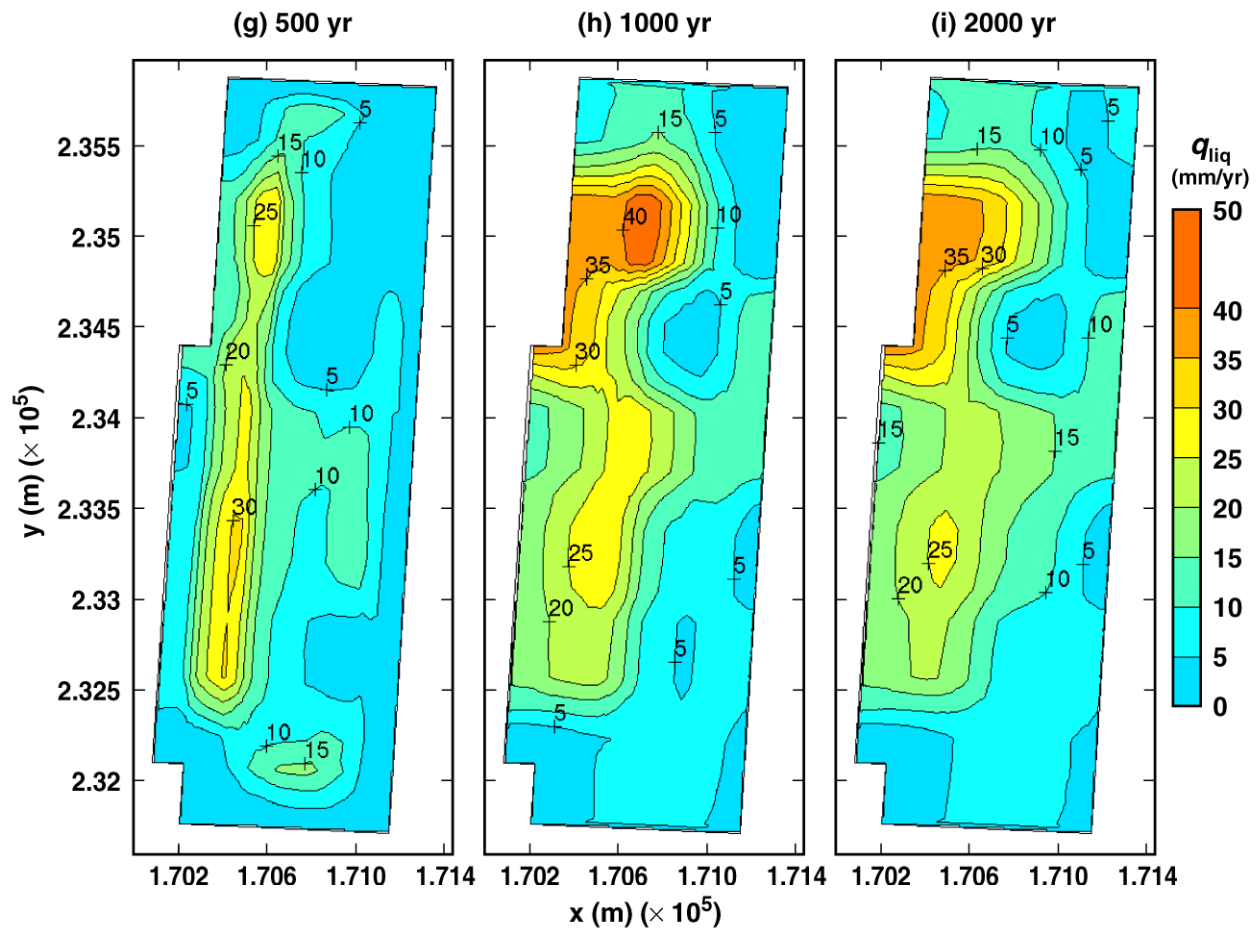
TB\_AMR\_mean\_qliq\_dw\_pwr2\_13-15

Figure 6-27. Liquid-phase flux 0.2 m above the crown of the drift for the mean infiltration-flux backfill case for the indicated times



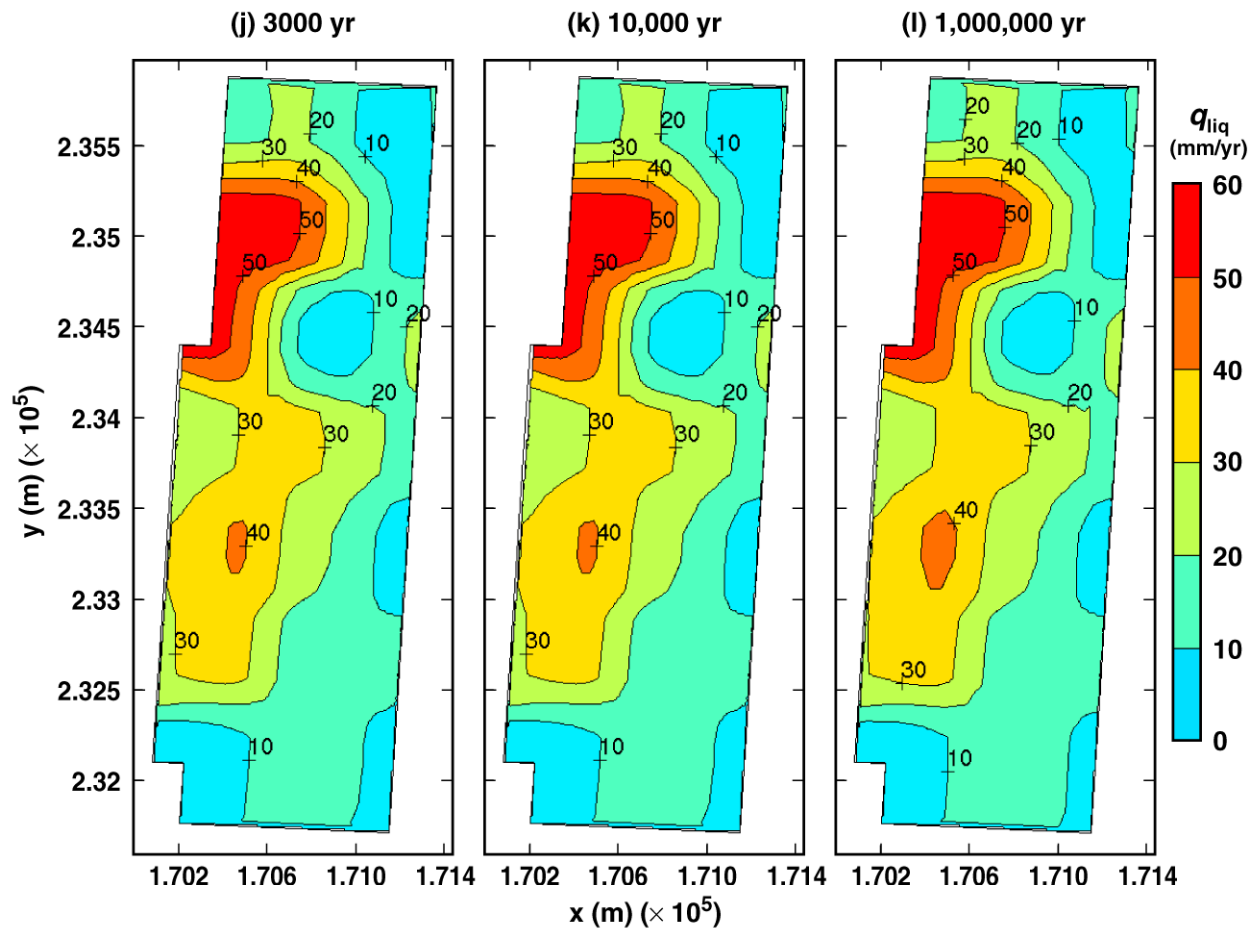
TB\_AMR\_mean\_qliq\_dw\_pwr2\_16-31

Figure 6-27. Liquid-phase flux 0.2 m above the crown of the drift for the mean infiltration-flux backfill case for the indicated times (Continued)



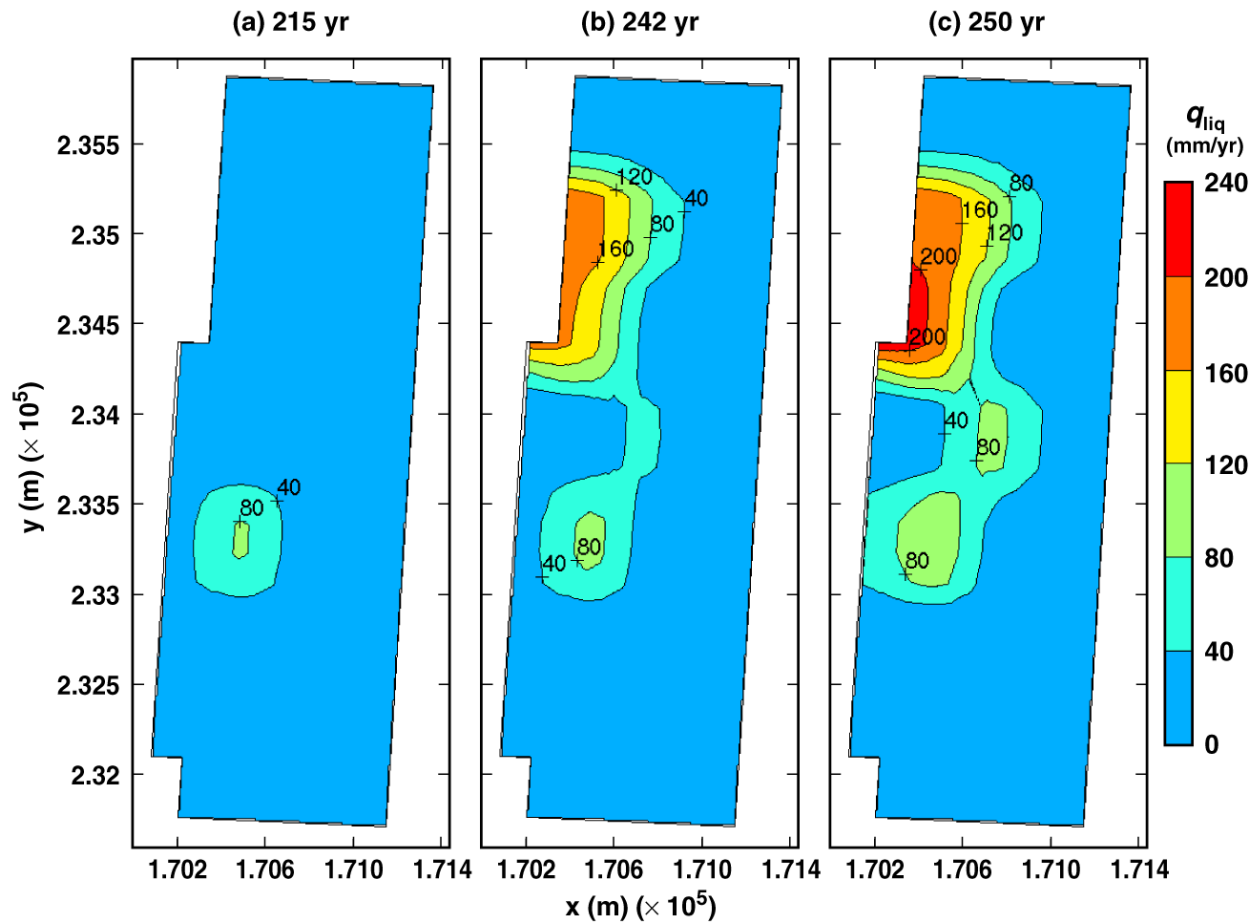
TB\_AMR\_mean\_qliq\_dw\_pwr2\_104-254

Figure 6-27. Liquid-phase flux 0.2 m above the crown of the drift for the mean infiltration-flux backfill case for the indicated times (Continued)



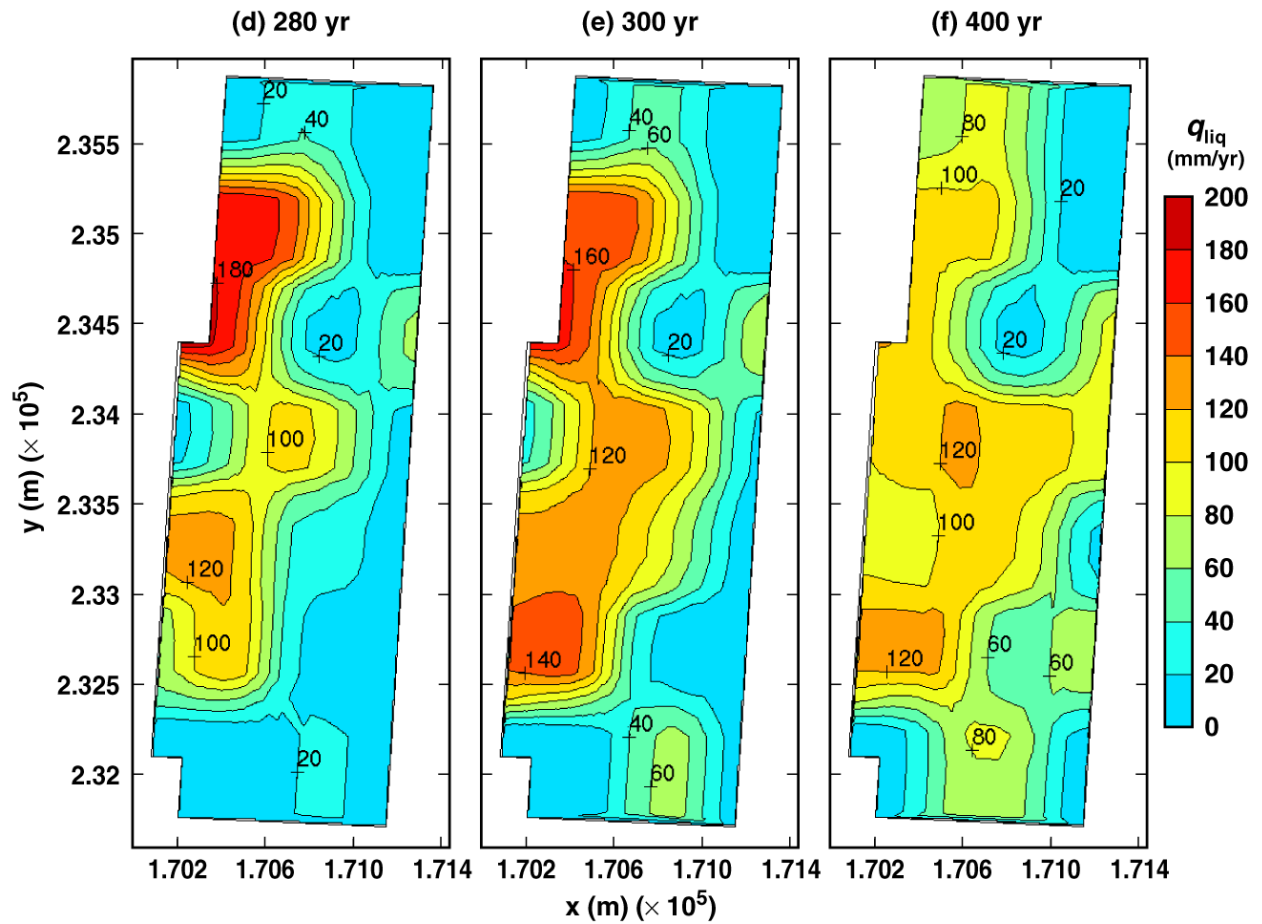
TB\_AMR\_mean\_qliq\_dw\_pwr2\_283-352

Figure 6-27. Liquid-phase flux 0.2 m above the crown of the drift for the mean infiltration-flux backfill case for the indicated times (Continued)



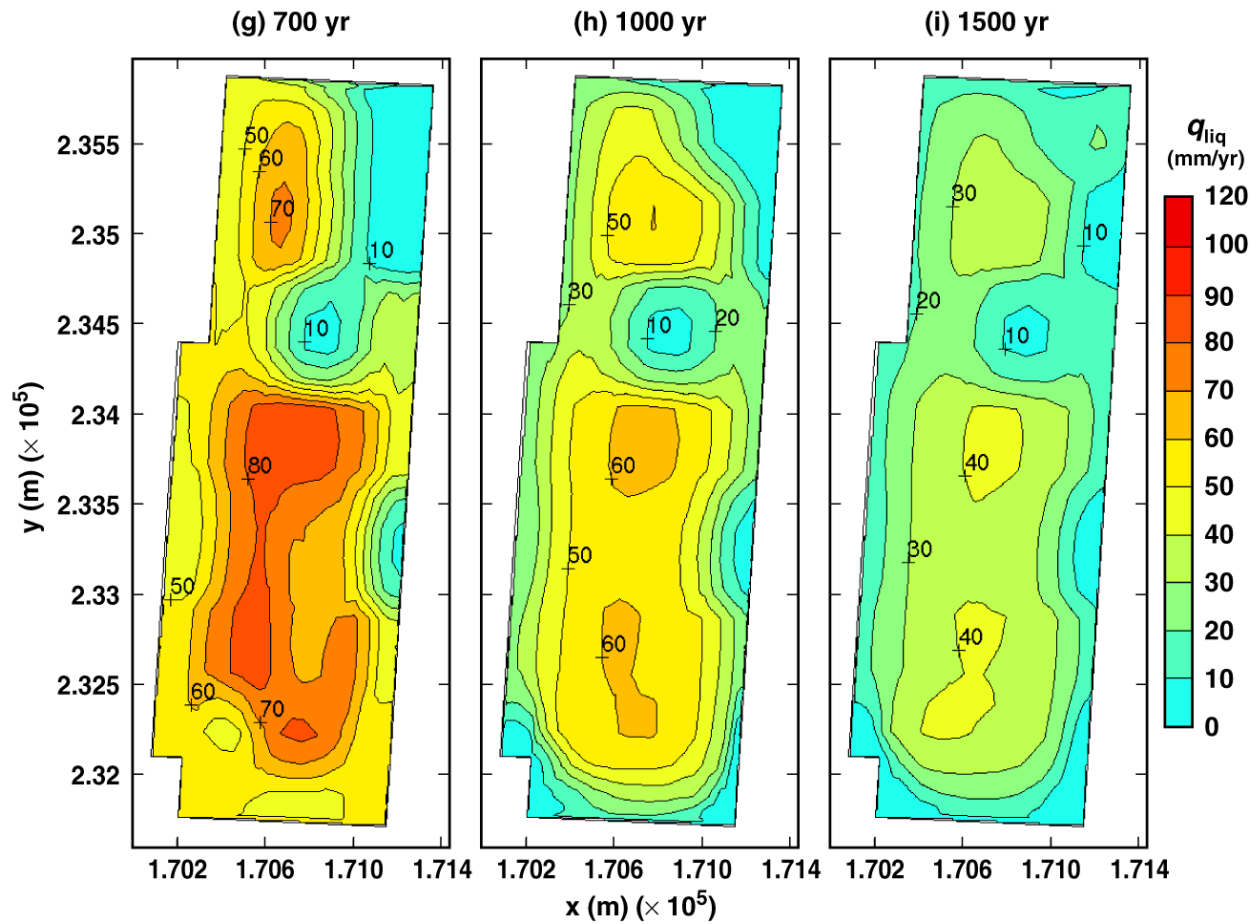
TB\_AMR\_mean\_qliq\_dsTop\_avg\_pwr2\_34-49

Figure 6-28. Liquid-phase flux averaged over the upper surface of the drip shield for the mean infiltration-flux backfill case for the indicated times



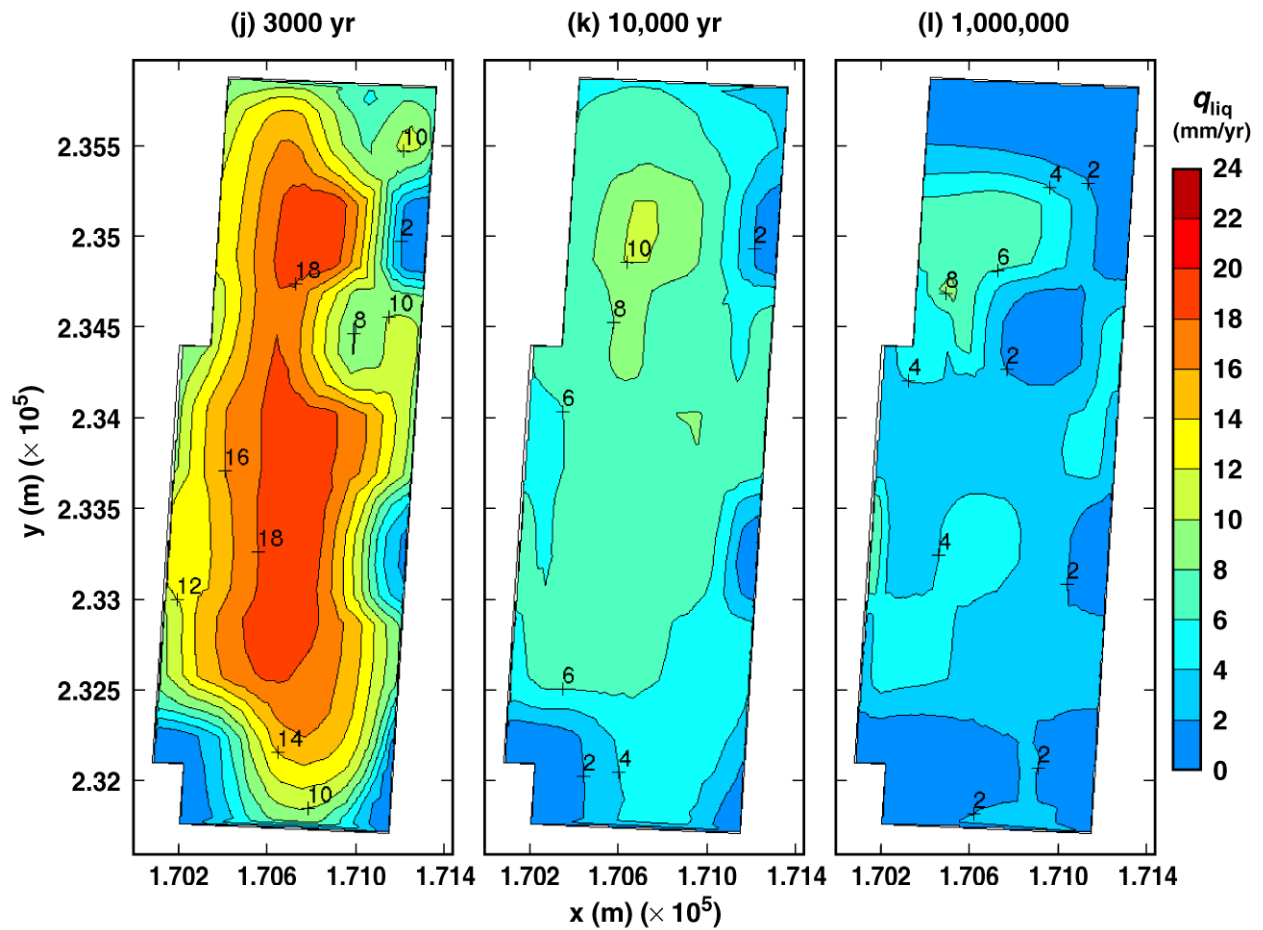
TB\_AMR\_mean\_qliq\_dsTop\_avg\_pwr2\_60-84

Figure 6-28. Liquid-phase flux averaged over the upper surface of the drip shield for the mean infiltration-flux backfill case for the indicated times (Continued)



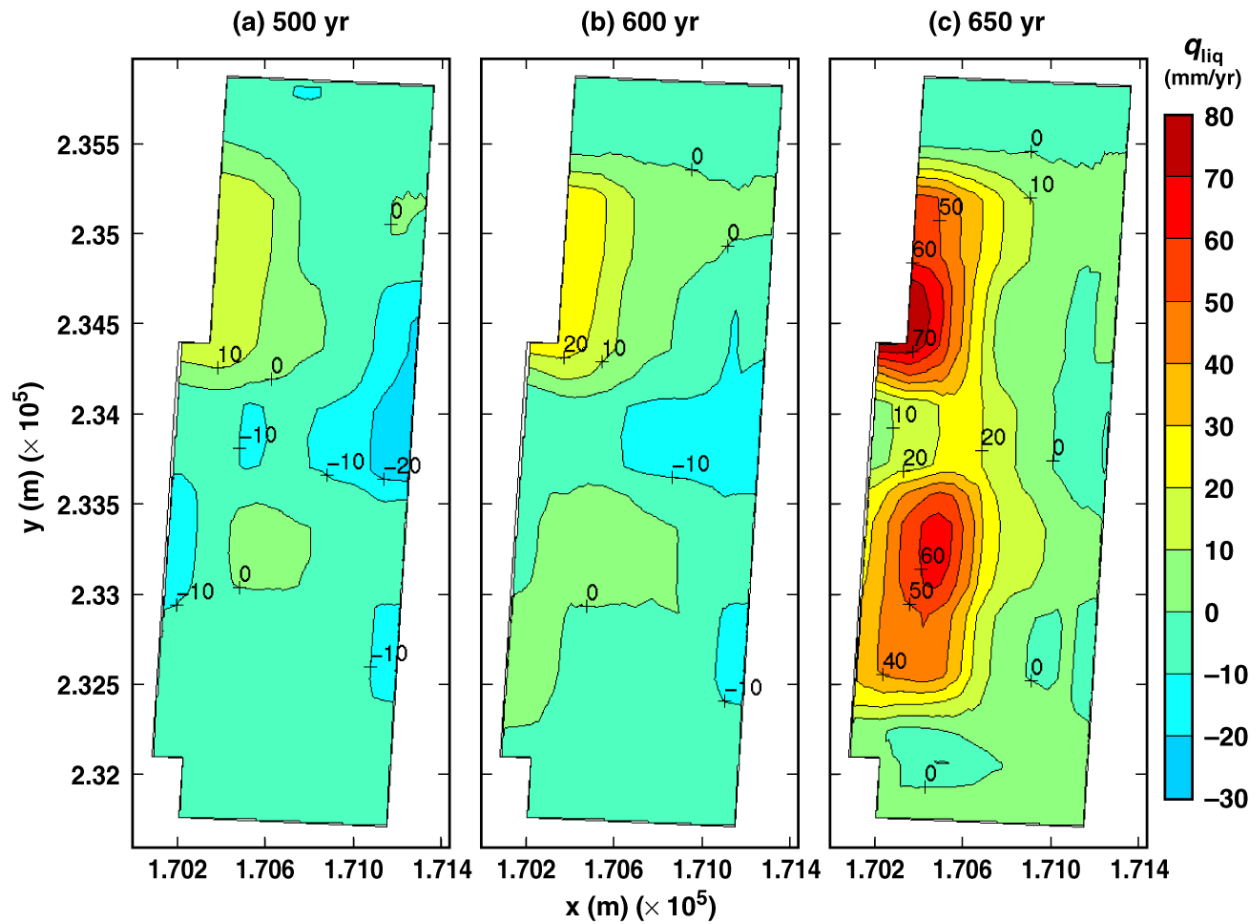
TB\_AMR\_mean\_qliq\_dsTop\_avg\_pwr2\_144-225

Figure 6-28. Liquid-phase flux averaged over the upper surface of the drip shield for the mean infiltration-flux backfill case for the indicated times (Continued)



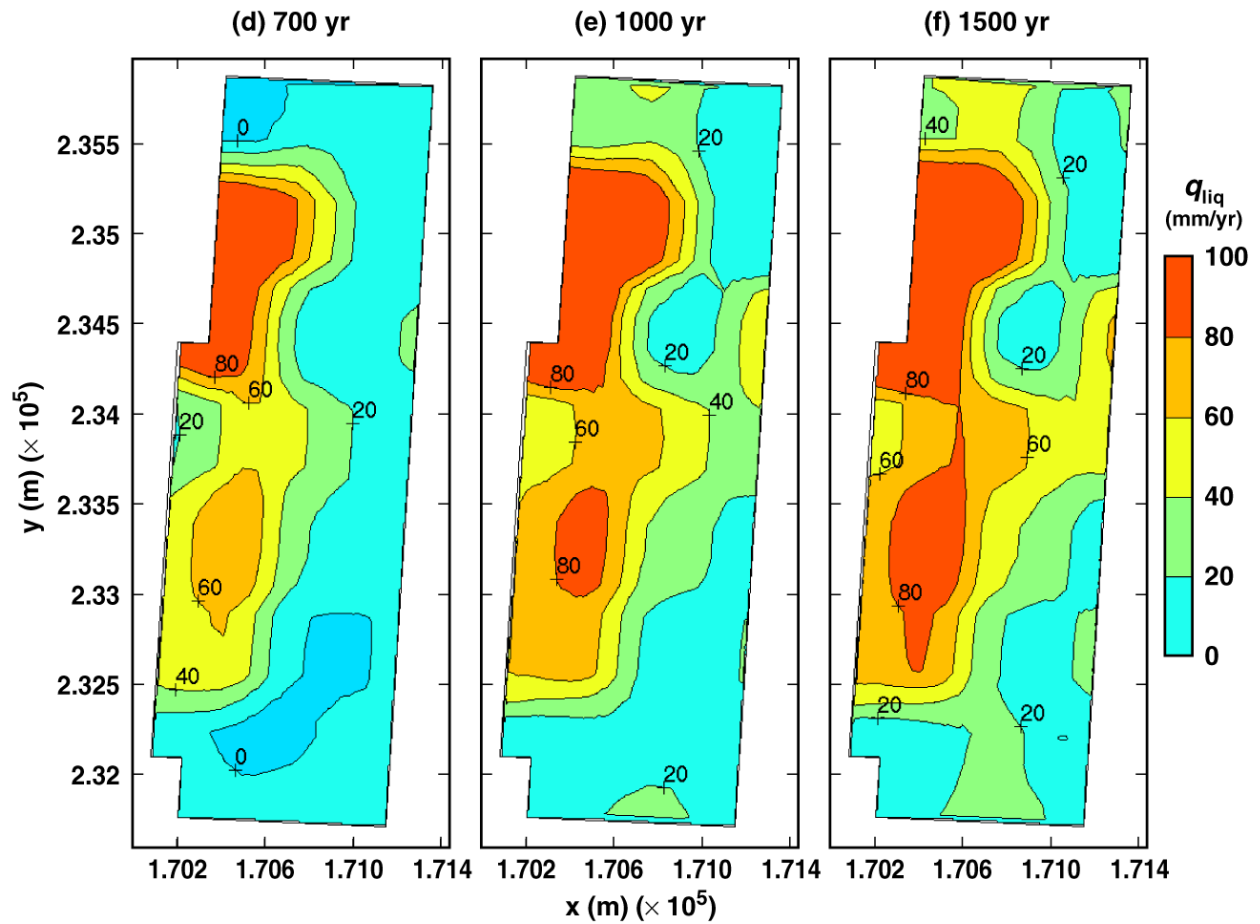
TB\_AMR\_mean\_qliq\_dsTop\_avg\_pwr2\_283-352

Figure 6-28. Liquid-phase flux averaged over the upper surface of the drip shield for the mean infiltration-flux backfill case for the indicated times (Continued)



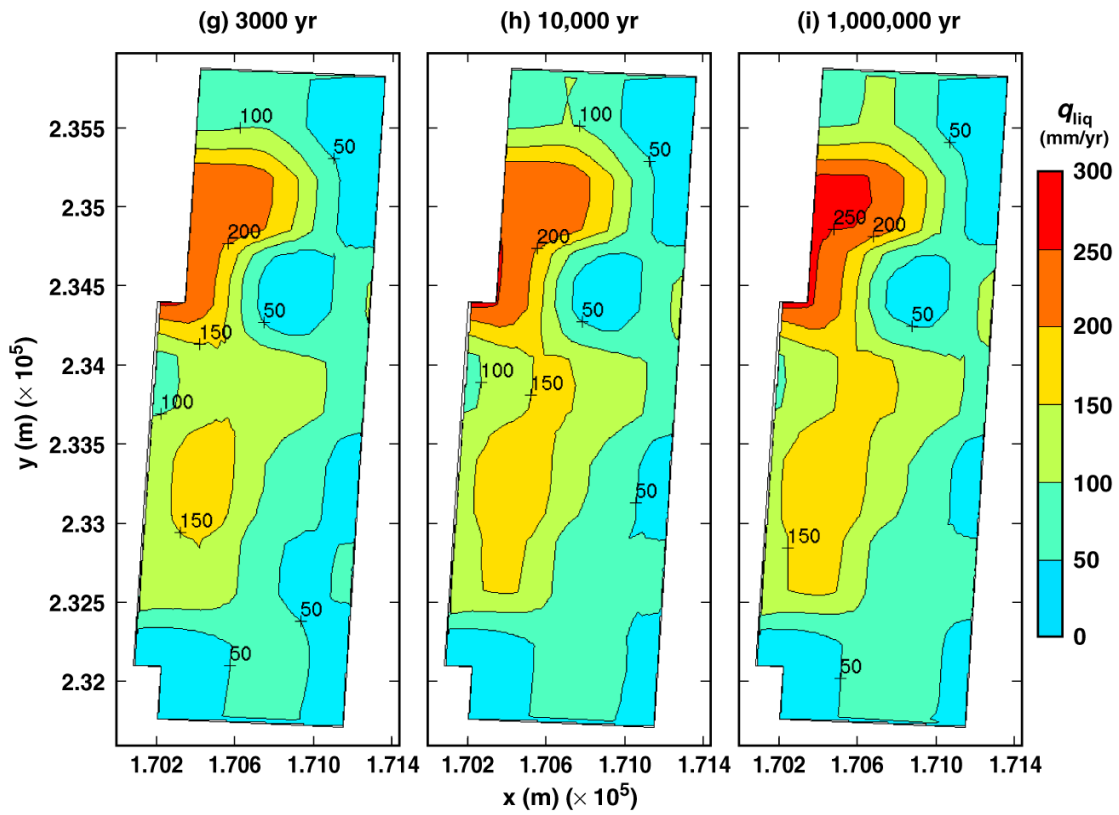
TB\_AMR\_mean\_qliq\_dsSide\_pwr2\_104-134

Figure 6-29. Liquid-phase flux adjacent to the lower side of the drip shield (i.e., adjacent to the base of the drip shield) for the mean infiltration-flux backfill case for the indicated times



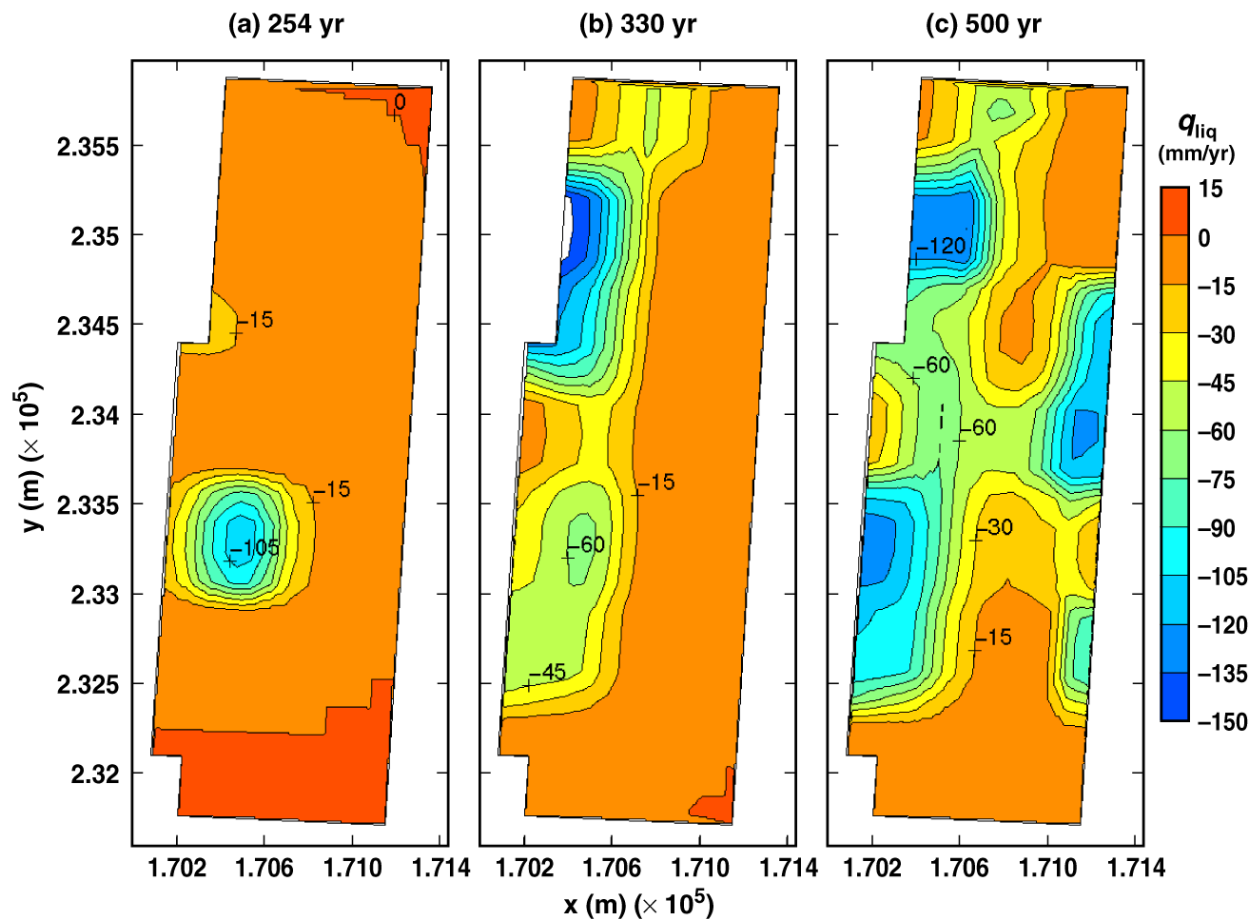
TB\_AMR\_mean\_qliq\_dsSide\_pwr2\_144-225

Figure 6-29. Liquid-phase flux adjacent to the lower side of the drip shield (i.e., adjacent to the base of the drip shield) for the mean infiltration-flux backfill case for the indicated times (Continued)



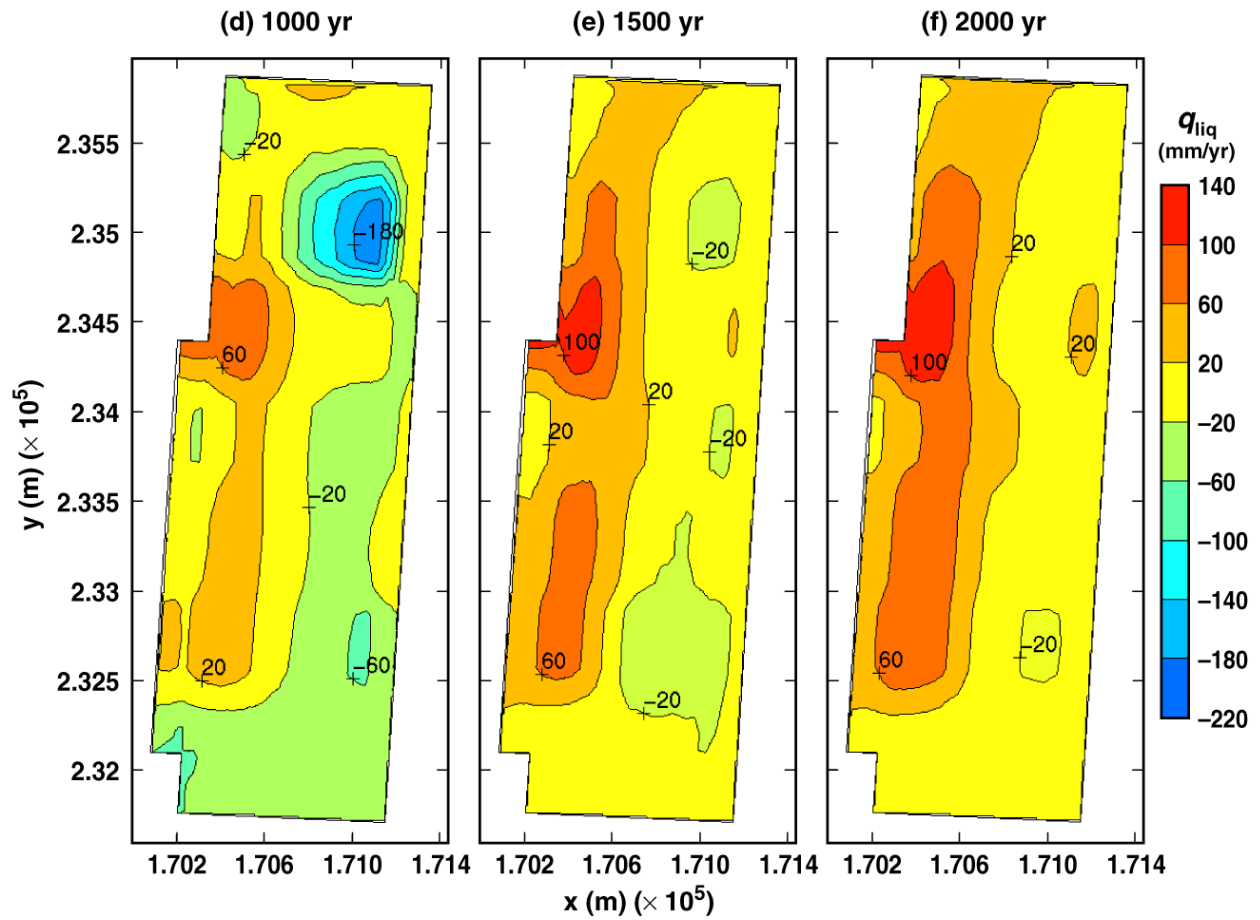
TB\_AMR\_mean\_qliq\_dsSide\_pwr2\_283-352

Figure 6-29. Liquid-phase flux adjacent to the lower side of the drip shield (i.e., adjacent to the base of the drip shield) for the mean infiltration-flux backfill case for the indicated times (Continued)



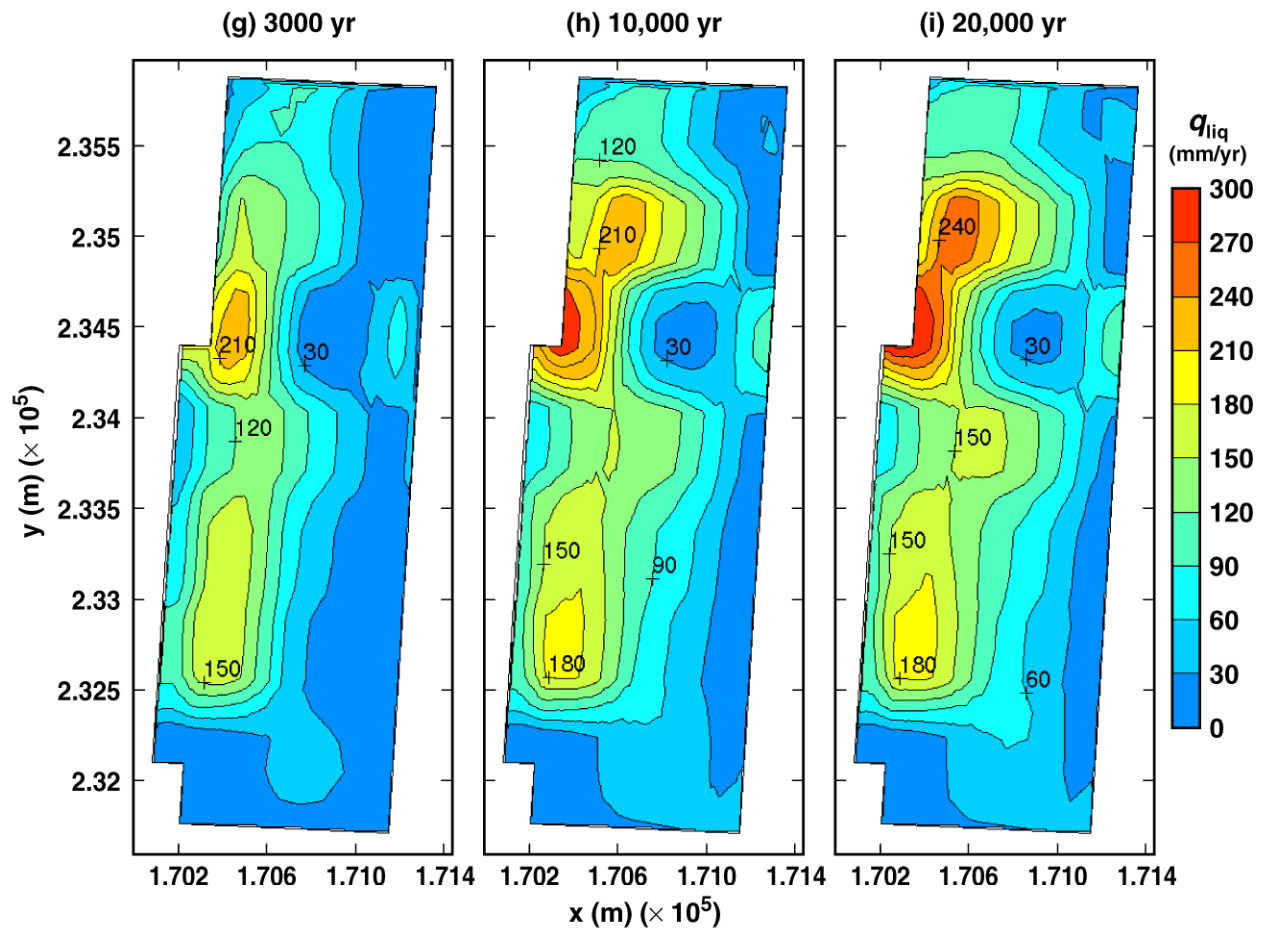
TB\_AMR\_mean\_qliq\_invert\_pwr2\_51-104

Figure 6-30. Liquid-phase flux averaged over the invert for the mean infiltration-flux backfill case for the indicated times



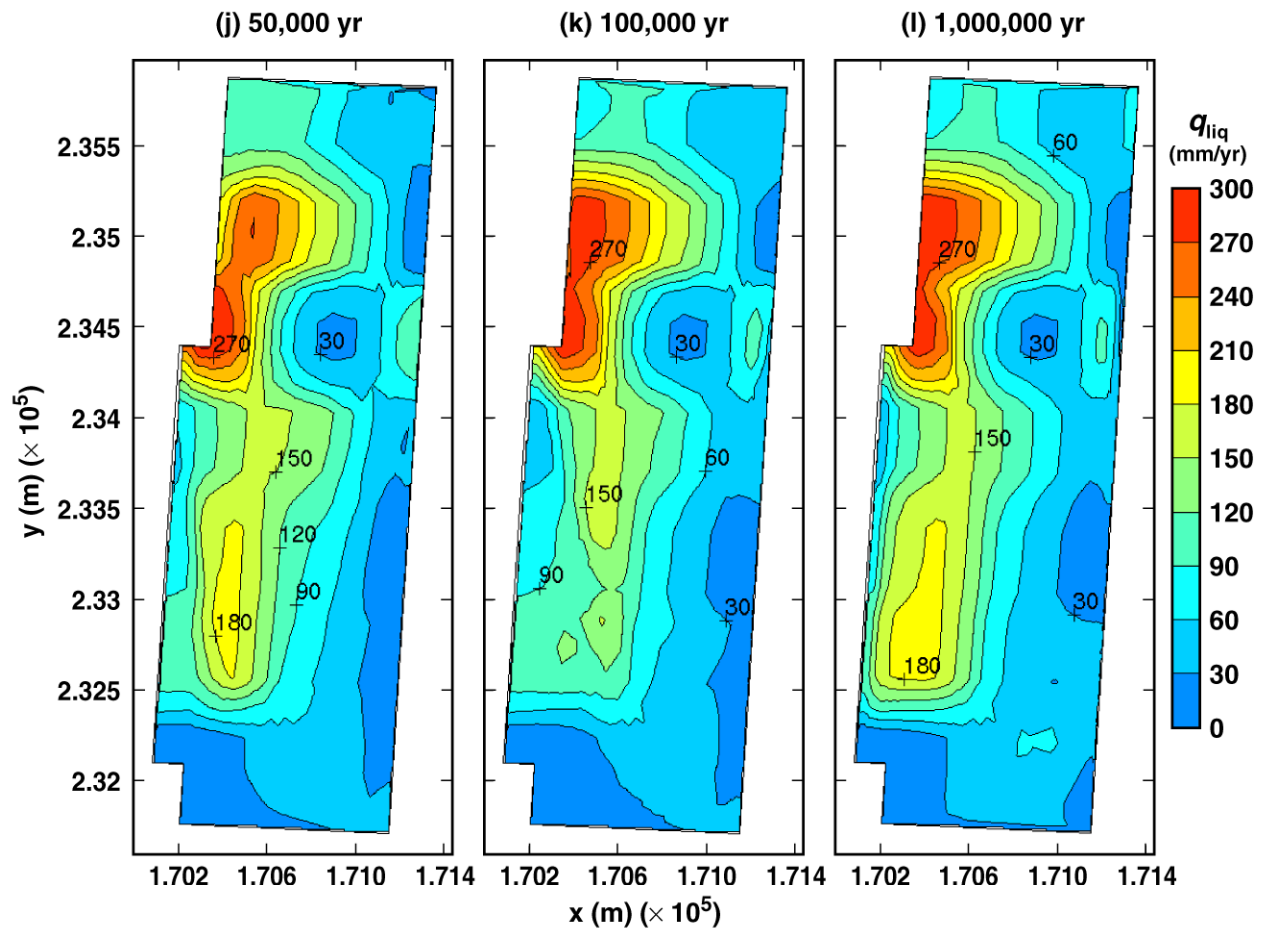
TB\_AMR\_mean\_qliq\_invert\_pwr2\_174-254

Figure 6-30. Liquid-phase flux averaged over the invert for the mean infiltration-flux backfill case for the indicated times (Continued)



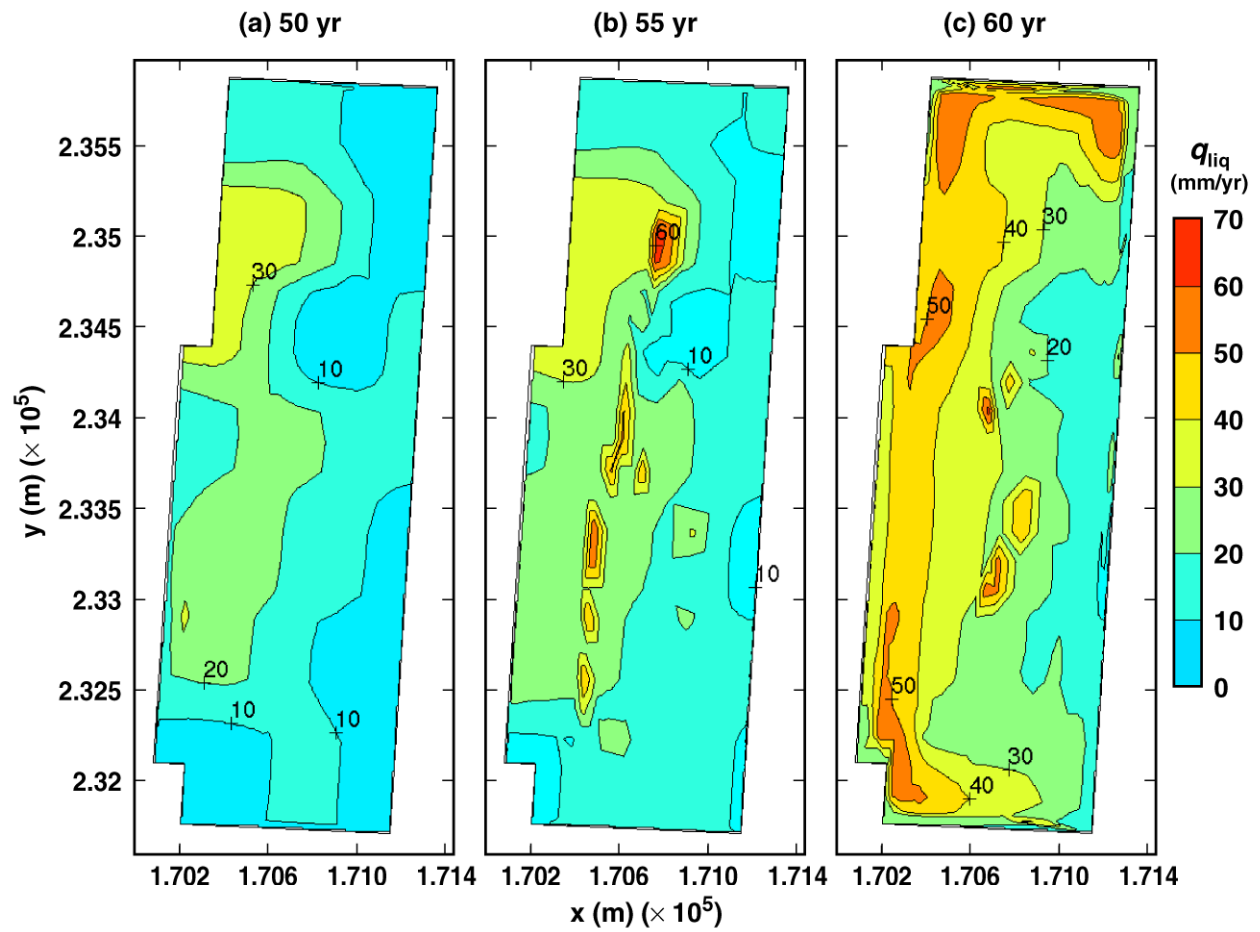
TB\_AMR\_mean\_qliq\_invert\_pwr2\_283-330

Figure 6-30. Liquid-phase flux averaged over the invert for the mean infiltration-flux backfill case for the indicated times (Continued)



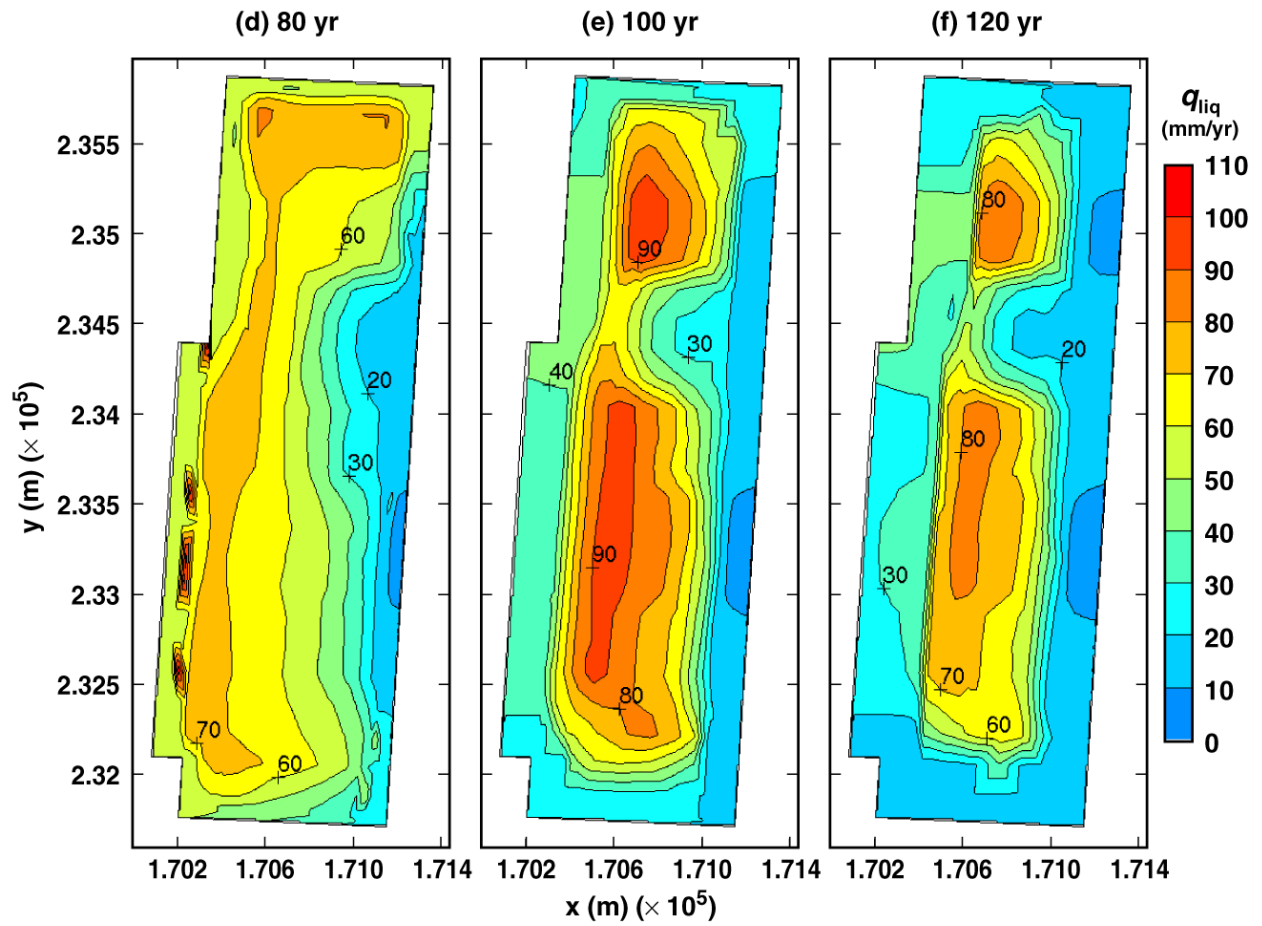
TB\_AMR\_mean\_qliq\_invert\_pwr2\_341-352

Figure 6-30. Liquid-phase flux averaged over the invert for the mean infiltration-flux backfill case for the indicated times (Continued)



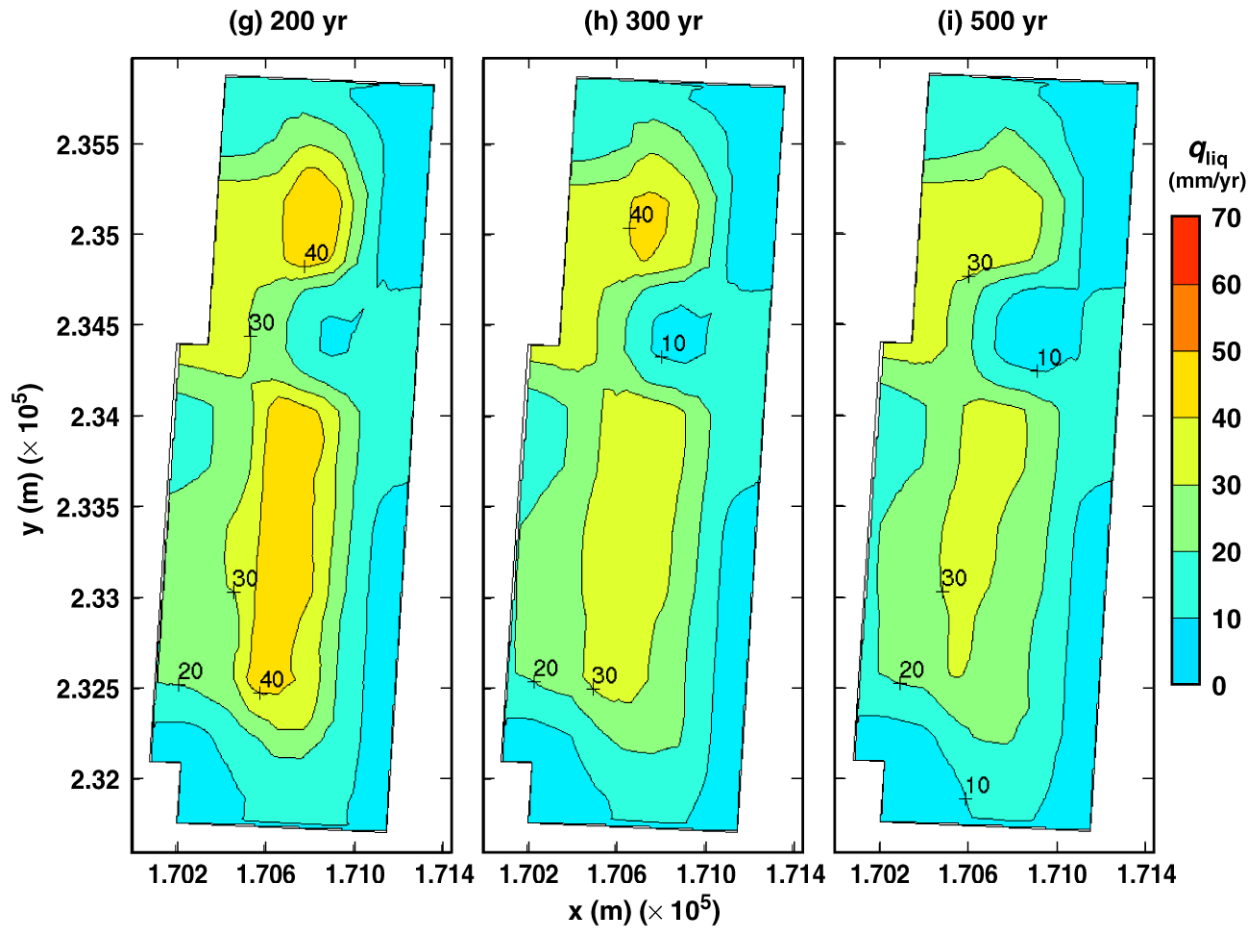
TB\_AMR\_upper\_qliq\_5m\_pwr2\_11-17

Figure 6-31. Liquid-phase flux 5 m above the crown of the drift for the high infiltration-flux backfill case for the indicated times



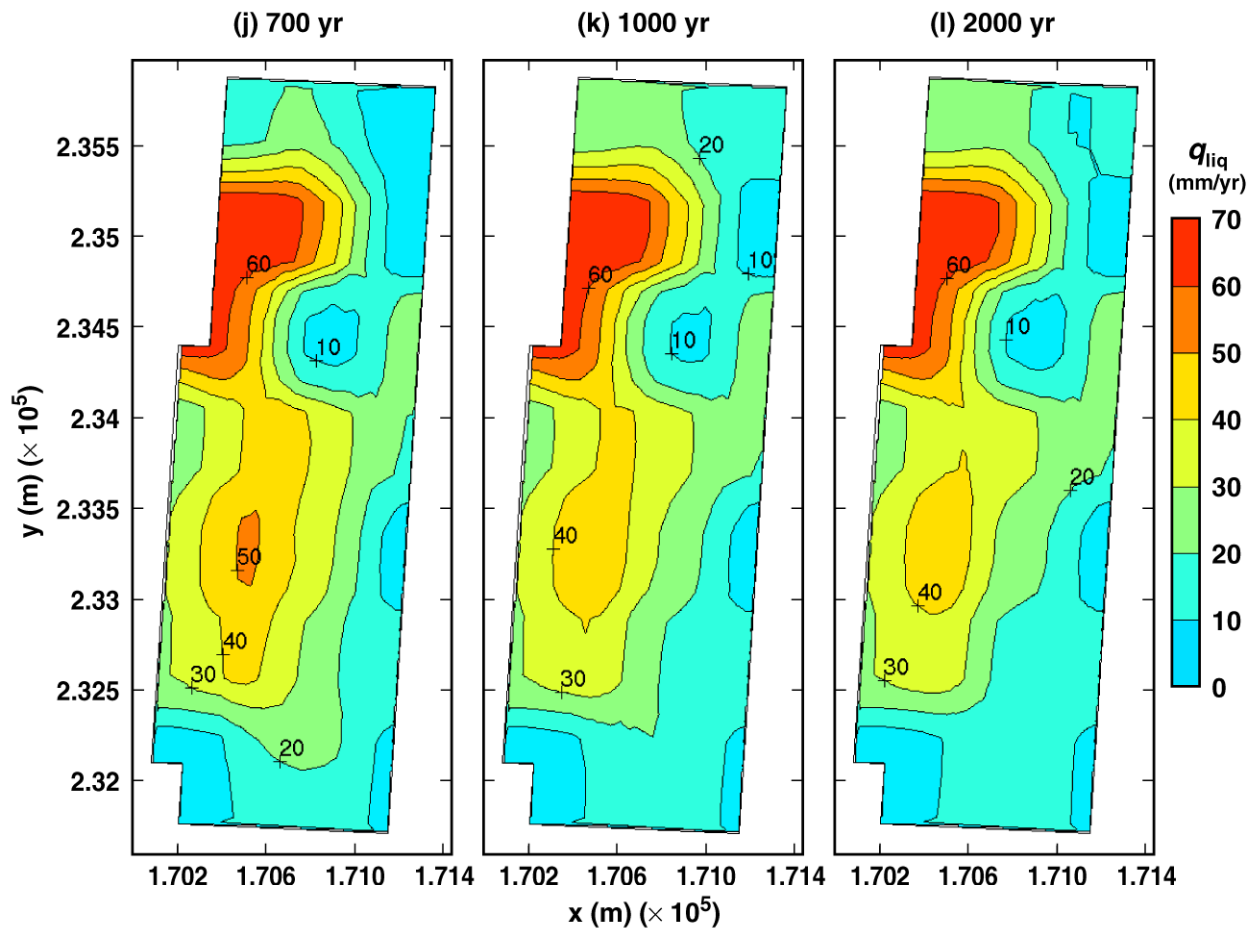
TB\_AMR\_upper\_qliq\_5m\_pwr2\_18-25

Figure 6-31. Liquid-phase flux 5 m above the crown of the drift for the high infiltration-flux backfill case for the indicated times (Continued)



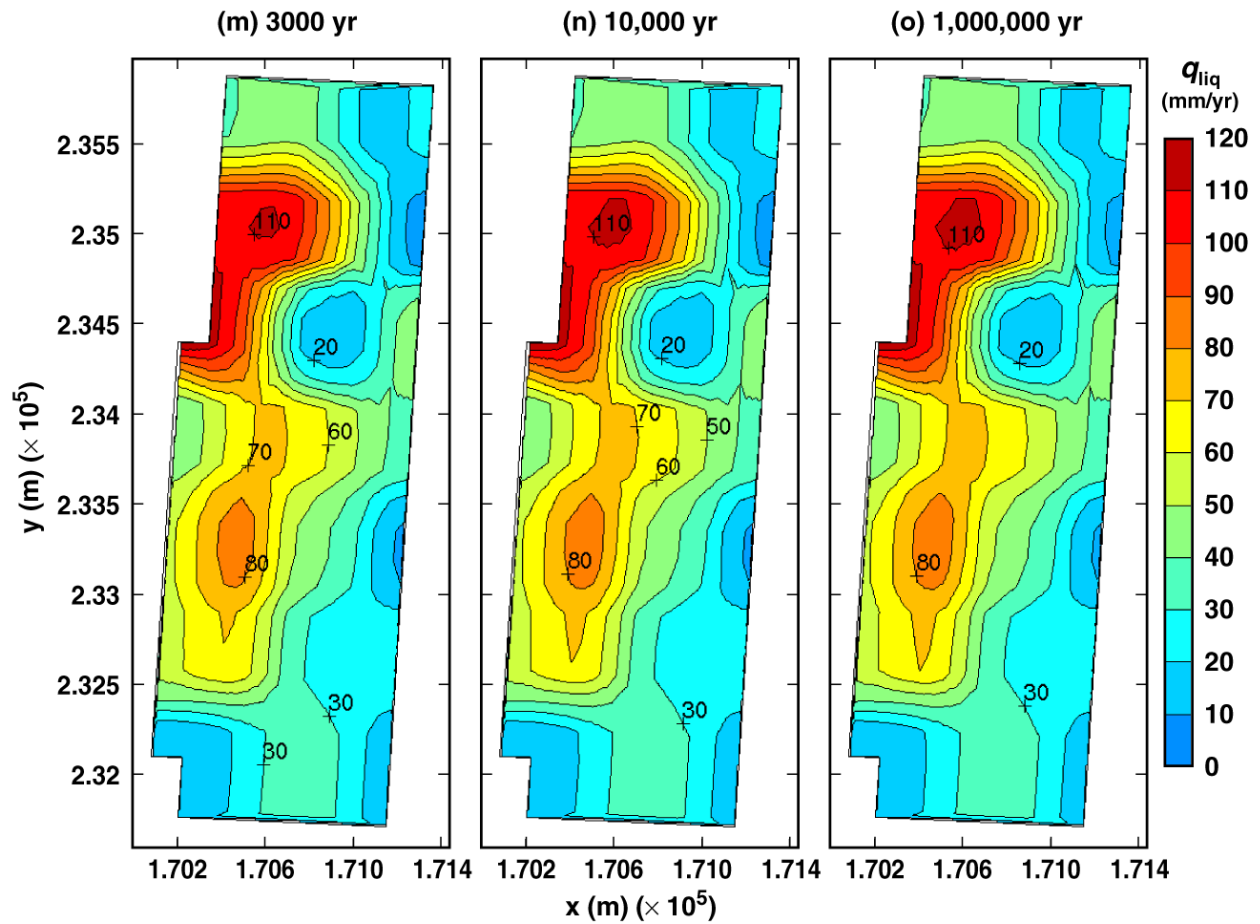
TB\_AMR\_upper\_qliq\_5m\_pwr2\_56-177

Figure 6-31. Liquid-phase flux 5 m above the crown of the drift for the high infiltration-flux backfill case for the indicated times (Continued)



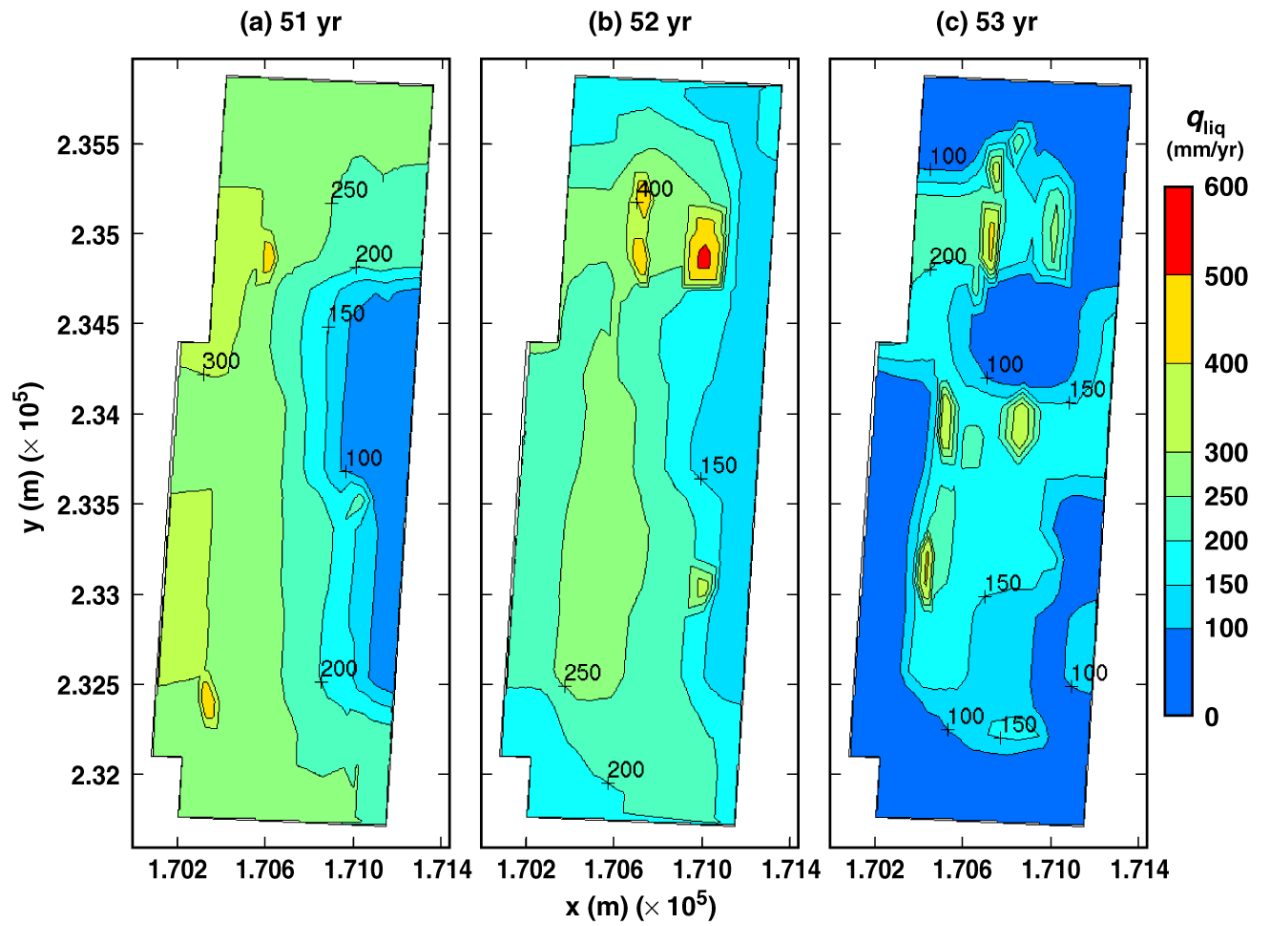
TB\_AMR\_upper\_qliq\_5m\_pwr2\_217-360

Figure 6-31. Liquid-phase flux 5 m above the crown of the drift for the high infiltration-flux backfill case for the indicated times (Continued)



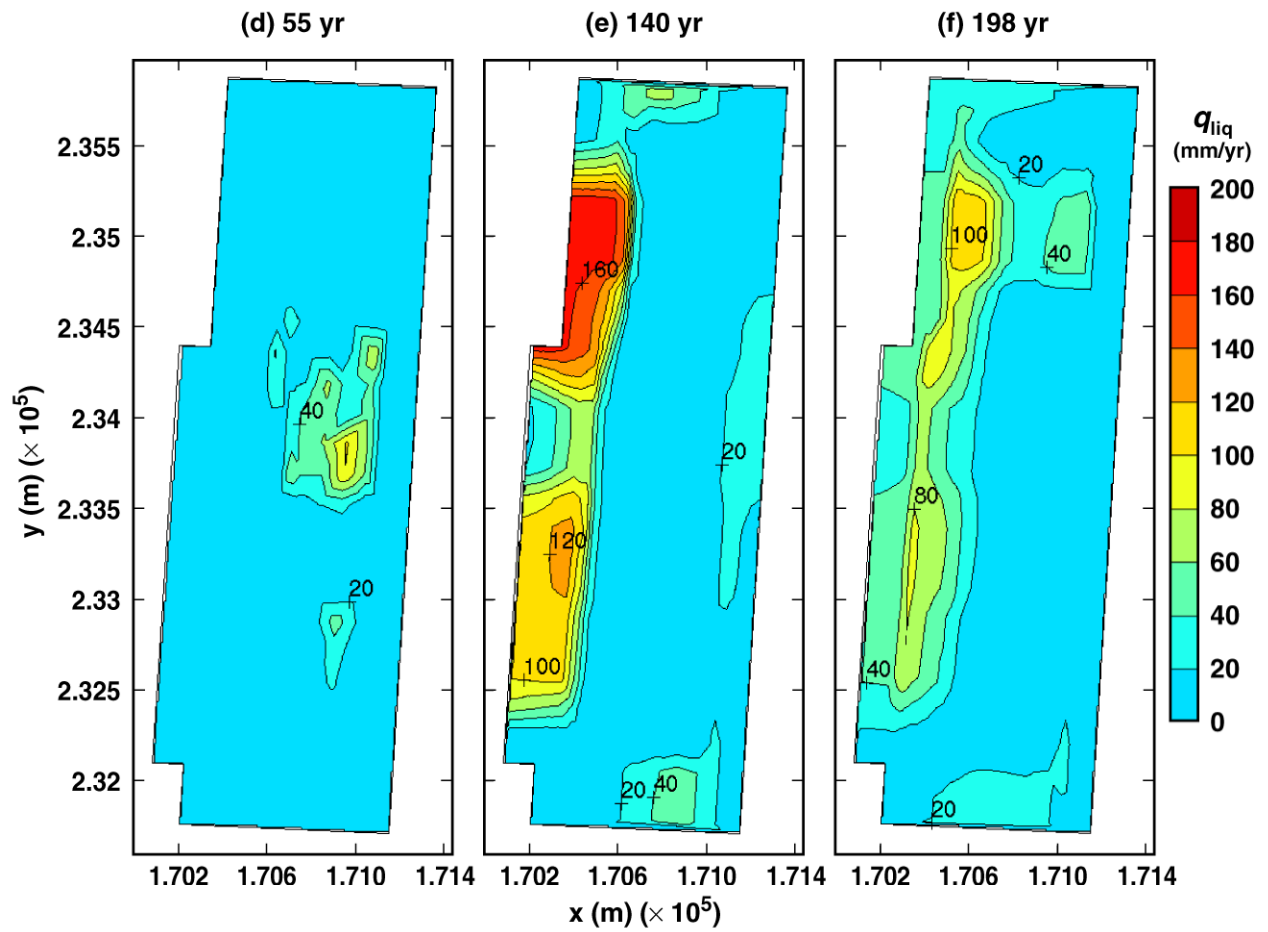
TB\_AMR\_upper\_qliq\_5m\_pwr2\_389-457

Figure 6-31. Liquid-phase flux 5 m above the crown of the drift for the high infiltration-flux backfill case for the indicated times (Continued)



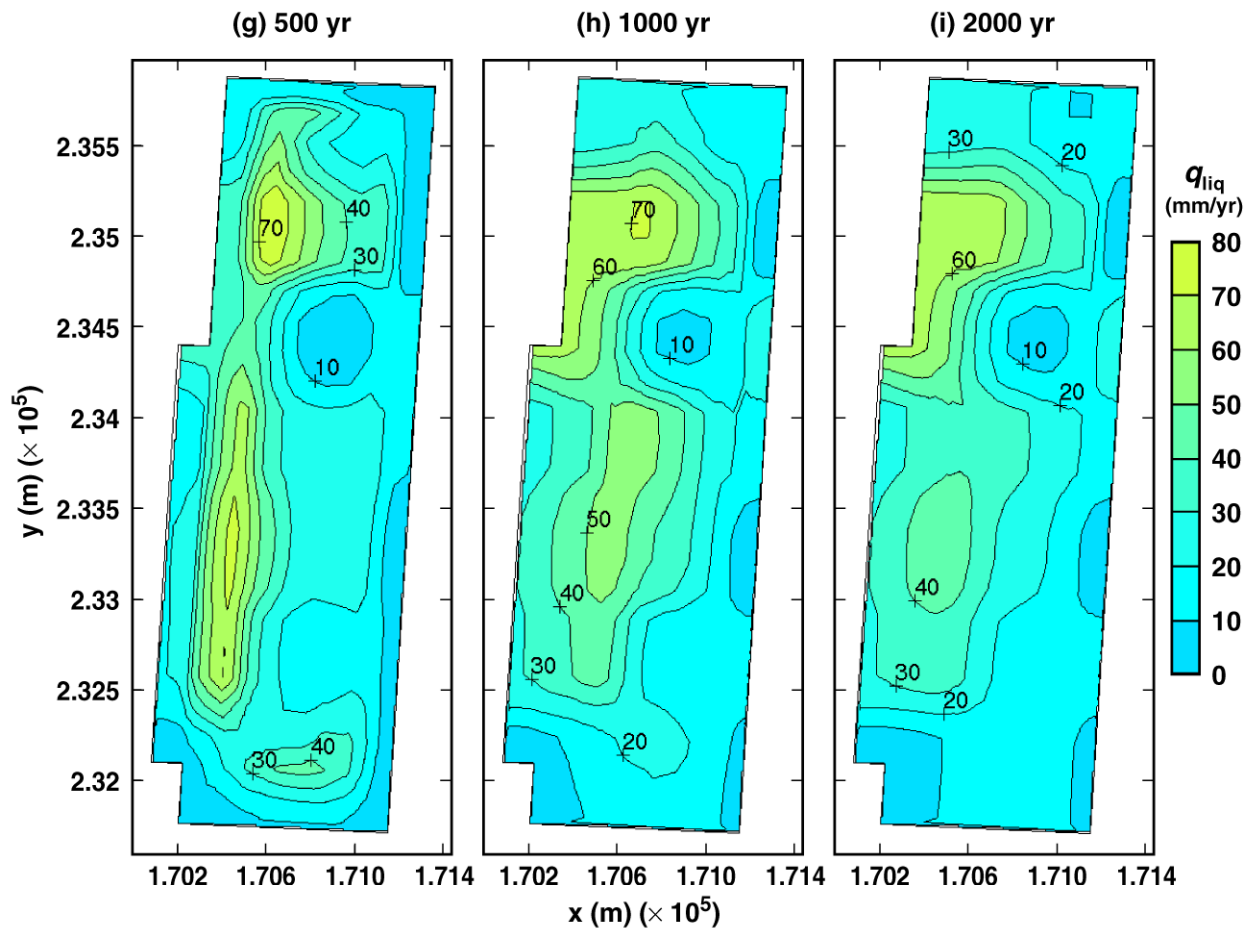
TB\_AMR\_upper\_qliq\_dw\_pwr1\_13-15

Figure 6-32. Liquid-phase flux 0.2 m above the crown of the drift for the high infiltration-flux backfill case for the indicated times



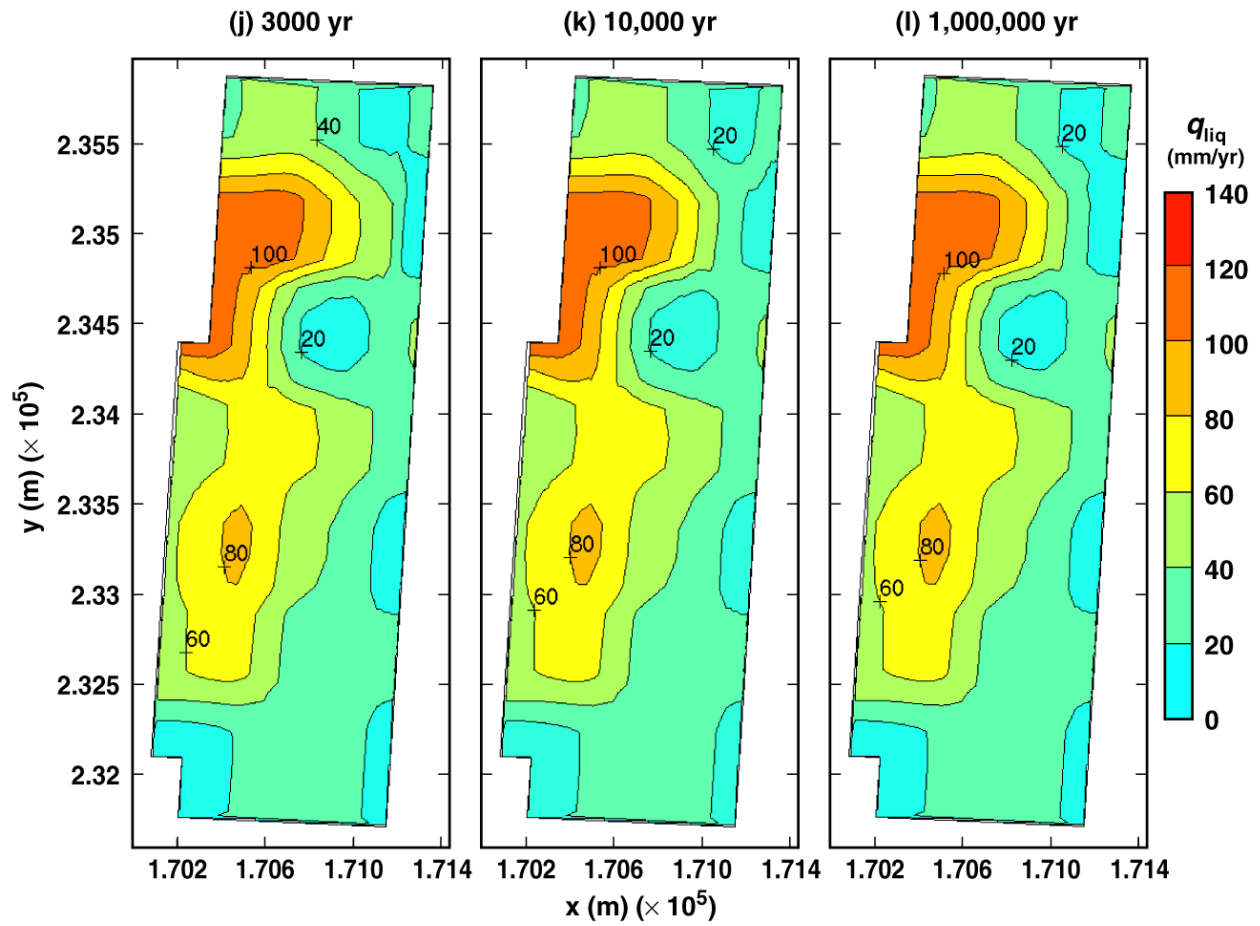
TB\_AMR\_upper\_qliq\_dw\_pwr1\_16-55

Figure 6-32. Liquid-phase flux 0.2 m above the crown of the drift for the high infiltration-flux backfill case for the indicated times (Continued)



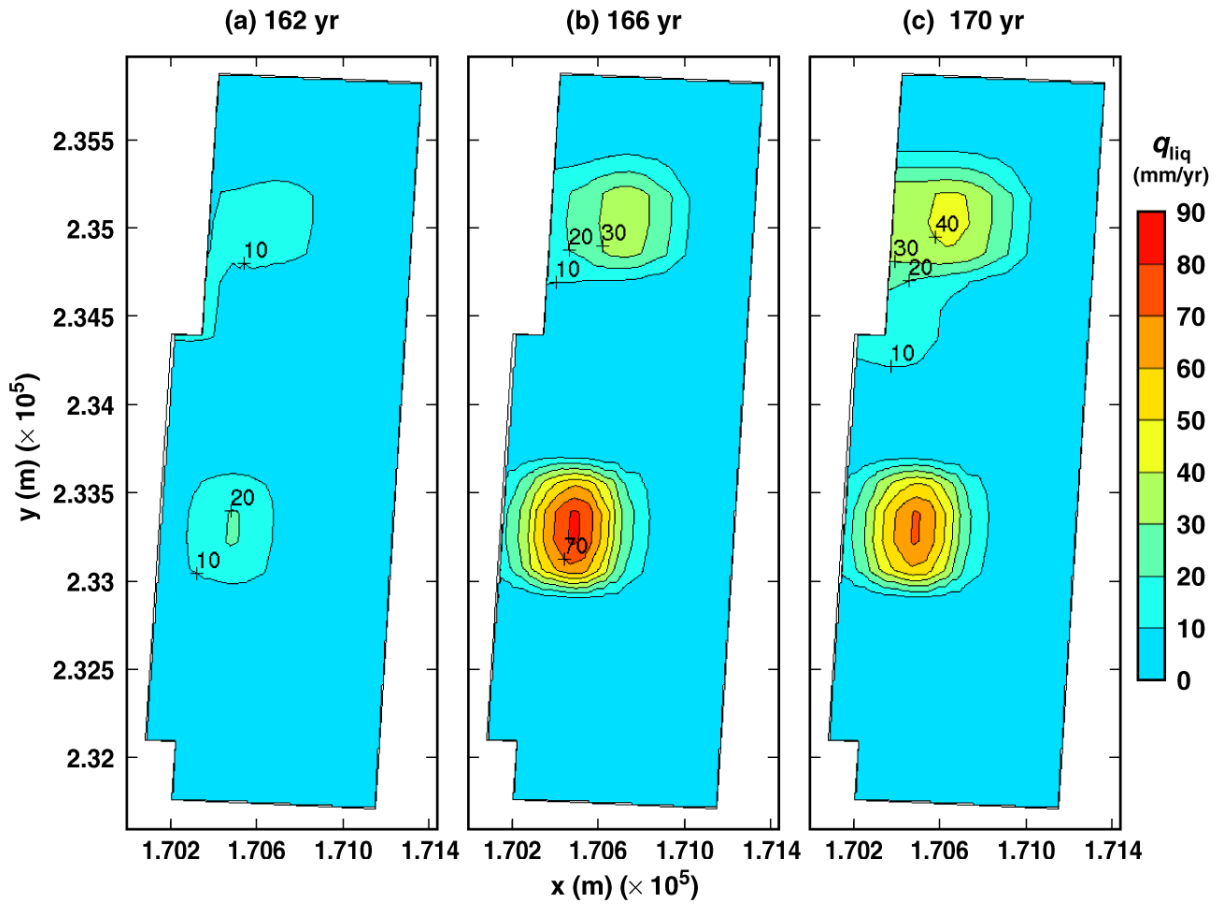
TB\_AMR\_upper\_qliq\_dw\_pwr1\_177-360

Figure 6-32. Liquid-phase flux 0.2 m above the crown of the drift for the high infiltration-flux backfill case for the indicated times (Continued)



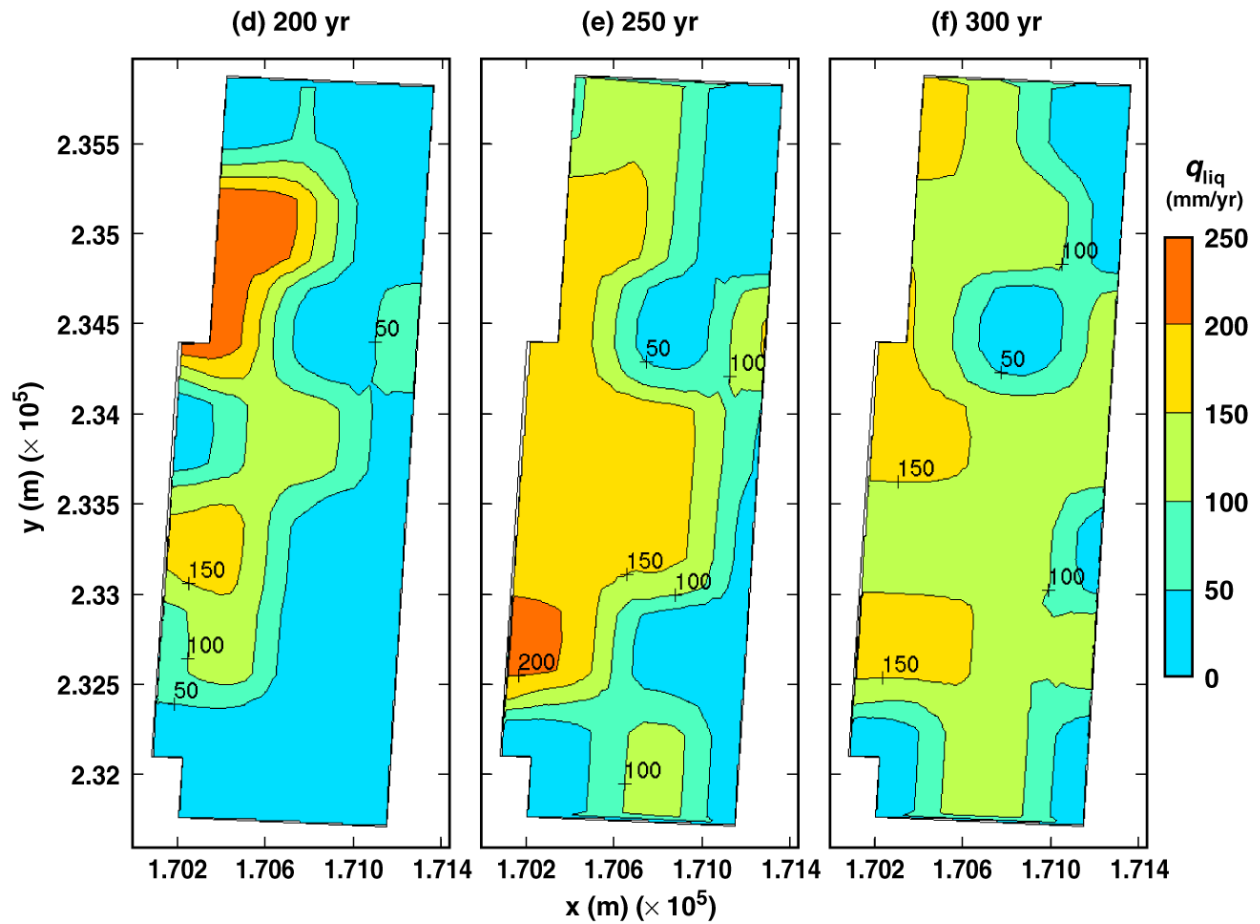
TB\_AMR\_upper\_qliq\_dw\_pwr1\_389-457

Figure 6-32. Liquid-phase flux 0.2 m above the crown of the drift for the high infiltration-flux backfill case for the indicated times (Continued)



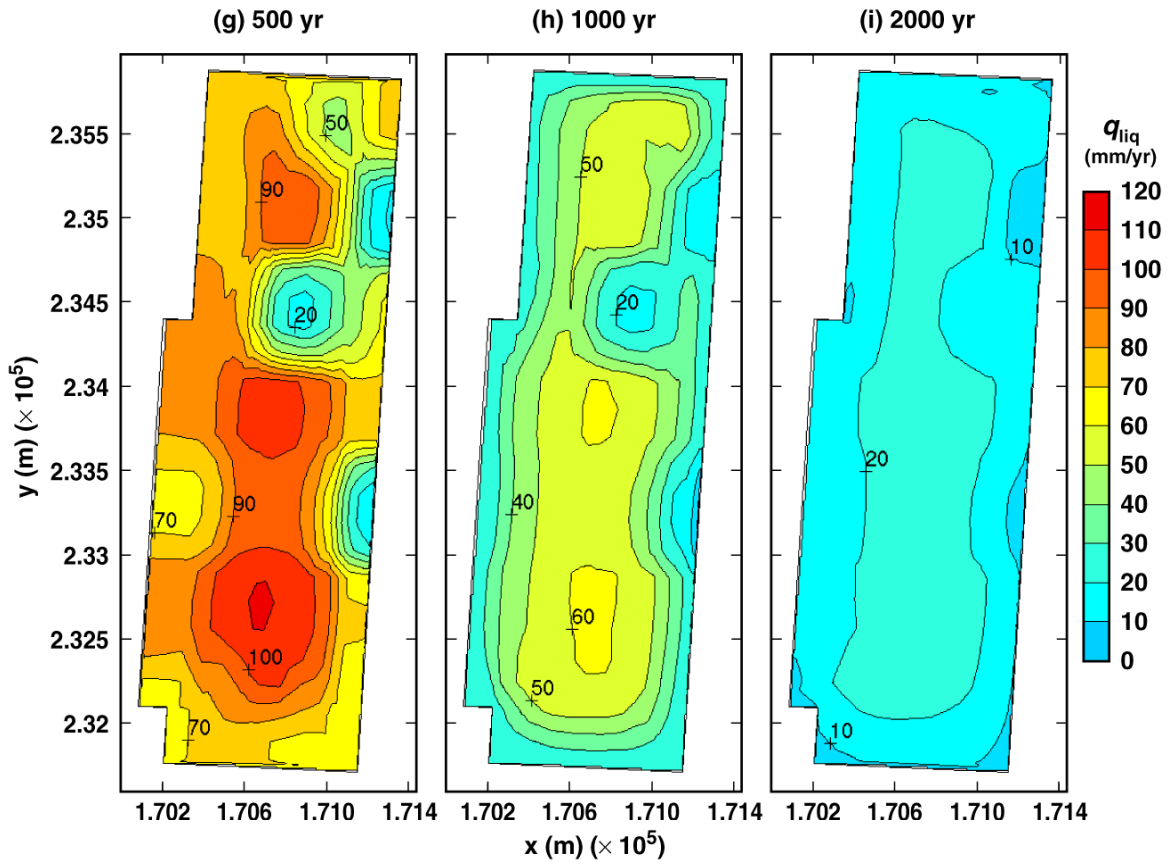
TB\_AMR\_upper\_qliq\_dsTop\_avg\_pwr2\_34-39

Figure 6-33. Liquid-phase flux averaged over the upper surface of the drip shield for the high infiltration-flux backfill case for the indicated times



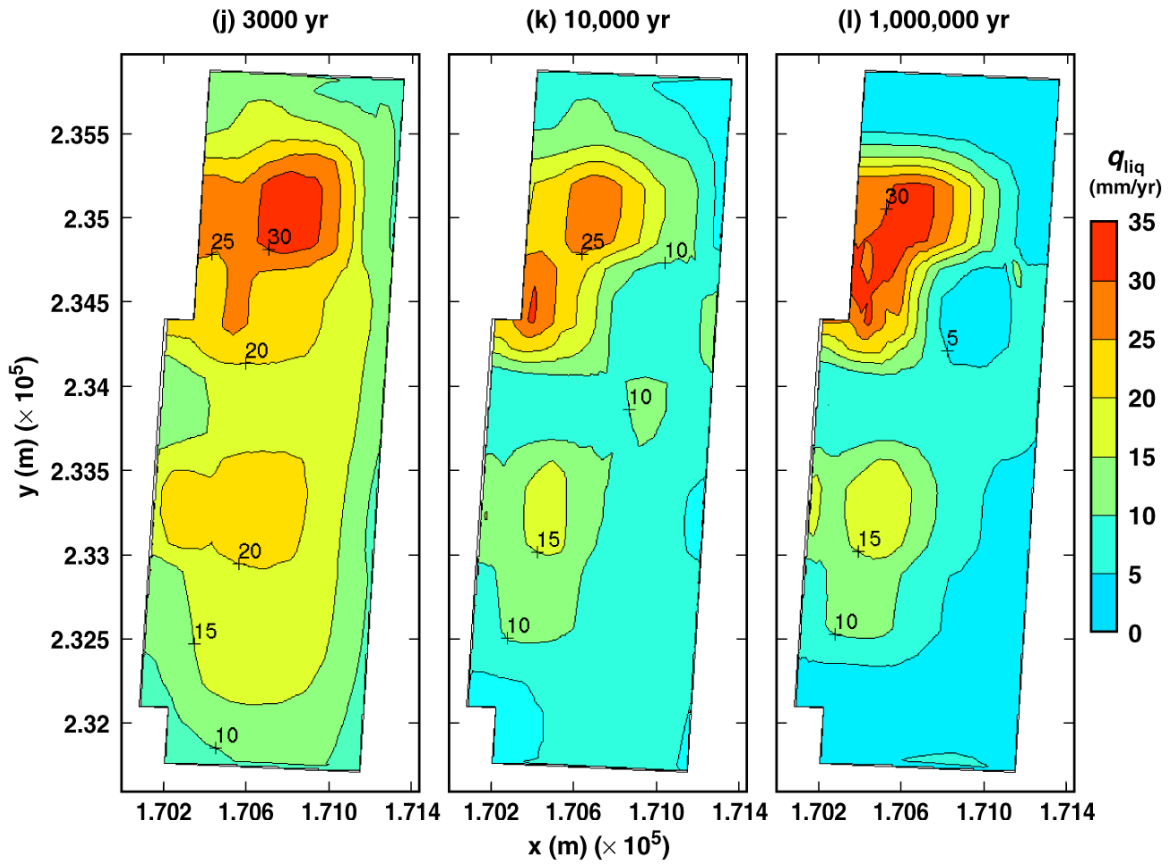
TB\_AMR\_upper\_qliq\_dsTop\_avg\_pwr2\_56-107

Figure 6-33. Liquid-phase flux averaged over the upper surface of the drip shield for the high infiltration-flux backfill case for the indicated times (Continued)



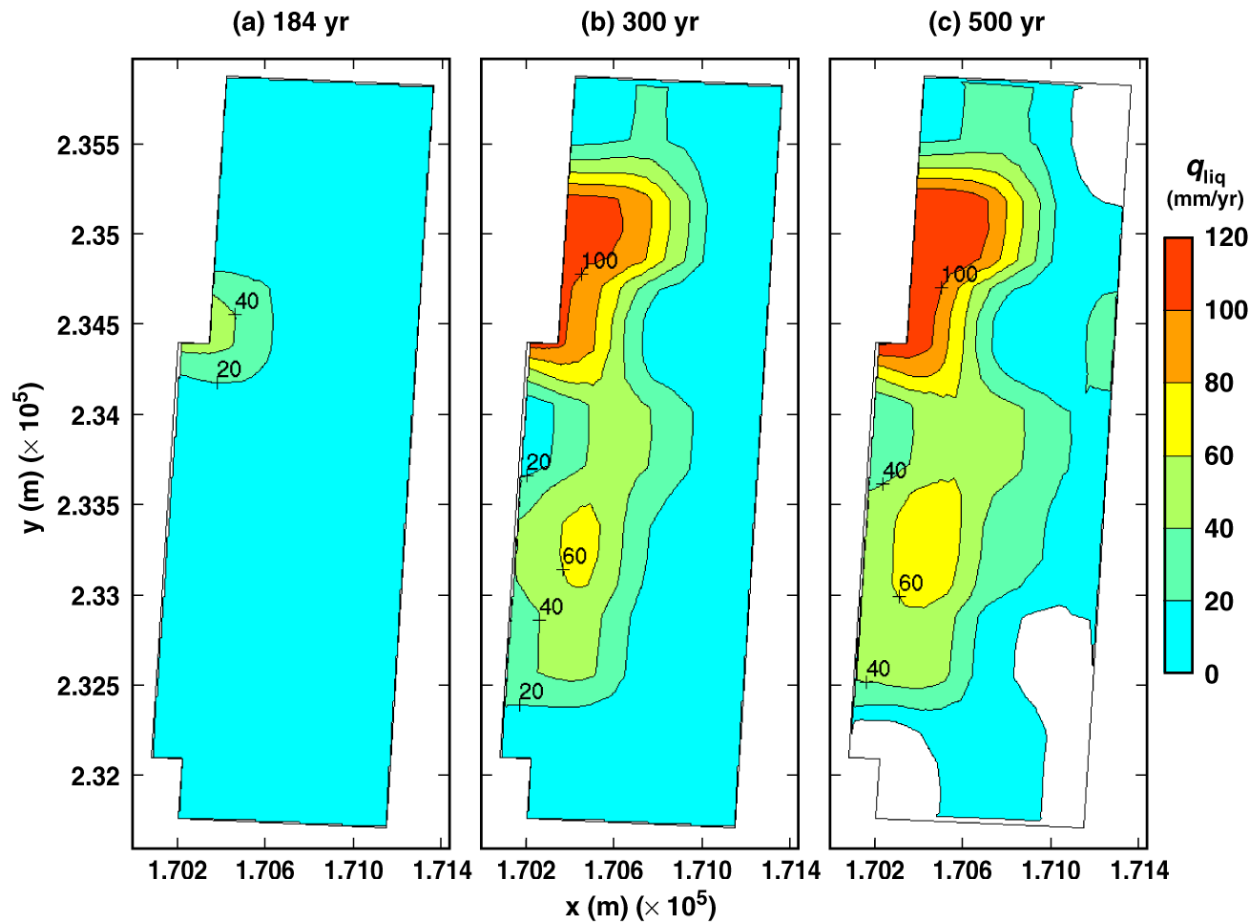
TB\_AMR\_upper\_qliq\_dsTop\_avg\_pwr2\_177-360

Figure 6-33. Liquid-phase flux averaged over the upper surface of the drip shield for the high infiltration-flux backfill case for the indicated times (Continued)



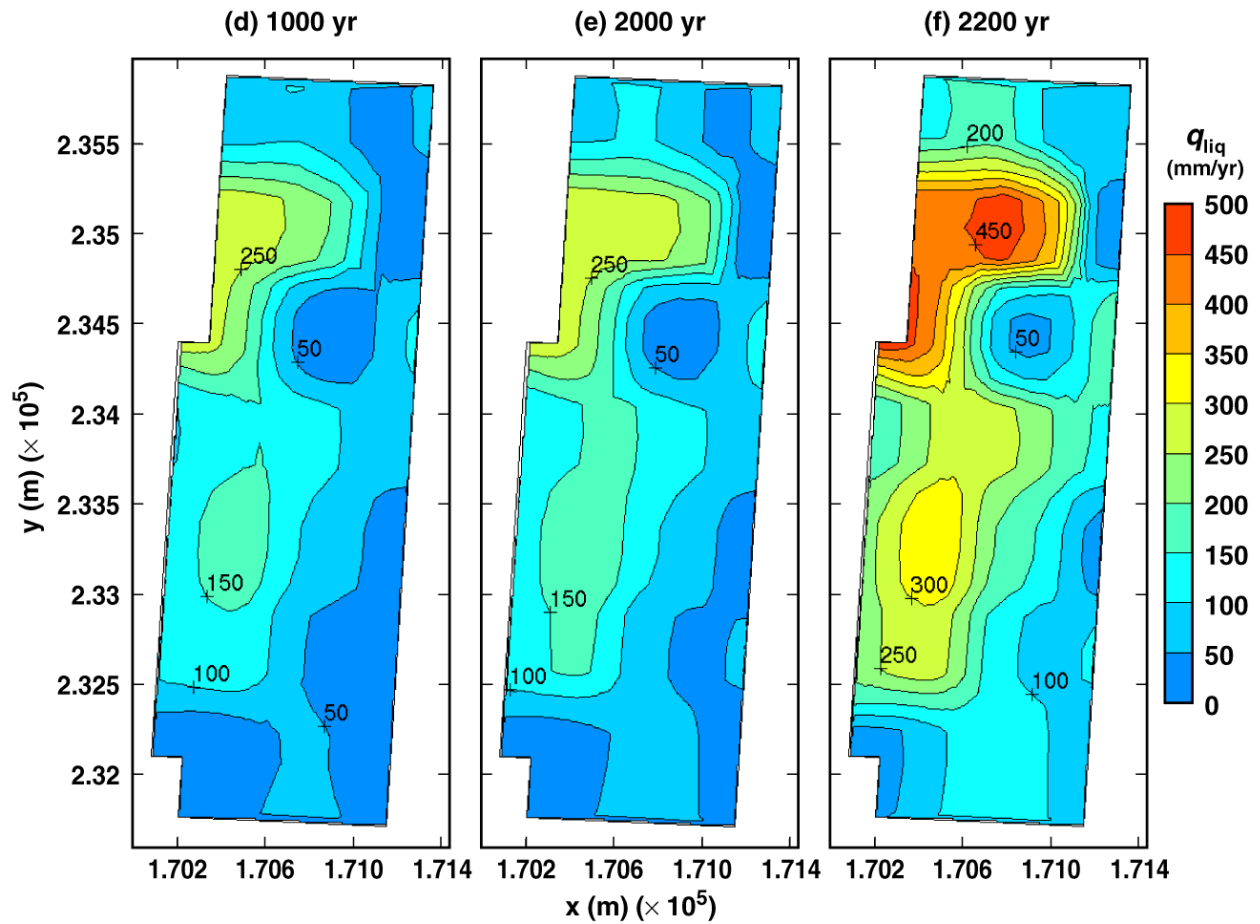
TB\_AMR\_upper\_qliq\_dsTop\_avg\_pwr2\_389-457

Figure 6-33. Liquid-phase flux averaged over the upper surface of the drip shield for the high | infiltration-flux backfill case for the indicated times (Continued)



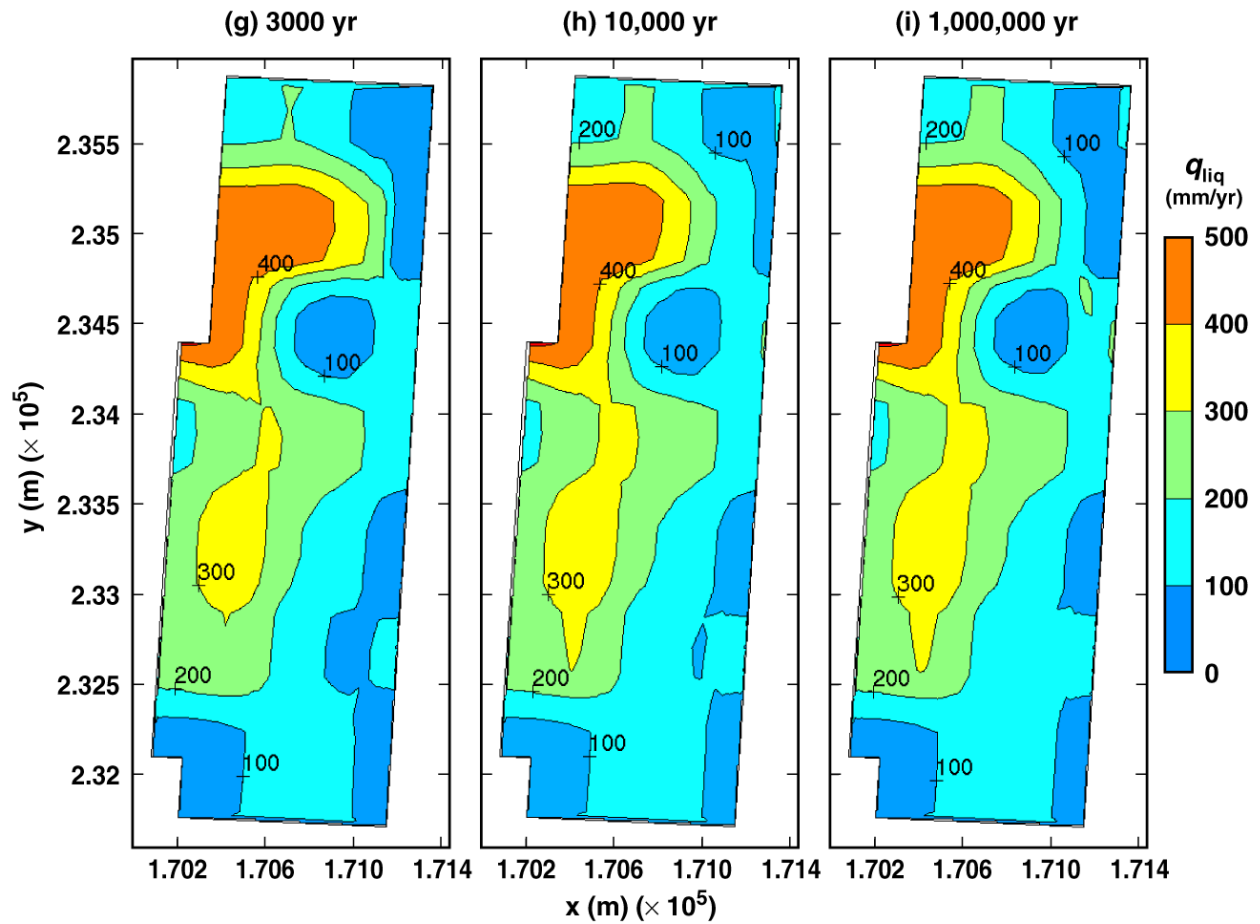
TB\_AMR\_upper\_qliq\_dsSide\_pwr1\_46-177

Figure 6-34. Liquid-phase flux backfill adjacent to the lower side of the drip shield (i.e., adjacent to the base of the drip shield) for the high infiltration-flux backfill case for the indicated times



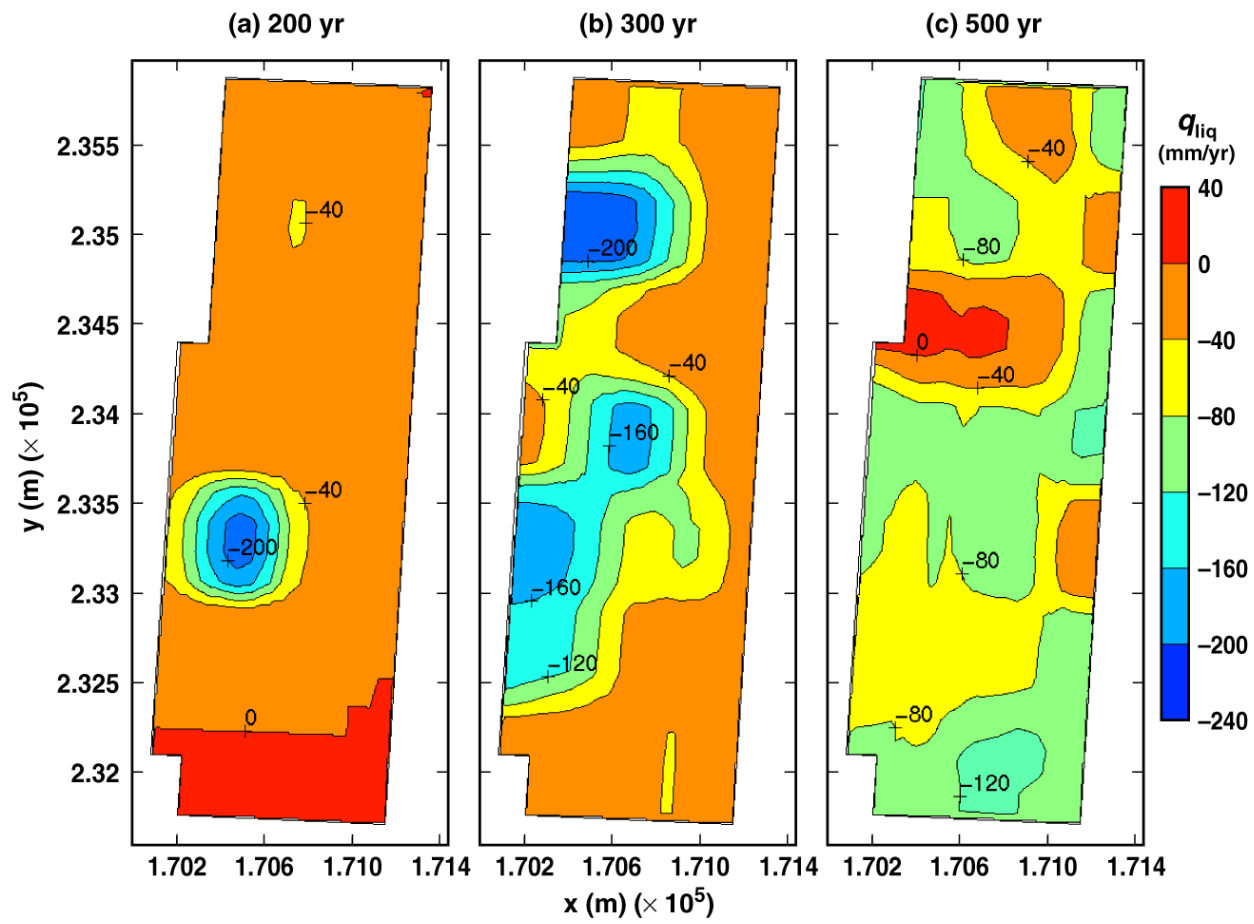
TB\_AMR\_upper\_qliq\_dsSide\_pwr1\_269-372

Figure 6-34. Liquid-phase flux backfill adjacent to the lower side of the drip shield (i.e., adjacent to the base of the drip shield) for the high infiltration-flux backfill case for the indicated times (Continued)



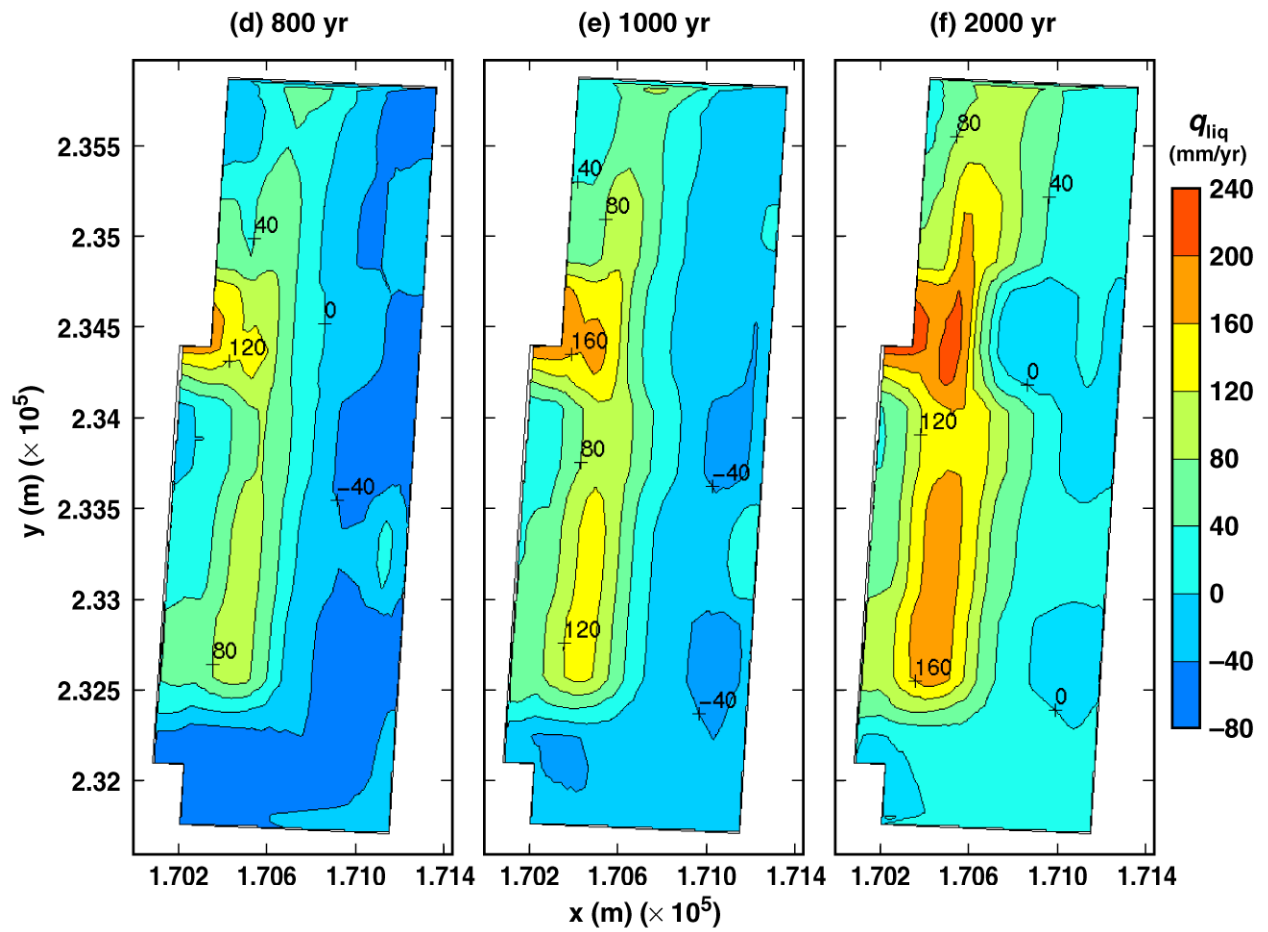
TB\_AMR\_upper\_qliq\_dsSide\_pwr1\_389-457

Figure 6-34. Liquid-phase flux backfill adjacent to the lower side of the drip shield (i.e., adjacent to the base of the drip shield) for the high infiltration-flux backfill case for the indicated times (Continued)



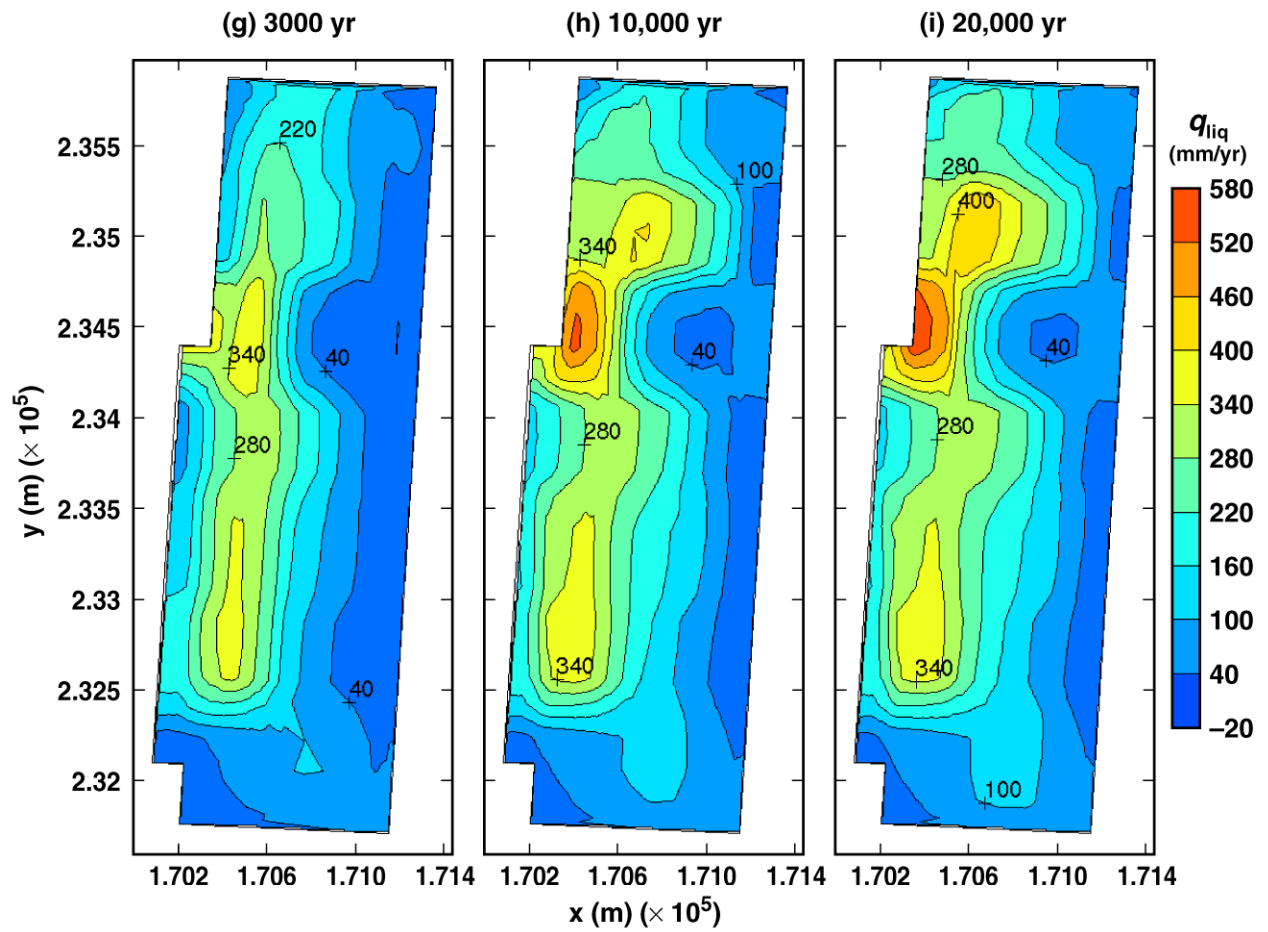
TB\_AMR\_upper\_qliq\_invert\_pwr2\_56-177

Figure 6-35. Liquid-phase flux backfill averaged over the invert for the high infiltration-flux backfill case for the indicated times



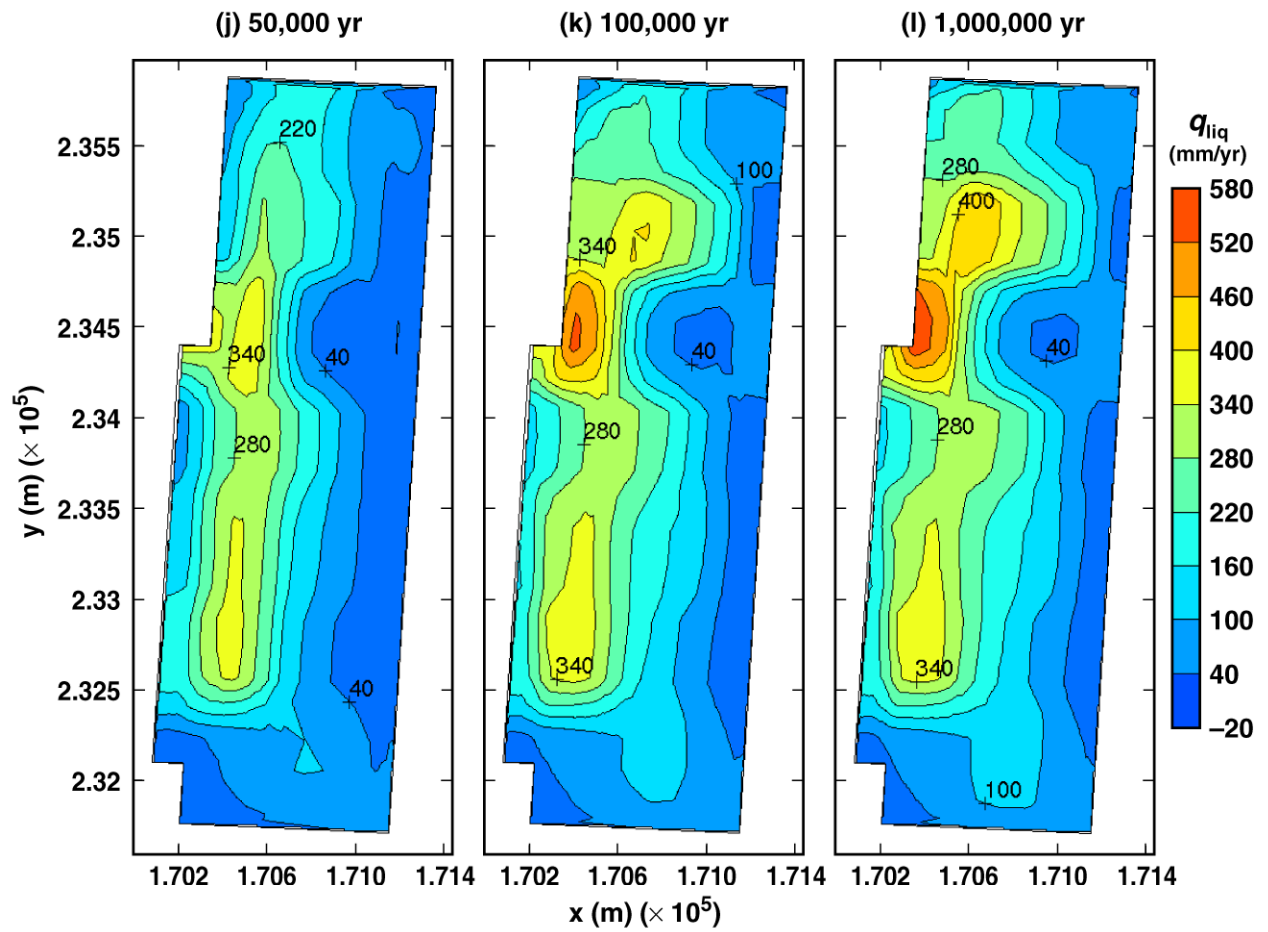
TB\_AMR\_upper\_qliq\_invert\_pwr2\_237-360

Figure 6-35. Liquid-phase flux backfill averaged over the invert for the high infiltration-flux backfill case for the indicated times (Continued)



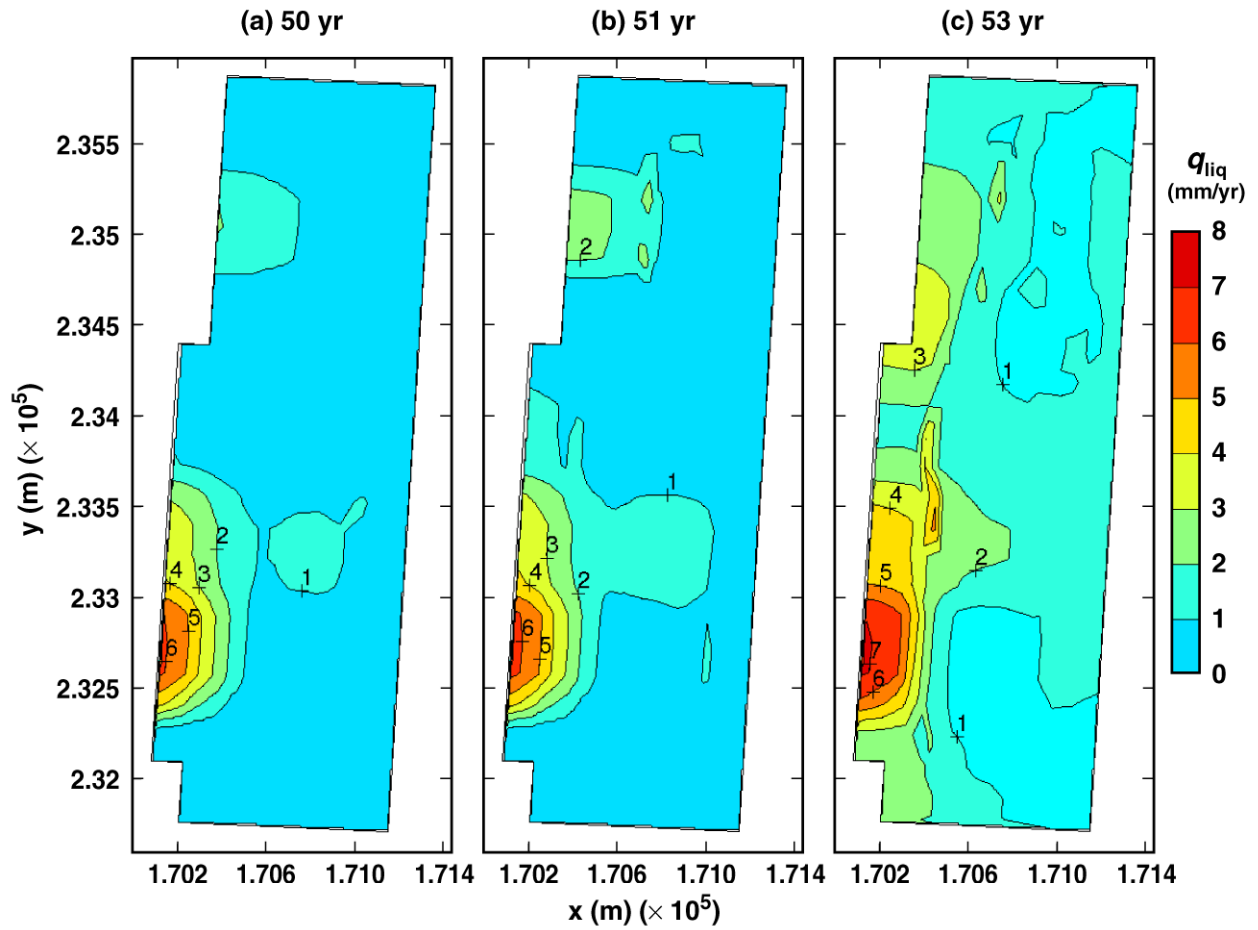
TB\_AMR\_upper\_qliq\_invert\_pwr2\_389-434

Figure 6-35. Liquid-phase flux backfill averaged over the invert for the high infiltration-flux backfill case for the indicated times (Continued)



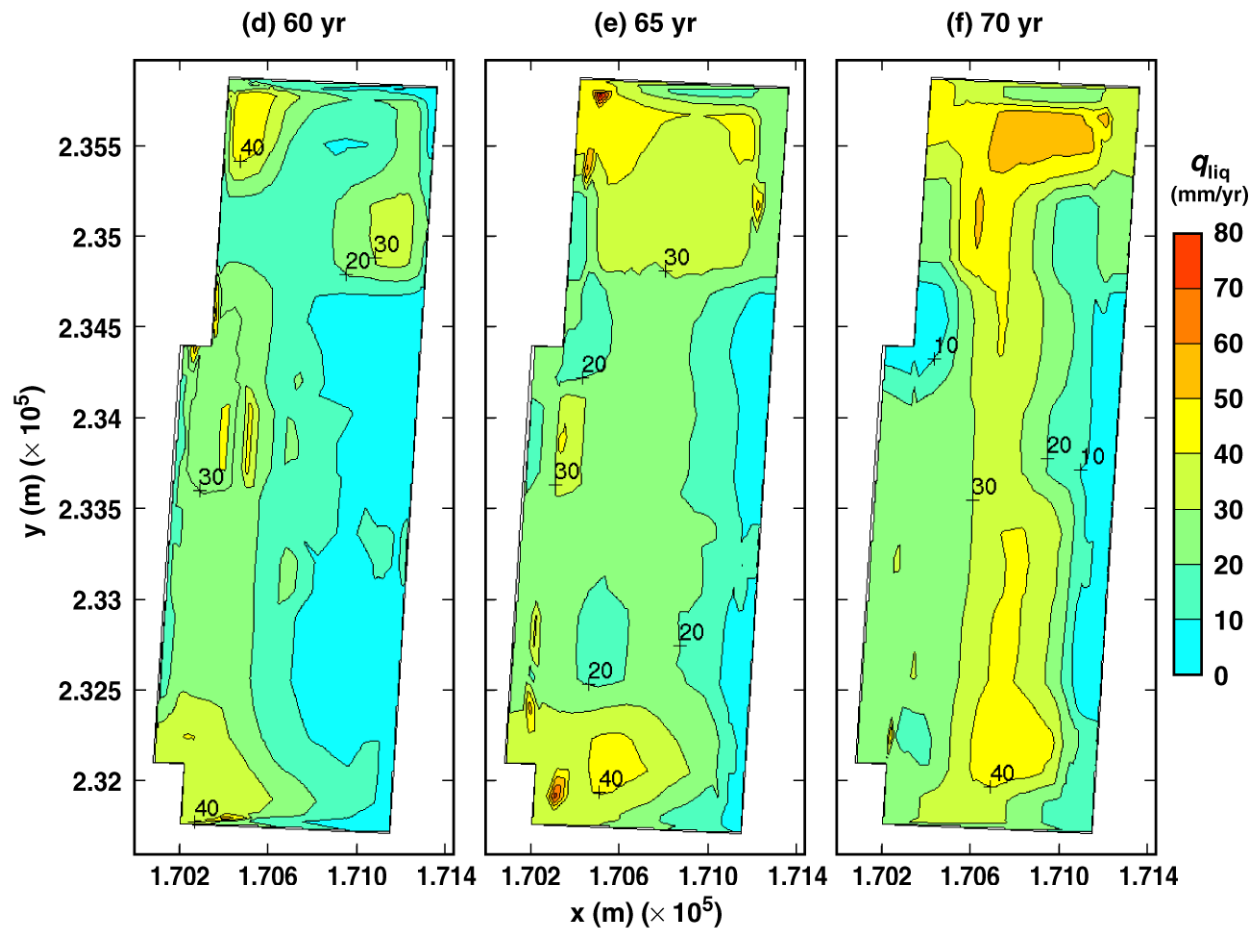
TB\_AMR\_upper\_qliq\_invert\_pwr2\_446-457

Figure 6-35. Liquid-phase flux backfill averaged over the invert for the high infiltration-flux backfill case for the indicated times (Continued)



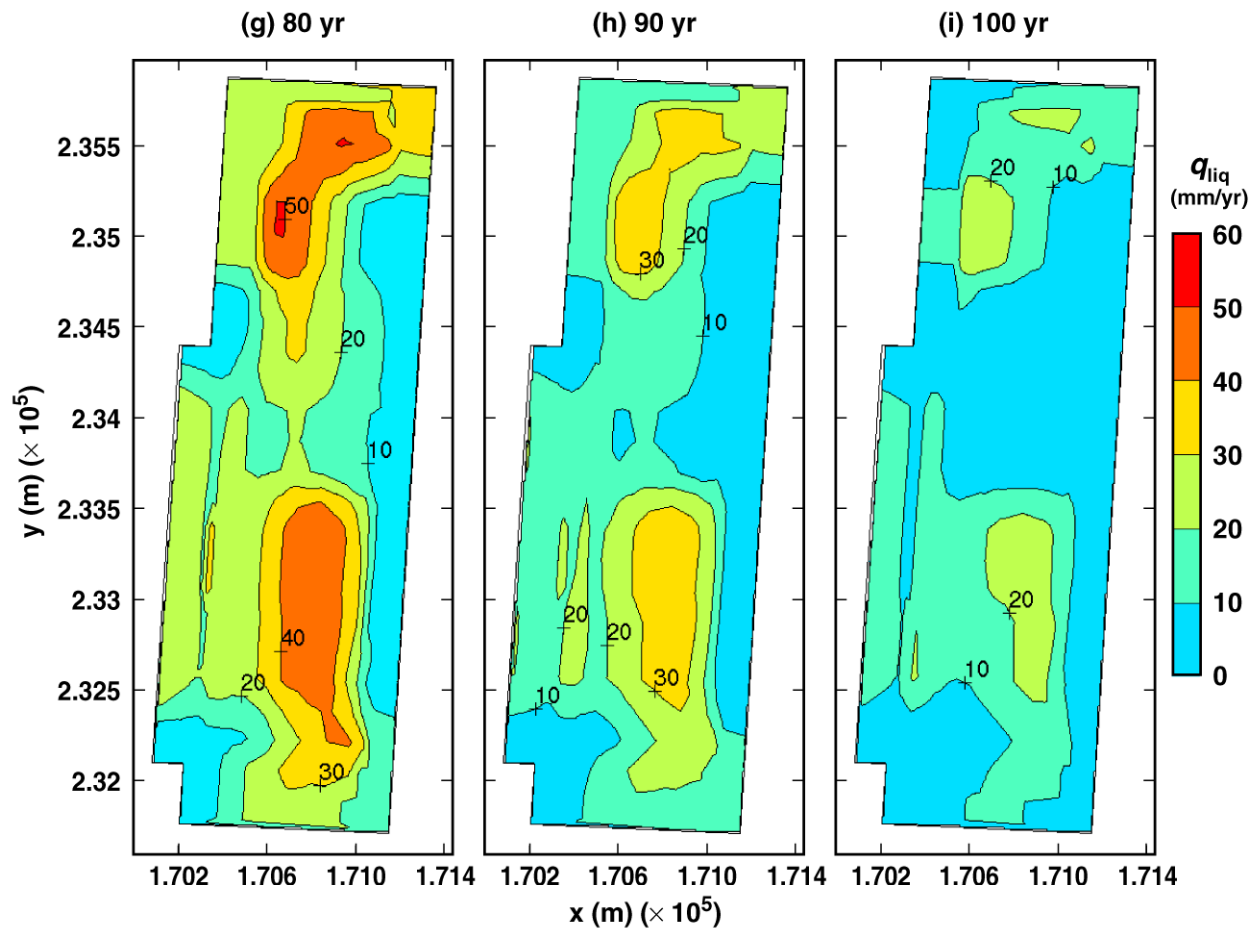
TB\_AMR\_lower\_qliq\_5m\_pwr2\_13-15

Figure 6-36. Liquid-phase flux backfill 5 m above the crown of the drift for the low infiltration-flux backfill case for the indicated times



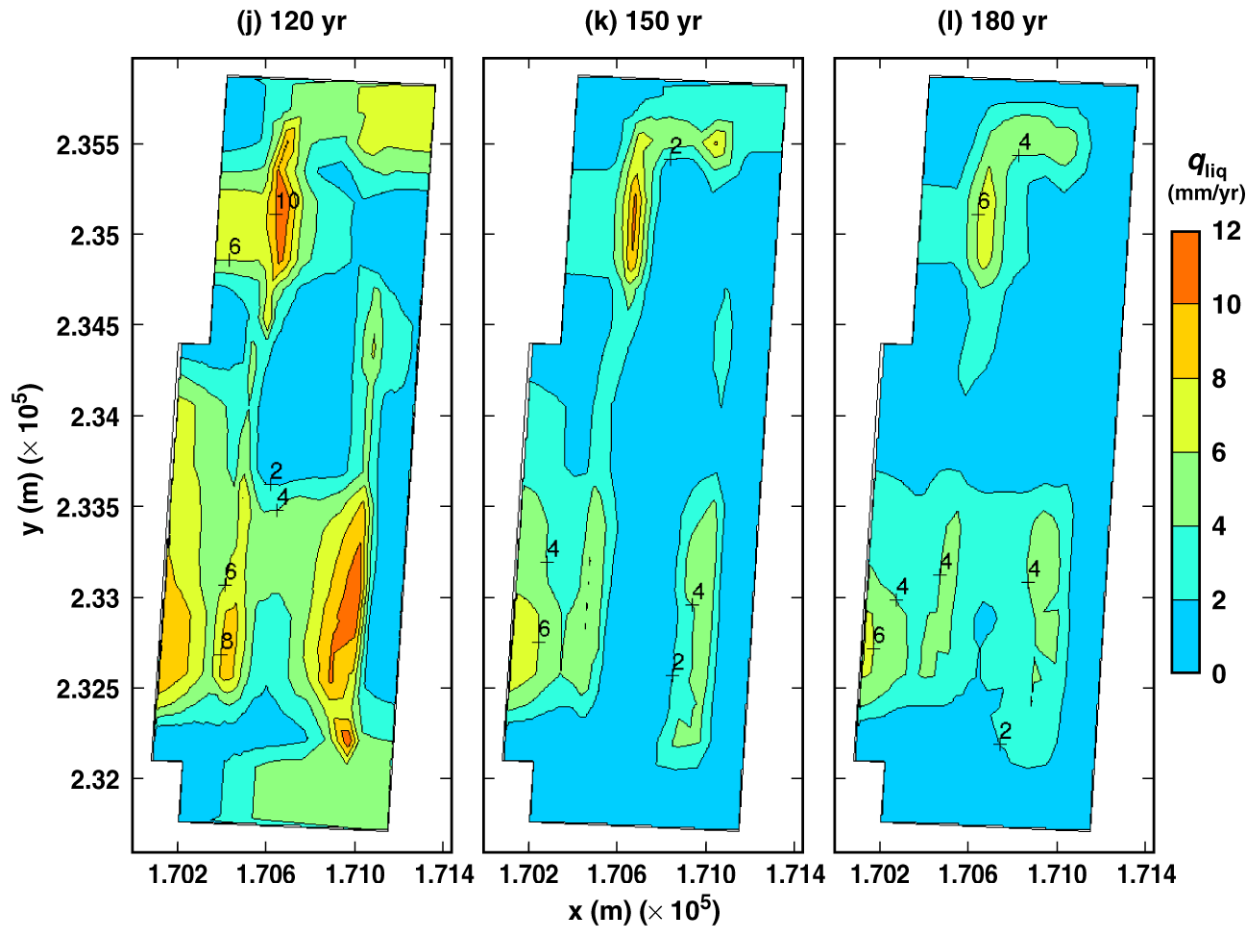
TB\_AMR\_lower\_qliq\_5m\_pwr2\_17-19

Figure 6-36. Liquid-phase flux backfill 5 m above the crown of the drift for the low infiltration-flux backfill case for the indicated times (Continued)



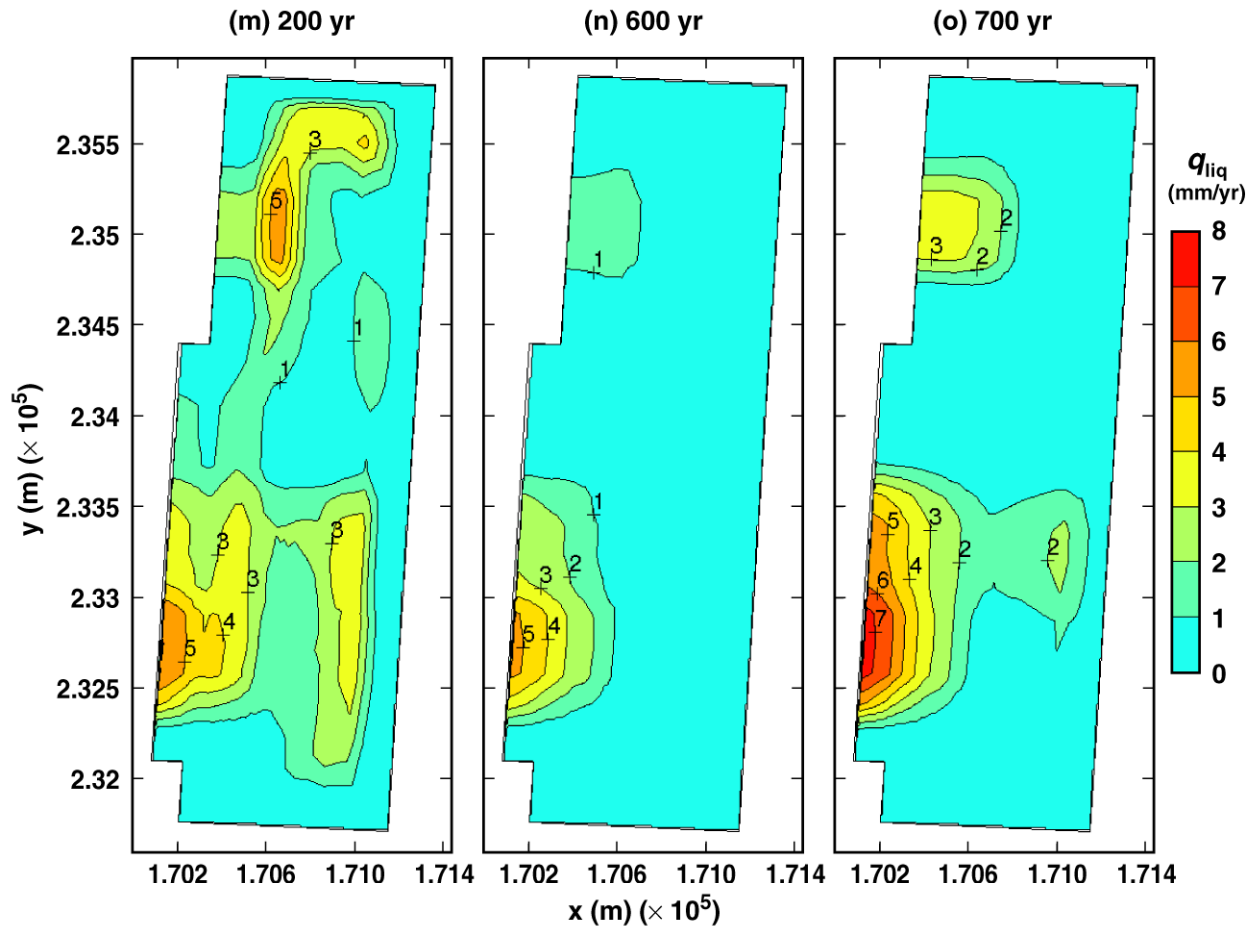
TB\_AMR\_lower\_qliq\_5m\_pwr2\_20-22

Figure 6-36. Liquid-phase flux backfill 5 m above the crown of the drift for the low infiltration-flux backfill case for the indicated times (Continued)



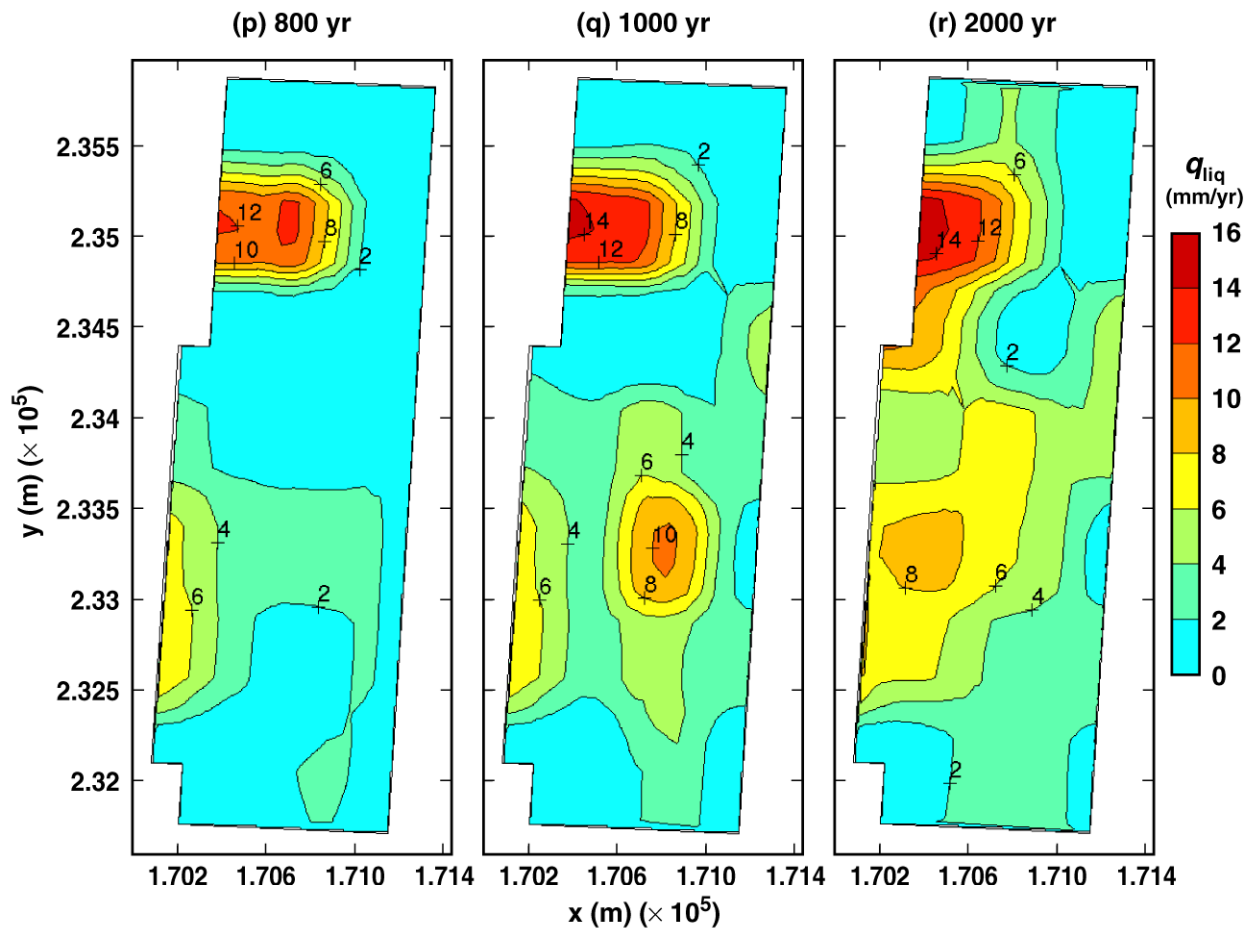
TB\_AMR\_lower\_qliq\_5m\_pwr2\_23-27

Figure 6-36. Liquid-phase flux backfill 5 m above the crown of the drift for the low infiltration-flux backfill case for the indicated times (Continued)



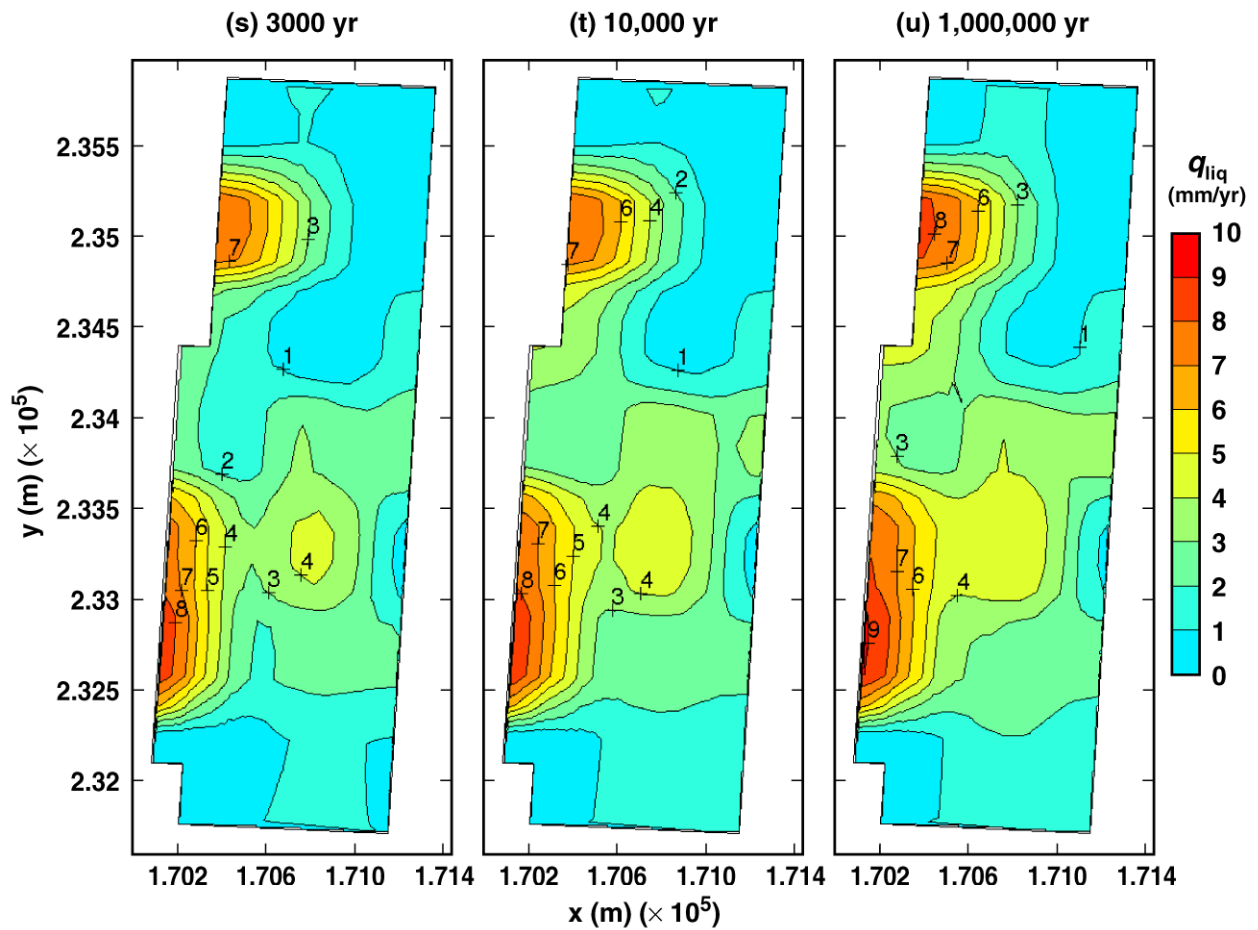
TB\_AMR\_lower\_qliq\_5m\_pwr2\_28-128

Figure 6-36. Liquid-phase flux backfill 5 m above the crown of the drift for the low infiltration-flux backfill case for the indicated times (Continued)



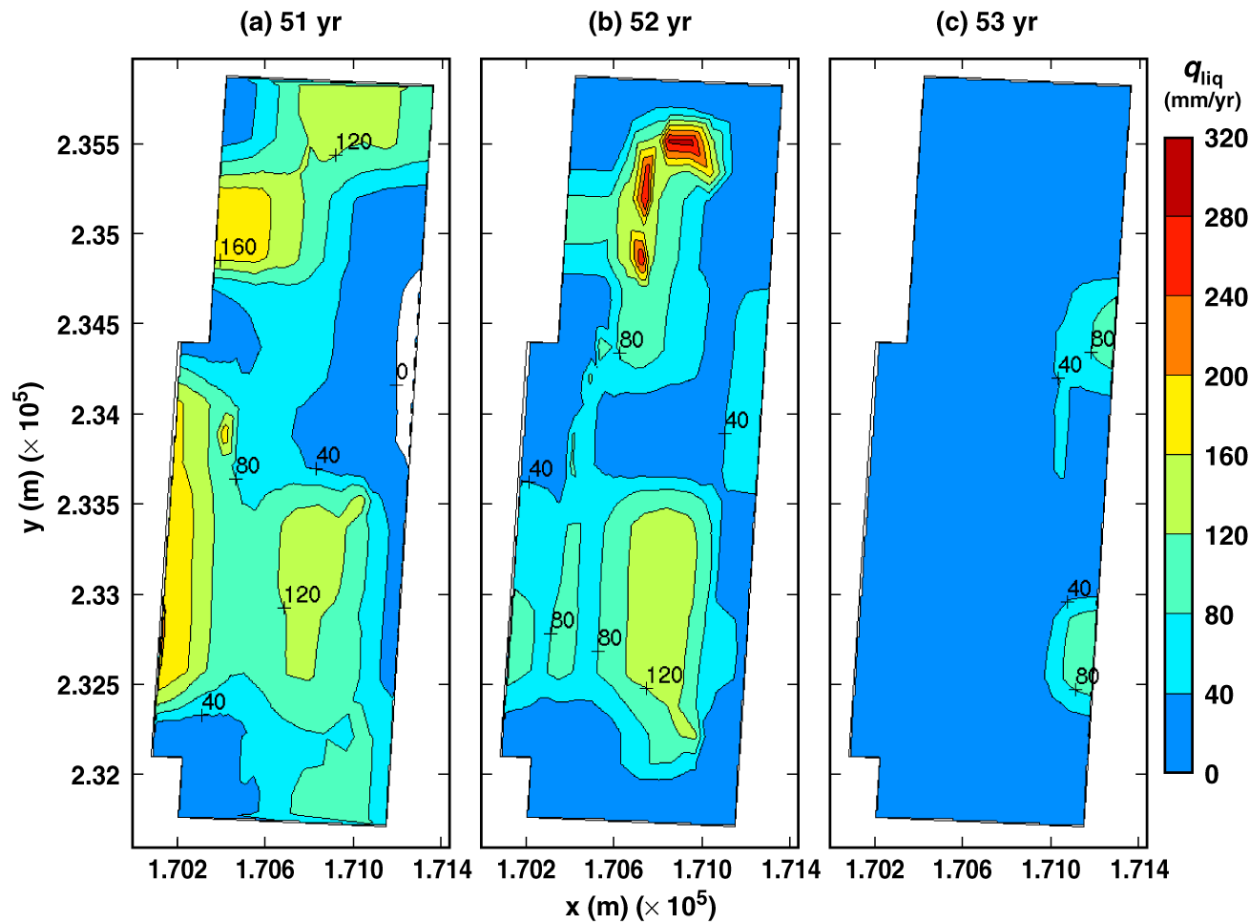
TB\_AMR\_lower\_qliq\_5m\_pwr2\_166-322

Figure 6-36. Liquid-phase flux backfill 5 m above the crown of the drift for the low infiltration-flux backfill case for the indicated times (Continued)



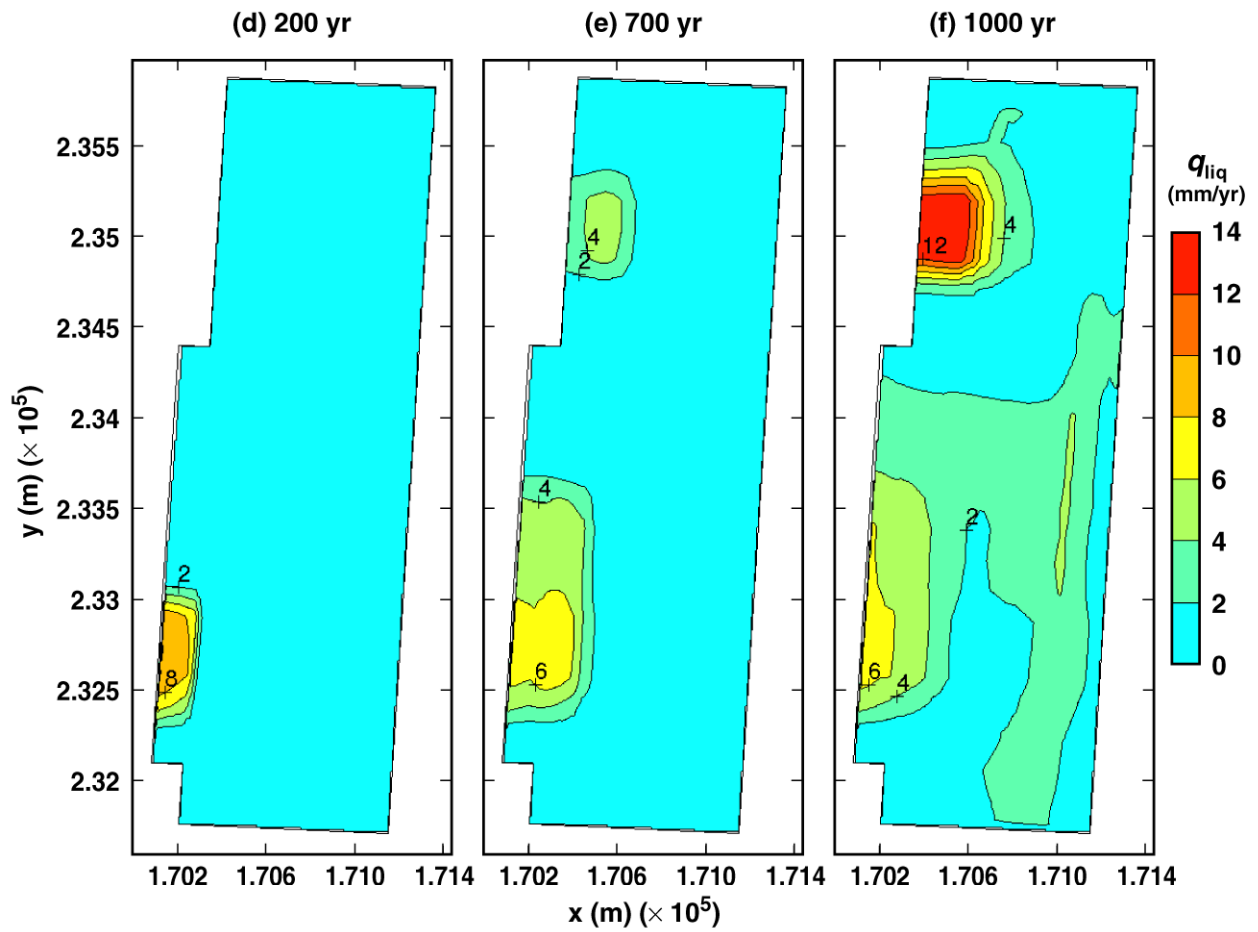
TB\_AMR\_lower\_qliq\_5m\_pwr2\_355-442

Figure 6-36. Liquid-phase flux backfill 5 m above the crown of the drift for the low infiltration-flux backfill case for the indicated times (Continued)



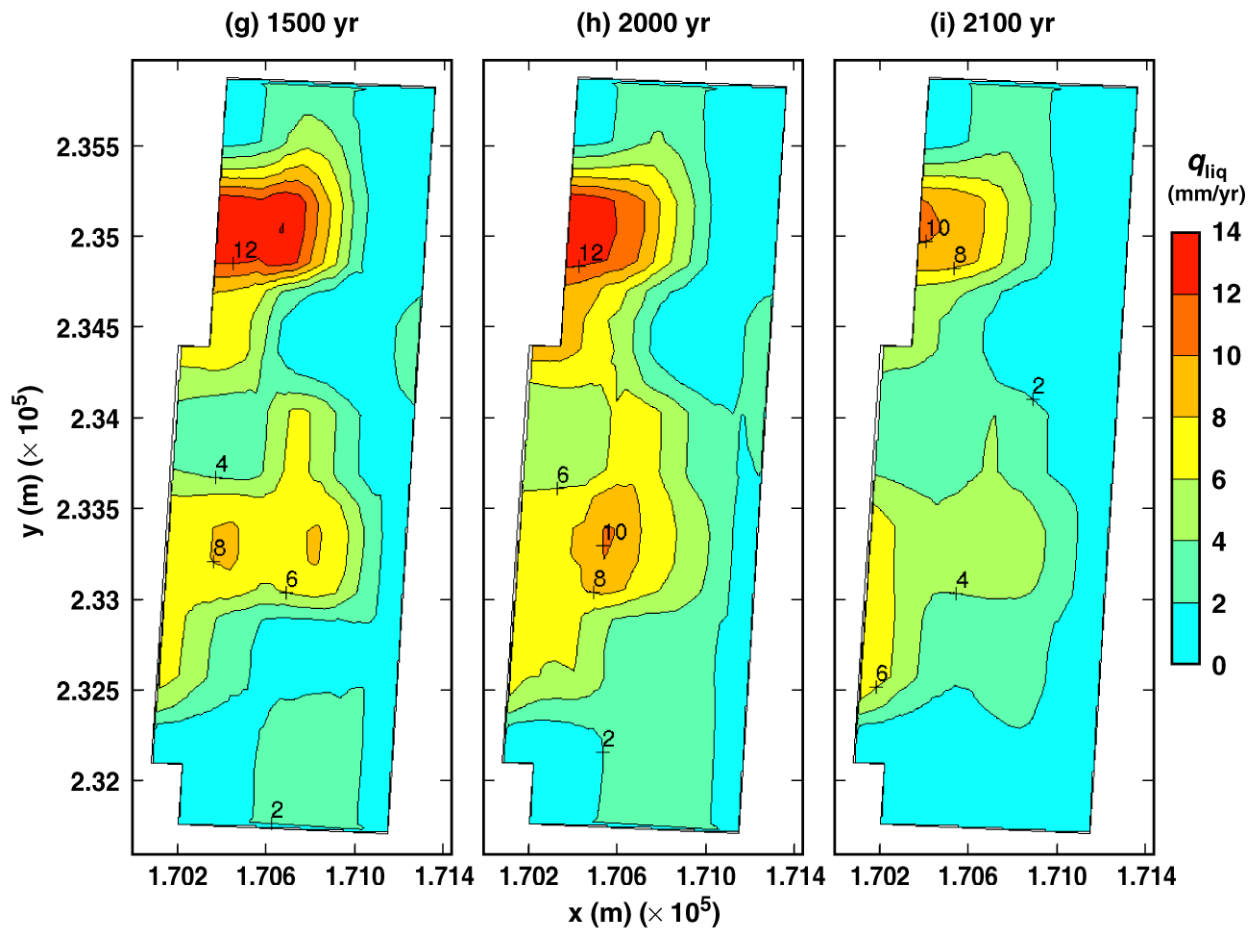
TB\_AMR\_lower\_qliq\_dw\_pwr2\_13-15

Figure 6-37. Liquid-phase flux backfill 0.2 m above the crown of the drift for the low infiltration-flux backfill case for the indicated times



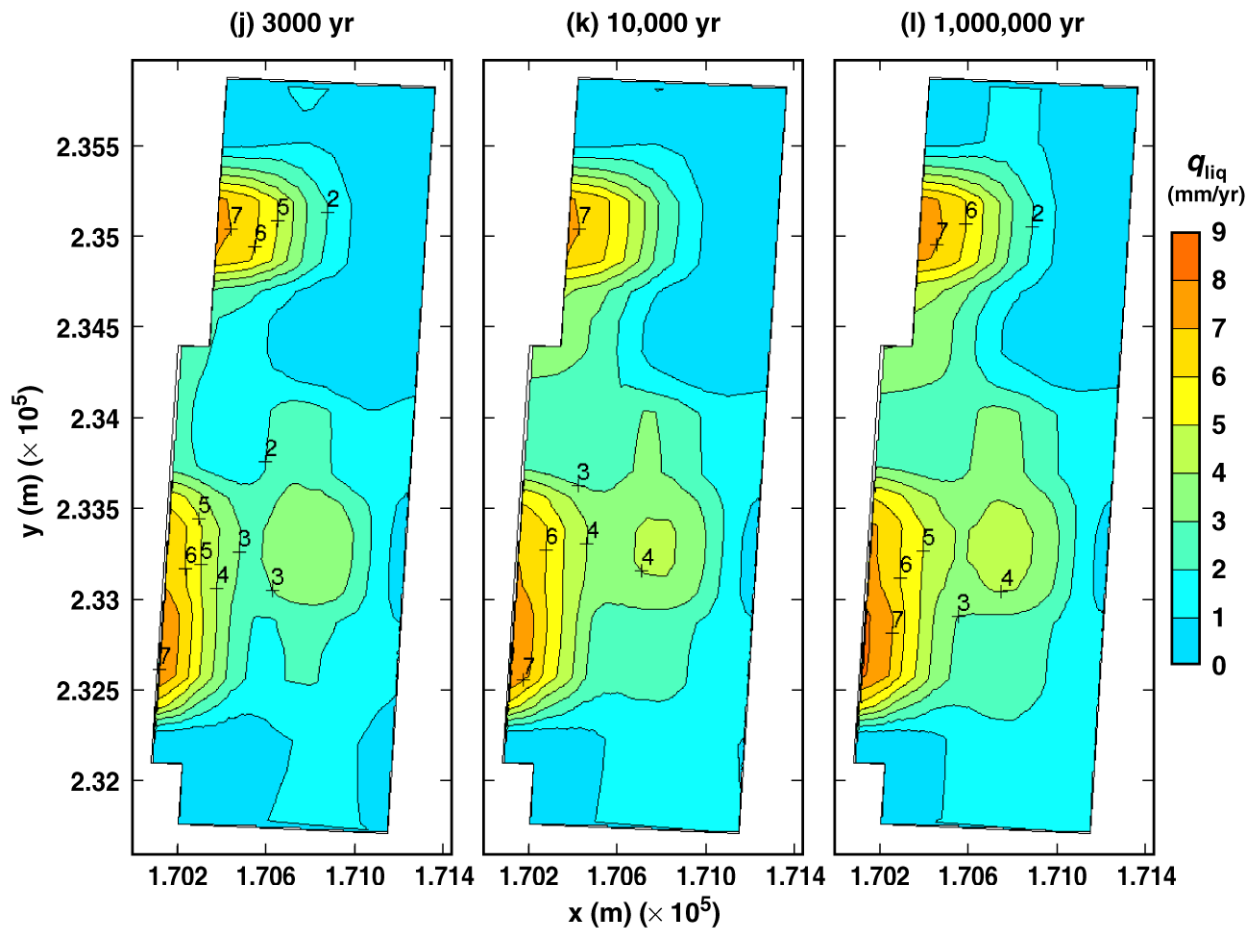
TB\_AMR\_lower\_qliq\_dw\_pwr2\_28-219

Figure 6-37. Liquid-phase flux backfill 0.2 m above the crown of the drift for the low infiltration-flux backfill case for the indicated times (Continued)



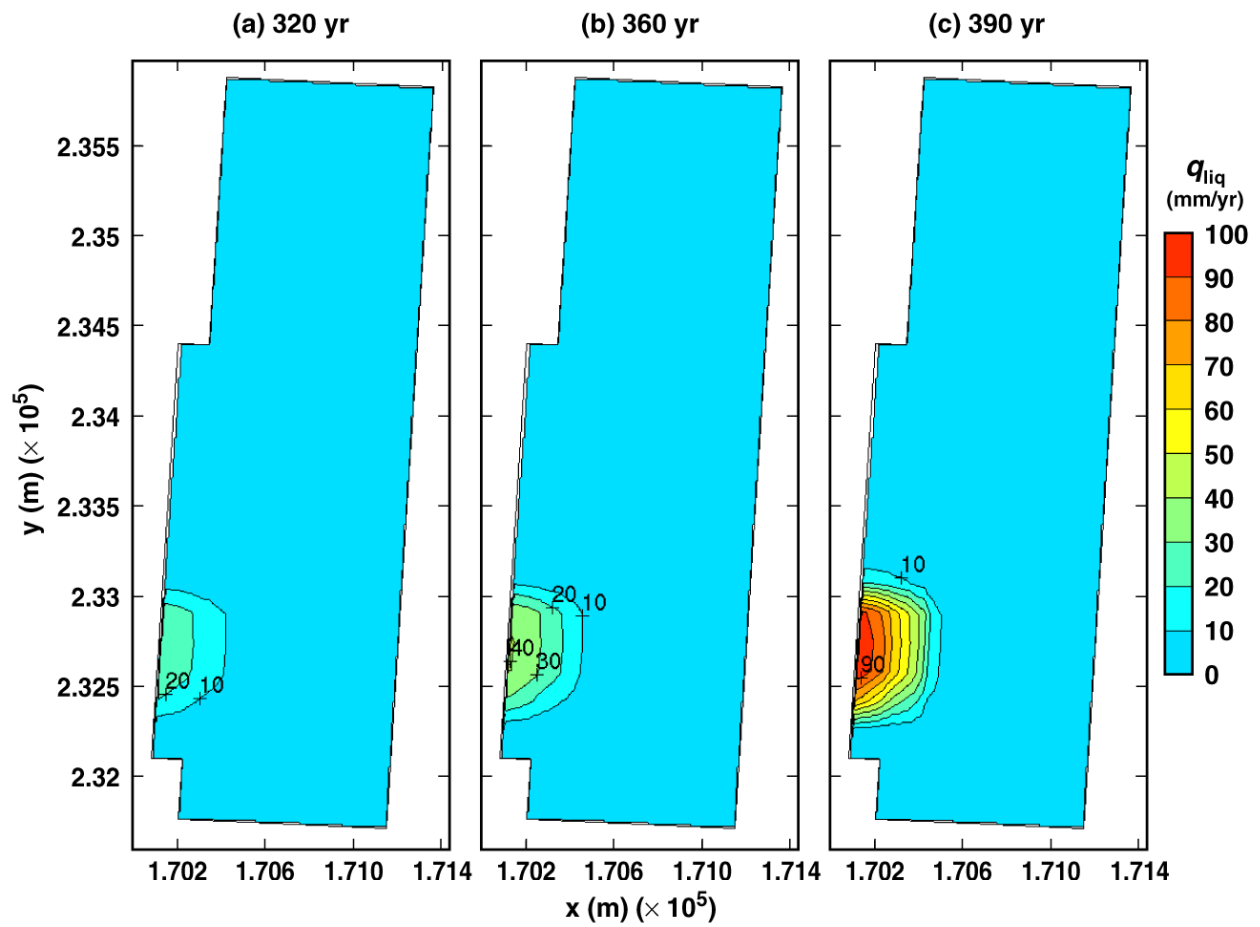
TB\_AMR\_lower\_qliq\_dw\_pwr2\_276-328

Figure 6-37. Liquid-phase flux backfill 0.2 m above the crown of the drift for the low infiltration-flux backfill case for the indicated times (Continued)



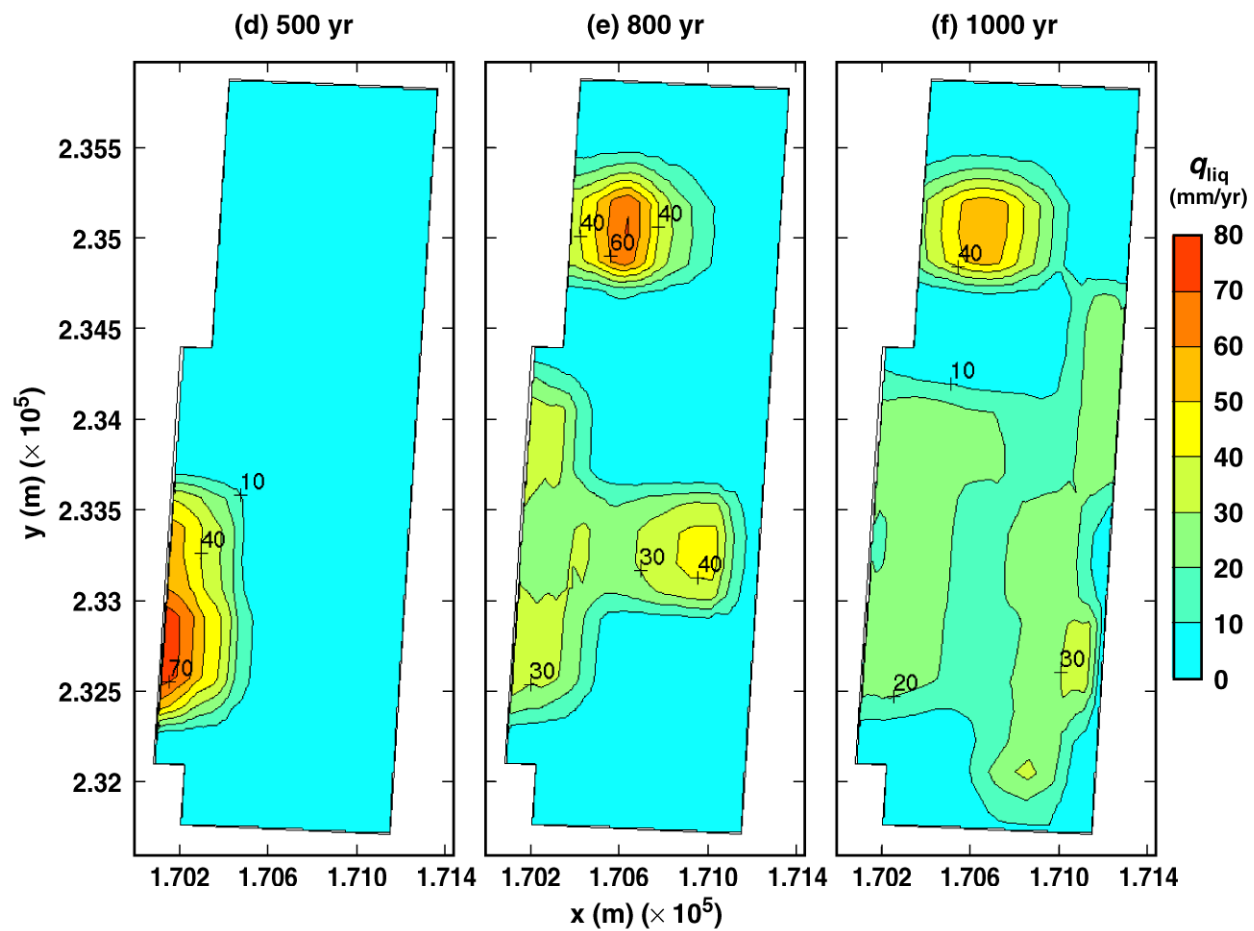
TB\_AMR\_lower\_qliq\_dw\_pwr2\_355-442

Figure 6-37. Liquid-phase flux backfill 0.2 m above the crown of the drift for the low infiltration-flux backfill case for the indicated times (Continued)



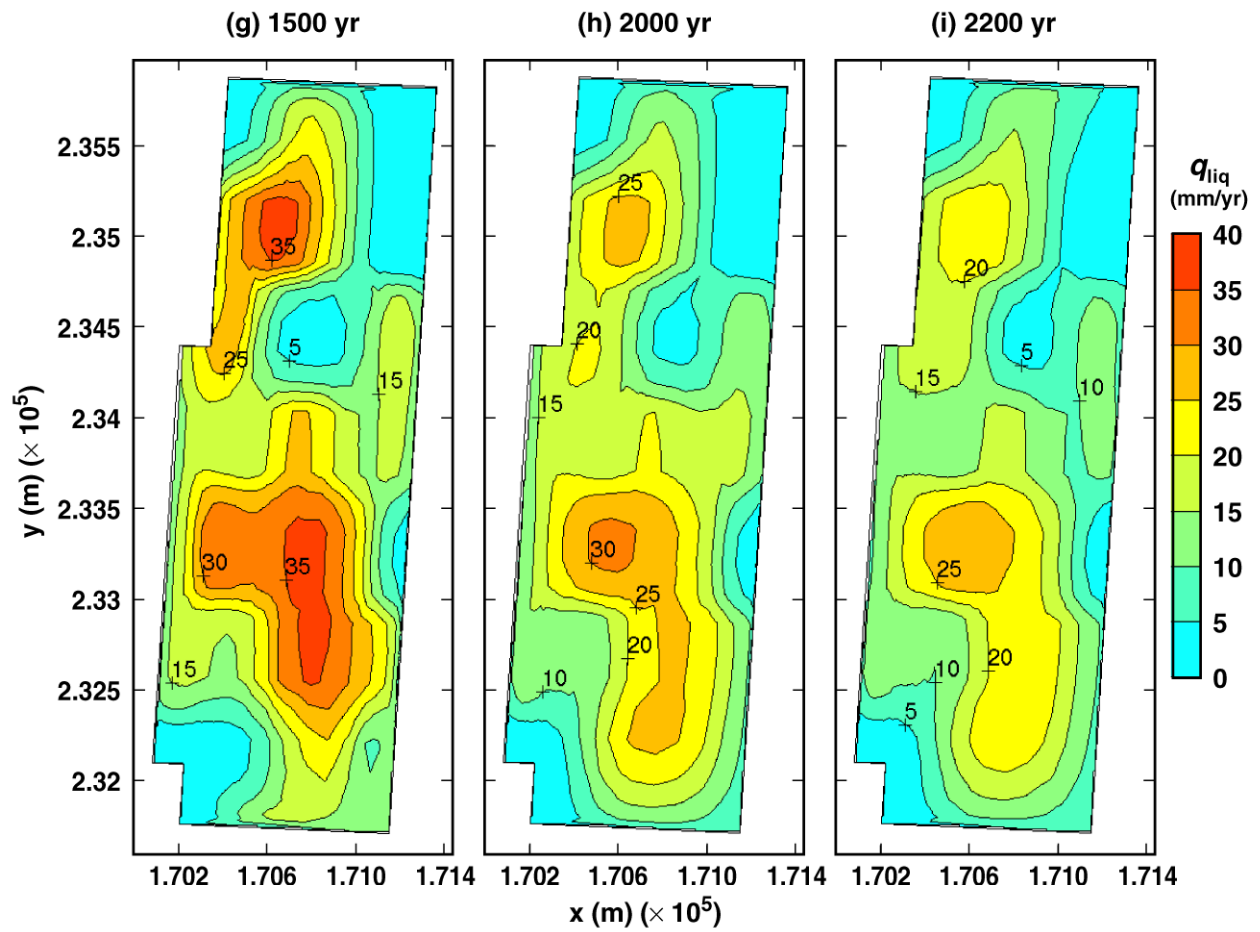
TB\_AMR\_lower\_qliq\_dsTop\_avg\_pwr2\_38-55

Figure 6-38. Liquid-phase flux averaged over the upper surface of the drip shield for the low infiltration-flux backfill case for the indicated times



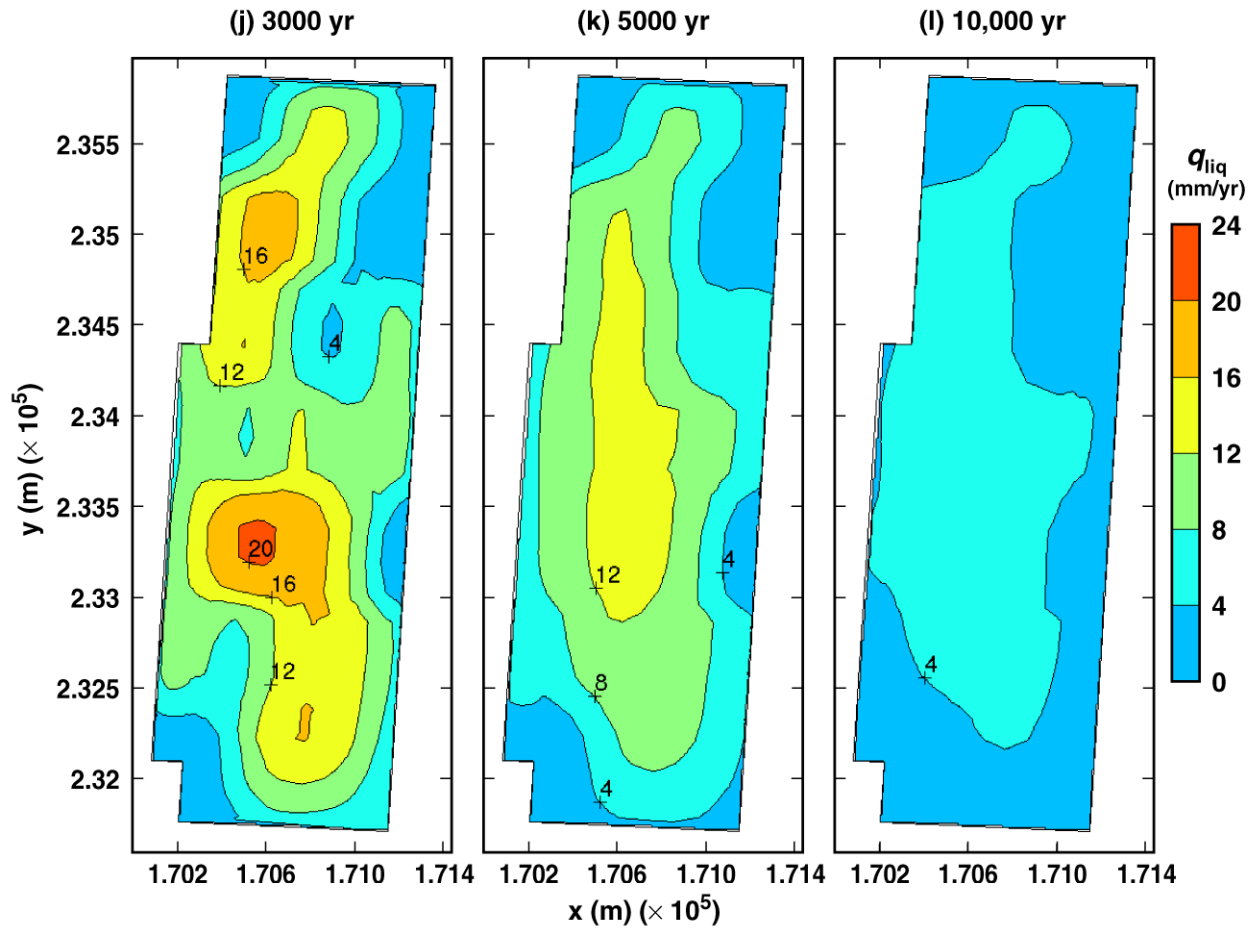
TB\_AMR\_lower\_qliq\_dsTop\_avg\_pwr2\_77-219

Figure 6-38. Liquid-phase flux averaged over the upper surface of the drip shield for the low infiltration-flux backfill case for the indicated times (Continued)



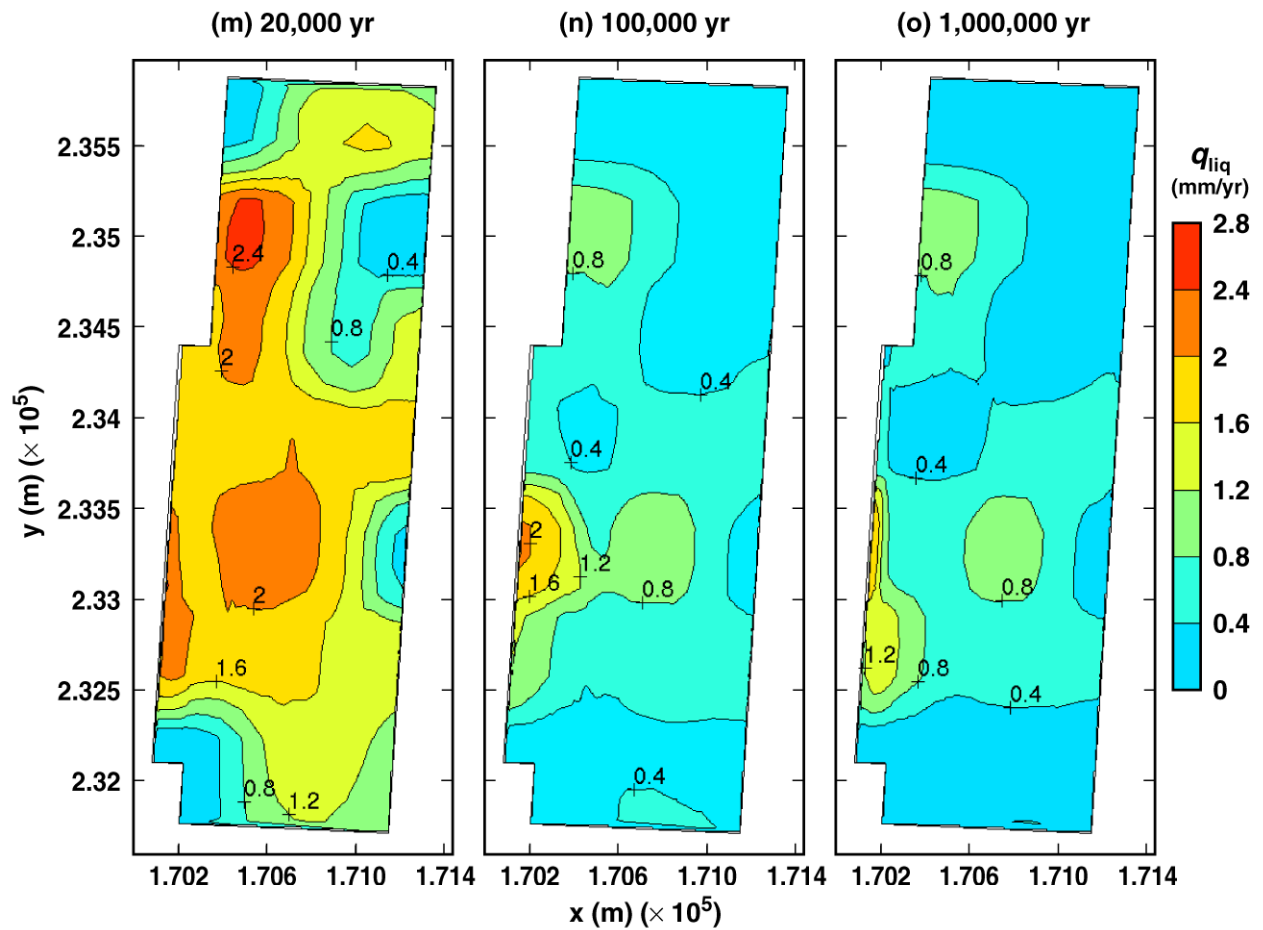
TB\_AMR\_lower\_qliq\_dsTop\_avg\_pwr2\_276-335

Figure 6-38. Liquid-phase flux averaged over the upper surface of the drip shield for the low infiltration-flux backfill case for the indicated times (Continued)



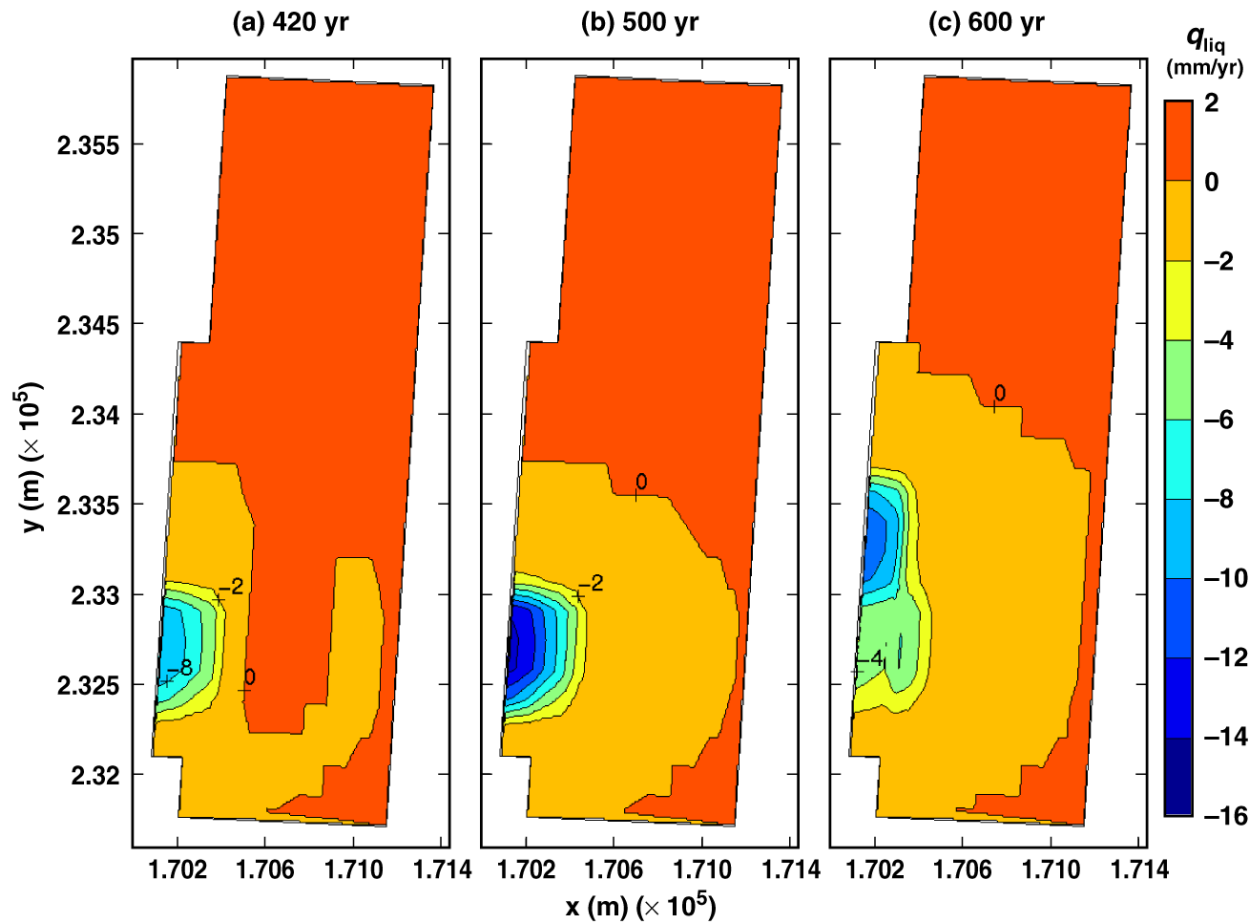
TB\_AMR\_lower\_qliq\_dsTop\_avg\_pwr2\_355-402

Figure 6-38. Liquid-phase flux averaged over the upper surface of the drip shield for the low infiltration-flux backfill case for the indicated times (Continued)



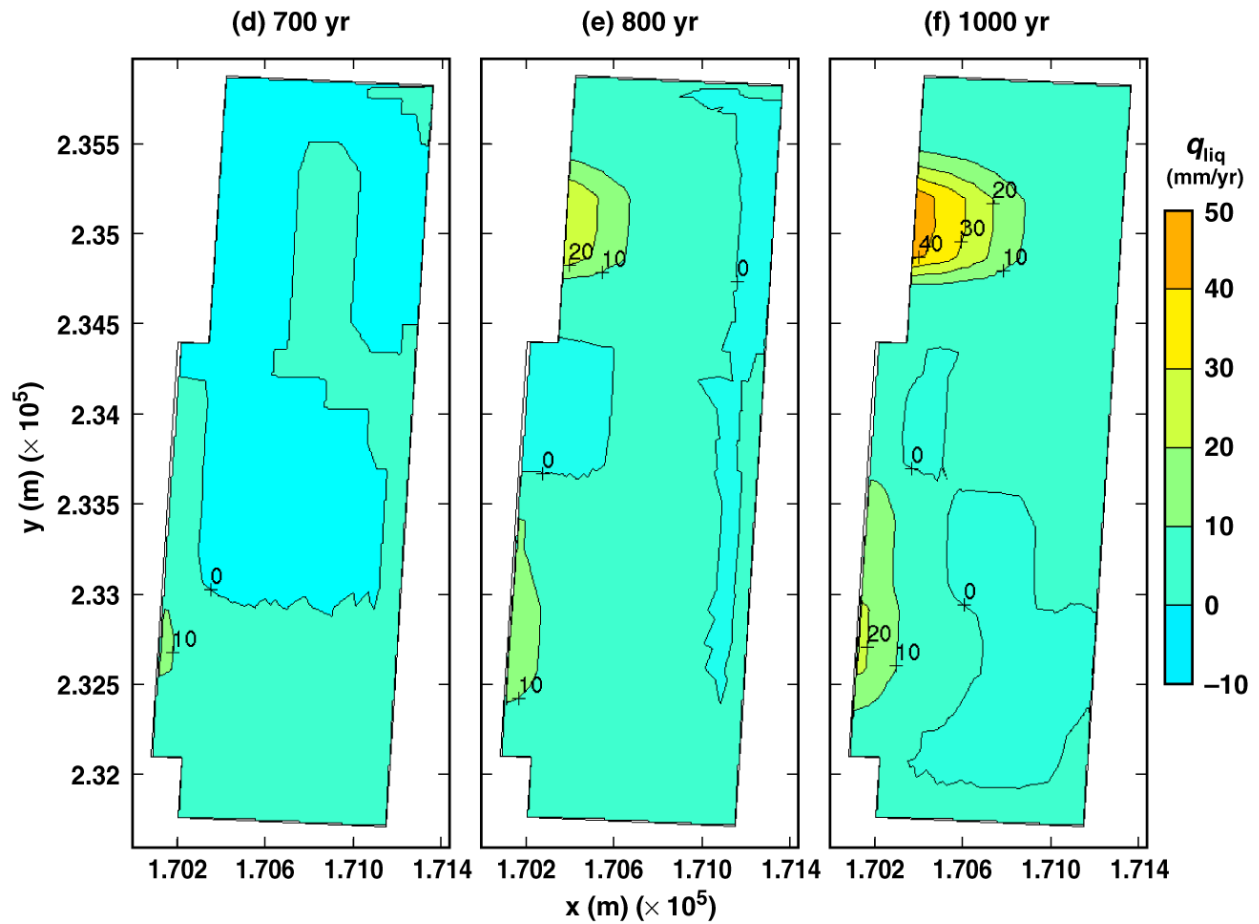
TB\_AMR\_lower\_qliq\_dsTop\_avg\_pwr2\_411-442

Figure 6-38. Liquid-phase flux averaged over the upper surface of the drip shield for the low infiltration-flux backfill case for the indicated times (Continued)



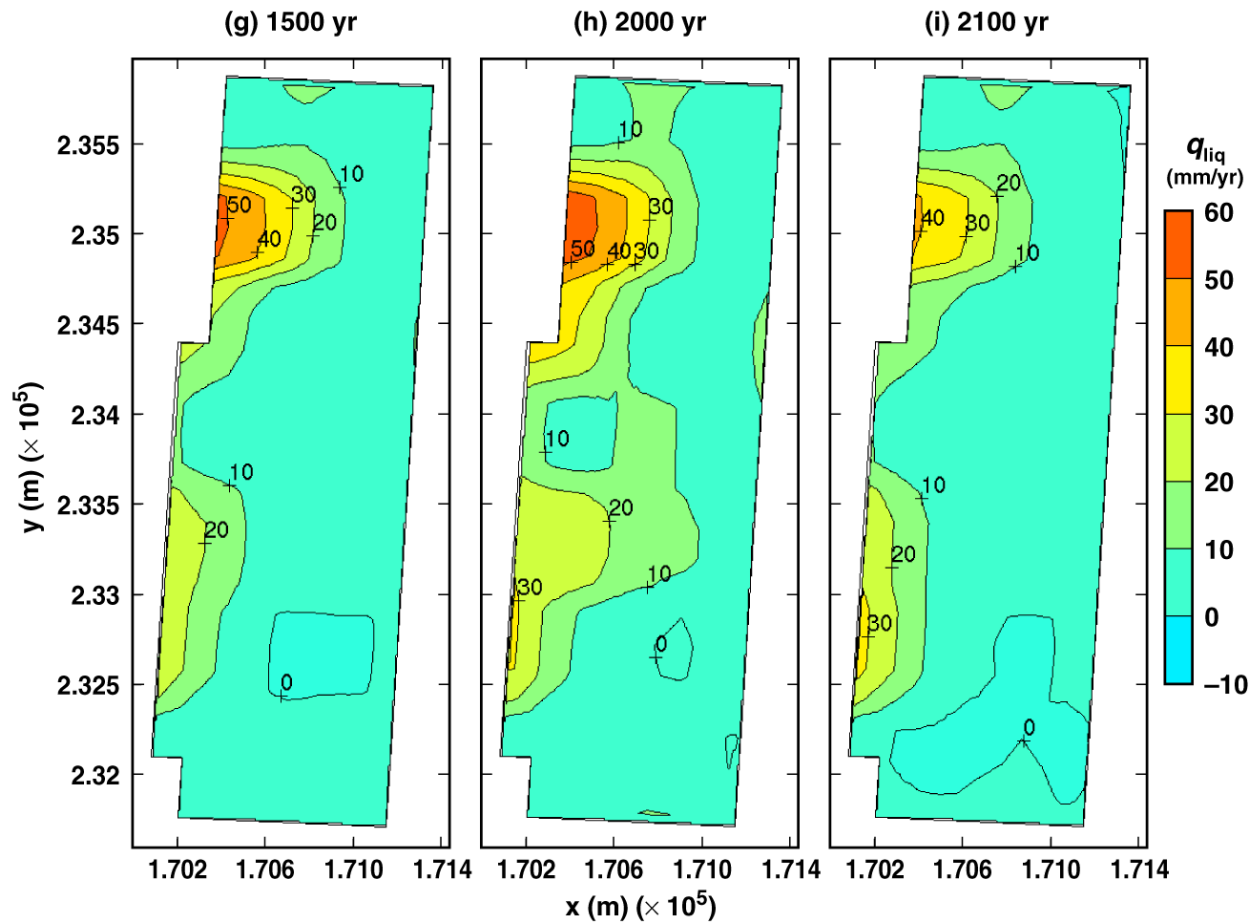
TB\_AMR\_lower\_qliq\_dsSide\_pwr2\_61-103

Figure 6-39. Liquid-phase flux adjacent to the lower side of the drip shield (i.e., adjacent to the base of the drip shield) for the low infiltration-flux backfill case for the indicated times



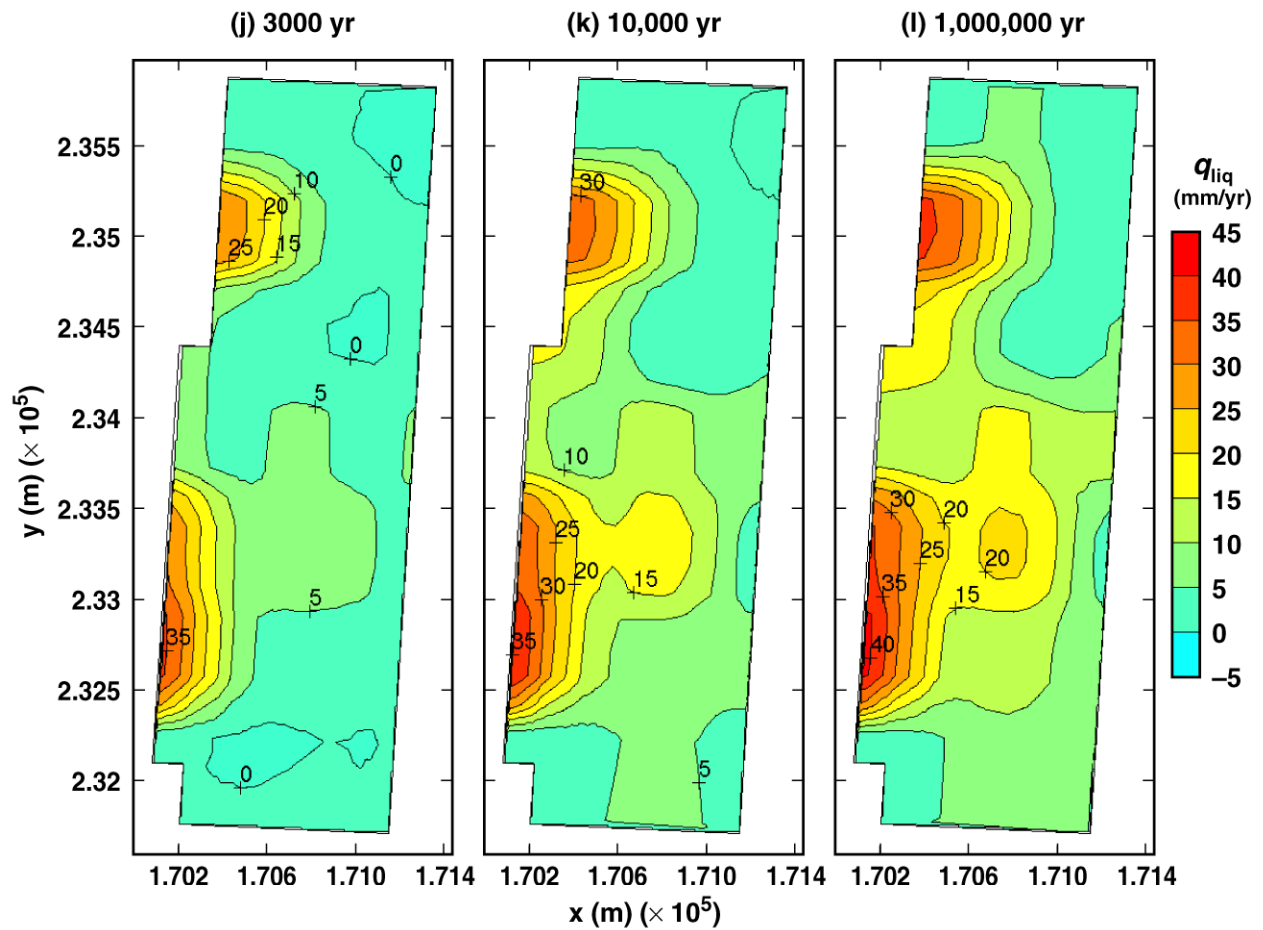
TB\_AMR\_lower\_qliq\_dsSide\_pwr2\_128-219

Figure 6-39. Liquid-phase flux adjacent to the lower side of the drip shield (i.e., adjacent to the base of the drip shield) for the low infiltration-flux backfill case for the indicated times (Continued)



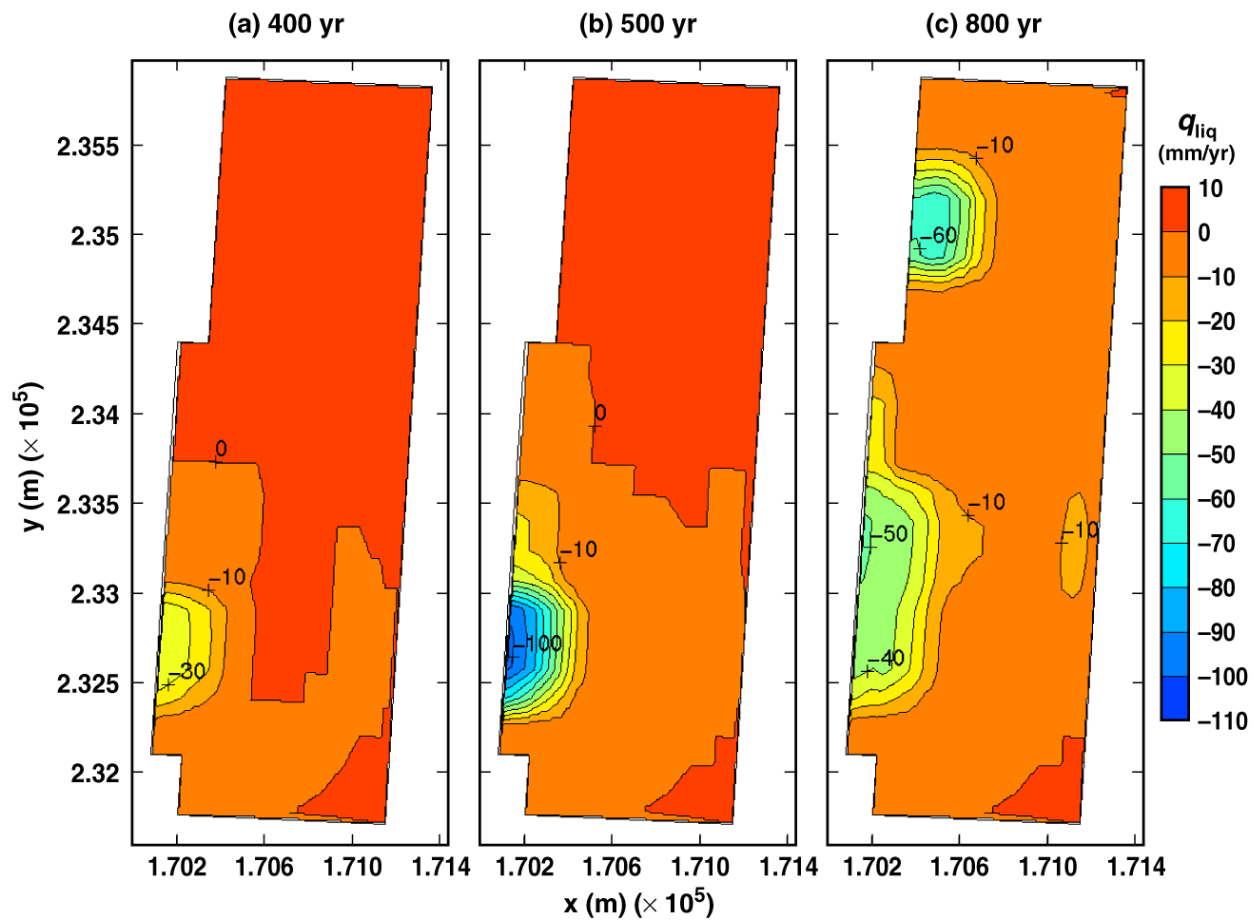
TB\_AMR\_lower\_qliq\_dsSide\_pwr2\_276-328

Figure 6-39. Liquid-phase flux adjacent to the lower side of the drip shield (i.e., adjacent to the base of the drip shield) for the low infiltration-flux backfill case for the indicated times (Continued)



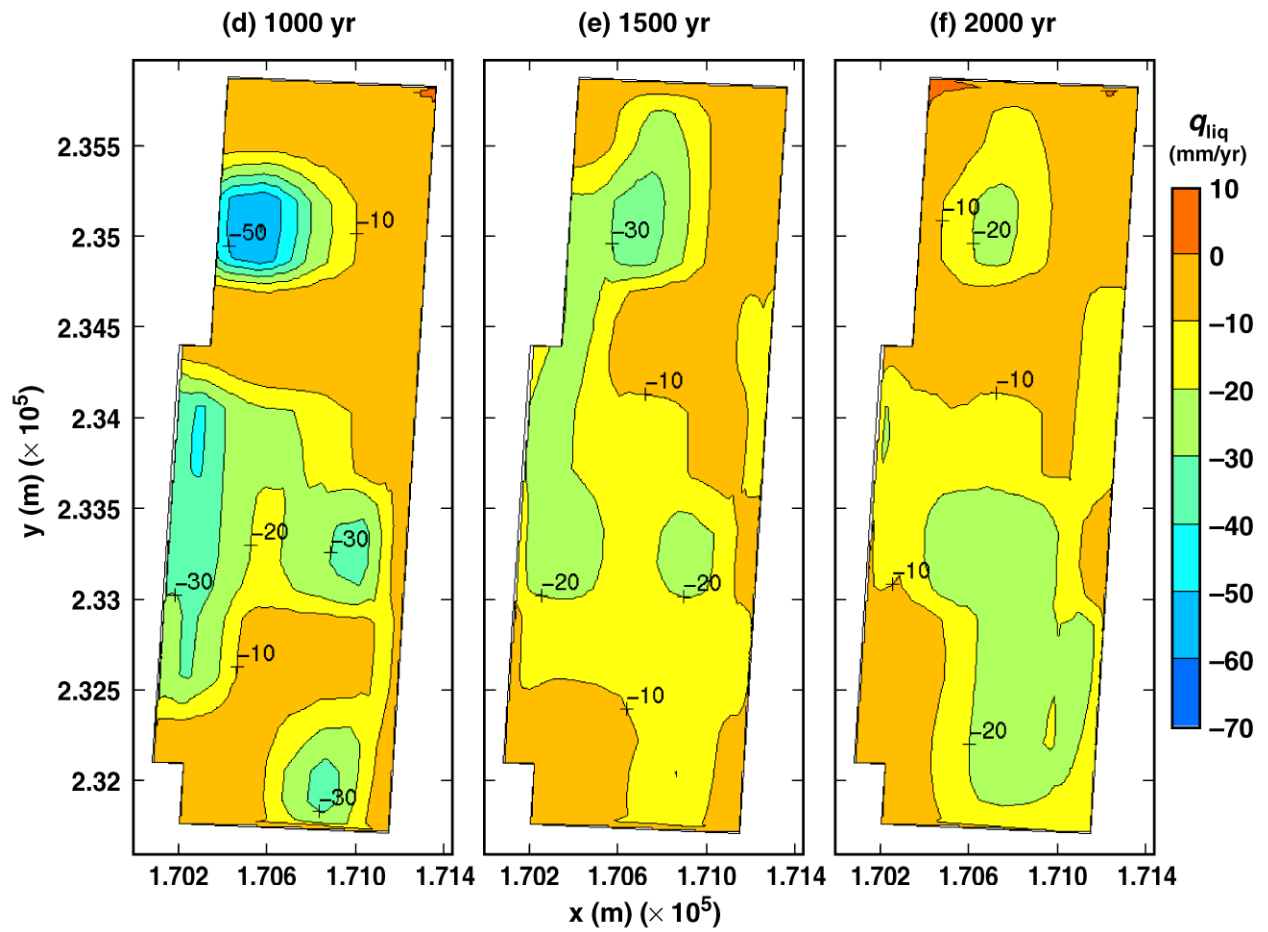
TB\_AMR\_lower\_qliq\_dsSide\_pwr2\_355-442

Figure 6-39. Liquid-phase flux adjacent to the lower side of the drip shield (i.e., adjacent to the base of the drip shield) for the low infiltration-flux backfill case for the indicated times (Continued)



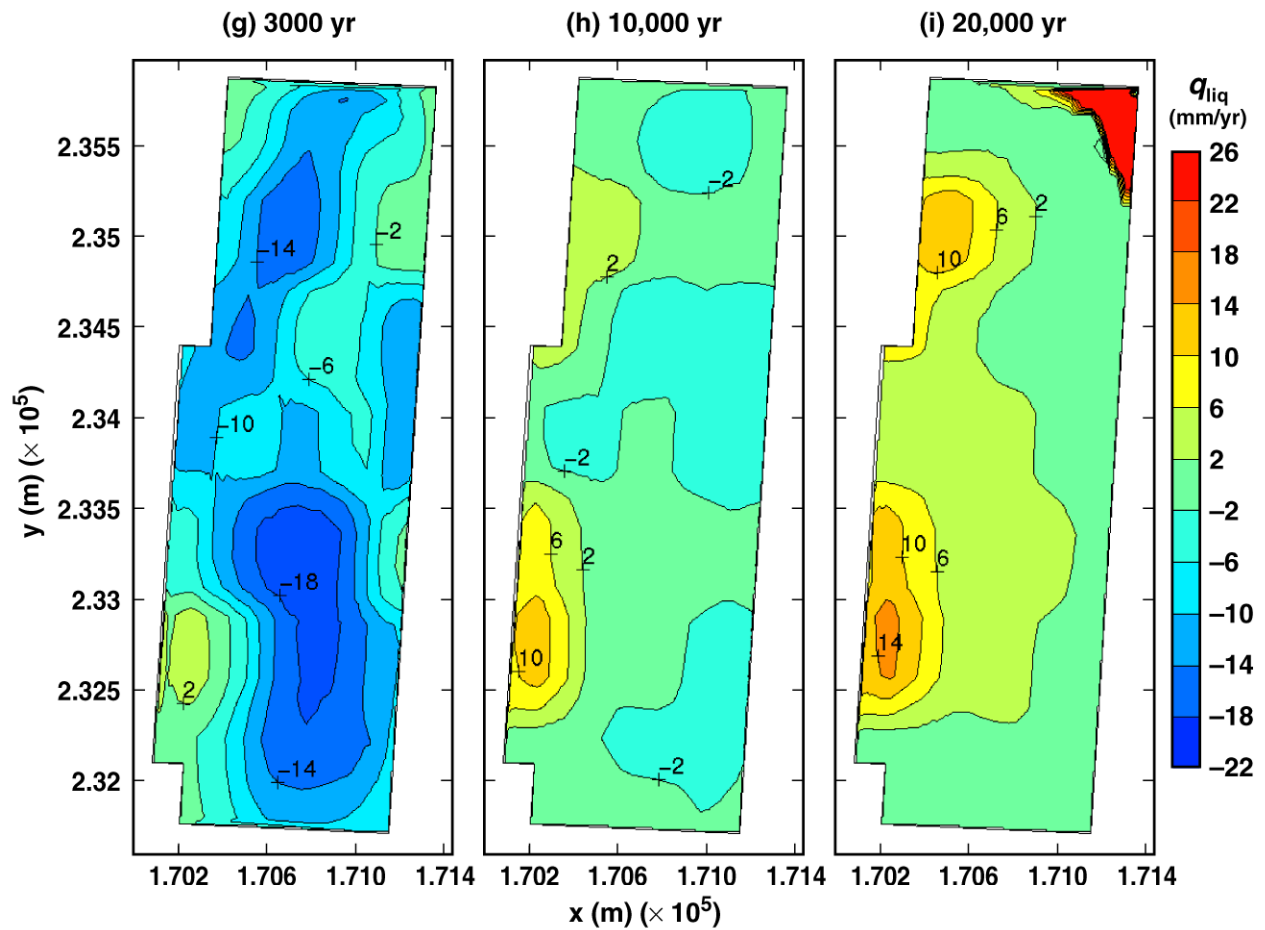
TB\_AMR\_lower\_qliq\_invert\_pwr2\_57-166

Figure 6-40. Liquid-phase flux averaged over the invert for the low infiltration-flux backfill case for the indicated times



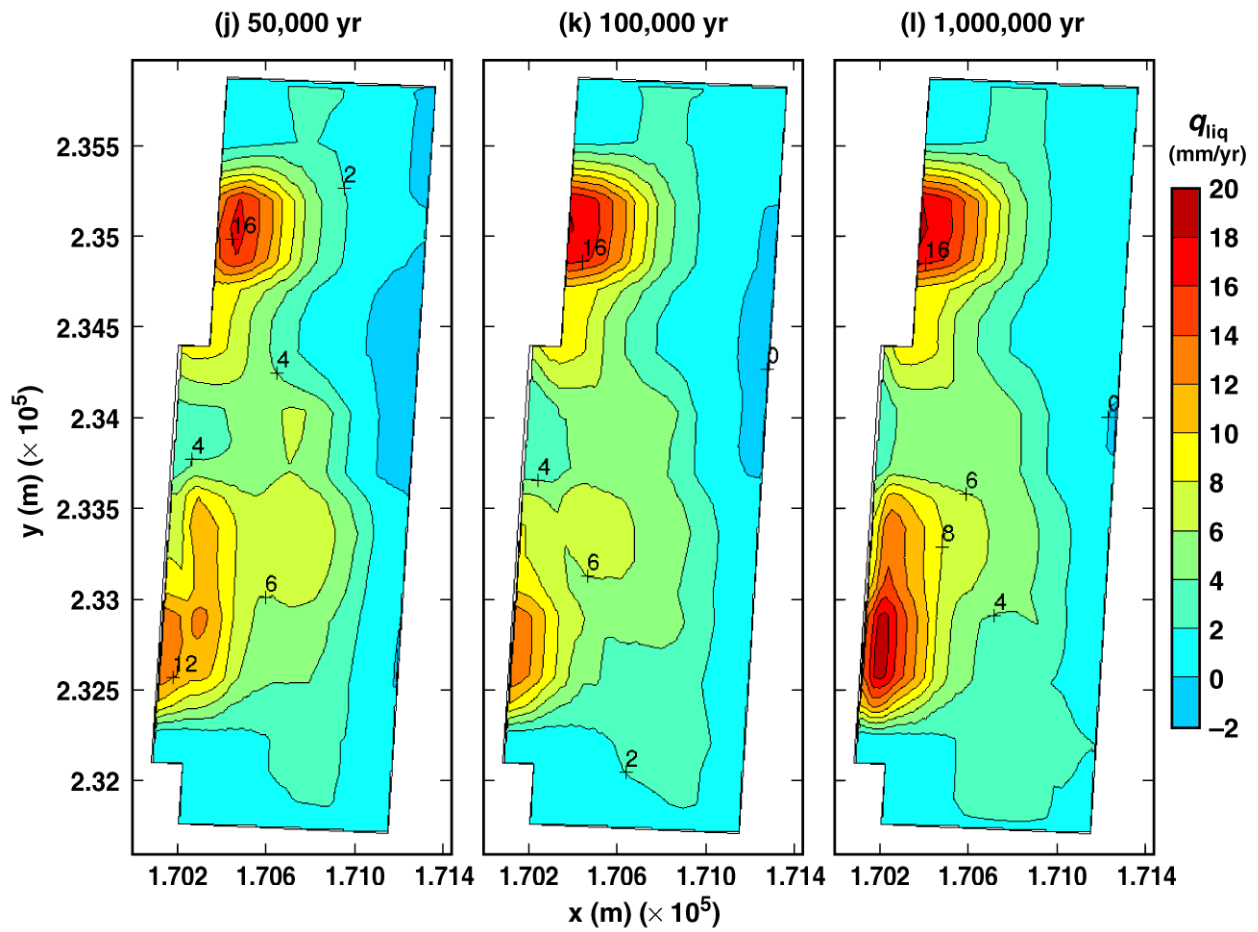
TB\_AMR\_lower\_qliq\_invert\_pwr2\_219-322

Figure 6-40. Liquid-phase flux averaged over the invert for the low infiltration-flux backfill case for the indicated times (Continued)



TB\_AMR\_lower\_qliq\_invert\_pwr2\_355-411

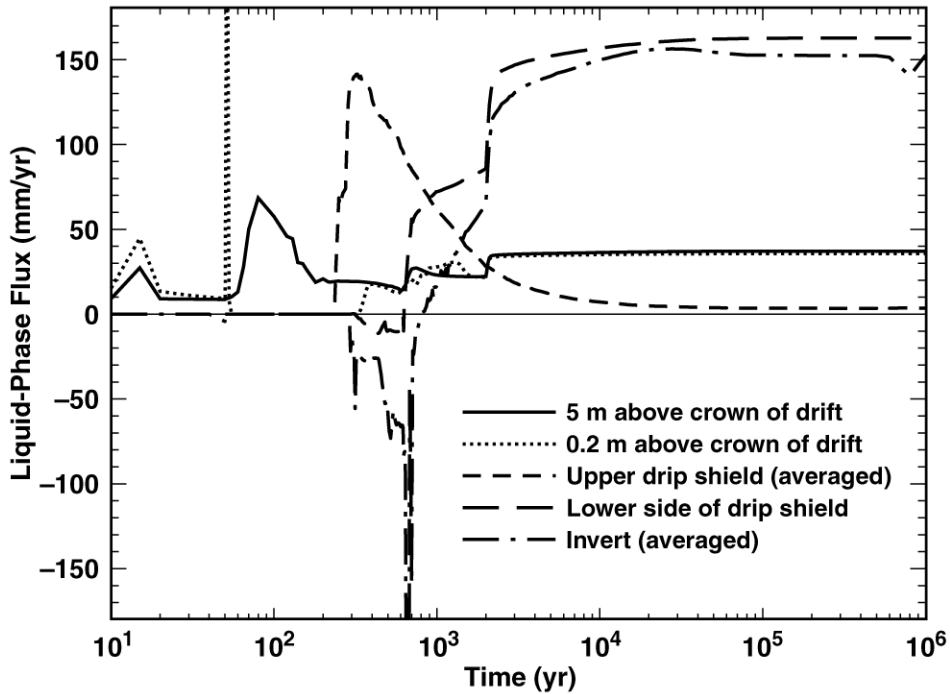
Figure 6-40. Liquid-phase flux averaged over the invert for the low infiltration-flux backfill case for the indicated times (Continued)



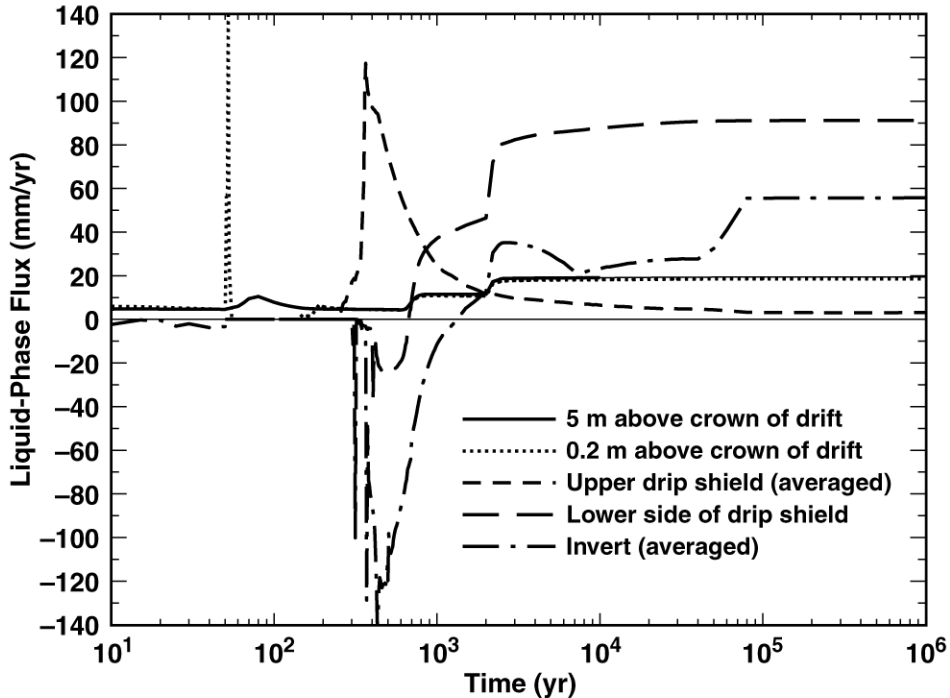
TB\_AMR\_lower\_qliq\_invert\_pwr2\_427-442

Figure 6-40. Liquid-phase flux averaged over the invert for the low infiltration-flux backfill case for the indicated times (Continued)

(a) Center of Repository  
 Nevada State Coordinates: Easting = 170535.03 m, Northing = 233640.08 m

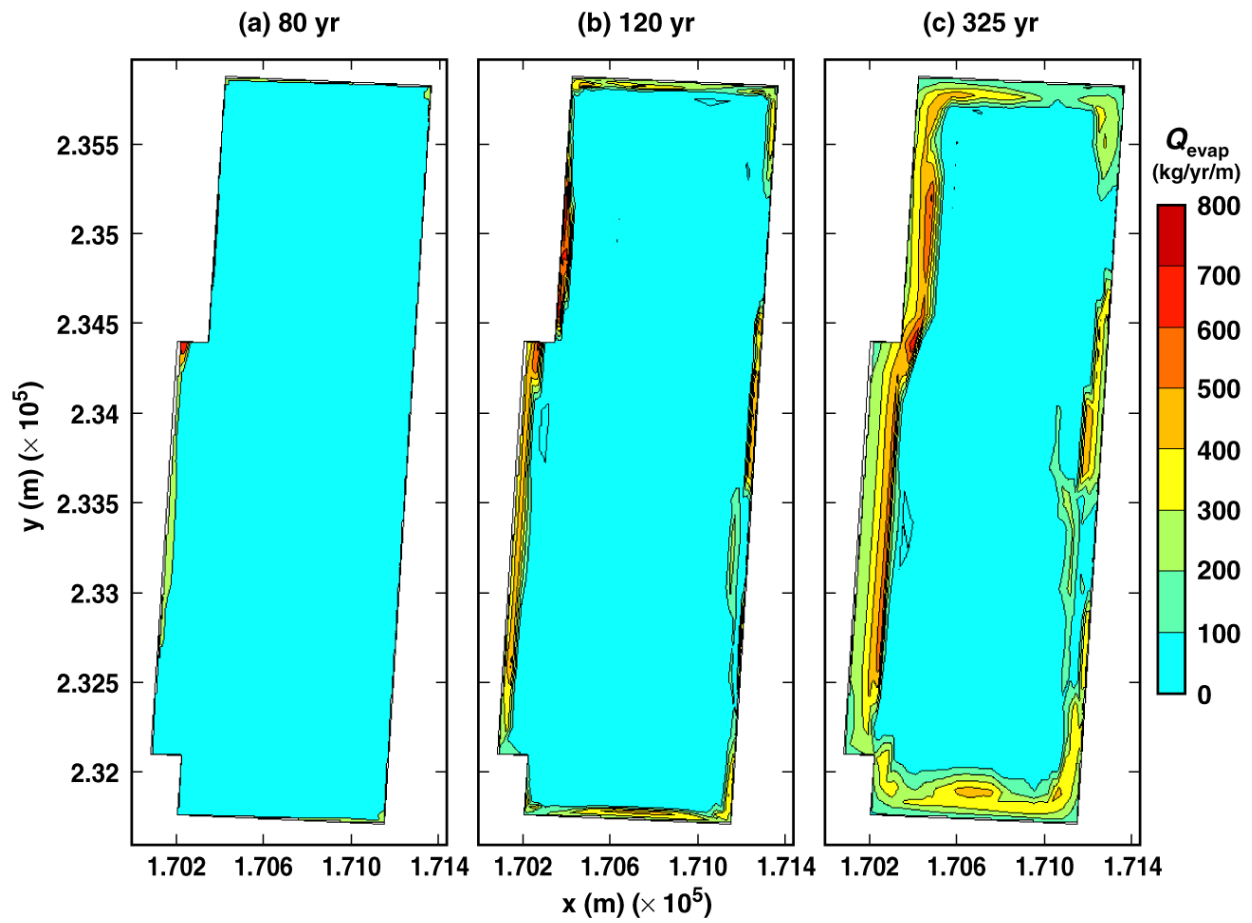


(b) Eastern Edge of Repository  
 Nevada State Coordinates: Easting = 171195.16 m, Northing = 233605.06 m



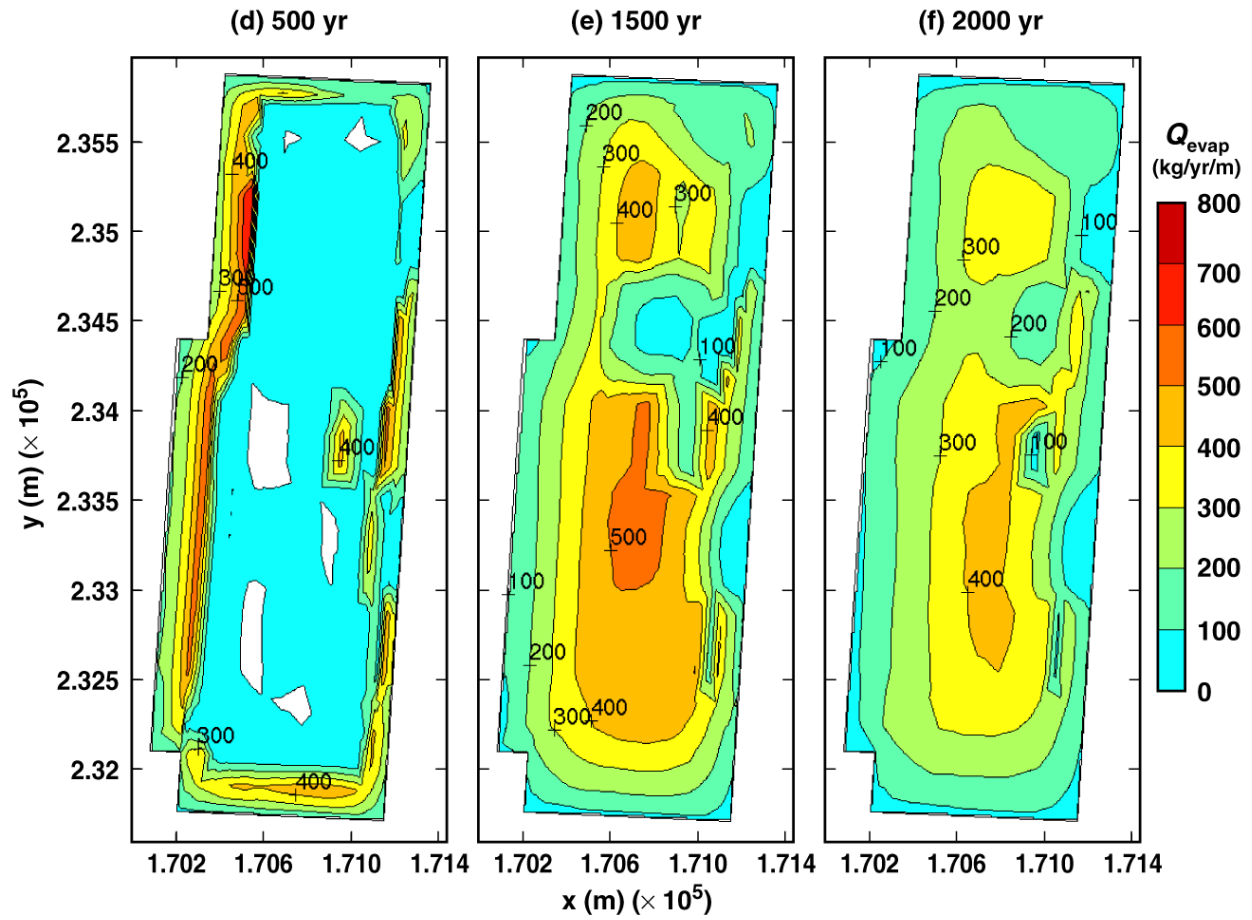
TB\_AMR\_qliq\_hist\_pwr2\_13&24\_17\_mean

Figure 6-41. Liquid-phase flux history at indicated drift-scale locations for the mean infiltration-flux case at (a) the geographical center of the repository and (b) a location 27.5 m from the eastern edge of the repository. Note that the Nevada State coordinates are given.



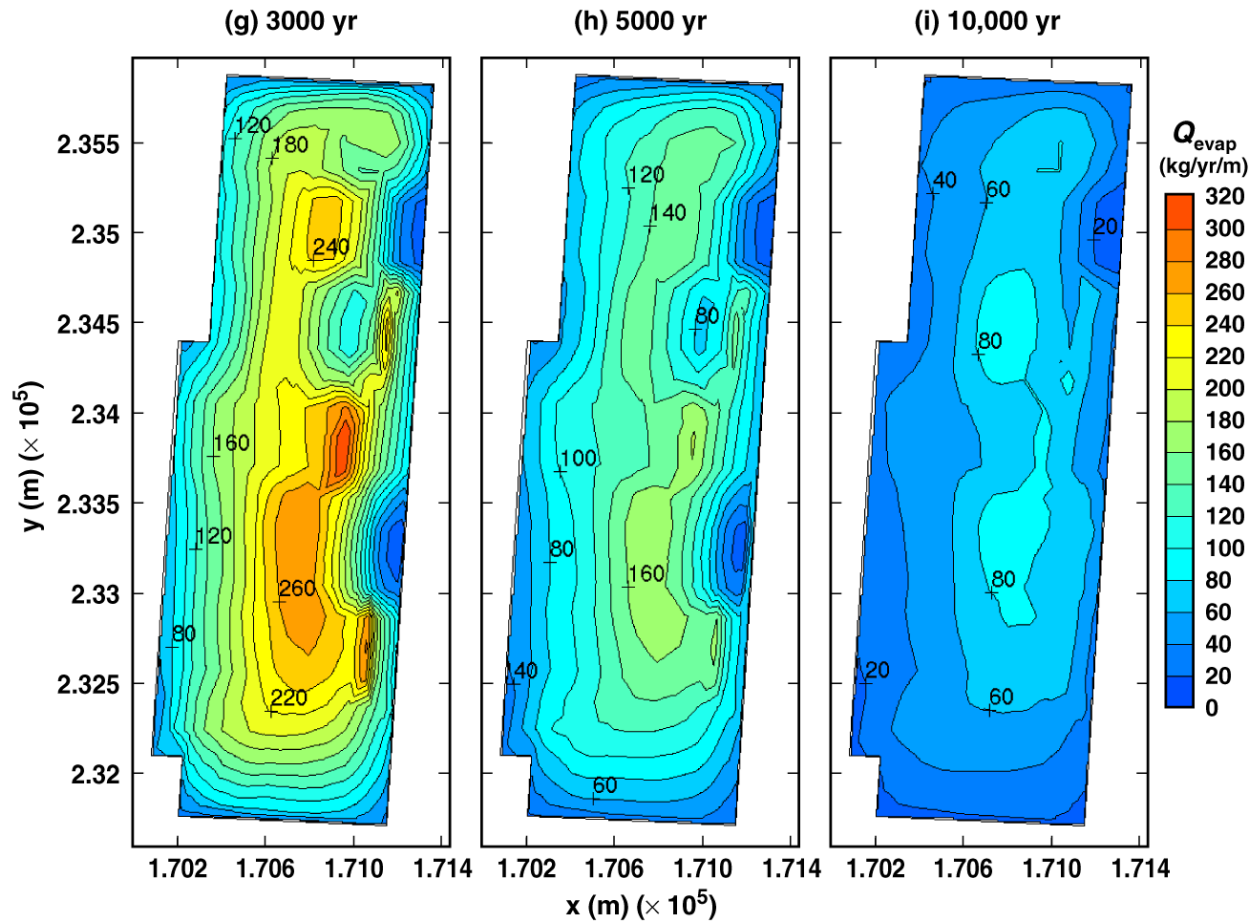
TB\_AMR\_Qevap\_dsPerim\_pwr2\_20-69

Figure 6-42. Evaporation rate summed over the upper surface of the drip shield for the mean infiltration-flux backfill case for the indicated times



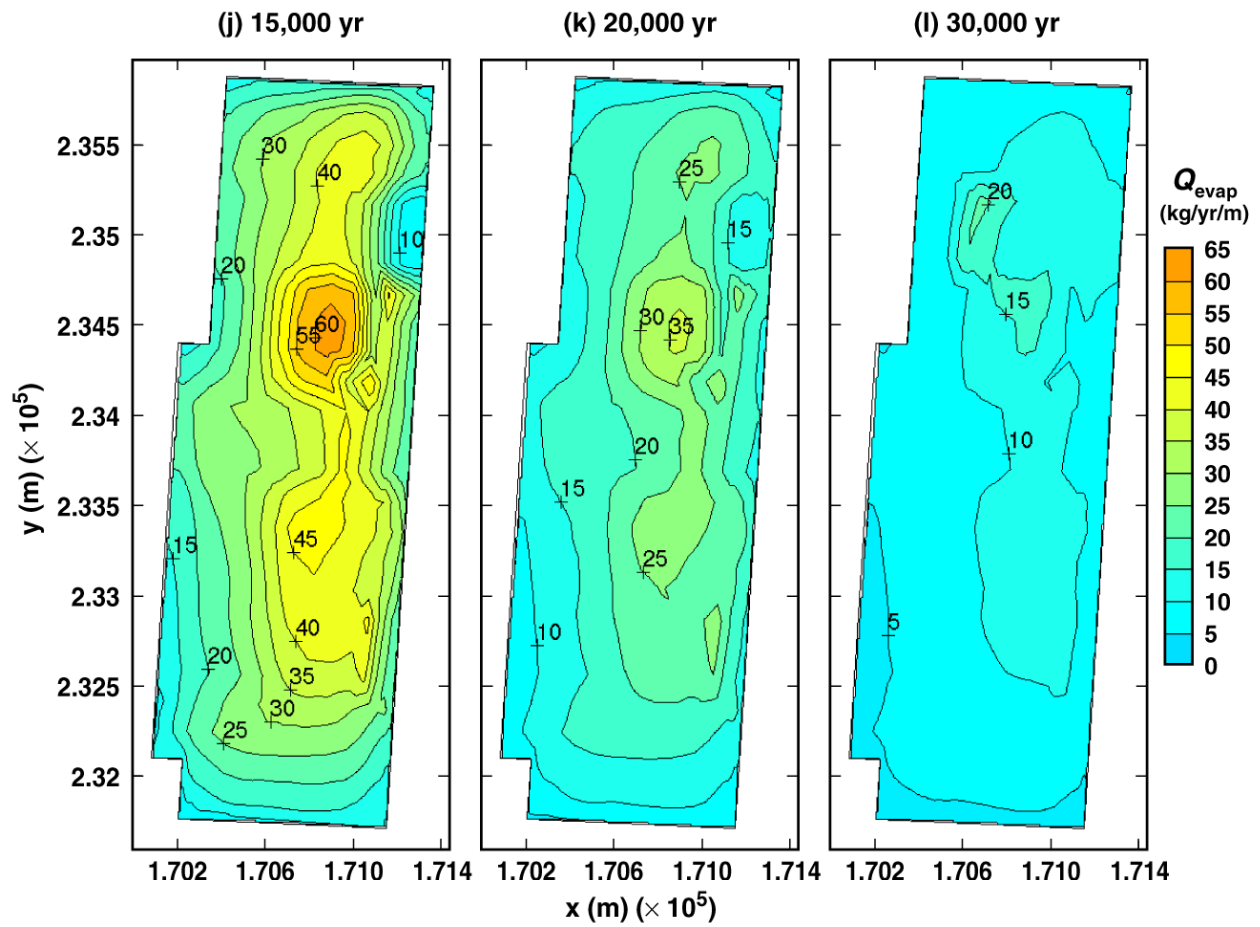
TB\_AMR\_Qevap\_dsPerim\_pwr2\_104-254

Figure 6-42. Evaporation rate summed over the upper surface of the drip shield for the mean infiltration-flux backfill case for the indicated times (Continued)



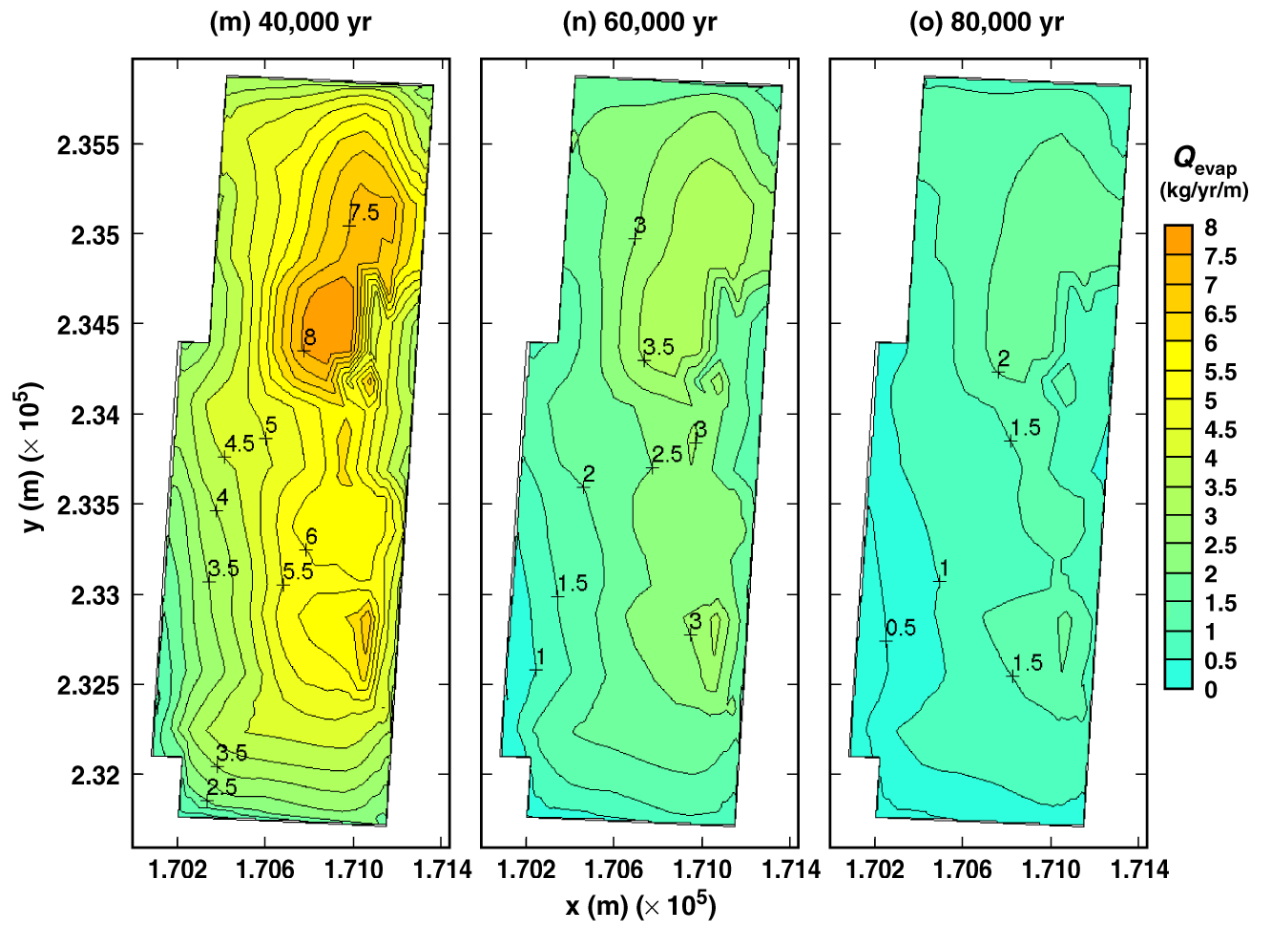
TB\_AMR\_Qevap\_dsPerim\_pwr2\_283-319

Figure 6-42. Evaporation rate summed over the upper surface of the drip shield for the mean infiltration-flux backfill case for the indicated times (Continued)



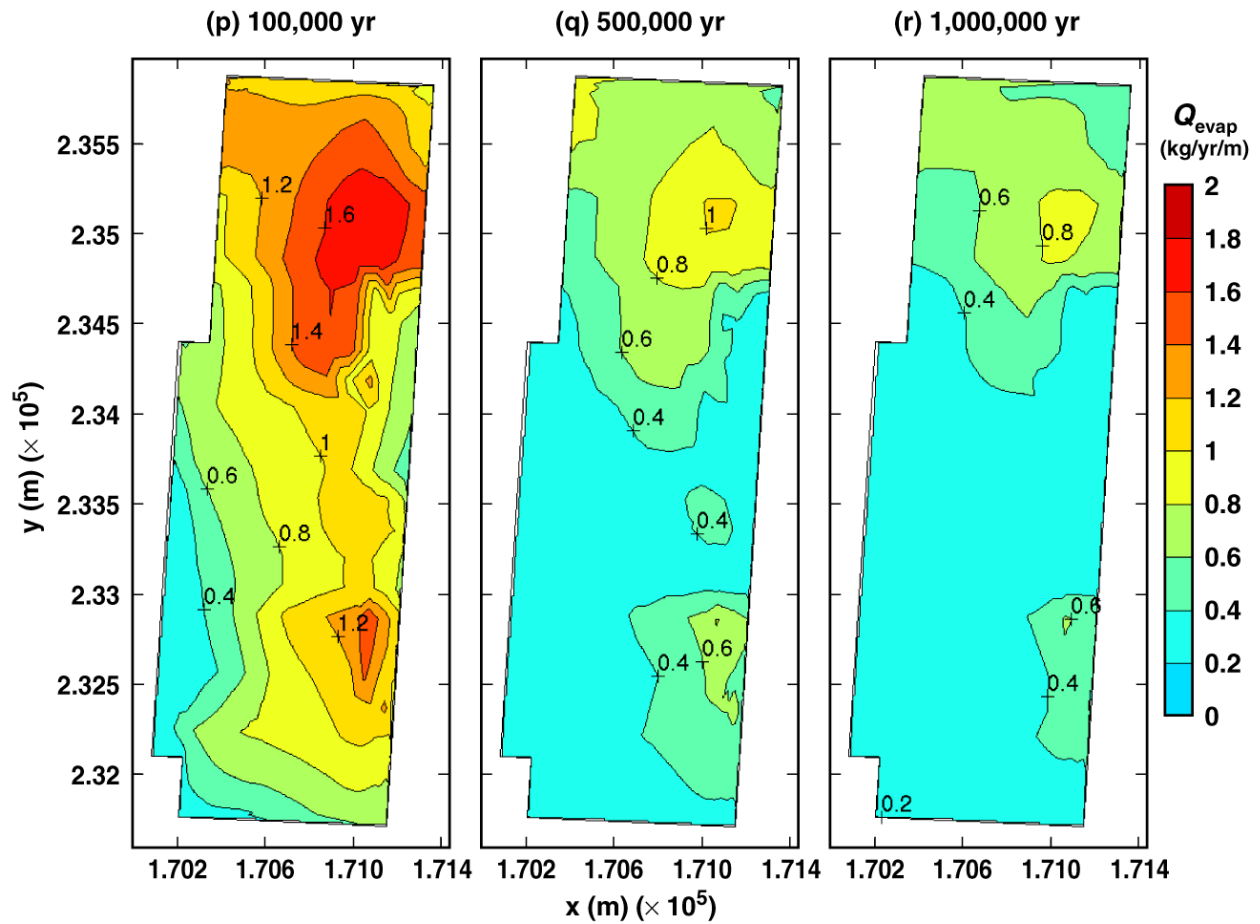
TB\_AMR\_Qevap\_dsPerim\_pwr2\_326-335

Figure 6-42. Evaporation rate summed over the upper surface of the drip shield for the mean | infiltration-flux backfill case for the indicated times (Continued)



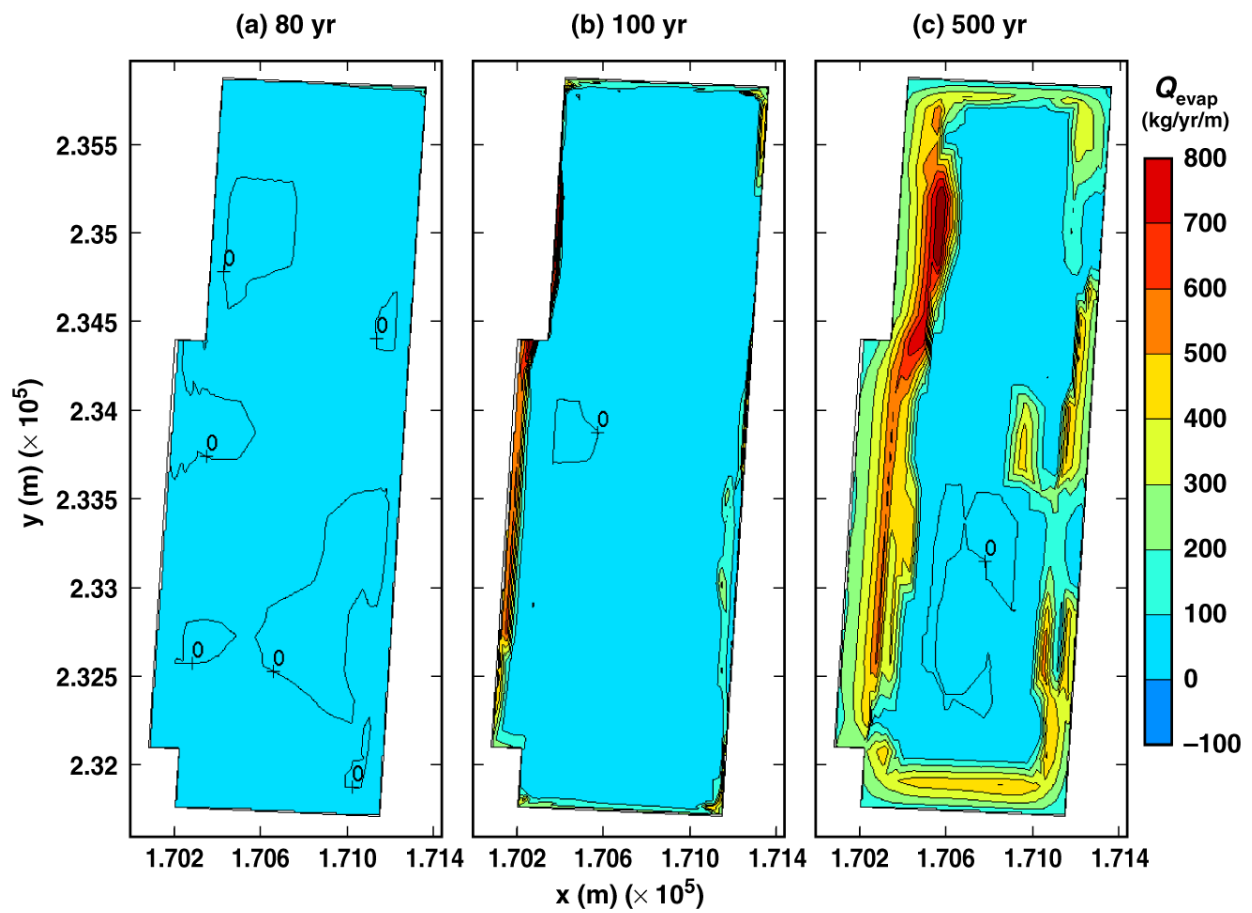
TB\_AMR\_Qevap\_dsPerim\_pwr2\_340-343

Figure 6-42. Evaporation rate summed over the upper surface of the drip shield for the mean infiltration-flux backfill case for the indicated times (Continued)



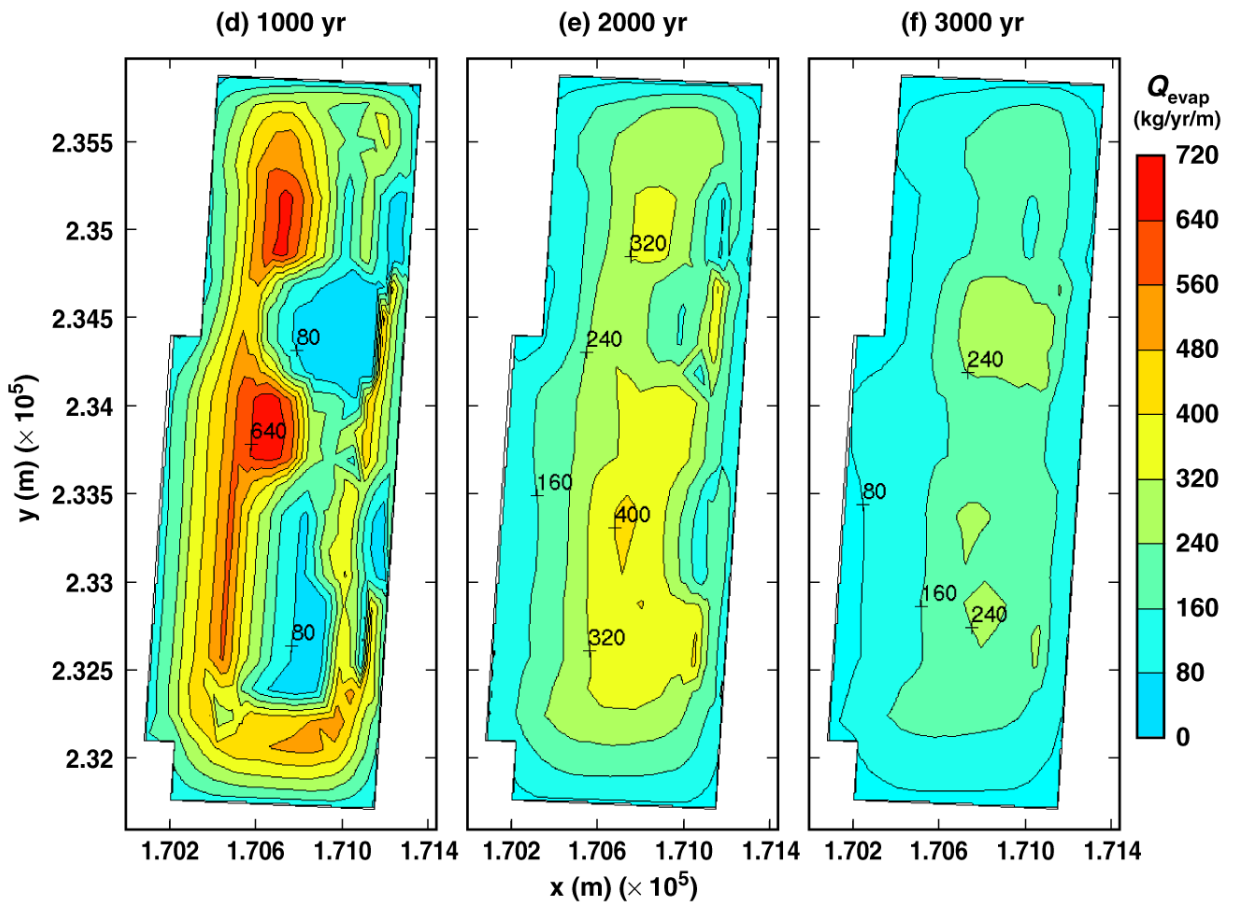
TB\_AMR\_Qevap\_dsPerim\_pwr2\_344-352

Figure 6-42. Evaporation rate summed over the upper surface of the drip shield for the mean | infiltration-flux backfill case for the indicated times (Continued)



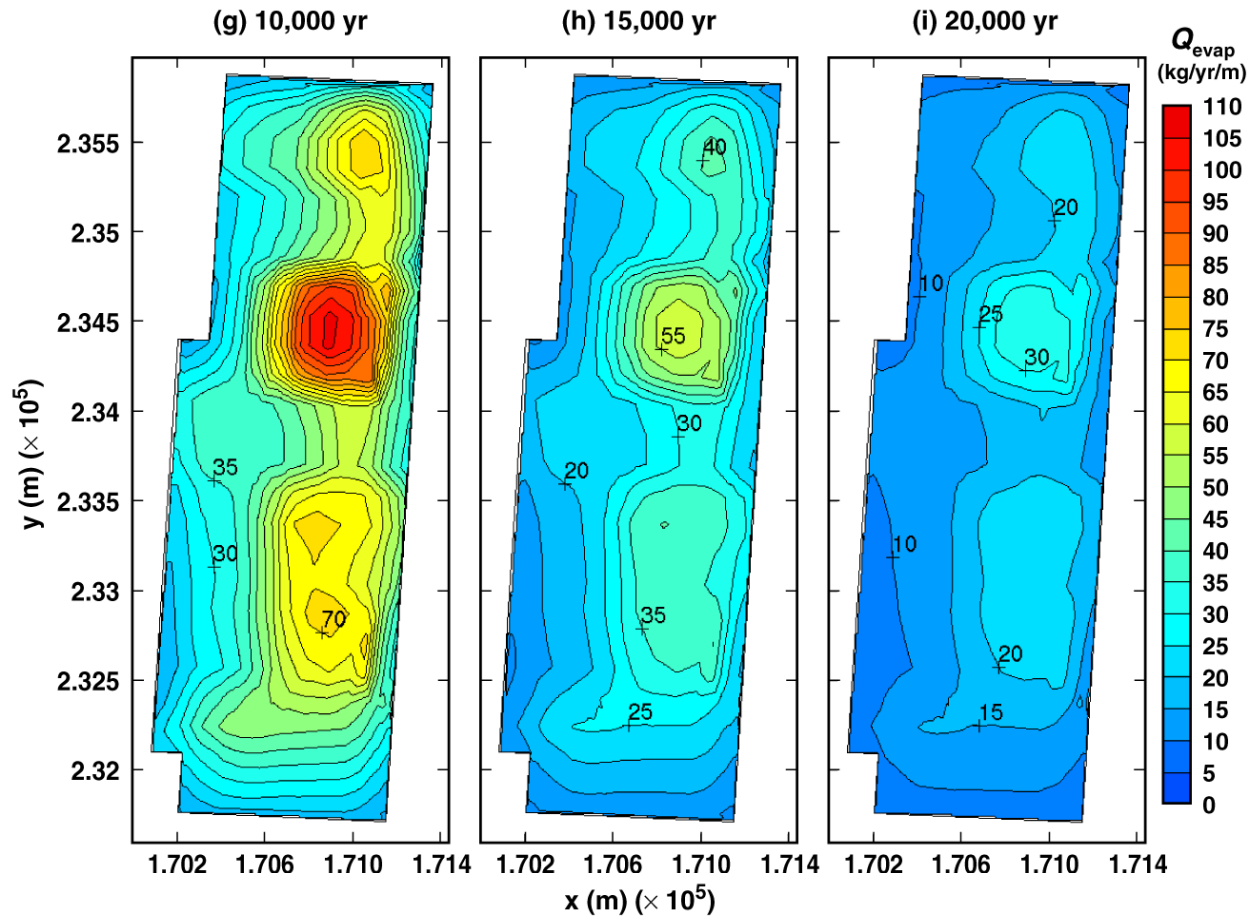
TB\_AMR\_upper\_Qevap\_dsPerim\_pwr2\_18-177

Figure 6-43. Evaporation rate summed over the upper surface of the drip shield for the high infiltration-flux backfill case for the indicated times



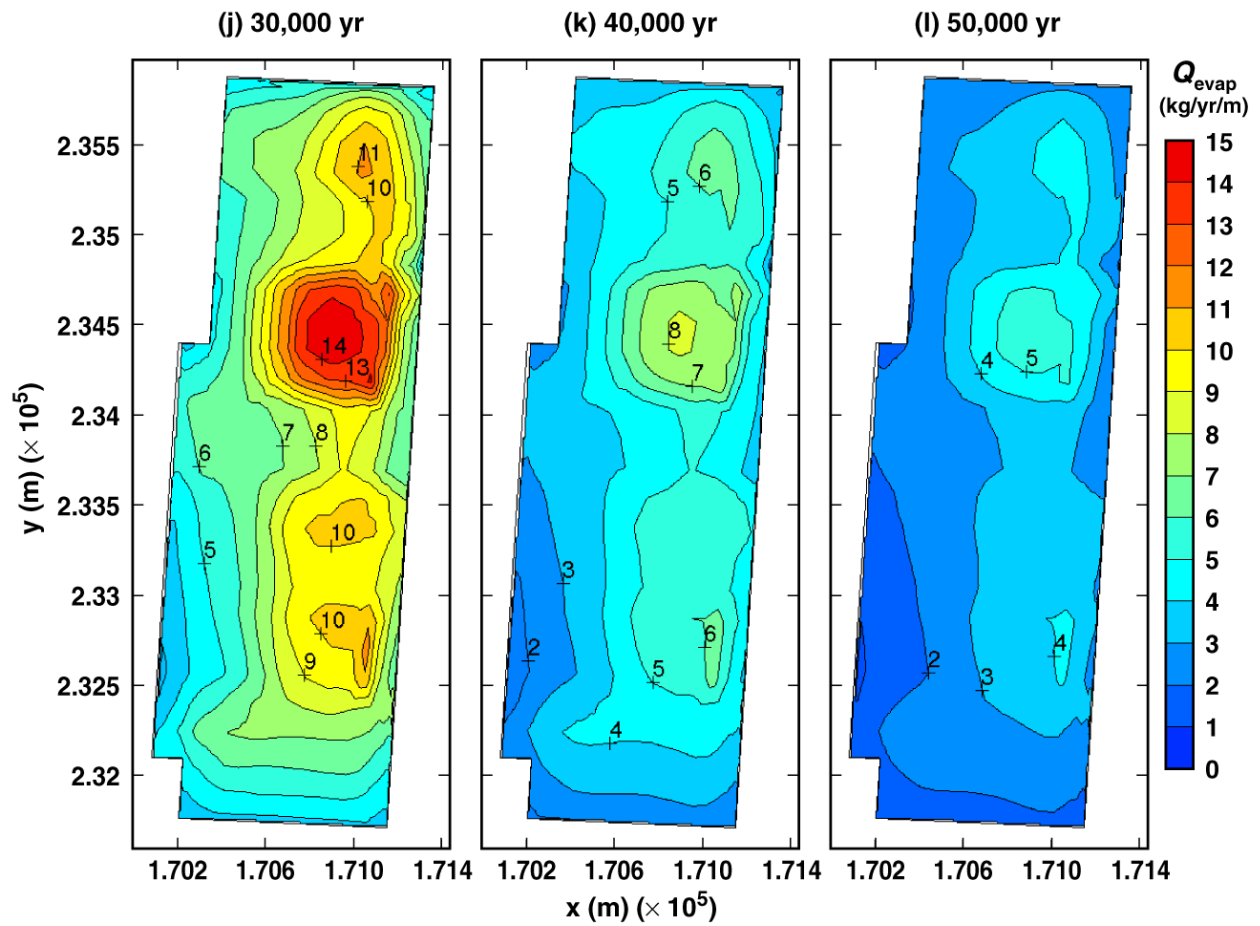
TB\_AMR\_upper\_Qevap\_dsPerim\_pwr2\_269-389

Figure 6-43. Evaporation rate summed over the upper surface of the drip shield for the high infiltration-flux backfill case for the indicated times (Continued)



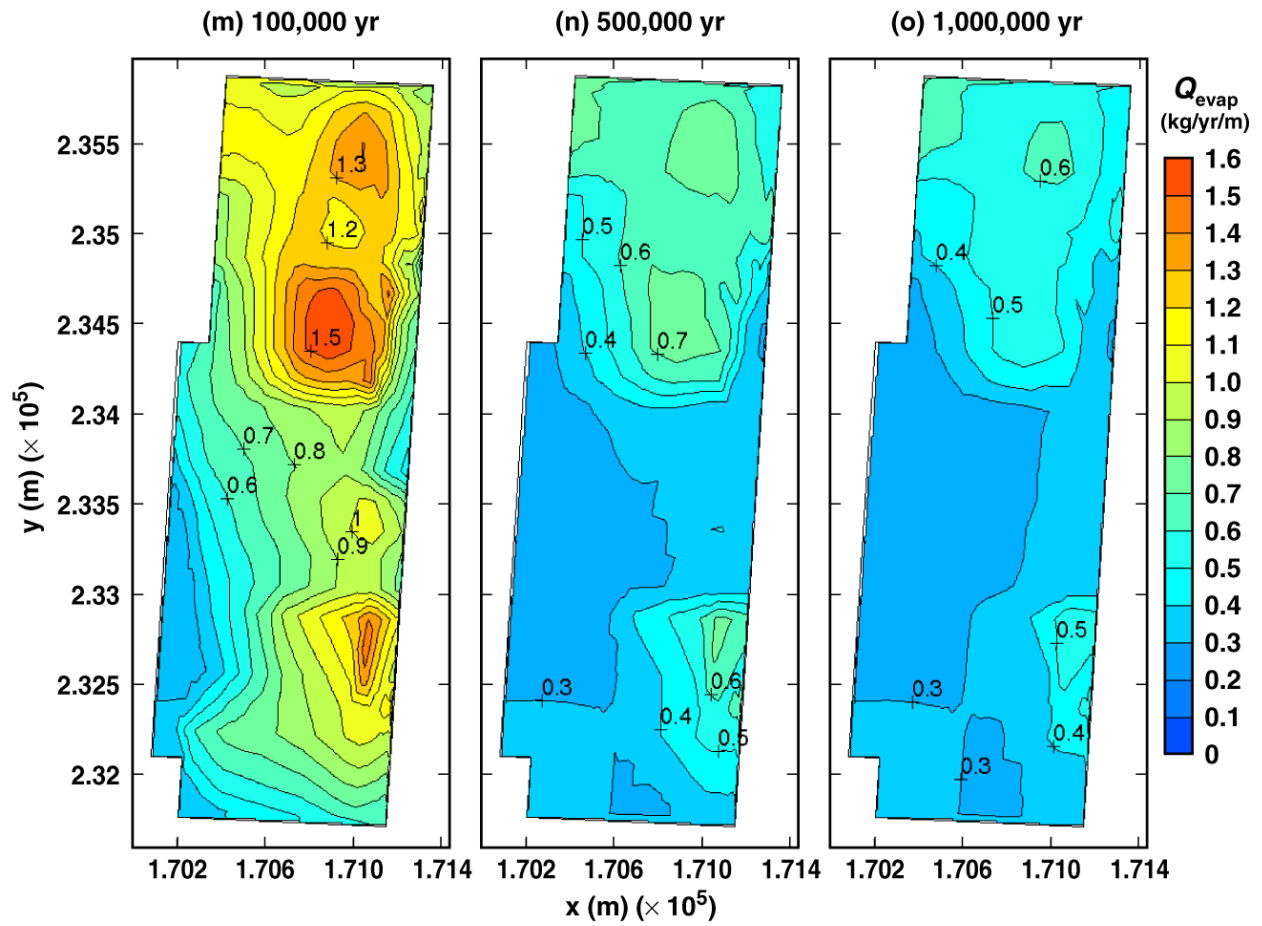
TB\_AMR\_upper\_Qevap\_dsPerim\_pwr2\_425-434

Figure 6-43. Evaporation rate summed over the upper surface of the drip shield for the high infiltration-flux backfill case for the indicated times (Continued)



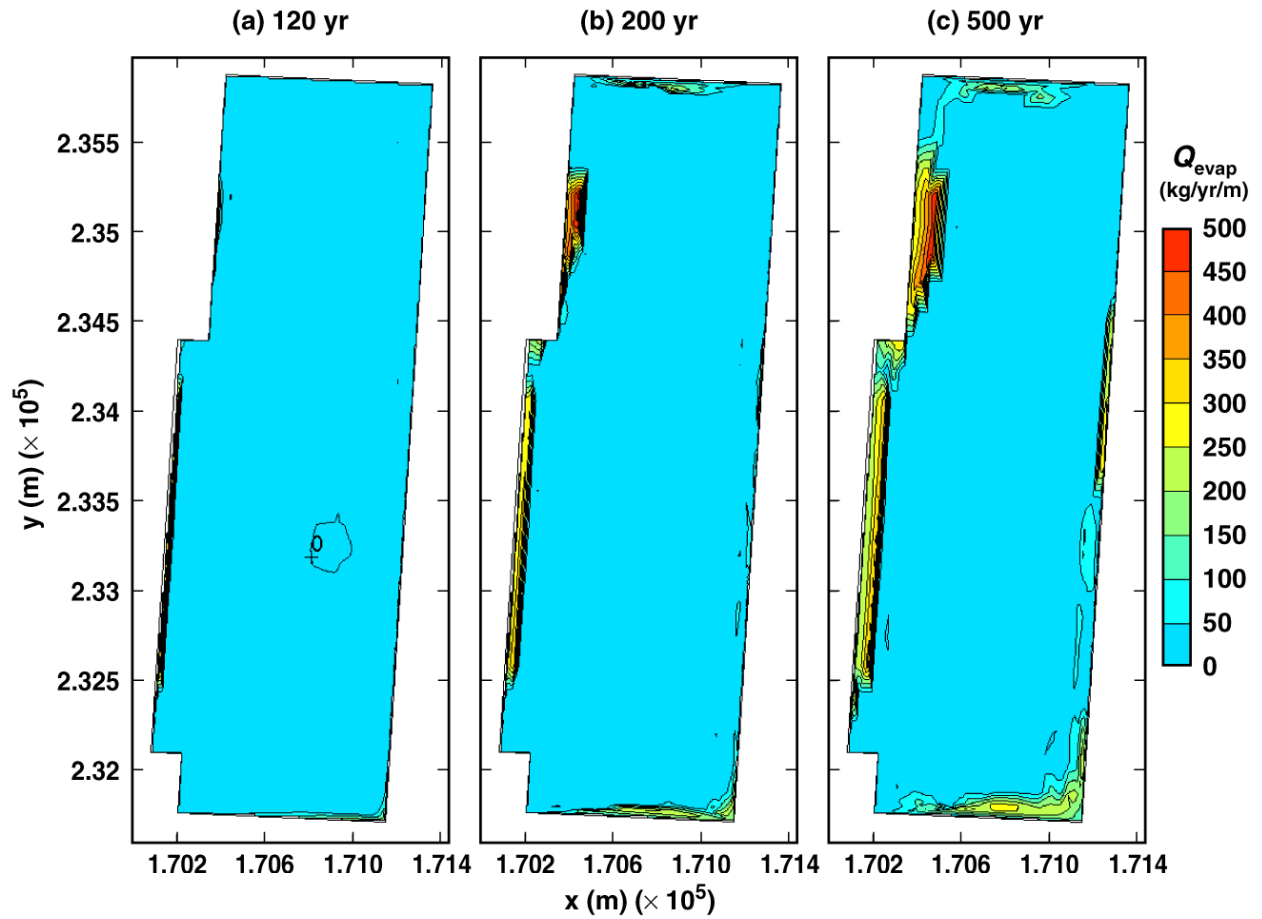
TB\_AMR\_upper\_Qevap\_dsPerim\_pwr2\_439-446

Figure 6-43. Evaporation rate summed over the upper surface of the drip shield for the high infiltration-flux backfill case for the indicated times (Continued)



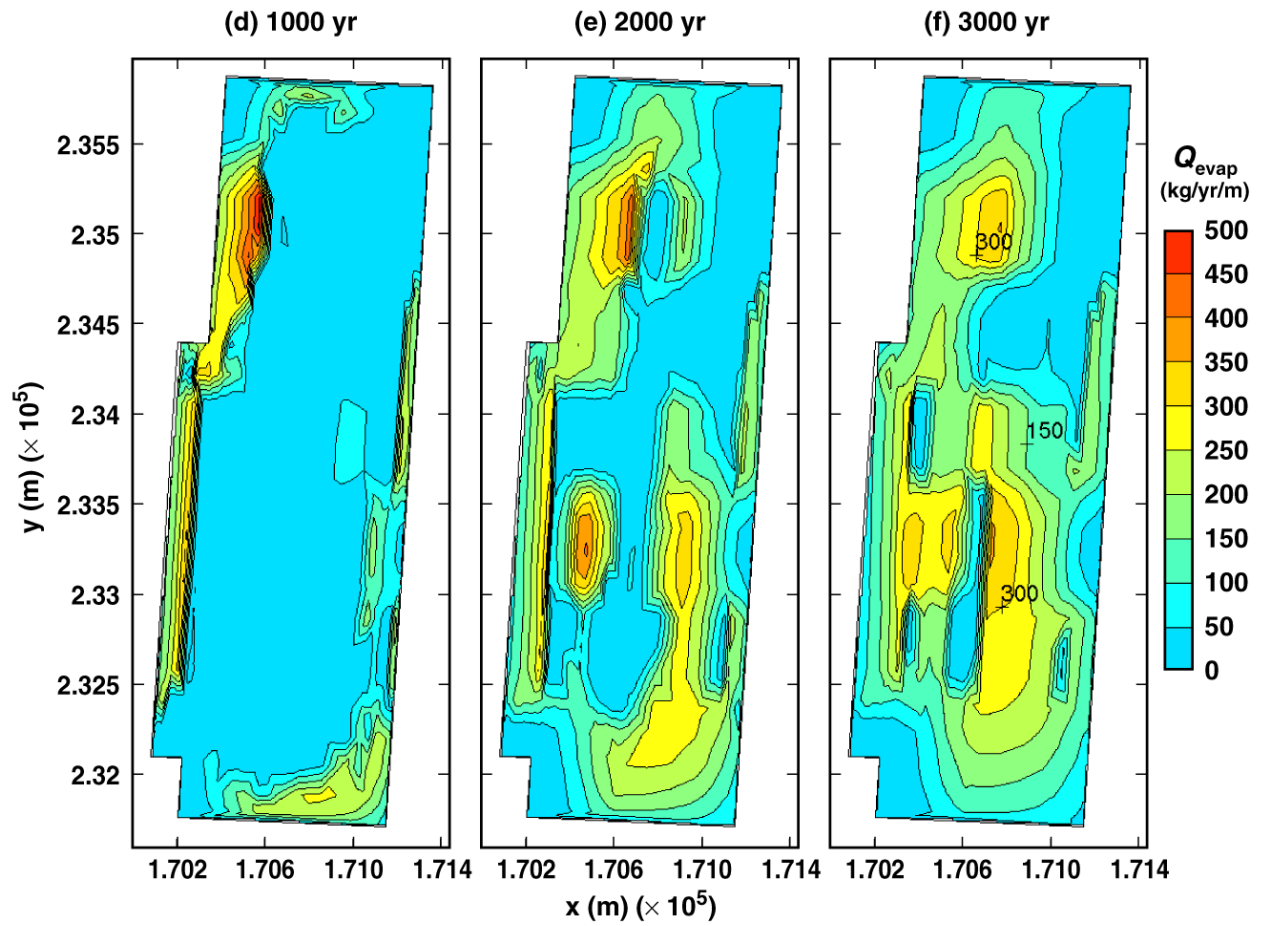
TB\_AMR\_upper\_Qevap\_dsPerim\_pwr2\_449-457

Figure 6-43. Evaporation rate summed over the upper surface of the drip shield for the high infiltration-backfill case for the indicated times (Continued)



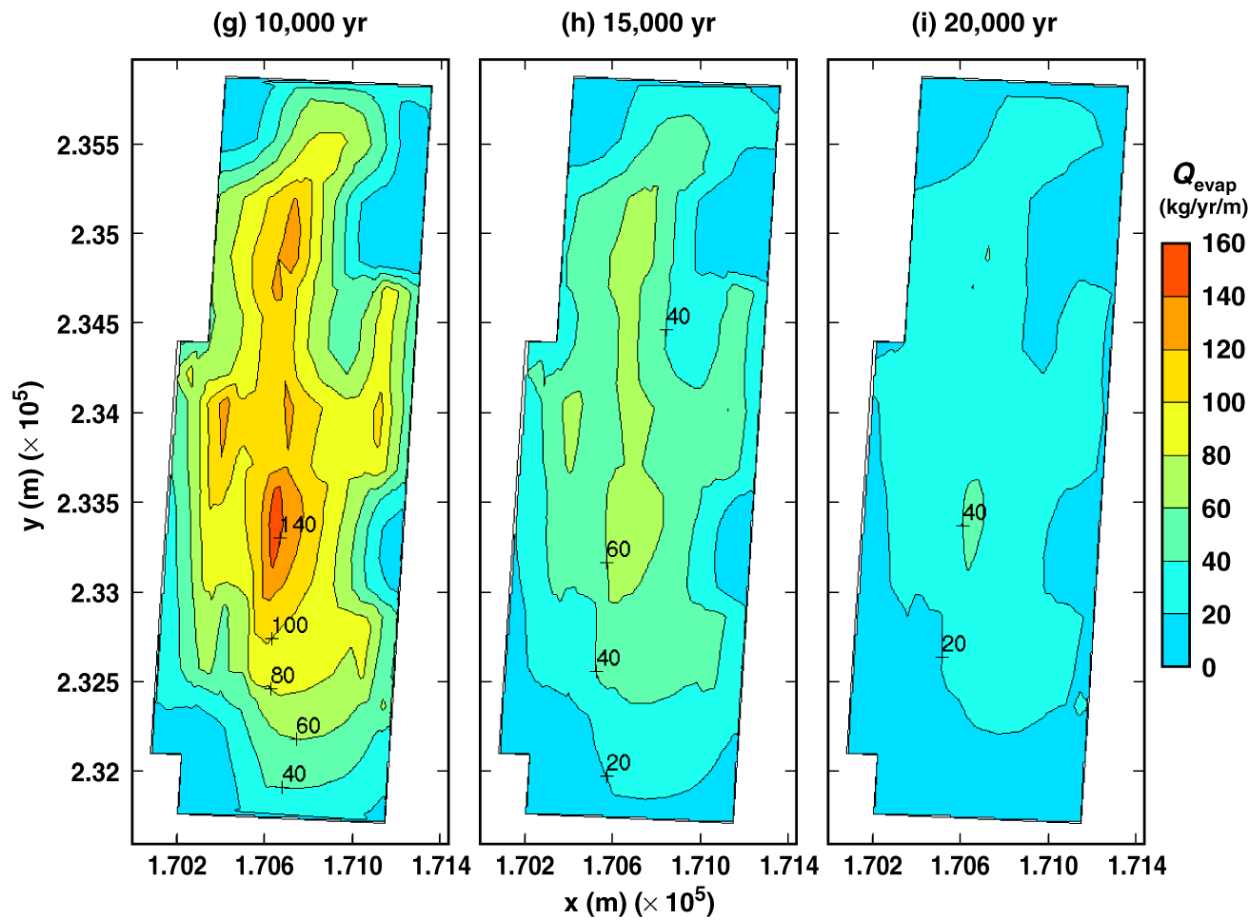
TB\_AMR\_lower\_Qevap\_dsPerim\_pwr2\_23-77

Figure 6-44. Evaporation rate summed over the upper surface of the drip shield for the low infiltration-backfill case for the indicated times



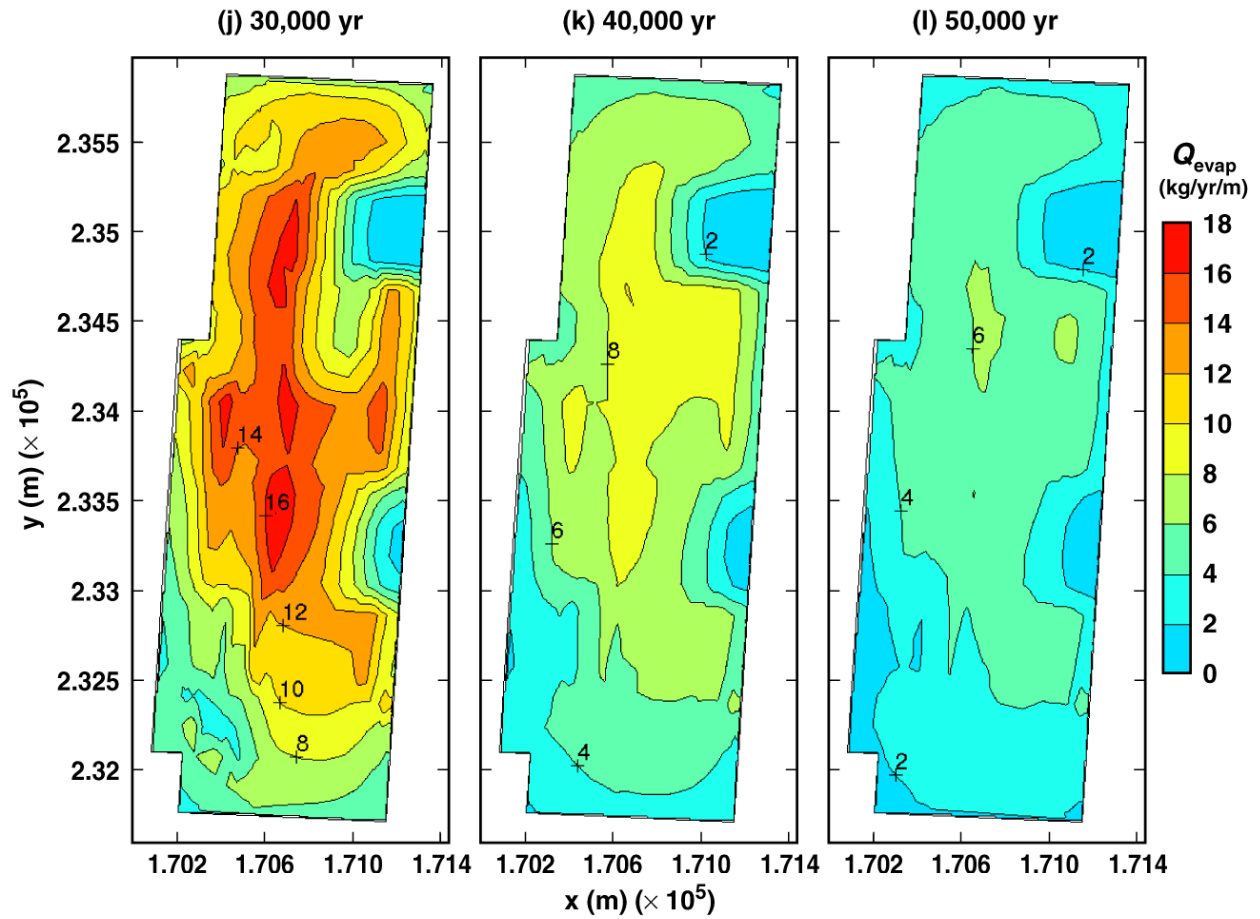
TB\_AMR\_lower\_Qevap\_dsPerim\_pwr2\_219-355

Figure 6-44. Evaporation rate summed over the upper surface of the drip shield for the low infiltration-backfill case for the indicated times (Continued)



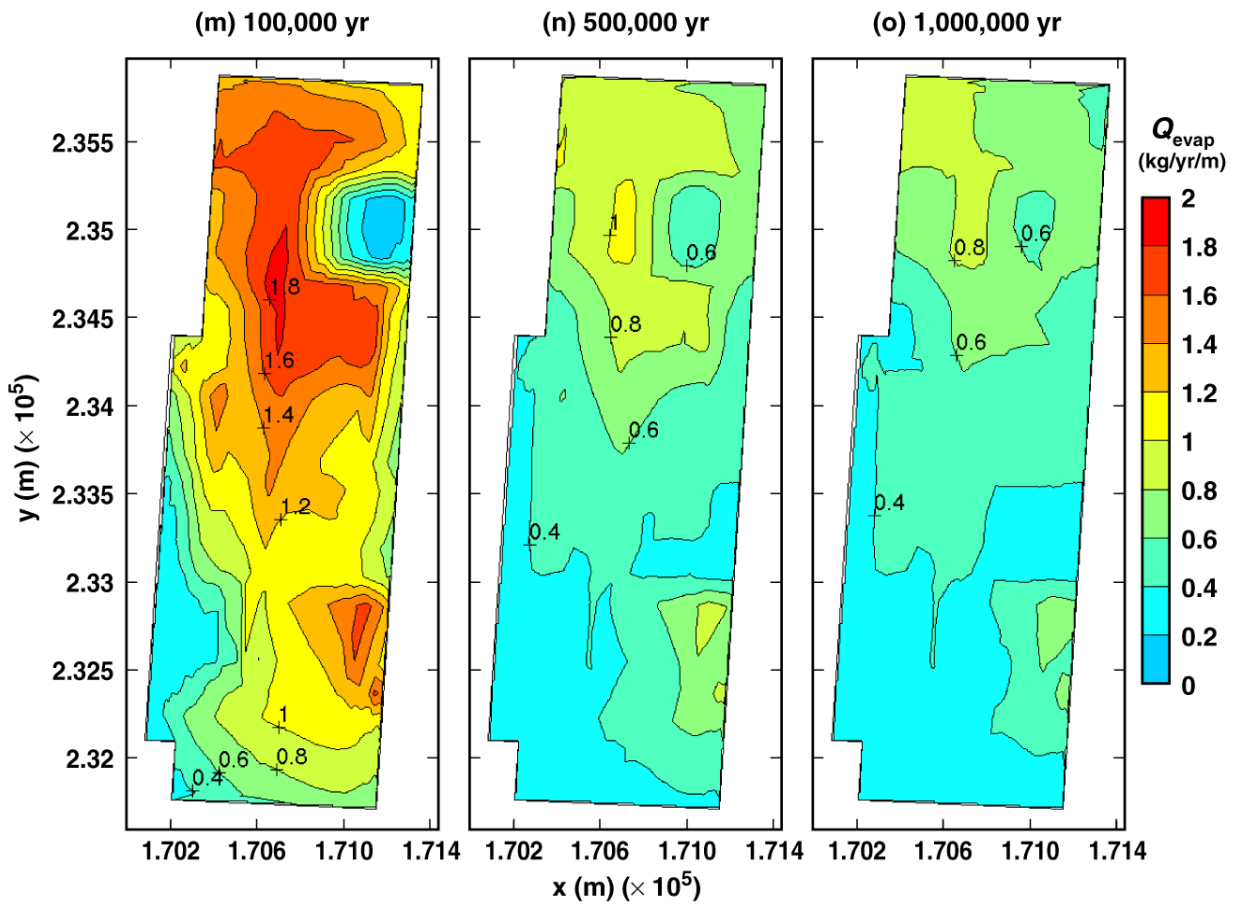
TB\_AMR\_lower\_Qevap\_dsPerim\_pwr2\_402-411

Figure 6-44. Evaporation rate summed over the upper surface of the drip shield for the low infiltration-backfill case for the indicated times (Continued)



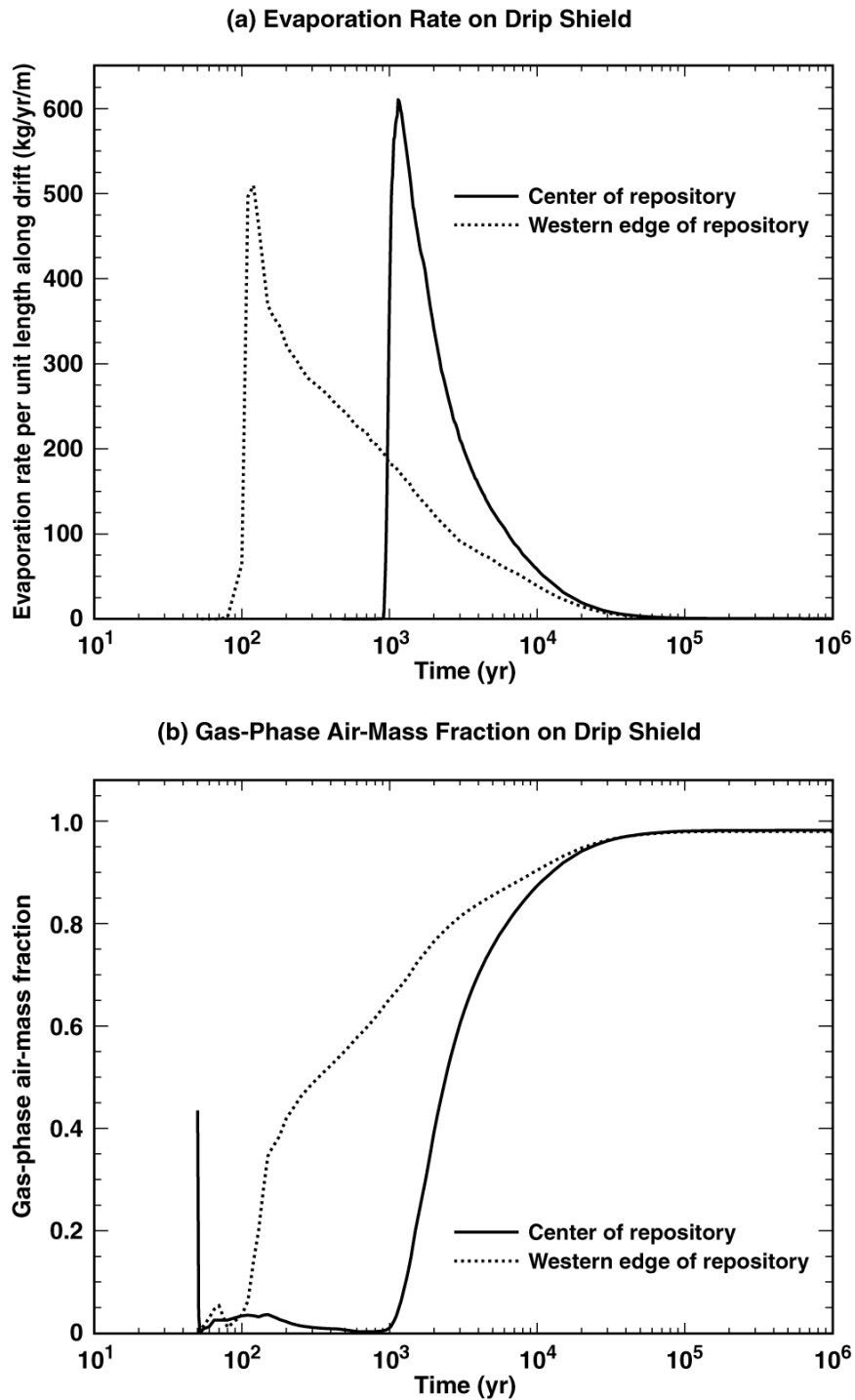
TB\_AMR\_lower\_Qevap\_dsPerim\_pwr2\_417-427

Figure 6-44. Evaporation rate summed over the upper surface of the drip shield for the low infiltration-flux backfill case for the indicated times (Continued)



TB\_AMR\_lower\_Qevap\_dsPerim\_pwr2\_434-442

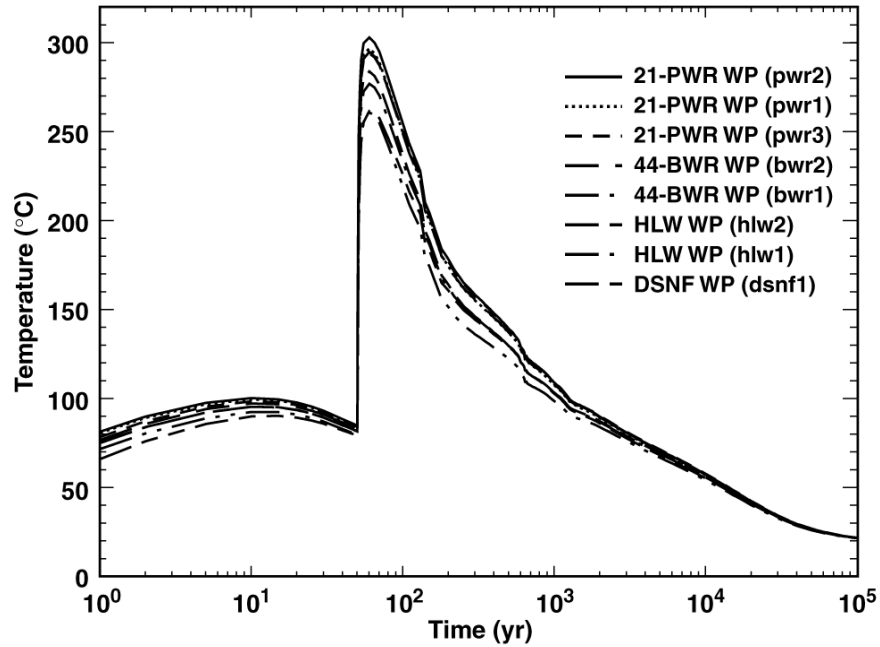
Figure 6-44. Evaporation rate summed over the upper surface of the drip shield for the low infiltration-flux backfill case for the indicated times (Continued)



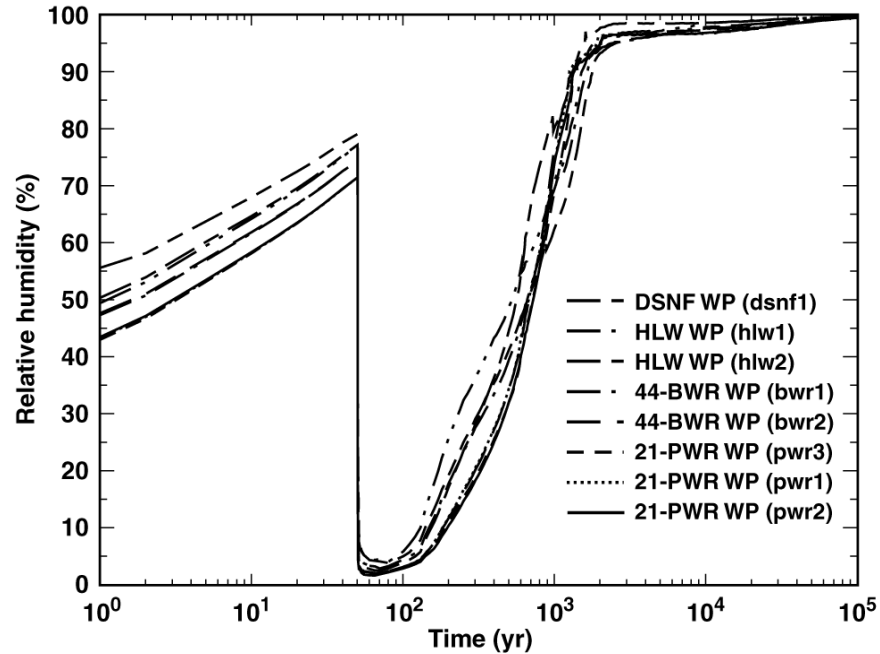
TB\_AMR\_Qevap&Xair\_ds\_hist\_mean

Figure 6-45. Evaporation rate summed over the upper surface of the drip shield for the mean infiltration-flux backfill case at (a) the geographical center of the repository and (b) a location 27.5 m from the eastern edge of the repository. Note that the Nevada State coordinates are given.

(a) Waste-Package Temperature  
 Nevada State Coordinates: Easting = 170535.03 m, Northing = 233640.08 m

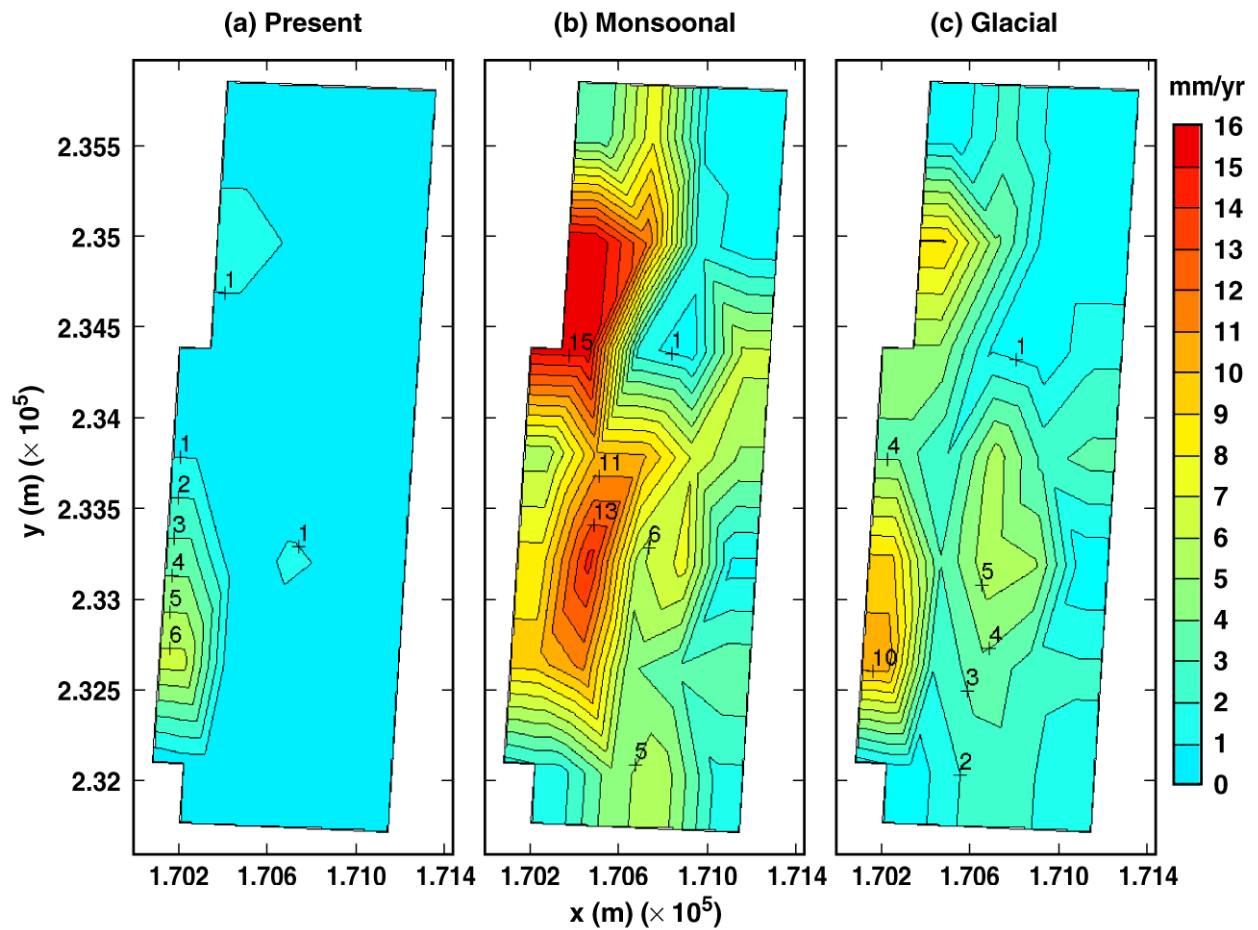


(b) Waste-Package Relative Humidity  
 Nevada State Coordinates: Easting = 170535.03 m, Northing = 233640.08 m



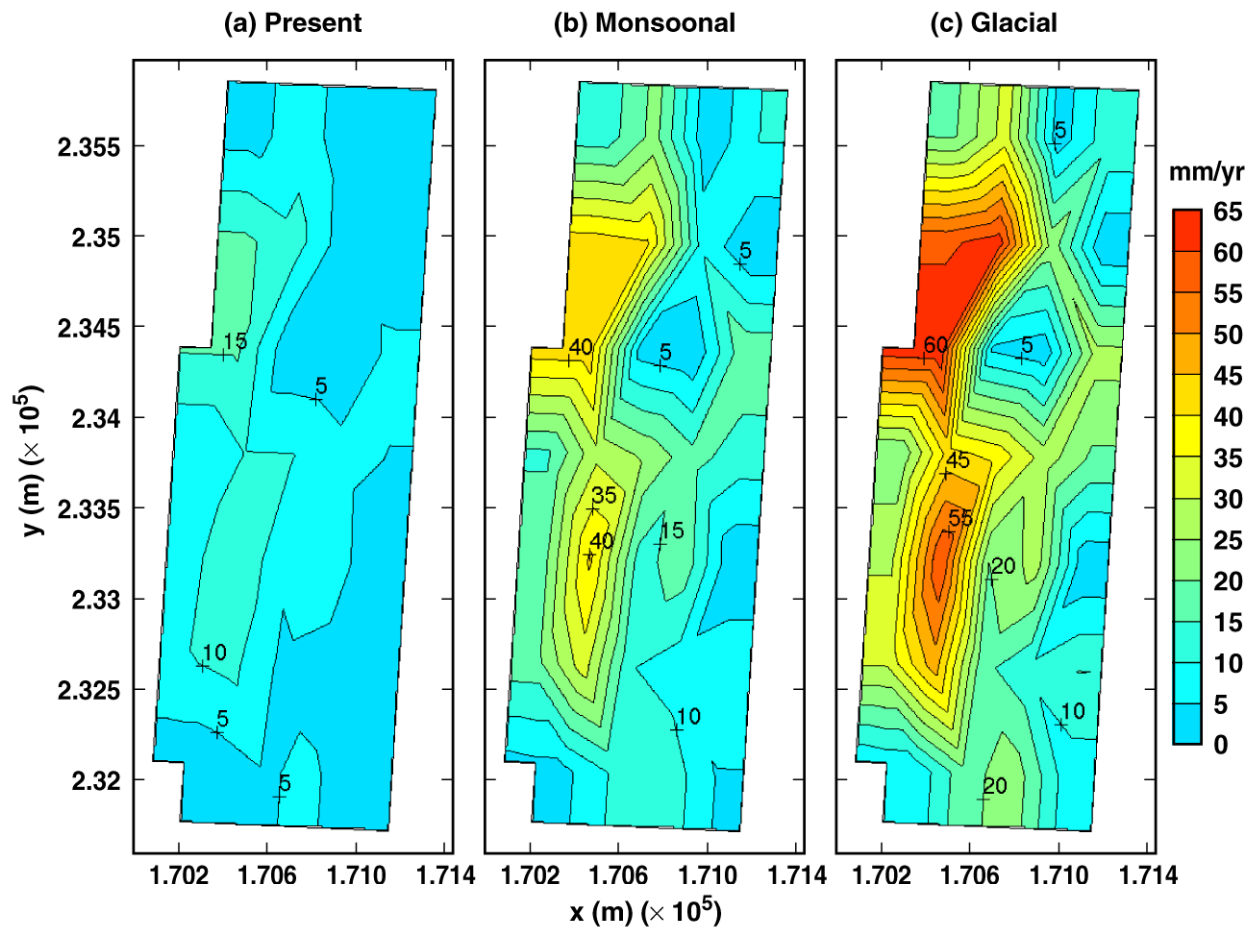
TB\_AMR\_T&RHwp\_13-17\_all

Figure 6-46. Temperature and relative humidity on the WP surface for the mean infiltration-flux backfill case is plotted at the geographical center of the repository for the 4 different WP types and 8 different WP locations (along the drift) considered in the MSTHM (see Figure 4-1 for WP locations)



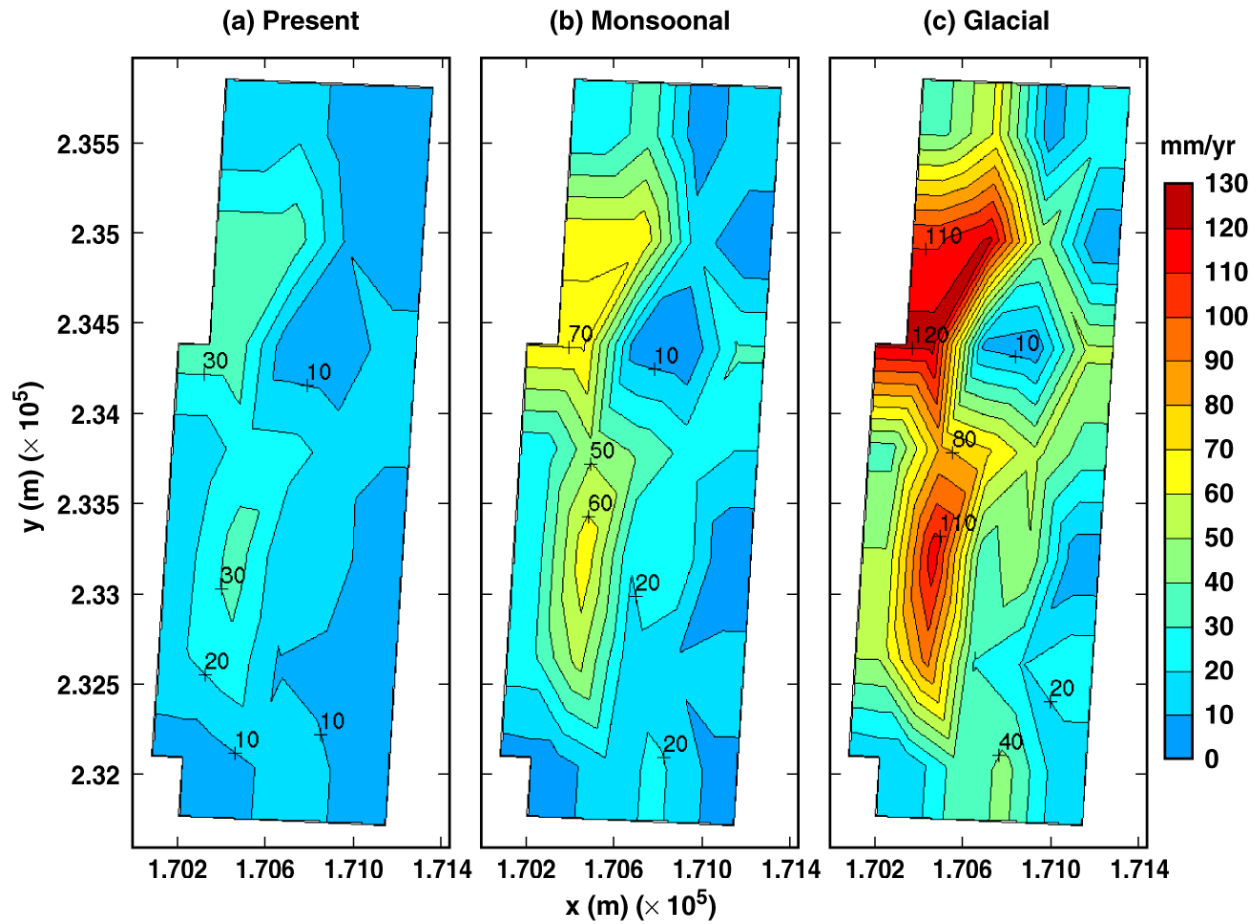
TB\_AMR\_infil\_lower\_p\_m\_g

Figure 6-47. The infiltration-flux distribution for the mean infiltration-flux case is plotted, including the present-day, monsoonal, and glacial climate periods



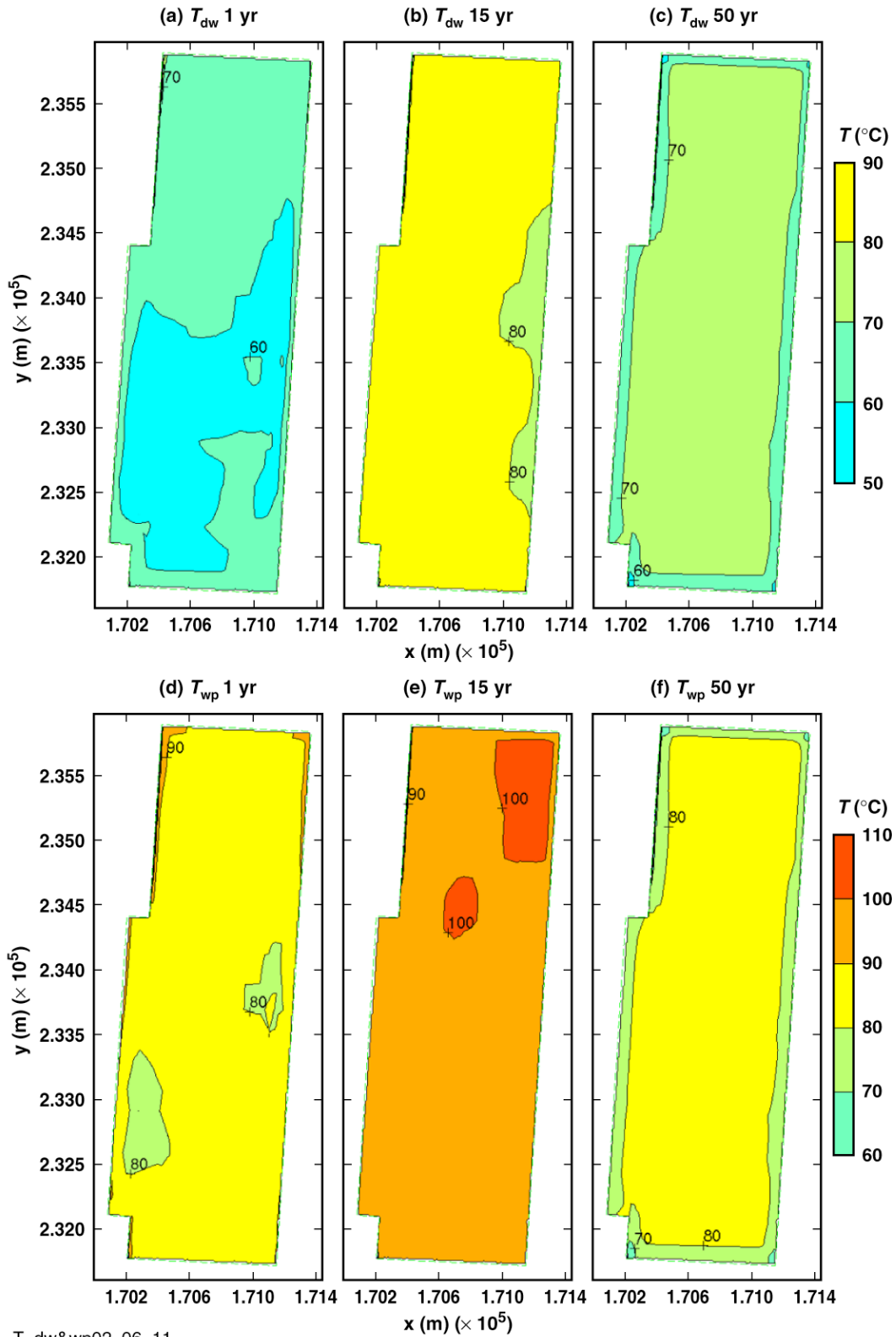
TB\_AMR\_infil\_medium\_p\_m\_g

Figure 6-48. The infiltration-flux distribution for the high infiltration-flux case is plotted, including the present-day, monsoonal, and glacial climate periods



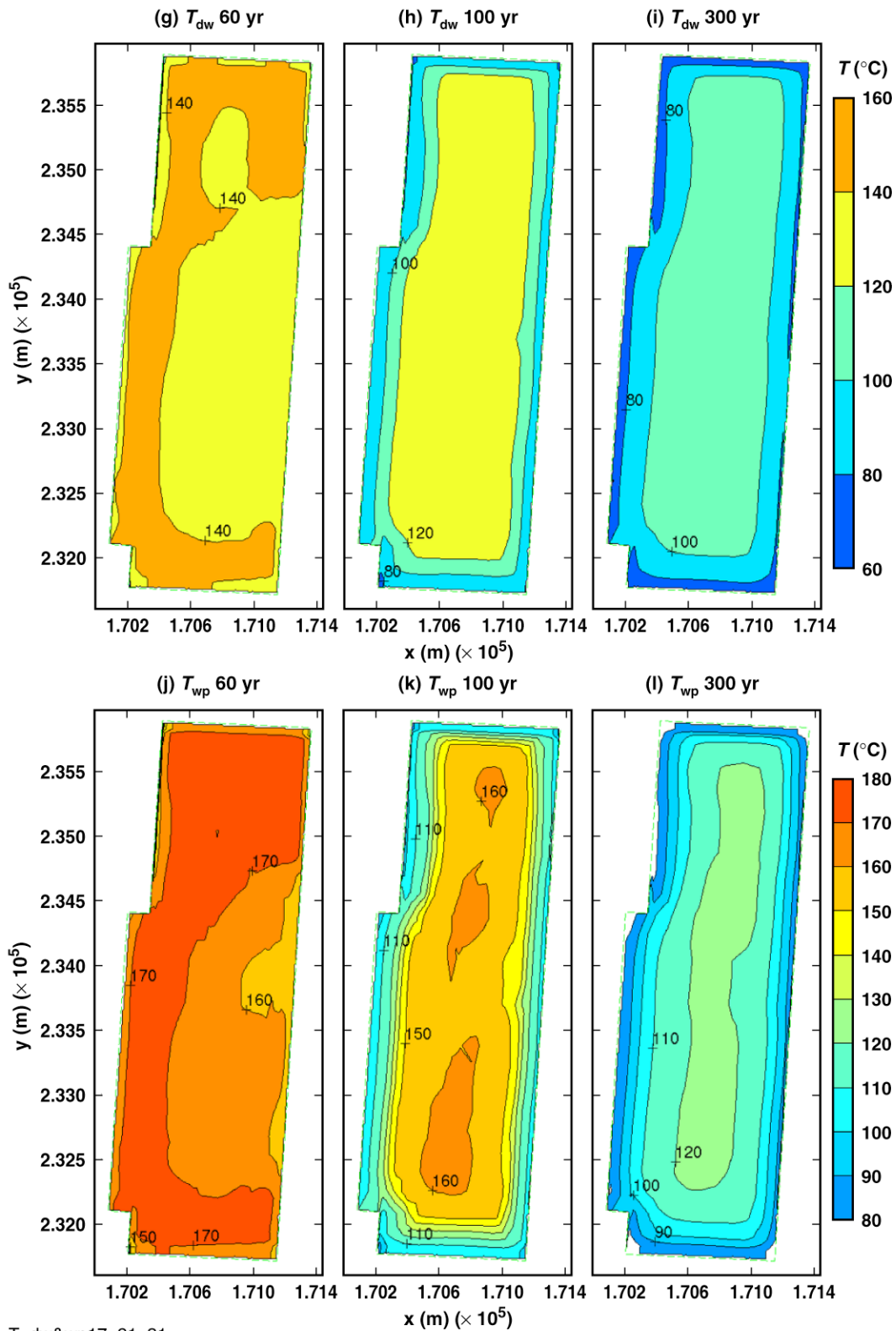
TB\_AMR\_infil\_upper\_p\_m\_g

Figure 6-49. The infiltration-flux distribution for the low infiltration-flux case is plotted, including the present-day, monsoonal, and glacial climate periods



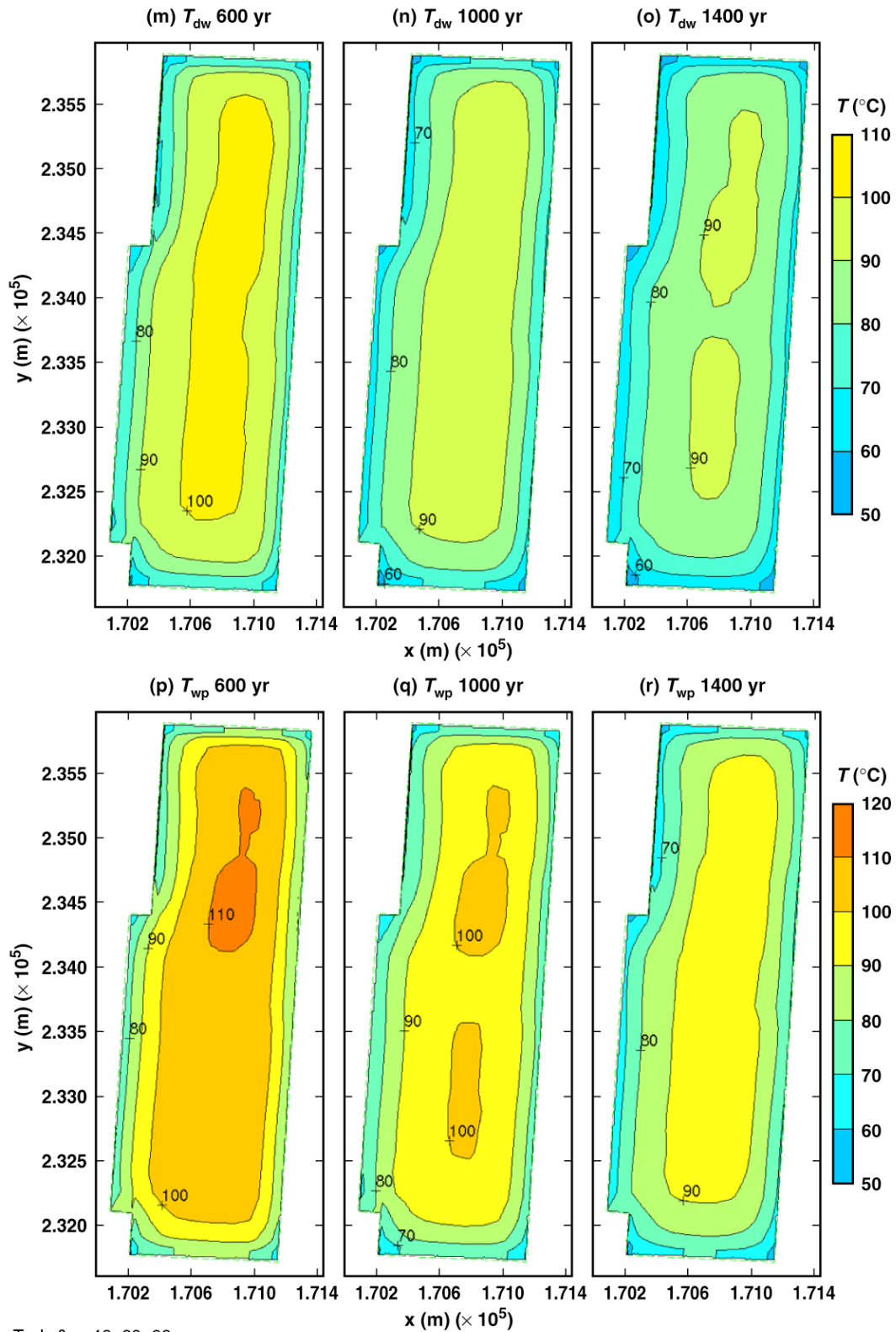
T\_dw&wp02\_06\_11

Figure 6-50. Perimeter-averaged temperature on the drift wall  $T_{dw}$  and temperature on the WP  $T_{wp}$  for a 21-PWR WP for the mean infiltration-flux no-backfill case for the indicated times



T\_dw&wp17\_21\_31

Figure 6-50. Perimeter-averaged temperature on the drift wall  $T_{dw}$  and temperature on the WP  $T_{wp}$  for a 21-PWR WP for the mean infiltration-flux no-backfill case for the indicated times (Continued)



T\_dw&wp46\_60\_66

Figure 6-50. Perimeter-averaged temperature on the drift wall  $T_{dw}$  and temperature on the WP  $T_{wp}$  for a 21-PWR WP for the mean infiltration-flux no-backfill case for the indicated times (Continued)

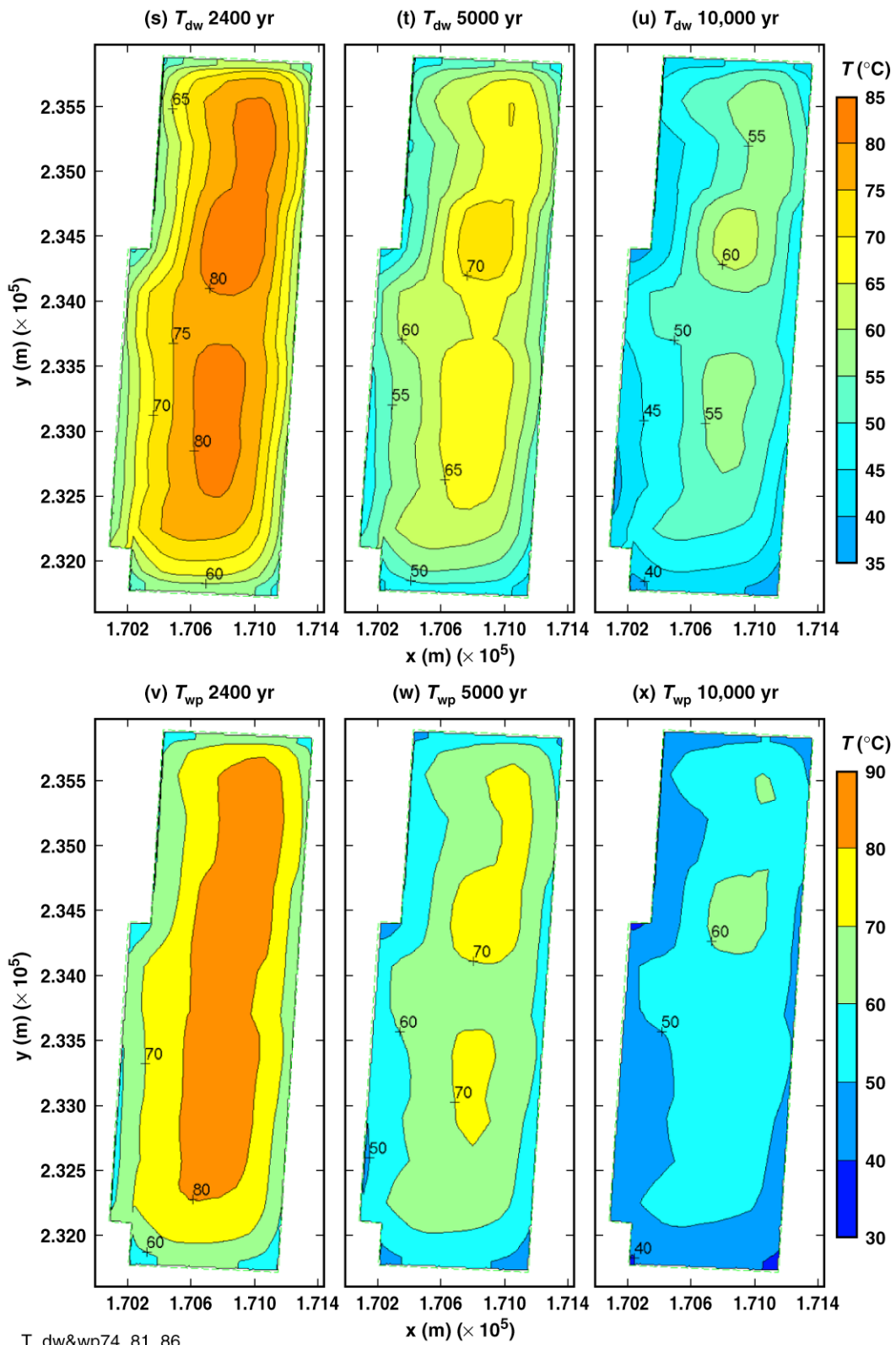
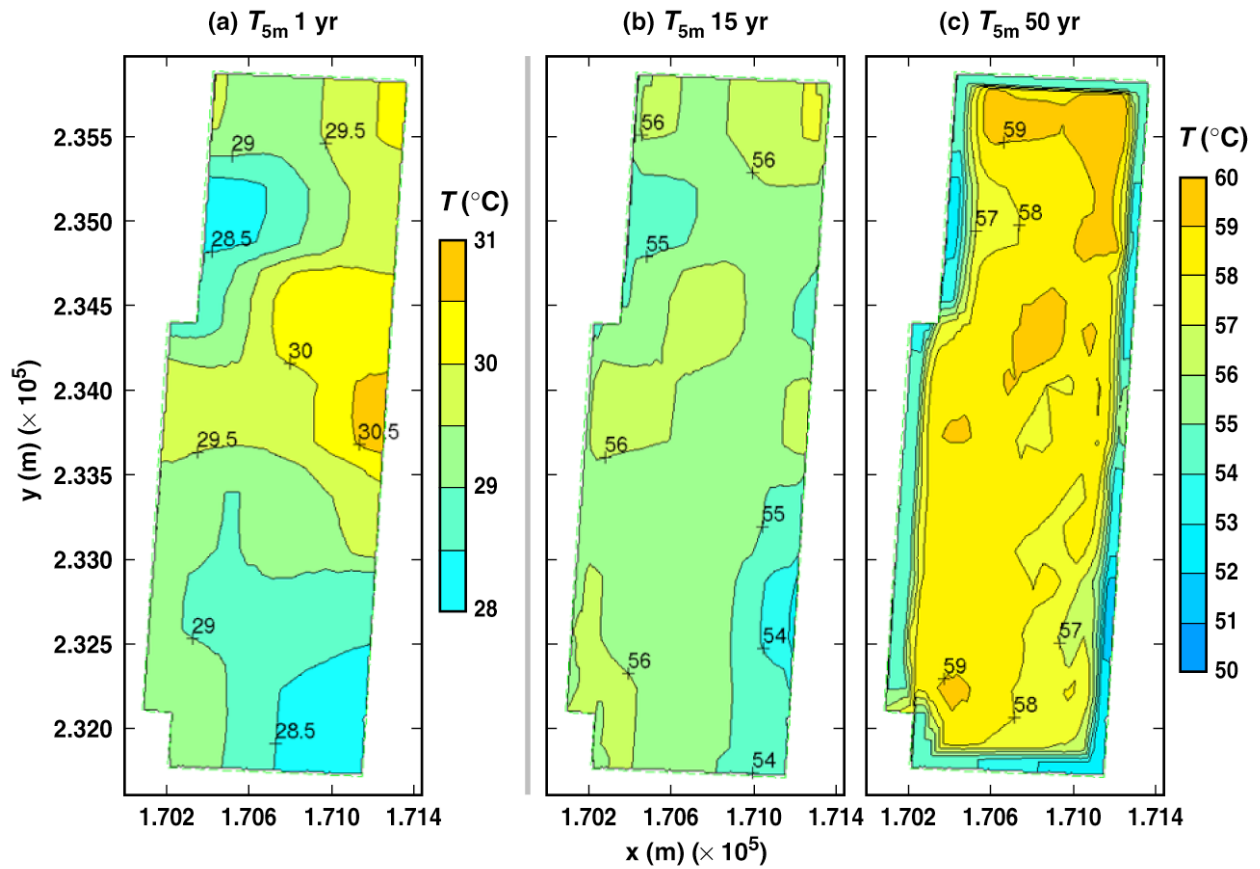
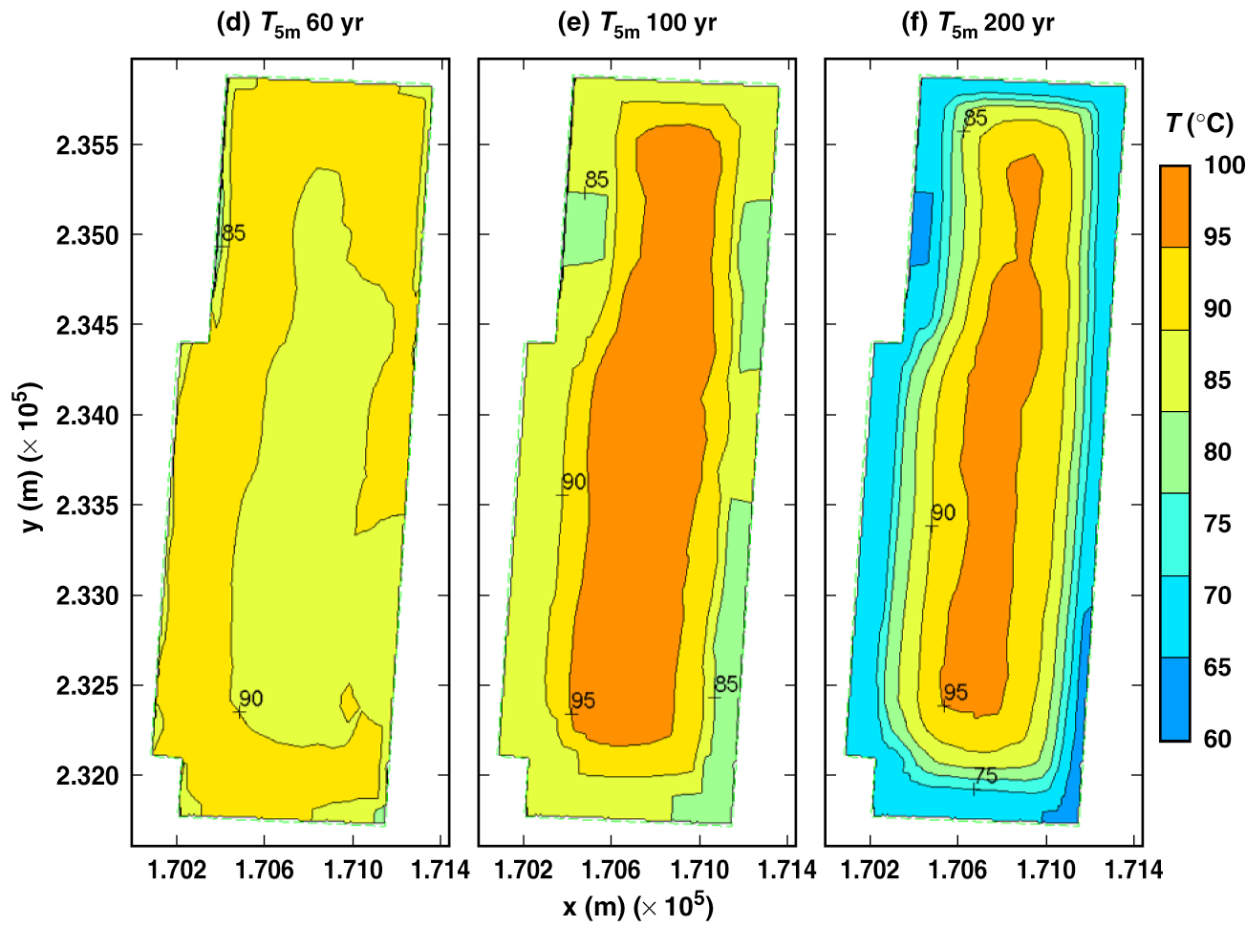


Figure 6-50 . Perimeter-averaged temperature on the drift wall  $T_{dw}$  and temperature on the WP  $T_{wp}$  for a 21-PWR WP for the mean infiltration-flux no-backfill case for the indicated times (Continued)



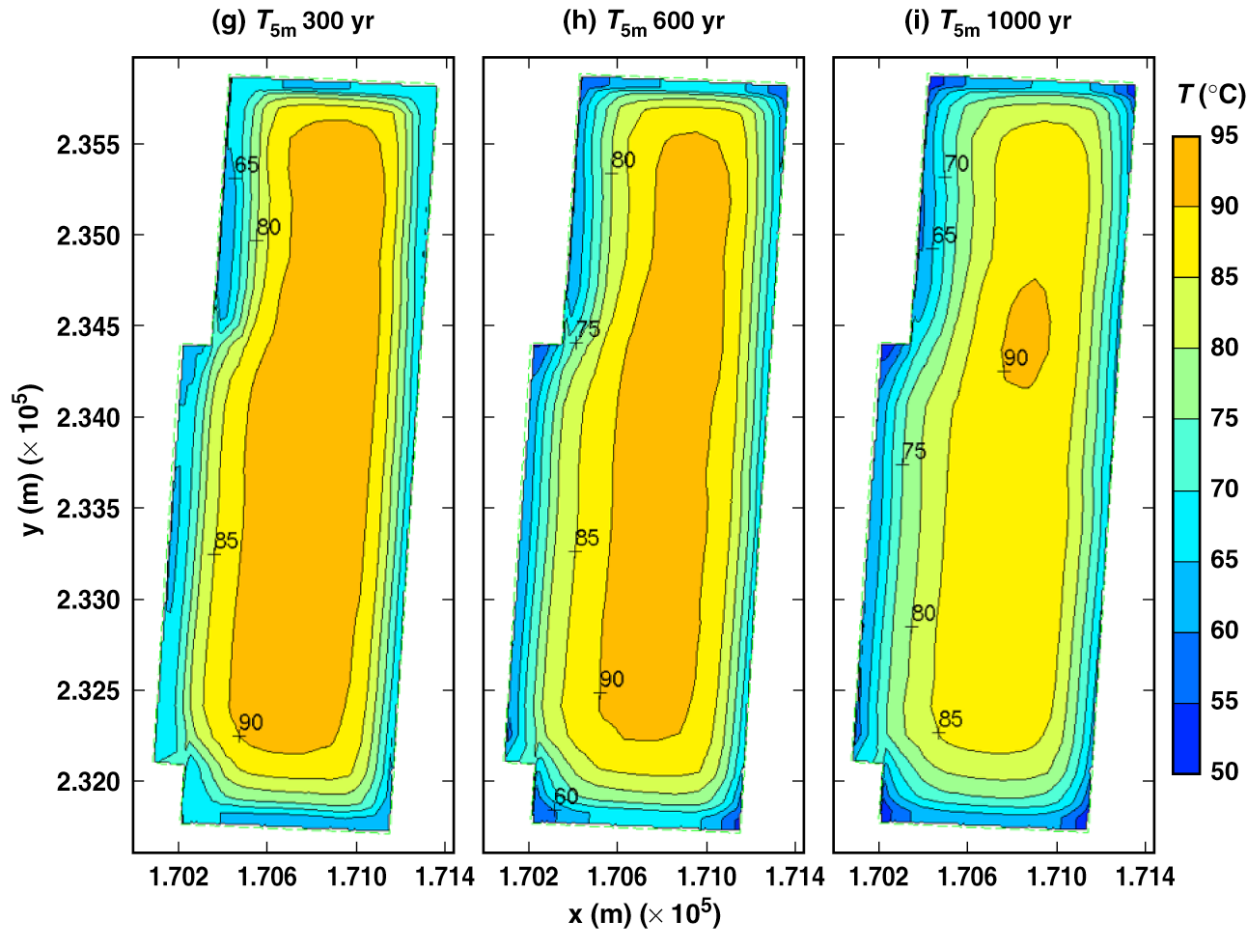
T\_5m02\_06\_11

Figure 6-51. Temperature 5 m above the crown of the drift in the vicinity of a 21-PWR WP for the mean infiltration-flux no-backfill case for the indicated times



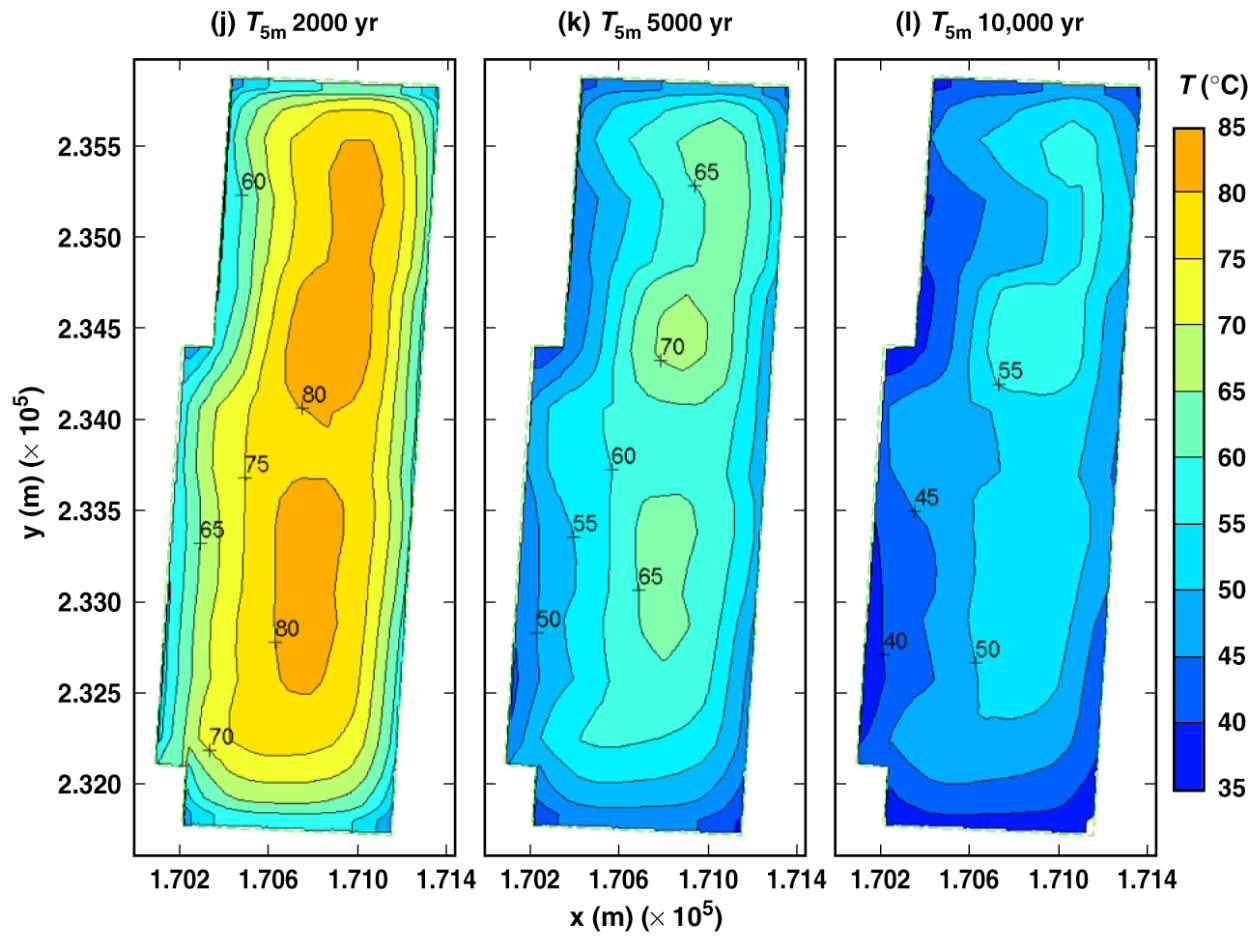
T\_5m17\_21\_26

Figure 6-51. Temperature 5 m above the crown of the drift in the vicinity of a 21-PWR WP for the mean infiltration-flux no-backfill case for the indicated times (Continued)



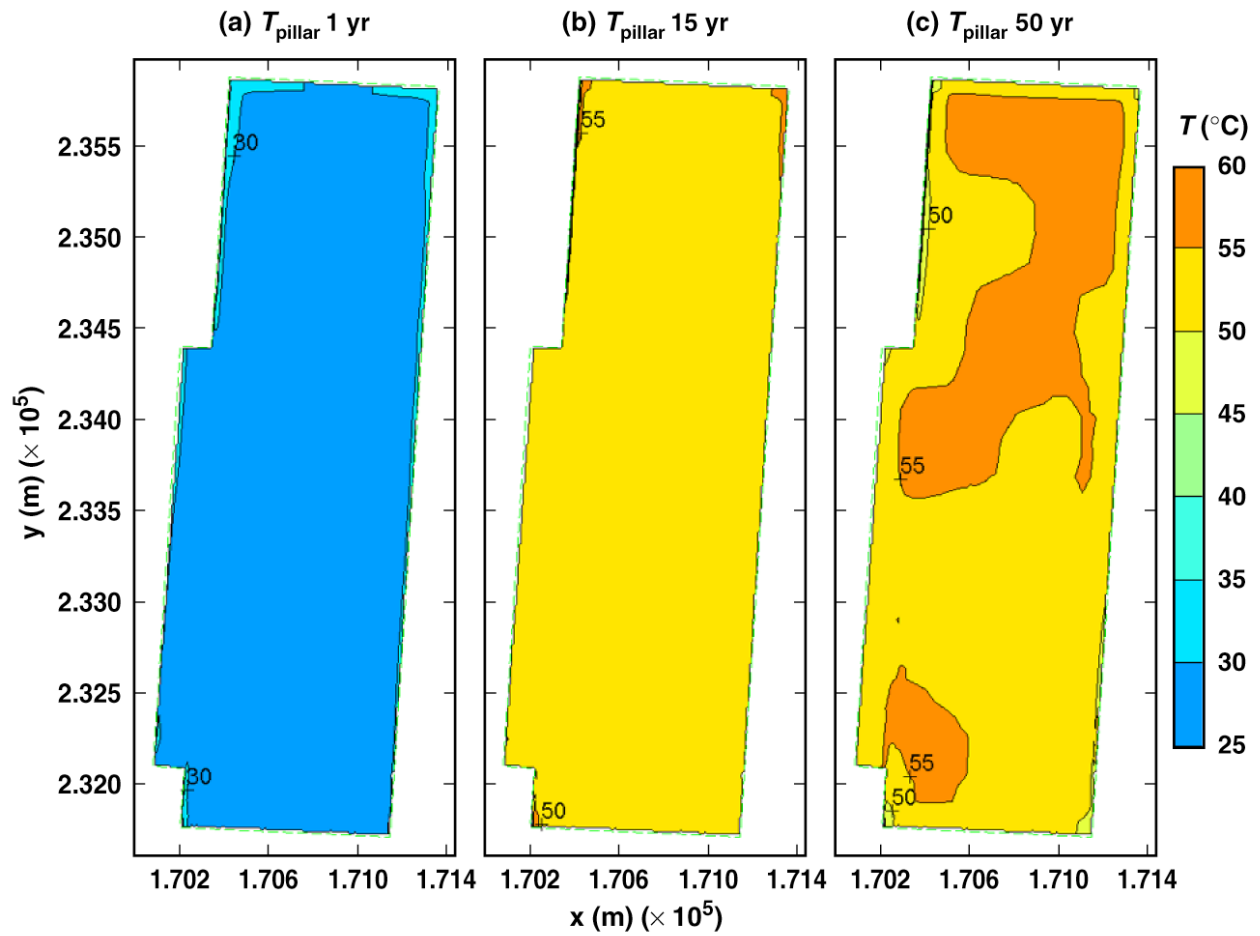
T\_5m31\_46\_60

Figure 6-51. Temperature 5 m above the crown of the drift in the vicinity of a 21-PWR WP for the mean infiltration-flux no-backfill case for the indicated times (Continued)



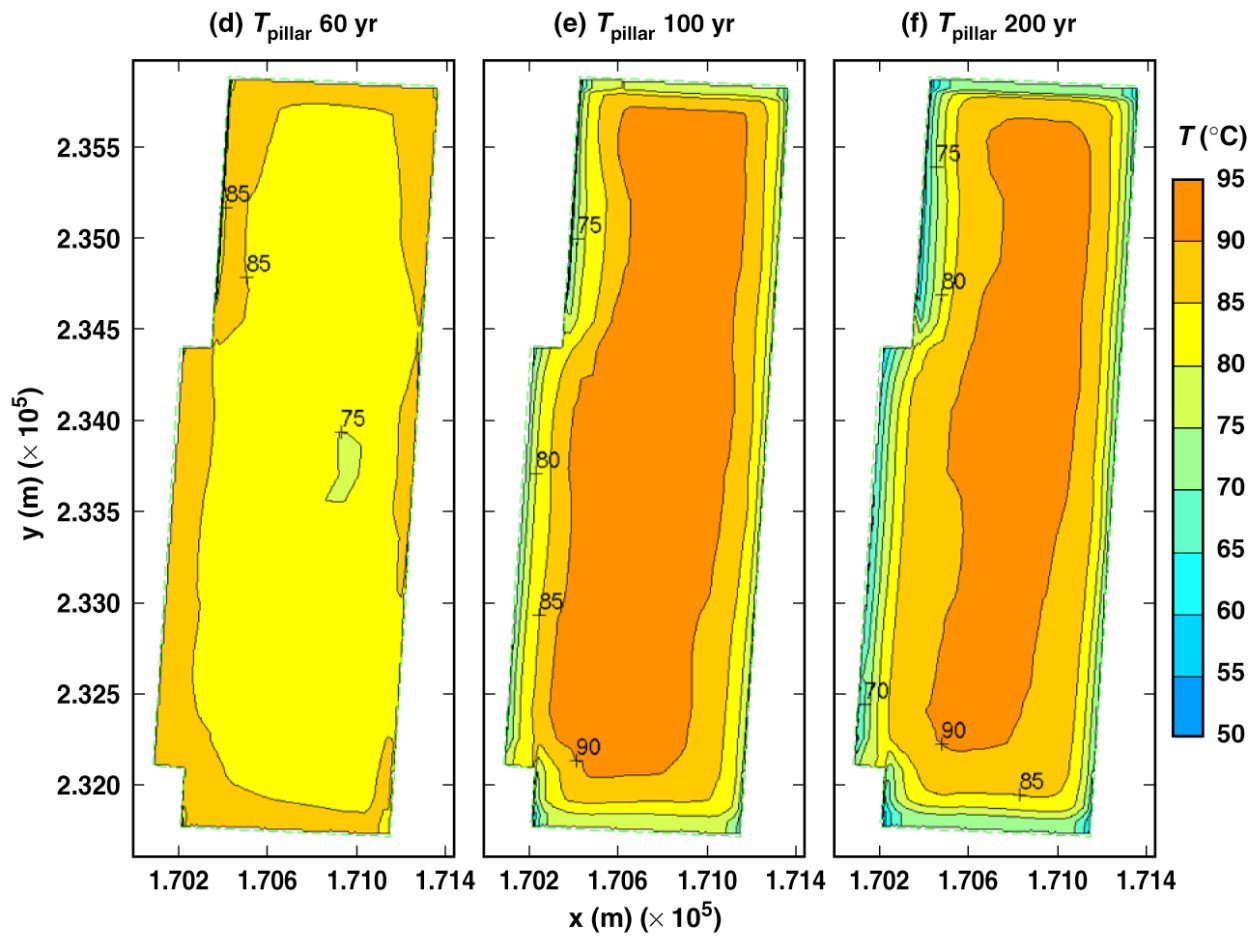
T\_5m72\_81\_86

Figure 6-51. Temperature 5 m above the crown of the drift in the vicinity of a 21-PWR WP for the mean infiltration-flux no-backfill case for the indicated times (Continued)



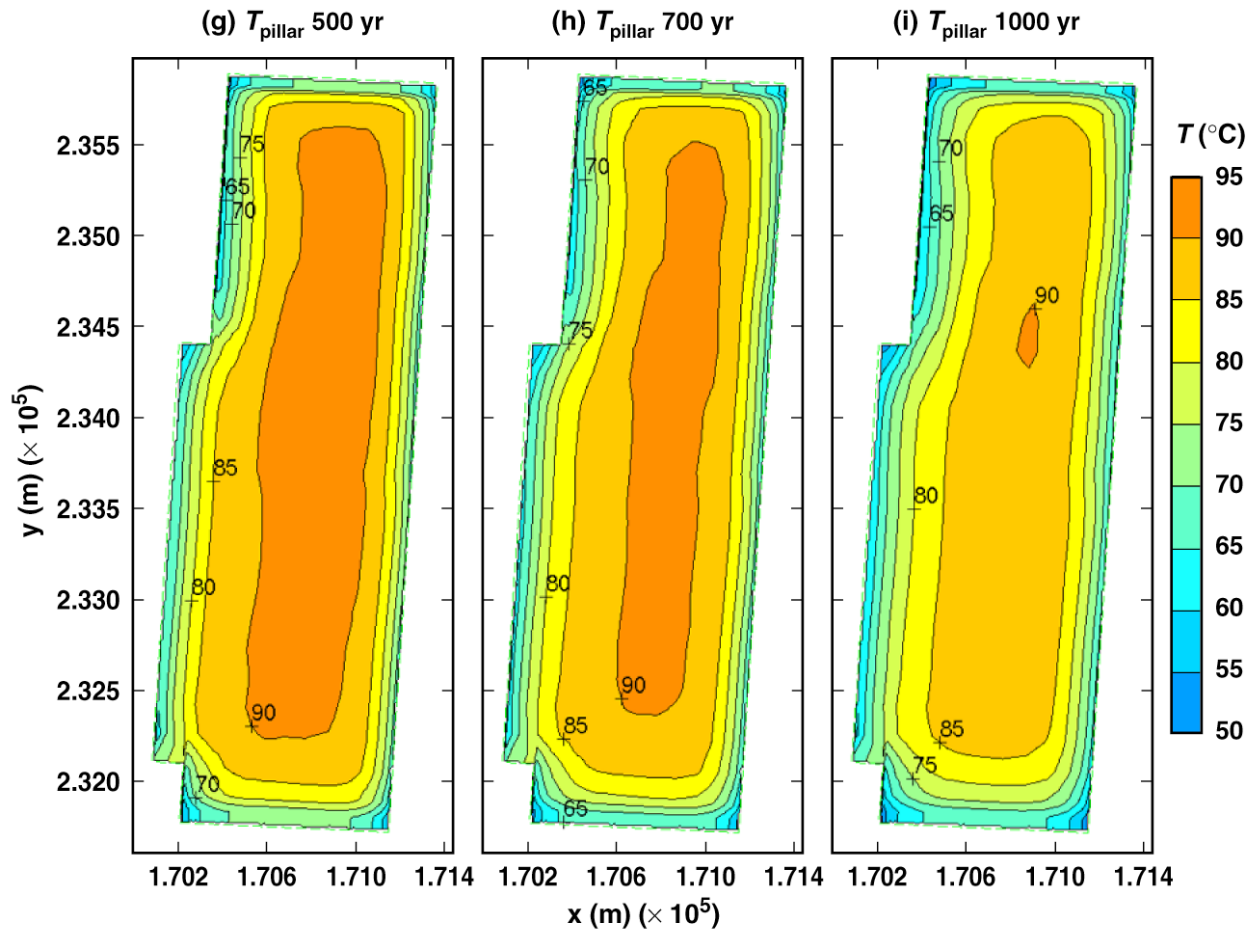
T\_pillar02\_06\_11

Figure 6-52. Temperature 7.39 m laterally away from the springline of the drift in the vicinity of a 21-PWR WP for the mean infiltration-flux no-backfill case for the indicated times. This location is almost exactly one-quarter of the distance in toward the midline of the pillar. This temperature is called  $T_{\text{pillar}}$ .



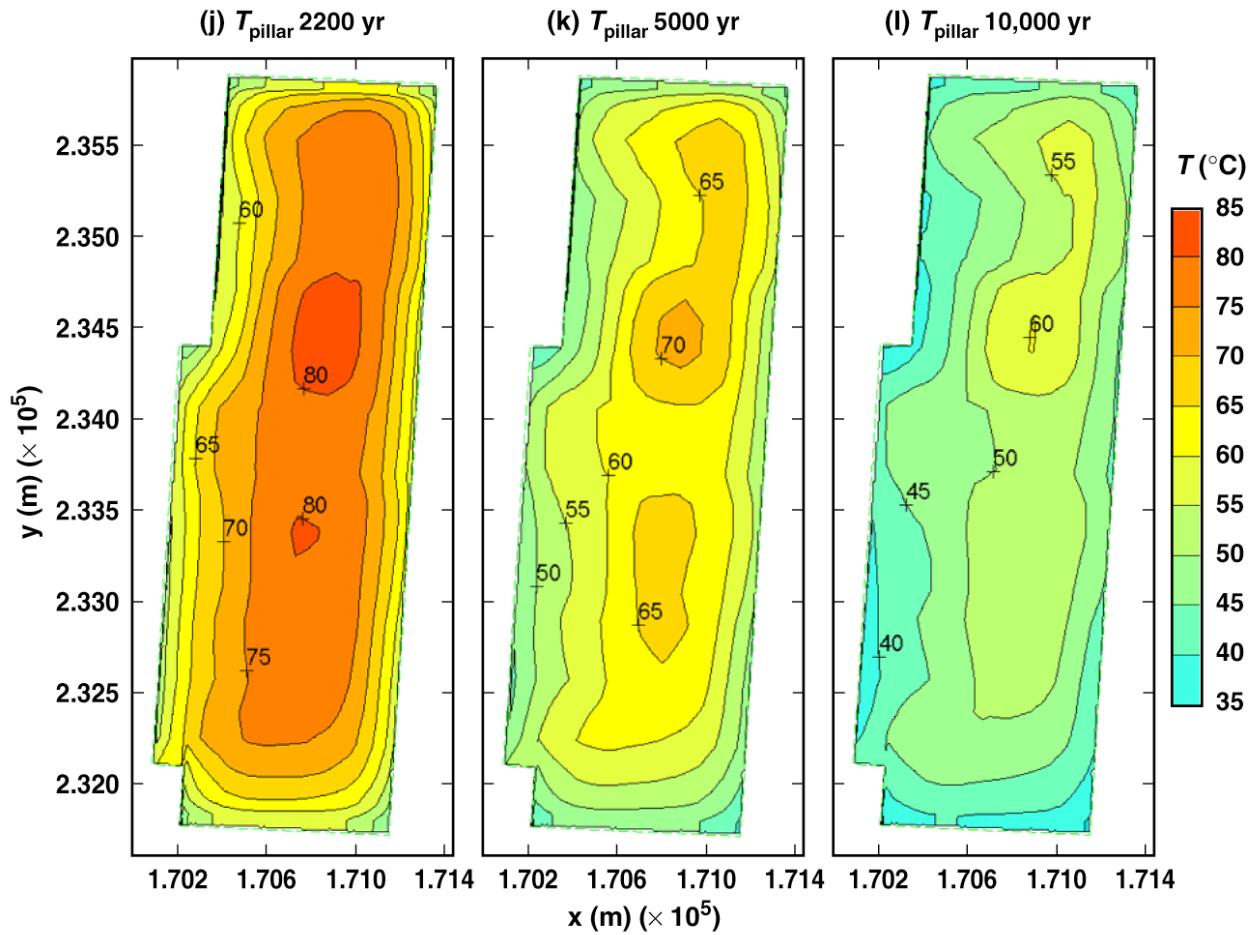
T\_pillar17\_21\_26

Figure 6-52. Temperature 7.39 m laterally away from the springline of the drift in the vicinity of a 21-PWR WP for the mean infiltration-flux no-backfill case for the indicated times. This location is almost exactly one-quarter of the distance in toward the midline of the pillar. This temperature is called  $T_{pillar}$ . (Continued)

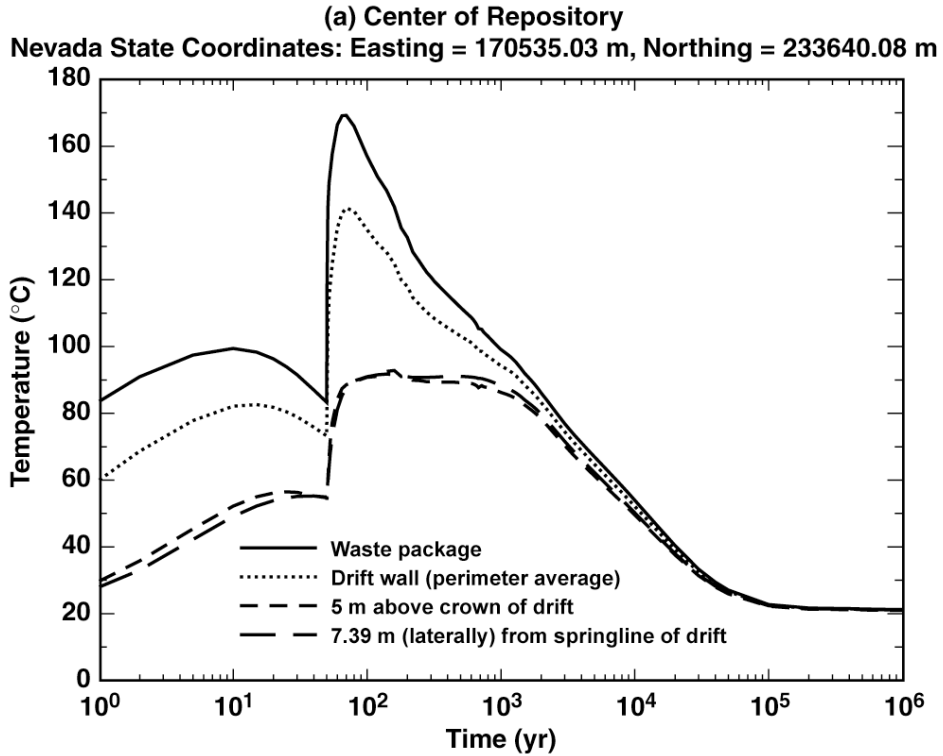


T\_pillar41\_51\_60

Figure 6-52. Temperature 7.39 m laterally away from the springline of the drift in the vicinity of a 21-PWR WP for the mean infiltration-flux no-backfill case for the indicated times. This location is almost exactly one-quarter of the distance in toward the midline of the pillar. This temperature is called  $T_{\text{pillar}}$ . (Continued)

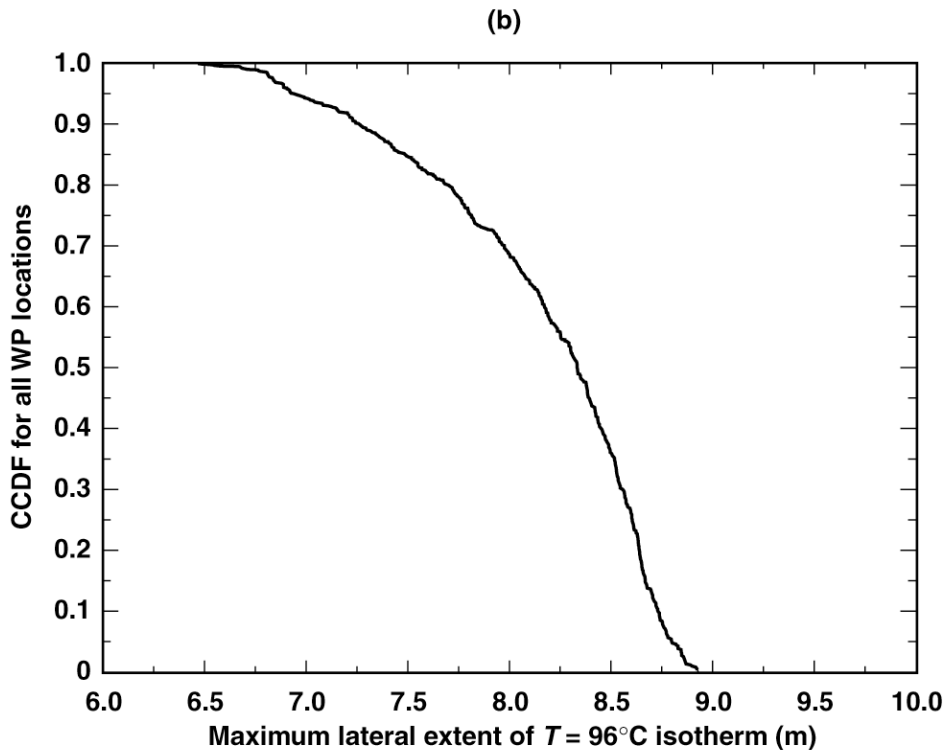
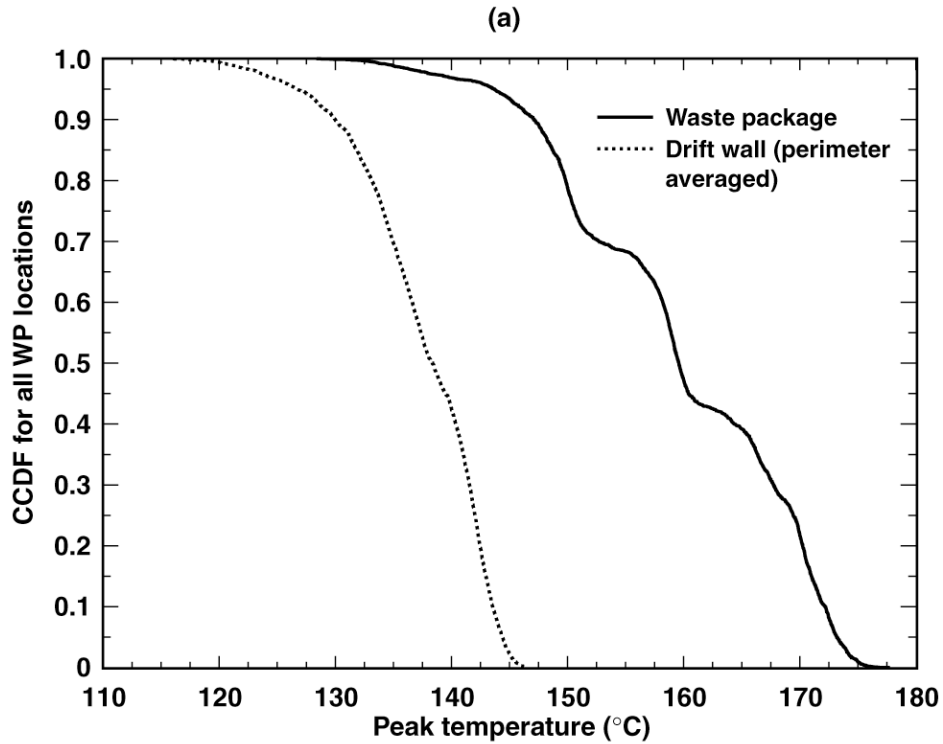


T\_pillar73\_81\_86  
 Figure 6-52. Temperature 7.39 m laterally away from the springline of the drift in the vicinity of a 21-PWR WP for the mean infiltration-flux no-backfill case for the indicated times. This location is almost exactly one-quarter of the distance in toward the midline of the pillar. This temperature is called  $T_{\text{pillar}}$ . (Continued)



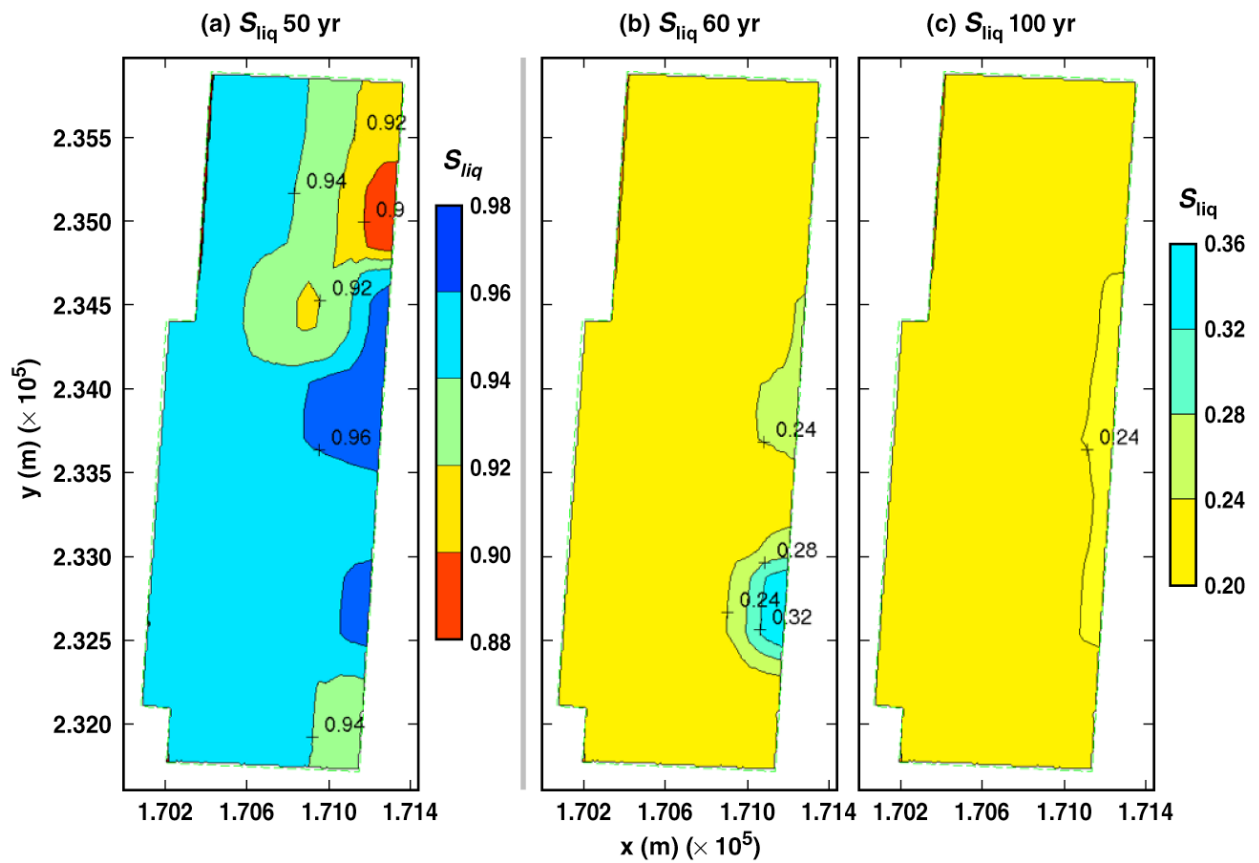
Tall\_16\_16-24\_16

Figure 6-53. Temperature history at the indicated locations at (a) the geographical center of the repository and (b) a location 27.5 m from the eastern edge of the repository. The temperatures occur in the vicinity of a 21-PWR WP for the mean infiltration-flux no-backfill case for the indicated times.



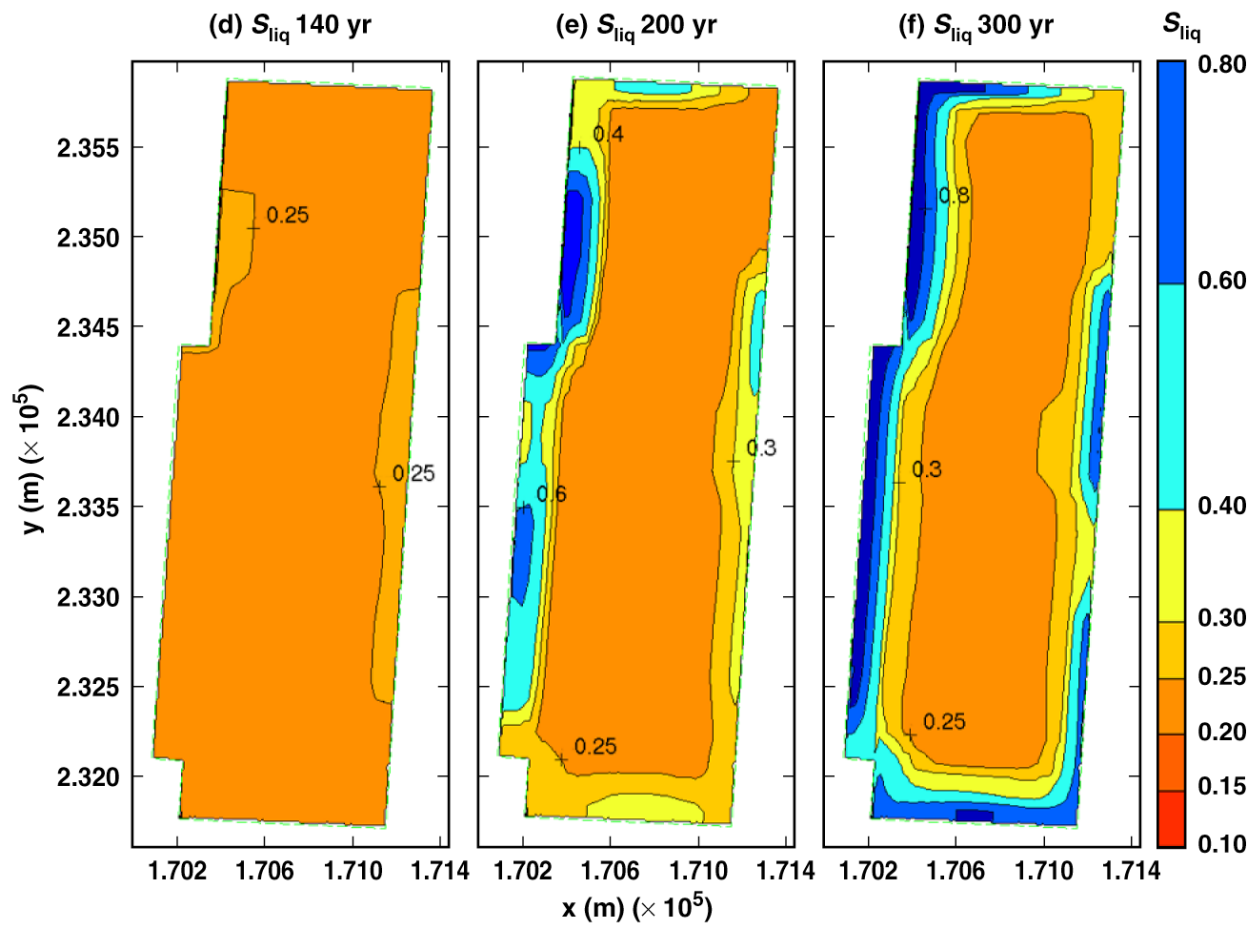
CCDF\_Tpeak\_T=96C

Figure 6-54. (a) The complementary cumulative distribution function (CCDF) for the peak temperature on waste packages and for the peak perimeter-averaged drift-wall temperature is plotted for the mean infiltration-flux no-backfill case. (b) The CCDF of the maximum lateral extent of the boiling point ( $T = 96^{\circ}\text{C}$ ) is plotted for the mean infiltration-flux case.



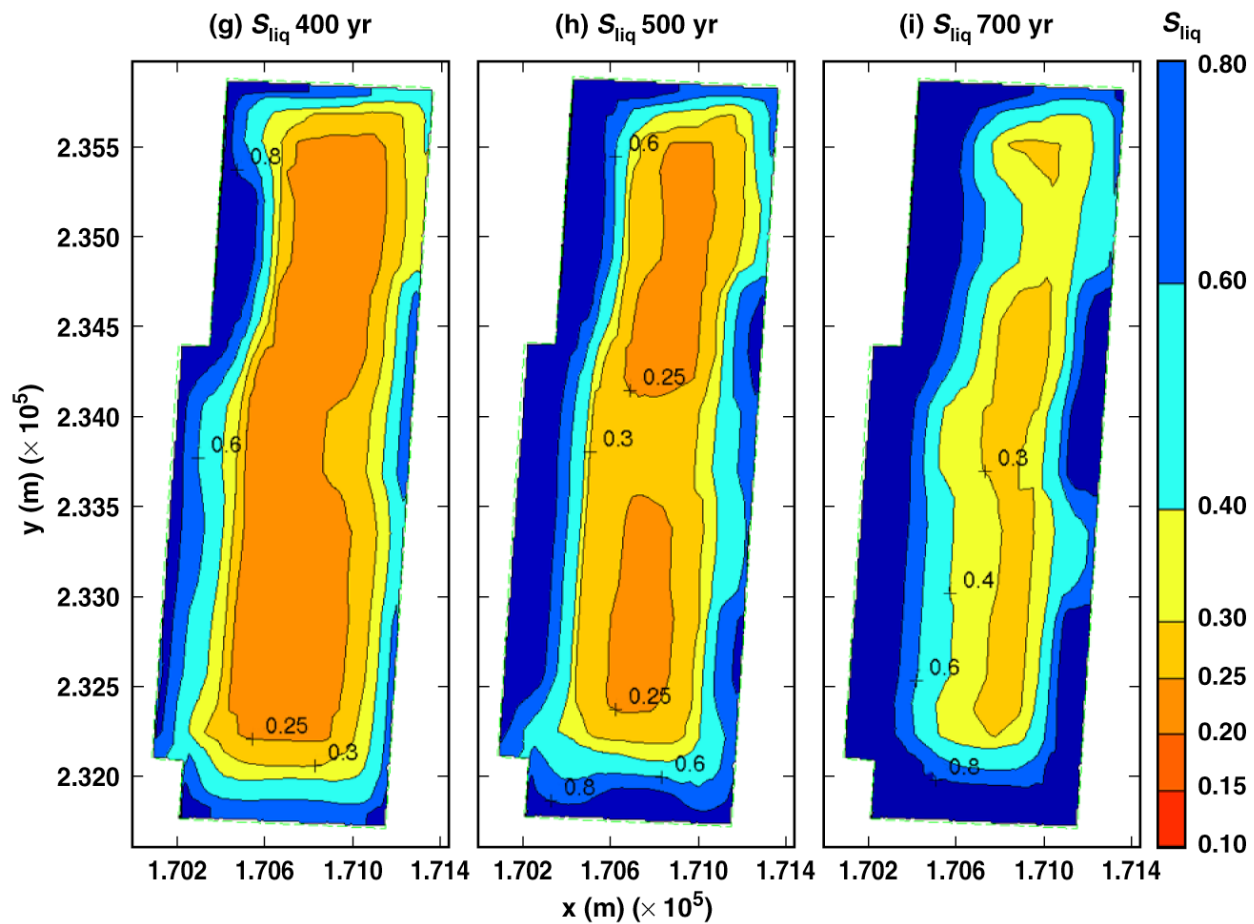
Sliq11\_17\_21

Figure 6-55. Liquid-phase saturation  $S_{liq}$  averaged around the perimeter of the drift wall in the vicinity of a 21-PWR WP for the mean infiltration-flux no-backfill case for the indicated times



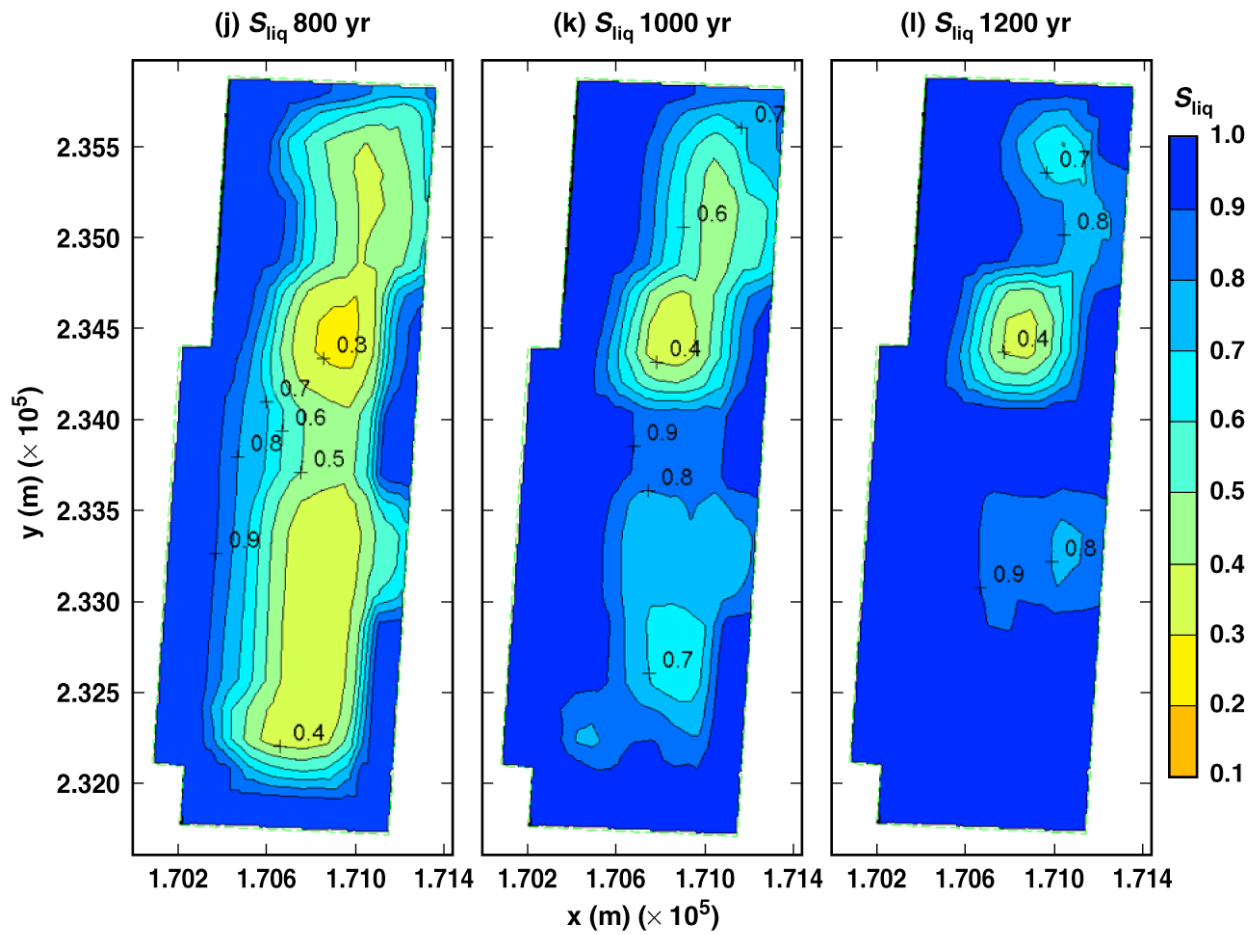
Sliq23\_26\_31

Figure 6-55. Liquid-phase saturation  $S_{liq}$  averaged around the perimeter of the drift wall in the vicinity of a 21-PWR WP for the mean infiltration-flux no-backfill case for the indicated times (Continued)



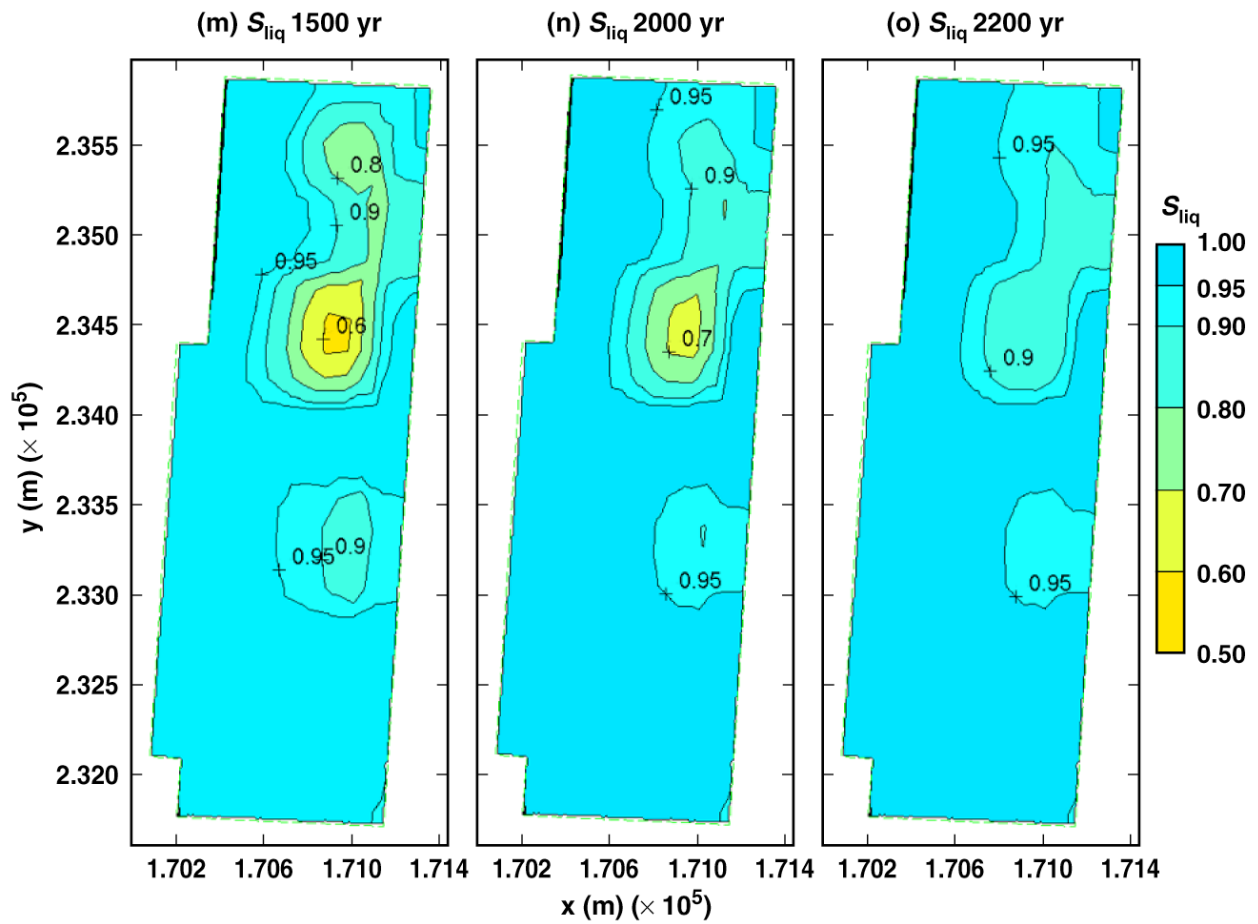
Sliq36\_41\_51

Figure 6-55. Liquid-phase saturation  $S_{liq}$  averaged around the perimeter of the drift wall in the vicinity of a 21-PWR WP for the mean infiltration-flux no-backfill case for the indicated times (Continued)



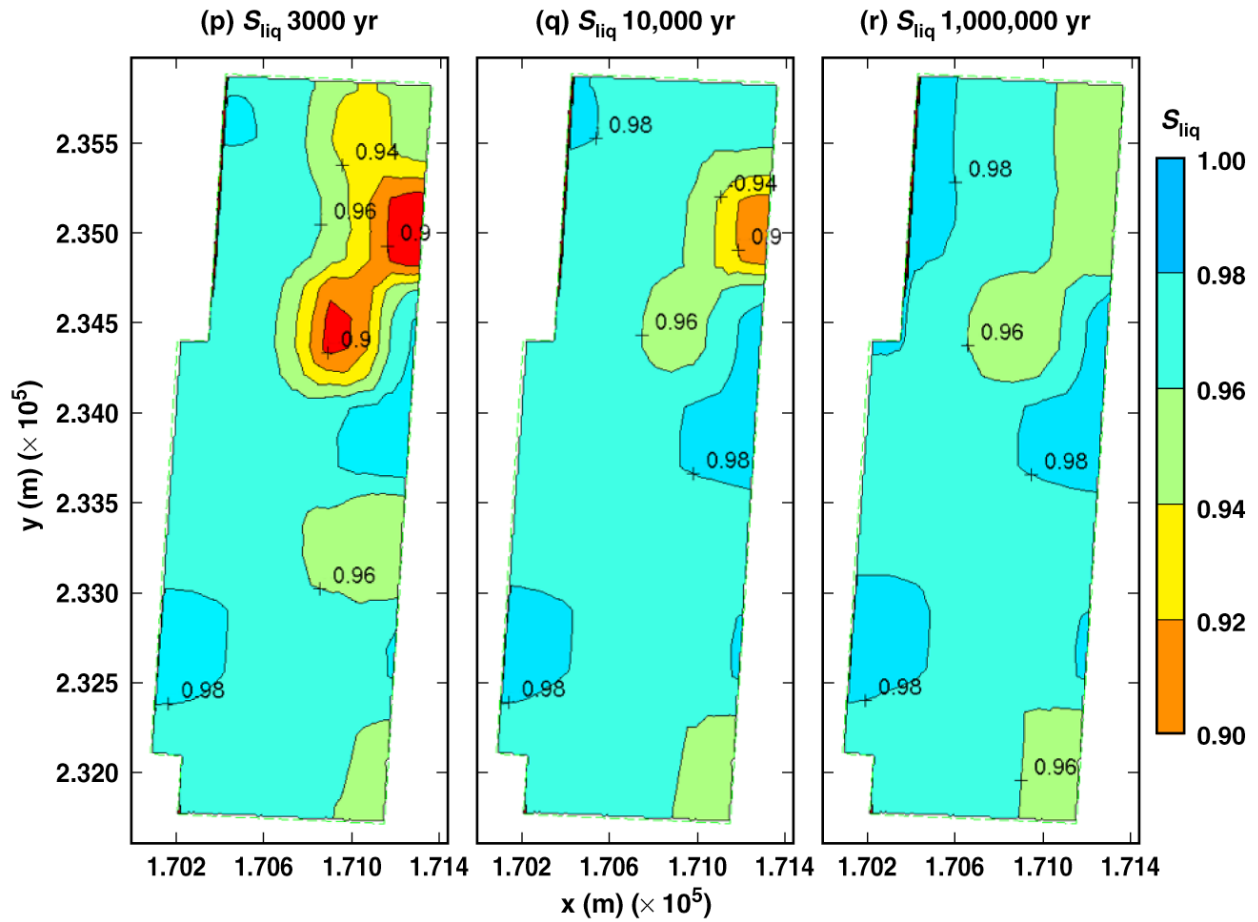
Sliq56\_60\_64

Figure 6-55. Liquid-phase saturation  $S_{liq}$  averaged around the perimeter of the drift wall in the vicinity of a 21-PWR WP for the mean infiltration-flux no-backfill case for the indicated times (Continued)



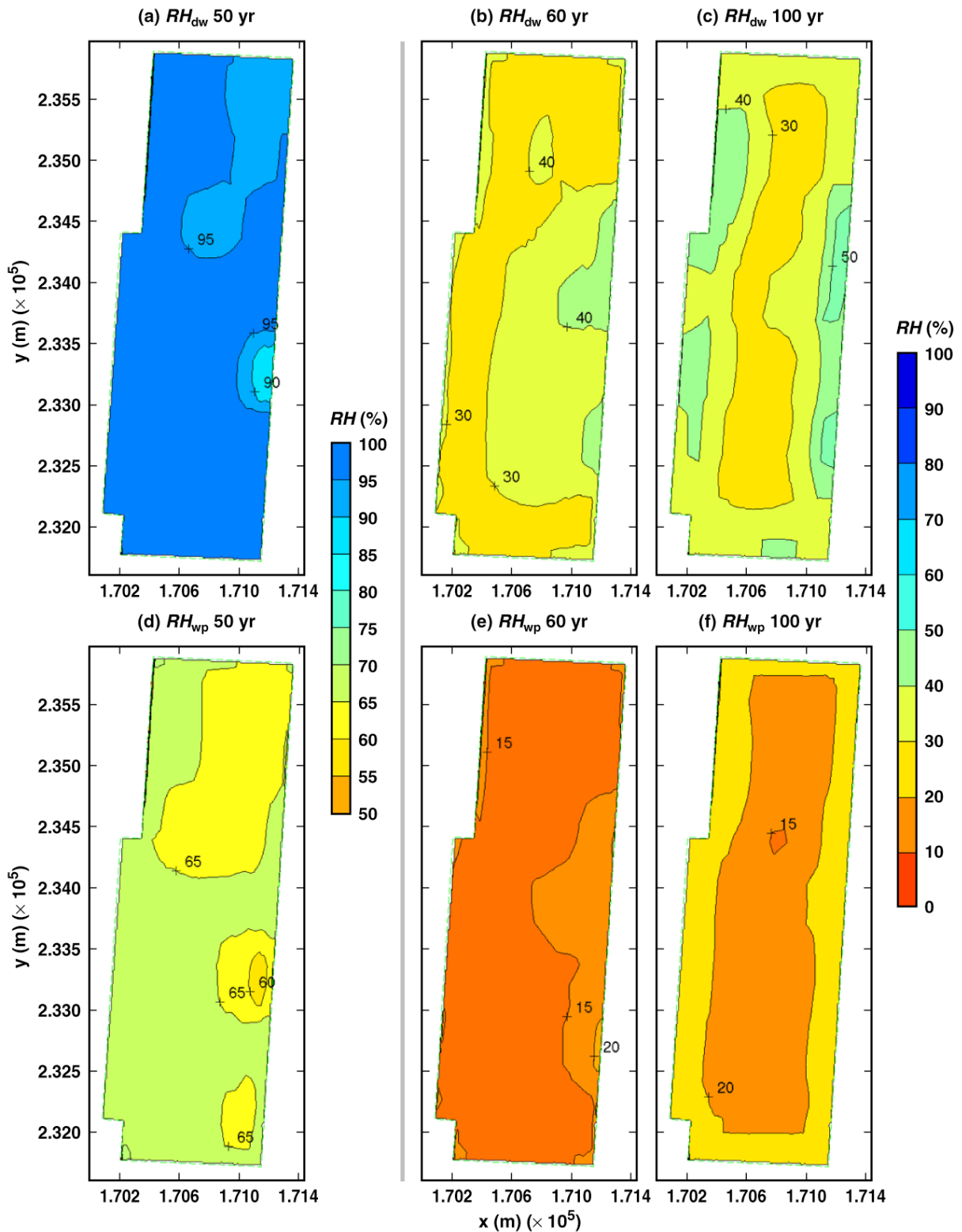
Sliq67\_72\_73

Figure 6-55. Liquid-phase saturation  $S_{liq}$  averaged around the perimeter of the drift wall in the vicinity of a 21-PWR WP for the mean infiltration-flux no-backfill case for the indicated times (Continued)



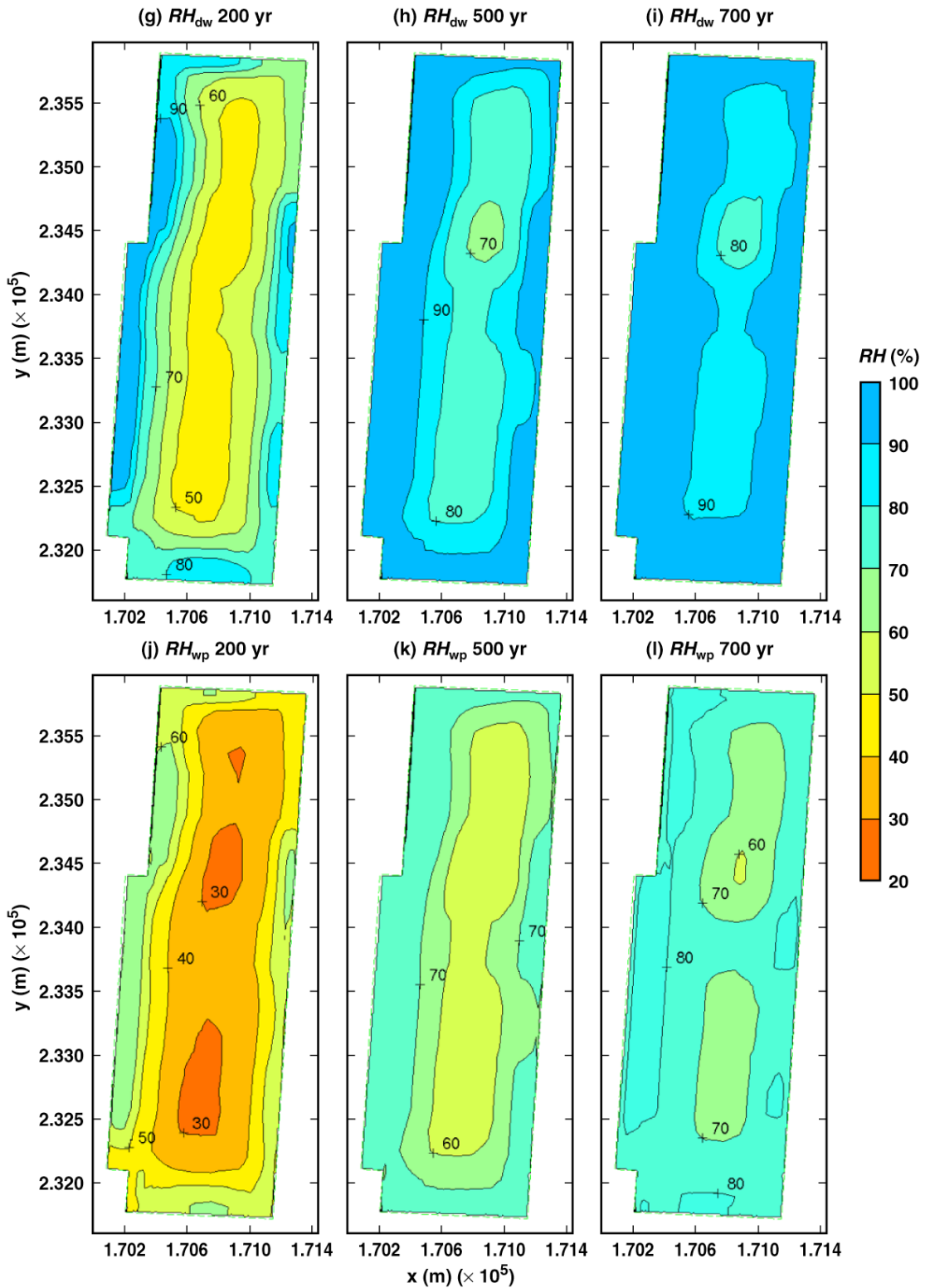
Sliq77\_86\_99  
Figure 6-55.

Liquid-phase saturation  $S_{liq}$  averaged around the perimeter of the drift wall in the vicinity of a 21-PWR WP for the mean infiltration-flux no-backfill case for the indicated times (Continued)



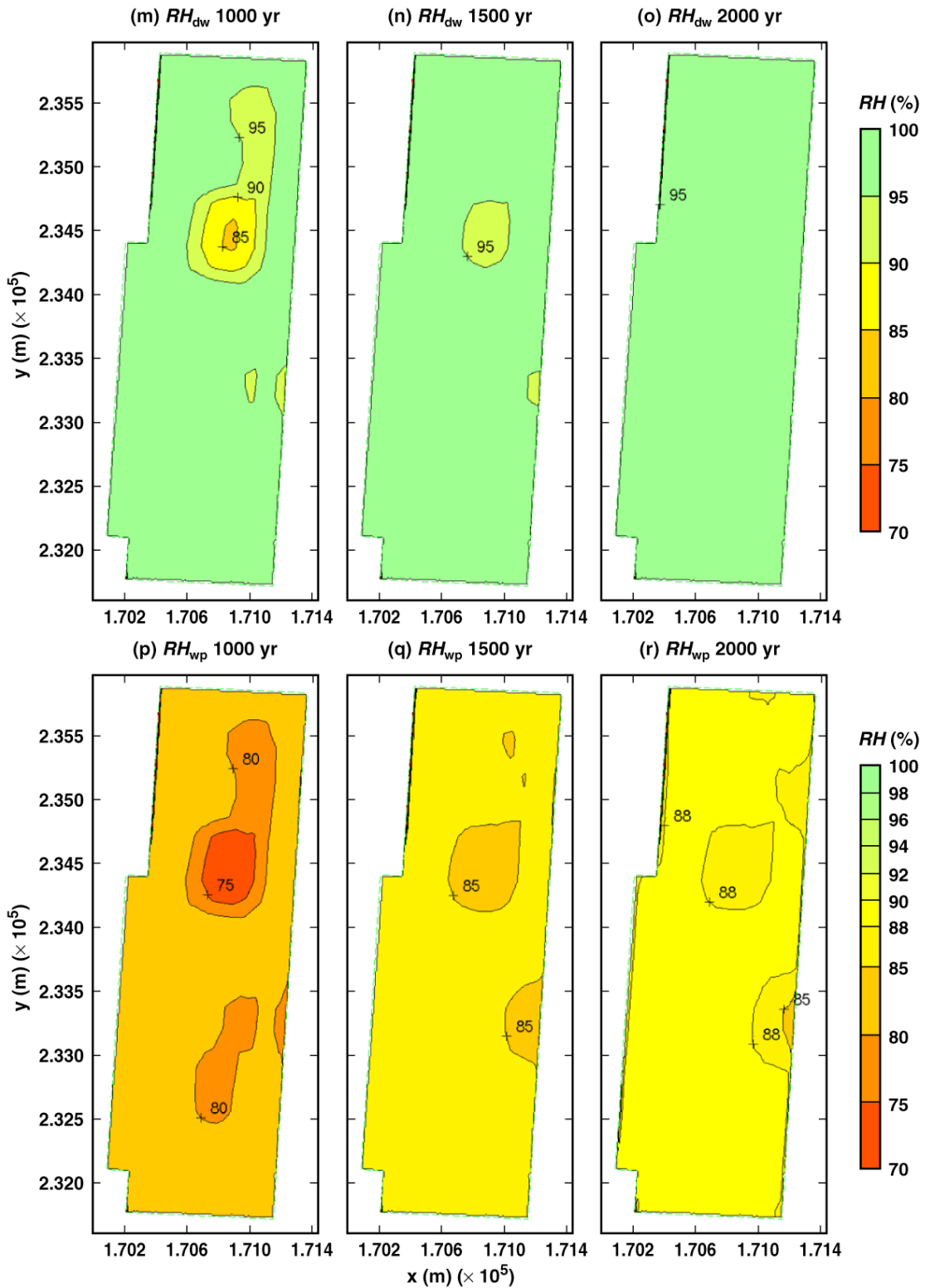
RH\_dw&wp11\_17\_21

Figure 6-56. Perimeter-averaged drift-wall relative humidity  $RH_{dw}$  and relative humidity on the surface of the WP  $RH_{wp}$  for a 21-PWR WP for the mean infiltration-flux no-backfill case for the indicated times



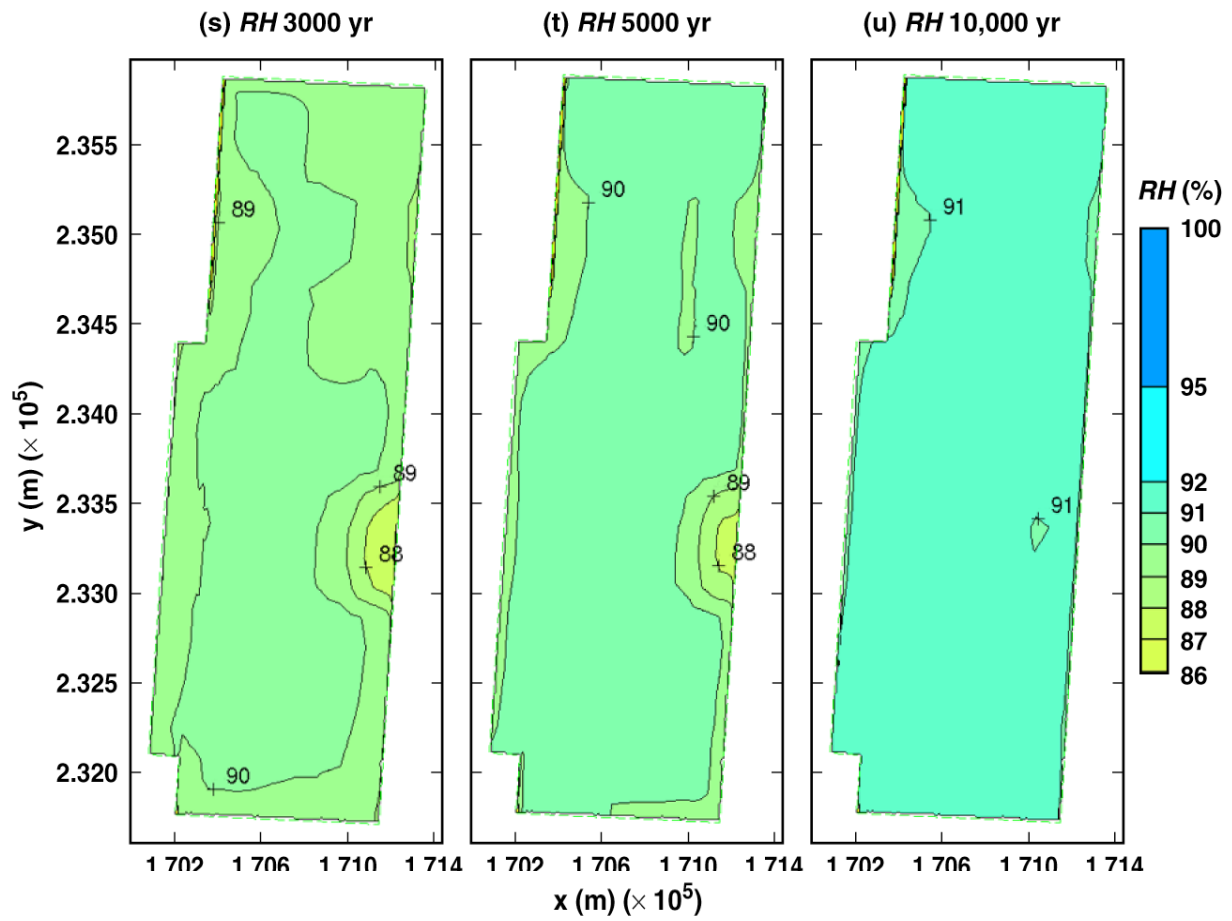
RH\_dw&wp26\_41\_51

Figure 6-56. Perimeter-averaged drift-wall relative humidity  $RH_{dw}$  and relative humidity on the surface of the WP  $RH_{wp}$  for a 21-PWR WP for the mean infiltration-flux no-backfill case for the indicated times (Continued)



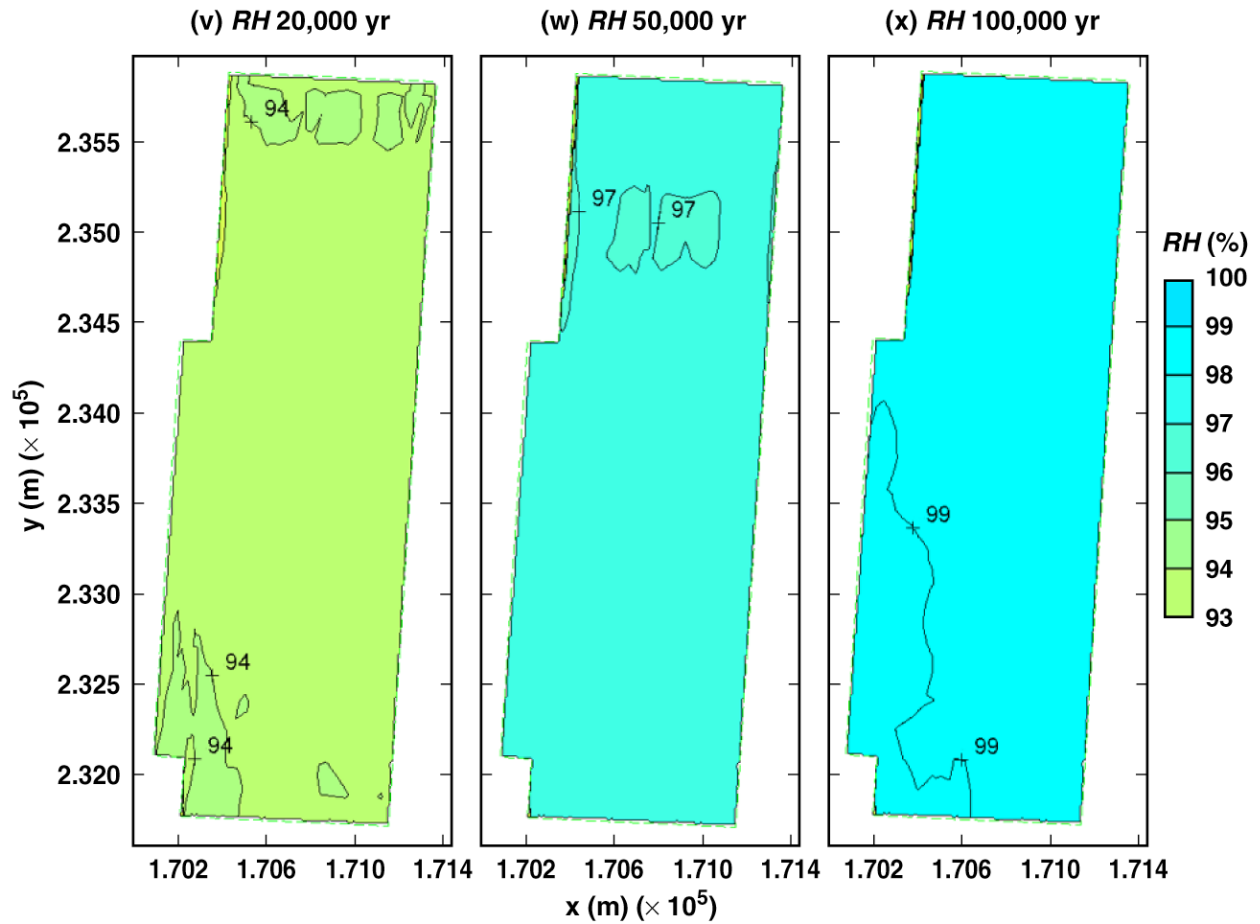
RH\_dw&wp60\_67\_72

Figure 6-56. Perimeter-averaged drift-wall relative humidity  $RH_{dw}$  and relative humidity on the surface of the WP  $RH_{wp}$  for a 21-PWR WP for the mean infiltration-flux no-backfill case for the indicated times (Continued)



RH\_wp77\_81\_86

Figure 6-56. Perimeter-averaged drift-wall relative humidity  $RH_{dw}$  and relative humidity on the surface of the WP  $RH_{wp}$  for a 21-PWR WP for the mean infiltration-flux no-backfill case for the indicated times (Continued)



RH\_wp88\_91\_92

Figure 6-56. Perimeter-averaged drift-wall relative humidity  $RH_{dw}$  and relative humidity on the surface of the WP  $RH_{wp}$  for a 21-PWR WP for the mean infiltration-flux no-backfill case for the indicated times (Continued)

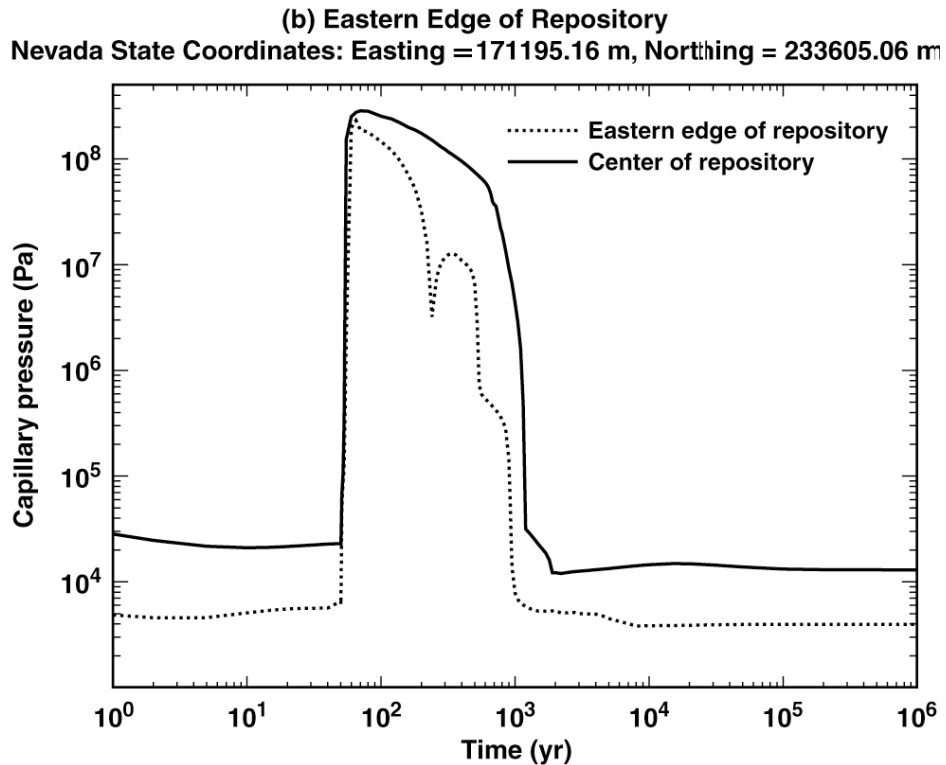
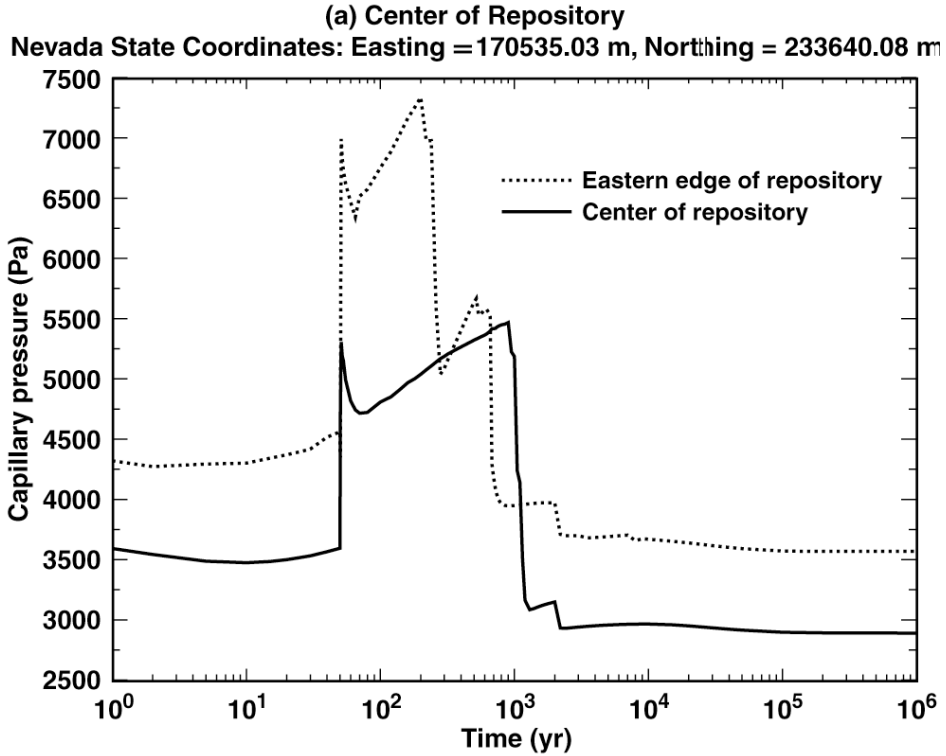
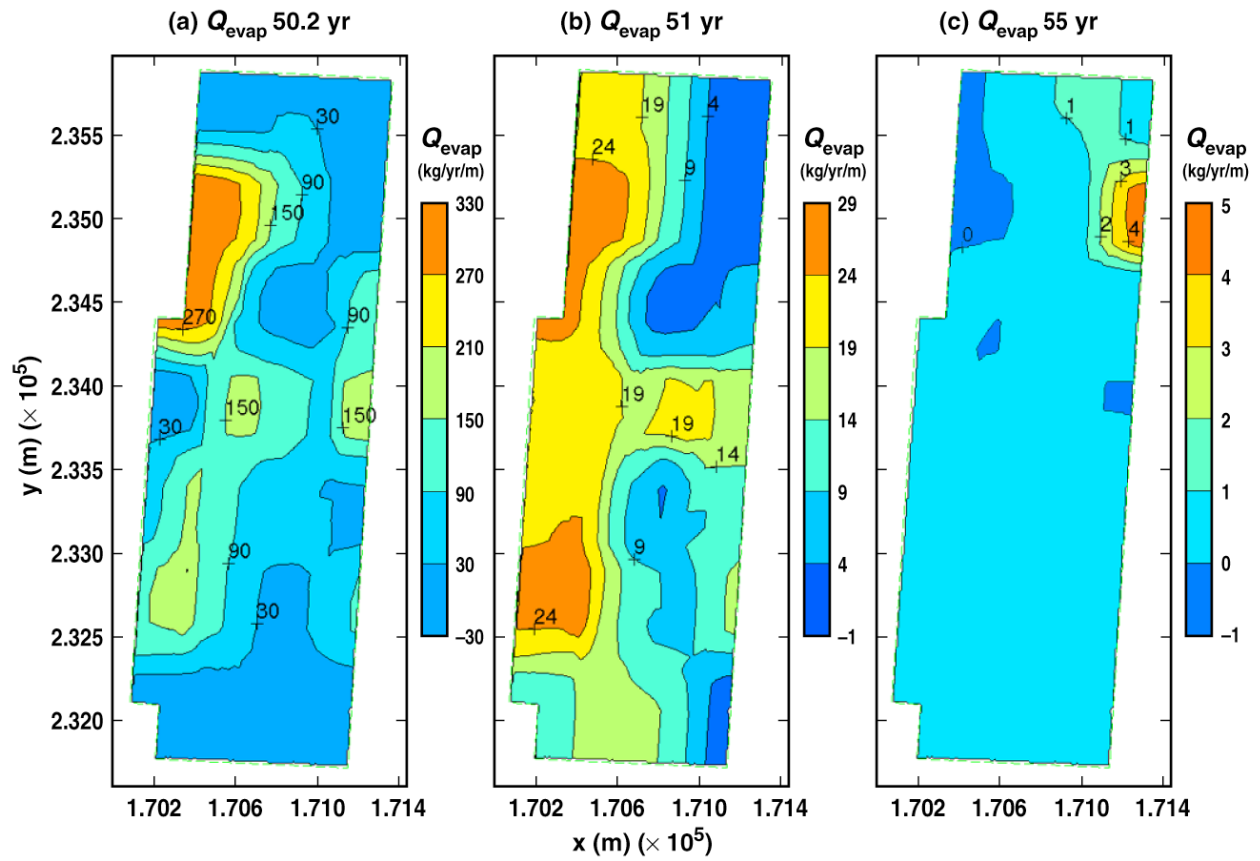
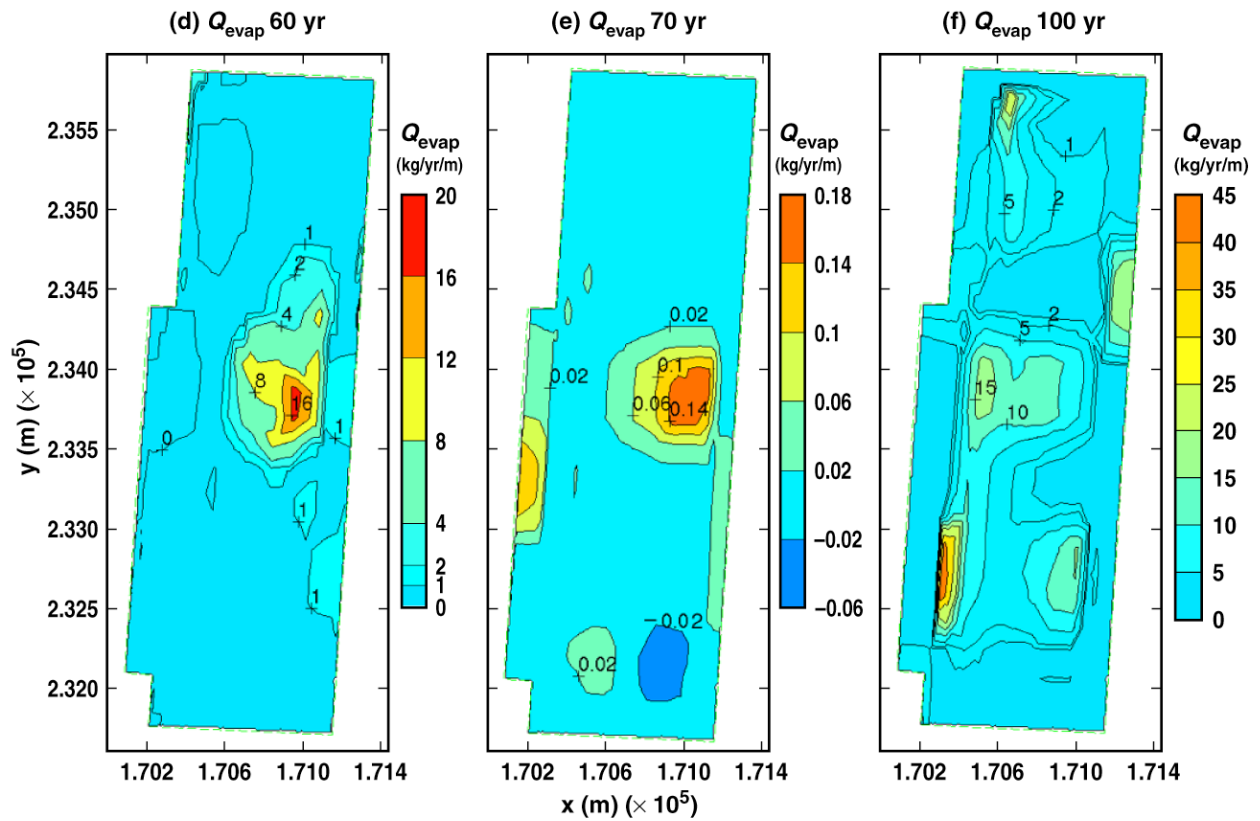


Figure 6-57 Pcap\_Fdw\_Mdw16\_16-24\_16  
Perimeter-averaged drift-wall liquid-phase saturation history and relative humidity history (a) at the geographical center of the repository and (b) a location 27.5 m from the eastern edge of the repository. These conditions occur in the vicinity of a 21-PWR WP for the mean infiltration-flux no-backfill case for the indicated times.



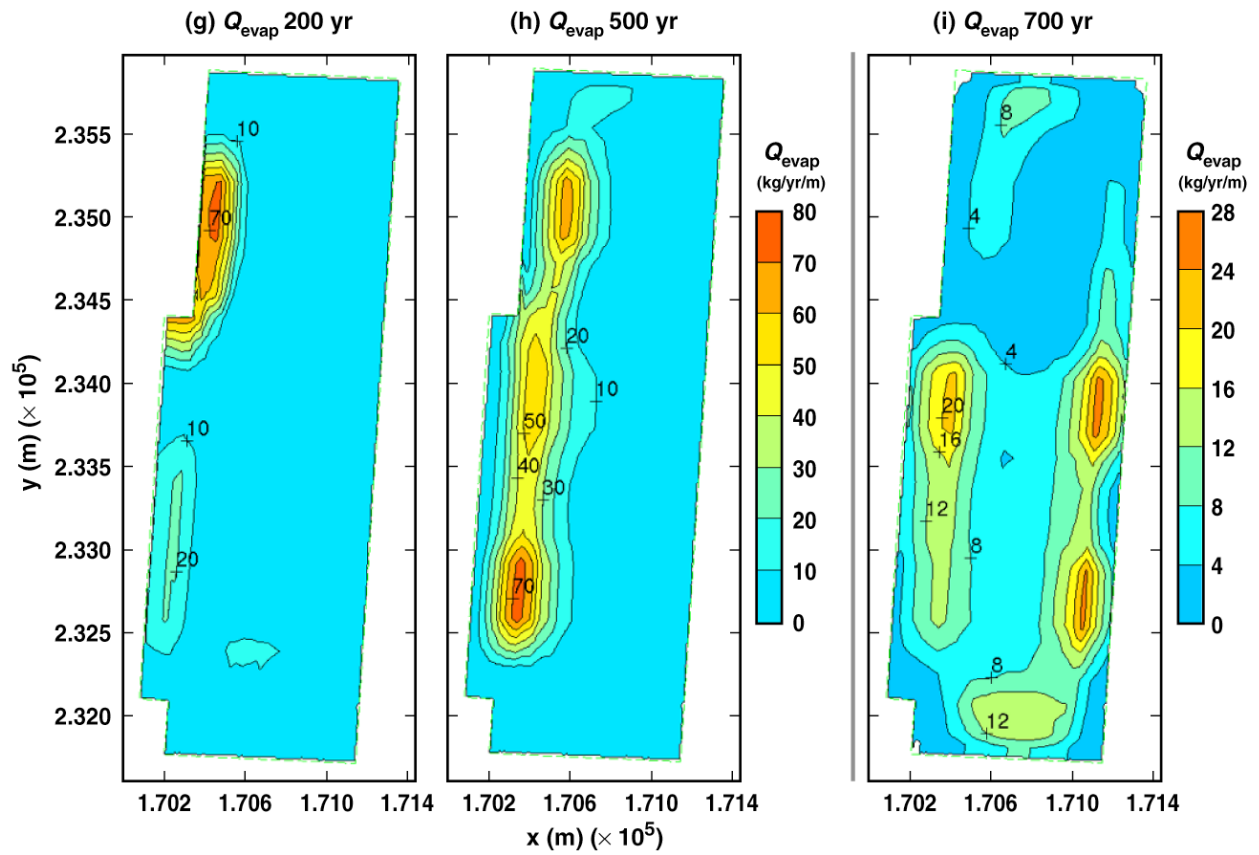
Qevap\_dwTop12\_13\_16

Figure 6-58 Evaporation rate  $Q_{\text{evap}}$  in the host rock at the crown of the drift in the vicinity of a 21-PWR WP for the mean infiltration-flux no-backfill case for the indicated times.



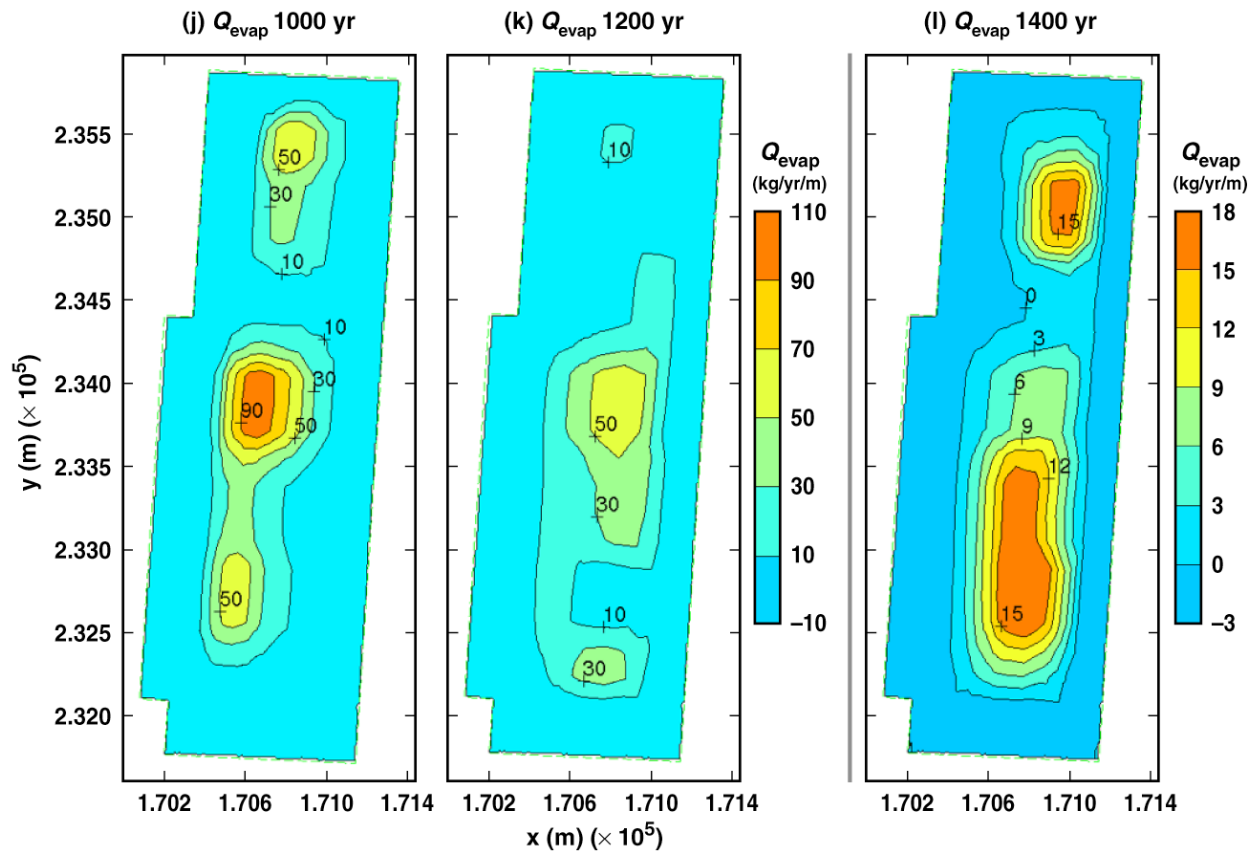
Qevap\_dwTop17\_19\_21

Figure 6-58. Evaporation rate  $Q_{\text{evap}}$  in the host rock at the crown of the drift in the vicinity of a 21-PWR WP for the mean infiltration-flux no-backfill case for the indicated times (Continued)



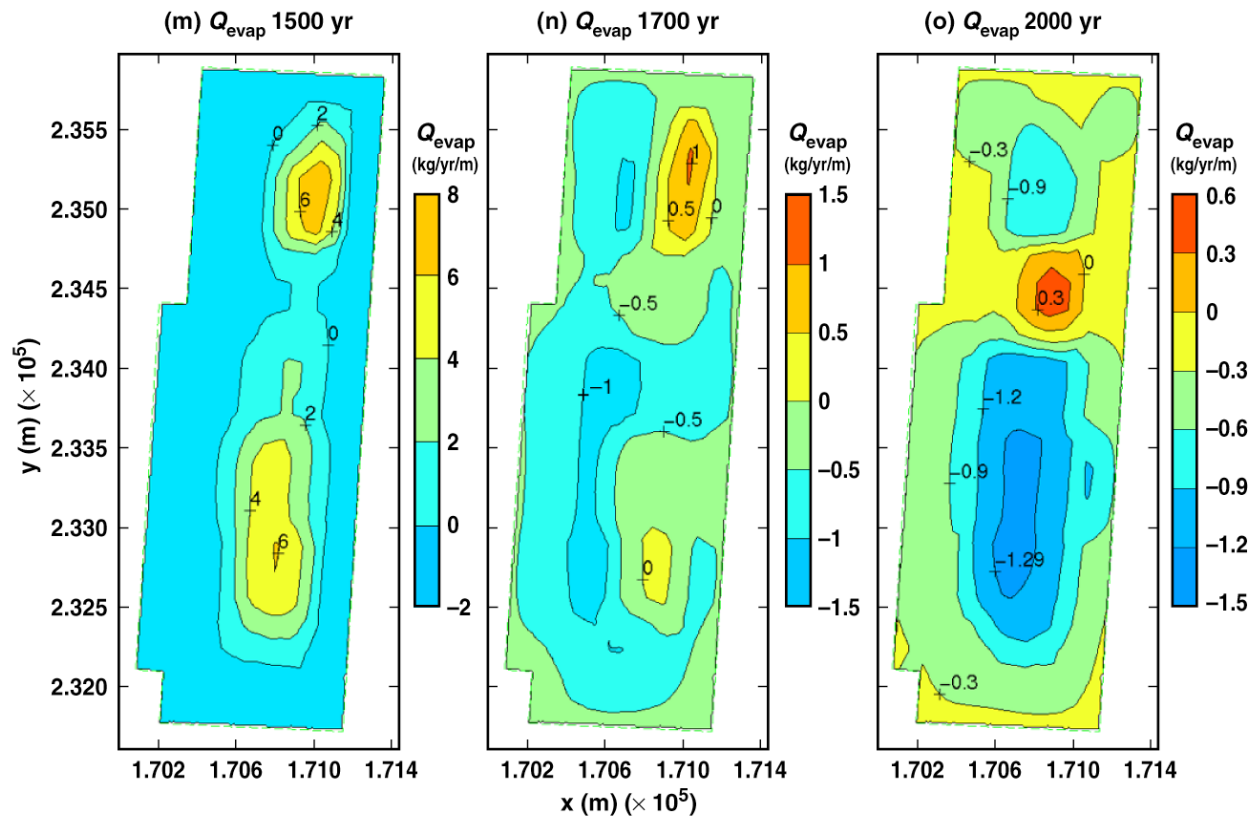
Qevap\_dwTop26\_41\_51

Figure 6-58. Evaporation rate  $Q_{\text{evap}}$  in the host rock at the crown of the drift in the vicinity of a 21-PWR WP for the mean infiltration-flux no-backfill case for the indicated times (Continued)



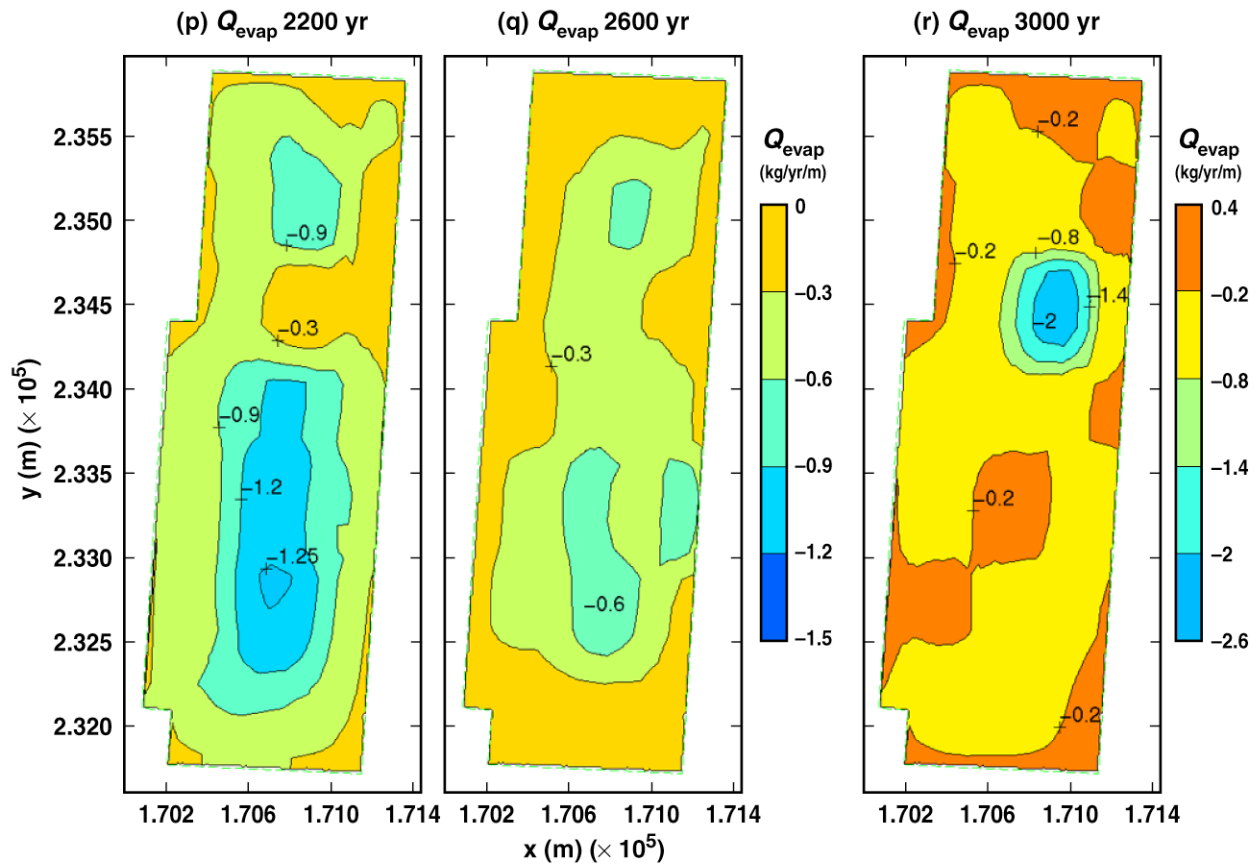
Qevap\_dwTop60\_64\_66

Figure 6-58. Evaporation rate  $Q_{\text{evap}}$  in the host rock at the crown of the drift in the vicinity of a 21-PWR WP for the mean infiltration-flux no-backfill case for the indicated times (Continued)



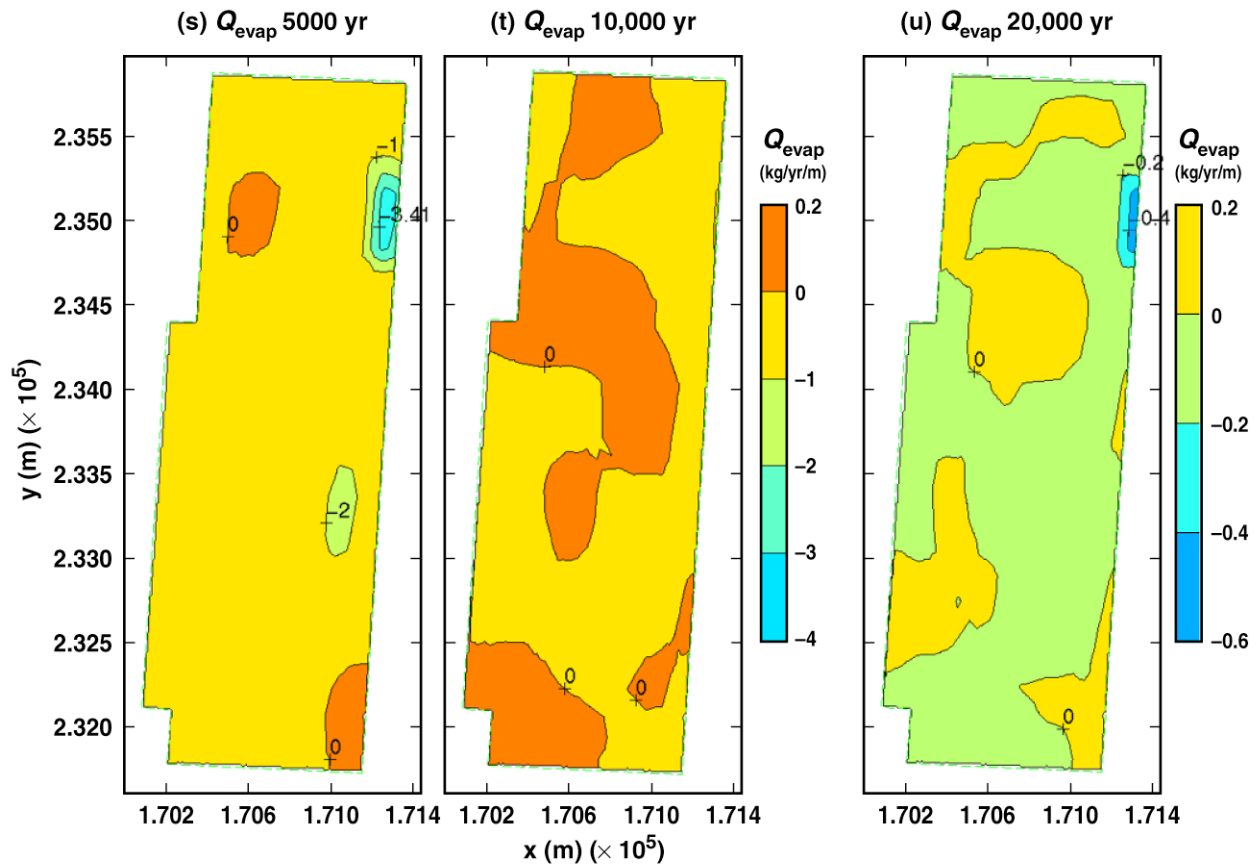
Qevap\_dwTop67\_69\_72

Figure 6-58. Evaporation rate  $Q_{\text{evap}}$  in the host rock at the crown of the drift in the vicinity of a 21-PWR WP for the mean infiltration-flux no-backfill case for the indicated times (Continued)



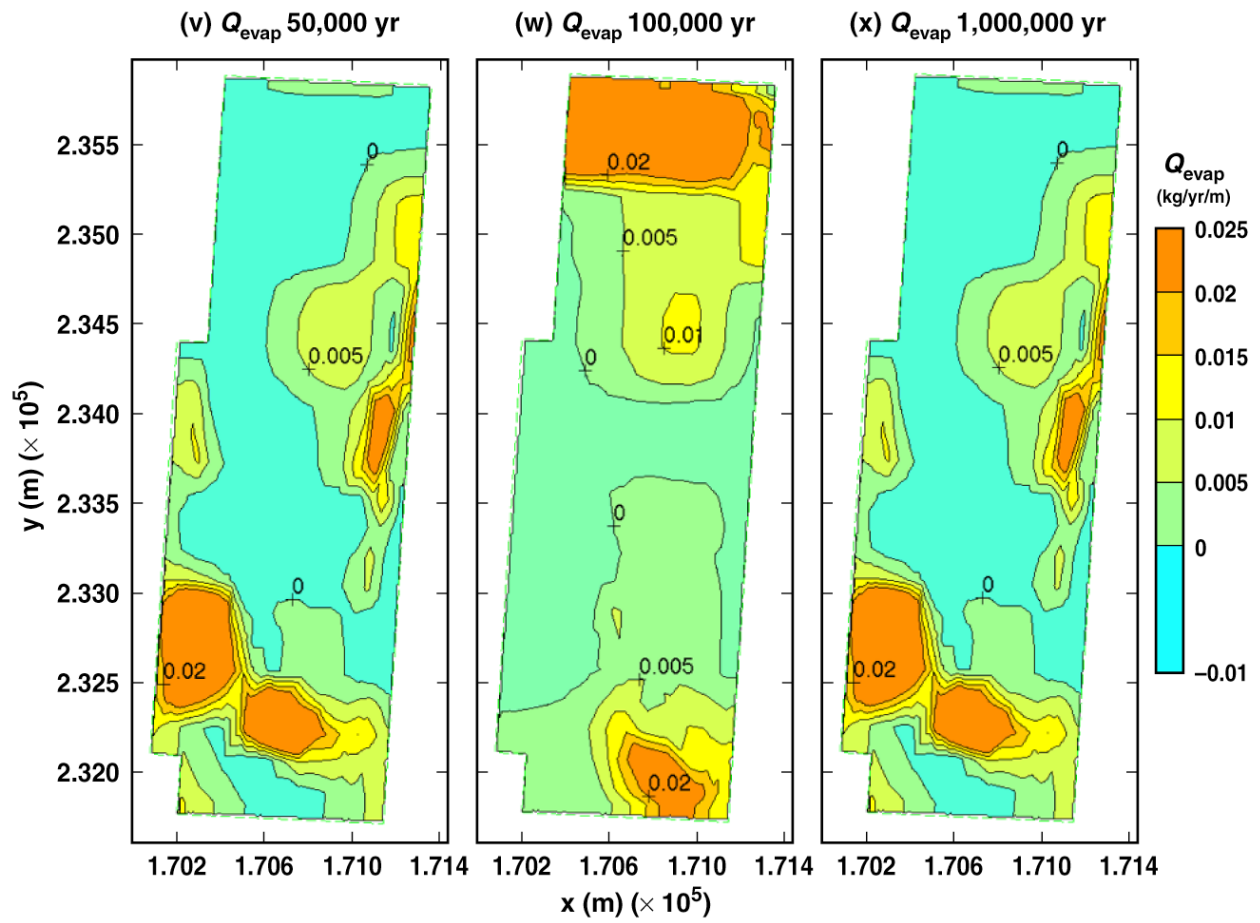
Qevap\_dwTop73\_75\_77

Figure 6-58. Evaporation rate  $Q_{\text{evap}}$  in the host rock at the crown of the drift in the vicinity of a 21-PWR WP for the mean infiltration-flux no-backfill case for the indicated times (Continued)



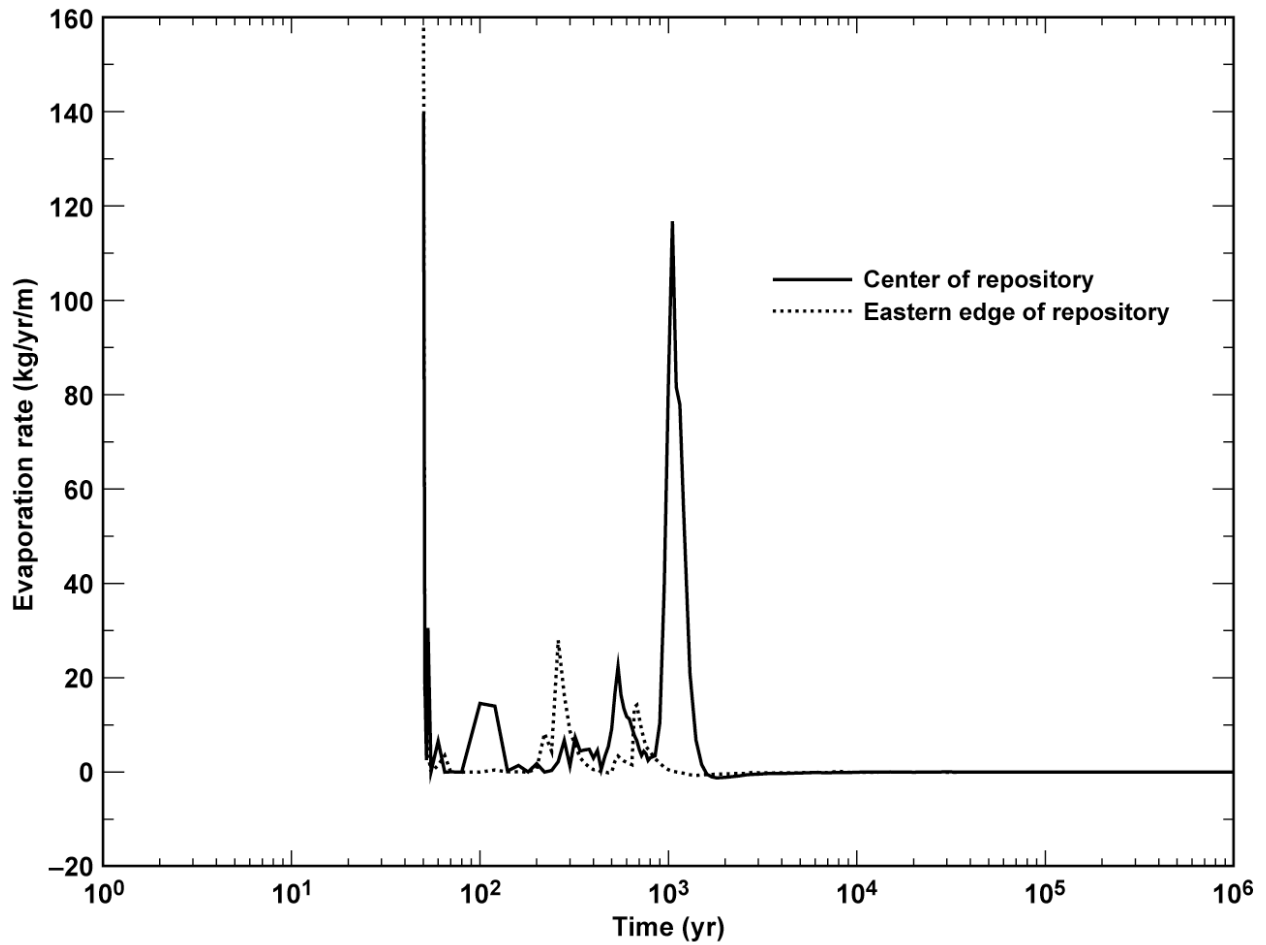
Qevap\_dwTop81\_86\_88

Figure 6-58. Evaporation rate  $Q_{\text{evap}}$  in the host rock at the crown of the drift in the vicinity of a 21-PWR WP for the mean infiltration-flux no-backfill case for the indicated times (Continued)



Qevap\_dwTop91\_92\_99

Figure 6-58. Evaporation rate  $Q_{\text{evap}}$  in the host rock at the crown of the drift in the vicinity of a 21-PWR WP for the mean infiltration-flux no-backfill case for the indicated times (Continued)



Qevap\_16\_16-24\_16

Figure 6-59. Evaporation rate history in the host rock at the crown of the drift at the geographical center of the repository and a location 27.5 m from the eastern edge of the repository. These conditions occur in the vicinity of a 21-PWR WP for the mean infiltration-flux no-backfill case for the indicated times. Center of repository, Nevada State coordinates: Easting = 170535.03 m, Northing = 233640.08 m. Eastern edge of repository, Nevada State coordinates: Easting = 171195.16 m, Northing = 233605.06 m.

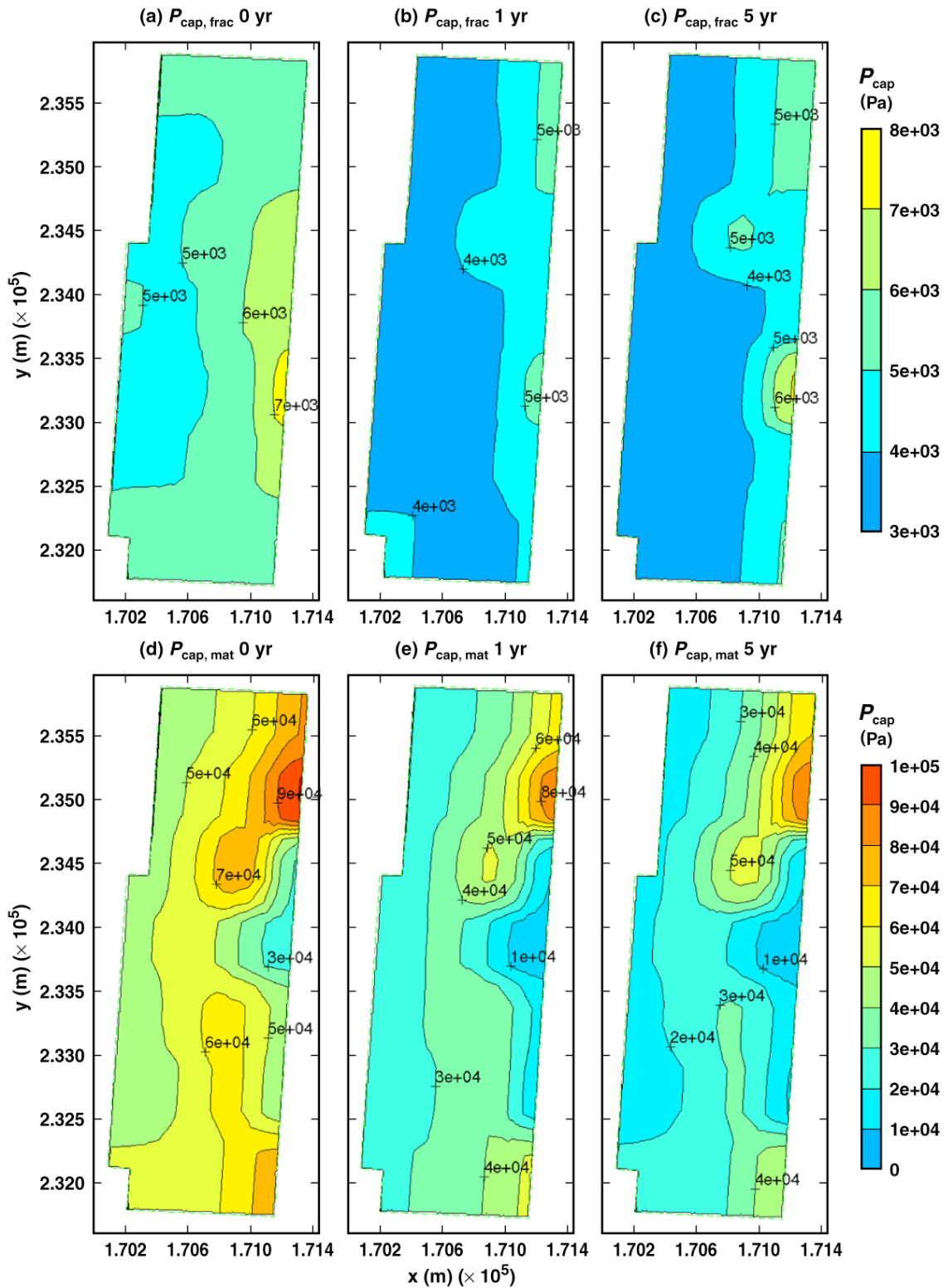
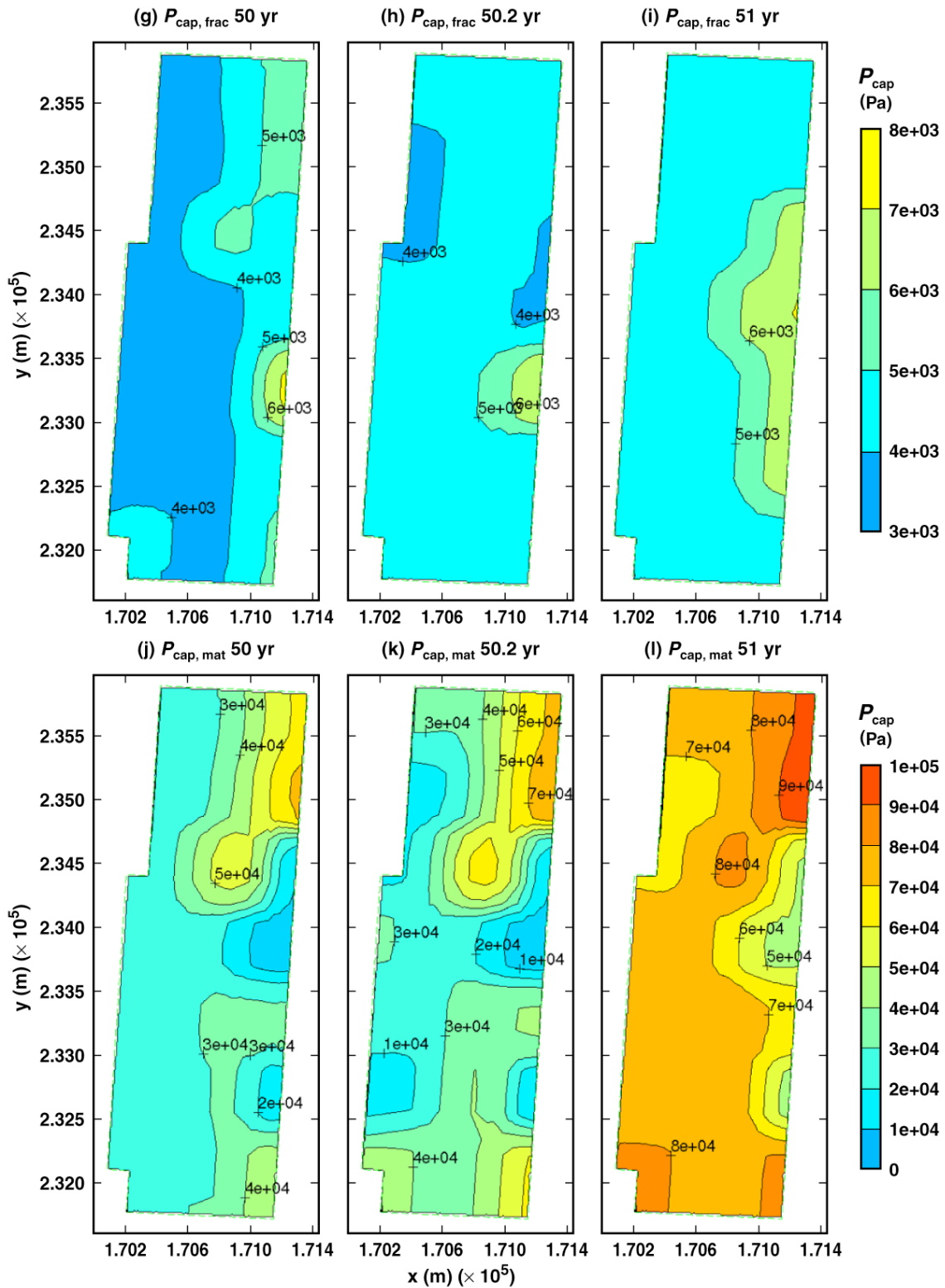
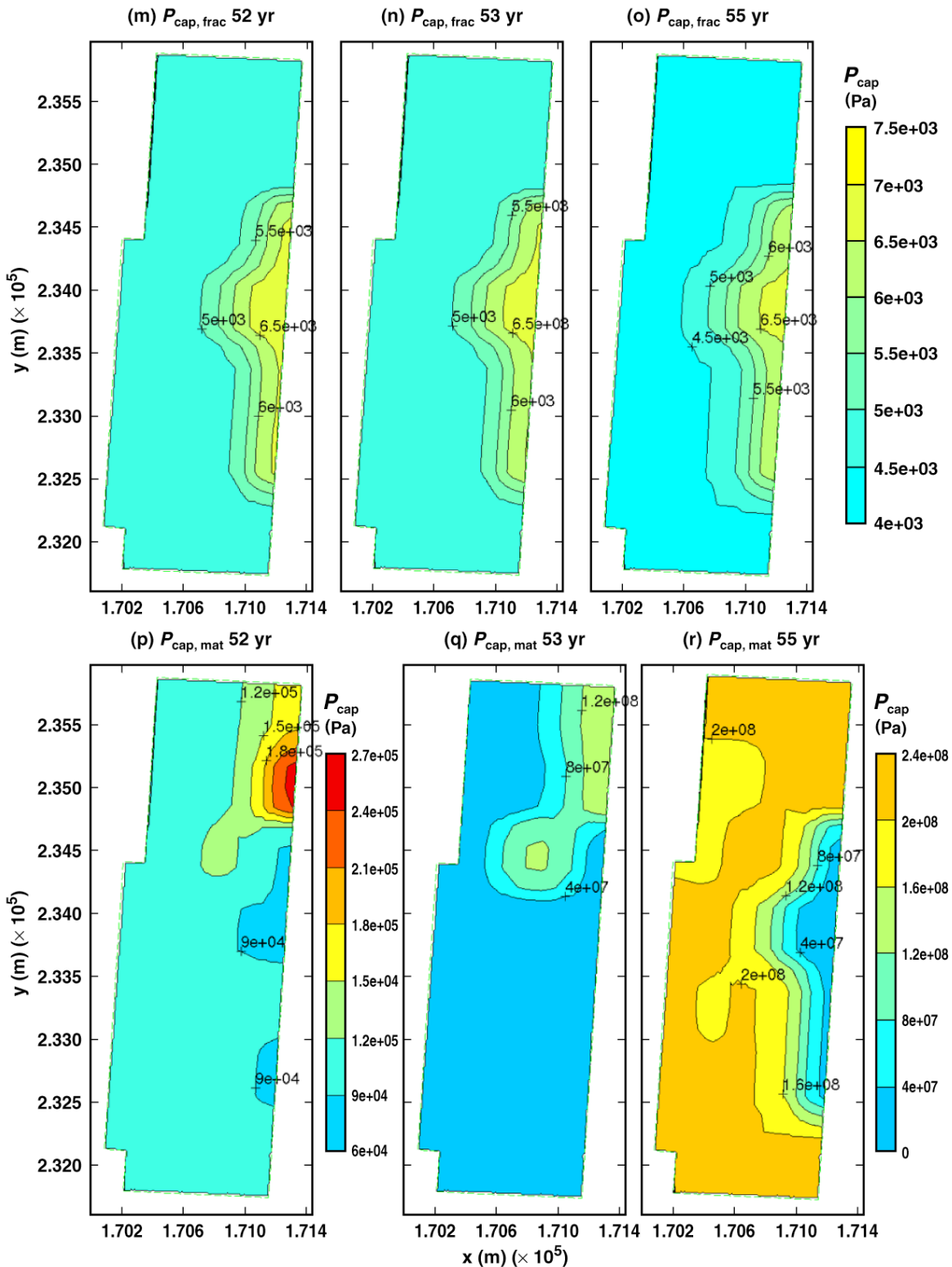


Figure 6-60. Capillary pressure in the fractures  $P_{cap, frac}$  and in the matrix  $P_{cap, mat}$  averaged around the perimeter of the drift wall in the vicinity of a 21-PWR WP for the mean infiltration-flux no-backfill case for the indicated times.



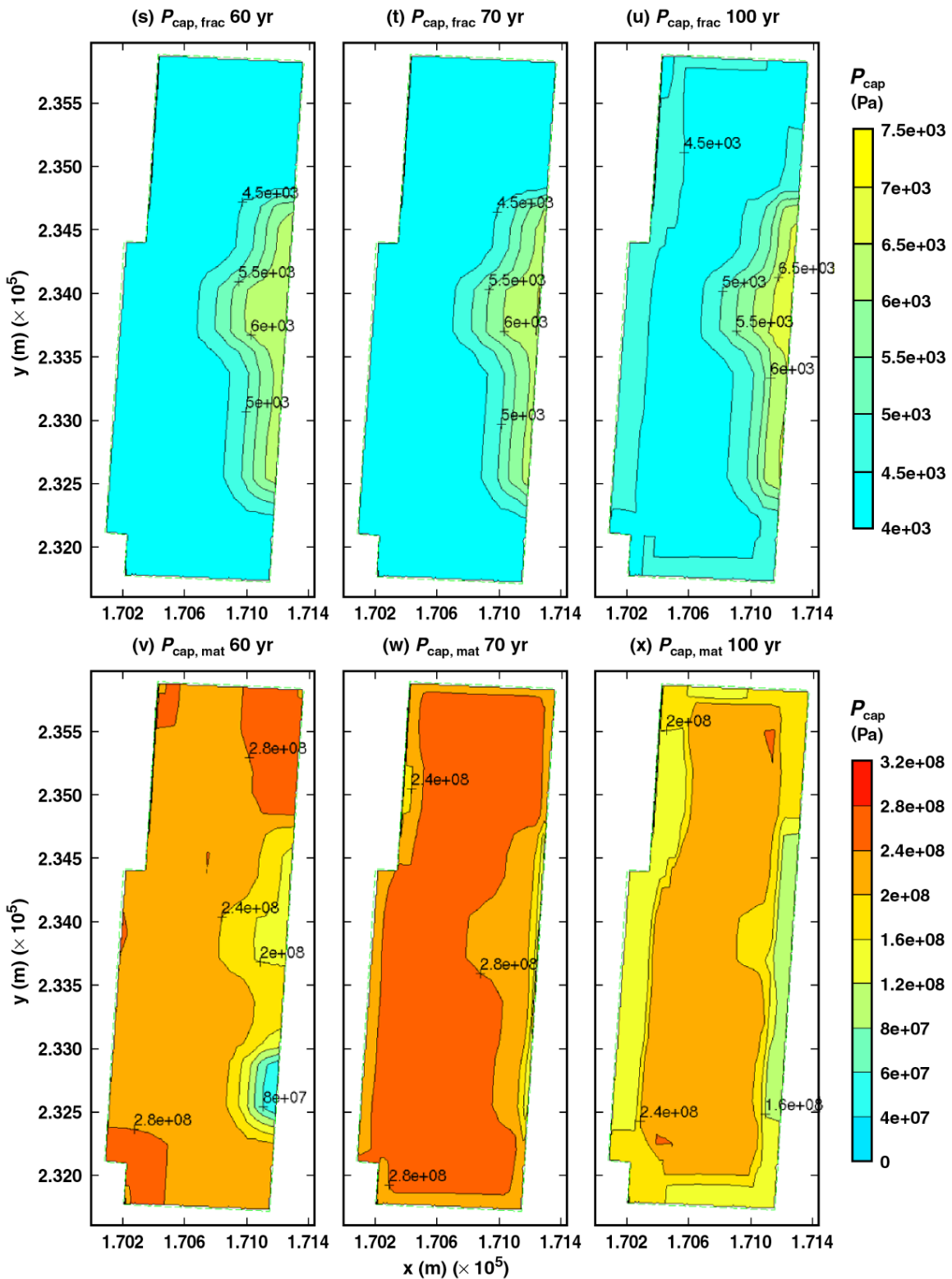
Pcap\_fdw&mdw11\_12\_13

Figure 6-60. Capillary pressure in the fractures  $P_{cap, frac}$  and in the matrix  $P_{cap, mat}$  averaged around the perimeter of the drift wall in the vicinity of a 21-PWR WP for the mean infiltration-flux no-backfill case for the indicated times (Continued)



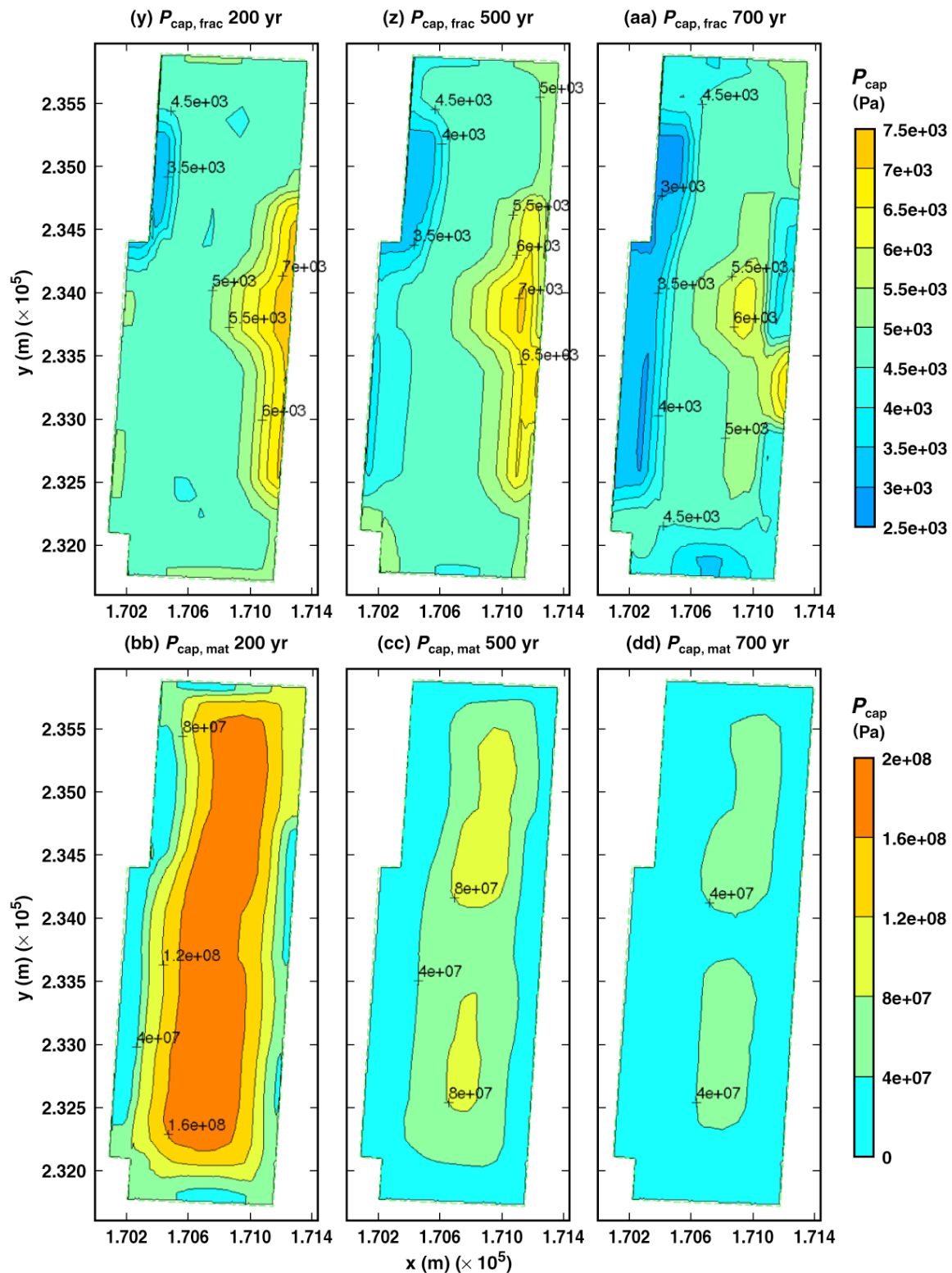
Pcap\_fdw&mdw14\_15\_16

Figure 6-60. Capillary pressure in the fractures  $P_{cap, frac}$  and in the matrix  $P_{cap, mat}$  averaged around the perimeter of the drift wall in the vicinity of a 21-PWR WP for the mean infiltration-flux no-backfill case for the indicated times (Continued)



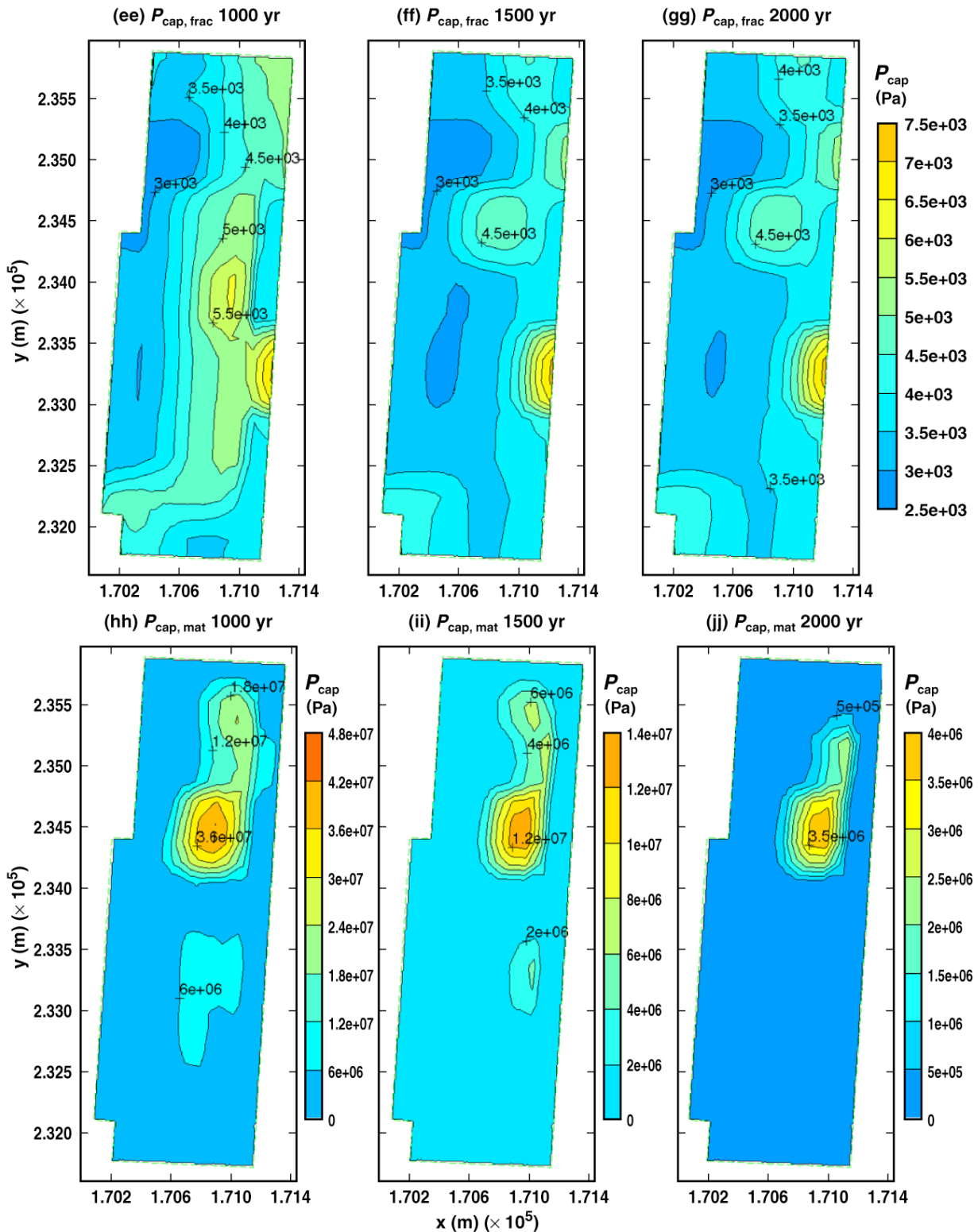
Pcap\_fdw&mdw17\_19\_21

Figure 6-60. Capillary pressure in the fractures  $P_{cap, frac}$  and in the matrix  $P_{cap, mat}$  averaged around the perimeter of the drift wall in the vicinity of a 21-PWR WP for the mean infiltration-flux no-backfill case for the indicated times (Continued)



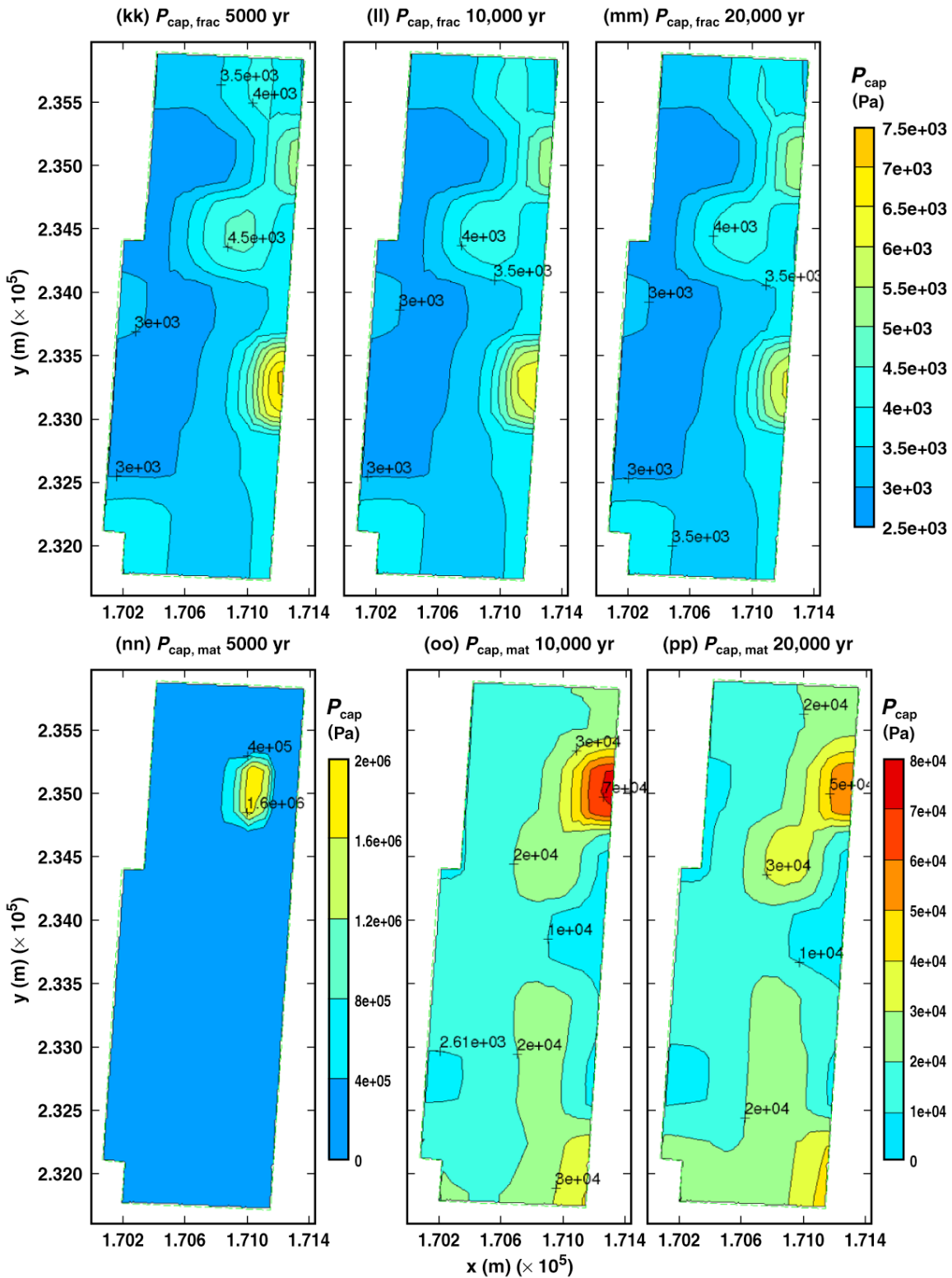
Pcap\_fdw&mdw26\_41\_51

Figure 6-60. Capillary pressure in the fractures  $P_{cap, frac}$  and in the matrix  $P_{cap, mat}$  averaged around the perimeter of the drift wall in the vicinity of a 21-PWR WP for the mean infiltration-flux no-backfill case for the indicated times (Continued)



Pcap\_fdw&mdw60\_67\_72

Figure 6-60. Capillary pressure in the fractures  $P_{cap, frac}$  and in the matrix  $P_{cap, mat}$  averaged around the perimeter of the drift wall in the vicinity of a 21-PWR WP for the mean infiltration-flux no-backfill case for the indicated times (Continued)



Pcap\_fdw&mdw81\_86\_88

Figure 6-60. Capillary pressure in the fractures  $P_{cap, frac}$  and in the matrix  $P_{cap, mat}$  averaged around the perimeter of the drift wall in the vicinity of a 21-PWR WP for the mean infiltration-flux no-backfill case for the indicated times (Continued)

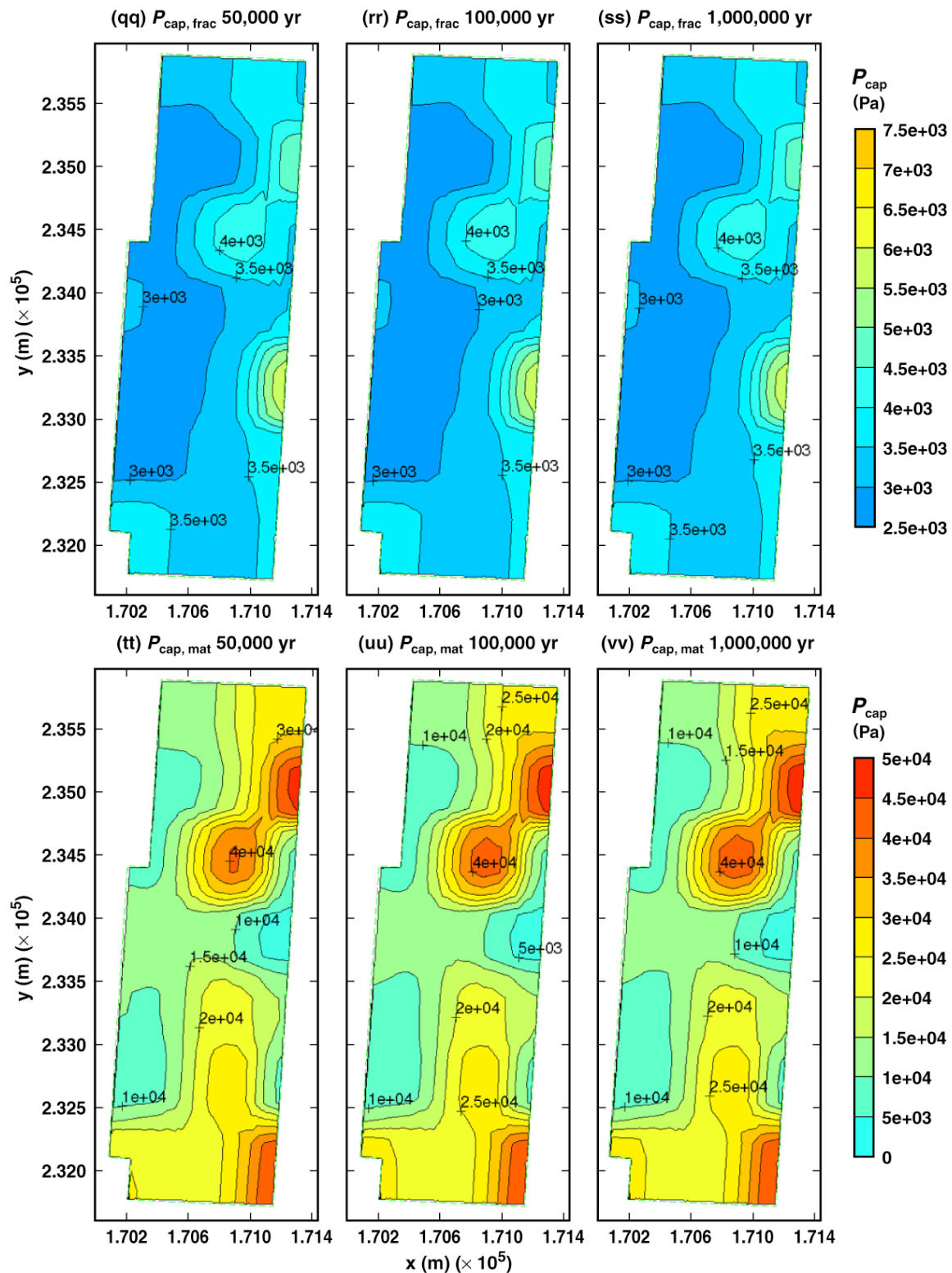
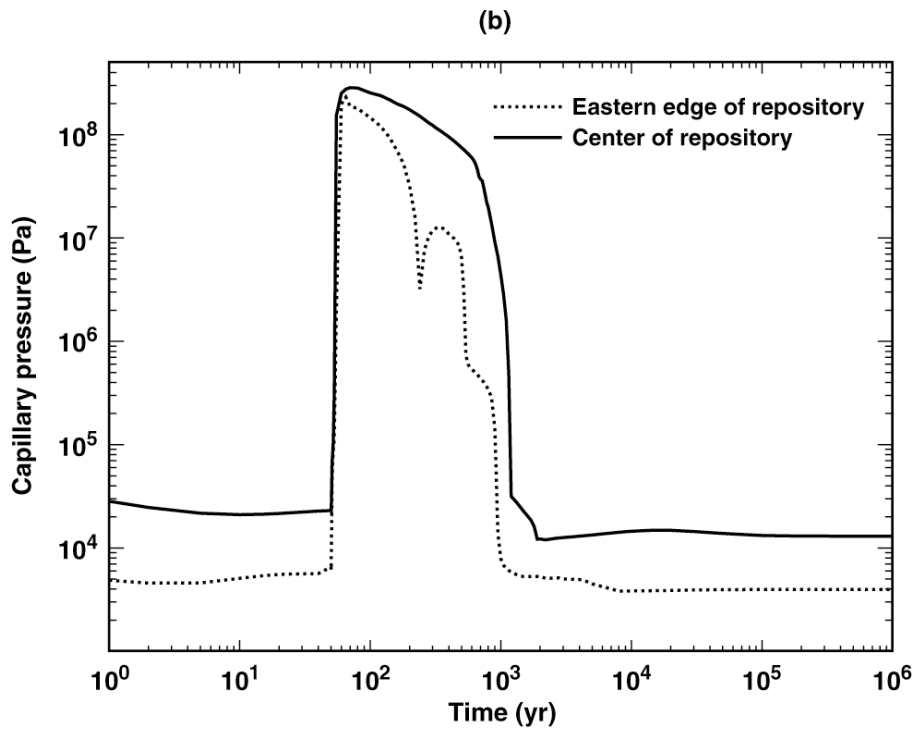
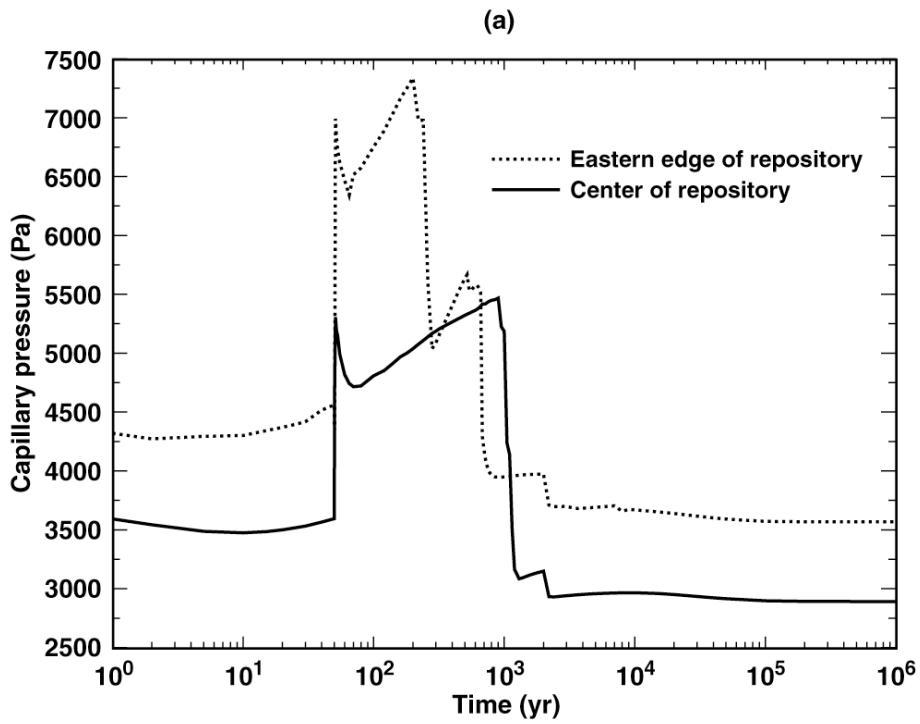
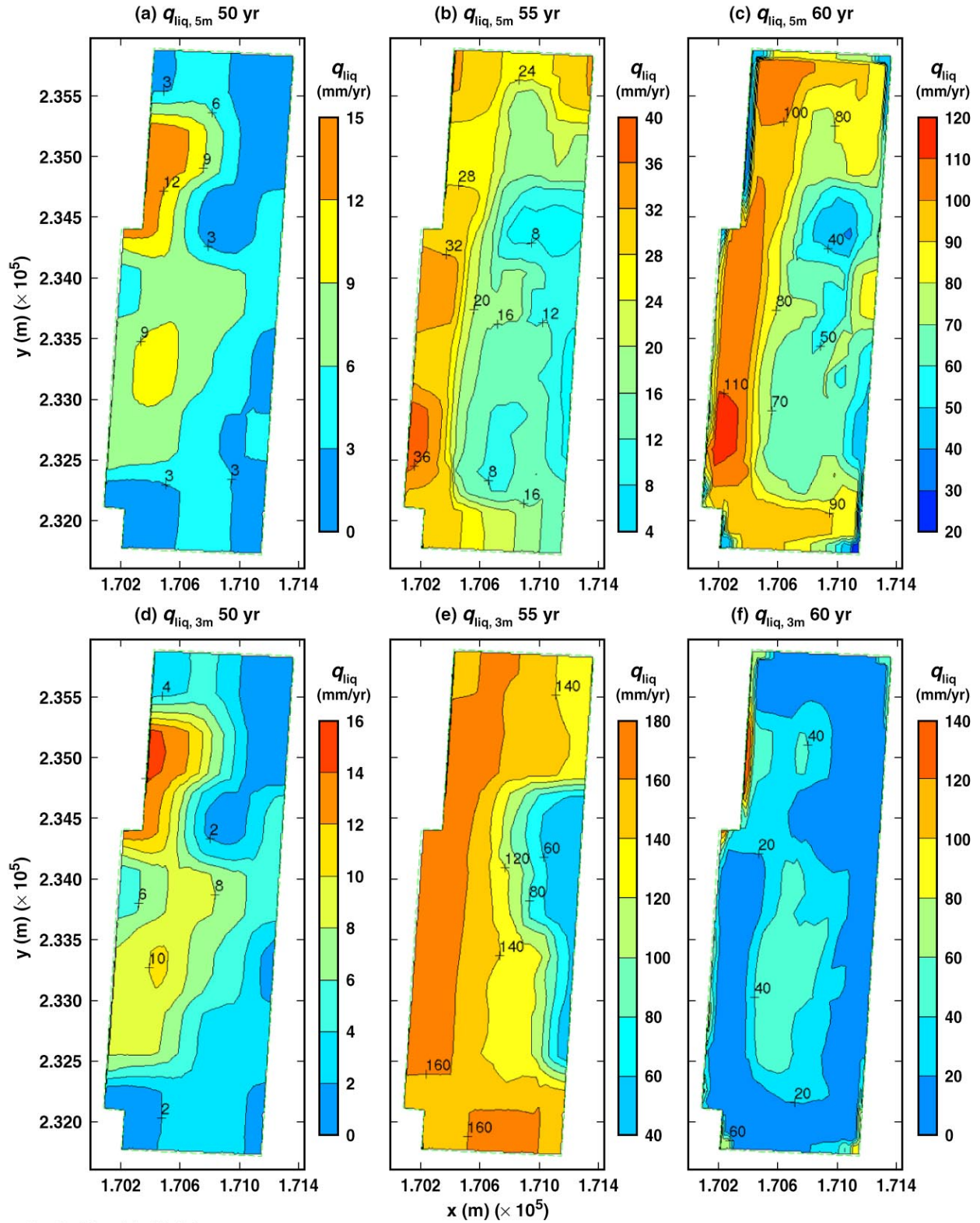


Figure 6-60. Capillary pressure in the fractures  $P_{cap, frac}$  and in the matrix  $P_{cap, mat}$  averaged around the perimeter of the drift wall in the vicinity of a 21-PWR WP for the mean infiltration-flux no-backfill case for the indicated times (Continued)



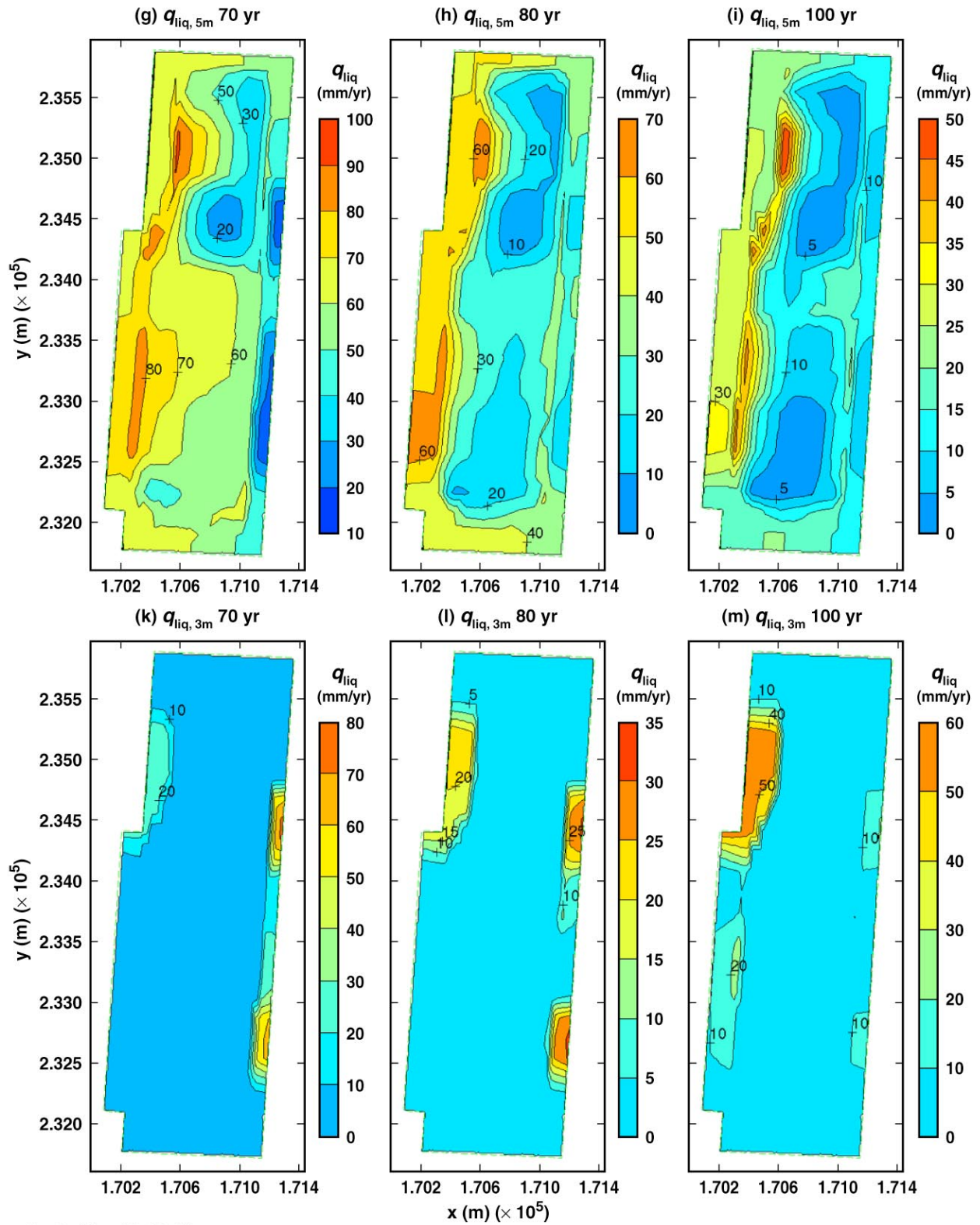
Pcap\_Fdw\_Mdw16\_16-24\_16

Figure 6-61 Capillary pressure history in (a) the fractures and in (b) the matrix averaged around the perimeter of the drift wall at the geographical center of the repository and a location 27.5 m from the eastern edge of the repository. These conditions occur in the vicinity of a 21-PWR WP for the mean infiltration-flux no-backfill case for the indicated times.



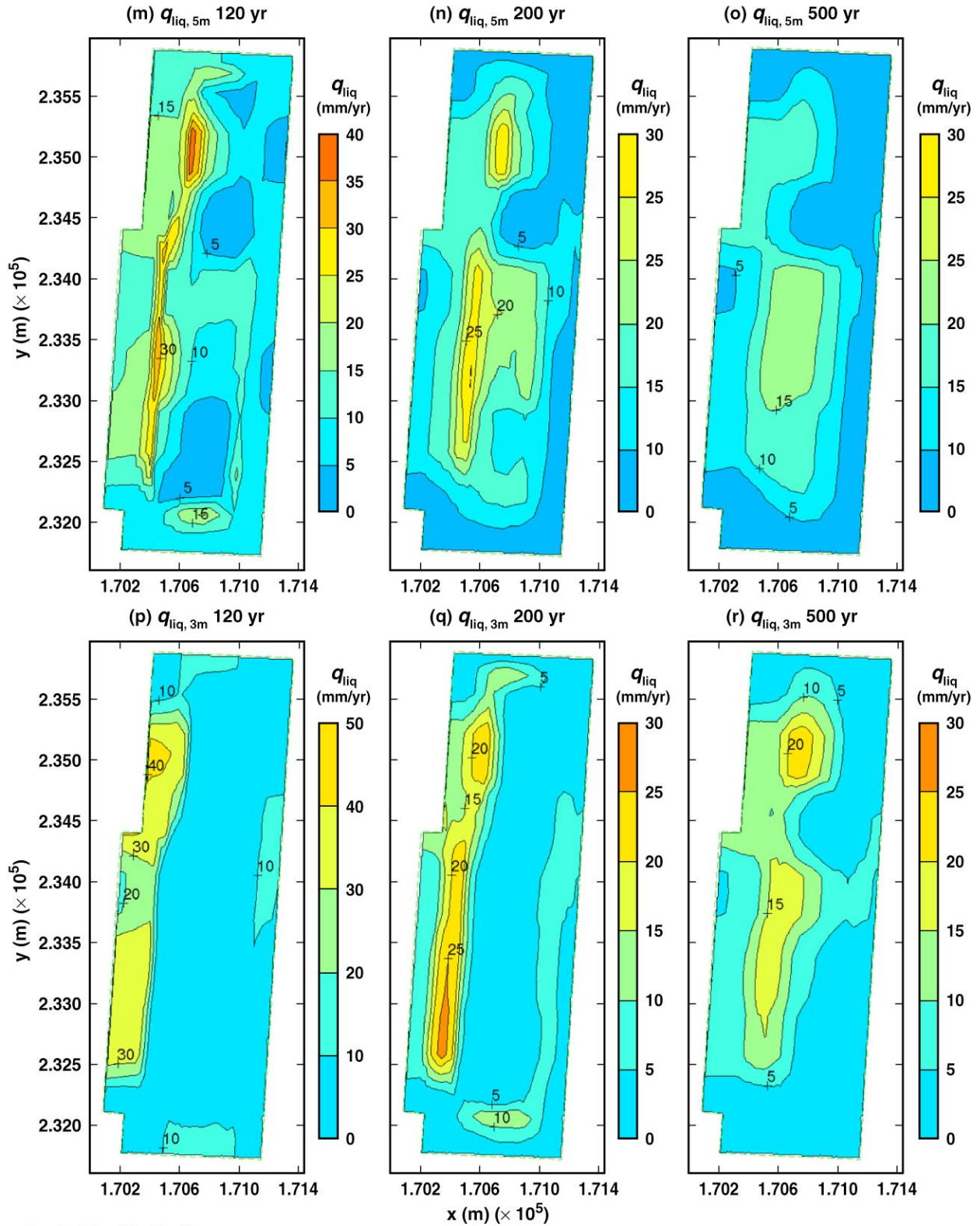
qliq\_5m&3m\_11\_16\_17

Figure 6-62 Liquid-phase flux 5 m and 3 m above the crown of the drift  $q_{liq,5m}$  and  $q_{liq,3m}$  in the vicinity of a 21-PWR WP for the mean infiltration-flux no-backfill case for the indicated times.



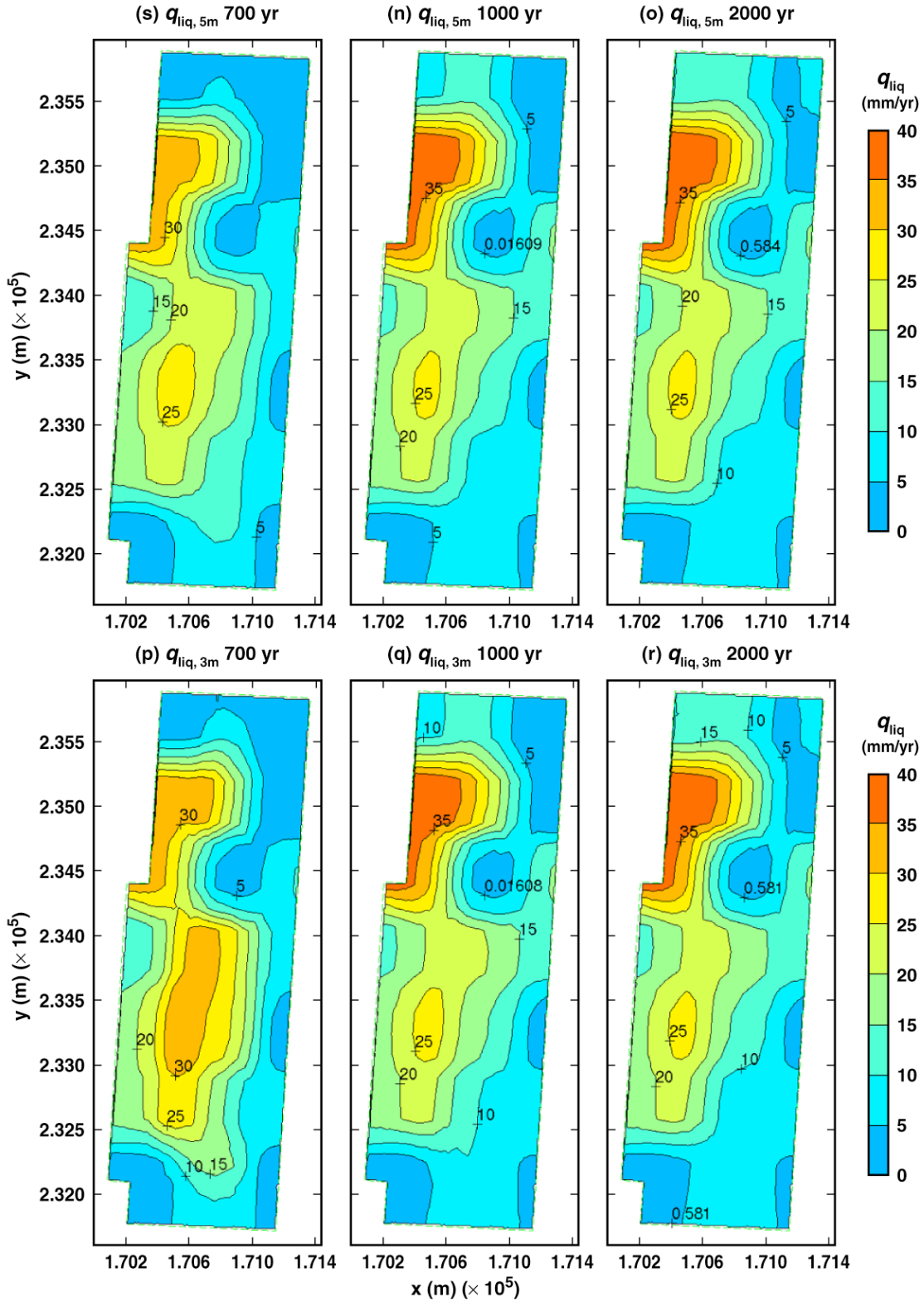
qliq\_5m&3m\_19\_20\_21

Figure 6-62. Liquid-phase flux 5 m and 3 m above the crown of the drift  $q_{liq,5m}$  and  $q_{liq,3m}$  in the vicinity of a 21-PWR WP for the mean infiltration-flux no-backfill case for the indicated times (Continued)



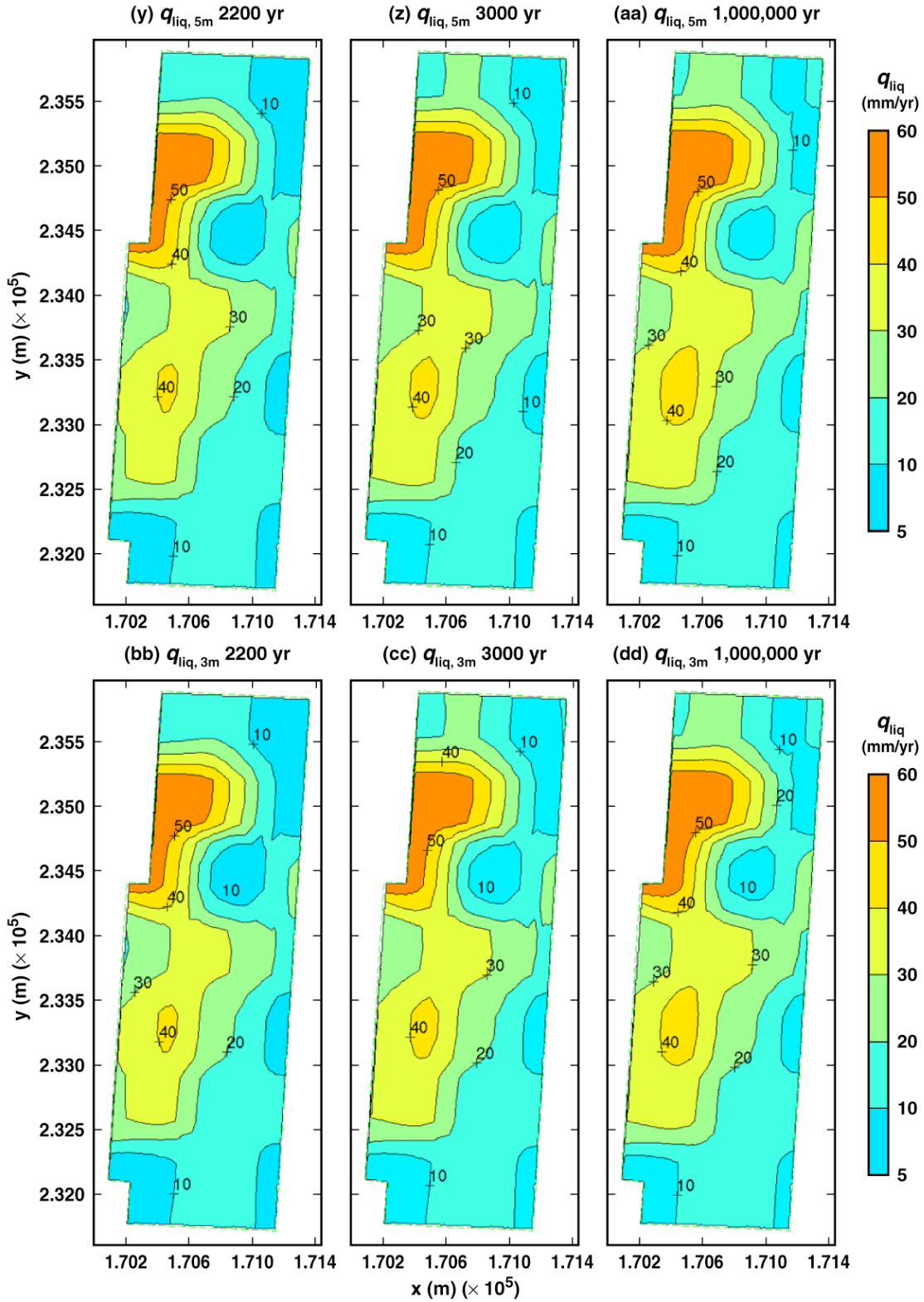
qliq\_5m&3m\_22\_26\_41

Figure 6-62. Liquid-phase flux 5 m and 3 m above the crown of the drift  $q_{liq,5m}$  and  $q_{liq,3m}$  in the vicinity of a 21-PWR WP for the mean infiltration-flux no-backfill case for the indicated times (Continued)



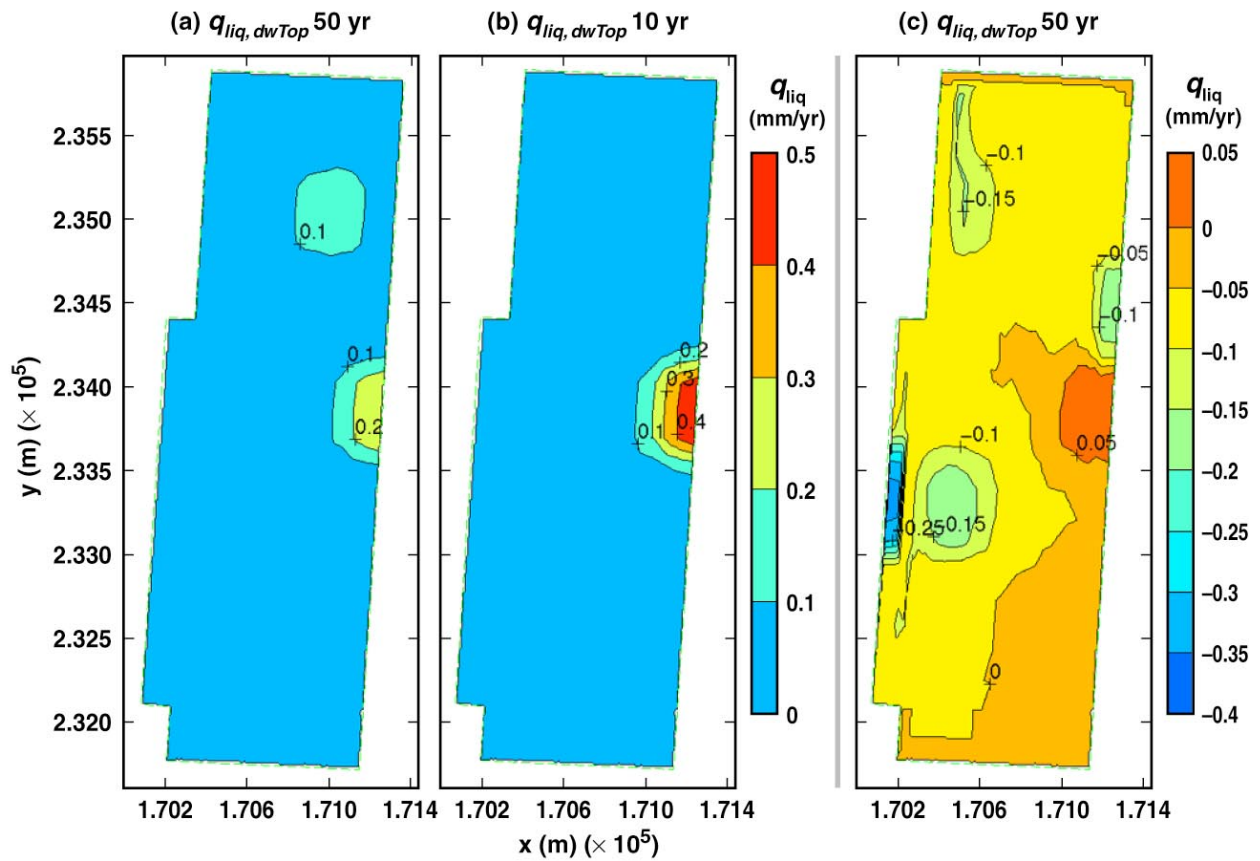
qliq\_5m&3m51\_60\_72

Figure 6-62 Liquid-phase flux 5 m and 3 m above the crown of the drift  $q_{liq,5m}$  and  $q_{liq,3m}$  in the vicinity of a 21-PWR WP for the mean infiltration-flux no-backfill case for the indicated times (Continued)



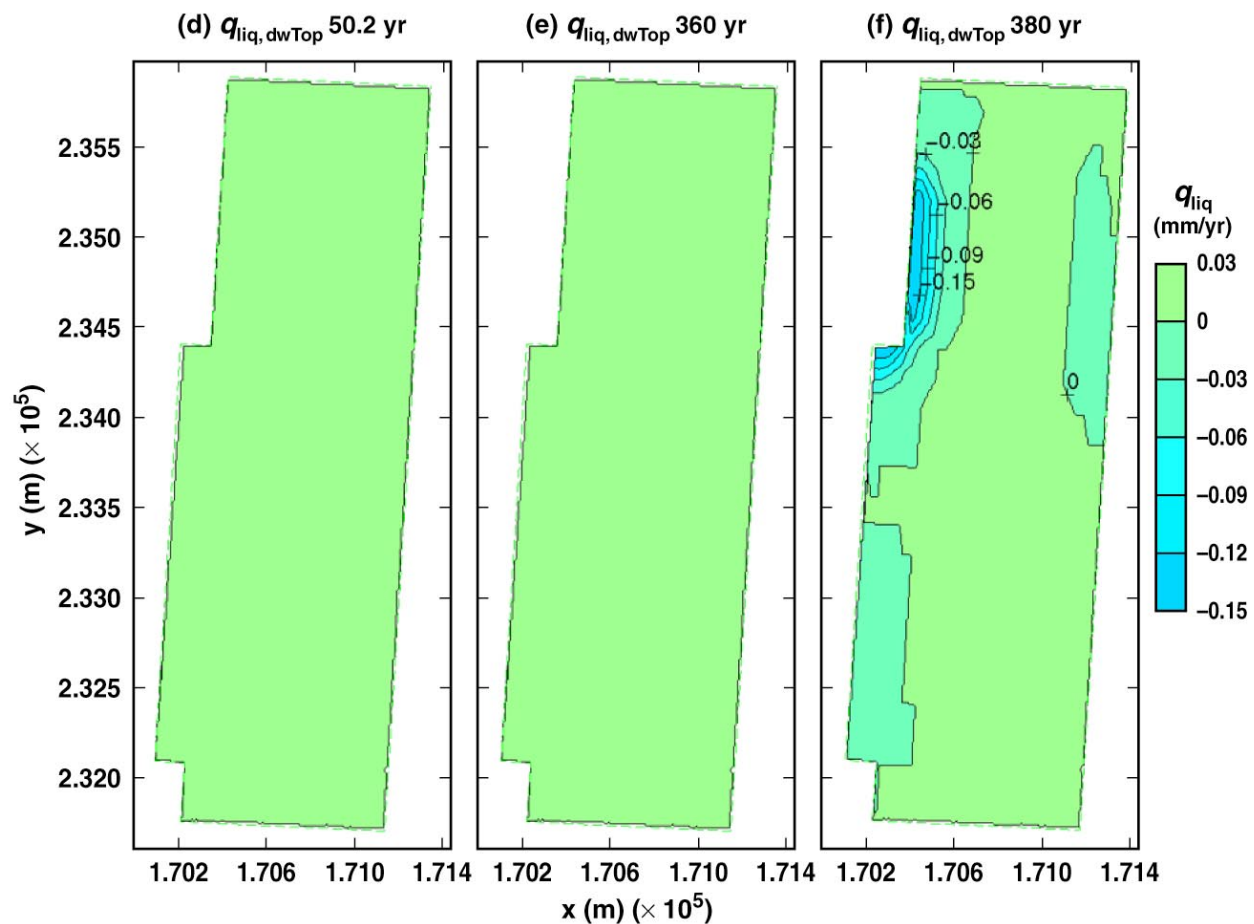
qliq\_5m&3m73\_77\_99

Figure 6-62. Liquid-phase flux 5 m and 3 m above the crown of the drift  $q_{liq,5m}$  and  $q_{liq,3m}$  in the vicinity of a 21-PWR WP for the mean infiltration-flux no-backfill case for the indicated times (Continued)



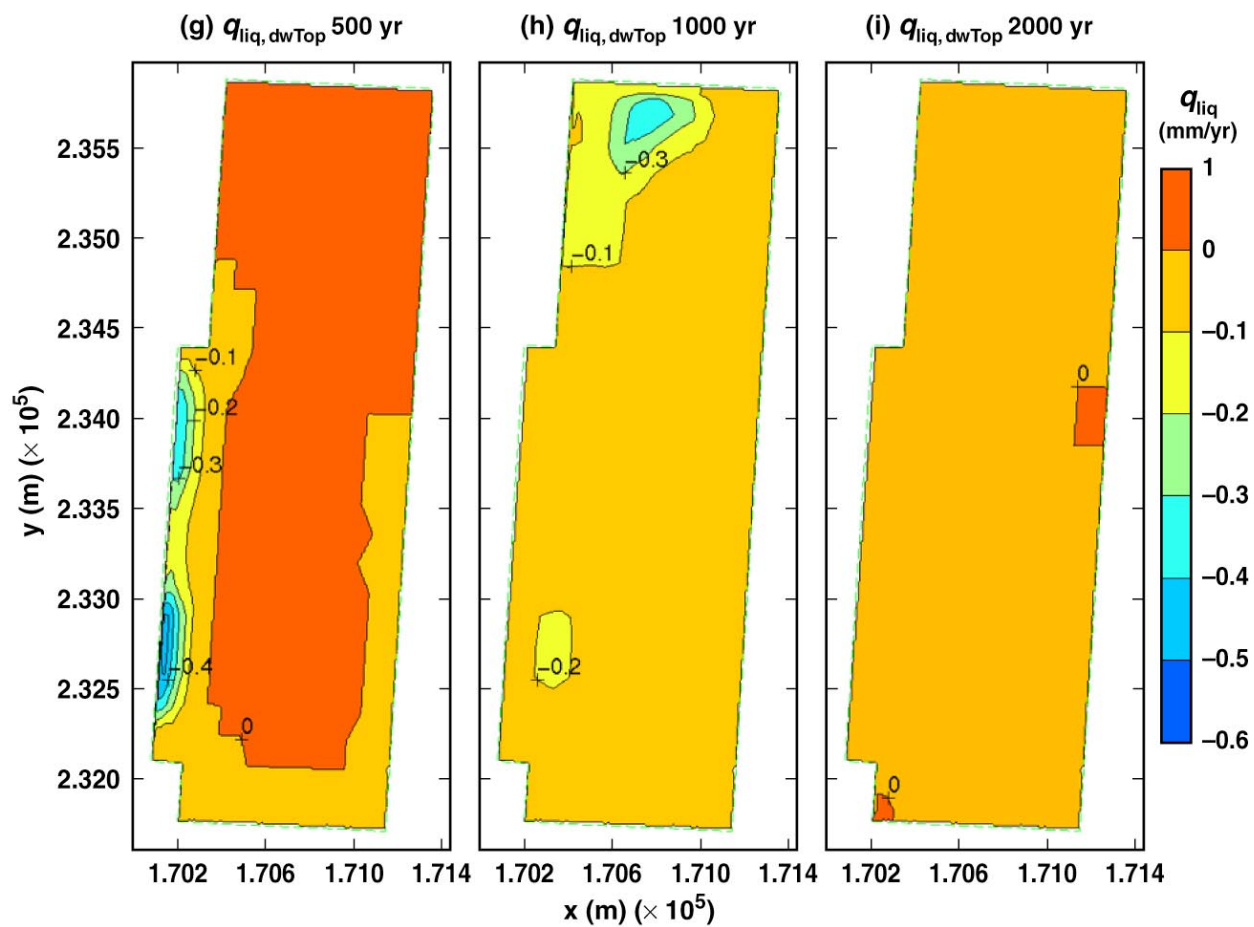
qliq\_dwTop03\_05\_11

Figure 6-63 Liquid-phase flux at the upper drift wall  $q_{liq, dwTop}$  in the vicinity of a 21-PWR WP for the mean infiltration-flux no-backfill case for the indicated times



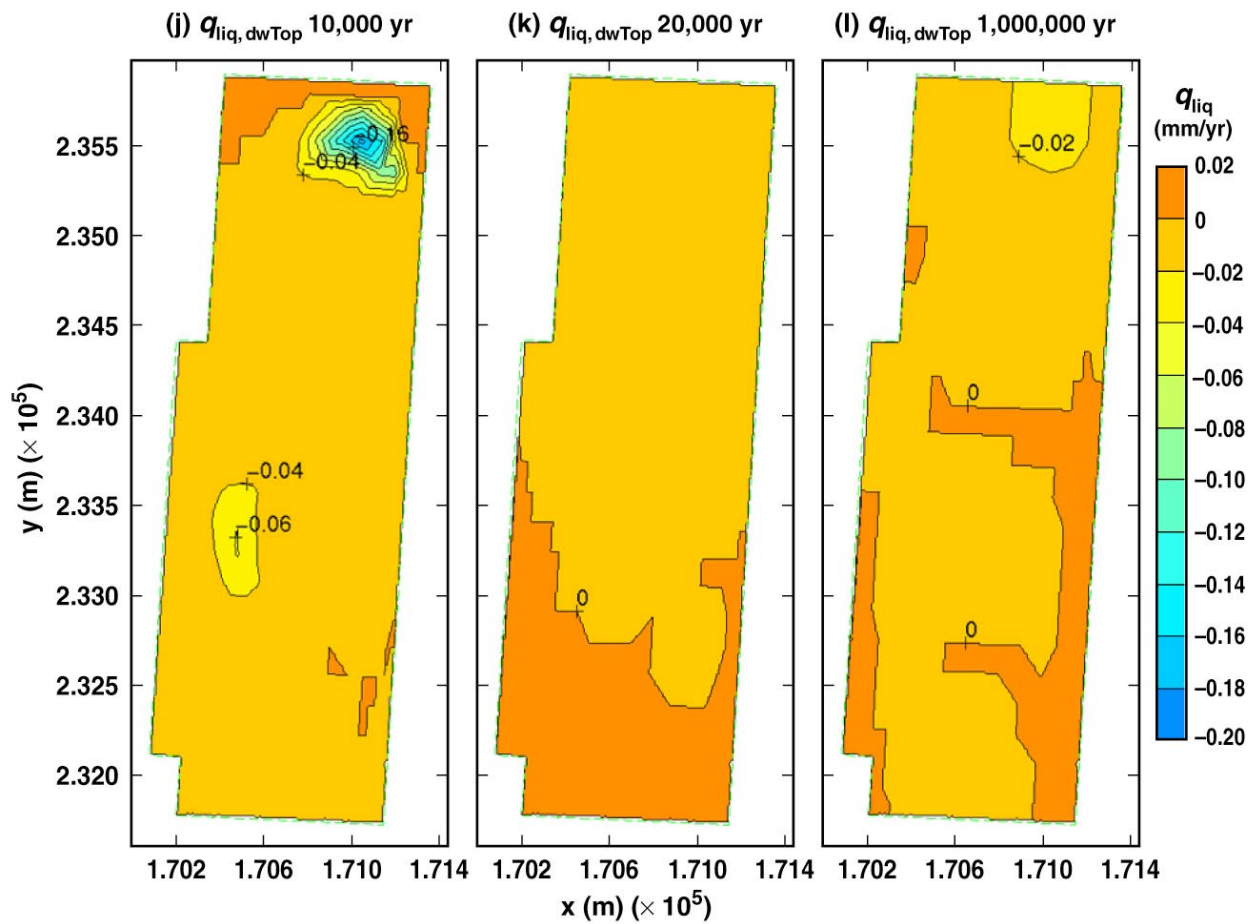
qliq\_dwTop12\_34\_35

Figure 6-63. Liquid-phase flux at the upper drift wall  $q_{liq,dwTop}$  in the vicinity of a 21-PWR WP for the mean infiltration-flux no-backfill case for the indicated times (Continued)



qliq\_dwTop41\_60\_72

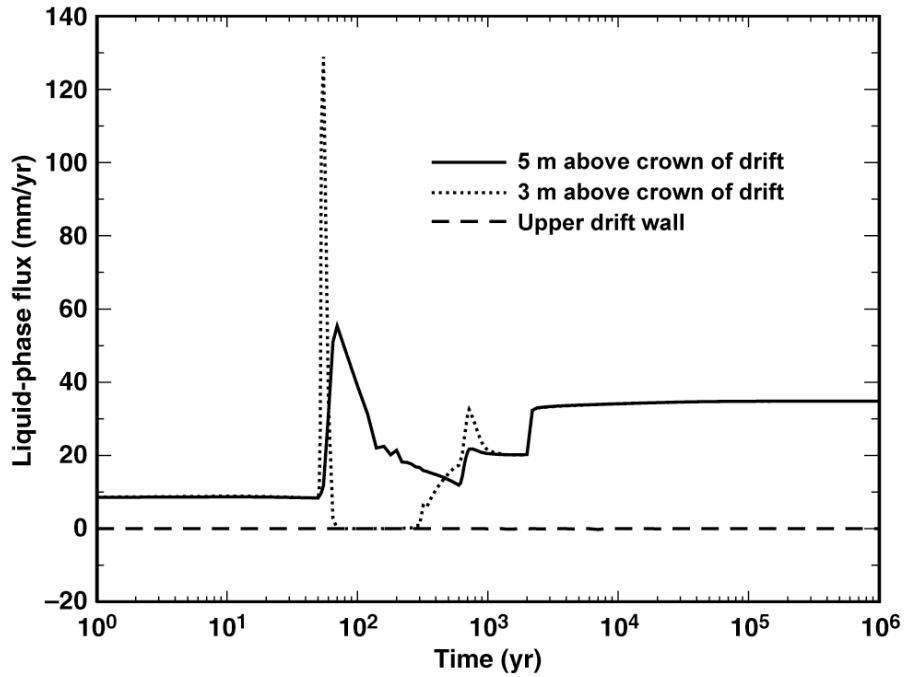
Figure 6-63. Liquid-phase flux at the upper drift wall  $q_{liq, dwTop}$  in the vicinity of a 21-PWR WP for the mean infiltration-flux no-backfill case for the indicated times (Continued)



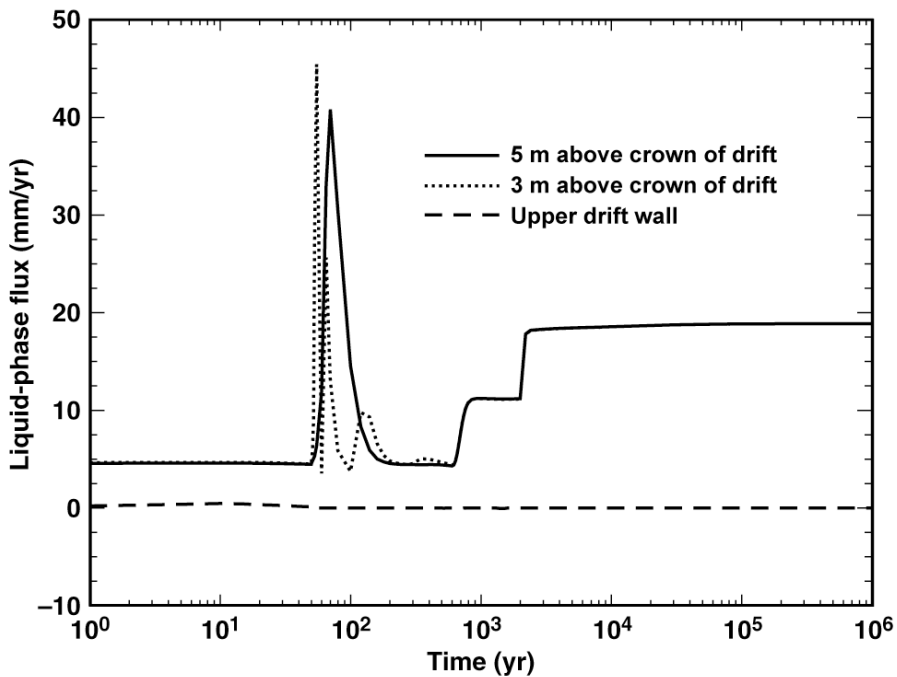
qliq\_dwTop86\_88\_99

Figure 6-63. Liquid-phase flux at the upper drift wall  $q_{liq, dwTop}$  in the vicinity of a 21-PWR WP for the mean infiltration-flux no-backfill case for the indicated times (Continued)

(a) Center of Repository  
 Nevada State Coordinates: Easting = 170535.03 m, Northing = 233640.08 m



(b) Eastern Edge of Repository  
 Nevada State Coordinates: Easting = 171195.16 m, Northing = 233605.06 m



qliq\_16\_16-24\_16

Figure 6-64. Liquid-phase flux history at the indicated locations above the drift at (a) the geographical center of the repository and (b) a location 27.5 m from the edge of the repository. These conditions occur in the vicinity of a 21-PWR WP for the mean infiltration-flux no-backfill case for the indicated times.

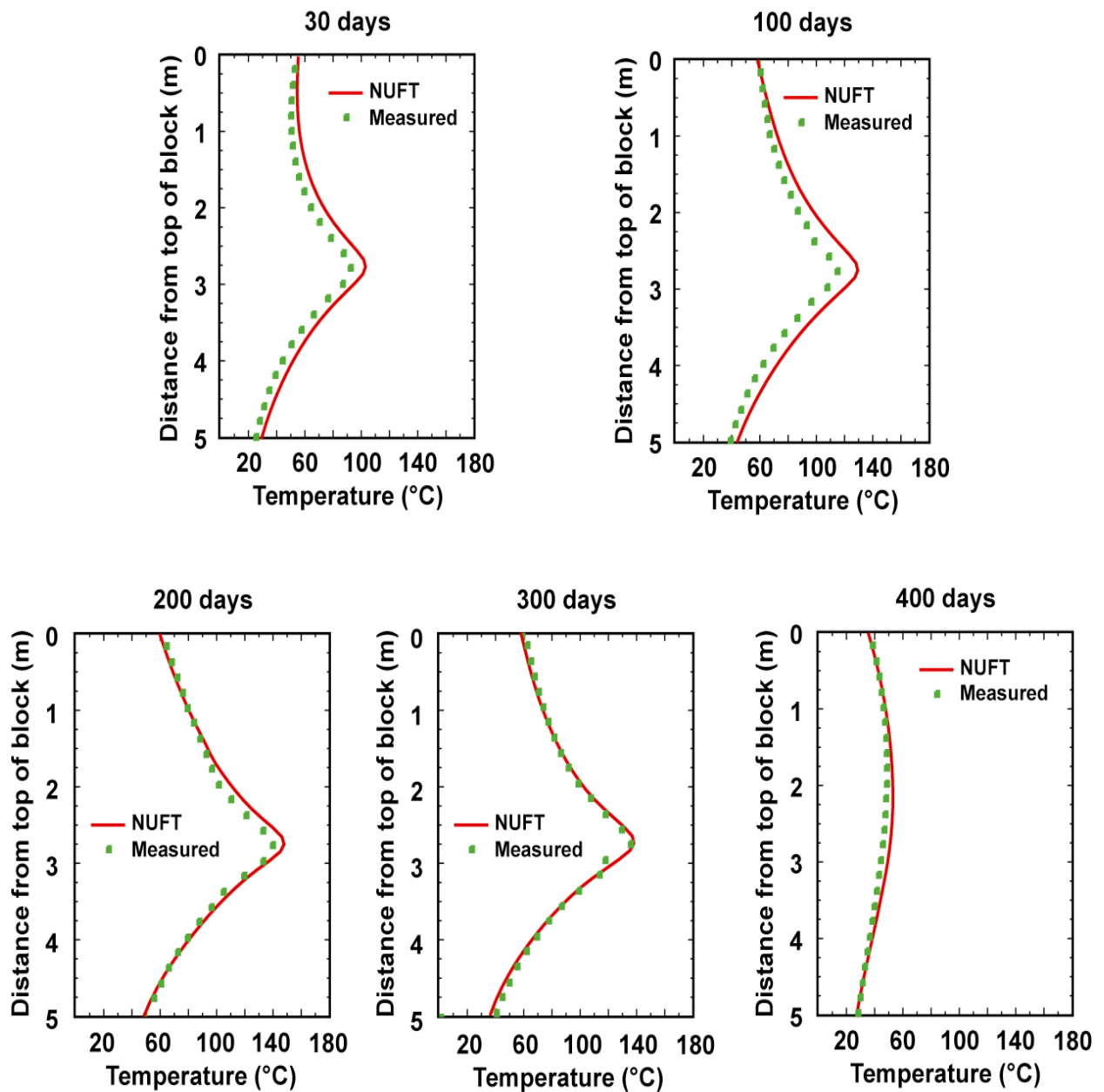


Figure 6-65. Comparison of the NUFT-simulated and measured temperatures along Borehole TT1 is given at six times from 30 to 400 days. The NUFT simulation used the drift-scale hydrologic property set that was used in the MSTHM calculations in this AMR.

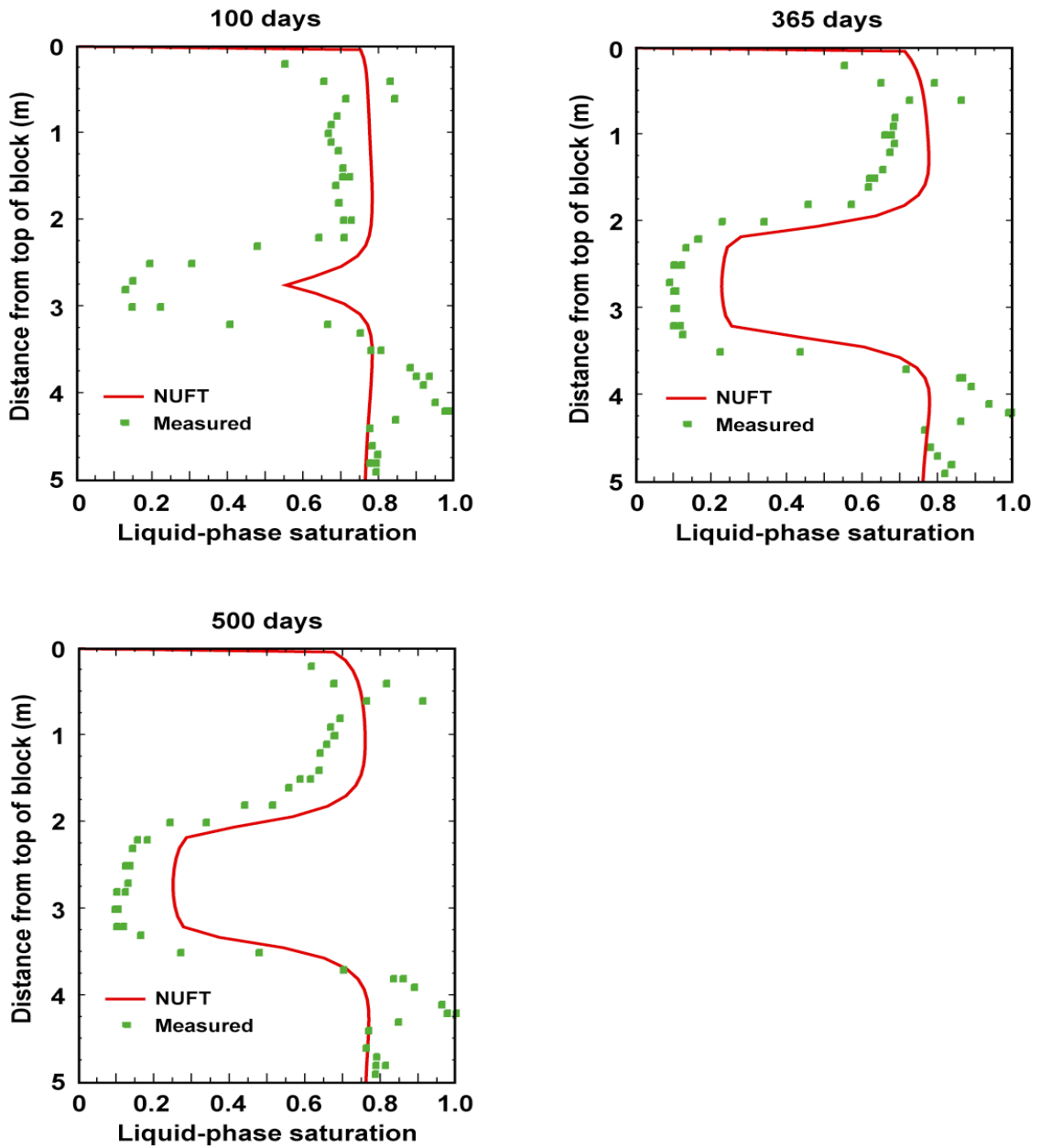


Figure 6-66. Comparison of the NUFT-simulated and measured liquid-phase saturation along Borehole TN3 is given at three times from 100 to 500 days. The NUFT simulation used the drift-scale hydrologic property set that was used in the MSTHM calculations in this AMR.

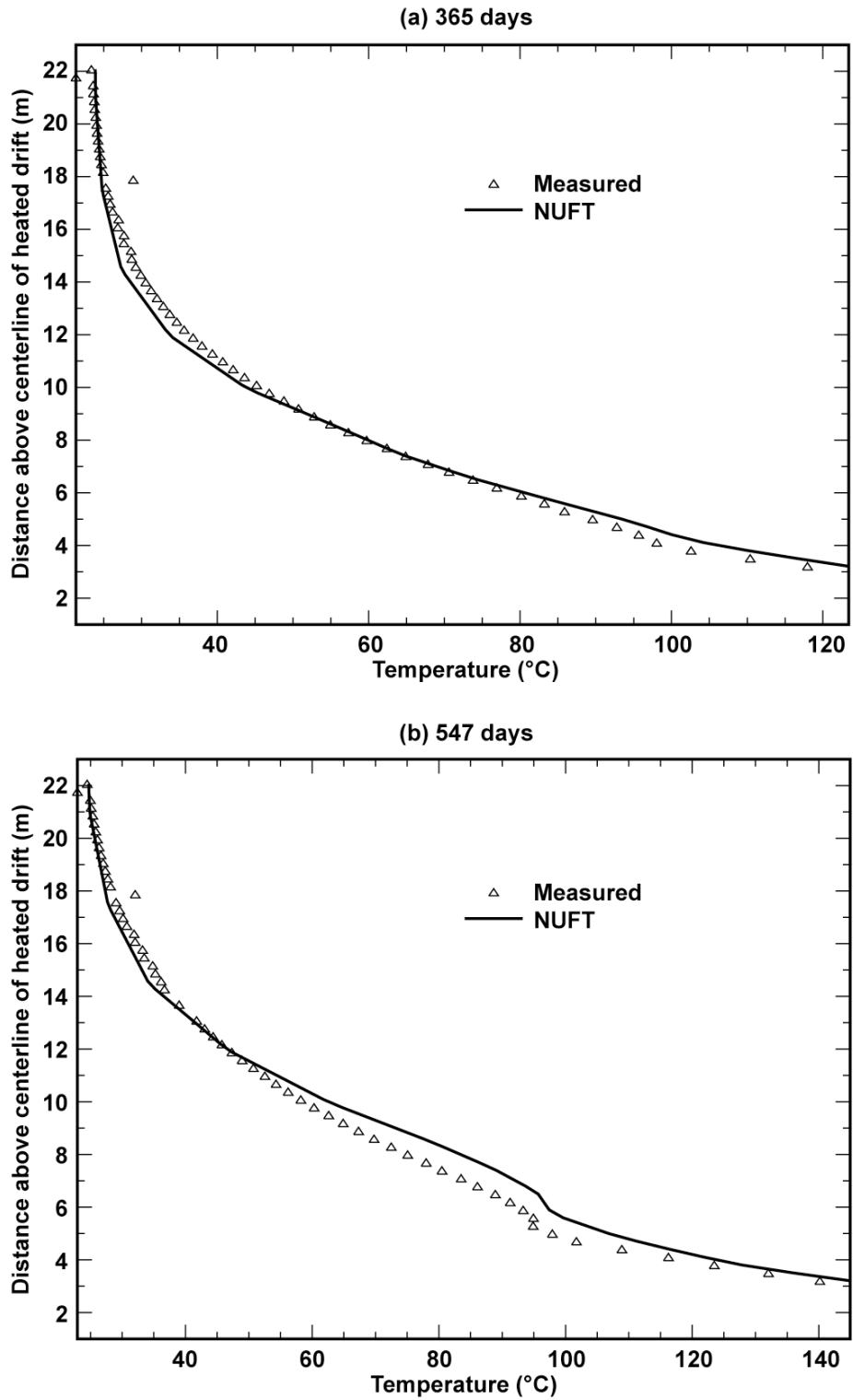


Figure 6-67. Comparison of the NUFT-simulated and measured temperatures along Borehole ESF-HD-137 is given at 365 and 547 days. The NUFT simulation used the drift-scale hydrologic property set that was used in the MSTHM calculations in this AMR.

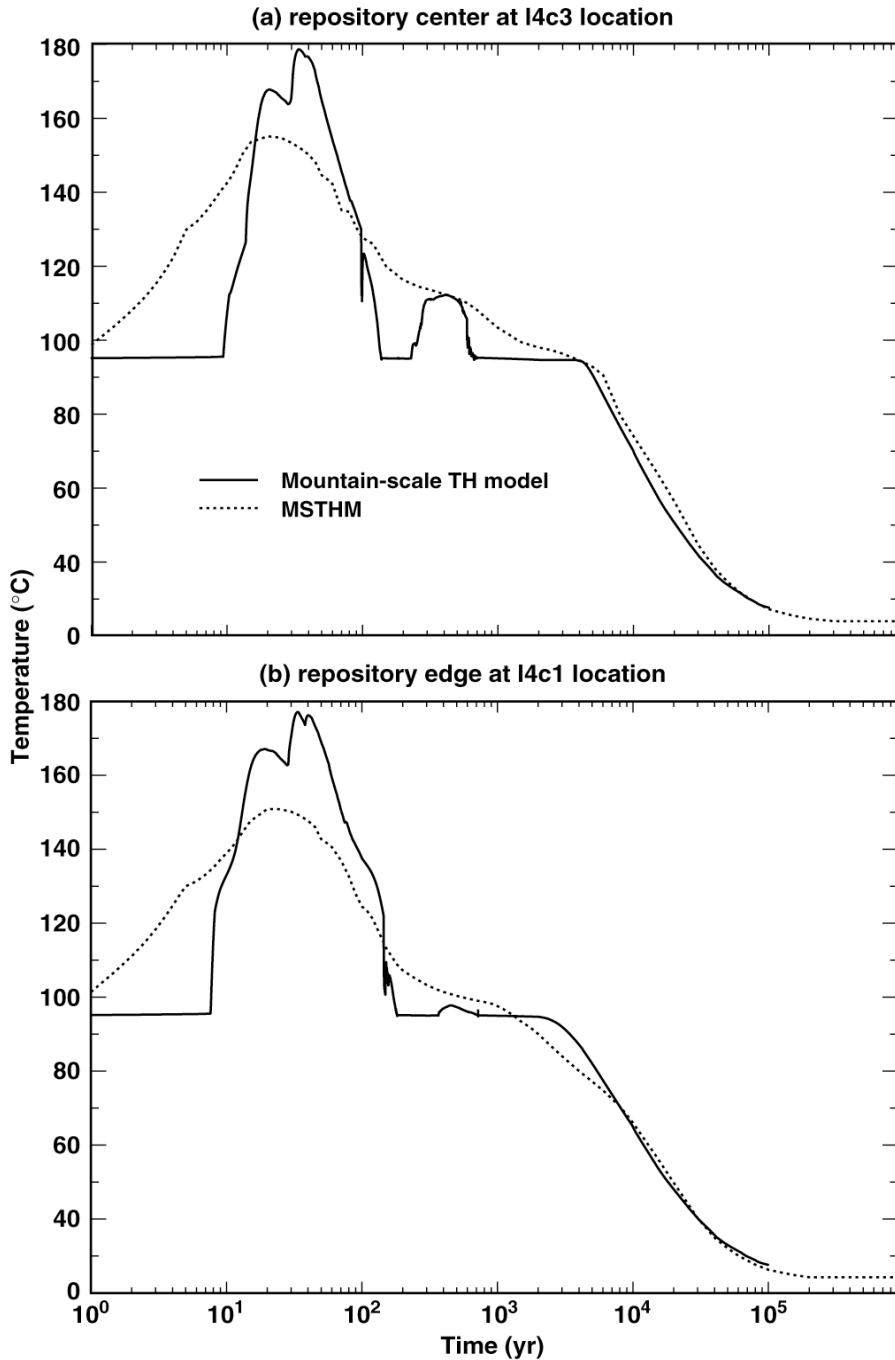
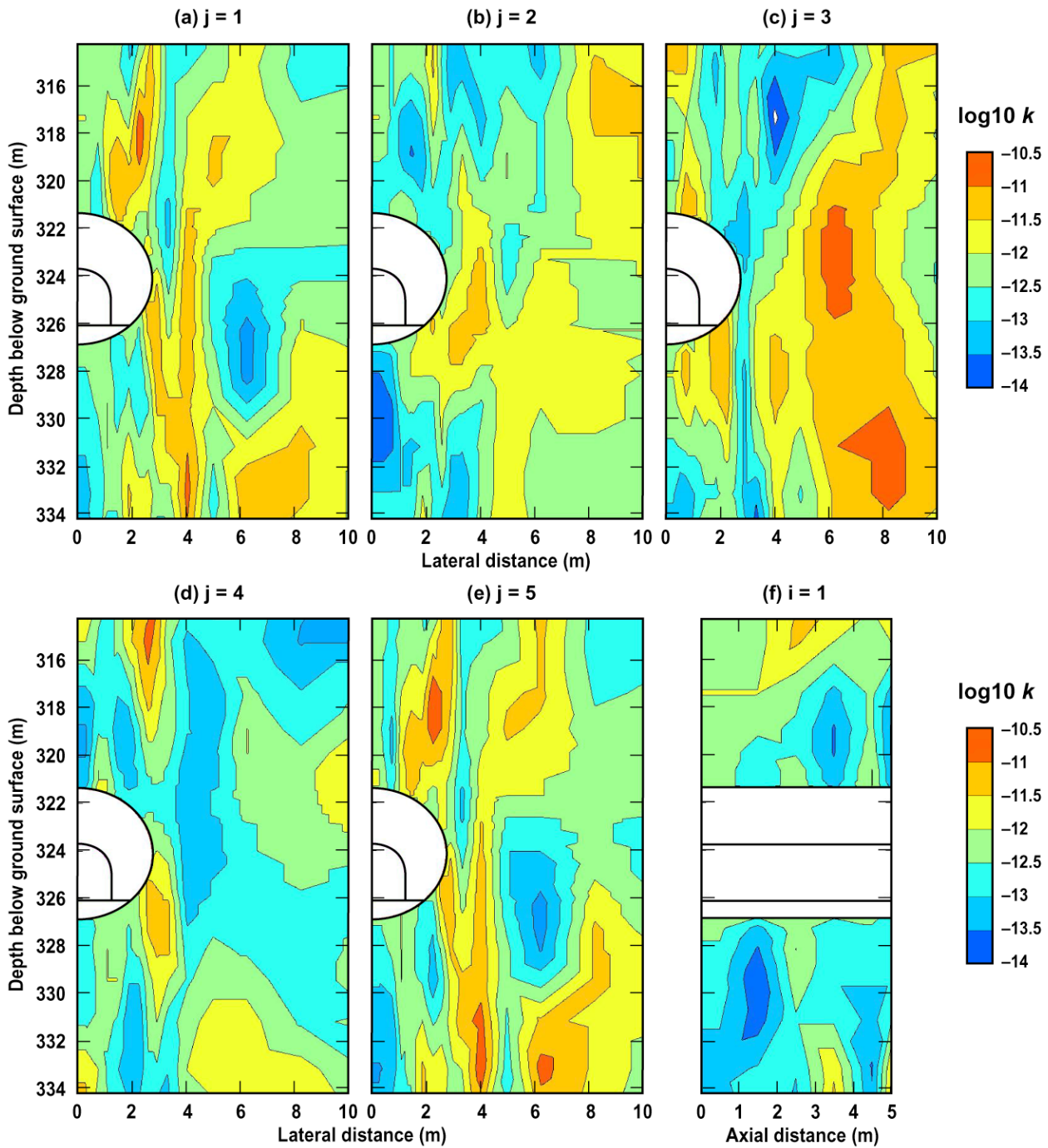


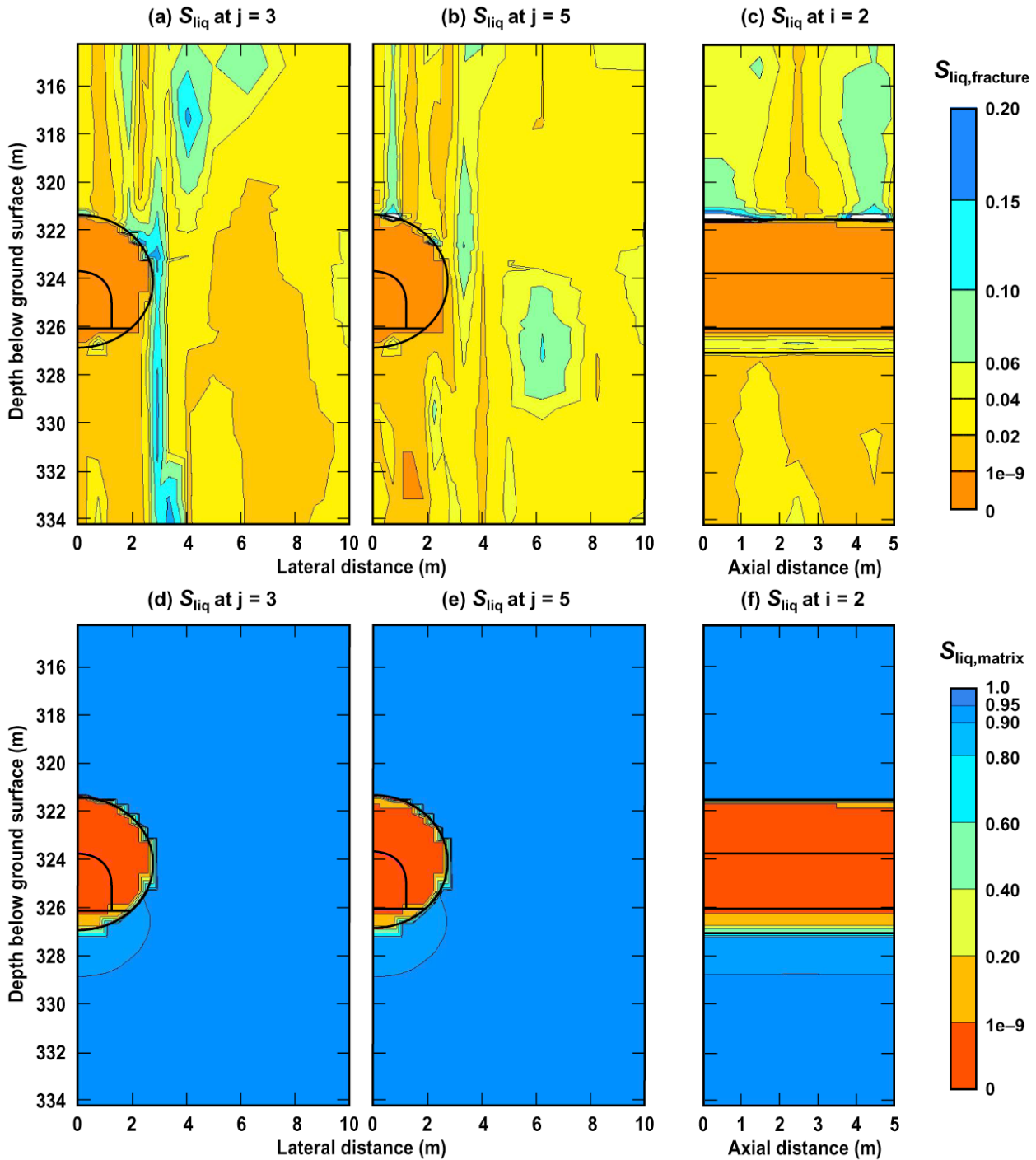
Figure 6-68. Comparison of predicted temperatures at (a) center of the repository (I4c3 location in Table 2-2 of Buscheck et al., 1998) and (b) 100 m from the edge of the repository (I4c1 location) for the 12/97 TSPA-VA base-case  $1 \times 1 \alpha_{f,mean}$  parameter set, where the symbol  $1$  stands for the nominal infiltration-flux  $q_{inf}$  map (average  $q_{inf} = 7.8$  mm/yr) for the present-day climate and the variable  $\alpha_f$  is the van Genuchten “alpha” parameter for fractures. The MSTHM is used to predict drift-wall temperature adjacent to an “average” 21-PWR medium-heat CSNF WP. The east-west cross-sectional mountain-scale TH model is used to predict the drift temperature, which is averaged over the cross section of the drift, arising from a line-averaged heat-source representation of WP decay heat.



K0xz&yz

Figure 6-69. Contours of the log<sub>10</sub> of the bulk permeability *k* field are plotted for stochastic realization A-56. Contours are given (a, b, c, d, e) for vertical xz planes at five locations (*j* = 1, 2, 3, 4, 5), located at axial distances of 0.5, 1.5, 2.5, 3.5, and 4.5 m, respectively. A contour plot is also given (f) for the vertical yz plane located along the central axis of the drift (*i* = 1).

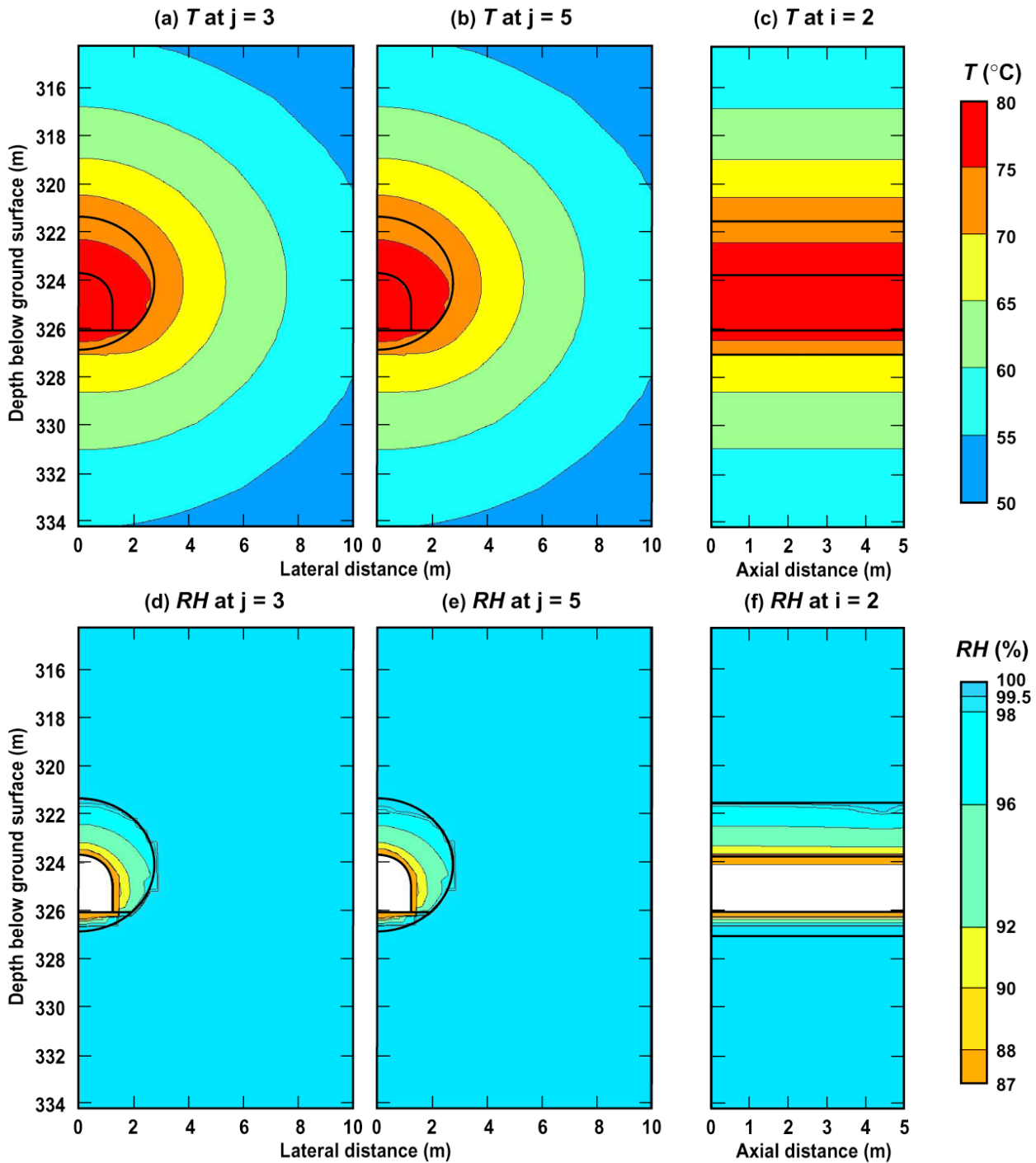
### Liquid-phase saturation at 50 yr



S02f&m\_50y\_xz-yz

Figure 6-70. Contours of liquid-phase saturation  $S_{liq}$  in the fractures (a, b, c) and in the matrix (d, e, f) at two vertical xz planes ( $j = 3, 5$ ) and one vertical yz plane ( $i = 2$ , which is 0.765 m from the centerline of the drift) plotted at 50 yr for stochastic realization A-56 and an AML of 56 MTU/acre

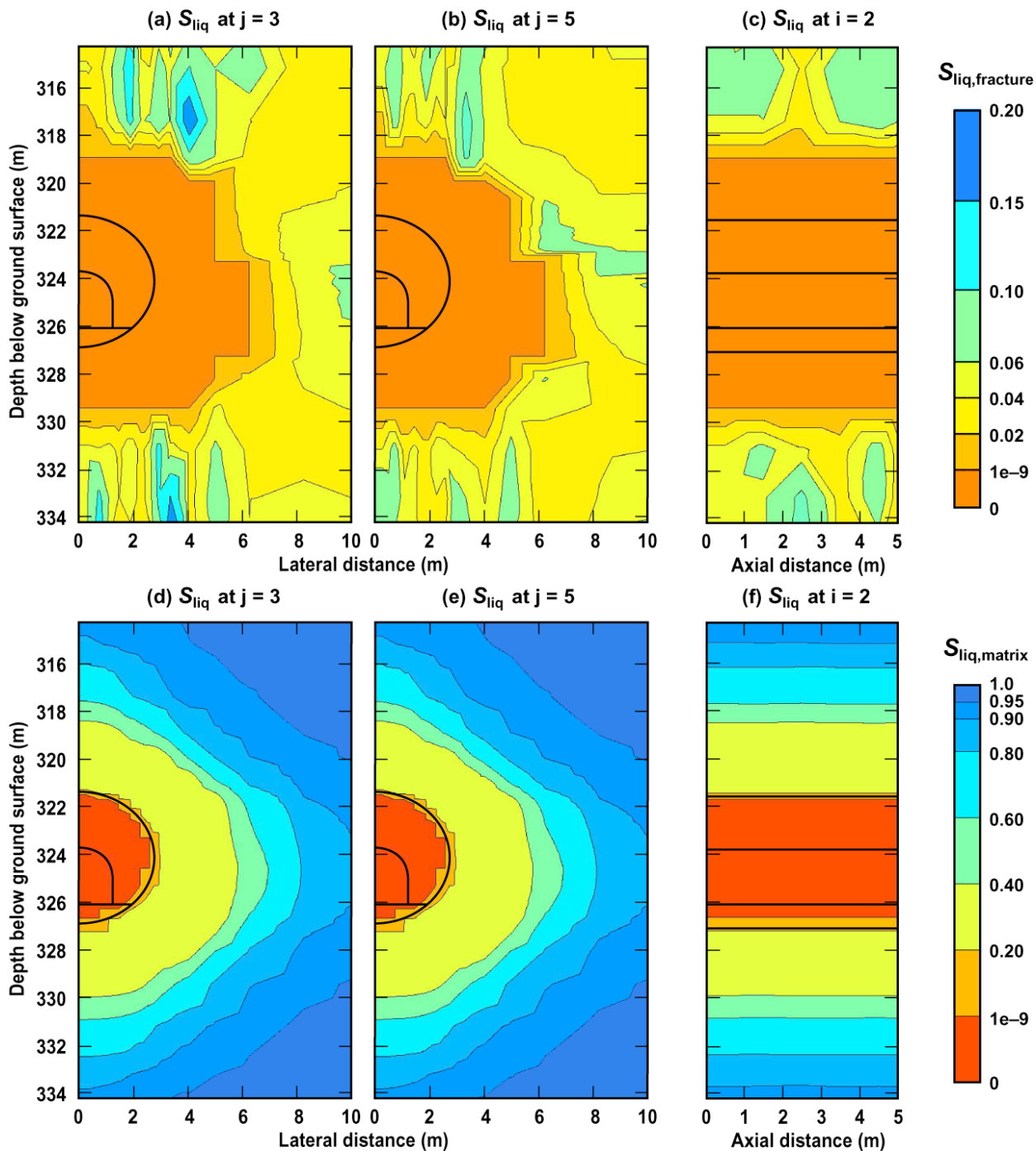
### Temperature and relative humidity at 50 yr



T&RH02m\_50y\_xz-yz

Figure 6-71. Contours of temperature  $T$  (a, b, c) and relative humidity  $RH$  (d, e, f) at two vertical  $xz$  planes ( $j = 3, 5$ ) and one vertical  $yz$  plane ( $i = 2$ , which is 0.765 m from the centerline of the drift), plotted at 50 yr for stochastic realization A-56 and an AML of 56 MTU/acre. Note that the white area in panels d, e, and f correspond to the region where  $RH$  is not predicted in the model.

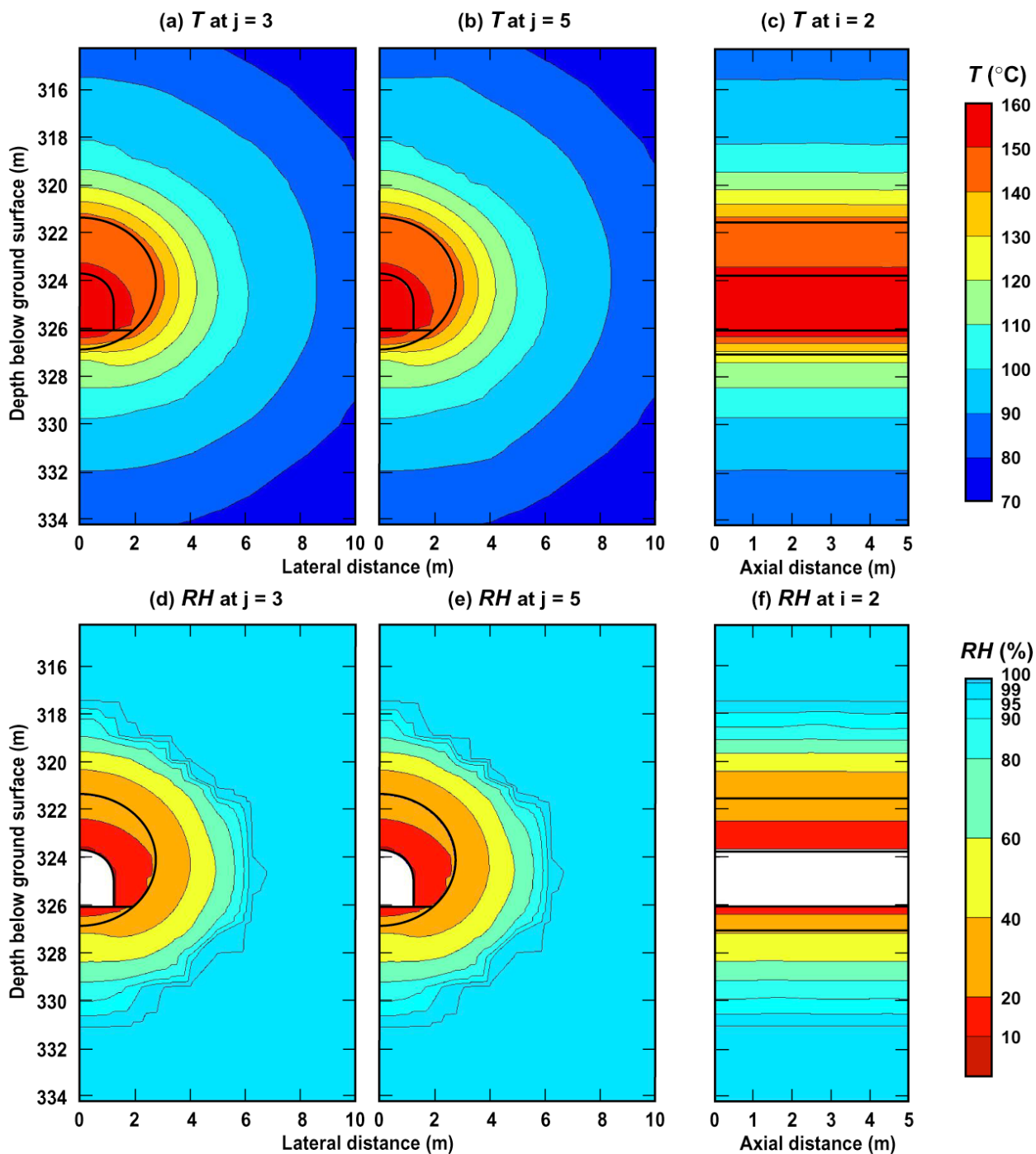
### Liquid-phase saturation at 60 yr



S02f&m\_60y\_xz-yz

Figure 6-72. Contours of liquid-phase saturation  $S_{liq}$  in the fractures (a, b, c) and in the matrix (d, e, f) at two vertical xz planes ( $j = 3, 5$ ) and one vertical yz plane ( $i = 2$ , which is 0.765 m from the centerline of the drift), plotted at 60 yr for stochastic realization A-56 and an AML of 56 MTU/acre

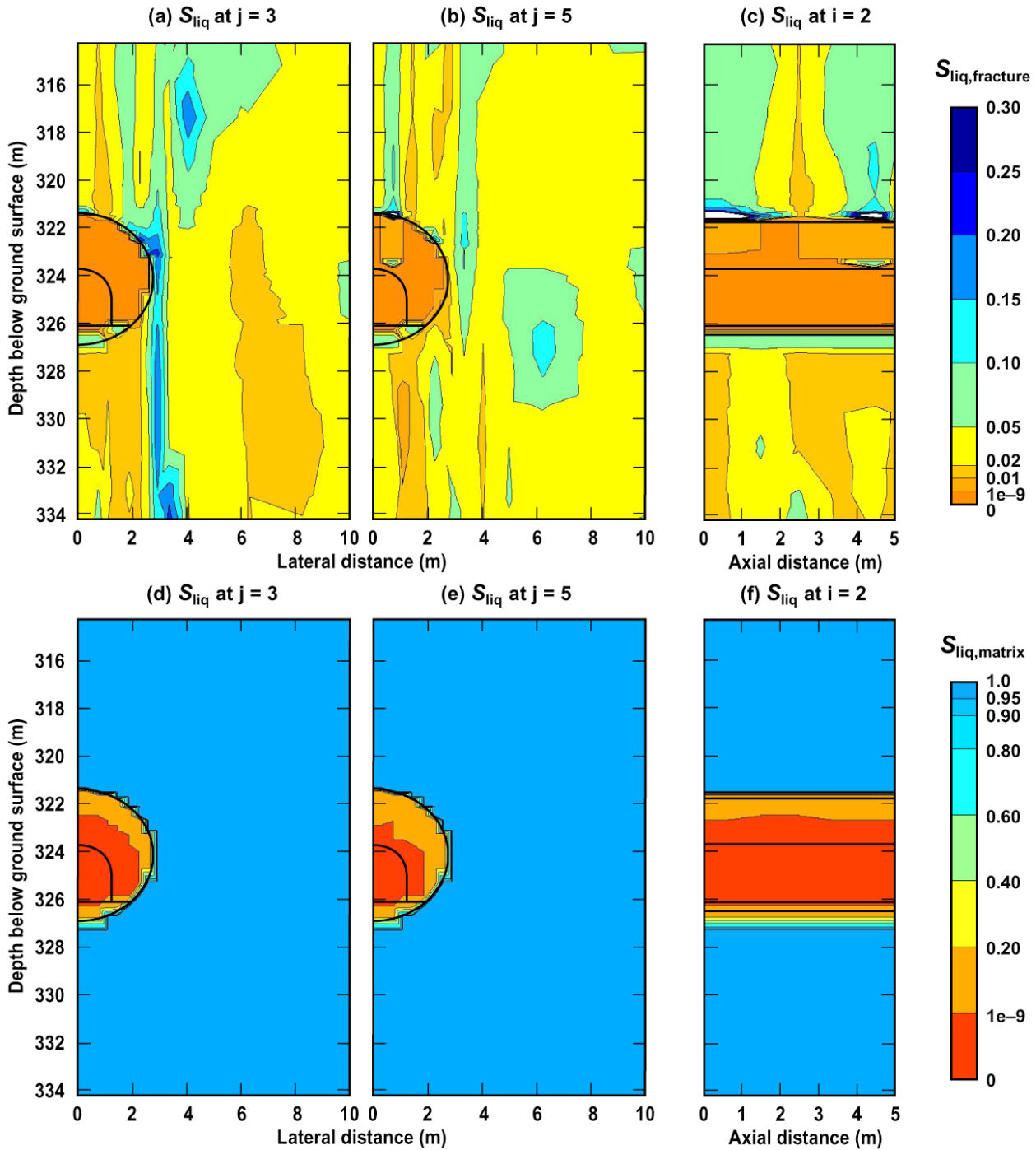
### Temperature and relative humidity at 60 yr



T&RH02m\_60y\_xz-yz

Figure 6-73. Contours of temperature  $T$  (a, b, c) and relative humidity  $RH$  (d, e, f) at two vertical  $xz$  planes ( $j = 3, 5$ ) and one vertical  $yz$  plane ( $i = 2$ , which is 0.765 m from the centerline of the drift) are plotted at 60 yr for stochastic realization A-56 and an AML of 56 MTU/acre. Note that the white area in panels d, e, and f correspond to the region where  $RH$  is not predicted in the model

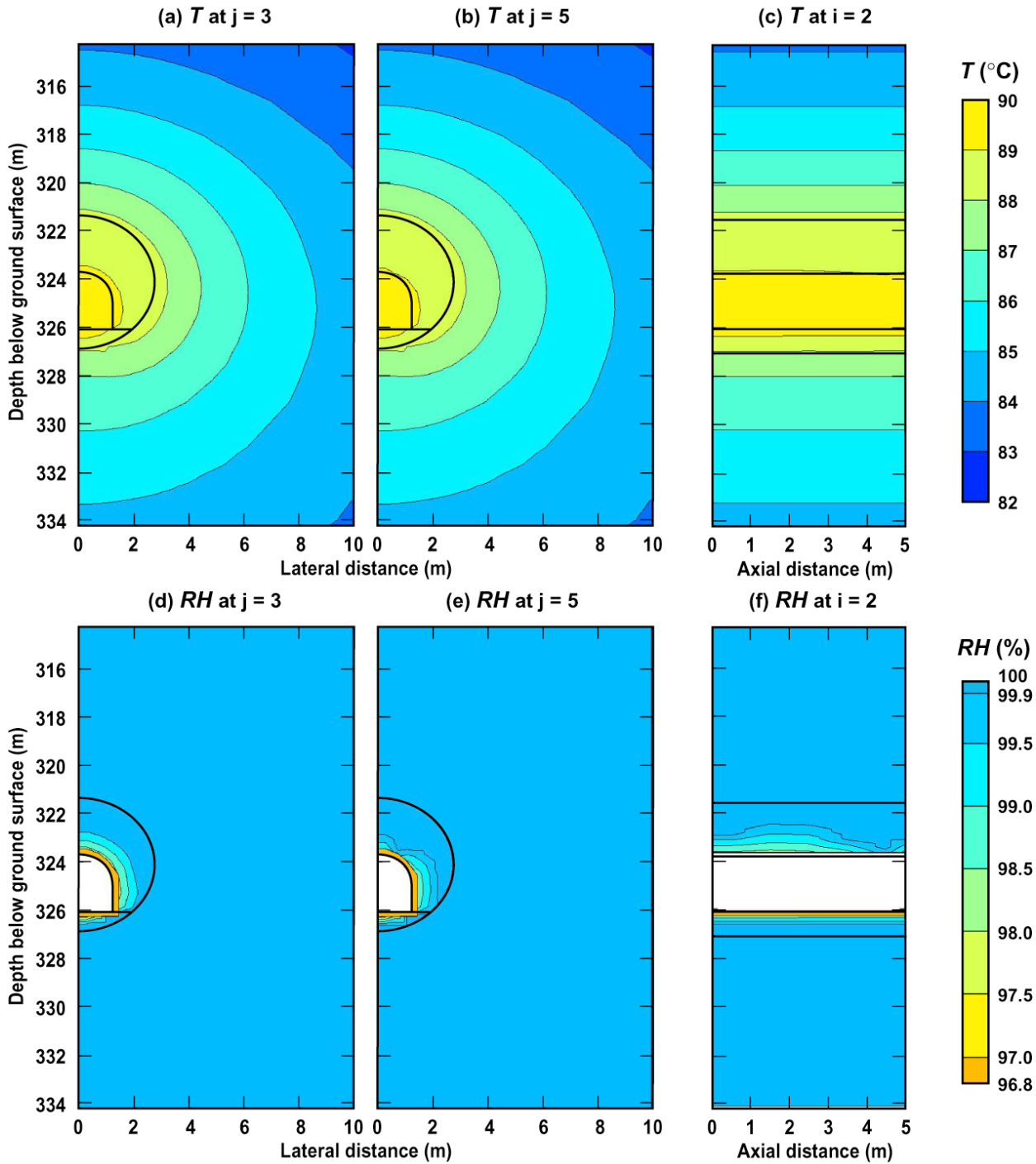
### Liquid-phase saturation at 1900 yr



S02f&m\_1900y\_xz-yz

Figure 6-74. Contours of liquid-phase saturation  $S_{liq}$  in the fractures (a, b, c) and in the matrix (d, e, f) at two vertical  $xz$  planes ( $j = 3, 5$ ) and one vertical  $yz$  plane ( $i = 2$ , which is 0.765 m from the centerline of the drift) are plotted at 1900 yr for stochastic realization A-56 and an AML of 56 MTU/acre

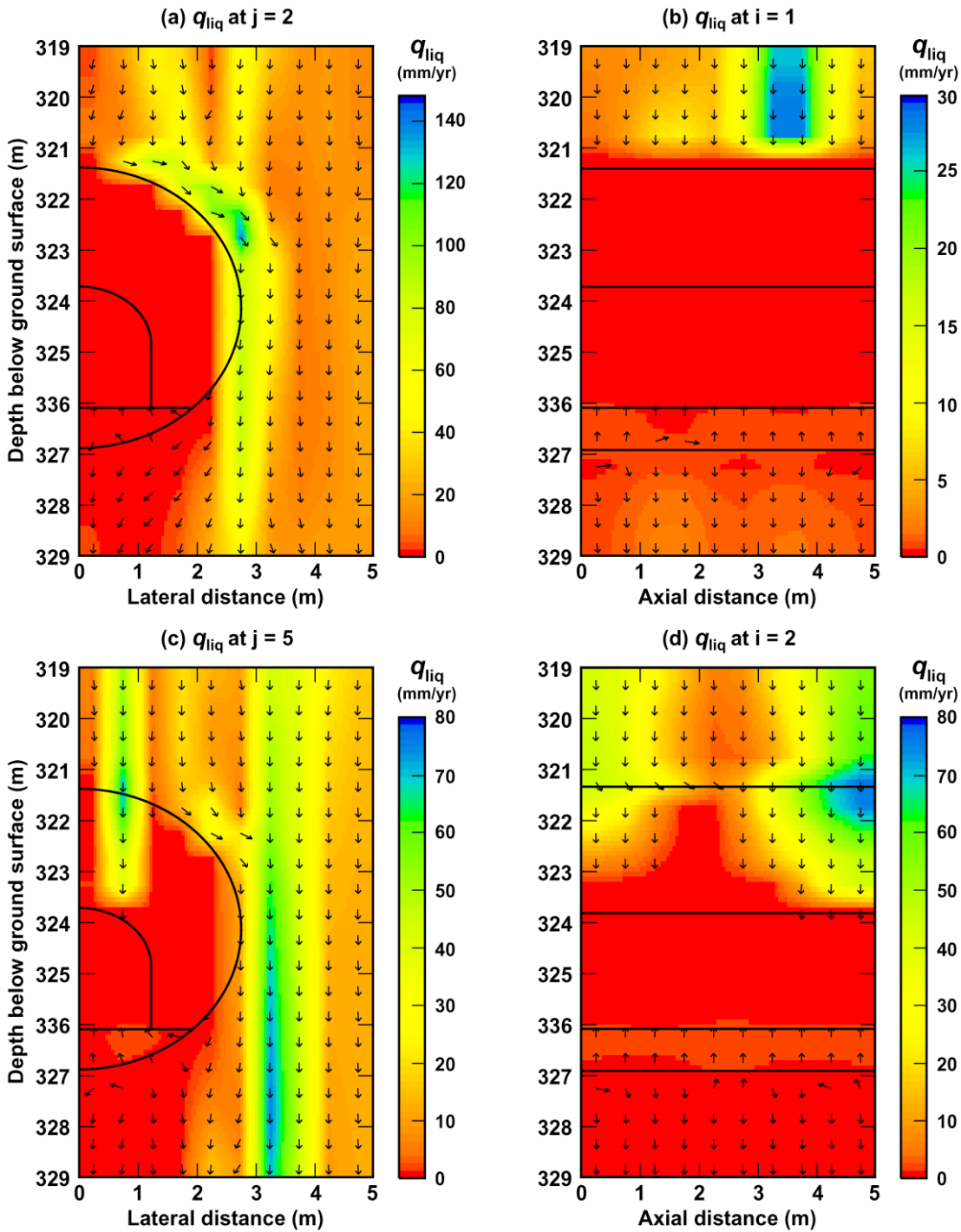
Temperature and relative humidity at 1900 yr



T&RH02m\_1900y\_xz-yz

Figure 6-75. Contours of temperature  $T$  (a, b, c) and relative humidity  $RH$  (d, e, f) at two vertical  $xz$  planes ( $j = 3, 5$ ) and one vertical  $yz$  plane ( $i = 2$ , which is 0.765 m from the centerline of the drift), are plotted at 1900 yr for stochastic realization A-56 and an AML of 56 MTU/acre. Note that the white area in panels d, e, and f correspond to the region where  $RH$  is not predicted in the model

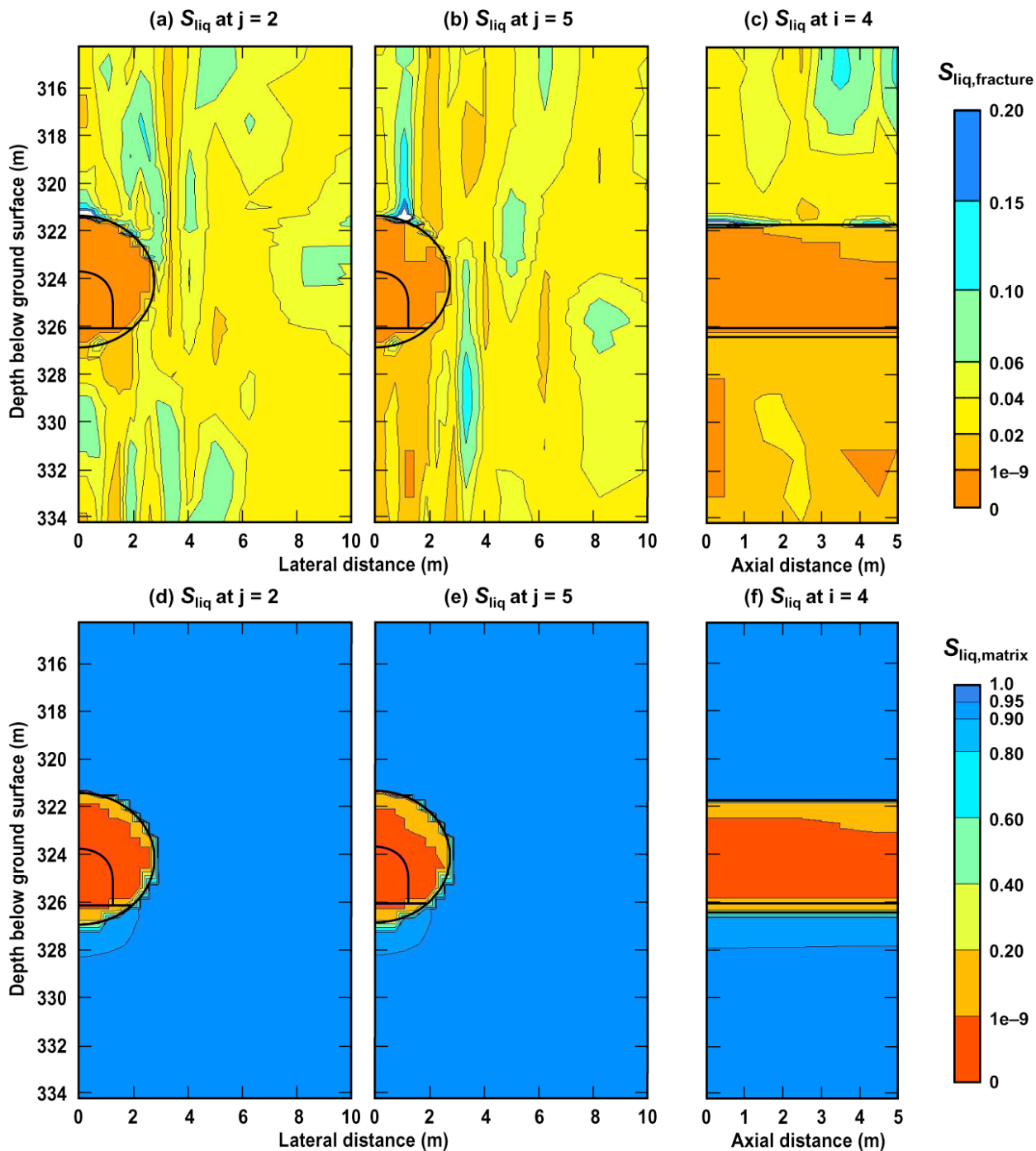
### Liquid-phase flux at 1900 yr



qliq56\_1900y\_xz-yz

Figure 6-76. Contours of liquid-phase flux  $q_{liq}$  in the fractures and in the drift at (a, c) two vertical xz planes ( $j = 2, 5$ ) and (b, d) two vertical yz planes ( $i=1$ , which is at the centerline of the drift and  $i = 2$ , which is 0.765m from the centerline of the drift) are plotted at 1900 yr for stochastic realization A-56 and an AML of 56 MTU/acre. The arrows show the direction of flow

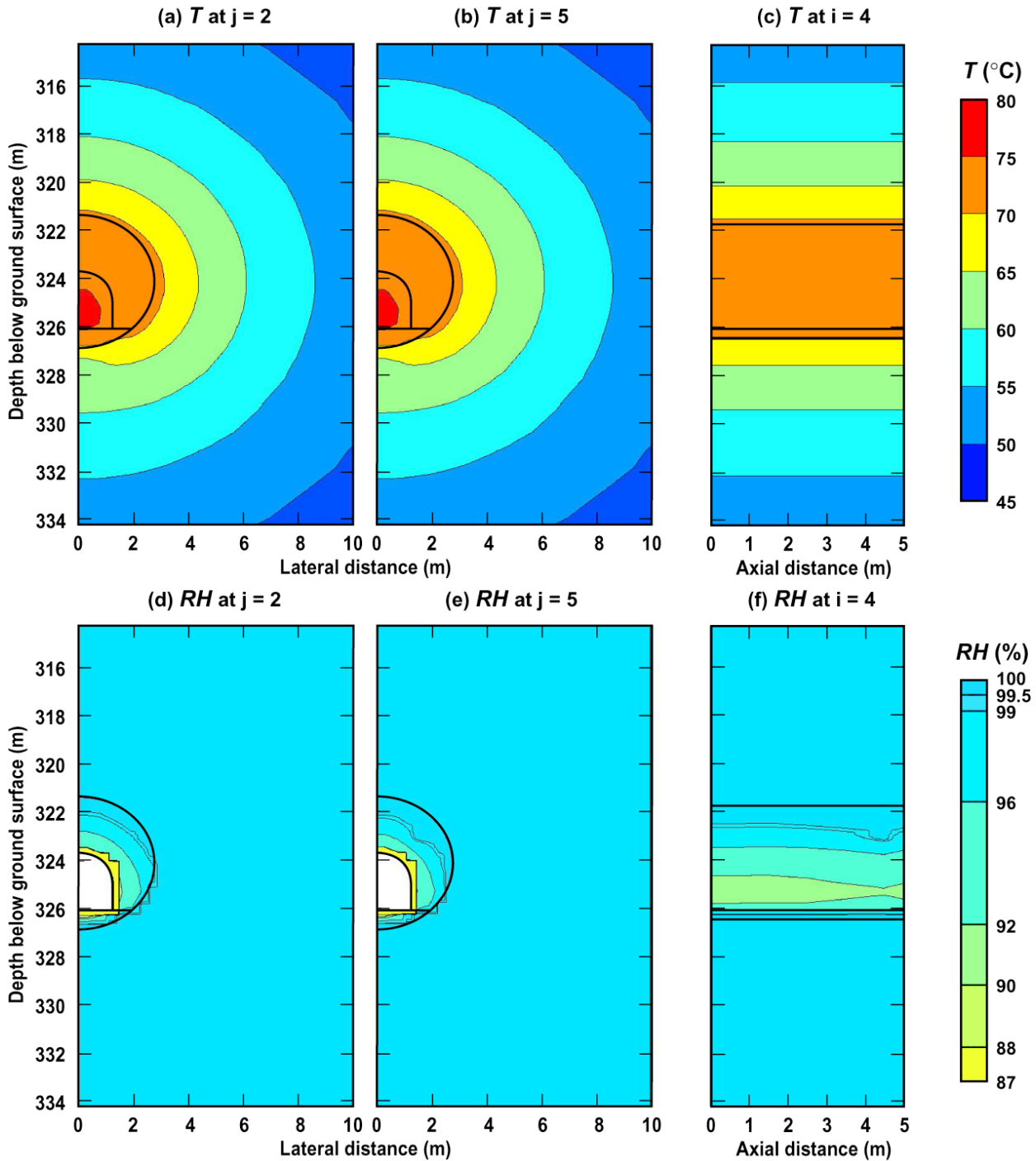
### Liquid-phase saturation at 50 yr



S34\_02f&m\_50y\_xz-yz

Figure 6-77. Contours of liquid-phase saturation  $S_{liq}$  in the fractures (a, b, c) and in the matrix (d, e, f) at two vertical xz planes ( $j = 2, 5$ ) and one vertical yz plane ( $i = 4$ , which is 1.4671 m from the centerline of the drift) are plotted at 50 yr for stochastic realization A-34 and an AML of 34 MTU/acre

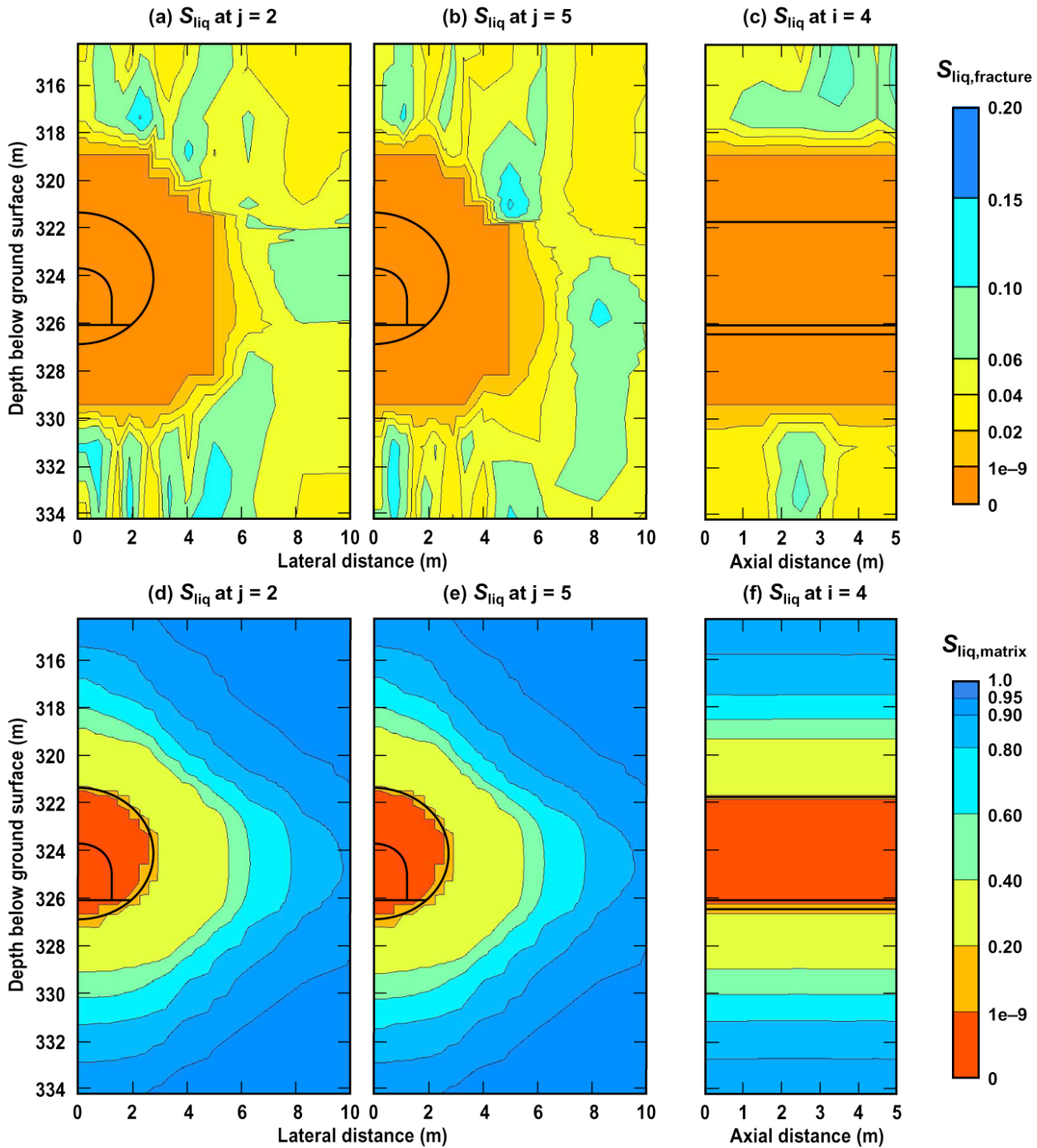
### Temperature and relative humidity at 50 yr



T&RH34\_02m\_50y\_xz-yz

Figure 6-78. Contours of temperature  $T$  (a, b, c) and relative humidity  $RH$  (d, e, f) at two vertical  $xz$  planes ( $j = 2, 5$ ) and one vertical  $yz$  plane ( $i = 4$ , which is 1.4671 m from the centerline of the drift) are plotted at 50 yr for stochastic realization A-34 and an AML of 34 MTU/acre. Note that the white area in panels d, e, and f correspond to the region where  $RH$  is not predicted in the model

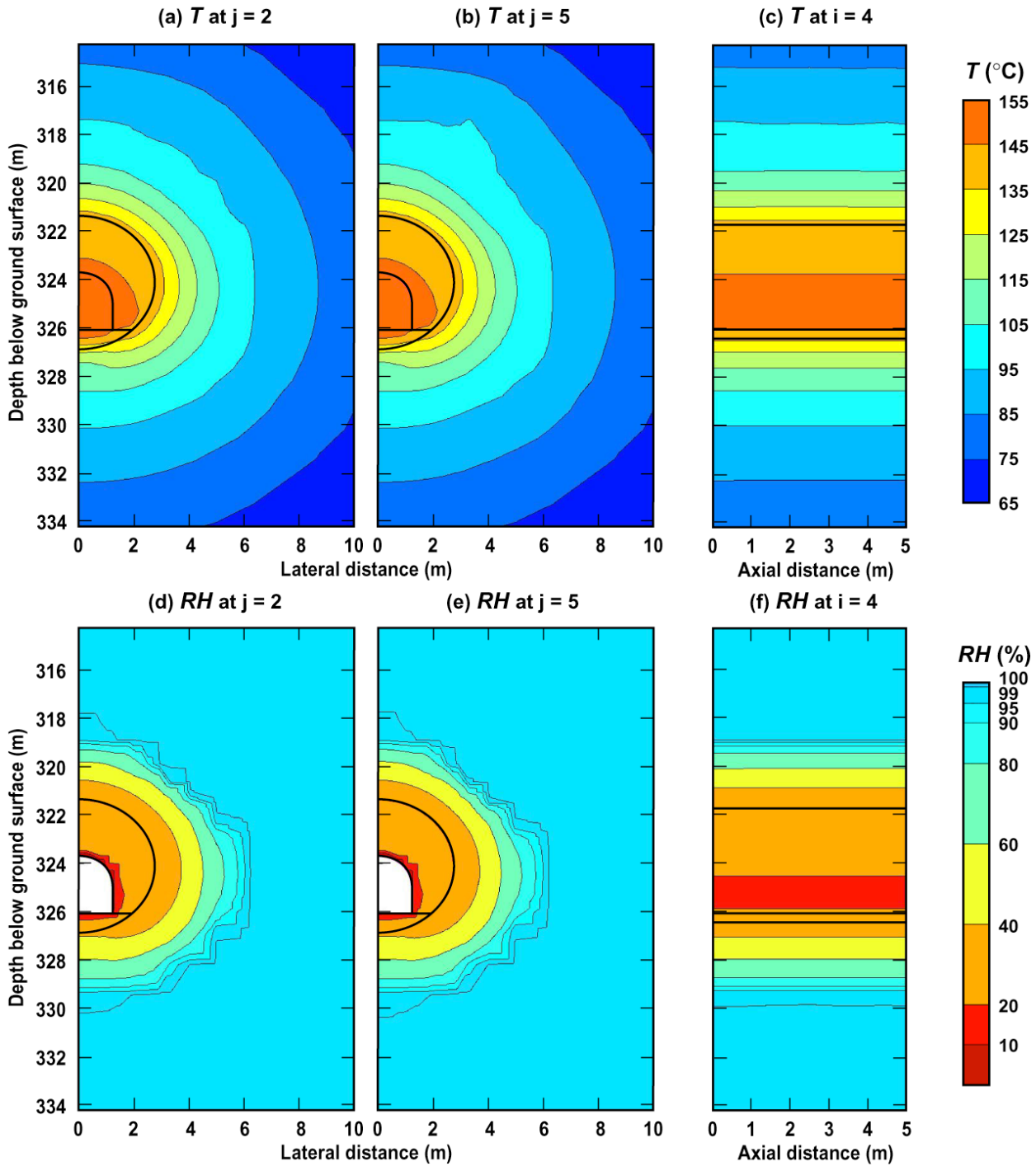
### Liquid-phase saturation at 60 yr



S34\_02f&m\_60y\_xz-yz

Figure 6-79. Contours of liquid-phase saturation  $S_{liq}$  in the fractures (a, b, c) and in the matrix (d, e, f) at two vertical xz planes ( $j = 2, 5$ ) and one vertical yz plane ( $i = 4$ , which is 1.4671 m from the centerline of the drift) are plotted at 60 yr for stochastic realization A-34 and an AML of 34 MTU/acre

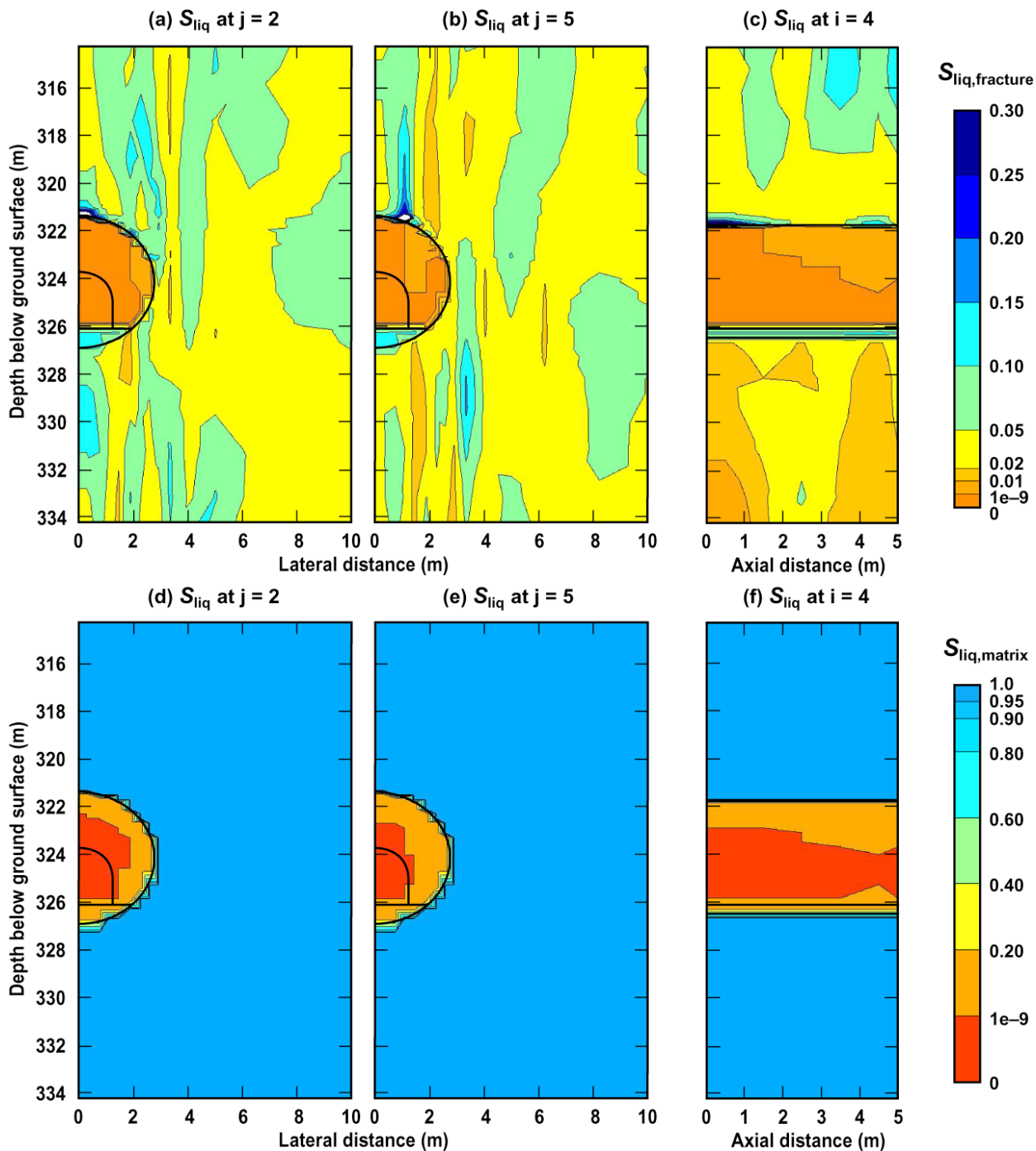
### Temperature and relative humidity at 60 yr



T&RH34\_02m\_60y\_xz-yz

Figure 6-80. Contours of temperature  $T$  (a, b, c) and relative humidity  $RH$  (d, e, f) at two vertical  $xz$  planes ( $j = 2, 5$ ) and one vertical  $yz$  plane ( $i = 4$ , which is 1.4671 m from the centerline of the drift) are plotted at 60 yr for stochastic realization A-34 and an AML of 34 MTU/acre. Note that the white area in panels d, e, and f correspond to the region where  $RH$  is not predicted in the model.

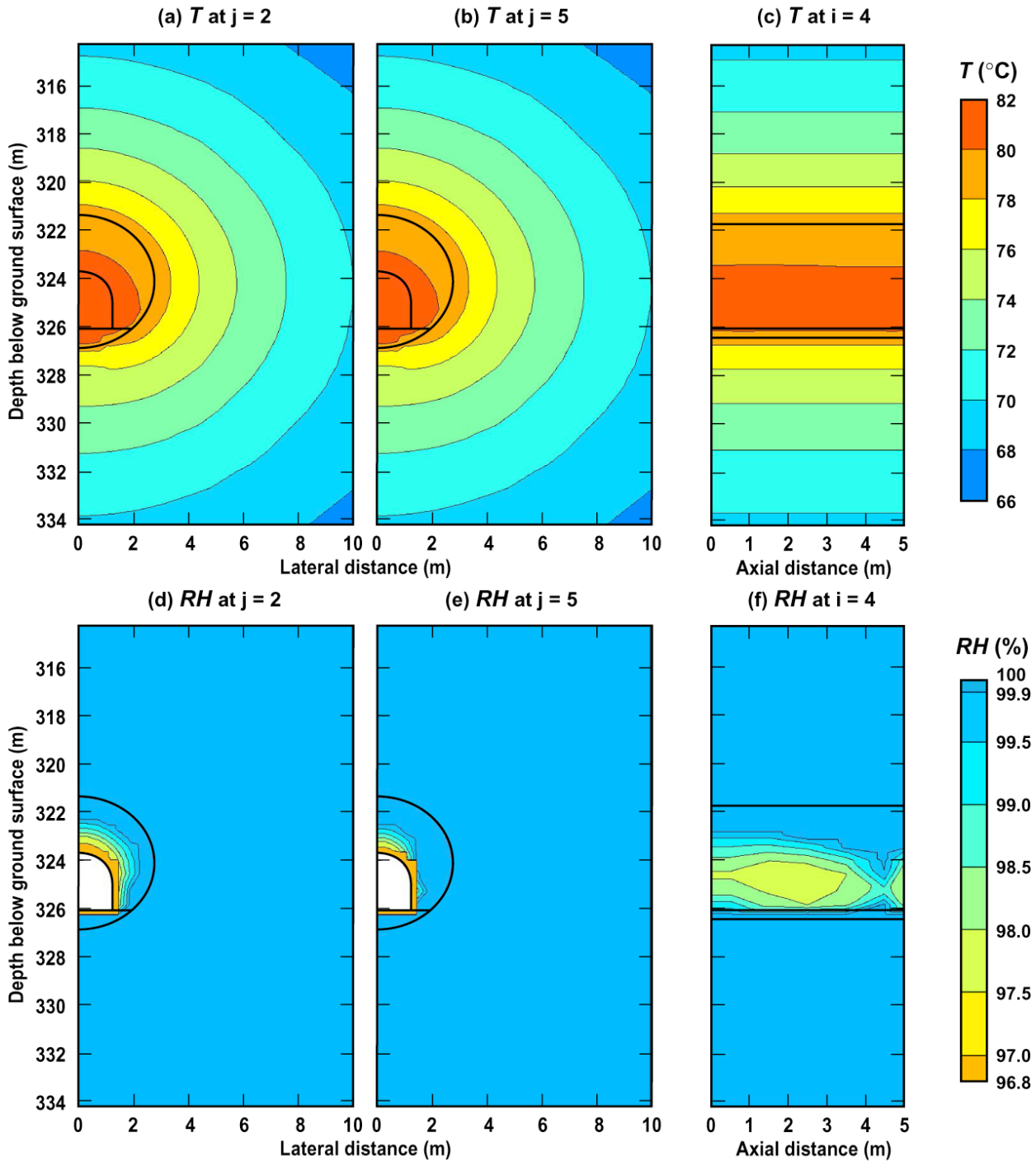
### Liquid-phase saturation at 700 yr



S34\_02f&m\_700y\_xz-yz

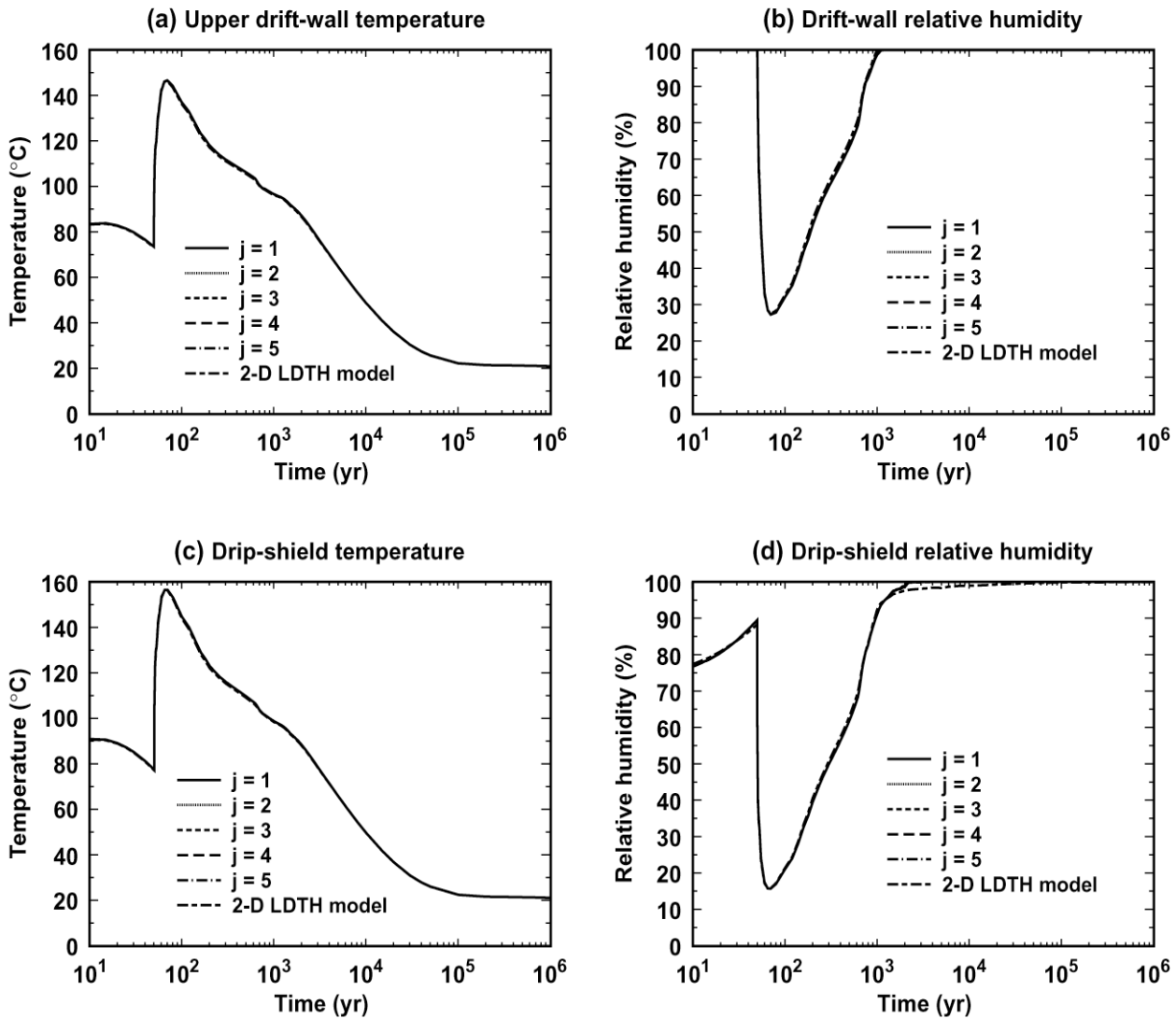
Figure 6-81. Contours of liquid-phase saturation  $S_{liq}$  in the fractures (a, b, c) and in the matrix (d, e, f) at two vertical xz planes ( $j = 2, 5$ ) and one vertical yz plane ( $i = 4$ , which is 1.4671 m from the centerline of the drift) are plotted at 700 yr for stochastic realization A-34 and an AML of 34 MTU/acre

Temperature and relative humidity at 700 yr



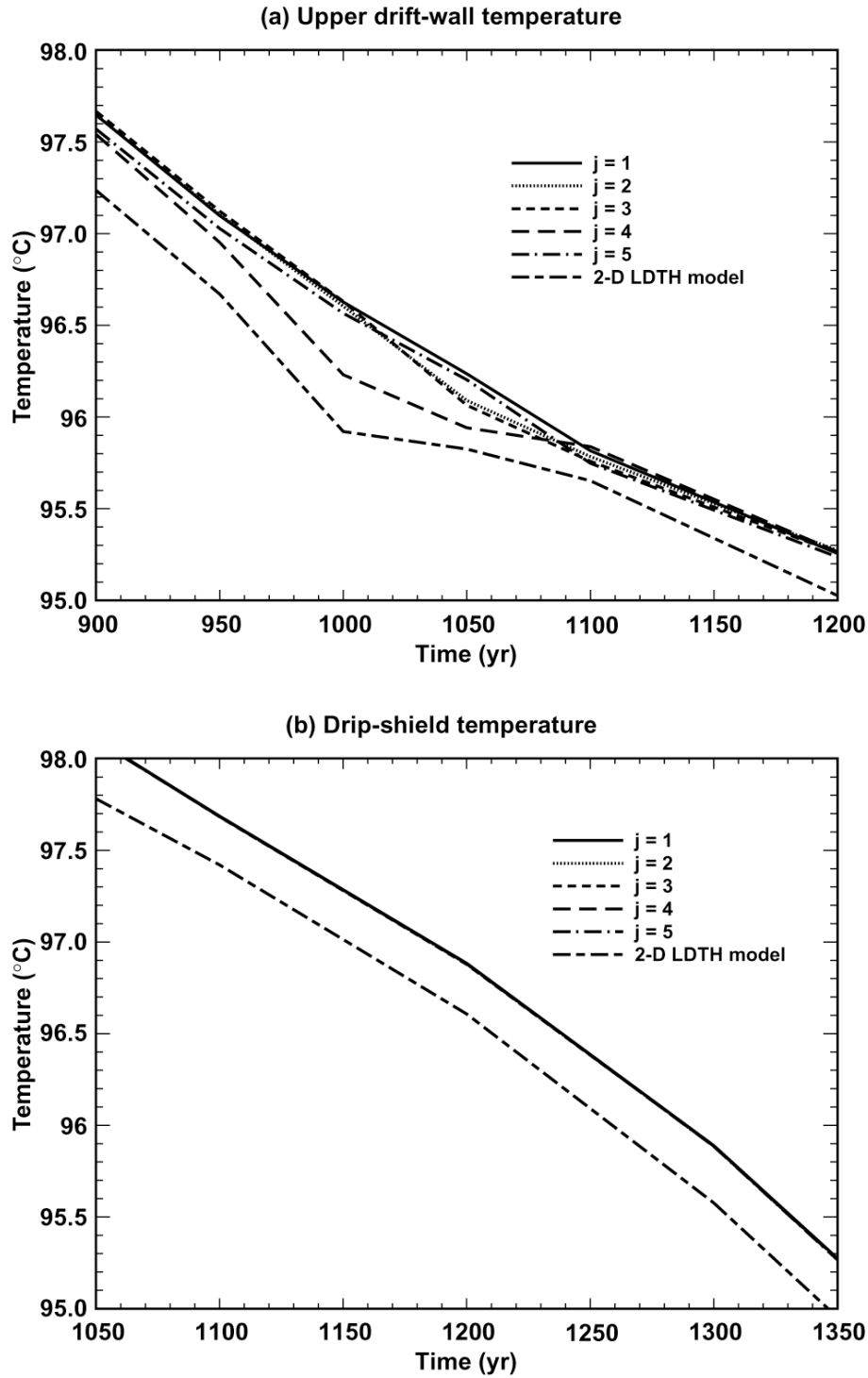
T&RH34\_02m\_700y\_xz-yz

Figure 6-82. Contours of temperature  $T$  (a, b, c) and relative humidity  $RH$  (d, e, f) at two vertical  $xz$  planes ( $j = 2, 5$ ) and one vertical  $yz$  plane ( $i = 4$ , which is 1.4671 m from the centerline of the drift) are plotted at 700 yr for stochastic realization A-34 and an AML of 34 MTU/acre. Note that the white area in panels d, e, and f correspond to the region where  $RH$  is not predicted in the model.



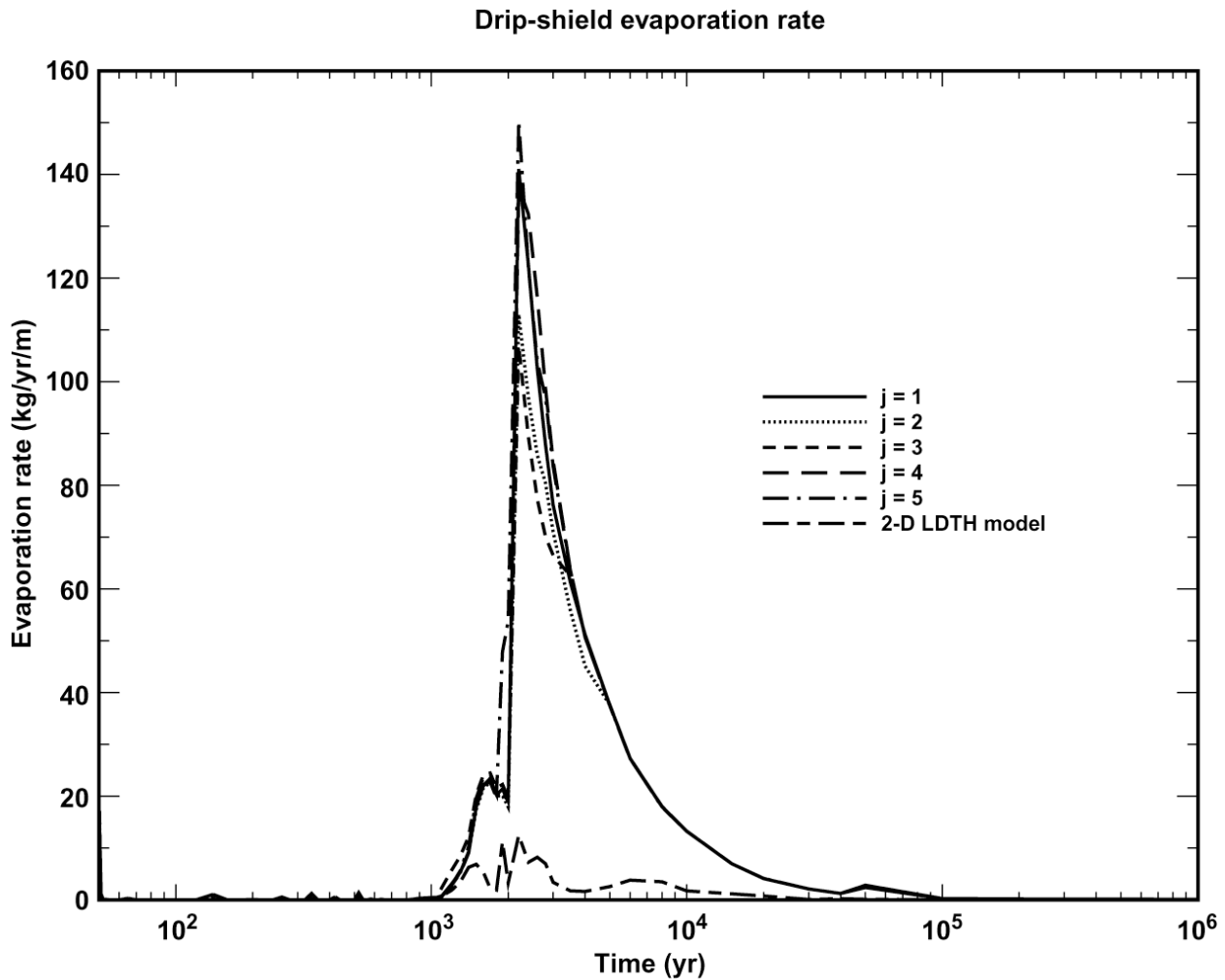
T&RH56-02\_j1-j5-2d

Figure 6-83. Temperature and relative-humidity histories are given at the drift wall and drip shield for stochastic realization A-56 and an AML of 56 MTU/acre. Temperature at the upper drift wall (a) is averaged from springline to springline. Relative humidity at the drift wall (b) is averaged over the entire perimeter of the drift. Drip-shield temperature (c) and relative humidity (d) are averaged over the entire drip shield. Histories are given at five axial locations ( $j = 1, 2, 3, 4,$  and  $5$ ) for the equivalent 2-D homogeneous LDTH model.



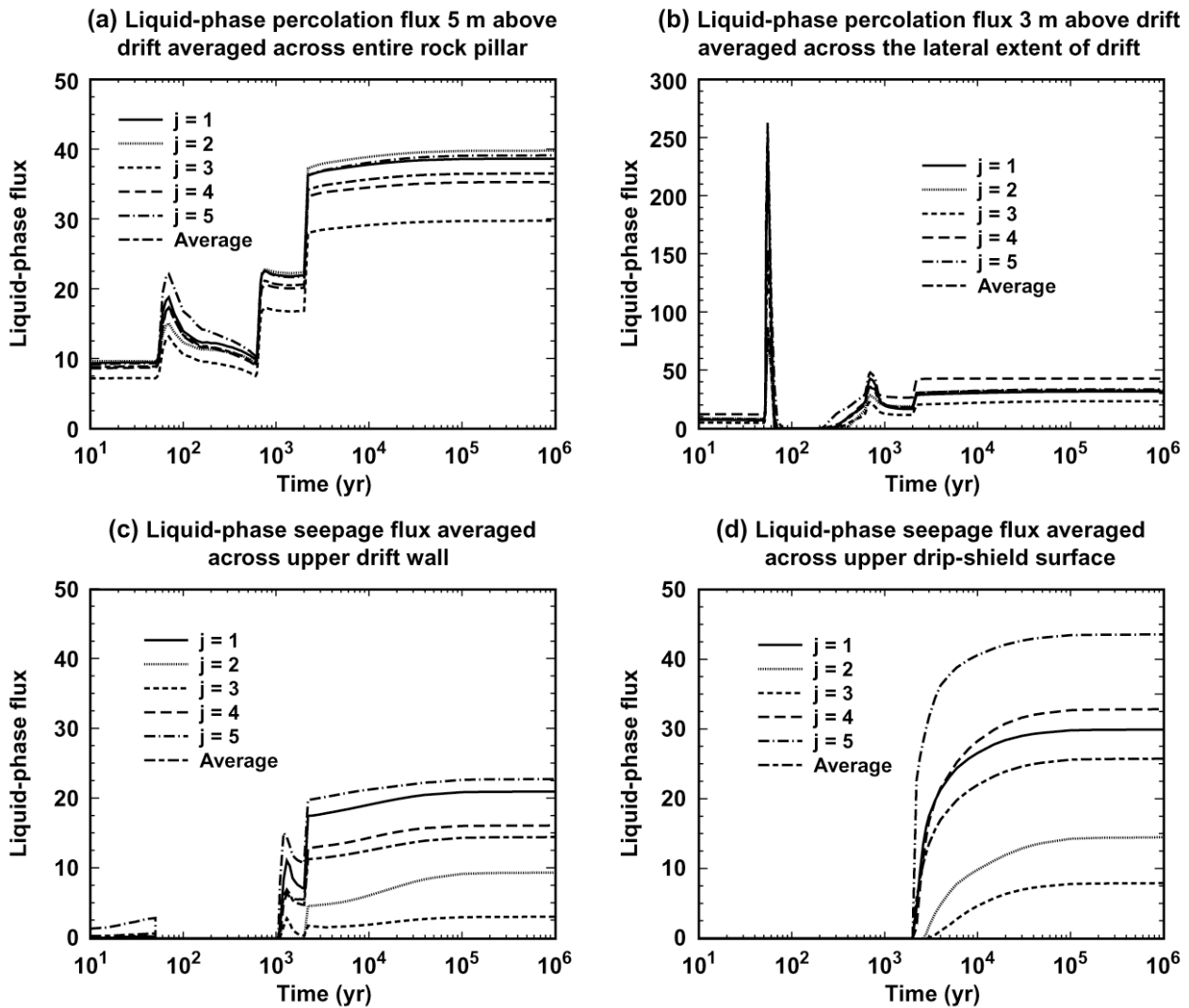
T56-02\_j1-j5-2d

Figure 6-84. Temperature histories are given at the drift wall and drip shield for stochastic realization A-56 and an AML of 56 MTU/acre. Temperature at the upper drift wall (a) is averaged from springline to springline. Drip-shield temperature (b) is averaged over the entire drip shield. Histories are given at five axial locations ( $j = 1, 2, 3, 4,$  and  $5$ ) for the corresponding 2-D LDTH model with an homogeneous drift-scale bulk permeability distribution. This plot focuses on the end of the boiling period.



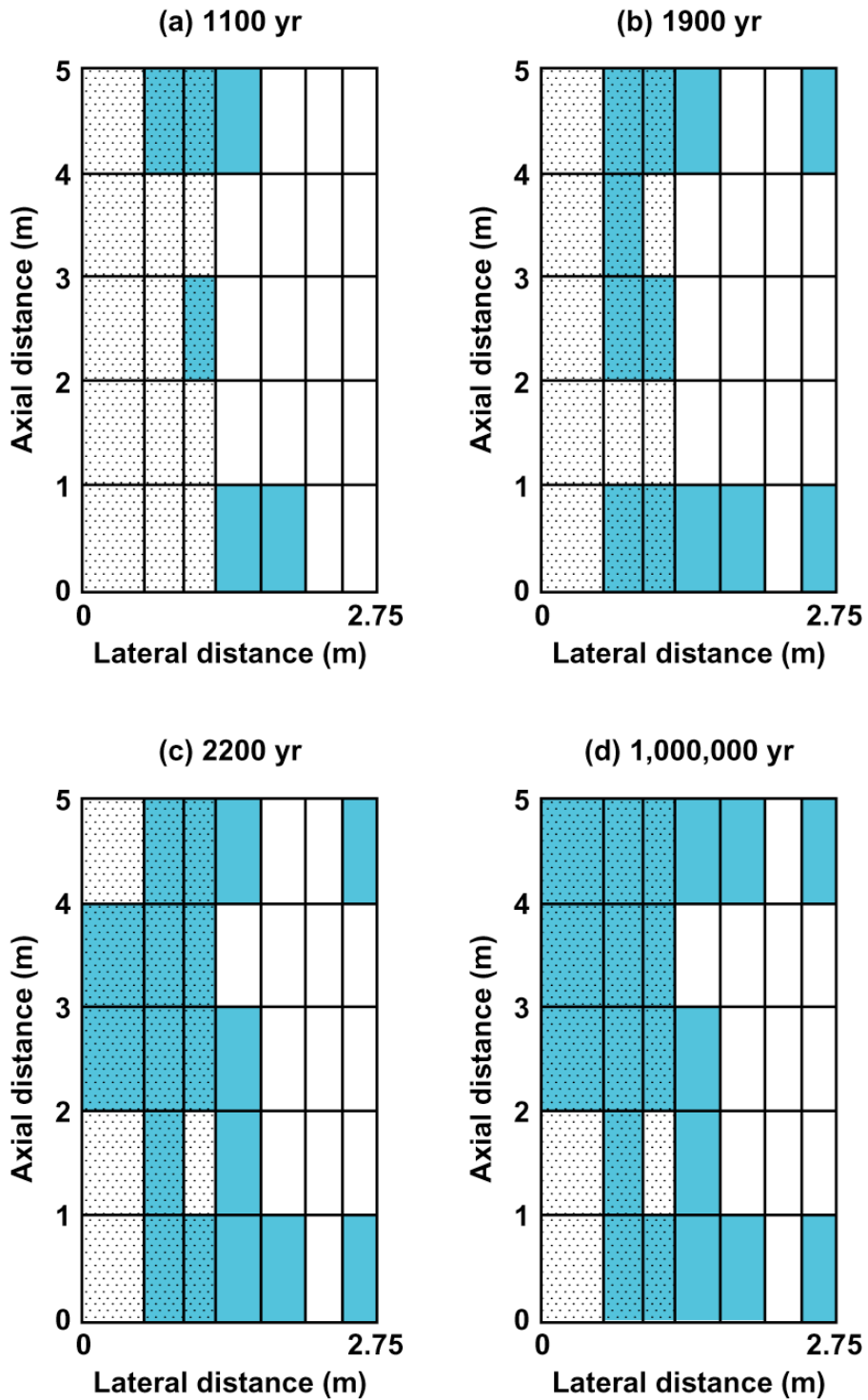
Qevapds56-02\_j1-j5-2D

Figure 6-85. Evaporation-rate history is given at the drip shield for stochastic realization A-56 and an AML of 56 MTU/acre. Drip-shield evaporation rate is averaged over the entire drip shield. Histories are given at five axial locations ( $j = 1, 2, 3, 4,$  and  $5$ ) and for the corresponding 2-D LDTH model with an homogeneous drift-scale bulk permeability distribution.



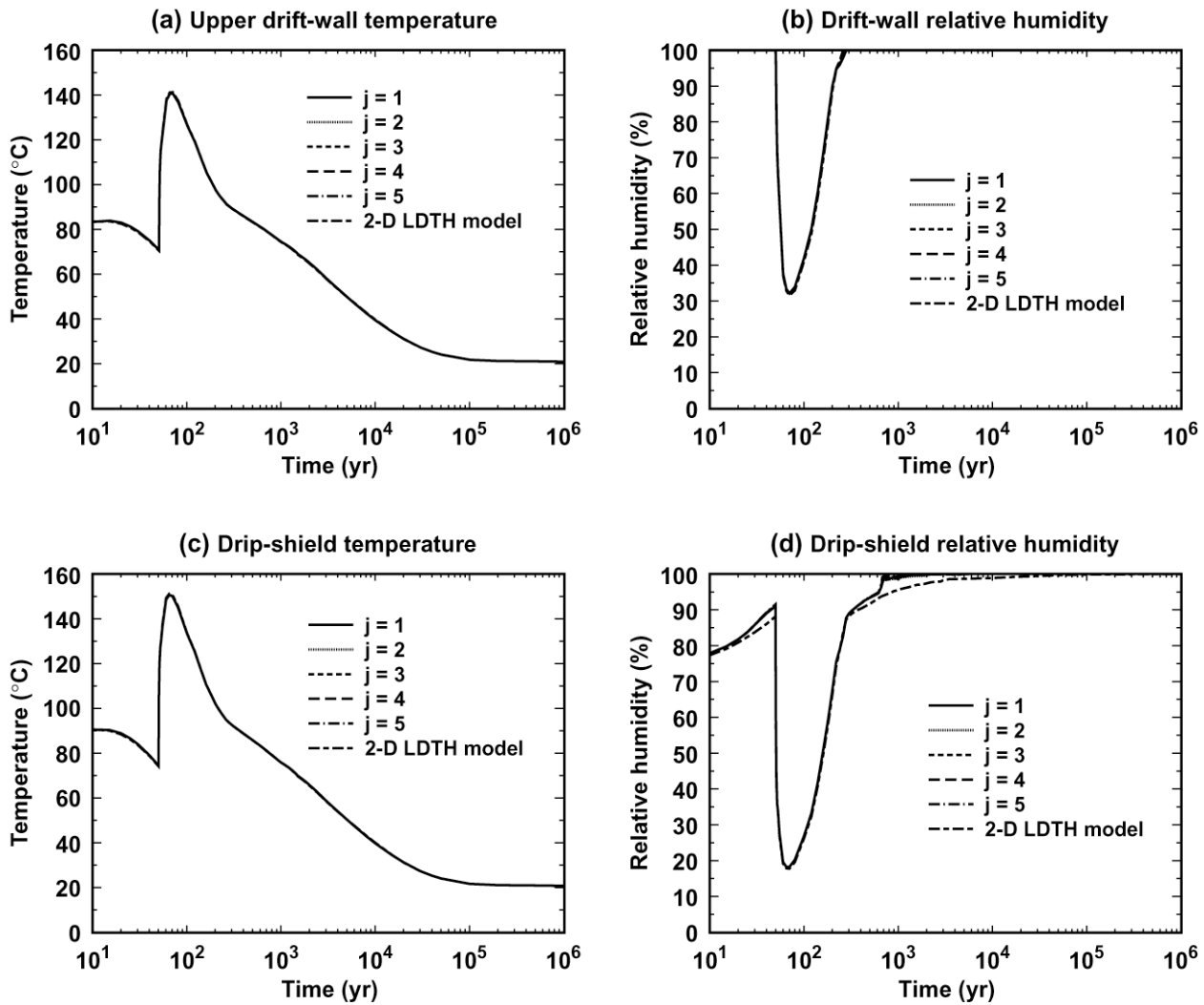
qliq56-02\_j1-j5-avg

Figure 6-86. Liquid-phase-flux histories are given at various locations in the host rock and in the drift for stochastic realization A-56 and an AML of 56 MTU/acre. Liquid-phase flux 5 m above the drift is averaged over the entire rock pillar from the drift centerline to the rock-pillar centerline. Liquid-phase flux 3 m above the drift is averaged over the lateral extent of the drift. Liquid-phase seepage flux at the upper drift wall is averaged from springline to springline. Liquid-phase seepage flux at the upper drip shield is averaged over the lateral extent of the drip shield. Histories are given at five axial locations ( $j = 1, 2, 3, 4,$  and  $5$ ), as well as for an average of the five axial locations.



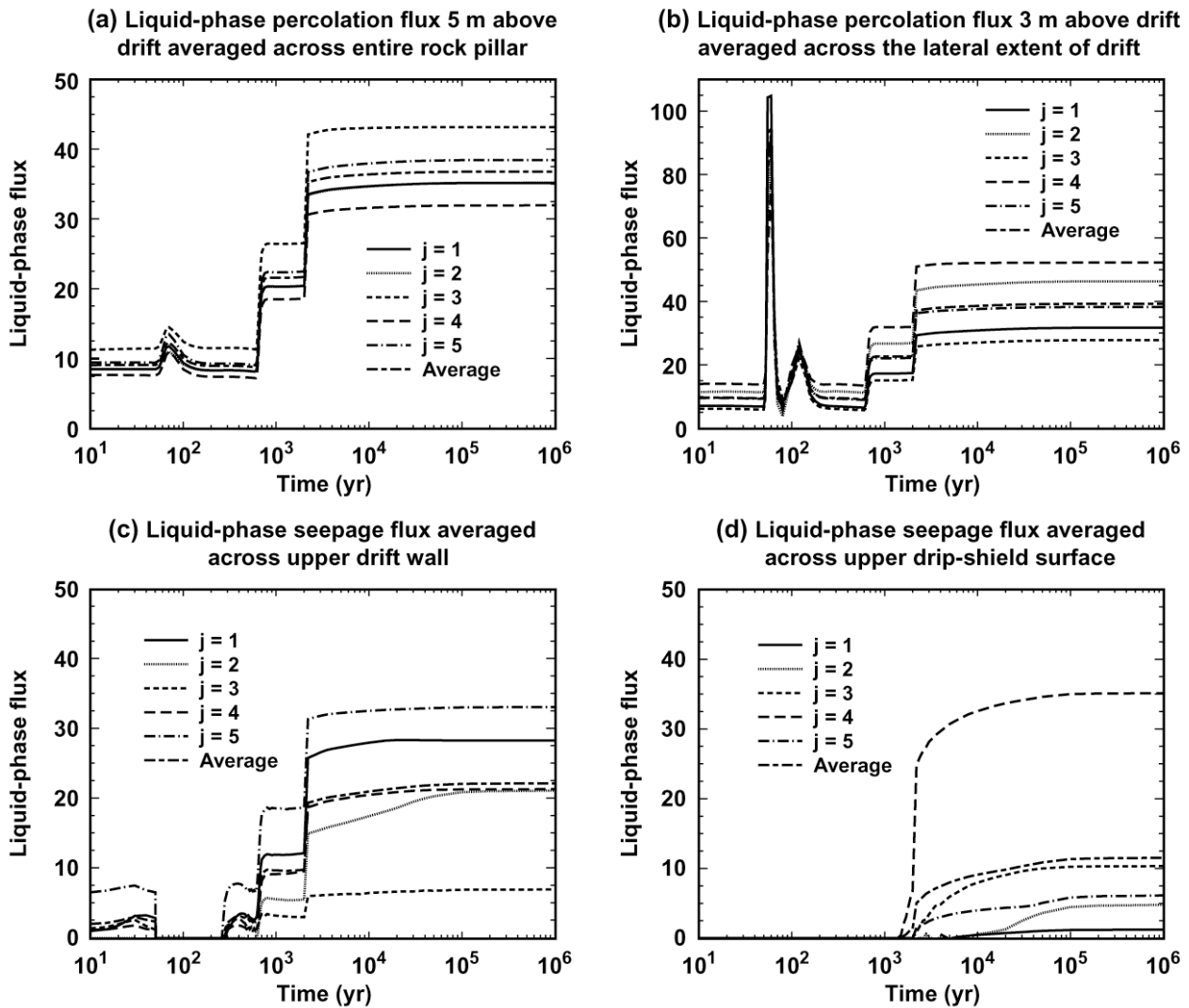
Seepage02

Figure 6-87. The distribution of seepage locations is plotted at (a) 1100 yr, (b) 1900 yr, (c) 2200 yr, and (d) 1,000,000 yr for stochastic realization A-56 and an AML of 56 MTU/acre. The light stippled blocks correspond to the footprint of the drip shield. The dark blue blocks correspond to blocks that have a non-zero liquid-phase seepage flux at the upper drift wall.



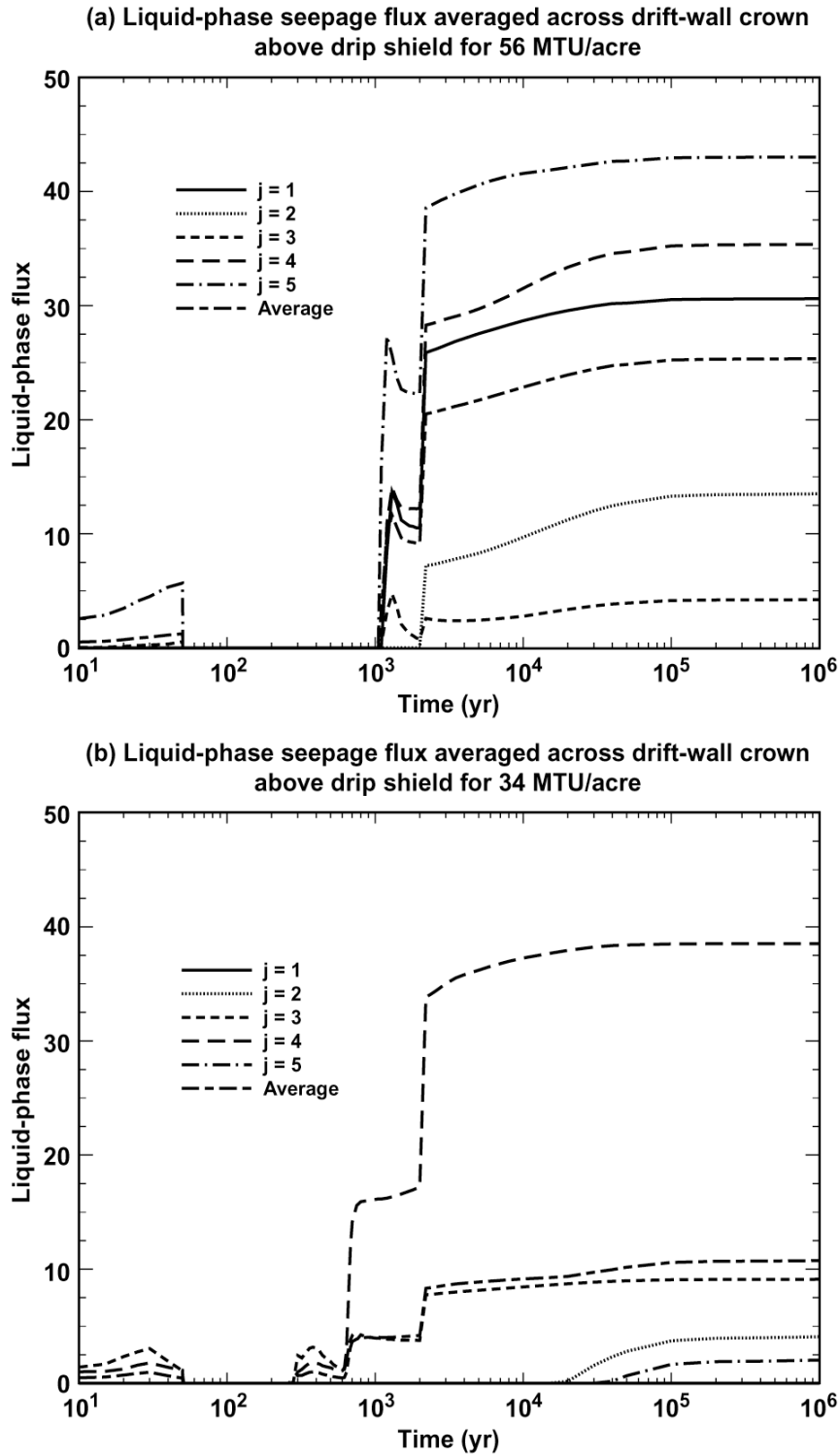
T&RH34-02\_j1-j5-2D

Figure 6-88. Temperature and relative-humidity histories are given at the drift wall and drip shield for stochastic realization A-34 and an AML of 34 MTU/acre. Temperature at the upper drift wall (a) is averaged from springline to springline. Relative humidity at the drift wall (b) is averaged over the entire perimeter of the drift. Drip-shield temperature (c) and relative humidity (d) are averaged over the entire drip shield. Histories are given at five axial locations ( $j = 1, 2, 3, 4,$  and  $5$ ) for the equivalent 2-D homogeneous LDTH model.



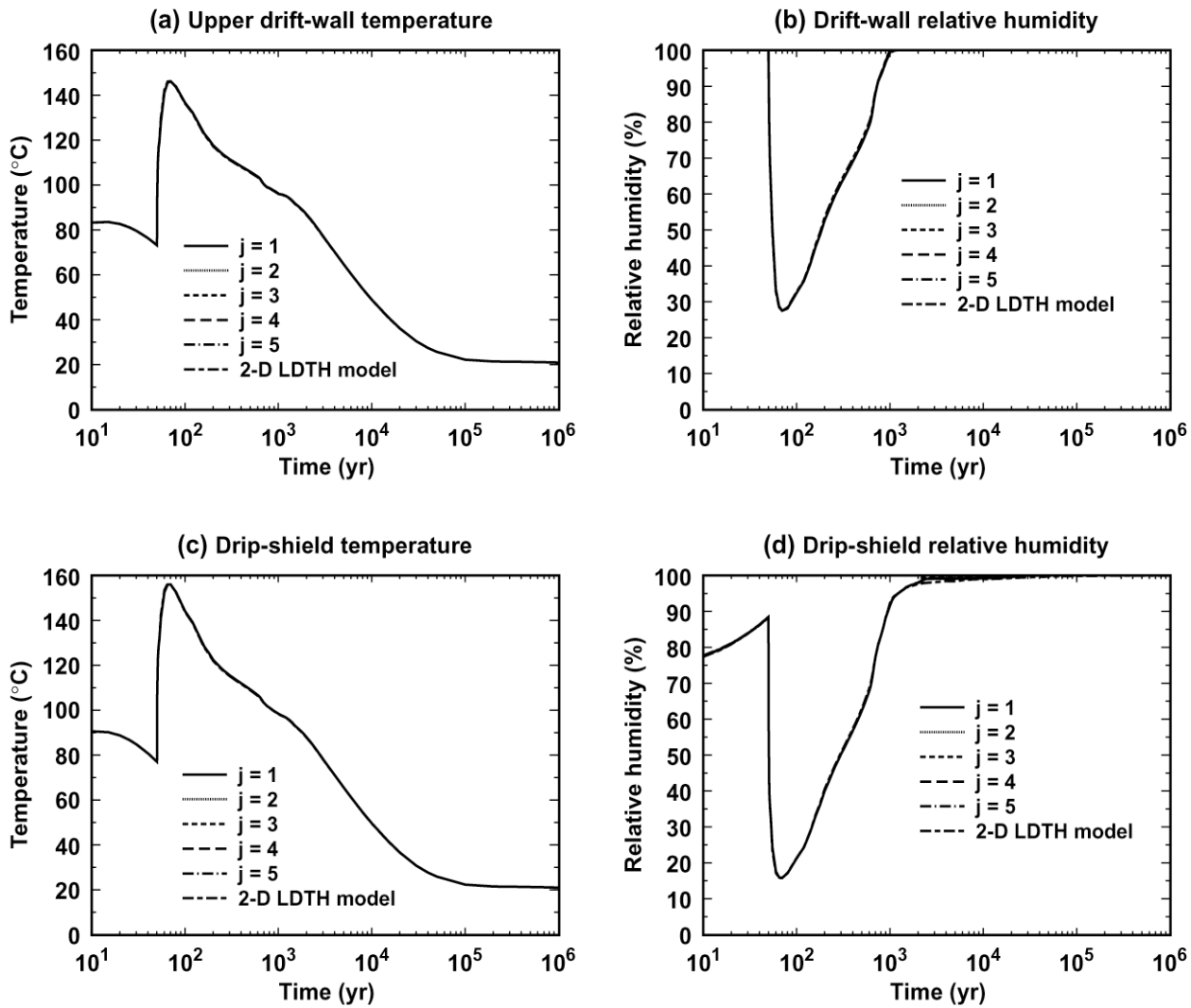
qilq34-02\_j1-j5-avg

Figure 6-89. Liquid-phase-flux histories are given at various locations in the host rock and in the drift for stochastic realization A-34 and an AML of 34 MTU/acre. Liquid-phase flux 5 m above the drift is averaged over the entire rock pillar from the drift centerline to the rock-pillar centerline. Liquid-phase flux 3 m above the drift is averaged over the lateral extent of the drift. Liquid-phase seepage flux at the upper drift wall is averaged from springline to springline. Liquid-phase seepage flux at the upper drip shield is averaged over the lateral extent of the drip shield. Histories are given at five axial locations ( $j = 1, 2, 3, 4,$  and  $5$ ), as well as for an average of the five axial locations.



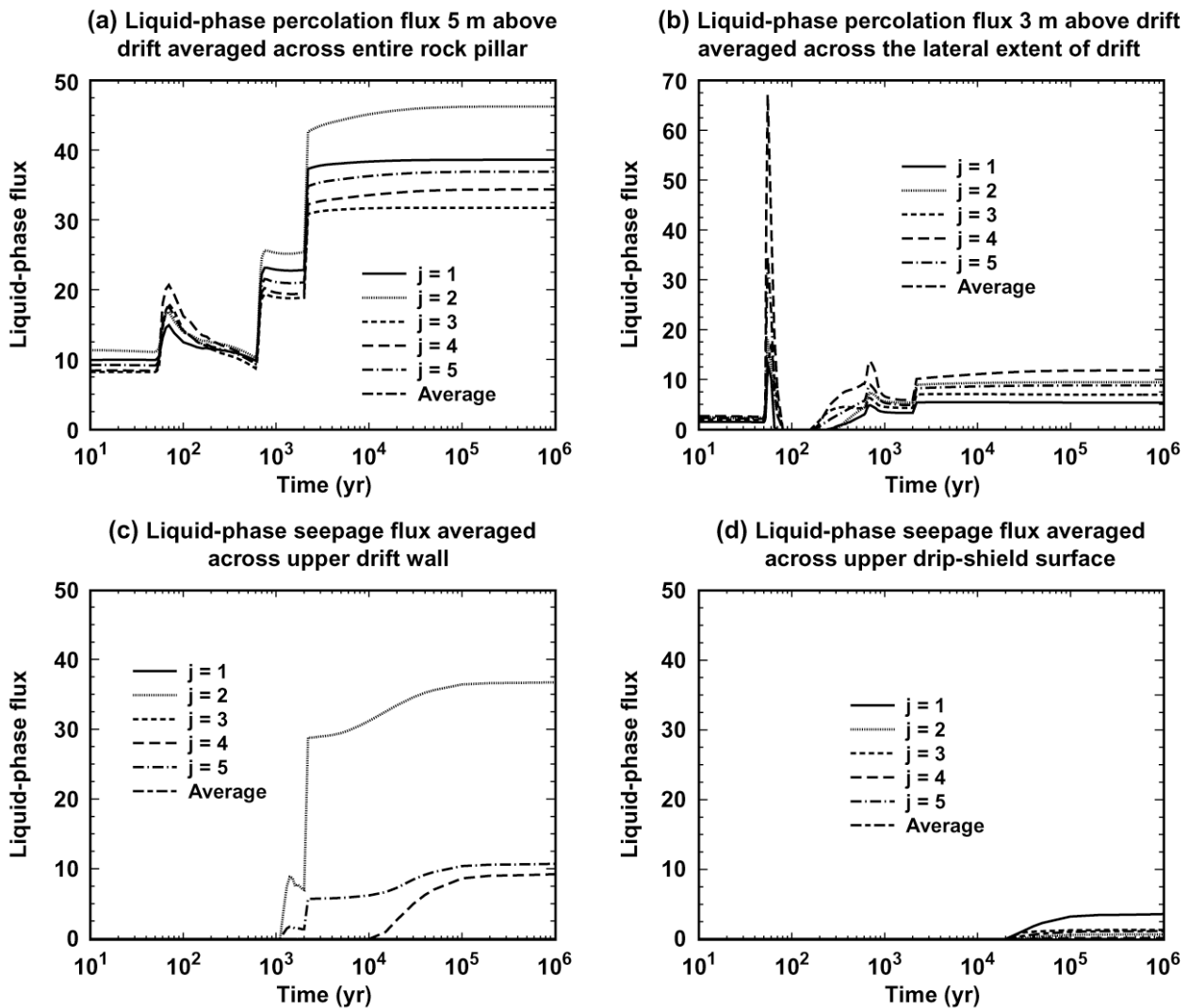
qliqdw\_cr34-02-j1-j5-avg

Figure 6-90. Liquid-phase-seepage-flux history at the crown of the drift for (a) stochastic realization A-56 and an AML of 56 MTU/acre and for (b) stochastic realization A-34 and an AML of 34 MTU/acre. This seepage flux is averaged over the lateral extent of the drip shield. Histories are given at five axial locations ( $j = 1, 2, 3, 4,$  and  $5$ ), as well as for an average of the five axial locations.



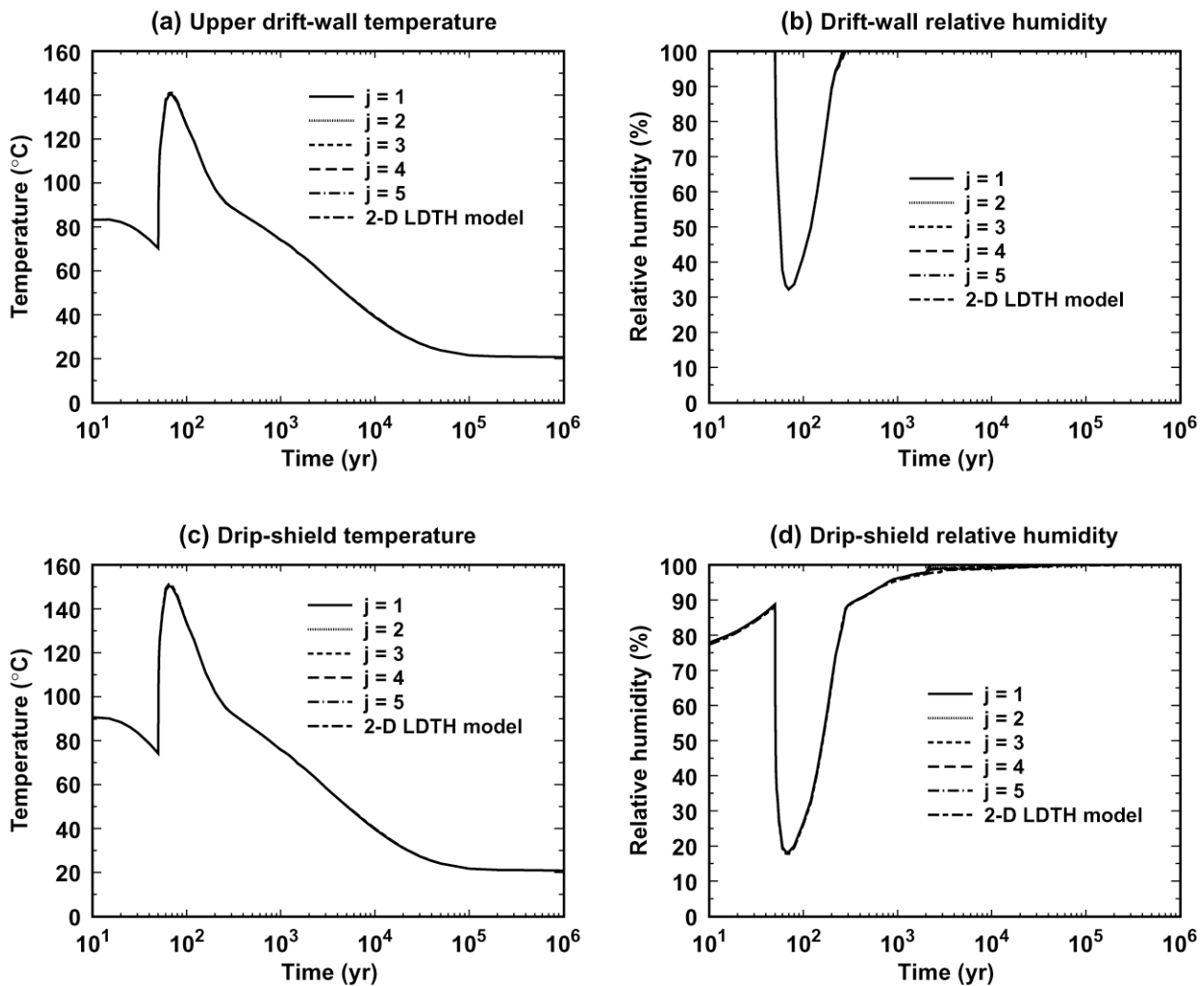
T&RH56-12\_j1-j5-2D

Figure 6-91. Temperature and relative-humidity histories are given at the drift wall and drip shield for stochastic realization B-56 and an AML of 56 MTU/acre. Temperature at the upper drift wall (a) is averaged from springline to springline. Relative humidity at the drift wall (b) is averaged over the entire perimeter of the drift. Drip-shield temperature (c) and relative humidity (d) are averaged over the entire drip shield. Histories are given at five axial locations ( $j = 1, 2, 3, 4,$  and  $5$ ) for the equivalent 2-D homogeneous LDTH model.



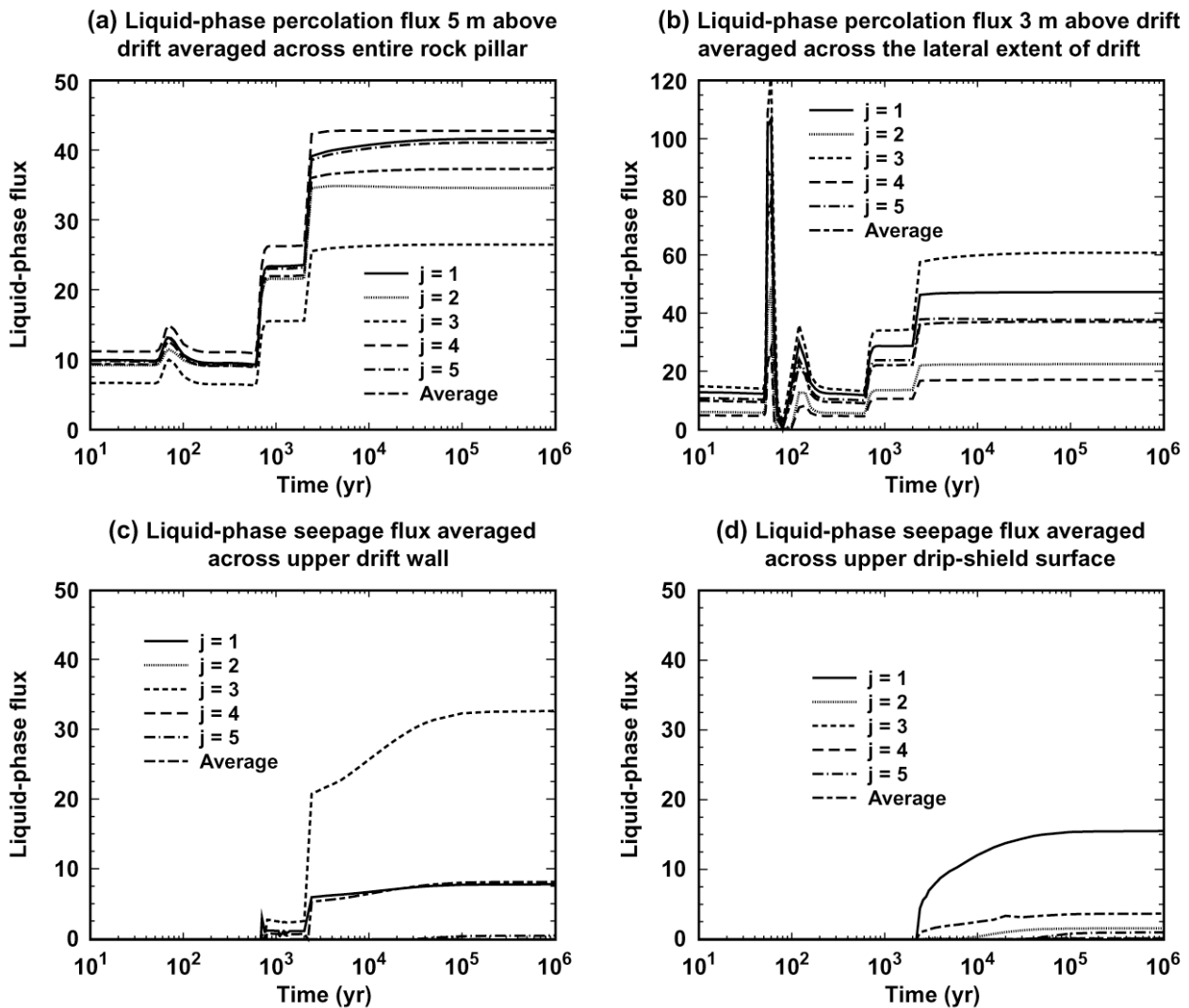
qilq56-12\_j1-j5-avg

Figure 6-92. Liquid-phase-flux histories are given at various locations in the host rock and in the drift for stochastic realization B-56 and an AML of 56 MTU/acre. Liquid-phase flux 5 m above the drift is averaged over the entire rock pillar from the drift centerline to the rock-pillar centerline. Liquid-phase flux 3 m above the drift is averaged over the lateral extent of the drift. Liquid-phase seepage flux at the upper drift wall is averaged from springline to springline. Liquid-phase seepage flux at the upper drip shield is averaged over the lateral extent of the drip shield. Histories are given at five axial locations ( $j = 1, 2, 3, 4,$  and  $5$ ), as well as for an average of the five axial locations.



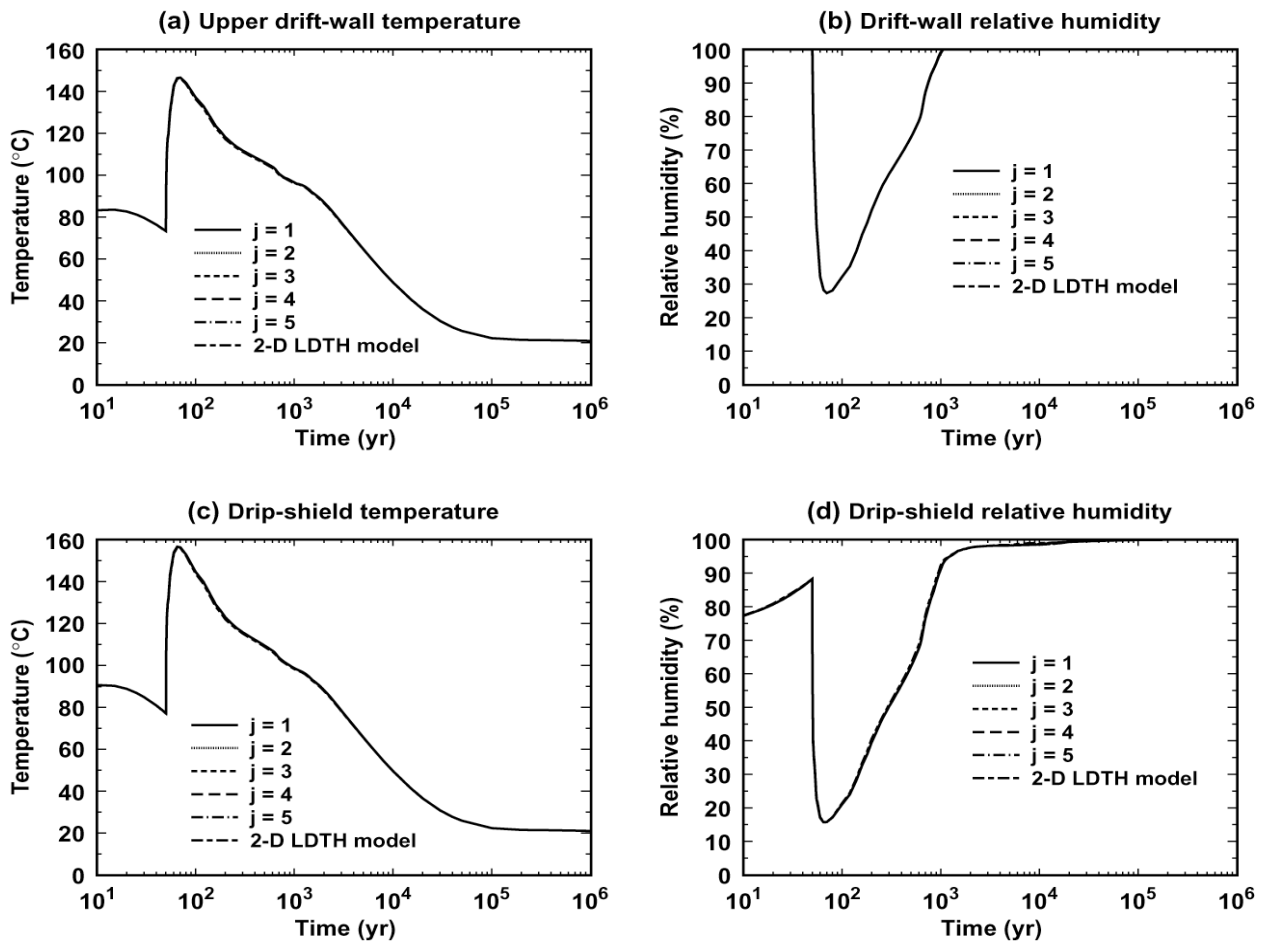
T&RH34-12\_j1-j5-2D

Figure 6-93. Temperature and relative-humidity histories are given at the drift wall and drip shield for stochastic realization B-34 and an AML of 34 MTU/acre. Temperature at the upper drift wall (a) is averaged from springline to springline. Relative humidity at the drift wall (b) is averaged over the entire perimeter of the drift. Drip-shield temperature (c) and relative humidity are (d) averaged over the entire drip shield. Histories are given at five axial locations ( $j = 1, 2, 3, 4,$  and  $5$ ) for the equivalent 2-D homogeneous LDTH model.



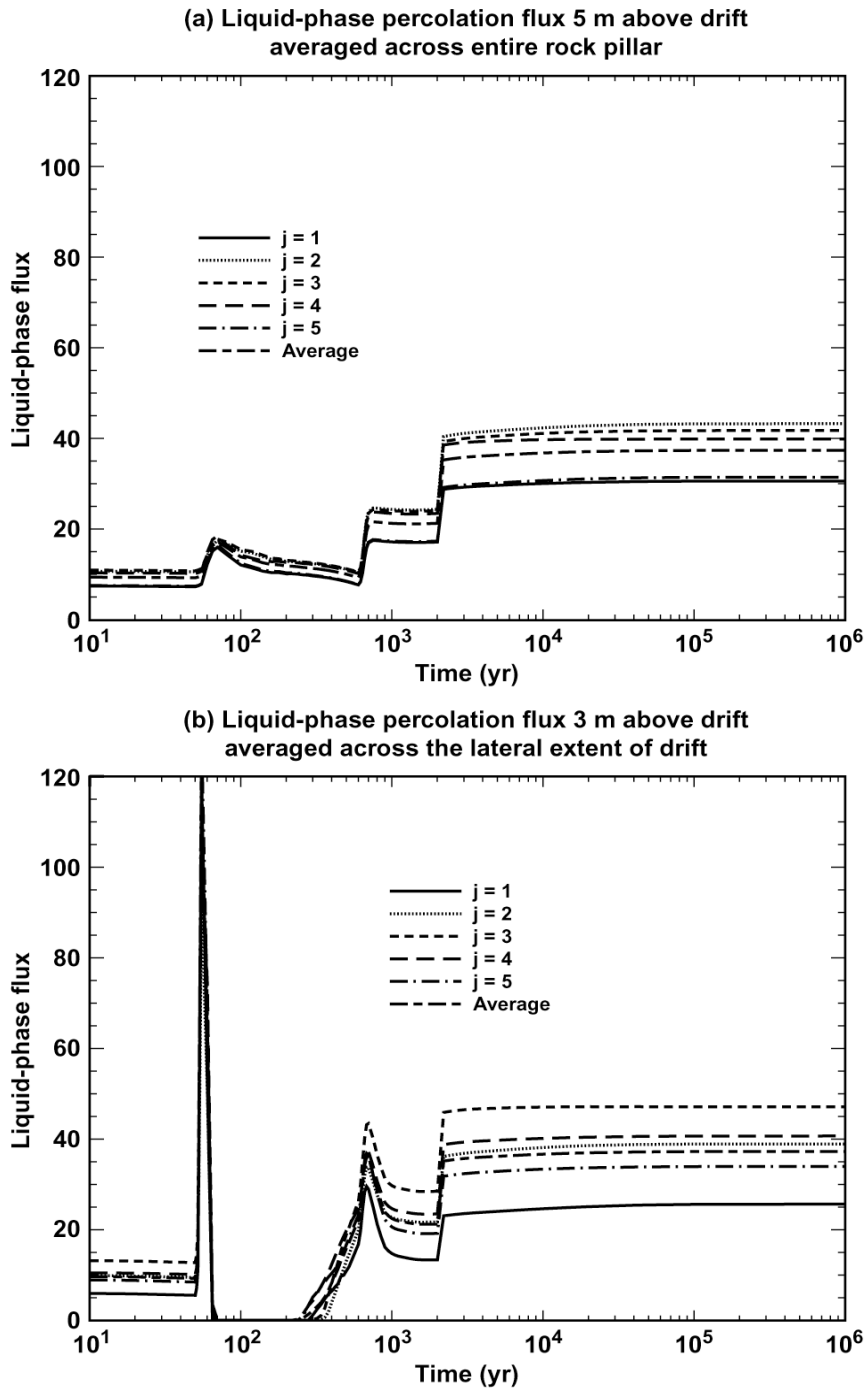
qilq34-12\_j1-j5-avg

Figure 6-94. Liquid-phase-flux histories are given at various locations in the host rock and in the drift for stochastic realization B-34 and an AML of 34 MTU/acre. Liquid-phase flux 5 m above the drift is averaged over the entire rock pillar from the drift centerline to the rock-pillar centerline. Liquid-phase flux 3 m above the drift is averaged over the lateral extent of the drift. Liquid-phase seepage flux at the upper drift wall is averaged from springline to springline. Liquid-phase seepage flux at the upper drip shield is averaged over the lateral extent of the drip shield. Histories are given at five axial locations ( $j = 1, 2, 3, 4,$  and  $5$ ), as well as for an average of the five axial locations.



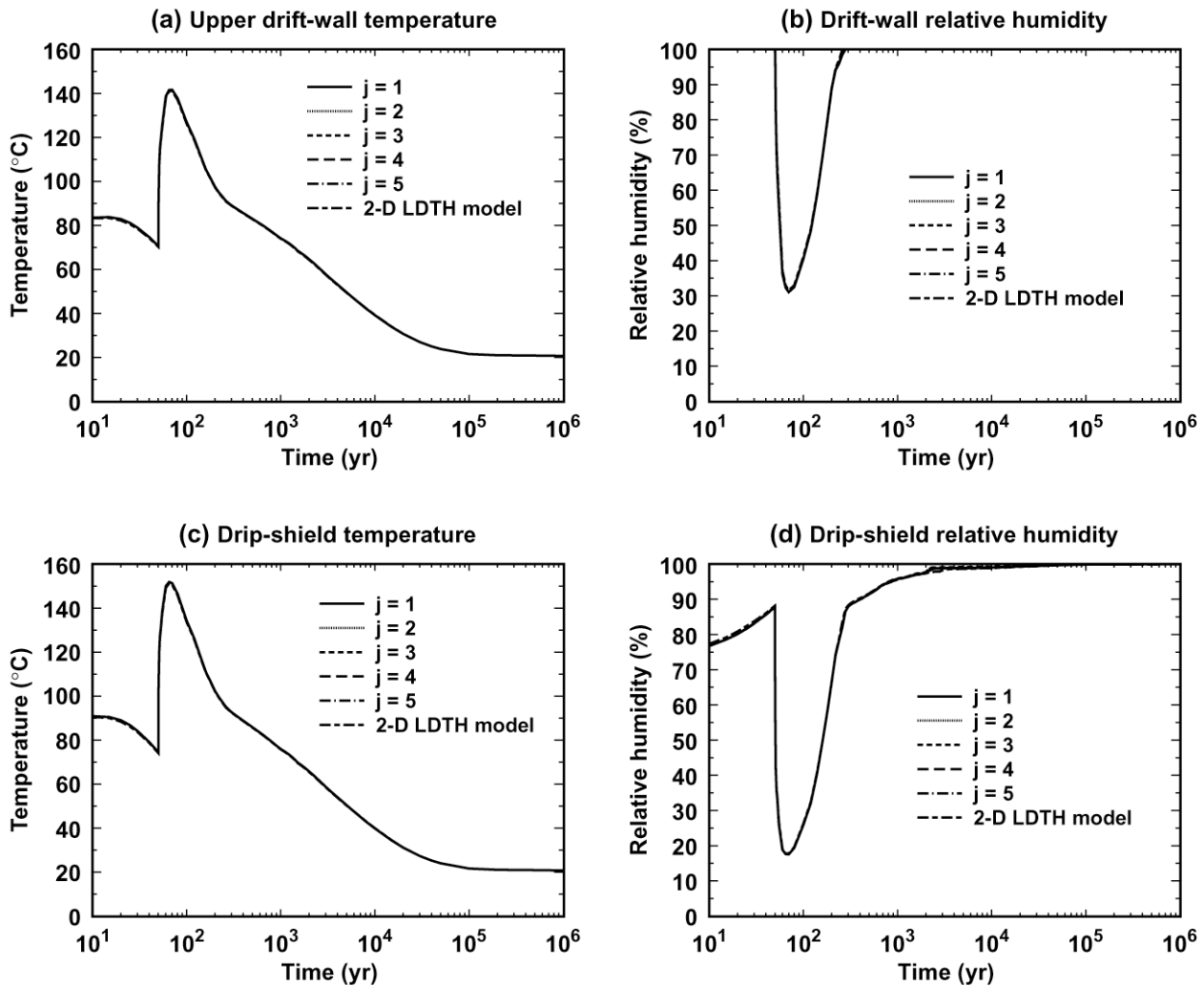
T&RH56-20\_j1-j5-2D

Figure 6-95. Temperature and relative-humidity histories are given at the drift wall and drip shield for stochastic realization C-56 and an AML of 56 MTU/acre. Temperature at the upper drift wall (a) is averaged from springline to springline. Relative humidity at the drift wall (b) is averaged over the entire perimeter of the drift. Drip-shield temperature (c) and relative humidity (d) are averaged over the entire drip shield. Histories are given at five axial locations ( $j = 1, 2, 3, 4,$  and  $5$ ) for the equivalent 2-D homogeneous LDTH model.



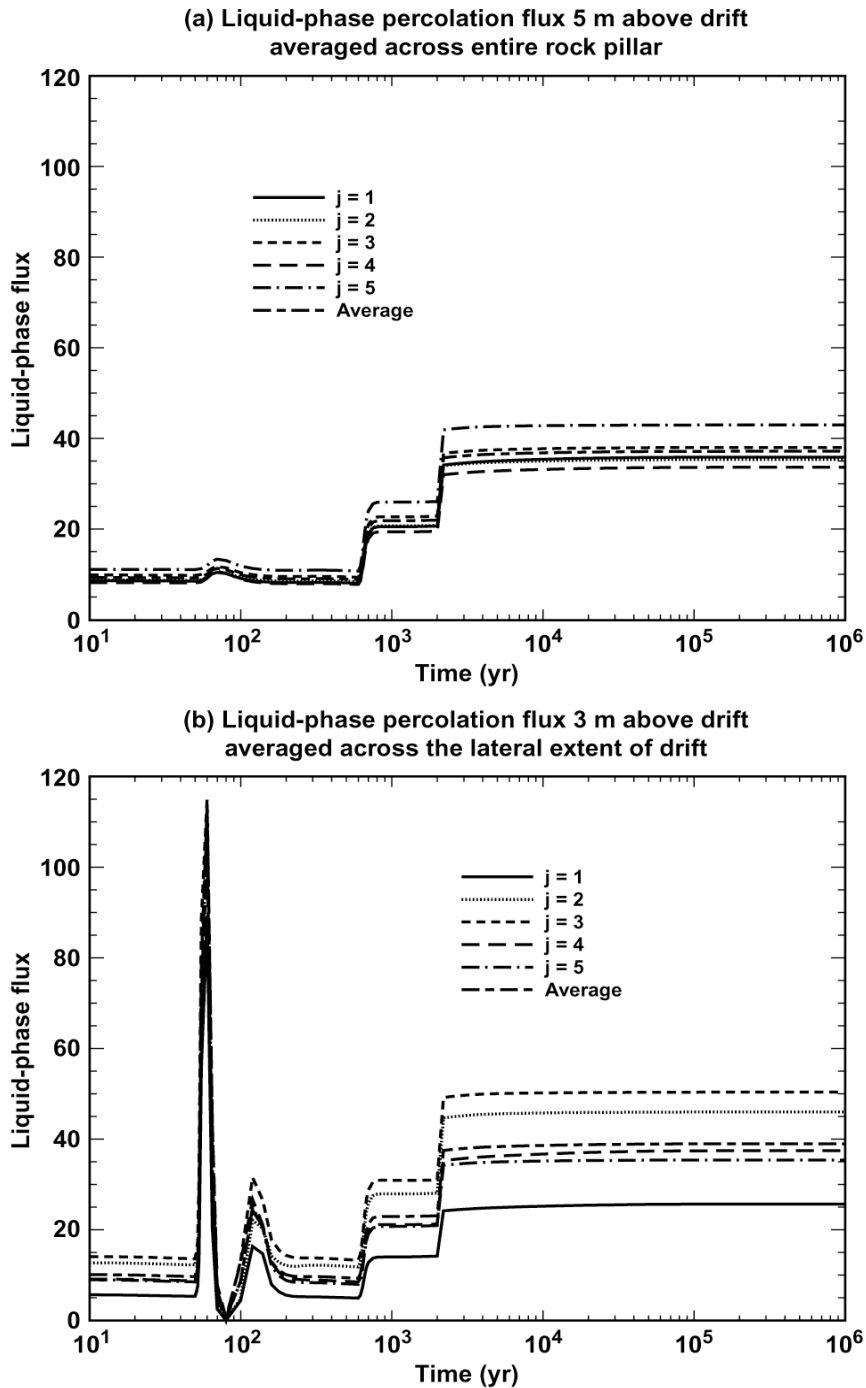
qliq56-20-j1-j5-avg

Figure 6-96. Liquid-phase-flux histories are given at various locations in the host rock for stochastic realization C-56 and an AML of 56 MTU/acre. Liquid-phase flux 5 m above the drift is averaged over the entire rock pillar from the drift centerline to the rock-pillar centerline. Liquid-phase flux 3 m above the drift is averaged over the lateral extent of the drift. All liquid-phase fluxes at the drift wall and in the drift are zero for this case. Histories are given at five axial locations ( $j = 1, 2, 3, 4,$  and  $5$ ), as well as for an average of the five axial locations. Note that there is no seepage flux across the upper drift wall or onto the drip shield for this realization.



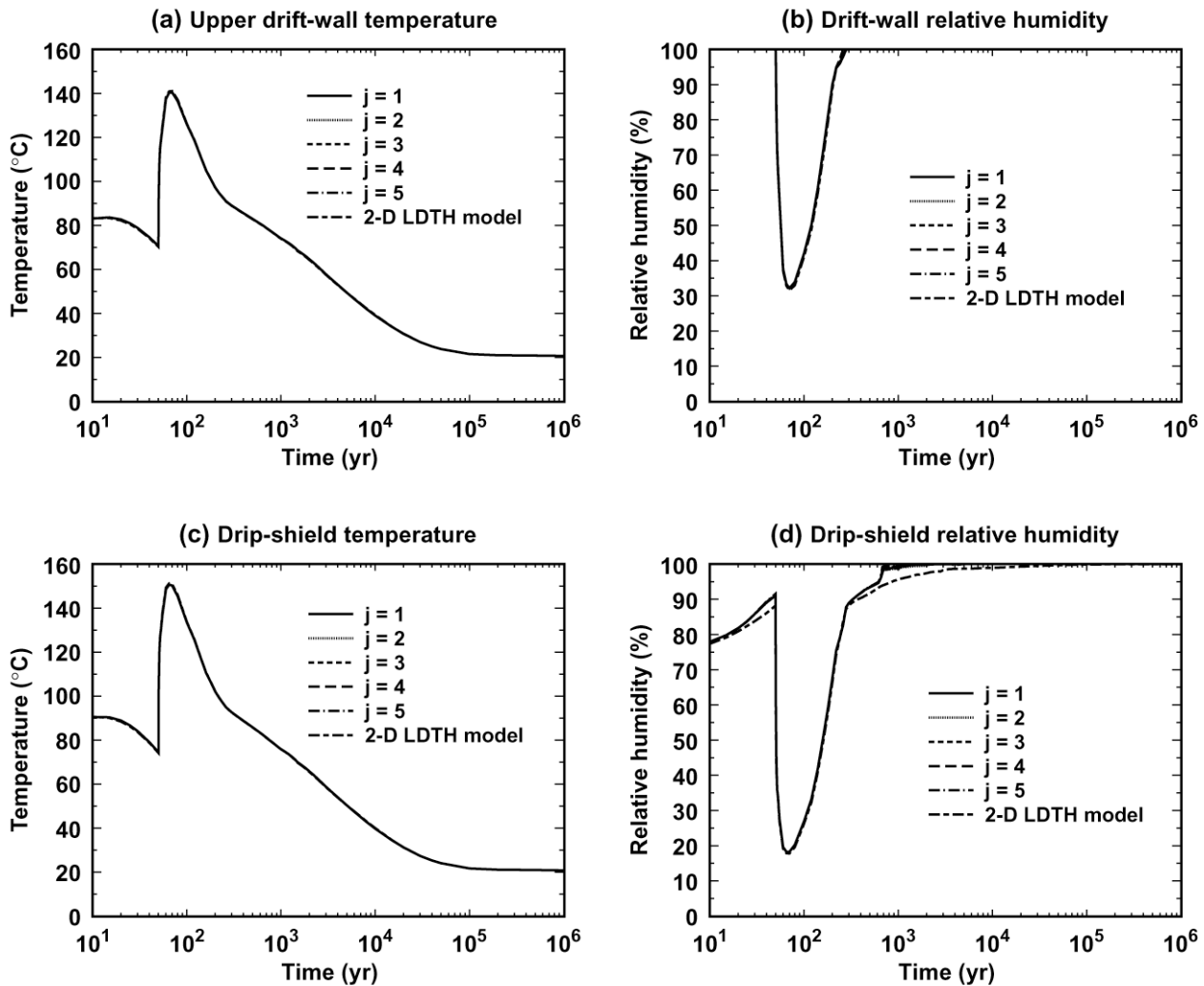
T&RH34-20\_j1-j5-2d

Figure 6-97. Temperature and relative-humidity histories are given at the drift wall and drip shield for stochastic realization C-34 and an AML of 34 MTU/acre. Temperature at the upper drift wall (a) is averaged from springline to springline. Relative humidity at the drift wall (b) is averaged over the entire perimeter of the drift. Drip-shield temperature (c) and relative humidity (d) are averaged over the entire drip shield. Histories are given at five axial locations ( $j = 1, 2, 3, 4,$  and  $5$ ) for the equivalent 2-D homogeneous LDTH model.



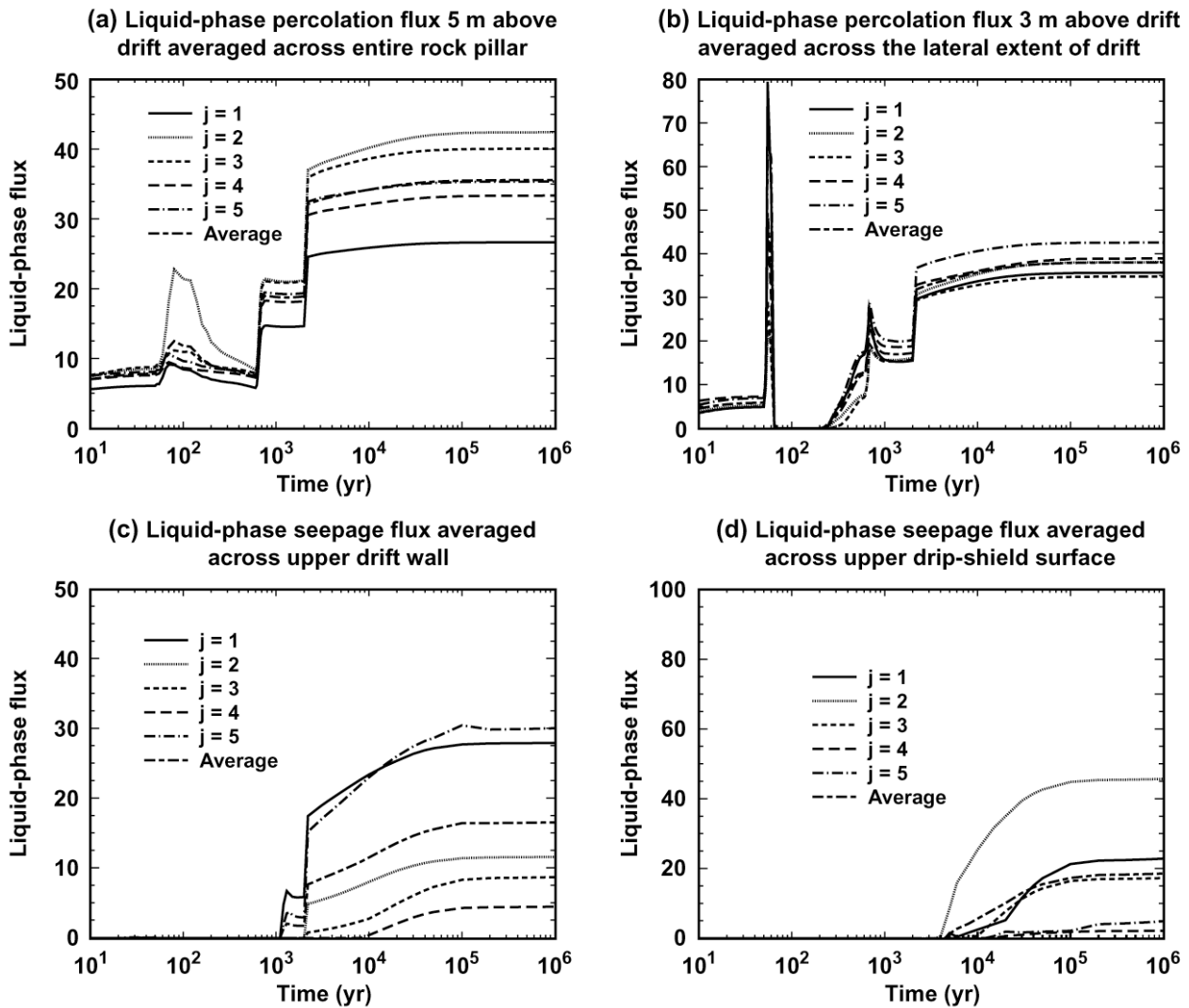
qliq34-20-j1-j5-avg

Figure 6-98. Liquid-phase-flux histories are given at various locations in the host rock for stochastic realization C-34 and an AML of 34 MTU/acre. Liquid-phase flux 5 m above the drift is averaged over the entire rock pillar from the drift centerline to the rock-pillar centerline. Liquid-phase flux 3 m above the drift is averaged over the lateral extent of the drift. All liquid-phase fluxes at the drift wall and in the drift are zero for this case. Histories are given at five axial locations ( $j = 1, 2, 3, 4,$  and  $5$ ), as well as for an average of the five axial locations. Note that there is no seepage flux across the upper drift wall or onto the drip shield for this realization.



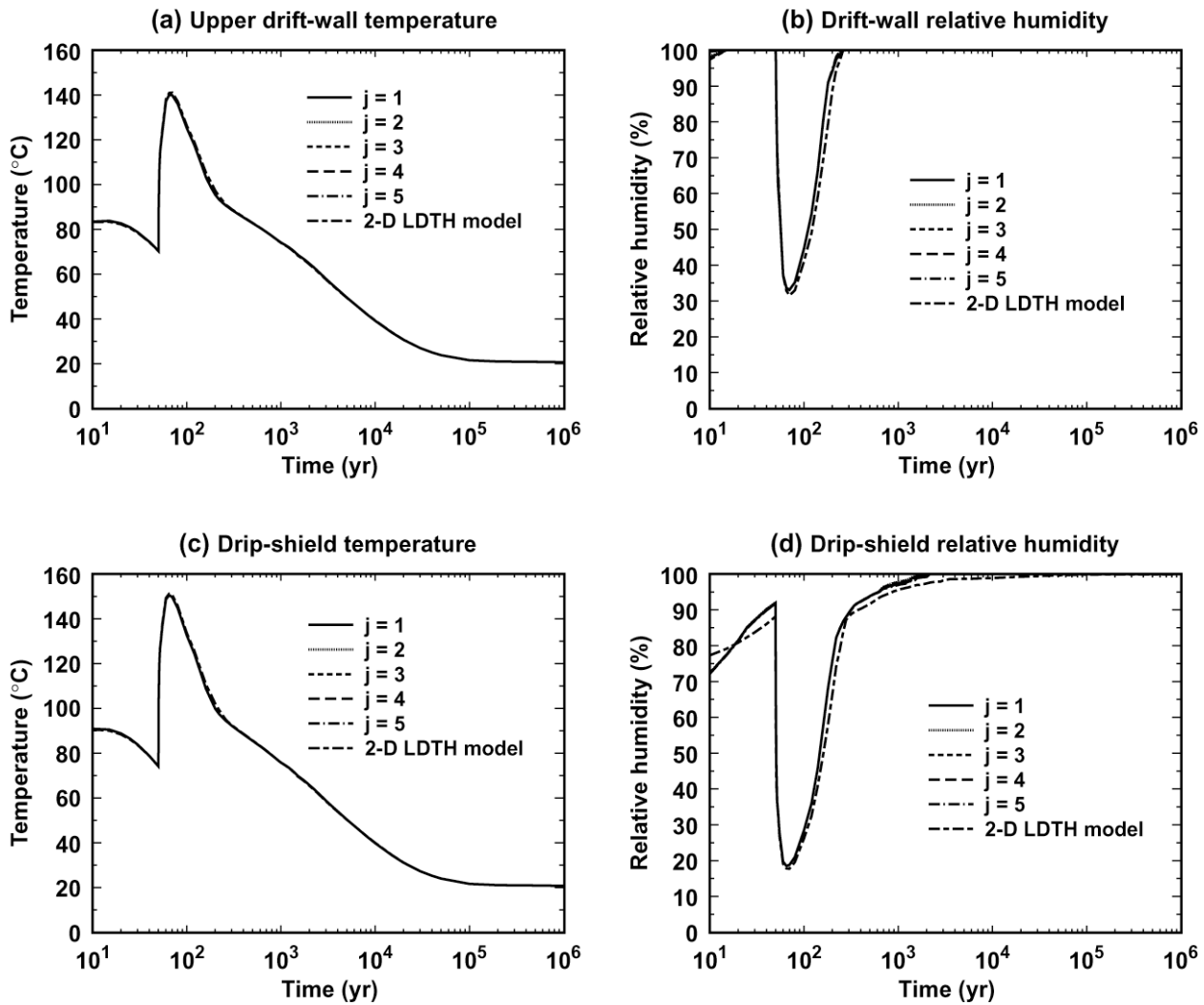
T&RH56-01\_j1-j5-2D

Figure 6-99. Temperature and relative-humidity histories are given at the drift wall and drip shield for stochastic realization D-56 and an AML of 56 MTU/acre. Temperature at the upper drift wall (a) is averaged from springline to springline. Relative humidity at the drift wall (b) is averaged over the entire perimeter of the drift. Drip-shield temperature (c) and relative humidity (d) are averaged over the entire drip shield. Histories are given at five axial locations ( $j = 1, 2, 3, 4,$  and  $5$ ) for the equivalent 2-D homogeneous LDTH model.



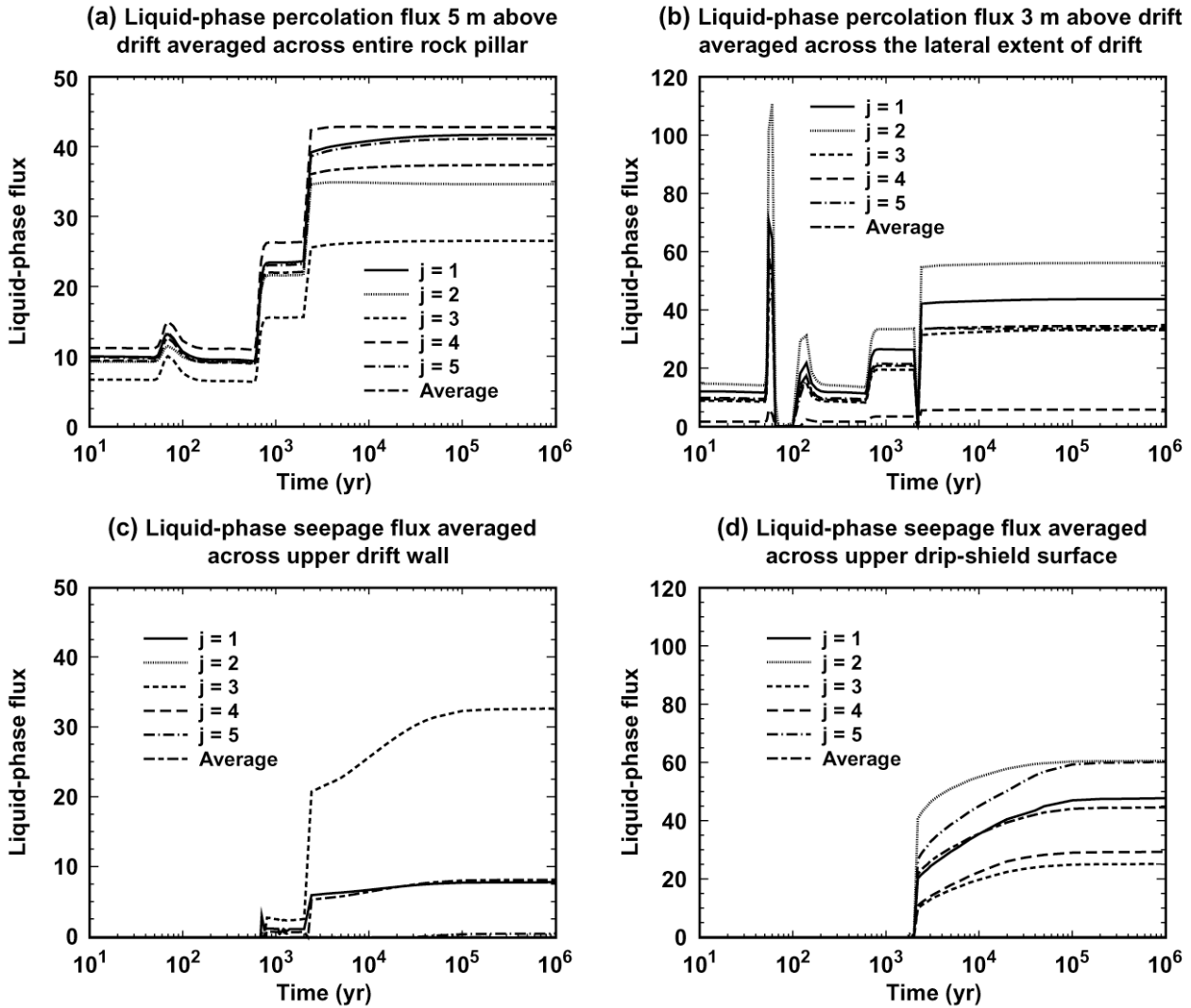
qilq56-01\_j1-j5-avg

Figure 6-100. Liquid-phase-flux histories are given at various locations in the host rock and in the drift for stochastic realization D-56 and an AML of 56 MTU/acre. Liquid-phase flux 5 m above the drift is averaged over the entire rock pillar from the drift centerline to the rock-pillar centerline. Liquid-phase flux 3 m above the drift is averaged over the lateral extent of the drift. Liquid-phase seepage flux at the upper drift wall is averaged from springline to springline. Liquid-phase seepage flux at the upper drip shield is averaged over the lateral extent of the drip shield. Histories are given at five axial locations ( $j = 1, 2, 3, 4,$  and  $5$ ), as well as for an average of the five axial locations.



T&RH34-01\_j1-j5-2D

Figure 6-101. Temperature and relative-humidity histories are given at the drift wall and drip shield for stochastic realization D-34 and an AML of 34 MTU/acre. Temperature at the upper drift wall (a) is averaged from springline to springline. Relative humidity at the drift wall (b) is averaged over the entire perimeter of the drift. Drip-shield temperature (c) and relative humidity (d) are averaged over the entire drip shield. Histories are given at five axial locations ( $j = 1, 2, 3, 4,$  and  $5$ ) for the equivalent 2-D homogeneous LDTH model.



qilq34-01\_j1-j5-avg

TT

Figure 6-102. Liquid-phase-flux histories are given at various locations in the host rock and in the drift for stochastic realization D-34 and an AML of 34 MTU/acre. Liquid-phase flux 5 m above the drift is averaged over the entire rock pillar from the drift centerline to the rock-pillar centerline. Liquid-phase flux 3 m above the drift is averaged over the lateral extent of the drift. Liquid-phase seepage flux at the upper drift wall is averaged from springline to springline. Liquid-phase seepage flux at the upper drip shield is averaged over the lateral extent of the drip shield. Histories are given at five axial locations (j = 1, 2, 3, 4, and 5), as well as for an average of the five axial locations.

## 7. CONCLUSIONS

The purpose of the MSTHM was to describe the thermohydrologic evolution of the NFE and EBS throughout the potential high-level nuclear waste repository at Yucca Mountain for a particular engineering design. TH information and data is provided throughout the entire repository area as a function of time in Figures 6-7 –6-102 and data in CRWMS M&O 2000a of which appropriate developed data was submitted to the TDMS and was assigned the following DTNs: LL000113904242.089, LL000114004242.090, and LL000114104242.091 for the backfill case. For the no-backfill case, the resulting DTNs are LL000509112312.003, LL000509012312.002, and LL000509212312.004. For the three-dimensional heterogeneous LDTH model, the resulting DTN is LL010802723122.019.

The MSTHM calculates 38 TH variables in the NFE and EBS for 623 subdomains in the repository and for 8 different WPs as a function of time for about 352 calculational timesteps for the backfill case. For the no-backfill case, the MSTHM calculates 38 TH variables for 610 subdomains and 99 calculational timesteps. The total of 38 TH arises from a combination of 10 thermodynamic variables (e.g., temperature  $T$  and relative humidity  $RH$ ) and 13 drift-scale locations (e.g., WP and drip-shield surface) These TH variables are determined for three infiltration-flux scenarios, including the mean, high, and low infiltration-flux scenarios. For each calculational timestep in the backfill case, the MSTHM calculates  $38 \times 623 \times 8$  TH data values, resulting in 189,392 data values. Multiplying by 352 calculational timesteps results in about 66 million TH data points for a complete time evolution of a given infiltration-flux scenario for the backfill case. For the no-backfill case, the MSTHM calculates  $38 \times 610 \times 8$  TH data values, resulting in 185,440 data values. Multiplying by 99 calculational timesteps results in more than 18 million TH data points for a complete time evolution of a given infiltration-flux scenario for the no-backfill case. These TH variables were requested by EBSO and PAO.

Temperature distributions in the NFE and EBS are influenced by a number of key factors:

- Repository-scale variability of percolation flux.
- Temporal variability of percolation flux (as influenced by climate change).
- Uncertainty in percolation flux (as addressed by the mean, high, and low infiltration-flux cases considered in this AMR).
- Repository-scale variability in hydrologic properties (e.g., those governing matrix imbibition diffusivity and capillary wicking in fractures).
- Edge-cooling effect (which increases with proximity to the edge of the repository).
- Dimensions and properties of the EBS components, such as the drip shield, engineered backfill and the invert.
- WP-to-WP variability in heat-generation rate.

- Repository-scale variability in overburden thickness.
- Repository-scale variability in thermal conductivity (with an emphasis on the host-rock units).

These factors, which are addressed in Sections 6.11 and 6.12, influence (to varying degrees) the time-evolution of the key TH variables, such as liquid-phase flux, temperature, relative humidity, gas-phase air-mass fraction, and evaporation rate.

Some software and inputs used in this AMR are TBV; therefore, the conclusions from this AMR are also TBV. The impact of the uncertainty of some of the most important input variables (e.g., infiltration flux and thermal conductivity of the host-rock units) were addressed in previous sections of this AMR. The impact of uncertainty in all of the model inputs was not completely addressed because it was outside of the scope of work of this AMR. Changes to the inputs and/or software will require reproducing this model.

Any changes to the document that may occur as a result of completing the confirmation activities will be reflected in subsequent revisions. The status of the input information quality may be confirmed by review of the Document Input Reference System database.

During the pre-closure period, host-rock temperatures for the backfill case remain below the boiling point for the mean and high infiltration flux cases while boiling occurred in the host rock for the low-flux case. During the pre-closure period peak WP temperatures of 100°C (for the mean-flux case) and 110°C (for the low-flux case) occur at 10 to 15 yr and at 20 to 25 yr peak drift-wall temperatures of 86°C (for the mean-flux case) and of 96°C (for the low-flux case) occur. Edge-cooling effects do not strongly affect pre-closure temperatures. After the initial heat-up stage, *RH* on WPs varies from 45 to 75% during the pre-closure period.

During the pre-closure period, host-rock temperatures for the no-backfill case remain below the boiling point for the mean, high, and low infiltration-flux cases. During the pre-closure period peak WP temperatures of 100°C (for the mean-flux case), 110°C (for the low-flux case), and 100°C (for the high-flux case) occur at 10 to 15 yr.

During the post-closure period of the backfill case, peak WP temperatures of 305°C (for the mean-flux case) and 315°C (for the low-flux case) occur at 60 yr. With regards to the influence of WP-to-WP variability in heat-generation rate, the difference in peak WP temperature between the hottest and coldest WP is 42°C for the backfill case.

During the post-closure period of the no-backfill case, peak WP temperatures of 177°C (for the mean-flux case), 187°C (for the low-flux case), and 172°C (for the high-flux case) occur at 60 yr. With regards to WP-to-WP variability in heat-generation rate, the difference in peak WP temperature between the hottest and coldest WP is 27°C for the no-backfill case.

For the backfill case, peak drift-wall temperatures have strong vertical asymmetry after the emplacement of backfill. During the post-closure period, peak temperatures on the lower drift wall of 195°C (for the mean-flux case) and 205°C (for the low-flux case) occur at 65 yr, upper

drift wall peak temperatures of 125°C (for the mean-flux case) and 134°C (for the low-flux case) occur at 65 yr. The large (70°C) temperature difference between the upper and lower drift wall arises from the WP, drip-shield, and backfill configuration in the emplacement drift. Because the Overton-sand backfill is a very effective insulator ( $K_{th} = 0.33$  W/m-K) and because there is much more of this effective insulator above the WP and drip shield than below, much of the heat generation from WPs is focussed to the floor of the drift causing the large disparity in temperature between the lower and upper drift wall. To reduce this disparity, it would be necessary to balance the amount of insulation above and below the WP and drip shield.

For the no-backfill case, there is very little vertical asymmetry in the drift-wall temperatures. Thermal radiation in the open drift cavity effectively distributes heat evenly over the drift-wall surfaces, resulting in uniform drift-wall temperatures around the circumference of the drift. During the post-closure period, peak drift-wall temperatures are 147°C (for the mean-flux case), 156°C (for the low-flux case), and 142°C (for the high-flux case).

During the very early post-closure period, the edge-cooling effect has a small effect on temperatures. By 100 yr, the influence of edge cooling is considerable, with WP temperatures varying by 120°C from the repository edge to the geographic center of the repository, with the outer 100 to 200 m of the repository are influenced by edge cooling at 100 yr. This large difference in temperature indicates a promising heat-management option for a repository with an extended ventilation period (e.g., 100 yr). Because the influence of edge-cooling has penetrated significantly (100 to 200 m) in from the edge by 100 yr, it would be possible to emplace the hottest WPs in this edge region without incurring very high peak temperatures. The cooler WPs would be emplaced in the central repository region that does not experience edge-cooling effects. Thus, the center of the repository (which is an inherently hotter region) could receive a disproportionate share of cooler WPs, thereby reducing peak WP temperatures at the center of the repository. This heat-load balancing would also serve to reduce the variability in *RH* histories on WPs between the edge and center locations in the repository.

Liquid-phase flux in the host rock above the drift is influenced by dryout and the heat-pipe effect. Although one of the important objectives of the repository design analyzed in this report was to eliminate condensate buildup above the repository horizon, and thereby greatly reduce the magnitude of the heat-pipe effect, heat-pipe behavior above the dryout zone still enhances liquid-phase flux to well above ambient percolation fluxes. However, the duration of time that decay heat significantly enhances liquid-phase flux above the dryout zone is greatly reduced relative to the 85 MTU/acre repository analyzed in TSPA-VA. A noticeable increase in liquid-phase flux lasts for less than the duration of the present-day climate period (of 600 yr). Moreover, the magnitude of ambient percolation flux during the monsoonal-climate period ( $600 < t < 2000$  yr) and during the glacial-climate period ( $2000 \text{ yr} < t$ ) is comparable to (or even greater than) that generated by decay heat from WPs during the early pre-closure period.

For the backfill case, three key factors (including processes and conditions) influence the manner in which water seeps into and then flows through the drifts. The distribution of liquid flux in inside the drift has a dominant influence on other TH variables in the drift, such as relative humidity *RH*. These three factors are as follows:

**Capillary wicking in the Overton-sand backfill**, in conjunction with temperatures at the drift wall, influences the onset of seepage into the drift. During the early part of the pre-closure period the backfill is dry. As the temperature at the drift wall declines below the boiling point, water is able to wick (by capillary flow) from the fractures into the Overton-sand backfill. This wicking is facilitated by the van Genuchten  $\alpha$  value for Overton sand being smaller than that of the fractures in the host-rock units. Had a coarser, well-sorted sand been used as backfill, with a value of  $\alpha$  larger than that of the fractures in the host-rock units, then this wicking would not have taken place. Wicking by the Overton-sand backfill augments the influence of gravity-driven fracture flow; “capturing” flow in fractures over a region that is wider than the footprint of the drift.

**Heat pipes**, which are the result of countercurrent water vapor and liquid water flow, strongly affect liquid-phase flux above the drip shield. Sometime after the onset of seepage, the magnitude of liquid-phase flux above the drip shield is much larger than the ambient percolation flux. Just as the magnitude of liquid-phase flux in the heat-pipe zone in the host-rock above the drift can greatly exceed the background percolation flux, the magnitude of liquid-phase flux in the heat-pipe zone in the backfill can greatly exceed the seepage flux entering the drift. The large temperature gradient in the backfill facilitates a large vapor flux away from the drip shield, while the high capillarity of the Overton sand facilitates a large liquid-phase flux of water returning to the drip shield. This capillary-driven heat-pipe system in the backfill results in a large evaporative flux on the surface of the drip shield. Because the onset of seepage generally occurs when temperature on the drift wall drops below the boiling point, the onset of evaporation on the drip shield occurs earliest at the repository edge and then proceeds in towards the center of the repository.

**Drip-shield, backfill, and invert geometry**, in conjunction with the hydrologic properties of the backfill and invert, strongly influence liquid-phase flux inside the drift. The liquid flow draining down the backfill along the side of the drip shield, encounters a restricted region for flow. If all of the water trying to shed around the drift were wicked into the drift, then this flux into the drift would be contributed by the percolation flux in a region that is at least 2.75 m wide (which corresponds to the half-width of the drift). Because the value of the van Genuchten  $\alpha$  in the Overton sand backfill is smaller than in the fractures of the host rock, water draining down the side of the drip shield does not want to leave the backfill and enter the host rock; instead, all of it drains into the invert. If all of the percolation flux over a 2.75 m wide zone were focussed into the 0.69 m wide zone next to the drip shield, this would result in a “focussing” factor of four, which is comparable to the ratio which is observed between the liquid-phase flux next to the lower side of the drip shield and the host-rock percolation flux.

Relative humidity inside the drift is very dependent on whether water has seeped into the drift; the magnitude of the seepage is also important. For the no-backfill case, very little seepage occurs and this very low occurrence is largely confined to the high-flux case. Moreover, for the no-backfill case the magnitude of seepage flux is always less than the percolation flux in the host rock; whereas, for the backfill case the magnitude of seepage flux can be greater than the percolation flux in the host rock. An important EBS performance measure is how long *RH* on the WPs is low. *RH* reduction on WPs results from the following:

**Relative humidity reduction at the drift wall** (and in the host rock) decreases strongly with proximity to the edge of the repository. Significant reduction in drift-wall *RH* persists for 100 to 1000 yr (depending on proximity to the edge) for the mean and high infiltration-flux cases and for about 200 to 2000 yr for the low-flux case.

**Relative humidity reduction on the drip shield** is relatively insensitive to proximity to the edge of the repository. For the backfill case, *RH* on the drip shield eventually equilibrates with that in the host rock, thereby becoming nearly 100%. For the mean and high-flux cases this takes about 1000 to 2000 yr to occur and for the low-flux case this takes about 3000 to 6000 yr to occur. The end of the period of *RH* reduction on the drip shield corresponds to the time that seepage in the backfill has reached a steady-state condition. Because very little seepage occurs in the no-backfill case, *RH* reduction on the drip shield persists throughout the 1 million year simulation period.

**Relative humidity reduction on the WP** persists long after *RH* reduction on the drip shield has ceased. The persistence of *RH* reduction between the drip shield and WP arises because of the temperature difference between the WP and drip shield. Because the interval between the WP and drip shield is an open cavity, thermal radiation controls this temperature difference. The use of an insulator (such as granular backfill) in the gap between the WP and drip shield would result in a much larger temperature difference, which would result in a much larger reduction in *RH* between the drip shield and WP.

The maximum lateral extent of boiling (away from the drift wall) is a good indication of spatial extent of rock dryout (and *RH* reduction) around the emplacement drifts. The lateral extent of boiling is considerably greater for the low infiltration-flux case than for the mean or high-flux cases. For the median WP location in the backfill case, the maximum lateral extent of boiling is 8.4 m, 9.1 m, and 10.5 m for the high, mean, and low-flux cases, respectively. The hottest (and driest) WP location in the no-backfill low-flux case has a maximum lateral extent of boiling of 18 m; therefore, because the drifts are 81 m apart (Figure 4-1), a maximum of 44.4% of the repository horizon is driven to the boiling point. The hottest (and driest) WP location in both the mean and high-flux cases have a maximum lateral extent of boiling of 9.7 m; therefore, a maximum of 24% of the repository horizon is driven to the boiling point. For the range of infiltration flux considered in this AMR, the maximum percentage of the repository horizon (between drifts) that can be driven to the boiling point lies between 24% and 44.4% for the backfill case.

The no-backfill case has a smaller maximum extent of boiling than in the backfill case. This smaller extent of boiling results because of the differences in the assumptions about thermal loading. For the backfill case, the initial lineal power density is assumed to be 1.54 kW/m, whereas, for the no-backfill case, the initial lineal power density is assumed to be 1.45 kW/m. For the median WP location in the no-backfill case, the maximum lateral extent of boiling is 7.4 m, 8.3 m, and 9.3 m for the high-, mean-, and low-flux cases, respectively. The hottest (and driest) WP location has a maximum lateral extent of boiling of 8.9, 8.9, and 12.4 m for the high-, mean-, and low-flux cases, respectively. For the range of infiltration flux considered in this AMR, the maximum percentage of the repository horizon (between drifts) that can be driven to the boiling point lies between 22% and 30.6% for the no-backfill case.

There is much greater difference in dryout behavior (as evidenced by the maximum lateral extent of boiling and as evidenced by *RH* reduction) between the mean and low infiltration-flux cases than between the mean and high-flux cases. Therefore, if one considers defining a percolation-flux threshold wherein rock dryout becomes significantly limited by percolation, then this percolation-flux threshold would appear to be close to that arising from the mean infiltration-flux case. Increasing percolation fluxes above those of the mean infiltration-flux case has a diminishing effect on decreasing the extent of boiling (and rock dryout).

## **7.1 UNCERTAINTIES OF THE AMBIENT AND THERMALLY PERTURBED SYSTEM**

There are two primary categories of uncertainties: those associated with the EBS and those associated with the natural system. The natural-system uncertainties of primary interest concern the rock properties values in repository host rock and the infiltration flux. The key rock properties of concern are those hydrologic properties governing capillarity (i.e., matrix imbibition and capillary wicking in fractures) and thermal conductivity. In addition to parameter uncertainty, there are uncertainties in the ability to understand and predict unsaturated flow processes in fractured rock under ambient conditions and to coupled thermal-hydrologic-chemical and thermal-hydrologic-mechanical behavior. The EBS uncertainties of primary interest concern the hydrologic and thermal properties of the backfill and invert and WP-to-WP variability in heat-generation rate. An uncertainty that involves both the natural system and EBS concerns the distribution of seepage flux along the drifts. A discussion of the major uncertainties and how they are addressed in this AMR follows:

- Infiltration-flux uncertainty affects the local percolation flux, which affects the duration of dryout in the near-field host rock surrounding the drifts as well as rewetting the backfill and invert to ambient (humid) conditions. Dryout duration increases with decreasing percolation flux. This uncertainty is addressed by including the mean, high, and low infiltration-flux cases in this AMR. These three cases are judged to adequately span the range of uncertainty of the infiltration flux. The low infiltration-flux cases had a considerably longer dryout duration than either the mean or high infiltration-flux cases.
- Matrix-imbibition diffusivity and capillary wicking in fractures uncertainty affects the duration of dryout in the near-field host rock surrounding the emplacement drifts. The rewetting of the host rock is also strongly affected by the magnitude of the local percolation flux, which depends on the ambient infiltration flux. Dryout duration increases with decreasing local percolation flux and with decreasing capillarity of the matrix and fractures in the host rock. This AMR considered a wide range of infiltration flux, which, in effect, is equivalent to considering a wide range of matrix-imbibition diffusivity and a wide range of capillarity of fractures in the host rock.
- Host-rock thermal-conductivity uncertainty affects the peak temperatures on the drift wall, drip shield, and WPs. It also has a minor influence on the duration of dryout of the near-field host rock surrounding the drifts. This uncertainty was addressed in Section 6.11.1.4.

- Backfill capillarity uncertainty affects the magnitude of the capillary wicking of water into the emplacement drifts. Coarse granular materials have low capillarity that result in low (or minimal) wicking of water into the drift, whereas fine granular materials have high capillarity that result in a high wicking flux into the drift, resulting in rapid wetting of the backfill to ambient (humid) conditions. The Overton sand backfill analyzed in this AMR results in very strong capillary wicking of water into the drift. After boiling ceases at the drift wall, the strong capillarity of the Overton sand causes wicking to wet the backfill relatively quickly to ambient (humid) conditions; therefore, it appears to be unlikely that this wetting behavior could occur significantly more quickly than predicted in this AMR. On the other hand, if the capillarity were found to be weaker than represented in this AMR, it is possible that the wetting could proceed significantly more slowly than predicted in this AMR.

Seepage-flux-distribution uncertainty can potentially affect how long it takes to wet the backfill and invert. Because of the high capillarity of the Overton sand backfill, water is wicked relatively quickly into the drift immediately after the drift-wall temperature has fallen below the nominal boiling point. Consequently, water enters the drift (by wicking) whether or not water would have seeped in the drift as a result of gravity drainage. The certainty with which water wicks into the drift (by capillarity) obviates the uncertainty of whether it would have seeped into the drift (by gravity drainage). Moreover, the large wicking capacity of the Overton sand also serves to attenuate (along the axis of the drift) any differences in local liquid-phase flux into the drift. Therefore, for the EBS design analyzed in this AMR (with Overton sand backfill), the uncertainty of seepage-flux distribution is negligible.

## 7.2 DRIFT-SCALE FRACTURE HETEROGENEITY

A sensitivity study with a 3-D LDTH model with heterogeneous fracture properties was conducted to determine which thermohydrologic variables predicted by the MSTHM would change as a result of drift-scale fracture heterogeneity. This study indicated that the thermohydrologic conditions calculated by the MSTHM for the no-backfill case (Section 6.12) would not be changed during the boiling period by virtue of adding the influence of drift-scale fracture heterogeneity. These observations also indicate that temperatures calculated by the MSTHM would not be significantly changed during either the boiling or postboiling period by virtue of adding the influence of fracture heterogeneity.

The primary thermohydrologic quantities predicted by the MSTHM for the no-backfill case that would be affected by the inclusion of drift-scale heterogeneity are as follows:

*RH* on the drip shield would be increased during the postboiling period only for cases where seepage contacted the drip shield. Because *RH* during the postboiling period is already relatively high for the postboiling period of the no-backfill case, the magnitude of the increase of *RH* would be relatively small. The probability of occurrence of increased *RH* on the drip shield would also be small.

Evaporation rate on the drip shield would be increased during the postboiling only for cases where seepage contacted the drip shield. The magnitude of this increase in evaporation rate

increases with the magnitude of seepage onto the drip shield and decreases with time (as the heat output from waste packages decreases).

## 8. INPUTS AND REFERENCES

### 8.1 DOCUMENTS CITED

ASME (American Society of Mechanical Engineers) 1995. "Materials." Section II of 1995 *ASME Boiler and Pressure Vessel Code*. New York, New York: American Society of Mechanical Engineers. TIC: 245287.

Avallone, E.A. and Baumeister, T., III, ed. 1987. *Marks' Standard Handbook for Mechanical Engineers*. 9th Edition. New York, New York: McGraw-Hill. TIC: 206891.

Bear, J., 1972. *Dynamics of Fluids in Porous Media*. American Elsevier Pub. Co., N.Y. TIC: 217356.

Bolz, R. E. and Tuve, G. L. 1973. *CRC Handbook of Tables for Applied Engineering Science*. 2<sup>nd</sup> Edition. Boca Raton, Florida: CRC Press. TIC: 246862.

BSC (Bechtel SAIC Company) 2001. *Technical Work Plan for EBS Department Modeling FY01 Work Activities*. TWP-MGR-MD-000015. Las Vegas, Nevada: BSC. ACC: MOL.20010924.0050.

Buscheck, T.A.; Gansemer, J.; Delorenzo, T. H.; Nitao, J. J.; and Shaffer, R. J. 1998. *Multiscale Thermohydrologic Model Sensitivity Analysis*. UCRL-ID-131489. Livermore, California: Lawrence Livermore National Laboratory. ACC: MOL.19980901.0245.

Buscheck, T.A. and Nitao, J. J. 1994. *The Impact of Buoyant, Gas-Phase Flow and Heterogeneity on Thermo-Hydrological Behavior at Yucca Mountain*. (UCRL-JC-115351) Livermore, California: Lawrence Livermore National Laboratory. ACC: NNA.19940524.0012.

CRWMS M&O 1999a. (Civilian Radioactive Waste Management System Management and Operating Contractor). Not Used.

CRWMS M&O 1999b. *Engineered Barrier System Performance Modeling (WP# 12012383MX)*. Activity Evaluation, July 12, 1999. Las Vegas, Nevada: CRWMS M&O. ACC: MOL.19990719.0317.

CRWMS M&O 1999c. *Classification of the MGR Ex-Container System*. ANL-XCS-SE-000001 REV 00. Las Vegas, Nevada: CRWMS M&O. ACC: MOL.19990928.0221.

CRWMS M&O 1999d. *Enhanced Design Alternative (EDA) II Repository Estimated Waste Package Types and Quantities*. Input Transmittal EBS-SR-99325.T. Las Vegas, Nevada: CRWMS M&O. ACC: MOL.19991103.0236.

CRWMS M&O 1999e. *ANSYS Calculations in Support of Enhanced Design Alternatives*. B00000000-01717-0210-00074 REV 00. Las Vegas, Nevada: CRWMS M&O. ACC: MOL.19990218.0240.

CRWMS M&O 1999f. *Request for Repository Subsurface Design Information to Support TSPA-SR*. Input Transmittal PA-SSR-99218.Ta. Las Vegas, Nevada: CRWMS M&O. ACC: MOL.19990901.0312.

CRWMS M&O 1999g. (Not Used).

CRWMS M&O 2000a. *Input Files for Revision 00 of the Multiscale Thermohydrologic Model*. (24 Compact Discs) ANL-EBS-MD-000049 REV 00. Las Vegas, Nevada: CRWMS M&O. ACC: MOL.20000706.0396.

CRWMS M&O 2000b. *Thermal Tests Thermal-Hydrological Analyses/Model Report*. ANL-NBS-TH-000001 REV 00. Las Vegas, Nevada: CRWMS M&O. ACC: MOL.20000505.0231.

CRWMS M&O 2000c. *Development Plan for Multiscale Thermohydrologic Model*. Development Plan TDP-EBS-MD-000024 REV 02. Las Vegas, Nevada: CRWMS M&O. ACC: MOL.20000417.0666.

CRWMS M&O 2000d. *Subsurface Facility System Description Document*. SDD-SFS-SE-000001 REV 01. Las Vegas, Nevada: CRWMS M&O. ACC: MOL.20000807.0078.

CRWMS M&O 2000e. *Emplacement Drift System Description Document*. SDD-EDS-SE-000001 REV 01. Las Vegas, Nevada: CRWMS M&O. ACC: MOL.20000803.0348.

CRWMS M&O 2000f. Not Used.

CRWMS M&O 2000g. *Repository Subsurface Design Information to Support TSPA-SR*. Input Transmittal PA-SSR-99218.Tc. Las Vegas, Nevada: CRWMS M&O. ACC: MOL.20000424.0690.

CRWMS M&O 2000h. Not Used.

CRWMS M&O 2000i. *Invert Effective Thermal Conductivity Calculation*. CAL-WIS-TH-000004 REV 00. Las Vegas, Nevada: CRWMS M&O. ACC: MOL.20000317.0593.

CRWMS M&O 2000j. *Seepage Calibration Model and Seepage Testing Data Analysis/Model Report*. MDL-NBS-HS-000004 REV00. Las Vegas, Nevada: CRWMS M&O. ACC: MOL.19990721.0521.

CRWMS M&O 2000k. Not Used.

CRWMS M&O 2000l. *Technical Work Plan: Subsurface Process Modeling FY 01 Work Activities*. TWP-MGR-MD-000013 REV00. Las Vegas, Nevada: CRWMS M&O. ACC: MOL.20001117.0052.

CRWMS M&O 2001a. *Drift-Scale Coupled Processes (Drift-Scale Test and THC Seepage) Models Analysis/Models Report*. MDL-NBS-HS-000001 REV01. Las Vegas, Nevada: CRWMS M&O. ACC: MOL.20010314.0003.

CRWMS M&O 2001b. Effective Thermal Conductivity for Drift-Scale Models Used in the TSPA-SR. CAL-EBS-HS-000001 REV00. Las Vegas, Nevada: CRWMS M&O. ACC: MOL.20010301.0252.

CRWMS M&O 2001c. Abstraction of NFE Drift Thermodynamic Environment and Percolation Flux. ANL-EBS-HS-000003 REV 00 ICN 02. Las Vegas, Nevada: CRWMS M&O. ACC: MOL.20010221.0160.

CRWMS M&O 2001d *Water Distribution and Removal Model Analysis/Model Report*. ANL-EBS-MD-000032 REV01. Las Vegas, Nevada: CRWMS M&O. ACC: MOL.20010214.0031.

DOE (U.S. Department of Energy) 2000. *Quality Assurance Requirements and Description*. DOE/RW-0333P, Rev. 10. Washington, D.C.: U. S. Department of Energy, Office of Civilian Radioactive Waste Management. ACC: MOL.20000427.0422.

Hardin, E.L. 1998. *Near-Field/Altered-Zone Models Report*. UCRL-ID-129179. Livermore, California: Lawrence Livermore National Laboratory. ACC: MOL.19980630.0560.

Haukwa, C.; Wu, Y.S.; Hinds, J.J.; Zhang, W.; Ritcey, A.C.; Pan, L.H.; Simmons, A.M.; and Bodvarsson, G.S. 1998. *Results of Sensitivity Studies of Thermo-Hydrologic Behavior Conducted on Hydrologic Parameter Sets*. Milestone SP3CK5M4. Berkeley, California: Lawrence Berkeley National Laboratory. ACC: MOL.19980918.0001.

Incropera, F. P. and DeWitt, D. P. 1996. *Fundamentals of Heat and Mass Transfer*. 4<sup>th</sup> Edition. New York, New York: John Wiley & Sons. TIC: 243950.

Isaaks, E. H. and Srivastava, R. M. 1989. *Applied Geostatistics*. New York, New York: Oxford University Press. TIC: 200301.

Keenan, J.H.; Keyes, F.G.; Hill, P.G.; and Moore, J.G. 1969. *Steam Tables, Thermodynamic Properties of Water Including Vapor, Liquid, and Solid Phases*. New York, New York: John Wiley & Sons. TIC: 246766.

Kitanidis, P. K. 1997. *Introduction to Geostatistics: Applications in Hydrogeology*. New York, New York: Cambridge University Press. TIC: 236758.

Leverett, M.C. 1941. "Capillary Behavior in Porous Solids." *AIME Transactions, Petroleum Development and Technology, Tulsa Meeting, October 1940*. 142, 152-169. New York, New York: American Institute of Mining and Metallurgical Engineers. TIC: 240680.

Liu, H.H.; Doughty, C.; and Bodvarsson, G.S. 1998. "An Active Fracture Model for Unsaturated Flow and Transport in Fractured Rocks." *Water Resources Research*, 34, (10), 2633-2646. Washington, D.C.: American Geophysical Union. TIC: 243012.

LLNL (Lawrence Livermore National Laboratory) 2001. *Electronic Management of Information Checklist for Management of Electronic Information Related to AMR ANL-EBS-MD-000049, Revision 00, ICN 2 and Calculation Report of TH Calculations Supporting SSPA*. LLYMP0109015A. ACC: MOL.20010925.0133.

Luckner, L., M.Th. van Genuchten, and D.R. Nielsen, 1989. "A consistent set of parametric models for the two-phase flow of immiscible fluids in the subsurface." *Water Resour. Res.* 25, 2187-2193. TIC: 224845.

Meyer, C. A.; McClintock, R. B.; Silvestri, G. J.; and Spencer, R. C., Jr. 1967. *1967 ASME Steam Tables, Thermodynamic and Transport Properties of Steam*. 2<sup>nd</sup> Ed. pages 13, 14, 17, 22. New York, New York: American Society of Mechanical Engineers. TIC: 246889.

Nitao, J.J., 1998. *Reference Manual fo the NUFT Flow and Transport Code*, UCRL-MA-130651, Lawrence Livermore National Laboratory. TIC: 238072.

Nitao, J.J., 1997. "Models for the Distribution of Percolation at the Repository Level and Seepage into Drifts under Pre-Emplacement Conditions." Milestone report for the CRWMS Management and Operating Contractor, U.S. Department of Energy. (SPLB2M4). Livermore, CA: Lawrence Livermore National Laboratory. ACC: MOL.20000728.0489.

Nitao, J.J., 1993. "The NUFT Code for Modeling Nonisothermal, Multiphase, Multicomponent Flow and Transport in Porous Media." In proceedings from *EOS*. Washington, DC. American Geophysical Union. Supplement 73:31. (Also UCRL-JC-14769 Abs, Lawrence Livermore National Laboratory, Livermore, CA). TIC: 226135

NRC (U.S. Nuclear Regulatory Commission) 2000. *Issue Resolution Status Report Key Technical Issue: Thermal Effects on Flow*. Rev. 3. Washington, D.C.: U.S. Nuclear Regulatory Commission. ACC: MOL.20010201.0106.

Pruess, K., 1997. "On vaporizing water flow in hot sub-vertical rock fractures." *Transp. Porous Media*, 28, 335-372. TIC: 238922.

Schreiner, R.L. 2001. *Stand Alone DR-39 Package for ANL-EBS-MD-000049. Rev. 00, ICN 01, Multiscale Thermohydrologic Model*. Las Vegas, Nevada: Bechtel SAIC Company. ACC: MOL.20010910.0181.

Stroupe, E. P. 2000. "Approach to Implementing the Site Recommendation Design Baseline." Interoffice Correspondence from E. P. Stroupe (CRWMS M&O) to Dr. D. R. Wilkins, January 26, 2000, LV.RSO.EPS.1/00-004, with attachment. Las Vegas, Nevada: CRWMS M&O. ACC: MOL.20000214.0480.

Tsang, C.-F., J. Birkholzer, G. Li, and Y. Tsang, 1997. "Drift Scale Modeling: Progress in Studies of Seepage into a Drift." Milestone report. (SP331CM4). Berkeley, CA: Lawrence Berkeley National Laboratory. ACC: MOL.19971204.0420.

Vanmarcke, E., 1983. *Random Fields: Analysis and Synthesis*. Cambridge, Massachusetts: Massachusetts Institute of Technology. TIC: 249691

Wilder, D.G., ed. 1996. *Near-Field and Altered-Zone Environment Report*. Volume II. UCRL-LR-124998. Livermore, California: Lawrence Livermore National Laboratory. ACC: MOL.19961212.0121; MOL.19961212.0122.

Williams, D. 2001., *TEF/ENFE Meeting Summary and Agreement Matrix*. E-mail from D. Williams to G. Hellstrom, January 16, 2001, with attachments. ACC: MOL.20010306.0262.

YMP (Yucca Mountain Site Characterization Project) 1998. *Q-List*. YMP/90-55Q, Rev. 5. Las Vegas, Nevada: Yucca Mountain Site Characterization Office. ACC: MOL.19980513.0132.

## 8.2 PROCEDURES CITED

AP-2.21Q, Rev 1, BSCN 1, *Quality Determinations and Planning for Scientific, Engineering, and Regulatory Compliance Activities*. Washington, D.C.: DOE OCRWM ACC: MOL.20010212.0018.

AP-3.4Q, Rev 2, ICN 2, *Level 3 Change Control*. Washington, D.C.: DOE OCRWM. ACC: MOL.20010927.0066.

AP-3.10Q, Rev 2, ICN 5, *Analyses and Models*. Washington, D.C.: DOE OCRWM. ACC: MOL.20011126.0261.

AP-3.15Q, Rev 3, *Managing Technical Product Inputs*. Washington, D.C.: DOE OCRWM. ACC: MOL. 20010801.0318.

AP-SI.1Q, Rev 3, ICN 2, ECN 1, *Software Management*. Washington, D.C.: DOE OCRWM. ACC: MOL. 20011030.0598.

AP-SIII.3Q, Rev 1, ECN 1, *Submittal and Incorporation of Data to the Technical Data Management System*. Washington, D.C.: DOE OCRWM. ACC: MOL.20011025.0001.

QAP-2-3, Rev 10, BSCN 2, *Classification of Permanent Items*. Las Vegas, Nevada: CRWMS M&O. ACC: MOL.20010212.0283.

## 8.3 SOURCE DATA

GS000308311221.005. Analysis of Infiltration Uncertainty, ANL-NBS-HS-000027, Rev 00, ICN 00. Submittal Date: 05/25/2000.

LB990701233129.001. 3-D UZ Model Grids for Calculation of Flow Fields for PA for AMR U0000, "Development of Numerical Grids for UZ Flow and Transport Modeling". Submittal Date: 09/24/1999.

LB990861233129.001. Drift Scale Calibrated 1-D Property Set, FY99. Submittal Date: 08/06/1999.

LB990861233129.002. Drift Scale Calibrated 1-D Property Set, FY99. Submittal Date: 08/06/1999.

LB990861233129.003. Drift Scale Calibrated 1-D Property Set, FY99. Submittal Date: 08/06/1999.

LB991091233129.006. Thermal Properties and Tortuosity Factor for the UZ Model Layers for AMR U0090, "Analysis of Hydrologic Properties Data". Submittal Date: 10/15/1999.

LB991201233129.001. The Mountain-Scale Thermal-Hydrologic Model Simulations for AMR U0105, "Mountain-Scale Coupled Processes (TH) Models". Submittal Date: 03/11/2000.

LL970803004244.036. Data on Temperature of the Large Block Test (LBT). Submittal Date: 08/08/1997.

LL971204304244.047. Neutron Logging Activities at the Large Block Test (LBT). Submittal Date: 12/08/1997.

LL980919304244.075. Neutron Logging Activities at the Large Block Test (LBT). Submittal Date: 09/30/1998.

MO9911MWDEBSWD.000. EBS Water Drainage Model. Submittal Date: 11/29/1999.

MO0009SEPTIHMP.000. Backfill and Crushed Tuff Invert Hydrological Properties. Submittal Date: 09/13/2000. Submit to RPC. URN-0602.

SN9907T0872799.002. Effective Thermal Conductivity for Drift-Scale Models Used in TSPA-SR (Total System Performance Assessment-Site Recommendation). Submittal Date: 03/26/1998.

SNT05071897001.004. Total System Performance Assessment-Viability Assessment (TSPA-VA) Heat Loading Data. Submittal Date: 03/26/1998.

SN9907T0872799.002. Effective Thermal Conductivity for Drift Scale Models Used in TSPA-SR (Total System Performance Assessment – Site Recommendation). Submittal Date: 07/27/1999.

#### **8.4 SOFTWARE SOURCES**

Lawrence Livermore National Laboratory. 1999. *Software Code: NUFT V3.0s*. V3.0s. 10088-3.0s-00.

Lawrence Livermore National Laboratory. 2001. *Software Code: NUFT V3.0s*. V3.0s. 10088-3.0s-01

Lawrence Livermore National Laboratory. 2000. *Software Routine: CONVERTCOORDS V1.1.* V1.1. 10209-1.1-00.

Lawrence Livermore National Laboratory. 2000. *Software Routine: YMESH V1.53.* V1.53. 10172-1.53-00.

Lawrence Livermore National Laboratory. 2000. *Software Routine: RADPRO V3.22.* V3.22. Sun Ultra10. 10204-3.22-00.

Lawrence Livermore National Laboratory. 2000. *Software Routine: XTOOL V10.1.* V10.1. Sun Ultra10. 10208-10.1-00.

Lawrence Livermore National Laboratory. 1999. *Software Code: MSTHAC V6.2.* V6.2. Sun Ultra10. 10290-6.2-00.

Lawrence Livermore National Laboratory 2001. *Software Routine: MSTHAC V6.3.* Sun. 10419-6.3-00.

## 8.5 OUTPUT DATA

LL000113904242.089. TSPA-SR Lower Calculations. Submittal Date: 1/28/2000.

LL000114004242.090. TSPA-SR Mean Calculations. Submittal Date: 1/28/2000.

LL000114104242.091. TSPA-SR Upper Calculations. Submittal Date: 1/28/2000.

LL000509012312.002. TSPA-SR Multiscale TH Results (E0120) Lower Calculations Using Drift Scale Property Set. Submittal Date: 05/18/2000.

LL000509112312.003. TSPA-SR Multiscale TH Results (E0120) Mean Calculations Using Drift Scale Property Set. Submittal Date: 05/18/2000.

LL000509212312.004. TSPA-SR Multiscale TH Results (E0120) Upper Calculations Using Drift Scale Property Set. Submittal Date: 05/18/2000.

LL010802723122.019. Three-Dimensional Heterogeneous LDTH Model Calculations for ANL-EBS-MD-000049 Rev 00 ICN 2. 03/22/2001.

## 9. ATTACHMENTS

	No. of Pages
Attachment I: LIST OF ATTACHMENTS FOR ICN 01 .....	2
Attachment II: INPUT AND OUTPUT FILES .....	13

## ATTACHMENT I

The following are a list of the attachments that were a part of ICN 01 of this AMR. The DR-39 Stand Alone package (Schreiner 2001) has modified and superceded these attachments. Software management reports will supercede the stand alone package at a later date.

Attachment I:	QUALIFICATION OF MakeColumns.....	2
Attachment II:	QUALIFICATION OF Define_EBS_fineGrid .....	6
Attachment III:	QUALIFICATION OF ReadUnits .....	2
Attachment IV:	QUALIFICATION OF AddLayers AND addlay .....	2
Attachment V:	QUALIFICATION OF Heat_DDT AND heat_SMT.....	3
Attachment VI:	QUALIFICATION OF Xairtab .....	3
Attachment VII:	QUALIFICATION OF Infiltab .....	2
Attachment VIII	QUALIFICATION OF Rock_sun .....	2
Attachment IX:	QUALIFICATION OF SMT_surf_bc AND SMT_bot_bc .....	4
Attachment X:	QUALIFICATION OF Bound .....	2
Attachment XI:	QUALIFICATION OF COREY ROUTINES.....	3
Attachment XII:	QUALIFICATION OF HeatgenAge .....	2
Attachment XIII:	QUALIFICATION OF Chim_Surf_TP AND Chim_wt_TP .....	2
Attachment XIV:	QUALIFICATION OF ColumnInfiltration.....	3
Attachment XV:	QUALIFICATION OF Cover .....	3
Attachment XVI:	QUALIFICATION OF Rme6.....	3
Attachment XVII:	NORMALIZED INFILTRATION RATES.....	4

Attachment XIX:	QUALIFICATION OF SplitEXT.....	7
Attachment XX:	DEVELOPMENT OF LINEAR EXTRAPOLATION FORMULA .....	2

## ATTACHMENT II INPUT AND OUTPUT FILE DESCRIPTION

### II.1 Input and Output Files Used in Rev 00

The input and output files that were used in Rev. 00 of this AMR (the backfill case) are contained on 24 CD's that have been entered in to the records system. These files are identified in Section 8 of this AMR as CRWMS M&O 2000a, *Input Files for Revision 00 of the Multiscale Thermohydrologic Model*. This reference is the document itself, and Document Control will issue it with or without the CDs, at the requesters preference. The CDs (and files on them) are not Attachments, but are stand-alone files with the same accession number.

### II.2 Input and Output Files Used in Rev 00 ICN 01

The list of input and output files for Rev 00 ICN 01 (the no-backfill case) was included as Attachment XVIII to that document, and the files themselves were included in three DTNs. In ICN 02, the file list appears below in this section (II.2), and the DTN citation is also included there.

The list of input and output files are for the following software codes and routines: RADPRO, XTOOL, MSTHAC, YMESH, and CONVERTCOORDS. These files are contained in DTNs LL000509112312.003, LL000509012312.002 and LL000509212312.004.

The input files for RADPRO v3.22 are DDT60-03v.radin, l4c3-DDT60-03v.radin, DDT60-03pbf.radin, l4c3-DDT60-03pbf.in and l4c3-DDT60-03bff.in and the output files are DDT60-03v.radout, DDT60-03pbf.radout and DDT60-03.radout (CRWMS M&O 2000a).

The input files for XTOOL v10.1 are the NUFT output files listed on Table 3-6 through Table 3-9 (CRWMS M&O 2000a). There are not output files since XTOOL is a graphical presentation routine.

The input files for MSTHAC v6.2 and v6.3 are the results from the NUFT output files listed on Table 3-6 through Table 3-9 and the outfiles are TSPA\_SR\_mean.ext, TSPA\_SR\_lower.ext and TSPA\_SR\_upper.ext (CRWMS M&O 2000a).

The input file for YMESH v1.53 is LBL99-YMESH and the output file is column.dat (CRWMS M&O 2000a).

The input files for CONVERTCOORDS v1.1 are ym\*.dat, monsoon\*.dat and glacial\*.dat and the output files are ym\*.NV, monsoon\*.NV and glacial\*.NV (CRWMS M&O 2000a).

## II.3 Input and Output Files Used in Rev 00 ICN 02

The list of input and output files for Rev 00 ICN 02 (the sensitivity study using the 3-D heterogeneous LDTH submodel) is included below in this section (II.3). The files themselves were included in DTNs cited below.

### II.3.1 Input Files for the Three-Dimensional Heterogeneous LDTH Submodel [lower level header]

Tables II-1 through II-10 list the input files used in the eight heterogeneous property cases and two homogeneous property cases. All of these files are found in DTN LL010802723122.019. The results are described in Section 6.14 of this AMR

Table II-1. NUFT Input Files for 3-D Heterogeneous LDTH Submodel Stochastic Realization A-56, which uses 56 MTU/acre

File Type	Filename
NUFT input (.in) file	I4c4-LDTH56-1Dds_mc-mi-40-02.in I4c4-LDTH56-1Dds_mc-mi-40-02b.in I4c4-LDTH56-1Dds_mc-mi-40-02c.in I4c4-LDTH56-1Dds_mc-mi-40-02dd.in I4c4-LDTH56-1Dds_mc-mi-40-02ee.in I4c4-LDTH56-1Dds_mc-mi-40-02ff.in
Ztab restart file from initialization run	I4c3-LMTH56-i.m.ztable I4c3-LMTH56-i.f.ztable
Restart file from previous run	I4c4-LDTH56-1Dds_mc-mi-40-02.re0 I4c4-LDTH56-1Dds_mc-mi-40-02b.re0 I4c4-LDTH56-1Dds_mc-mi-40-02c.re0 I4c4-LDTH56-1Dds_mc-mi-40-02dd.re1 I4c4-LDTH56-1Dds_mc-mi-40-02ee.re0
Rock properties file	dkm_afc-1Dds-mc-mi-00
EBS properties file	dkm-afc-EBS_Rev20a dkm-afc-EBS_Rev21
Thermal conductivity "modification" file	modprop_dr-20
Heat generation file	LDTH-SDT-0.3Qheat-50y_vent-20-3D
Solver control file	vtough.pkg
Run control file	run_control_param_LDTH-v01, run_control_param_LDTH-v10, etc
Time steps for ext file output	output.times-56-40

Table II-2. NUFT Input Files for 3-D Heterogeneous LDTH Submodel Stochastic Realization A-34, which uses 34 MTU/acre

File Type	Filename
NUFT input (.in) file	l4c4-LDTH34-1Dds_mc-mi-40-02.in l4c4-LDTH34-1Dds_mc-mi-40-02b.in l4c4-LDTH34-1Dds_mc-mi-40-02c.in l4c4-LDTH34-1Dds_mc-mi-40-02d.in l4c4-LDTH34-1Dds_mc-mi-40-02e.in l4c4-LDTH34-1Dds_mc-mi-40-02f.in l4c4-LDTH34-1Dds_mc-mi-40-02g.in l4c4-LDTH34-1Dds_mc-mi-40-02h.in l4c4-LDTH34-1Dds_mc-mi-40-02i.in l4c4-LDTH34-1Dds_mc-mi-40-02j.in l4c4-LDTH34-1Dds_mc-mi-40-02k.in l4c4-LDTH34-1Dds_mc-mi-40-02l.in l4c4-LDTH34-1Dds_mc-mi-40-02m.in
Ztab restart file from initialization run	l4c3-LMTH56-i.m.ztable l4c3-LMTH56-i.f.ztable
Restart file from previous run	l4c4-LDTH34-1Dds_mc-mi-40-02.re1 l4c4-LDTH34-1Dds_mc-mi-40-02b.re0 l4c4-LDTH34-1Dds_mc-mi-40-02c.re1 l4c4-LDTH34-1Dds_mc-mi-40-02d.re0 l4c4-LDTH34-1Dds_mc-mi-40-02e.re0 l4c4-LDTH34-1Dds_mc-mi-40-02f.re1 l4c4-LDTH34-1Dds_mc-mi-40-02g.re0 l4c4-LDTH34-1Dds_mc-mi-40-02h.re0 l4c4-LDTH34-1Dds_mc-mi-40-02i.re0 l4c4-LDTH34-1Dds_mc-mi-40-02j.re0 l4c4-LDTH34-1Dds_mc-mi-40-02k.re1 l4c4-LDTH34-1Dds_mc-mi-40-02l.re1
Rock properties file	dkm_afc-1Dds-mc-mi-00
EBS properties file	dkm-afc-EBS_Rev20a dkm-afc-EBS_Rev21
Thermal conductivity "modification" file	modprop_dr-20
Heat generation file	LDTH-SDT-0.3Qheat-50y_vent-20-3D
Solver control file	vtough.pkg
Run control file	run_control_param_LDTH-v01, run_control_param_LDTH-v10, etc
Time steps for ext file output	output.times-56-40

Table II-3. NUFT Input Files for 3-D Heterogeneous LDTH Submodel Stochastic Realization B-56, which uses 56 MTU/acre

File Type	Filename
NUFT input (.in) file	I4c4-LDTH56-1Dds_mc-mi-40-12.in I4c4-LDTH56-1Dds_mc-mi-40-12b.in I4c4-LDTH56-1Dds_mc-mi-40-12c.in I4c4-LDTH56-1Dds_mc-mi-40-12d.in I4c4-LDTH56-1Dds_mc-mi-40-12e.in I4c4-LDTH56-1Dds_mc-mi-40-12f.in
Ztab restart file from initialization run	I4c3-LMTH56-i.m.ztable I4c3-LMTH56-i.f.ztable
Restart file from previous run	I4c4-LDTH56-1Dds_mc-mi-40-12.re1 I4c4-LDTH56-1Dds_mc-mi-40-12b.re0 I4c4-LDTH56-1Dds_mc-mi-40-12c.re1 I4c4-LDTH56-1Dds_mc-mi-40-12d.re1 I4c4-LDTH56-1Dds_mc-mi-40-12e.re1
Rock properties file	dkm_afc-1Dds-mc-mi-00
EBS properties file	dkm-afc-EBS_Rev20a dkm-afc-EBS_Rev21
Thermal conductivity "modification" file	modprop_dr-20
Heat generation file	LDTH-SDT-0.3Qheat-50y_vent-20-3D
Solver control file	vtough.pkg
Run control file	run_control_param_LDTH-v01, run_control_param_LDTH-v10, etc
Time steps for ext file output	output.times-56-40

Table II-4. NUFT Input Files for 3-D Heterogeneous LDTH Submodel Stochastic Realization B-34, which uses 34 MTU/acre

<b>34 MTU/acre; Stochastic Realization B-34</b>	
<b>File Type</b>	<b>Filename</b>
NUFT input (.in) file	I4c4-LDTH34-1Dds_mc-mi-40-12.in I4c4-LDTH34-1Dds_mc-mi-40-12b.in I4c4-LDTH34-1Dds_mc-mi-40-12c.in I4c4-LDTH34-1Dds_mc-mi-40-12d.in I4c4-LDTH34-1Dds_mc-mi-40-12e.in I4c4-LDTH34-1Dds_mc-mi-40-12f.in I4c4-LDTH34-1Dds_mc-mi-40-12g.in I4c4-LDTH34-1Dds_mc-mi-40-12h.in
Ztab restart file from initialization run	I4c3-LMTH56-i.m.ztable I4c3-LMTH56-i.f.ztable
Restart file from previous run	I4c4-LDTH34-1Dds_mc-mi-40-02.re0 I4c4-LDTH34-1Dds_mc-mi-40-02b.re0 I4c4-LDTH34-1Dds_mc-mi-40-02c.re0 I4c4-LDTH34-1Dds_mc-mi-40-02d.re1 I4c4-LDTH34-1Dds_mc-mi-40-02e.re0 I4c4-LDTH34-1Dds_mc-mi-40-02f.re0 I4c4-LDTH34-1Dds_mc-mi-40-02g.re0
Rock properties file	dkm_afc-1Dds-mc-mi-00
EBS properties file	dkm-afc-EBS_Rev20a dkm-afc-EBS_Rev21
Thermal conductivity "modification" file	modprop_dr-20
Heat generation file	LDTH-SDT-0.3Qheat-50y_vent-20-3D
Solver control file	vtough.pkg
Run control file	run_control_param_LDTH-v01, run_control_param_LDTH-v10, etc
Time steps for ext file output	output.times-56-40

Table II-5. NUFT Input Files for 3-D Heterogeneous LDTH Submodel Stochastic Realization C-56, which uses 56 MTU/acre

<b>56 MTU/acre; Stochastic Realization C-56</b>	
<b>File Type</b>	<b>Filename</b>
NUFT input (.in) file	I4c4-LDTH56-1Dds_mc-mi-40-20.in I4c4-LDTH56-1Dds_mc-mi-40-20b.in
Ztab restart file from initialization run	I4c3-LMTH56-i.m.ztable I4c3-LMTH56-i.f.ztable
Restart file from previous run	I4c4-LDTH56-1Dds_mc-mi-40-20.re1
Rock properties file	dkm_afc-1Dds-mc-mi-00
EBS properties file	dkm-afc-EBS_Rev20a dkm-afc-EBS_Rev21
Thermal conductivity "modification" file	modprop_dr-20
Heat generation file	LDTH-SDT-0.3Qheat-50y_vent-20-3D
Solver control file	vtough.pkg
Run control file	run_control_param_LDTH-v01, run_control_param_LDTH-v10, etc
Time steps for ext file output	output.times-56-40

Table II-6. NUFT Input Files for 3-D Heterogeneous LDTH Submodel Stochastic Realization C-34, which uses 34 MTU/acre

<b>34 MTU/acre; Stochastic Realization C-34</b>	
<b>File Type</b>	<b>Filename</b>
NUFT input (.in) file	I4c4-LDTH34-1Dds_mc-mi-40-20.in I4c4-LDTH34-1Dds_mc-mi-40-20b.in
Ztab restart file from initialization run	I4c3-LMTH56-i.m.ztable I4c3-LMTH56-i.f.ztable
Restart file from previous run	I4c4-LDTH34-1Dds_mc-mi-40-20.re1 I4c4-LDTH34-1Dds_mc-mi-40-20b.re1 I4c4-LDTH34-1Dds_mc-mi-40-20c.re0
Rock properties file	dkm_afc-1Dds-mc-mi-00
EBS properties file	dkm-afc-EBS_Rev20a dkm-afc-EBS_Rev21
Thermal conductivity "modification" file	modprop_dr-20
Heat generation file	LDTH-SDT-0.3Qheat-50y_vent-20-3D
Solver control file	vtough.pkg
Run control file	run_control_param_LDTH-v01, run_control_param_LDTH-v10, etc
Time steps for ext file output	output.times-56-40

Table II-7. NUFT Input Files for 3-D Heterogeneous LDTH Submodel Stochastic Realization D-56, which uses 56 MTU/acre

<b>56 MTU/acre; Stochastic Realization D-56</b>	
<b>File Type</b>	<b>Filename</b>
NUFT input (.in) file	I4c4-LDTH56-1Dds_mc-mi-40-01.in I4c4-LDTH56-1Dds_mc-mi-40-01b.in I4c4-LDTH56-1Dds_mc-mi-40-01c.in I4c4-LDTH56-1Dds_mc-mi-40-01d.in I4c4-LDTH56-1Dds_mc-mi-40-01e.in I4c4-LDTH56-1Dds_mc-mi-40-01f.in
Ztab restart file from initialization run	I4c3-LMTH56-i.m.ztable I4c3-LMTH56-i.f.ztable
Restart file from previous run	I4c4-LDTH56-1Dds_mc-mi-40-01.re1 I4c4-LDTH56-1Dds_mc-mi-40-01b.re0 I4c4-LDTH56-1Dds_mc-mi-40-01c.re0 I4c4-LDTH56-1Dds_mc-mi-40-01d.re1 I4c4-LDTH56-1Dds_mc-mi-40-01e.re0
Rock properties file	dkm_afc-1Dds-mc-mi-00
EBS properties file	dkm-afc-EBS_Rev20a dkm-afc-EBS_Rev21
Thermal conductivity "modification" file	modprop_dr-20
Heat generation file	LDTH-SDT-0.3Qheat-50y_vent-20-3D
Solver control file	vtough.pkg
Run control file	run_control_param_LDTH-v01, run_control_param_LDTH-v10, etc
Time steps for ext file output	output.times-56-40

Table II-8. NUFT Input Files for 3-D Heterogeneous LDTH Submodel Stochastic Realization D-34, which uses 34 MTU/acre

<b>34 MTU/acre; Stochastic Realization D-34</b>	
<b>File Type</b>	<b>Filename</b>
NUFT input (.in) file	I4c4-LDTH34-1Dds_mc-mi-40-01.in I4c4-LDTH34-1Dds_mc-mi-40-01b.in I4c4-LDTH34-1Dds_mc-mi-40-01c.in I4c4-LDTH34-1Dds_mc-mi-40-01d.in I4c4-LDTH34-1Dds_mc-mi-40-01e.in I4c4-LDTH34-1Dds_mc-mi-40-01f.in I4c4-LDTH34-1Dds_mc-mi-40-01g.in I4c4-LDTH34-1Dds_mc-mi-40-01h.in I4c4-LDTH34-1Dds_mc-mi-40-01i.in
Ztab restart file from initialization run	I4c3-LMTH56-i.m.ztable I4c3-LMTH56-i.f.ztable
Restart file from previous run	I4c4-LDTH34-1Dds_mc-mi-40-01.re1 I4c4-LDTH34-1Dds_mc-mi-40-01b.re1 I4c4-LDTH34-1Dds_mc-mi-40-01c.re0 I4c4-LDTH34-1Dds_mc-mi-40-01d.re1 I4c4-LDTH34-1Dds_mc-mi-40-01e.re0 I4c4-LDTH34-1Dds_mc-mi-40-01f.re0 I4c4-LDTH34-1Dds_mc-mi-40-01g.re1 I4c4-LDTH34-1Dds_mc-mi-40-01h.re1
Rock properties file	dkm_afc-1Dds-mc-mi-00
EBS properties file	dkm-afc-EBS_Rev20a dkm-afc-EBS_Rev21
Thermal conductivity "modification" file	modprop_dr-20
Heat generation file	LDTH-SDT-0.3Qheat-50y_vent-20-3D
Solver control file	vtough.pkg
Run control file	run_control_param_LDTH-v01, run_control_param_LDTH-v10, etc
Time steps for ext file output	output.times-56-40

Table II-9. NUFT Input Files for the 56 MTU/acre 2-D Homogeneous LDTH Submodel Case

<b>56 MTU/acre; Homogeneous 2-D Case</b>	
<b>File Type</b>	<b>Filename</b>
NUFT input (.in) file	I4c4-LDTH56-1Dds_mc-mi-40.in
Ztab restart file from initialization run	I4c3-LMTH56-i.m.ztable I4c3-LMTH56-i.f.ztable
Rock properties file	dkm_afc-1Dds-mc-mi-00
EBS properties file	dkm-afc-EBS_Rev20a
Thermal conductivity "modification" file	modprop_dr-20
Heat generation file	LDTH-SDT-0.3Qheat-50y_vent-20
Solver control file	vtough.pkg
Run control file	run_control_param_LDTH-v01
Time steps for ext file output	output.times-56-40

Table II-10. NUFT Input Files for the 34 MTU/acre 2-D Homogeneous LDTH Submodel Case

<b>34 MTU/acre; Homogeneous 2-D Case</b>	
<b>File Type</b>	<b>Filename</b>
NUFT input (.in) file	I4c4-LDTH34-1Dds_mc-mi-40.in
Ztab restart file from initialization run	I4c3-LMTH56-i.m.ztable I4c3-LMTH56-i.f.ztable
Rock properties file	dkm_afc-1Dds-mc-mi-00
EBS properties file	dkm-afc-EBS_Rev20a
Thermal conductivity "modification" file	modprop_dr-20
Heat generation file	LDTH-SDT-0.3Qheat-50y_vent-20
Solver control file	vtough.pkg
Run control file	run_control_param_LDTH-v01
Time steps for ext file output	output.times-56-40

### II.3.2 Output Files for the Three Dimensional Heterogeneous LDTH Submodel

Tables II-11 through II-20 list the input files used in the eight heterogeneous property cases and two homogeneous property cases. All of these files are found in DTN LL01009812342.004. The results are described in Section 6.14 of this AMR.

Table II-11. NUFT Output Files for 3-D Heterogeneous LDTH Submodel Stochastic Realization A-56, which uses 56 MTU/acre

<b>56 MTU/acre; Stochastic Realization A-56</b>	
<b>File Type</b>	<b>Filename</b>
NUFT output (.in) file for matrix	I4c4-LDTH56-1Dds_mc-mi-40-02.m.EBS.ext I4c4-LDTH56-1Dds_mc-mi-40-02b.m.EBS.ext I4c4-LDTH56-1Dds_mc-mi-40-02c.m.EBS.ext I4c4-LDTH56-1Dds_mc-mi-40-02dd.m.EBS.ext I4c4-LDTH56-1Dds_mc-mi-40-02ee.m.EBS.ext I4c4-LDTH56-1Dds_mc-mi-40-02ff.m.EBS.ext
NUFT output (.in) file for fracture	I4c4-LDTH56-1Dds_mc-mi-40-02.f.EBS.ext I4c4-LDTH56-1Dds_mc-mi-40-02b.f.EBS.ext I4c4-LDTH56-1Dds_mc-mi-40-02c.f.EBS.ext I4c4-LDTH56-1Dds_mc-mi-40-02dd.f.EBS.ext I4c4-LDTH56-1Dds_mc-mi-40-02ee.f.EBS.ext I4c4-LDTH56-1Dds_mc-mi-40-02ff.f.EBS.ext

Table II-12. NUFT Output Files for 3-D Heterogeneous LDTH Submodel Stochastic Realization A-34, which uses 34 MTU/acre

<b>34 MTU/acre; Stochastic Realization A-34</b>	
<b>File Type</b>	<b>Filename</b>
NUFT output (.in) file for matrix	l4c4-LDTH34-1Dds_mc-mi-40-02.m.EBS.ext l4c4-LDTH34-1Dds_mc-mi-40-02b.m.EBS.ext l4c4-LDTH34-1Dds_mc-mi-40-02c.m.EBS.ext l4c4-LDTH34-1Dds_mc-mi-40-02d.m.EBS.ext l4c4-LDTH34-1Dds_mc-mi-40-02e.m.EBS.ext l4c4-LDTH34-1Dds_mc-mi-40-02f.m.EBS.ext l4c4-LDTH34-1Dds_mc-mi-40-02g.m.EBS.ext l4c4-LDTH34-1Dds_mc-mi-40-02h.m.EBS.ext l4c4-LDTH34-1Dds_mc-mi-40-02i.m.EBS.ext l4c4-LDTH34-1Dds_mc-mi-40-02j.m.EBS.ext l4c4-LDTH34-1Dds_mc-mi-40-02k.m.EBS.ext l4c4-LDTH34-1Dds_mc-mi-40-02l.m.EBS.ext l4c4-LDTH34-1Dds_mc-mi-40-02m.m.EBS.ext
NUFT output (.in) file for fracture	l4c4-LDTH34-1Dds_mc-mi-40-02.f.EBS.ext l4c4-LDTH34-1Dds_mc-mi-40-02b.f.EBS.ext l4c4-LDTH34-1Dds_mc-mi-40-02c.f.EBS.ext l4c4-LDTH34-1Dds_mc-mi-40-02d.f.EBS.ext l4c4-LDTH34-1Dds_mc-mi-40-02e.f.EBS.ext l4c4-LDTH34-1Dds_mc-mi-40-02f.f.EBS.ext l4c4-LDTH34-1Dds_mc-mi-40-02g.f.EBS.ext l4c4-LDTH34-1Dds_mc-mi-40-02h.f.EBS.ext l4c4-LDTH34-1Dds_mc-mi-40-02i.f.EBS.ext l4c4-LDTH34-1Dds_mc-mi-40-02j.f.EBS.ext l4c4-LDTH34-1Dds_mc-mi-40-02k.f.EBS.ext l4c4-LDTH34-1Dds_mc-mi-40-02l.f.EBS.ext l4c4-LDTH34-1Dds_mc-mi-40-02m.f.EBS.ext

Table II-13. NUFT Output Files for 3-D Heterogeneous LDTH Submodel Stochastic Realization B-56, which uses 56 MTU/acre

<b>56 MTU/acre; Stochastic Realization B-56</b>	
<b>File Type</b>	<b>Filename</b>
NUFT output (.in) file for matrix	l4c4-LDTH56-1Dds_mc-mi-40-12.m.EBS.ext l4c4-LDTH56-1Dds_mc-mi-40-12b.m.EBS.ext l4c4-LDTH56-1Dds_mc-mi-40-12c.m.EBS.ext l4c4-LDTH56-1Dds_mc-mi-40-12d.m.EBS.ext l4c4-LDTH56-1Dds_mc-mi-40-12e.m.EBS.ext l4c4-LDTH56-1Dds_mc-mi-40-12f.m.EBS.ext
NUFT output (.in) file for fracture	l4c4-LDTH56-1Dds_mc-mi-40-12.f.EBS.ext l4c4-LDTH56-1Dds_mc-mi-40-12b.f.EBS.ext l4c4-LDTH56-1Dds_mc-mi-40-12c.f.EBS.ext l4c4-LDTH56-1Dds_mc-mi-40-12d.f.EBS.ext l4c4-LDTH56-1Dds_mc-mi-40-12e.f.EBS.ext l4c4-LDTH56-1Dds_mc-mi-40-12f.f.EBS.ext

Table II-14. NUFT Output Files for 3-D Heterogeneous LDTH Submodel Stochastic Realization B-34, which uses 34 MTU/acre

<b>34 MTU/acre; Stochastic Realization B-34</b>	
<b>File Type</b>	<b>Filename</b>
NUFT output (.in) file for matrix	I4c4-LDTH34-1Dds_mc-mi-40-12.m.EBS.ext I4c4-LDTH34-1Dds_mc-mi-40-12b.m.EBS.ext I4c4-LDTH34-1Dds_mc-mi-40-12c.m.EBS.ext I4c4-LDTH34-1Dds_mc-mi-40-12d.m.EBS.ext I4c4-LDTH34-1Dds_mc-mi-40-12e.m.EBS.ext I4c4-LDTH34-1Dds_mc-mi-40-12f.m.EBS.ext I4c4-LDTH34-1Dds_mc-mi-40-12g.m.EBS.ext I4c4-LDTH34-1Dds_mc-mi-40-12h.m.EBS.ext
NUFT output (.in) file for fracture	I4c4-LDTH34-1Dds_mc-mi-40-12.f.EBS.ext I4c4-LDTH34-1Dds_mc-mi-40-12b.f.EBS.ext I4c4-LDTH34-1Dds_mc-mi-40-12c.f.EBS.ext I4c4-LDTH34-1Dds_mc-mi-40-12d.f.EBS.ext I4c4-LDTH34-1Dds_mc-mi-40-12e.f.EBS.ext I4c4-LDTH34-1Dds_mc-mi-40-12f.f.EBS.ext I4c4-LDTH34-1Dds_mc-mi-40-12g.f.EBS.ext I4c4-LDTH34-1Dds_mc-mi-40-12h.f.EBS.ext

Table II-15. NUFT Output Files for 3-D Heterogeneous LDTH Submodel Stochastic Realization C-56, which uses 56 MTU/acre

<b>56 MTU/acre; Stochastic Realization C-56</b>	
<b>File Type</b>	<b>Filename</b>
NUFT output (.in) file for matrix	I4c4-LDTH56-1Dds_mc-mi-40-20.m.EBS.ext I4c4-LDTH56-1Dds_mc-mi-40-20b.m.EBS.ext
NUFT output (.in) file for fracture	I4c4-LDTH56-1Dds_mc-mi-40-20.f.EBS.ext I4c4-LDTH56-1Dds_mc-mi-40-20b.f.EBS.ext

Table II-16. NUFT Output Files for 3-D Heterogeneous LDTH Submodel Stochastic Realization C-34, which uses 34 MTU/acre

<b>34 MTU/acre; Stochastic Realization C-34</b>	
<b>File Type</b>	<b>Filename</b>
NUFT output (.in) file for matrix	I4c4-LDTH34-1Dds_mc-mi-40-20.m.EBS.ext I4c4-LDTH34-1Dds_mc-mi-40-20b.m.EBS.ext
NUFT output (.in) file for fracture	I4c4-LDTH34-1Dds_mc-mi-40-20.f.EBS.ext I4c4-LDTH34-1Dds_mc-mi-40-20b.f.EBS.ext

Table II-17. NUFT Output Files for 3-D Heterogeneous LDTH Submodel Stochastic Realization D-56, which uses 56 MTU/acre

<b>56 MTU/acre; Stochastic Realization D-56</b>	
<b>File Type</b>	<b>Filename</b>
NUFT output (.in) file for matrix	I4c4-LDTH56-1Dds_mc-mi-40-01.m.EBS.ext I4c4-LDTH56-1Dds_mc-mi-40-01b.m.EBS.ext I4c4-LDTH56-1Dds_mc-mi-40-01c.m.EBS.ext I4c4-LDTH56-1Dds_mc-mi-40-01d.m.EBS.ext I4c4-LDTH56-1Dds_mc-mi-40-01e.m.EBS.ext I4c4-LDTH56-1Dds_mc-mi-40-01f.m.EBS.ext
NUFT output (.in) file for fracture	I4c4-LDTH56-1Dds_mc-mi-40-01.f.EBS.ext I4c4-LDTH56-1Dds_mc-mi-40-01b.f.EBS.ext I4c4-LDTH56-1Dds_mc-mi-40-01c.f.EBS.ext I4c4-LDTH56-1Dds_mc-mi-40-01d.f.EBS.ext I4c4-LDTH56-1Dds_mc-mi-40-01e.f.EBS.ext I4c4-LDTH56-1Dds_mc-mi-40-01f.f.EBS.ext

Table II-18. NUFT Output Files for 3-D Heterogeneous LDTH Submodel Stochastic Realization D-34, which uses 34 MTU/acre

<b>34 MTU/acre; Stochastic Realization D-34</b>	
<b>File Type</b>	<b>Filename</b>
NUFT output (.in) file for matrix	I4c4-LDTH34-1Dds_mc-mi-40-01.m.EBS.ext I4c4-LDTH34-1Dds_mc-mi-40-01b.m.EBS.ext I4c4-LDTH34-1Dds_mc-mi-40-01c.m.EBS.ext I4c4-LDTH34-1Dds_mc-mi-40-01d.m.EBS.ext I4c4-LDTH34-1Dds_mc-mi-40-01e.m.EBS.ext I4c4-LDTH34-1Dds_mc-mi-40-01f.m.EBS.ext I4c4-LDTH34-1Dds_mc-mi-40-01g.m.EBS.ext I4c4-LDTH34-1Dds_mc-mi-40-01h.m.EBS.ext I4c4-LDTH34-1Dds_mc-mi-40-01i.m.EBS.ext
NUFT output (.in) file for fracture	I4c4-LDTH34-1Dds_mc-mi-40-01.f.EBS.ext I4c4-LDTH34-1Dds_mc-mi-40-01b.f.EBS.ext I4c4-LDTH34-1Dds_mc-mi-40-01c.f.EBS.ext I4c4-LDTH34-1Dds_mc-mi-40-01d.f.EBS.ext I4c4-LDTH34-1Dds_mc-mi-40-01e.f.EBS.ext I4c4-LDTH34-1Dds_mc-mi-40-01f.f.EBS.ext I4c4-LDTH34-1Dds_mc-mi-40-01g.f.EBS.ext I4c4-LDTH34-1Dds_mc-mi-40-01h.f.EBS.ext I4c4-LDTH34-1Dds_mc-mi-40-01i.f.EBS.ext

Table II-19. NUFT Output Files for the 56 MTU/acre 2-D Homogeneous LDTH Submodel Case

<b>56 MTU/acre; Homogeneous 2-D Case</b>	
<b>File Type</b>	<b>Filename</b>
NUFT output (.in) file for matrix	I4c4-LDTH56-1Dds_mc-mi-40.m.EBS.ext
NUFT output (.in) file for fracture	I4c4-LDTH56-1Dds_mc-mi-40.f.EBS.ext

Table II-20. NUFT Output Files for the 34 MTU/acre 2-D Homogeneous LDTH Submodel Case

<b>34 MTU/acre; Homogeneous 2-D Case</b>	
<b>File Type</b>	<b>Filename</b>
NUFT output (.in) file for matrix	I4c4-LDTH34-1Dds_mc-mi-40.m.EBS.ext
NUFT output (.in) file for fracture	I4c4-LDTH34-1Dds_mc-mi-40.f.EBS.ext